FEUP Universidade do Porto
Faculdade de Engenharia

ADVANCED METHODOLOGIES FOR THE FATIGUE ANALYSIS OF REPRESENTATIVE DETAILS OF METALLIC BRIDGES

António Luís Lima da Silva

2015

Thesis presented to the Faculty of Engineering of the University of Porto
for the Doctor Degree in Mechanical Engineering

Supervisors
António Augusto Fernandes *Full Professor*
Abílio Manuel Pinho de Jesus *Assistant Professor*

To my wife Andreia

and my daughter Áurea.

ACKNOWLEDGMENTS

This thesis was possible due to the assistance received from many individuals and organizations. Acknowledgments have to be addressed to a large number of persons and institutions. The words and feelings expressed in these acknowledgments express my genuine gratitude to those who have provided important assistance and support during my studies. The order of appearance of individuals and organizations does not reflect in any way the level of importance of their contribution to the success of the research presented in this thesis.

- To my supervisors, Professor António Augusto Fernandes and Professor Abílio Manuel Pinho de Jesus, who gave me far more help and assistance than that I could expect. Their guidance and discussion about the structure of the thesis and several theoretical and methodological aspects of the research is recognized; their assistance on pointing out me the right direction regarding the experimental and numerical analysis were also enthusiastically appreciated;
- To the Portuguese Foundation for Science and Technology (FCT) and the European Commission, respectively in the context of the doctoral scholarship SFRH/BD/72434/2010 and FADLESS project (RFSR-CT-2009-00027), that provided the necessary funds to carry out the work;
- To the University of Trás-os-Montes e Alto Douro for providing the access to their laboratories;
- To the INSA-Lyon and particularly to Prof. Maigre and Prof. Gravouil for their support and help, during a 3 months internship, that allowed me to understand the XFEM methodology;

- To Dr. José Xavier for his unconditional support and help in the development of experimental procedures and also several algorithms used in this thesis, in particular what concerns the use of DIC;
- To my collegues from the Civil Engineering Department of the Faculty of Engineering of the University of Porto, Carlos Albuquerque and Fernando Marques, for their sympathy, partnership and collaboration;
- To Professors Rui Calçada and Álvaro Cunha for their leadership in the FADLESS project context and for their key contributions for the presented research;
- To Engº Miguel Figueiredo from the Mechanical Department of the Faculty of Engineering of the University of Porto and responsible for LET, Dr. Cristóvão Santos, Prof. Paula Braga both from the University de Trás-os-Montes and Alto Douro for their support in their respective work domain, particularity concerning the experimental activities;
- My fraternal thanks to João Pereira and Fábio Pereira; without their friendship and help, this PhD would be more burdensome;
- Lastly, but certainly not least at all, I am very grateful to my wife Andreia for her love and continuous understanding and support.

Abstract

Advanced methodologies for the fatigue analysis of metallic bridges are investigated in this thesis. Local approaches to fatigue are proposed for complex bridge details leading to multi-scale problems requiring efficient tools to allow feasible solutions for real bridge components under actual traffic conditions. The current doctoral thesis was prepared within the framework of the FADLESS European project (*Fatigue Damage Control and Assessment for Railways Bridges*) where two bridge case studies were investigated, and selected representative details supported the analyses presented in this thesis. Trezói and Alcácer do Sal Railway Bridges, respectively riveted and welded bridges, motivated a significant experimental study aiming the characterization of the fatigue behaviour of riveted and welded joints, as well as the fatigue characterisation of respective materials (S235 and S355 structural steels). The generated experimental data was important to provide basic material data for models identification as well as for the models validation. The down-scale fatigue testing of riveted and welded components and the mixed-mode fatigue crack propagation tests assisted by Digital Image Correlation could be emphasized as noteworthy contributions from the experimental program.

This doctoral research also included significant numerical fatigue investigation. Both local approaches to fatigue and Fracture Mechanics were applied to simulate the fatigue crack initiation and propagation of tested details. Several finite element models of tested riveted and welded connections were developed in order to validate fatigue life prediction models. Distinct finite element approaches were used to simulate the fatigue crack propagation. This included the finite element method and the extended finite method, the latter being attractive since it does not require remeshing operations.

In general, it was observed a good compromise between simulations and experimental results.

Finally, numerical fatigue studies were developed for selected structural details of the Trezói and Alcácer do Sal railway bridges. With respect to the first case study, it was recognized the necessity to develop multiaxial fatigue analyses. Also, non-proportionality of stress states and their random time history nature were verified, demanding specialized damage models. For riveted joints, the simulation of rivets using contact elements is crucial to obtain reliable critical locations. An innovative approach for the fatigue damage assessment based on modal stress intensity factors superposition was also addressed in this doctoral thesis. The key objective of this methodology aims an efficient fatigue damage analysis considering the concept of modal stress intensity factors. It was found that the approach was able to simulate the residual fatigue life of a welded detail of the Alcácer do Sal Railway Bridge, for a significant traffic sample from the monitoring system.

RESUMO

Metodologias avançadas para análise à fadiga de pontes metálicas são objeto de estudo nesta dissertação. As abordagens locais de fadiga propostas para detalhes complexos de pontes conduzem a problemas multiescala que requerem ferramentas eficientes de modo a permitir soluções confiáveis para detalhes de pontes reais sob a ação de condições de tráfego representativas. A presente tese foi realizada no contexto do projeto Europeu FADLESS onde dois casos de estudo foram investigados, tendo-se selecionado dois detalhes estruturais representativos para suportar as análises realizadas nesta dissertação. As pontes ferroviárias de Trezói e Alcácer do Sal, respetivamente rebitadas e soldadas, motivaram um programa experimental visando a caracterização do comportamento à fadiga de ligações rebitadas e soldadas, assim como a caracterização à fadiga dos respetivos materiais (aços estruturais S235 e S355). Os resultados experimentais providenciaram informação essencial relativa aos materiais, necessária à identificação dos modelos, assim como a informação para a validação dos mesmos modelos. Merecem destaque os ensais de fadiga em ligações rebitadas e soldadas, construídas numa escala reduzida dos detalhes reais das pontes, assim como os ensaios de propagação de fendas em modo misto, assistidos por técnicas de correlação digital de imagem.

A presente tese de doutoramento também contempla uma componente numérica importante que visa a simulação do comportamento à fadiga de detalhes estruturais recorrendo a modelos de iniciação e de propagação de fendas, baseados em abordagens locais da fadiga e Mecânica da Fratura. Foram propostos vários modelos de elementos finitos dos componentes rebitados e soldados testados, no sentido de validar modelos de previsão de vida à fadiga. Neste domínio, a presente tese de doutoramento abrange diversas metodologias numéricas para a modelação de propagação de fendas de fadiga. A metodologia XFEM foi considerada para modelar a propagação de fendas de fadiga em ligações, sem haver a necessidade de refazer a

malha de elementos finitos, para cada incremento de fenda de fadiga. Em geral foi observado um bom compromisso entre as simulações e os resultados experimentais.

Finalmente foram desenvolvidos estudos numéricos incidindo nos detalhes estruturais selecionados das pontes ferroviárias de Trezói e Alcácer do Sal. No que diz respeito ao primeiro caso de estudo, foi reconhecida a necessidade de uma análise de fadiga multiaxial. Foi também observada a não-proporcionalidade do estado de tensões e a natureza aleatória da sua história, o que exige a utilização de modelos de dano especializados. A simulação do comportamento à fadiga de ligações rebitadas requer o uso de elementos finitos de contacto para estimativas fiáveis das zonas críticas. Foi ainda testada uma abordagem inovadora para a determinação de vidas residuais de componentes recorrendo à Mecânica da Fratura, com a história dos fatores de intensidade de tensões simulada através da sobreposição modal de fatores de intensidade de tensões. Esta abordagem foi demonstrada para um detalhe soldado da ponte de Alcácer do Sal permitindo a computação, de forma eficiente, da evolução do dano de fadiga considerando uma amostra significativa de comboios resultante de um sistema de monitorização.

CONTENTS

Chapter III - Fatigue characterization of structural steels

Chapter IV - Fatigue behaviour of relevant riveted and welded details of railway bridges

Chapter V - Welded joint fatigue behaviour assessment using mesh insensitive procedures and S-N master curve concepts

Chapter VI - Finite element modelling of experimental details

Chapter VII - Fatigue modelling of a relevant detail from the Trezói bridge

Chapter VIII - Finite element modelling of a relevant detail of the Alcácer do Sal Bridge

Chapter IX - Final conclusion and future works

LIST OF FIGURES

LIST OF TABLES

NOMENCLATURE

Latin

a	*Fatigue crack size*
$\boldsymbol{B}$	*Pre-logarithmic energy factor*
b	*Fatigue strength exponent*
b_γ	*torsional cyclic fatigue strength exponent*
C	*Paris law's coeficient*
c	*Fatigue ductility exponent*
D	*Fatigue damage*
$\mathbf{D}$	*Damping matrix*
$\frac{da}{dN}$	*Fatigue crack growth rate*
dA	*Infinitesimal area segment*
E	*Young modolus*
$Fmax$	*Maximum load in a load range*
$Fmin$	*Minimum load in a load range*
$\boldsymbol{f}$	*Body force per volume unit*
f_j	*Modal forces, for the j^{th} mode of vibration*
G	*Elastic shear modulus*
$\bar{J}$	*Energy release rate calculated with respect to a finite segment*
J_{aux}	*J-integral related to the auxiliary field*

J_{int}	*J-integral from the interaction integral*
J_{tot}	*Total J-integral*
K	*Stiffness matrix*
K'	*Cyclic strain hardening coefficient*
K_I	*Mode I stress intensity factor*
K_{II}	*Mode II stress intensity factor*
K_{Ic}.	*Material toughness*
K_{eq}	*Equivalent stress intensity factor*
k	*Number of specimens for statically analysis*
k_t	*Elastic stress concentration factor*
M	*Mass matrix*
M_{kn}	*Magnification stress intensity factor parameter(S-N Master Curve)*
m	*Paris law's exponent*
n'	*Cyclic strain hardening exponent*
$2N_f$/ N_f	*Number of reversals to failure/ Number of cycles to failure*
R_σ	*Stress ratio*
R1	*Riveted specimens (configuration 1)*
R2	*Riveted specimens (configuration 2)*
R3	*Riveted specimens (configuration 3)*
Rp	*Yield stress*
Rm	*Rupture stress*
R	*Rigid body rotation*
S^2	*Variance*
S	*Standard deviation*
T_x	*Rigid body translation along the x directions*

T_y	*Rigid body translation along the y directions*
t	*Thickness*
W	*Width of the Compact Tension specimens*
W1	*Welded specimens 1 (configuration 1)*
W2	*Welded specimens 2 (configuration 2)*
W3	*Welded specimens 3 (configuration 3)*
W4	*Welded specimens 4 (configuration 4)*
$\overline{X}$	*Mean value of the independent variable X*
$\overline{Y}$	*Mean value of the independent variable Y*
Y_j , $Y_j(t)$	*Modal coordinate, modal coordinates time histories*
t_r	*Reference length of the final crack depth at failure (S-N Master Curve)*

Greek

$\varepsilon_f{}'$	*Fatigue ductility coefficient*
γ	*Material constant of the Walker model*
μ	*Friction coefficient*
ν	*Poisson ratio*
$\sigma_{n,\max}$	*Maximum direct stress acting on the principal strain range plane assessed during principal strain cycle counting procedure*
σ_b	*Bending stress component for structural stress computation*
$\sigma_f{}'$	*Fatigue strength coefficient*
σ_m	*Membrane stress component for structural stress computation*
τ_m	*Transverse shear component for structural stress computation*
ΔF	*Load range*
$\overline{\Delta K}$	*Equivalent Stress intensity factor range of the Walker model*

ΔK	*Stress intensity factor range*
ΔK_{th}	*Crack propagation threshold stress intensity factor range*
ΔS_s	*Equivalent structural stress range*
$\Delta \gamma$	*Shear strain range*
$\Delta \varepsilon$	*Total strain range*
$\Delta \varepsilon_1$	*Maximum principal strain range*
$\Delta \varepsilon^E$	*Elastic strain range*
$\Delta \varepsilon^P$	*Plastic strain range*
$\Delta \varepsilon_{loc}$	*Local strain range*
$\Delta \sigma$	*Stress range*
$\Delta \sigma_s$	*Structural stress range*
$\Delta \sigma_{loc}$	*Local stress range*
$\Delta \sigma_{nom}$	*Nominal stress range*
ξ_j	*Modal damping ratio*
τ'_f	*Torsional cyclic fatigue strength coefficient*
$\phi(x)$	*Normal level set function*
$\varphi(x)$	*Tangential level set function*
ω_j	*Natural frequency*

ACRONYMS

AASHTO	*American Association of State Highway Traffic Officials*
ANSYS	*Swanson Analysis Systems*
AREA	*American Railway Engineering Association*
ASTM	*American society for testing and materials*

BS	*British Standards Institution*
BS	*Bannantine and Socie*
CT	*Compact Tension*
DIC	*Digital image correlation*
DE	*Displacement Extrapolation method*
EC_3	*Eurocode 3*
EPFM	*Elastoplastic Fracture Mechanics*
FADLESS	*Fatigue Damage Control and Assessment for Railways Bridges*
FE	*Finite element*
FS	*Fatemi and Socie*
IDMEC	*Institute of Mechanical Engineering*
IIW	*International Institute of Welding*
LEFM	*Linear Elastic Fracture Mechanic*
MCS	*Maximum Circumferential Stress criteria*
MERR	*Maximum Energy Release Rate*
MTS	*Maximum Tangential Stress criteria*
SIF	*Stress intensity factor*
SWT	*Smith-Watson-Topper*
VCCT	*Virtual Crack Closure Technique*

Chapter I

Introduction

1.1. INTRODUCTION

Bridges are very complex structures that are built to support dynamic loads resulting from traffic actions (e.g. cars, trucks, trains, etc). The action of the dynamic loads over these structures is responsible for their progressive damaging due to fatigue. This is a major concern of designers and owners of the structures since they need to guarantee significant operational safety levels in order to avoid catastrophic collapses with strong social and economic impact.

The awareness of fatigue behaviour of bridges did not appear with the construction of the first metallic riveted bridges at the end of XIX century. Only some decades ago, the fatigue design became a concern of engineers. This happened with the development of the first design rules that included a fatigue design section. Nowadays there is a full awareness for the need of a fatigue design of metallic bridges (e.g. bolted, welded, composite bridges) and design codes are strictly observed. The traffic intensity (e.g. axle loads, speed and frequency) on modern bridges is very high and with an increasing trend which requires constant attention in order to avoid fatigue cracks and in case they cannot be avoided, maintenance plans supported on residual life calculations need to be implemented.

Although fatigue modelling has suffered significant advances for mechanical engineering applications, the fatigue methodologies preconized in design codes for bridges have a very simple form, despite the enormous complexity of the generality of those structures. The question that may be advanced is why the state-of-the art fatigue models are not being explored for bridge fatigue assessment? One answer that could be formulated is the fact that the most advanced fatigue models are local models that recognize the local nature of the fatigue damage. The application of those local models to bridges is cumbersome since a multi-scale problem needs to be faced. A global model of the structure is required to account conveniently for the traffic loads, but local information (e.g. strains, stresses, stress intensity factors) at critical hot spots is also

required to provide the required input information to the fatigue models. The conciliation of these two scales of analyses is currently an open problem that requires significant contributions in other to allow the progress of current design code approaches which are based on global S-N approaches.

1.2. AIM OF THE THESIS

The main goal of the present dissertation was to develop advanced methodologies to be applied in the fatigue assessment of structural details from metallic bridges, including welded and riveted joints. Local models for the fatigue analysis were preferably followed in the proposed research, in alternative to traditional global S-N approaches, and strategies proposed to overcome the difficulties introduced by the multi-scale problem that this kind of fatigue models introduces.

The present research was performed within the framework of the FADLESS European project, entitled *Fatigue Damage Control and Assessment for Railways Bridges* [1]. This European project aimed at the development of methodologies for the assessment of the fatigue behaviour of critical details, to be demonstrated for several European railway bridges, selected as case studies. Regarding the Portuguese case studies, two railway bridges were selected, namely the Trezói Railway Bridge and the new Alcácer do Sal Railway Bridge (see Figure 1.1).

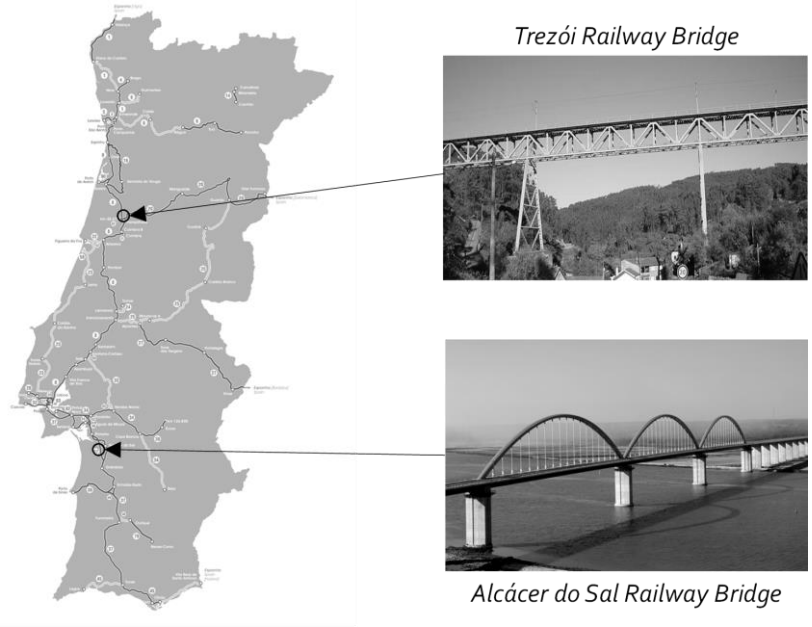

Figure 1.1 - Location of the Trezói and Alcácer do Sal Railway Bridges.

The research proposed in this PhD work was focused on the local fatigue assessment methodologies for bridge details, the global structural dynamic behaviour of the bridges, another important counterpart of a fatigue assessment procedure, was out of scope of this PhD work. However, information from global dynamic analysis, such as displacement/member forces histories required for the local fatigue approaches, were made available from the other partners involved in the FADLESS project. The research proposed in this PhD work also benefitted from field monitoring data that was gathered during the FADLESS project, in particular for the two selected Portuguese case studies, which allowed the validation of the proposed models in terms of reproducibility of the local stresses and strains.

The Portuguese cases studies selected in the FADLESS project involved two types of bridge construction, namely riveted and welded construction. Therefore the proposed research focused on both types of details. In addition to the fatigue simulation activities, this PhD research also aimed at the development of a significant experimental program focused on base materials and riveted/welded joints, representative of the two Portuguese case studies investigated within the FADLESS project. The generated fatigue data was used as an input for the numerical models. Also, it was used to allow the application of assessment procedures under controlled

laboratory conditions, where fatigue damage was possible to be generated and controlled. This is an important issue of the research, since the selected bridge case studies did not exhibit any visible fatigue damage, disabling the possibility of testing the models reliability for fatigue simulation in the case studies. However, the case studies are still very important since they represent the complexity of real bridge details, requiring several strategies for the mitigation of the important computational costs this kind of problems poses to the structural analysts. Also, stress fields in real bridge details are not fully represented using laboratory specimens.

Concerning the fatigue simulation strategies, both crack initiation and crack propagation fatigue damages should be addressed. While fatigue crack propagation has been understood as the governing damage process for welded joints, fatigue crack initiation may not be neglected for riveted joints (unwelded material/details).

Recognising the central role of the FADLESS case studies in this research, the following subsections give an overview of those case studies and the respective selected details that deserved major attention in this PhD dissertation.

1.2.1. Trezói Railway Bridge case study

The Trezói Bridge (Figure 1.2) is located in the international Beira Alta railway line that links Portugal to Spain. This bridge is located at the km 62, north of Mortágua in the village of Trezói. The bridge was constructed as part of a project aiming the replacement of existing bridges in the railway line, carried out during the decade of 50 of last century, and was opened to traffic in August 1956. The project was funded by the Marshall Plan and the conception, manufacturing and erection, together with 6 other bridges of larger span on the same line, were of the responsibility of the German House Fried Krupp.

The metallic riveted bridge is formed by three spans of 39 m, 48 m and 39 m, representing a total length of 126 m (see Figure 1.3). The two inverted Warren truss girders that compose the metallic deck of the bridge are 5.68 m height. The girder panels are 6.50 m wide in the central span and 6.00 m in the end spans. Two trapezoidal shape trusses acting as columns and two granite masonry abutments transmit the loads

carried out by the structure to the foundation. The bridge has a constant width of 4.4om throughout its length.

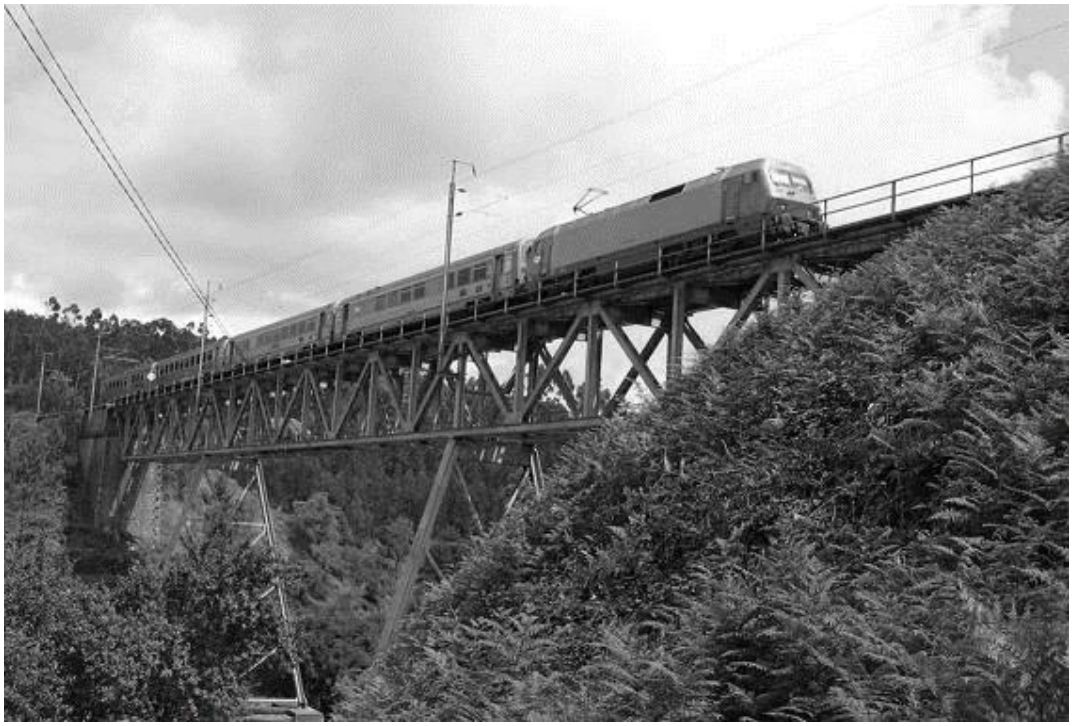

Figure 1.2 - General view of the Trezói Bridge [1].

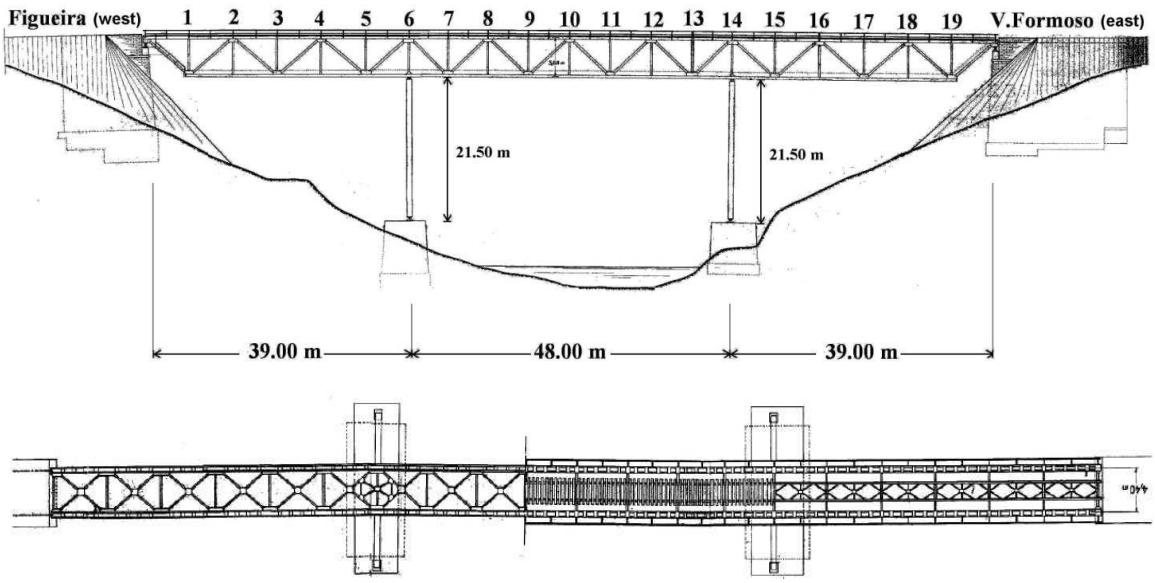

Figure 1.3 - Technical representation of the Trezói Bridge: elevation and plan view [1].

The cross girders, as well as the stringers resting on them, were built using "I-shaped" sections, as shown in Figure 1.4. The cross girders are 71 cm height and are connected to the lateral vertical elements with riveted plates. The chords and diagonals of the truss girders are formed by double "U-shape" sections. The bearing supports of the superstructure are metallic and allow free rotations in the structure plane. At the east support, the longitudinal displacements are constrained, while at the west support displacements caused by longitudinal horizontal forces (thermal actions, braking, etc.) are allowed. Figure 1.5 illustrates the selected node of the bridge that was investigated in this research. This is a representative node of the bridge that was demonstrated in the FADLESS project as the one most fatigue sensitive node [1]. The cross girder receives directly the traffic load action and transfers it to the two Warren truss girders.

Figure 1.4 - Partial view of the upper structure

Figure 1.5 – Selected structural detail. Connection between the cross girder and the main chord [1].

1.2.2. Alcácer do Sal Railway Bridge case study

The new Alcácer do Sal railway bridge is located in the Lisbon – Algarve railway line, in south of Portugal (Figure 1.6). It was designed for passenger trains (as the Alfa Pendular tilting train and the Intercity train) running at speeds up to 220 km/h. Since it is also part of the main railway connection to the sea port of Sines, it is also designed for freight trains with up to 25 tons per axle. The bridge has a continuous composite deck that covers three spans (160 m per span). The deck is suspended from 3 arches. Each arch holds one span of the deck, with 18 vertical hangers, 8 m apart from each other. The structure is preceded by the north and south access viaducts (with 1115 m and 1140 m, respectively). Both viaducts and bridge were designed to hold two ballasted tracks even if only the upstream track is on service, at the current time. A reinforced concrete slab, above a U-shaped steel box, forms the deck. The 15.85 m wide concrete slab has a maximum thickness of 0.43 m. The steel box, with sloped webs, was built up by welding steel plates. Maximum plate thickness is 120 mm. A diaphragm reinforces the deck at each hanger connection. Two diagonals per hanger distribute the suspension force into the deck (see Figure 1.7). The arches present a hexagonal hollow section with variable height and width.

Figure 1.6 - Overview of the bridge of the new railway crossing of the river Sado (adapted from [2]).

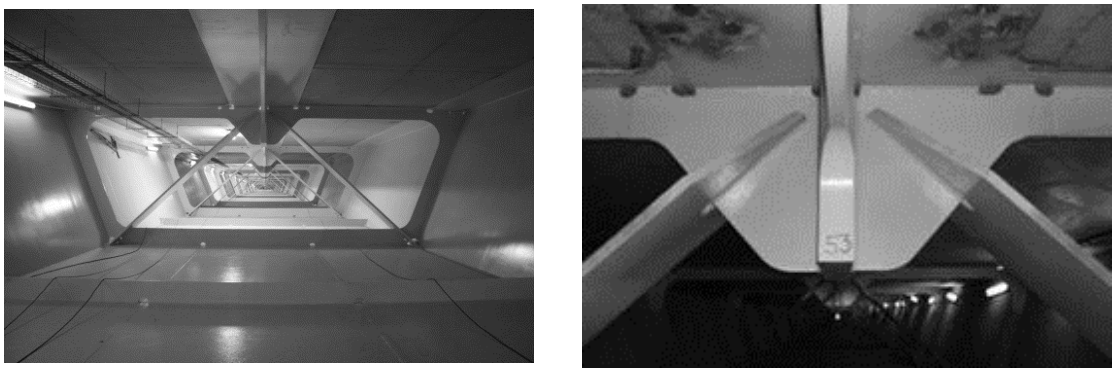

a) b)

Figure 1.7 - Diaphragm 54 of the Alcácer do Sal Bridge: global overview of the diaphragm; b) detail of the welded joint at the diaphragm to central gusset plate.

The welded connection between the diaphragm diagonals and the vertical gusset (Figures 1.7a) and b)) were selected for the fatigue assessment. Stress analysis revealed relatively small stress levels in the steel structure which is an indication of the absence of fatigue damage concerning this structure. Nevertheless, the referred welded joint exhibited a design deviation with respect to existing recommendations such the Eurocode 3 fatigue classes. Therefore, the proposed research concerning the Alcácer do Sal Bridge is twofold: i) to assess the influence of the design variation of the detail on fatigue behaviour; ii) to propose an efficient methodology to assess such a detail in the context of a very complex structure.

1.3. OUTLINE OF THE THESIS

A brief outline of the thesis is given in this section. This dissertation is organized into nine chapters, including the present one. Chapter II presents a review about fatigue assessment methodologies for bridge details. A brief introduction to the fatigue of steel structures is also presented in the first part of chapter. Then, a review of experimental and numerical research concerning riveted and welded joints is performed.

Chapter III presents the results of an experimental work that was performed within this PhD work, in order to characterize the fatigue behaviours of the structural steels S235 and S355. Elastoplastic cyclic behaviours, fatigue behaviours based on smooth

specimens and fatigue crack propagation rates were assessed for both materials. Concerning the fatigue crack propagation, special mixed-mode fatigue crack propagation tests were performed and digital image correlation (DIC) used in data reduction. The investigated steels were used to produce riveted and welded connections that were also fatigue tested and results presented in Chapter IV.

Chapter IV deals with an experimental campaign of riveted and welded joints. Regarding riveted specimens, 1 down-scale specimen and 2 small-scale specimens were considered. Code-based S-N curves were validated. About the welded specimens, 4 small-scale specimens were tested, aiming to represent distinct weld/geometry variations. While the riveted specimens were motivated by the Trezói bridge case study, the welded specimens were motivated by the Alcácer do Sal bridge.

In Chapter V the master S-N curve concept presented by Dong [3] is applied to the investigated welded joints. The equivalent structural stress concept is computed for each investigated welded joint and respective experimental results where then compared with the master S-N curve, based on existing literature.

Chapter VI presents a numerical analysis of the specimens presented in Chapter IV. Finite elements models of riveted and welded were described. The fatigue lives are assessed using local strain and Fracture Mechanics approaches. The fatigue crack propagation is simulated using both standard finite element method and extended finite elements method.

Chapter VII presents a numerical analysis of the selected riveted detail from the Trezói bridge. Both continuous and riveted models were considered in the analysis. Sub-models of the node were proposed and validated using monitoring fatigue data. Multiaxial local fatigue criteria were applied in the analysis of the detail aiming the fatigue crack initiation simulation.

Chapter VIII was dedicated to the analysis of a selected welded detail of the Alcácer do Sal bridge. A new and efficient computational method to assess stress intensity factors is presented, based on modal superposition analysis. The proposed approach is demonstrated for a residual fatigue life assessment.

Finally, Chapter VIII summaries the main conclusions of each chapter and also suggests some future works.

1.4. REFERENCES

[1] Lippi, F., Salvatore, W., Braconi, A., Finetto, M., Wenzel, H., De Roeck, G., Peeters, B., Könke C., Zabel, V., Cunha, A.,"Fatigue damage control and assessment for railway bridge", Research Fund for Coal and Steel, Directorate-General for Research and Innovation, 2014.

[2] Rede Ferroviária Nacional, R.E., Variante de Alcácer, Lisboa: REFER, 187 p., 2010.

[3] Dong, P., Hong, J. K., Cao, Z., "Structural stress based master S- N curve for welded joints", IIW Doc. XIII -1930-02/XV-1119-02, pp. 24, 2002.

Chapter II

A review of fatigue assessment methodologies for bridge details

2.1. INTRODUCTION

Metallic bridges are important structures that are susceptible to fatigue damage due to the nature of the loads they are subjected during their operation. These loads are mainly due to the traffic action, which is variable in nature and may include amplification dynamic effects, leading to variable amplitude stress histories. The fatigue loads and consequent fatigue damage is more severe for railway bridges than for highway/road bridges. In the context of railway bridges, the freight traffic is the one that raises more concerns from the perspective of fatigue. The panorama of existing metallic bridges may be classified into old riveted metallic bridges and bolted/welded bridges.

Concerning the old metallic bridges, there are an important number of these structures in Europe and North America, constructed during the second half of the 19th century up to the middle of the 20th century which, due to economic reasons, are still in operation. Since they have been subjected to increasing traffic intensity along their operational lives, both in terms of vehicle gross weights/axle loads as well as truck/train frequencies, their damage levels need to be assessed in order to decide about possible repairs. Thus, the maintenance and safety of these existing bridges is a major concern of governmental agencies. In order to assure high safety levels in old riveted steel bridges, highway and railway authorities have to invest heavily in their maintenance and retrofitting. In particular, fatigue failures are a concern for riveted steel bridges since they were not originally designed taking into account fatigue. The fatigue phenomenon was only intensively investigated in the second half of the 20th century, when the riveted construction was no longer applied in new bridge structures. Therefore, for the exposed reasons, these structures require a special attention aiming at their fatigue damage assessment and the establishment of reliability levels.

Bolted and welded bridges may be constructed with an integral steel configuration or a composite technology (steel/concrete). In general, the fatigue concern is focused on the

steel components. The necessity of a fatigue design must be assessed for new structures and in the case it would be required, a fatigue assessment methodology should be implemented.

The usual approach for the fatigue assessment of steel structures is based on S-N approach, which is understood as a global approach, i.e., an approach for the prediction of the complete failure of components. Damage accumulation theories (e.g. Miner), when applied with the global S-N approach, are not capable to give a real picture of the damage progression in the details being assessed. The S-N approach is the basis of the main design codes for steel structures such as the Eurocode 3 [1]. This S-N approach requires the use of nominal stresses in members being compatible with the development of global finite element models of the structure. For some details (e.g. complex ones) geometric/structural stresses are required, which demands for bridge models of more local nature in order to include the required geometric details with more refinement. Local models are, however, computationally demanding since they lead to a multi-scale problem, requiring strategies for computational costs mitigation.

The research in fatigue of steel bridges has attracted a lot of attention in the last years, several national and European projects being performed [2-6]. The investigated topics ranged from dynamic effects assessment for railway traffic, traffic loads monitoring, materials/connections fatigue characterization and local fatigue modelling. Local fatigue modelling emerged as an attractive approach for fatigue analysis of bridge details since it is direct linked with the fatigue damage mechanism occurring in the details. For example, fracture mechanics based fatigue approach allows the simulation of a fatigue crack, starting at a specific location and propagating along a specific path. Notch strain/notch stress approaches to fatigue may be used to simulate a macroscopic crack initiation at a specific spot.

Chapter I referred two metallic railway bridges that have been the focus of the research activities within this work. The current chapter aims at the presentation and discussion of some relevant available fatigue approaches, some of them could be selected for the analysis of the referred structures. Others have been applied in similar type of structures. This chapter starts with an overview of fatigue fundamentals. Afterwards, a reference to existing research works in the field of fatigue behaviour/characterization of bridge components is presented, namely on riveted and welded joints.

2.2. GENERAL CONSIDERATIONS ON FATIGUE OF STEEL STRUCTURES

A fatigue assessment usually involves two fundamental stages: fatigue actions and fatigue resistance of structural details assessments. The knowledge of the actions is important to simulate the stress histories at locations to be fatigue assessed. Both fatigue actions and fatigue resistance data usually shows various sources of uncertainties. The load information is normally provided by the responsible authorities or is based in existing standards and monitoring activities. Concerning the fatigue resistance assessment, usually it is defined in the form of experimental S-N curves, where N is the predicted number of cycles to failure for a given stress range, $\Delta\sigma$. Since the current investigation is focused on fatigue resistance side, the proposed literature review will refer the aspects concerning the fatigue characterization of riveted and welded connections, discussing the S-N approach and alternative approaches referred in the literature. A review of existing fatigue resistance assessment methodologies for bridge details is primarily described in this chapter.

2.2.1. Stress-based fatigue approach

The stress-based fatigue approach, very often known as S-N approach, results from fatigue tests of specimens performed under constant amplitude loading, for different stress ranges, $\Delta\sigma$, keeping constant the stress ratio, R_σ, or the mean stress. The stress range $\Delta\sigma$ is defined as the difference between the maximum stress (σ_{max}) and the minimum stress (σ_{min}) of the cyclic loading, while the stress ratio R_σ is defined as the ratio between the minimum stress and the maximum stress ($\sigma_{min}/\sigma_{max}$). S-N curves results generally from the stress range, $\Delta\sigma$, or stress amplitude $\Delta\sigma/2$, plotted against the number of cycles to failure, N_f. Plotting the test data on logarithmic scales, it commonly leads to an approximately linear correlation for steel details, in the finite life regime:

$$\log(N)=\log(C)-m\log(\Delta\sigma) \tag{2.1}$$

where $1/m$ is the slope of the straight line and C is a constant, both depending on material and loading conditions. Equation (2.1) is often found in the following power form:

$$N(\Delta\sigma)^m=C \tag{2.2}$$

Figure 2.1 illustrates a typical S-N curve where a stress range, $\Delta\sigma_0$, below which no fatigue failure occurs, is called the fatigue limit. In practice, the fatigue limit of unnotched steel specimens is approximately equal to the half of the ultimate tensile strength of the material and is highly dependent on the surface conditions of the material [7]. The fatigue behaviour depends on several phenomena such as the stress ratio R_σ and the residual stresses. Smith [8] refers that zero-to-tension loading (R_σ =0) results in lower fatigue lives than full stress reversals (R_σ = -1) and, in general, the increase in the mean stress results in a decrease in fatigue life. Besides the mean stress effects, residual stresses also affect the fatigue life, particularly compressive residual stresses are beneficial since they hinder fatigue crack initiation or may even stop the fatigue crack propagation. This type of compressive residual stresses can be introduced by various fatigue life-enhancing methods such as shot peening, plastic hole expansion, cold rolling, overloading and grinding [9]. On the other hand, tensile residual stresses, as often found in welded details, promote crack opening and hence tend to reduce fatigue life [10].

Fatigue crack initiation in structural details is generally expected where stress concentrations may occur, such as at sharp corners, grooves, holes and weld toes. The stress concentration factor (k_t), defined as the ratio of the peak stress to the nominal stress, is frequently used to quantify the notch severity. For simple geometries, the stress concentration factor parameter can be computed analytically by means of elasticity theory and solid mechanics [7]; finite element analysis (FEA) may be used to characterise more complicated geometries.

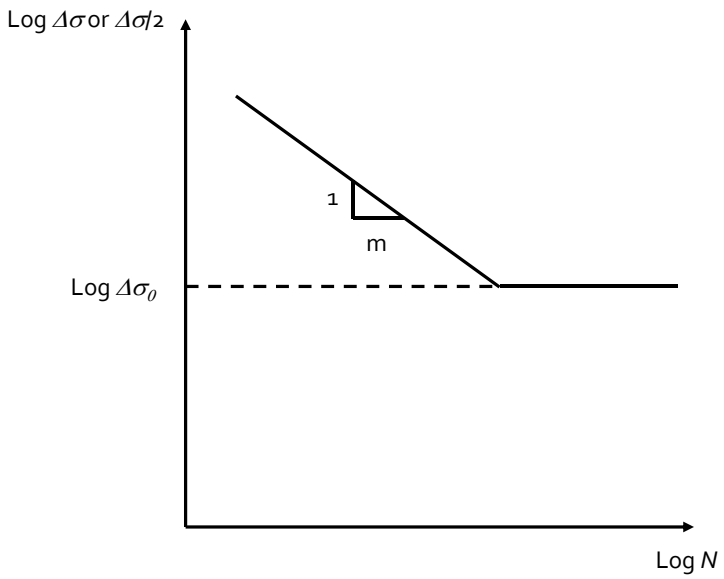

Figure 2. 1 – Schematic S-N curve.

The use of smooth specimens based S-N curves in conjunction with appropriate k_t to predict the fatigue life of notched details may be implemented. However fatigue lives of notched specimens generally yield longer fatigue lives than the ones predicted using the k_t-corrected stresses. In fact, the actual fatigue strength reduction, which can be expressed by the fatigue notch factor k_f, is usually less than the reduction obtained by using k_t. The notch sensitivity of a material can be defined by

$$q = \frac{k_f - 1}{k_t - 1} \tag{2.3}$$

In Equation (2.3), q = 0 indicates that the notch does not impact the fatigue life, whereas q = 1 suggests that the notch cause the maximum possible effect ($k_t = k_f$).

The statistical size effect is another well-known influent phenomenon on fatigue behaviour. The reason for the existence of such effect is generally justified by the fact that larger volumes of stressed material contains a higher number of defects which results in a larger probability of finding crack initiation defects.

2.2.2. Fracture mechanics based fatigue approach

The fatigue life prediction for components with incipient cracks can be evaluated using a Fracture Mechanics approach. Generally, the Fracture Mechanics approach is performed as a complement to the stress-based approach, the latter being adopted to model the fatigue crack initiation. The Fracture Mechanics is usually divided into two main groups, namely the Linear Elastic Fracture Mechanic (LEFM) and Elastoplastic Fracture Mechanic (EPFM). Irwin [11] proposed the stress intensity factor to describe the severity of the stresses around a crack tip. The stress intensity factor can be defined as:

$$K = Y\sigma\sqrt{\pi a} \tag{2.4}$$

where σ is the remotely applied stress, a is the crack length and Y is the stress intensity magnification factor which depends on the geometry and loading conditions. The stress intensity factor solutions are available in the literature for a wide range of cracked geometries [11-12].

An effort has been made in order to relate the fatigue crack growth with the stress intensity factor range, ΔK, at the crack tip. Many relations between the fatigue crack growth rates and the stress intensity factor range have been proposed in the literature, such as the well-known Paris law [14]:

$$\frac{da}{dN} = C\left(\Delta K\right)^m \tag{2.5}$$

where m and C are experimentally measured material constants. On a log-log plot, Equation (2.5) yields to a linear relation, known as Region II of the typical fatigue crack propagation curve, shown in Figure 2.2. Two more distinct regions can be point out in the Figure 2.2, namely the asymptotic Region I, which is associated to a fatigue threshold below which fatigue cracks are non-propagating and the Region III, where fatigue cracks accelerates toward an unstable propagation.

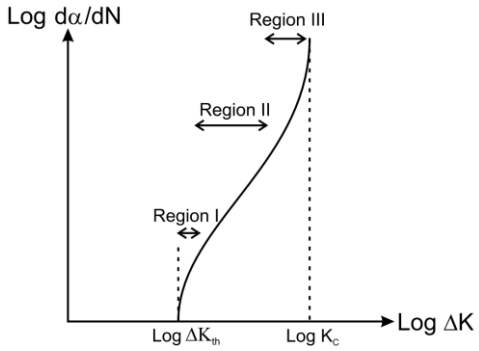

Figure 2.2 – Schematic da/dN *versus* ΔK curve.

2.2.3. Variable amplitude stress conditions

Large structures such as metallic bridges are usually subjected to variable amplitude loading histories. In order to perform fatigue assessments on such structures, several models have been proposed to compute cumulative damage under variable loading stress ranges [15]. The most common method is based on the linear damage accumulation assumption. This assumption does not consider the loading sequence effects, assuming that the fatigue crack growth during a given cycle is not affected by prior loading history. However, Skorupa [16] refers some sequence load effects such as overloads or underloads which can retard or accelerate fatigue crack growth. However, in the case of very irregular random stress histories, the retardation and acceleration effects may cancel out each other effects. Therefore, linear damage accumulation may be a considered a proper choice. The linear Palmgren-Miner's rule is the most widely used model for calculating fatigue damage due to variable amplitude loading [17]. The Miner sum is expressed as:

$$D = \sum \frac{n_i}{N_{fi}} \tag{2.6}$$

where D is the total damage, n_i is the applied number of cycles at a specific stress amplitude or stress range, and N_{fi} is the fatigue life corresponding to the same stress

amplitude or stress range. The Palmgren-Miner's rule postulates that failure occurs when D =1.

2.2.4. Multiaxial fatigue

The majority of the studies in fatigue have been performed under uniaxial loading conditions, and this is the basis of the main approaches being proposed in the literature, including the design codes for bridge structures. However, in some cases, the local stresses developed at critical details of metallic bridges are multiaxial. Besides the stress multiaxiality, the principal stress directions may change over time, defining non-proportional stress histories. In addition to the non-proportional multiaxial stress histories, variable amplitude stress histories are frequent [18].

Although over the years, different methods have been proposed for fatigue life prediction under multiaxial stress states, currently, there is no universally accepted approach to the problem [19]. Due to its simplicity, one of the most common approaches is the transformation of the multiaxial stress state into an equivalent uniaxial stress state with the same fatigue life characteristics [18, 20-22]. The transformation is usually performed using the well-known Von Mises or Tresca equivalent stress criteria and replacing the principal stresses with their ranges. However, this approach has been found to give non-conservative results for the cases of non-proportional loading [20, 22-23]. Another type of approaches that appears to be more successful in multiaxial fatigue data description [19] is the critical plane based approaches, on which fatigue damage is assumed to take place. Combinations of shear and normal stresses on the critical plane are assumed to govern the fatigue behaviour [21-22]. For proportional and constant amplitude loading, the critical planes are usually identified as being the ones experiencing the maximum normal or shear stress. On the other hand, for multiaxial variable amplitude loading, the critical plane is identified, having investigated different plane orientations, as the one experiencing the highest value of different shear and normal stress combinations [19, 24]. Further, the complex multiaxial loading histories can be resolved into individual cycles by using modified forms of the rainflow counting method and then applying Miner's rule [18, 25-28].

2.2.5. Code-based S-N fatigue curves for structural details

Methods for fatigue analysis available in structural design codes of practice are based on S-N fatigue curves which are applicable to distinct details such as, for example, riveted, bolted and welded joints. A family of parallel S-N curves is proposed, with the same slope (m), each one representing the fatigue resistance of a group of details, often called fatigue class [1]. For constant amplitude loading, a fatigue limit $\Delta\sigma_0$ is specified for a given number of cycles (e.g. $N=10^7$ [7]). Below this fatigue limit no damage occurs, if constant amplitude loading is applied. For variable amplitude loading conditions, a second S-N segment with a slope m+2 is proposed, for stress ranges below constant amplitude fatigue limit. The fatigue curves are assumed independent of the stress ratio, R_σ [31]. The detrimental effects of positive mean stresses are included in the S-N curves. Usually, the S-N curves slope is equal to 3, this value being based on Fracture Mechanics principles [10].

The BS5400 standard [29] presents 9 fatigue classes, designated as B, C, D, E, F, F2, G, W and S. This standard allows different target failure probabilities by parallel shifting of the S-N curves.

EC3 [1] considers 14 fatigue strength curves, characterizing 14 fatigue classes. The fatigue class designation results from the fatigue strength at $N=2\times10^6$ cycles. For variable amplitude loading, and for all fatigue classes, a S-N curve slope of m=5 is assumed beyond $N=5\times10^6$.

The American Association of State Highway Traffic Officials (AASHTO) code [30] proposes the use of 7 detail categories (A, B, Bo, C, D, E, and E) with various modifications. Variable amplitude loading is assessed by lowering the cutoff constant amplitude fatigue limit for each fatigue category, calculating an effective constant amplitude stress range and comparing it with the modified fatigue limit.

The American Railway Engineering Association (AREA) standard [31] is very similar to the AASHTO code, the only differences being the S-N curves suggested for riveted details.

The UK railway assessment code [32] adopts the BS5400 fatigue classes but it provides two additional fatigue classes for plain and riveted wrought-iron details (class WI-rivet). Furthermore, cut-off limits at $N = 10^8$ cycles are suggested for all detail classes. Riveted details are considered in the BS5400, AASHTO, AREA and UK railway assessment codes but are not explicitly considered in Eurocode 3. BS5400 suggests the use of its Class D for lapped or spliced riveted connections. In AASHTO, category D is suggested for riveted connections. On the other hand, the AREA code suggests the use of its category D with a distinction being made between riveted connections with high or low clamping force and with drilled or punched holes. However riveted joints are not explicitly referred in the EC3. Meanwhile some recommendations [33] suggest the use of the Class 71 S-N curve from EC3 for any type of riveted joint. Recent studies conducted by Taras and Greiner [34] suggested an alternative approach to the universal slopes proposed by existing codes, and several fatigue classes of riveted joints.

The assessment of riveted joints using code-based S-N curves should be based on net stresses which are nominal stresses computed at cross sections containing the riveted holes. Concerning the welded joints, several types of stress categories may be used in conjunction with the proposed code-based S-N curves. The nominal stress approach is the basic stress form proposed to be used with some types of bridge details in many codes, including the EC3 and the International Institute of Welding (IIW) recommendations [35]. Structural or geometric stresses are also proposed for use with the with the S-N curves of some details. In many cases structural details are assessed on the basis of the maximum principal stress range in the section where potential fatigue cracking is expected. However, maximum shear stress range is required for shear loaded details. Distinct S-N curves are provided for normal or shear loaded welds.

2.3. OVERVIEW OF EXISTING RESEARCH ON RIVETED MEMBERS AND CONNECTIONS

A significant number of fatigue assessment studies for riveted railway bridges have been proposed in the past. An investigation about the fatigue performance of existing steel and composite bridges collected fatigue damage cases for various bridge types and details [36]. Reza Haghani [37] reported more than 100 damage cases which were studied and categorized according to the type of detail and/or the mechanism behind the observed fatigue cracking. The results of this study showed that more than 90% of all reported cases are caused by secondary effects, so-called deformation-induced cracking. This type of fatigue damage is often the result of secondary restraining forces generated by overlooked interaction between different members in the bridge. Poor detailing, along with unstiffened gaps and abrupt changes in stiffness at the connections between different members, also contributes to fatigue cracking in most details. Design codes and evaluation methods generally provide very little guidance on how fatigue damage should be accounted for or prevented. It is the responsibility of the bridge designer to ensure—through good detailing—that these secondary effects and the kind of fatigue damage associated with them are avoided. Figure 2.3 shows collected damage cases categorized according to detail type. The most common types of deformation-induced fatigue damage can be found in the connections between stringers and floor beams, between the latter and the main load-carrying elements in the bridge and at the connections of diaphragms and cross-bracings.

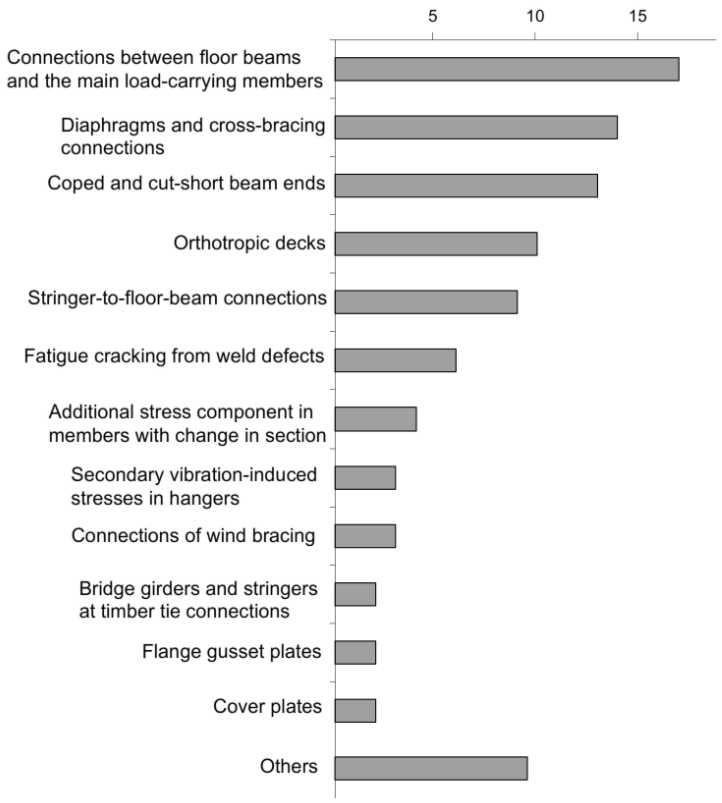

Figure 2.3 – Collected fatigue damage cases listed according to the type of detail in which they were met [37].

Brühwiler *et al.* [38] presented a fatigue research comprising full scale tests on three different girder types, four rolled girders with an extra cover plate riveted to the lower flange and six built up girders, and finally three lattice girders made of wrought iron. The author concluded that the corrosion of riveted girders did not provide lower fatigue life than the one non-corroded. A corrosion loss of ~10 % of the cross section did not give a combined effect worse than the conditions of rivet holes. Wrought iron elements showed fatigue strength similar to steel. The failures in the lattice girders were always in the rivets due to shear stresses component. EC3 fatigue class 71 provided a reasonable estimation of the fatigue life. The constant amplitude fatigue limit of riveted wrought iron girders was estimated to be 70 MPa. For mild steel as well as for girders with punched holes the level was believed to be lower. The shear resistance of rivets may be the governing failure mode for connections.

Adamson *et al.* [39] investigated the fatigue behaviour of stringers retrieved from a bridge built in 1911. From the load history and strain measurements, it was concluded that the accumulated fatigue damage was negligible. Presence of corrosion on the

stringers was also believed to have a negligible effect on the fatigue performance. The investigation included five full scale tests on stringers. Non-bearing riveted details showed a tendency of having fatigue resistance higher than bearing details. The results of the fatigue endurance of the stringers were covered by the AASHTO fatigue class category.

Helmerich *et al.* [40] investigated the fatigue life of girders from three bridges. The results from the tests were used to develop a non-destructive inspection technique, for identification of cracks in bridges. Nine full scale tests were performed, and the results indicated that the EC_3 fatigue class 71 could be used to assess the fatigue life of riveted bridges. The influence of corroded material impact damages and structural defects were covered by the fatigue class. The fatigue endurance of wrought iron was not worse than that of mild steel. Considering appropriate values of Young's modulus and the yield strength, wrought iron bridges can be assessed as steel bridges accordingly to the author.

DiBattista *et al.* [41] made fatigue tests on seven full-scale tension members. The tension members were retrieved from the same bridge as the tests of Adamson *et al.* [39]. A uniform corrosion was observed on all tension members. The tests showed that the fatigue resistance of the diagonals and their connections to the bottom chord could be evaluated by AREA detail fatigue class D, depending on definition of net section area. Non-bearing riveted details showed a tendency of having fatigue resistance higher than bearing details. Repairing cracked connections between tension members and the gusset plate, with preloaded bolts, extended the life of the connections significantly.

Out *et al.* [42] investigated the fatigue resistance of four riveted stringers. The tests focused on corroded girders. Measurements conducted on the girders while still in service showed that 1 % of the stress cycles exceeded 48 MPa, thus the cumulative fatigue damage from service was believed to be negligible. The resistances of the corroded sections were between AASHTO fatigue class E and C (EC_3 fatigue class 56 and 80) depending on the loss of cross section. The riveted beams showed redundancy, the stresses being redistributed to nearby parts when cracks were formed. Tests performed at reduced temperatures did not result in unstable crack growth.

Zhou *et al.* [43] investigated the effect of hole preparation methods on the fatigue life of riveted structures. Investigations concerning the fatigue limit were also performed.

Fatigue tests were carried out at stress ranges between 44 MPa to 54 MPa. A total of 20 tests were performed, 12 at constant amplitude and 8 with a variable load spectra. The result showed that rivet holes were the most frequent origin for crack initiation and was believed to be an effect of the surface condition of the holes. Girders with punched holes provided lower fatigue endurance than drilled or sub punched and reamed. Five tests reached $1x10^8$ cycles, after which the tests were terminated and examination of the girders showed that no fatigue cracking had occurred. The fatigue limit was determined to be 41 MPa. The AREA fatigue class D1 was believed to provide a lower bound for riveted girders in general. The investigations also showed that wrought iron girders exhibited lower fatigue endurance than steel.

Abouelmaaty *et al.* [44] carried out constant amplitude fatigue tests on two deliberately constructed full-scale models of a typical stringer-to-cross-girder steel connection (Figure 2.4). Due to stringer rotation, both test specimens failed at the cross-girder web with fatigue cracks initiating at the locations where the upper and lower flanges of the stringer came into contact with the cross-girder web. More cracks were also detected in the cross-girder web around the double-angle connection and in the stringer web. A considerable amount of bending moment (approximately 8.5% of the stringer fixed-end moment) was found to be carried by the double-angle connection.

Al-Emrani [45] fatigue tested three full-scale bridge parts, which were extracted from an old mild steel railway bridge. Each part consisted of four riveted built-up stringers connected through double angles to three riveted built-up cross-girders (Figure 2.5). Some connection angles were found to contain fatigue cracks prior to testing. The specimens failed either by fatigue cracking in the connection angle, due to out-of-plane distortion of the outstanding legs, or fatigue cracking of the rivets connecting the outstanding legs of the angles to the web of the cross-girder. Fatigue cracks were always found to initiate near the angle fillet at the upper row and after slowly vertical propagation, they were self-arrested due to the gradual reduction in the rotational stiffness of the connections. Fatigue failures of rivets were attributed to combined bending and tensile stresses being present in the rivets, the flexure of the outstanding legs and the stress concentration between the shank and the head. It was found that the double-angle connections were capable of developing up to 67% of the corresponding moment of a fully continuous beam.

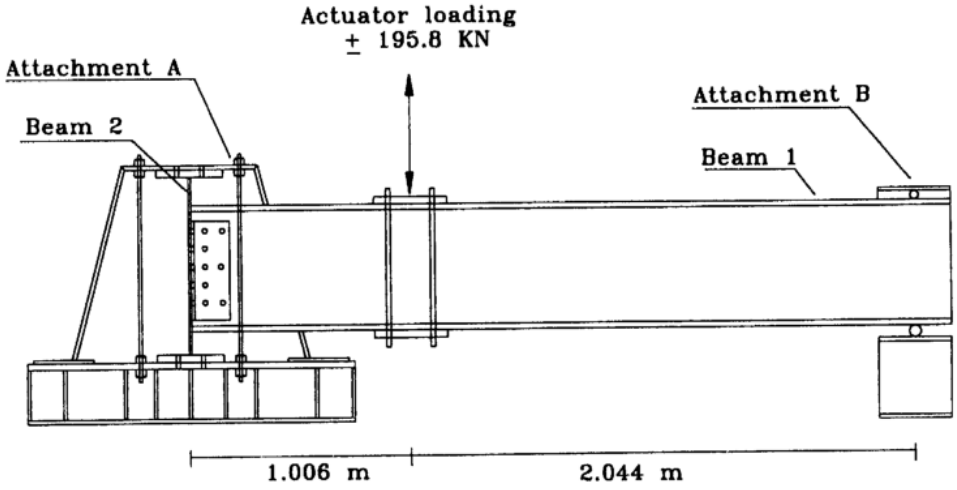

Figure 2.4 – Stringer-to-cross-girder assembly tested by Abouelmaaty *et al.* [44].

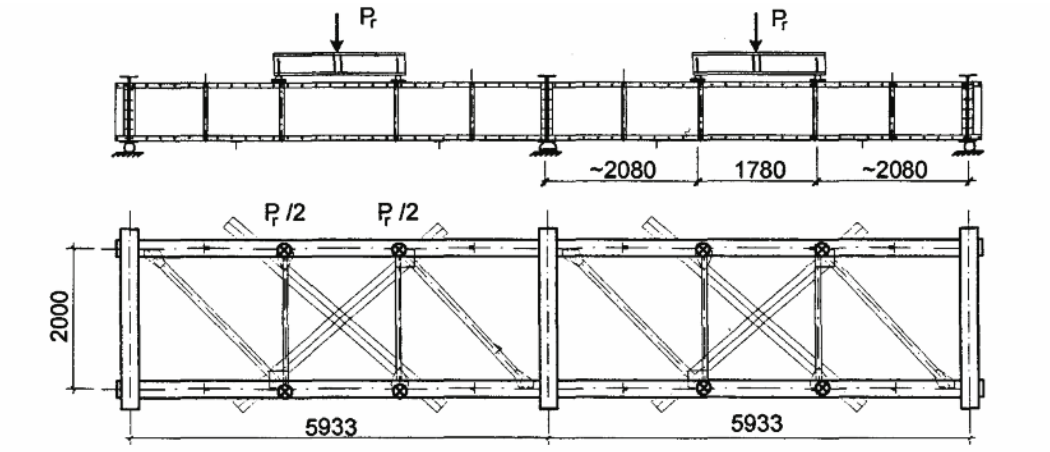

Figure 2.5 – Stringer-to-cross-girder assembly tested by Al-Emrani [45] (dimensions in mm).

Based on previous works by Taras and Greiner [34], Bertram Kühn [46] presented guidelines for the fatigue assessment of existing steel structures supported with information about old materials and non-destructive testing methods for the evaluation of details. Particular attention is paid on remedial measures which are proposed for weak details and damages caused by fatigue. The developed fatigue assessment procedure can be applied to existing steel structures under cyclic loading in general, but the guideline concentrates on the existing traffic infrastructure made from old steel, because of the public importance. The proposed procedure summarizes, regroups and

arranges the knowledge in the field of assessment on existing steel to be applied by practicing engineers.

Previous analytical and numerical investigations on bridge riveted members and connections are sparse. A bibliographical review of FE methods applied to various types of connections, including bolted and riveted connections, was given by Mackerle [47].

Al-Emrani [48] developed a simple analytical model to estimate the rotational stiffness of a stringer-to-cross-girder connection by using the assumption of Wilson and Coombe [49] regarding the fixity of the angle. The connection was divided into a number of segments which had the same axial stiffness. The author also assumed that the cross-girder web remains rigid and that the connection follows a linear load-deformation behaviour.

Paasch and DePiero [50] and DePiero *et al.* [51] carried out 3-D FE analyses on a global model of a riveted highway bridge and on a local model of a stringer to-cross-girder connection. In the global model, beam elements were used to model the cross-girders and the stringers, whereas the reinforced concrete deck was modelled using orthotropic plate elements. The boundary conditions created by the clip angles in the stringer-to-cross-girder connections were also modelled by using very short beam elements. The model was loaded by one axle of a standard fatigue truck. The midspan moments obtained from the global model were compared with field measurements. The measured stresses were found to be considerably lower than their FE counterparts and this was attributed to the composite interaction between the deck and the stringers, which was not taken into account in the FE analyses. The local model of the stringer-to cross-girder connection consisted of a stringer, part of the cross-girder and a connection angle, all of which were modelled using brick elements. Contact was modelled between the different parts of the connection. The root of the angle fillet at the top part of the connection was found to be the most highly stressed region. The clip angles of the riveted connections situated in the interior spans of the bridge were found to be more highly stressed than the connections situated at the end spans of the bridge.

Roeder *et al.* [52] presented a method for estimating the stiffness of bolted and riveted connections based on experimental tests on various connections. The connection stiffness was related to the second moment of area of the bolt or rivet group by a least squares fit on the experimental results.

Lee and Moon [53] developed an analytical model in order to describe the nonlinear moment-rotation behaviour of semi-rigid connections with web angles. The behaviour of the angle segment was investigated by assuming small connection deformation and negligible slip. The authors assumed that the angle was fixed at the edge of the bolt nut and at the leg connected to the beam web. Furthermore, the leg of the angle adjacent to the beam was assumed to behave as a rigid body. In the case of bolts, the full length of the angle was assumed to resist the bending moment, whereas in the case of rivets, an effective length equal to the diameter of the rivet times the number of rivets was suggested. The model predictions for the initial connection stiffness were found to be in good agreement with experimental findings, with the maximum discrepancy being 22%.

Al-Emrani and Kliger [54] carried out FE analyses of a riveted, double-angle, stringer to-cross-girder connection of a railway bridge. Exploiting symmetry, the authors used a 3-D model of a half-stringer and one connection angle connected to a rigid surface representing the cross-girder web (Figure 2.6). The stringer was modelled with shell elements, whereas 8-noded brick elements were used for the connection angles and the rivets. The assembly was loaded statically by two point loads as shown in Figure 2.6. Contact between the rivets and the connection angle and the connection angle and the rigid surface was modelled assuming Coulomb friction with a friction coefficient of 0.3. Three different clamping force values were used for the rivets (30, 65 and 140 MPa). Bending stresses in the stringer near the connection, which were calculated through the FE model, were compared to values obtained through measurements on full-scale assemblies [54]. It was found that the model was capable of reproducing rather accurately the stresses and rotational stiffness of the connection. The analyses revealed that the rotational stiffness of the connection was not affected by the magnitude of the clamping force. However, increase in the clamping force was found to result in the reduction of the axial stress range in the rivets caused by the external loads, the stress range corresponding to an applied load range from 0 to 180 kN. Bending stresses of the outstanding leg were found to increase along the gauge distance reaching a maximum at the fillet of the angle. These, however, were not affected by the rivet clamping force. Finally, the local stress range at the junction between the rivet shank and head due to bending of the rivet was found to decrease with increasing clamping force.

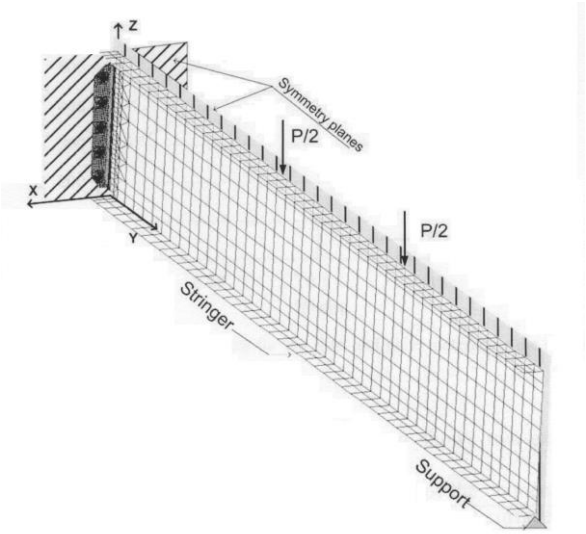

Figure 2.6 – Finite element model of a stringer-to-cross-girder assembly developed by Al-Emrani and Kliger [54].

Al-Emrani *et al.* [55] built a 3D FE model of part of a truss bridge, which included a cross-girder, two pairs of stringer halves and bracings. The model is shown in Figure 2.7. The cross-girder, stringers and the double-angle connections were modelled by using shell elements. Beam elements were used to model the bracings. By statically traversing a train over the bridge, secondary forces of considerable magnitude were found to develop on different members and connections. In particular, secondary axial forces in the stringers and bending of the cross-girders along their weak axis were identified as critical and could lead to fatigue cracking of these members or the connections. The connections between the stringers and cross-girders were found to possess considerable fixity resulting in negative bending moments at the stringer ends and secondary stresses in the connection angles and the rivets.

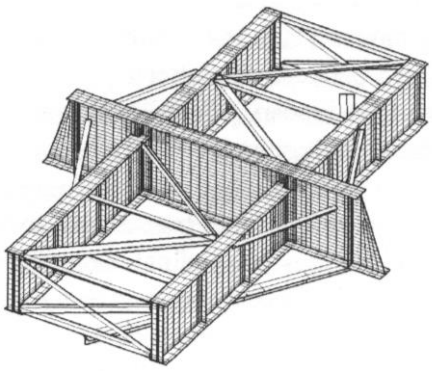

Figure 2.7 – 3-D finite element model developed by Al-Emrani *et al.* [55].

Lemonis and Gantes [56] developed a two-dimensional analytical model for T-stub bolted steel connections. In their work, the authors modelled the T-stub as a continuous beam and the bolts as springs and used classical beam theory in order to derive the load *versus* displacement behaviour of the connection.

An analytical model for estimating the initial stiffness as well as the bending and rotation capacities of beam-to-girder bolted connections was developed by Oliveira and Batista [57]. The main components that contribute to joint deformation were modelled by translational springs. Contributions from bolts in tension, bolts in shear, angles in bending, web angles in bearing and beam web in bearing were taken into account. The analytically derived initial rotational stiffness was found to agree well with experimental results.

Imam [58] built a global FE model of a bridge module composed of stringer-to-cross-girder connections, using shell elements (Figures 2.8). The individual members (I-sections) were tied to each other at the locations of the connections, a condition which corresponds to fully fixed connections. A local solid FE model was built in order to model the riveted connection at the stringer-to-cross-girder connection shown in Figure 2.8. The shell-to-solid interface was considered in order to allow the transition from the 8-noded shell elements away from the connection to the 8-noded brick elements. The bridge is loaded with the BS5400 train No. 7 which has a maximum axle load of 25 t. The axle loads are applied directly to the top flange of the stringers neglecting any load spread due to the rails and sleepers. The self-weight of the bridge members and the superimposed dead load due to the sleepers and rails are also taken into account in the global-local FE model. The loads are quasi-statically applied and dynamic amplification is not considered. Several fatigue damage scenarios were investigated using among others the recently developed theory of critical distances [59] for the fatigue assessment of notched components.

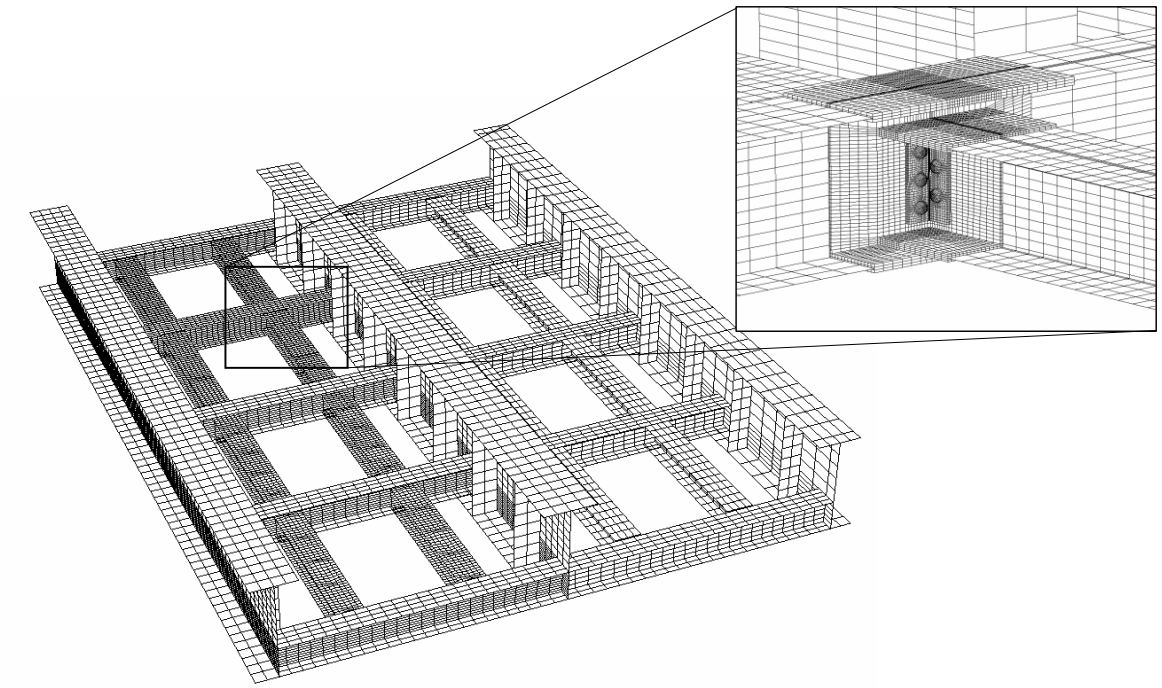

Figure 2. 8 – Global-local FE models of a riveted bridge module proposed by Imam [58].

Pantoli *et al.* [60] presented a finite element model of a bridge (Figure 2.9) which was calibrated using available dynamic experimental data (first natural frequencies and mode shapes) [61]. Then, the actual fatigue loading spectrum was evaluated taking the actual traffic flows into account. Train transit on the bridge was simulated in order to find the structural elements where local vibrations can be significant. Different numbers of trains on the bridge are considered in order to define the load combinations giving the most significant effect in terms of local vibrations. After having identified the members potentially subject to local vibrations, a substructure finite element model is studied for the detail. Starting from the stresses obtained in the detailed FE model, the crack growth is studied using Paris's relationship.

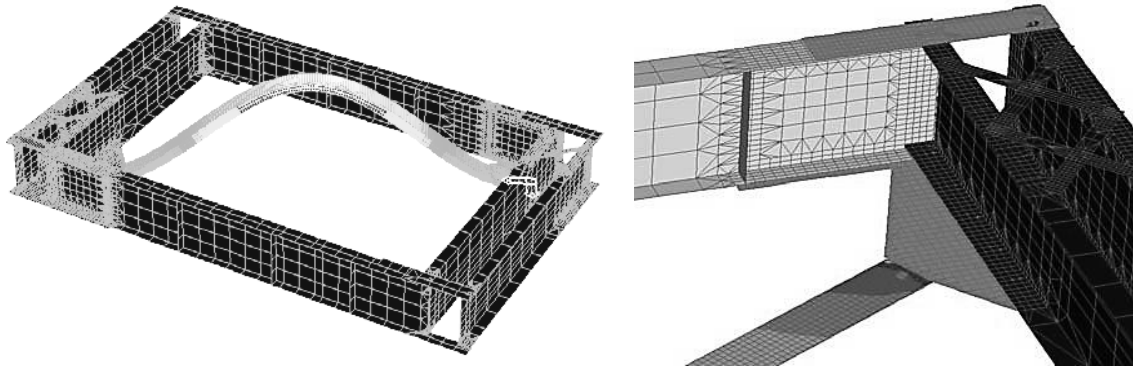

a) b)

Figure 2. 9 – FE model of the substructure elements from the local analysis proposed by Pantoli *et al.* [60].

The effect of un-bonded carbon fibre reinforced polymer post-tensioning retrofit system on the fatigue vulnerability of an existing bridge in Münchenstein, Switzerland, is explored by E. Ghafoori *et al.* [62]. Finite elements models were considered (Figure 2.10) in order to determine critical fatigue locations and to investigate the relative effects of the post-tensioning retrofit on these locations. Fatigue analyses with and without the retrofit are considered. Submodeling was considered in order to assess this multi-scale problem.

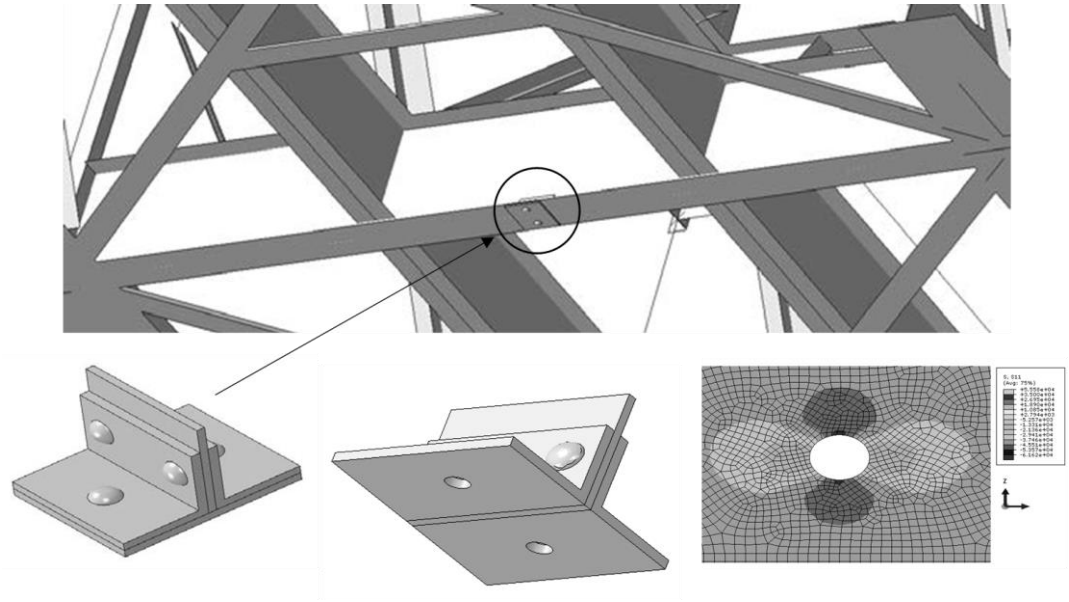

Figure 2.10 – FE model of the substructure elements according Ghafoori *et al.* [62].

Regarding Portuguese research about the fatigue resistance assessment of bridge details, several works were performed in order to model S-N curves of riveted connections. Correia *et al.* [63, 65] presented a numerical and experimental procedure aiming the simulation and validation of S-N curves for an original simple riveted joint from a Portuguese railway bridge (see Figure 2.11). Crack initiation and crack propagation phases were considered. Several parameters such as the evolution of the stress concentration factors with the clamping stress were investigated. Concerning the crack propagation phase, through thickness fatigue cracks were simulated emanating from rivet holes.

Correia *et al.* [65] has also investigated the single riveted joint presented in [63], using both solid and shell finite elements (Figure 2.12). The second modelling approach may be convenient if a reduction in computation effort is required. Several numerical parameters were investigated such the friction coefficient, the clamping stress, the stress concentration factor, the normal penalty stiffness factor (FKN) and the penetration tolerance (FTOLN).

Jesus *et al.* [64] presented the results of an experimental program aiming the evaluation of the fatigue behaviour of two types of joints (single and double shear) with preloaded resin-injected bolts. Results are compared with test data obtained with standard preloaded bolts, revealing a systematic fatigue strength reduction when preloaded resin-injected bolts were used.

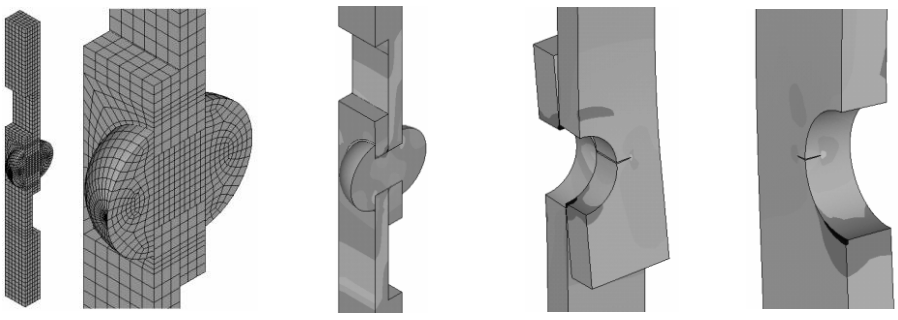

Figure 2.11 – FE model of a single rivet connection from the Trezói railway bridge proposed by Correia *et al.* [65].

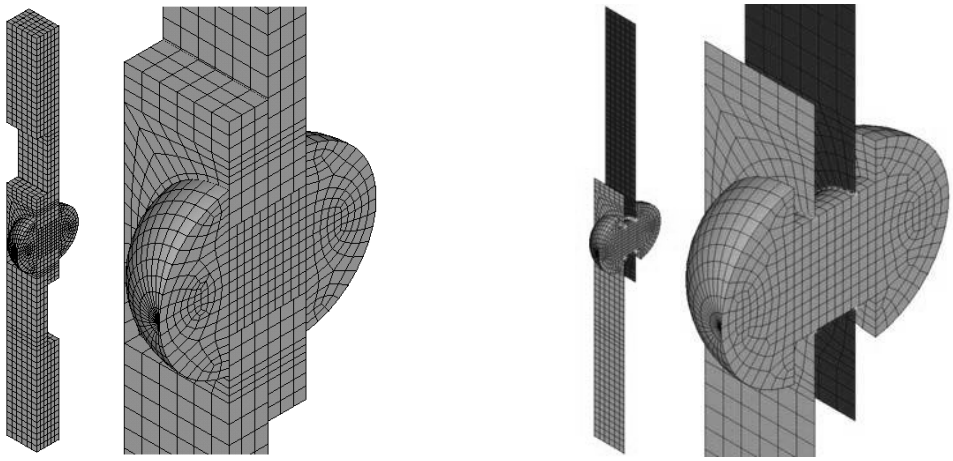

a) b)

Figure 2.12 – Finite element models of a single riveted connection: a) Solid finite element models; b) Shell finite element model (Correia *et al.* [65]).

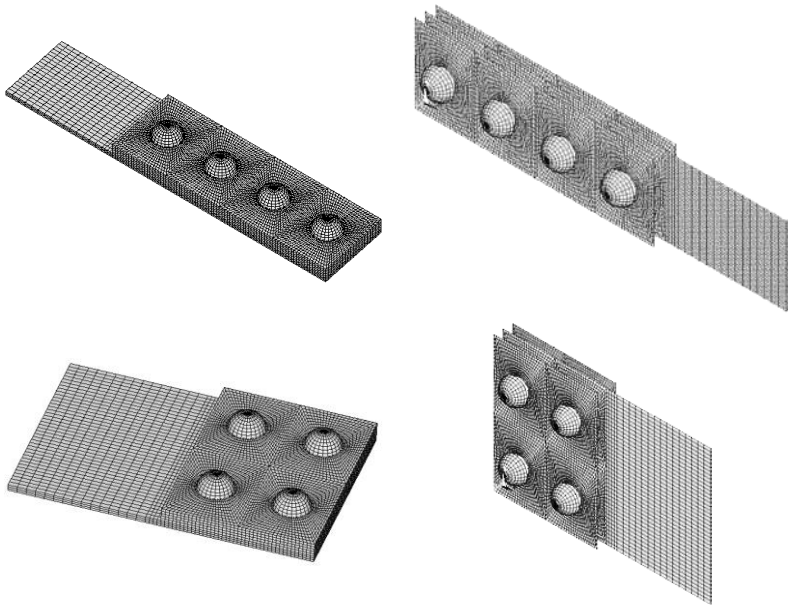

a) b)

Figure 2.13 – Finite element models of a multiple rivets connections: a) solid finite element models; b) shell finite element models (Rodrigues *et al.* [66]).

Connections with multiple rivets were investigated by Rodrigues *et al.* [66] (Figure 2.13). The author also proposes a comparison of two alternative finite element modelling strategies for riveted connections, which may be used for fatigue assessments. In the first approach, the plates of the connection are modelled using finite solid elements; the second approach uses finite shell elements. Based on proposed finite element models, some riveted connections are analysed to assess the local stresses, namely the elastic stress concentration factors for uncracked geometries and the stress intensity factors,

for cracked geometries. The stress intensity factors are evaluated using the virtual crack closure technique (VCCT technique) (Krueger [67]). The effects of friction and clamping stresses on rivets are accounted in the models.

2.4. OVERVIEW OF EXISTING RESEARCH ON WELDED MEMBERS AND CONNECTIONS

The research on fatigue behaviour of welded details for generic applications is too wide to be covered in this section. Therefore this section presents a selection of research works performed on welded members and connections for applications in bridge structures.

Frýba [68] investigated the fatigue properties of orthotropic decks of steel railway bridges with open ribs. Being fully welded, the orthotropic decks are sensitive to fatigue. Fatigue tests were carried out on several series of specimens (see Figure 2.14). The shape of cut-outs in the web of the cross-girder, the effect of shear forces and the weld penetration appeared to be very important factors influencing the fatigue behaviour.

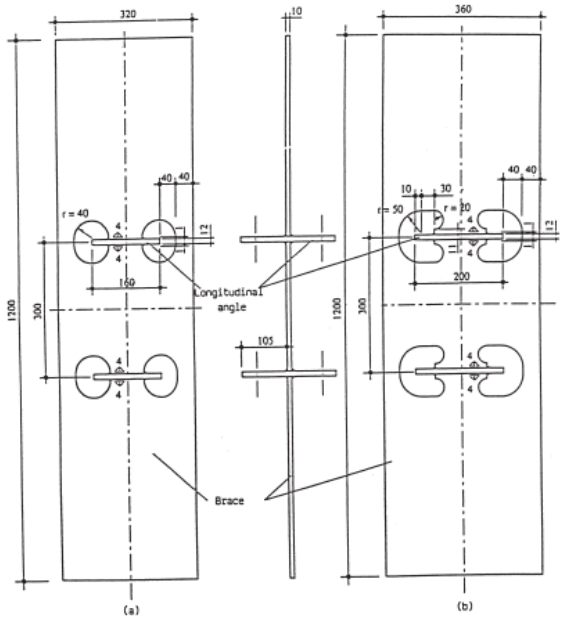

Figure 2.14 – Small ICOM specimens tested by Frýba [68]: a) specimen with circular cut-outs; b) specimens with cut-outs with apple form.

Clubley *et al.* [69] presented the consequences of a fatigue analysis on the structural integrity of the River Mardle Viaduct. The River Mardle Viaduct is a curved, twin box girder bridge, spanning a total length of 177 m. Four continuous spans carry the A38 trunk road over the River Mardle and Old Totnes Road. The bridge forms an important part of the heavy loaded network in and out of the tourist areas of Devon and Cornwall. In September 2001, an initial inspection of the site splice welds joining the box girders detected a series of large imperfections. These weld defects were confirmed by a further independent inspection 6 months later and the results subsequently analysed using detailed fracture mechanics.

Schumacher [70] presented fatigue tests carried out on welded circular hollow section K-joints typical on bridges. The tests specimens were large-scale (approximately 9 m long and 2 m high) trusses loaded in the plane of the truss (see Figure 2.15). Measured member stresses showed that a significant proportion of the load in a truss member may be due to bending, underlining the importance of considering correctly this load case in the design of these structures. Measured hot-spot stresses in the joints were compared with hot-spot stresses calculated using the current design guidelines. The authors found that the measured values are considerably lower than the calculated values, calling into question the applicability of the design guidelines to these types of (bridge) structures. The S-N fatigue results from the current study, on the other hand, showed that the fatigue resistance of the joints that were tested is lower than the corresponding S-N design curves. This means that when the considerably higher calculated hot-spot stress range is applied to the corresponding design curve, the predicted resistance is similar to the resistance predicted using the lower measured hot-spot stresses in combination with the lower measured S-N curve too. This has highlighted the importance of relating hot-spot stresses to the appropriate, corresponding S-N curves. Evidence from the fatigue tests has clearly demonstrated the effect of size on the fatigue strength of welded tubular joints. A comparison of fatigue S–N results from smaller and larger welded circular hollow section joints has shown the same trend indicated in design specifications: a thicker failed member results in lower fatigue strength. The size correction factor integrated into the S-N design curves of the specifications, however, does not seem to represent this significant effect in a fairly manner.

Righiniotis *et al.* [71] considered the application of a probabilistic fracture mechanics approach to predict the fatigue life of welded steel details in the presence of cracks under bridge spectrum loading, based on a recently proposed bi-linear relationship to model fatigue crack growth. The fatigue model incorporates a failure criterion to describe the interaction between fracture and plastic collapse.

Ghahremani *et al.* [72] presented fatigue tests results of needle peened structural steel weld specimens loaded under simulated in-service loading histories typical of highway bridges (see Figure 2.16). A strain-based fracture mechanics model was then validated by comparison with the test results and used to perform additional studies. Similar welds were analysed under loading histories encompassing a wider range of influence lines and bridge spans. Ghahremani *et al.* concluded that the applied model is well suited for studying the effects of peening on the fatigue performance of highway bridge welds under in-service loading conditions. The consideration of tensile dead load stresses and periodic overload trucks is seen to decrease the predicted benefit of peening. This benefit can still be substantial, however, for a wide range of loading conditions likely to occur in highway bridges.

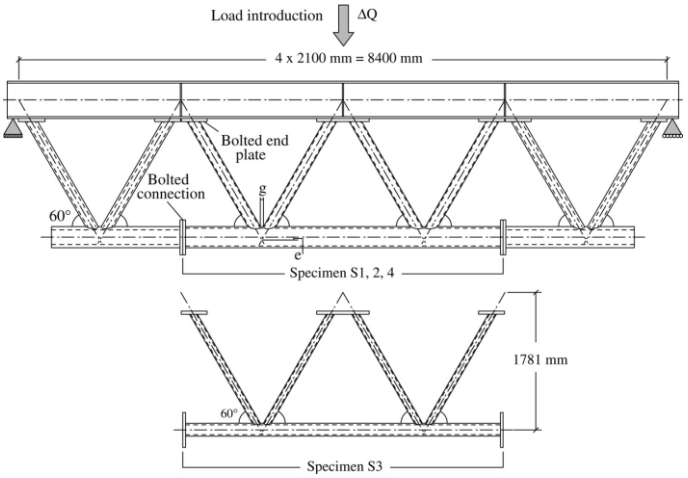

Figure 2.15 –Truss girder tested by Schumacher, general geometric configuration and dimensions [70].

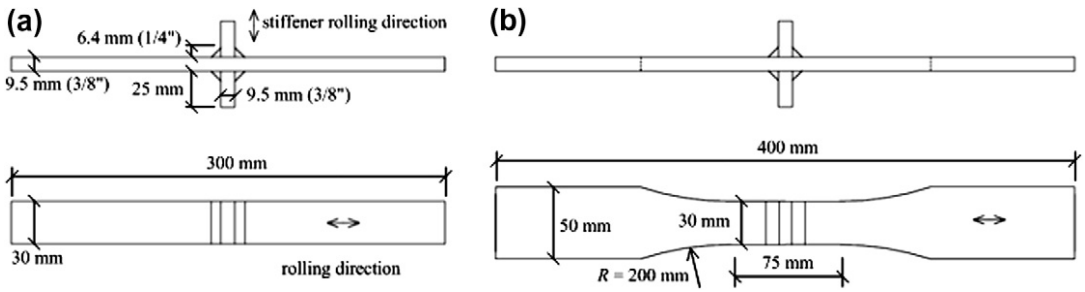

Figure 2.16 – Transverse stiffener specimen geometries tested by Ghahremani *et al.*: a) straight geometry; b) variable width geometry [72].

The transverse distribution of wheel loads in orthotropic decks generates significant out-of-plane bending moments in the deck plate and rib wall at the rib-to-deck joint. Due to the relatively small thickness of both the deck plate and rib wall, the out-of-plane bending moments result in high local flexural stresses causing fatigue cracks to develop at the joints. Xiao *et al.* [73] investigated the transverse stresses within the joint region that arise under the action of wheel loads are investigated using finite element analyses (see Figure 2.17). Based on the stress results and the basic theories of linear elastic fracture mechanics, the design fatigue strength was determined for the investigated joint. Factors affecting the stress range were also studied. The authors reveal that the surface stresses in the deck plate are much larger than those in the rib wall, in the case of 75% weld penetration into the rib wall, indicating that the fatigue strength of the joint is governed by the fatigue cracks propagating into the thickness of deck plate.

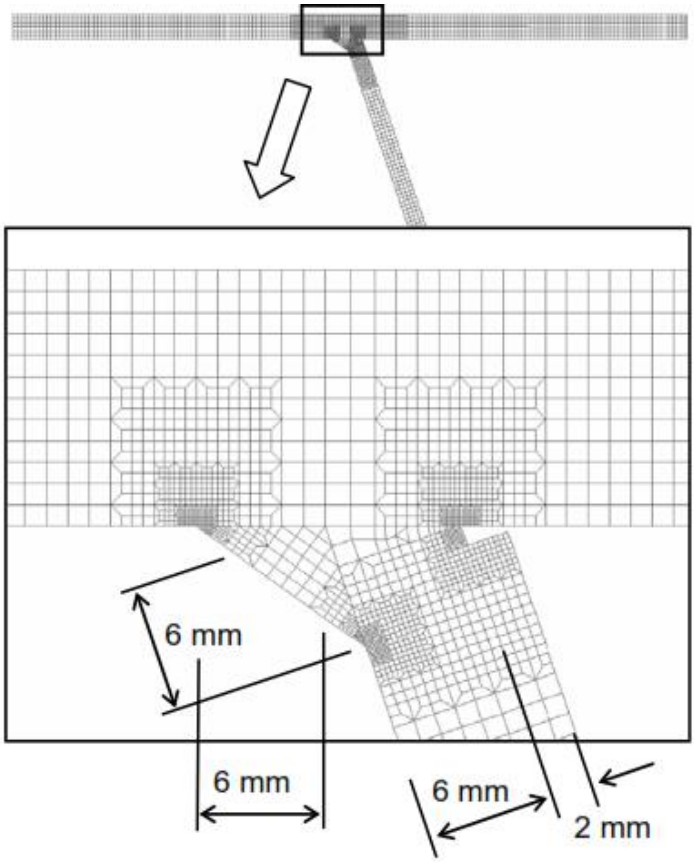

Figure 2.17 – Finite element model of a welded joint investigated by Xiao *et al* [73].

The EC3 is the governing design code for steel structures in Europe. In this design code, the nominal stress method is the predominant approach for fatigue design. However, the limitations of this method along with new advanced computational possibilities, have allowed the way for more accurate stress based fatigue design approaches. The structural hot spot stress (SHSS) and the effective notch stress (ENS) methods are among those which have widely drawn engineers' attention since their advent. These approaches take advantage of new computational modelling possibilities and designate the basic stress by taking into account the geometrical variations of the detail at the expected fatigue crack initiation location (hot spot). As a result, a higher variation of constructional details can be assessed more accurately by these methods. Although the SHSS and ENS approaches have been extensively exploited in other industries, both methods are considered inexperienced in the field of bridge engineering.

Heshmati [74] assessed the fatigue strengths of the welded details using the structural hot spot stress and the effective notch stress methods. Finite elements models were carried out using different modelling techniques mainly based on the well-known IIW modelling instructions (see Figure 2.18). Furthermore, the thickness effects, weld shape and overall member geometry on the computed stress concentration factor were studied and discussed by the author. A large database including available fatigue test was built up and used to produce S-N curves using structural hot spot stress and effective notch stress definitions. The effects of altering the geometric shape of the cope-holes were also investigated using finite element analysis. The fatigue strength enhancement of cope-hole details by means of post-weld treatment is experimentally evaluated by conducting constant amplitude fatigue tests. Based on the test results, a new fatigue strength category for improved cope-hole details is proposed by Heshmati.

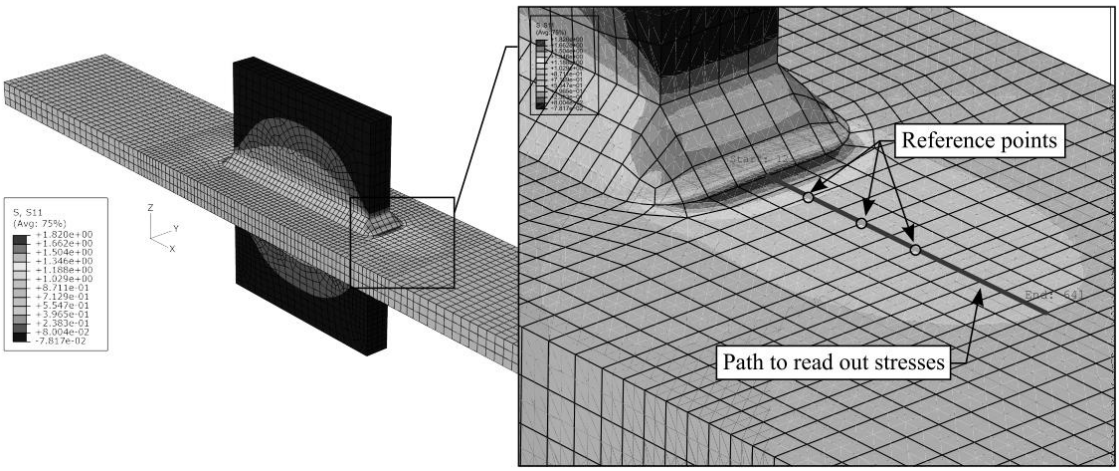

Figure 2.18 – Finite element models of an investigated welded joint by Heshmati [74].

Aygül [75] studied the fatigue life estimation of orthotropic steel bridge decks using the finite element method (see Figure 2.19). The application of the structural hot spot stress approach or the effective notch stress approach to a welded joint with cut-out holes in orthotropic bridge decks was made. Aygül compared the results of the finite element calculations with the results of the fatigue tests which were carried out on full-scale specimens. The results of the finite element analyses revealed that the structural hot spot stresses obtained from the shell element models were unrealistically high when the welds were omitted. The author also underlined that the way in which the welds were represented had a substantial influence on the magnitude of the hot spot stress. The results of the analysis when using the effective notch stress approach showed that the agreement between the estimated fatigue life using this approach and the fatigue life obtained from the fatigue tests was good.

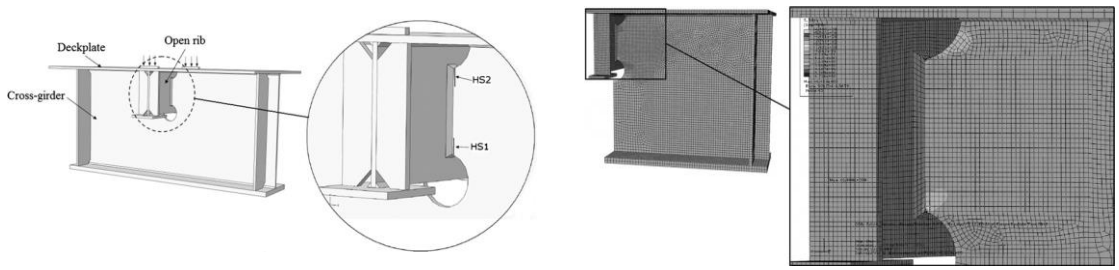

Figure 2.19 – Welded detail investigated by Aygül [75]: a) Fatigue test specimen loading and investigated hot spot points; b) solid element model with an element size of 4 mm.

Taras *et al.* [76] presented an investigation regarding the effects of thickness steps or transitions of weld joints, which are often used in flanges of bridge girders in order to adapt the bending resistance of the cross-sections to variable bending moment distributions. Taras *et al.* [76] focused his work primarily on the stress raising effects for the longitudinal stresses near the butt weld, at the thickness transition.

Klinger *et al.* [77] investigated fatigue cracks on specific steel components and joints of a railway bridge over the Elbe River at Lutherstadt Wittenberg, Germany, due to wind induced vibrations. The authors adopted Fracture Mechanic calculations to assess the remaining service life of the welded joints.

Binhua Wang [78] presents a comparison study of specimens with two types of cut-out holes, namely the circular arc transition configuration and the vertical transition configuration. The fatigue life estimation of specimens was investigated with the application of the structural hot spot stress approach by using finite element analyses (see Figure 2.20). Structural stresses were computed using the Dong method [79]. The author observed that compared with the measured results, the solid element models, both using contact elements and non-contact elements, presented a good estimation of the hot spot stresses. Aiming the simplification, the solid element model with non-contact elements is recommended. The results that were obtained through the shell increased thickness model were not in good agreement with the test result. The Dong's method yielded good results for the investigated points because the calculated stress was obtained from stress distributions obtained using the solid FE analysis.

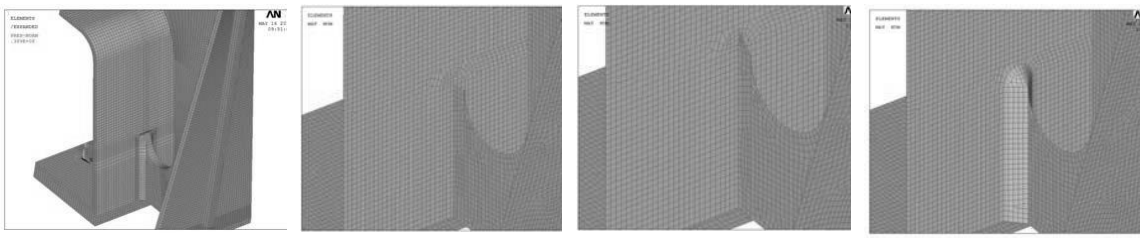

Figure 2.20 – Finite element models of a welded connection investigated in [78].

2.5. CONCLUDING REMARKS

Reliable fatigue assessment of bridge details still is quite a challenging problem involving many complexities, despite much research work being performed and referred in the literature. The previous literature review, despite not fully comprehensive, gave an overview of important works in the field of experimental fatigue testing and numerical simulation of bridge details. Both fields need further developments, but the field of numerical simulation of bridge details (riveted and welded) seems to be the one that needs substantial work in order to provide and demonstrate reliable alternative tools to the conventional blind and over conservative S-N approaches. The development of numerical models in the literature has been presented in the form of non-integrated approaches. The models of the details have been mainly simulated under theoretical well-behaved simplified loading histories in contradiction with the real loading histories originated by actual traffic histories experienced by the bridges.

2.6. REFERENCES

[1] EC3, Eurocode 3, "Design of steel structures. Part 1-9: Fatigue. ENV 1993-1-9", Enevoldsen, I., Pedersen, C., Axhag, F., Johansson, O., and Toyra, B. (2002). Assessment and measurement of the Forsmo bridge, Sweden. Structural Engineering International, 4:254–257, 2005.

[2] Avaliação da Integridade Estrutural de Pontes Metálicas Ferroviárias/ Assessment of the Structural Integrity of Metalic Railway Bridges, POCTI/ECM/57286/2004, FEUP, 2005-2008.

[3] Comportamento à Fadiga de Ligações Rebitadas em Pontes Metálicas Antigas, PTDC/EME-PME/78833/2006, 2007-2010.

[4] Burchi, S., Lippi F., V., Salvatore W., "Design for optimal performance of high-speeed railway bridges by enhanced monitoring systems", European research project details, ISBN 978-88-579-0047-6, 2009.

[5] Lippi, F., Salvatore, W., Braconi, A., Finetto, M., Wenzel, H., De Roeck, G., Peeters, B., Könke, C., Zabel, V., Cunha, A., "Fatigue damage control and assessment for railway bridge", Research Fund for Coal and Steel, Directorate-General for Research and Innovation, Grant Agreement RFSR-CT-2009-00027, 1 July 2009 to 30 June 2012

[6] Lukić, M., Al-Emrani, M., Aygül, M., Bokesjö, Urushadze, M.S., Frýba, L., Škaloud, M., Collin, P., Nilsson, M., Eichler, B., Schillo, N., Wieschollek, M., Imam, B., Righiniotis, T., Kaliyaperumal, G., Pitsolis, A., "Bridge fatigue guidance - meeting sustainable design and assessment", Research Fund for Coal and Steel, ISBN 978-92-79-28958-3, 2013.

[7] Iman, B., "Fatigue analysis of riveted railway bridges", Ph.D. Thesis, School of Engineering, University of Surrey, UK, 2006.

[8] Smith, J.O., "The effect of range of stress on the fatigue strength of metals", Engineering Experimental Station Bulletin, University of Illinois, p. 481, 1942.

[9] Skorupa, M., "Load interaction effects during fatigue crack growth under variable amplitude loading - A literature review. part I: Empirical trends", Fatigue and Fracture of Engineering Materials and Structures 21(8), pp.987–1006, 1998.

[10] Gurney, T.R., "Fatigue of Welded Structures", Cambridge University Press, second edition, 1979.

[11] Irwin, G.R., "Analysis of stresses and strains near the end of a crack traversing a plate", Transactions of the ASME, Journal of Applied Mechanics 24, pp.361–364, 1957.

[12] Murakami, Y. "Stress Intensity Factors Handbook, volume 1". Pergamon Press. Oxford, UK, 1987.

[13] Tada, H., Paris, P. C., Irwin, G.R., "The Stress Analysis of Cracks Handbook", ASME, 2000.

[14] Paris, P., Erdogan, F., "A critical analysis of crack propagation laws", Journal of Basic Engineering 85, pp. 528-534, 1963.

[15] Fatemi, A., Yang, L., "Cumulative fatigue damage and life prediction theories: A survey of the state of the art for homogeneous materials" International Journal of Fatigue 20(1),pp.9–34, 1998.

[16] Skorupa, M., "Load interaction effects during fatigue crack growth under variable amplitude loading - A literature review. part I: Empirical trends", Fatigue and Fracture of Engineering Materials and Structures 21(8), pp.987–1006, 1998.

[17] Miner, M. A., "Cumulative damage in fatigue", Journal of Applied Mechanics 12, pp.159–164, 1945.

[18] Socie, D.F., Marquis, G. B., "Multiaxial Fatigue", Society of Automotive Engineers (SAE International). USA, 2000.

[19] Das, J., Sivakumar, S. M., "An evaluation of multiaxial fatigue life assessment methods for engineering components", International Journal of Pressure Vessels and Piping 76(10), pp.741–746, 1999.

[20] Garud, Y. S. "Multiaxial fatigue: A survey of the state of the art", Journal of Testing and Evaluation 9(3), pp.165–178, 1981.

[21] You, B. R., Lee, S.B. "A critical review on multiaxial fatigue assessment of metals", International Journal of Fatigue 18(4), pp.235–244, 1996.

[22] Tipton, S.M., Nelson, D.V., "Advances in multiaxial fatigue life prediction for components with stress concentrations", International Journal of Fatigue 19(6), pp.503–515, 1997.

[23] Sonsino, C.M., "Multiaxial fatigue of welded joints under in-phase and out of-phase local strains and stresses", International Journal of Fatigue 17(1), pp.55–70, 1995.

[24] Bannantine, J.A., Socie, D.F., "A multiaxial fatigue life estimation technique", In Mitchell, M. R. and Landgraf, R. W., editors, Advances in Fatigue Lifetime Predictive Techniques, ASTM STP 1122, American Society for Testing and Materials. Philadelphia, pp.249–275.

[25] Wang, C.H., Brown, M.W., "Life prediction techniques for variable amplitude multiaxial fatigue - Part 1: Theories", Journal of Engineering Materials and Technology, 118, pp.367–370, 1996.

[26] Weber, B., Carmet, A., Kenmeugne, B., "A stress-based approach for fatigue assessment under multiaxial variable amplitude loading", In Proceedings of the 5th

International Conference on Biaxial/Multiaxial Fatigue and Fracture, Cracow, Poland, pp. 218–231, 1997.

[27] Carpinteri, A., Spagnoli, A., Vantadori, S., "A multiaxial fatigue criterion for random loading", Fatigue and Fracture of Engineering Materials and Structures 26(6), pp.515–522, 2003.

[28] Langlais, T.E., Vogel, J.H., Chase, T.R., "Multiaxial cycle counting for critical plane methods. International Journal of Fatigue, 25(7):641–647, 2003.

[29] BS5400, "Steel, concrete and composite bridges: Part 10 : Code of practice for fatigue", British Standards Institute, London, 1980.

[30] AASHTO, "Standard specifications for highway bridges. Technical report", American Association of State Highway Traffic Officials (AASHTO). Washington D.C, 1977.

[31] AREA, "Manual for railway engineering", American Railway Engineering Association (AREA). Washington D. C, 1996.

[32] Railtrack, RT/CE/C/025, "Railtrack line code of practice: The structural assessment of underbridges", Railtrack, 2001.

[33] Kühn, B., Lukić, M., Nussbaumer, A, Günther, H.P., Helmerich, R., Herion, S., Kolstein ,M.H., Walbridge, S., Androic, B., Dijkstra, O., Bucak, Ö., "Assessment of Existing Steel Structures: Recommendations for Estimation of Remaining Fatigue Life - EUR 23252 EN", Sedlacek G, Bijlaard F, Géradin M, Pinto A and Dimova S (eds.), JRC – ECCS, Fist edition, 2008.

[34] Taras, A., Greiner, R., "Statistical Background to the Proposed Fatigue Class Catalogue for Riveted Components. Report: Contribution to WG6.1 – Assessment of Existing Steel Structures", ECCS TC6 – 2010, Spring Meeting – Lausanne – March 22-23, 2010.

[35] Hobbacher, A., "Fatigue Design of Welded Joints and Components", XIII-1539-96/XV-845-96 doc., International Institute of Welding: Cambridge, England, 1996.

[36] Olofsson, I., Elfgren, L., "Sustainable Bridges-Assessment for Future Traffic Demands and Longer Lives", Taylor & Francis: Oxford, UK, p. 369, 2004.

[37] Haghani, R., Al-Emrani, M., Heshmati, M., "Fatigue-Prone Details in Steel Bridges", Buildings, 2, 456-476; doi:10.3390/buildings2040456, 2012

[38] Bruhwiler, E., Smith, I.F.C., Hirt, M.A., "Fatigue and fracture of riveted bridge members", Journal of Structural Engineering (ASCE) 116(1), pp.198–214, 1990.

[39] Adamson, D.E., Kulak, G.L., "Fatigue tests of riveted bridge girders", Structural Engineering Report No 210. Department of Civil Engineering, University of Alberta, Edmonton, Canada, 1995.

[40] Helmerich, R., Brandes, K., Herter, J., "Full scale laboratory fatigue tests on riveted steel bridges", In Report of IABSE Workshop, Lausanne : Evaluation of Existing Steel and Composite Bridges, Zurich, pp. 191–200, 1997.

[41] DiBattista, J.D., Adamson D.E.J., Kulak G.L., "Evaluation of remaining fatigue life for riveted truss bridges", Canadian Journal of Civil Engineering, Vol. 25, No.4, pp. 678-691, 1998.

[42] Out, J.M.M., Fisher, J.W., Yen, B.T., "Fatigue strength of weathered and deteriorated riveted members", Transportation Research Record, Transportation Research Board, Washington D.C, pp.950:10–20, 1984.

[43] Zhou, Y.E., Yen, B.T., Fisher, J.W., and Sweeney, R.A.P., "Examination of fatigue strength (Sr-N) curves for riveted bridge members", In Proceedings of the 12th Annual Bridge Conference, Engineer's Society of Western Pennsylvania. Pittsburgh, PA, pp. 102–109, 1995.

[44] Abouelmaaty, W., Maragakis, E., Itani, A., and Douglas, B., "Fatigue testing of double-angle connections of steel railroad bridges", Transportation Research Record, Transportation Research Board, Washington D.C 1688, pp. 46–52, 1999.

[45] Al-Emrani, M., "Fatigue in riveted railway bridges – a study of the fatigue performance of riveted stringers and stringer-floor-beam connections", Ph.D. Thesis, Department of Structural Engineering, Chalmers University of Technology, Goteborg, Sweden, 2002.

[46] Kühn, B., "Assessment of existing steel structures - Recommendations for estimation of the remaining fatigue life", 5th Fatigue Design Conference, Fatigue Design, Procedia Engineering 66, pp.3 – 11, 2013.

[47] Mackerle, J., "Finite element analysis of fastening and joining: A bibliography (1990-2002)", International Journal of Pressure Vessels and Piping, 80(4), pp.253–271, 2003.

[48] Al-Emrani, M., Crocetti, R., Akesson, B., Edlund, B., "Fatigue damage retrofitting of riveted steel bridges using stop-holes". In Makelainen, P. and Hassinen, P., editors, 4th International Conference on Light-Weight Steel and Aluminium Structures, Espoo, Finland, pp.223–230, 1999.

[49] Wilson, W.M., Coombe, J.V., "Fatigue tests of connection angles", Engineering Experiment Station Bulletin, University of Illinois, p. 317, 1939.

[50] Paasch, R.K., DePiero, A.H., "Fatigue Crack Modeling in Bridge Deck Connection Details, Final Report SPR 380, Oregon Department of Transportation, 1999.

[51] DePiero, A.H., Paasch, R.K., Lovejoy, S.C., "Finite-element modeling of bridge deck connections details", Journal of Bridge Engineering. 7, No. 4, pp. 229-235, 2002.

[52] Roeder, C. W., MacRae, G. A., Kalogiros, A. Y., and Leland, A. "Fatigue cracking of riveted, coped, stringer-to-floorbeam connections, Research report WA- RD 494.1", Washington State Department of Transportation, 2001.

[53] Lee, S. S. and Moon, T. S., "Moment-rotation model of semi-rigid connections with angles. Engineering Structures 24(2), pp.227–237, 2002.

[54] Al-Emrani, M., Kliger, R., "FE analysis of stringer-to-floor-beam connections in riveted railway bridges", Journal of Constructional Steel Research 59(7), pp.803– 818, 2003.

[55] Al-Emrani, M., Akesson, B., Kliger, R., "Overlooked secondary effects in open-deck truss bridges", Structural Engineering International 4, pp.307–312, 2004.

[56] Lemonis, M., Gantes, C., "An analytical elastic-plastic model for T-stub steel connections", In Hoffmeister, B. and Hechler, O., editors, Proceedings of the 4th European Conference on Steel and Composite Structures, Eurosteel 2005, volume C, Maastricht, The Netherlands, pp. 41–48,2005.

[57] Oliveira, T., Batista, E., "Experimental analysis of composite semi-rigid beam-to-girder connections", In Hoffmeister, B. and Hechler, O., editors, Proceedings of the 4th European Conference on Steel and Composite Structures, Eurosteel 2005, volume C, Maastricht, The Netherlands, pp.107–114, 2005.

[59] Imam, B.M, Chryssanthopoulos, M.K., Frangopol, D.M., "System effects on the fatigue reliability of deteriorating riveted railway bridges", Structural safety and reliability; Safety, reliability and risk of structures, infrastructures and engineering systems; ICOSSAR2009 International Conference; 10th, Structural safety and reliability;

Safety, reliability and risk of structures, infrastructures and engineering systems; ICOSSAR2009;p. 545, 2010.

[59] Taylor, D., Wang, G,. "The validation of some methods of notch fatigue analysis", Fatigue and Fracture of Engineering Materials and Structures 23(5), pp. 387-394, 2000.

[60] Pantoli, E., Vincenzi, L., Savoia, M., Testa, R., "The effect of local vibrations on fatigue in old steel riveted bridges. A case study: the Manhattan Bridge", Proceedings of the 8th International Conference on Structural Dynamics, EURODYN, Leuven, Belgium, 4-6 July 2011

[61] Mayer, L., Yanev, B., Olson, L.D., Smyth, A., "Monitoring of the Manhattan Bridge for Vertical and Torsional Performance with GPS and Interferometric Radar Systems", Transportation Research Board 89th Annual Meeting, 2010.

[62] Ghafoori, E., Prinz, G.S., Mayor, E., Nussbaumer, A., Herwig, M.M.A., Fontana, M., "Finite Element Analysis for Fatigue Damage Reduction in Metallic Riveted Bridges Using Pre-Stressed CFRP Plates", doi:10.3390/polym6041096, Polymers 6, pp.1096-1118, 2014.

[63] José, A.F.O.C., Jesus A.M.P., Figueiredo, M.A.V., Ribeiro, A.S., Fernandes, A.A., "Fatigue Assessment of Riveted Railway Bridge Connections. Part I: Experimental Investigations", 7th International Conference on Steel Bridges, Guimarães, Portugal, 4-6 June 2008.

[64] Jesus, A.M.P., Silva, J.F.N., Figueiredo, M.A.V., Ribeiro, A.S., Fernandes, A.A., José, A.F.O.C., Silva, A.L.L., Maeiro, J.M.C., "Fatigue Behaviour of Resin-Injected Bolts: An Experimental Approach", berian Conference on Fracture and Structural Integrity 2010 - CIFIE'2010, FEUP, Porto, Portugal, 2010.

[65] Correia, J.A.F.O., Jesus, A.M.P. Silva, A.L.L., "Simulação por Elementos Finitos de Curvas S-N de Ligações Rebitadas", 8º Congresso Nacional de Mecânica Experimental – APAET 2010, Univ. Minho, Guimarães, 21-23 Abril, 2010

[66] Rodrigues, M.P.G., Jesus, A.M.P., Silva, A.L.L., "Comparison Between Alternative FE Modelling Strategies for Riveted Connections Concerning Fatigue Assessments", 8º Congresso Nacional de Mecânica Experimental Guimarães, 21-23 de Abril, 2010.

[67] Krueger, R., "Virtual crack closure technique: History, approach, and applications", Applied Mechanics Reviews, p. 109-143, 2004.

[68] Frýba, L., Gajdoš, L.,"Fatigue properties of orthotropic decks on railway bridges", Engineering Structures 21, pp. 639–652, 1999.

[69] Simon, K., Clubley, Stephen N., "On the fatigue and fracture of site splice welds at the River Mardle Viaduct", Engineering Failure Analysis 10, pp. 593–604, 2003

[70] Schumacher, A., Nussbaumer, A., "Experimental study on the fatigue behaviour of welded tubular K-joints for bridges", Engineering Structures 28, pp. 745–755, 2006.

[71] Righiniotis, T. D., Chryssanthopoulos, M.K., "Fatigue and fracture simulation of welded bridge details through a bi-linear crack growth law", Structural Safety 26, pp. 141–158, 2004.

[72] Ghahremani, K., Walbridge, S., "Fatigue testing and analysis of peened highway bridge welds under in-service variable amplitude loading conditions", International Journal of Fatigue 33, pp. 300–312, 2011.

[73] Xiao, Z.G., Yamada, K., Samol, Y., Zhao, X.L., "Stress analyses and fatigue evaluation of rib-to-deck joints in steel orthotropic decks", International Journal of Fatigue 30, pp. 1387–1397, 2008.

[74] Heshmati, M., "Fatigue Life Assessment of Bridge Details Using Finite Element Method", Master's thesis in the Master's Programme Structural Engineering and Building Performance Design, Department of Civil and Environmental Engineering Division of Structural Engineering Steel and Timber Structures CHALMERS UNIVERSITY OF TECHNOLOGY Gothenburg, Sweden 2012

[75] Aygül, M., Al-Emrani, M., Urushadze, S., "Modelling and fatigue life assessment of orthotropic bridge deck details using FEM", International Journal of Fatigue 40, pp. 129–142, 2010

[76] Taras, A., Unterweger, H., "Proposal for a stress modification factor for the fatigue design of flange thickness transitions in welded girders", Engineering Structures 56, pp. 1758–1774, 2013.

[77] Klinger, C., Michael, T., Bettge,D., "Fatigue cracks in railway bridge hangers due to wind induced vibrations – Failure analysis, measures and remaining service life estimation, Engineering Failure Analysis, 2014.

[78] Wang, B., Lu, P., Shao, Y., "Fatigue Test and Simulation Research of Rib-to-Diaphragm Welded Connection", Journal of Convergence Information Technology (JCIT) Volume8, Number9, May 2013

[79] Dong, P., "A Structural Stress Definition and Numerical Implementation for Fatigue Analysis of Welded Joints", International Journal of Fatigue 23, pp. 865-876, 2001

Chapter III

Fatigue characterization of structural steels

3.1. INTRODUCTION

This chapter presents an experimental campaign that was carried out in order to characterize the fatigue behaviour of two current structural steels. The investigated materials were used in the production of welded and riveted joints fatigue tested within this research, the respective results being presented in Chapter IV. The materials under consideration are the S355 and S235 structural steels, which were used respectively in the manufacturing of welded and riveted joints. Concerning the riveted joints, the number of cycles required to initiate a crack may be significant, when compared with the total fatigue life of the structural component. In order to be able to appropriately characterize the crack initiation behaviour, strain-controlled fatigue tests were performed on smooth specimens according to the ASTM E606 [1] standard. These tests were performed for both structural steels. Classically, fatigue behaviour of welded joints is understood as a process of fatigue crack propagation. It is assumed that welded joints show intrinsic defects whose cyclic growth controls the fatigue life of the welded component. Fracture Mechanics is commonly used to model the fatigue crack propagation, allowing the assessment of the failure life of the component. In order to facilitate the application of the Fracture Mechanics to the assessment of the crack propagation fatigue live of structural components, fatigue crack propagation tests were carried out according to the ASTM E647 standard [2], on the referred structural streels, in order to allow the derivation of the fatigue crack growth rates. Besides the pure mode I fatigue crack propagation tests, mixed mode (I+II) fatigue crack propagation tests were also performed for the S235 material. This kind of fatigue data is very important, since for real details the mode mixity is very common. The results analysis for the mixed mode fatigue crack propagation tests was performed using Digital Image Correlation (DIC). DIC was used for assessing both the crack path as well as the stress intensity factors.

3.2. MICROSTRUCTURES OF THE S355 AND S235 STRUCTURAL STEELS

The Figure 3.1 presents the microstructures of the S355 and S235 structural steels. The observations were performed using an optical microscope on previously polished and etched surfaces. Several magnifications were considered: 200x (Figure 3.1a) and b)), 500x (Figure 3.1c) and d)) and 100x (Figure 3.1e) and f)) for both S355 and S235 steels. A global analysis of Figure 3.1 allows the following considerations:

i) Both materials show an aligned grain microstructure which results from the rolling process;

ii) Both materials show a ferrite/perlite microstructure with is typical of carbon steels;

iii) The S355 steel shows higher perlite zones which results from higher carbon content;

iv) The S355 steel exhibits smaller grain sizes than the S235 steel.

3.3. ASSESSMENT OF CYCLIC ELASTOPLASTIC AND FATIGUE BEHAVIOURS OF THE S355 AND S235 STRUCTURAL STEELS

This section presents a cyclic elastoplastic characterization of the S355 and S235 structural steels. Strain-controlled cyclic tests were performed for both materials using smooth specimens, following the recommendations of the ASTM E606 standard [1]. Besides the fatigue behaviour, these tests allowed the assessment of the cyclic elastoplatic behaviours of the structural steels under consideration. All specimens were tested under strain control, with null strain R-ratio (R_ε=0.0), on a servo-hydraulic machine rated to 100kN (see Figure 3.2a)). Test frequencies ranged between 0.4 and 1.6Hz, depending on the strain ranges applied to the specimens. An average strain rate of 0.8 %/s was kept constant in the test programme. The strain control was guaranteed by means of a clip gauge with a maximum displacement of ±2.5mm, as shown in Figure 3.2b).

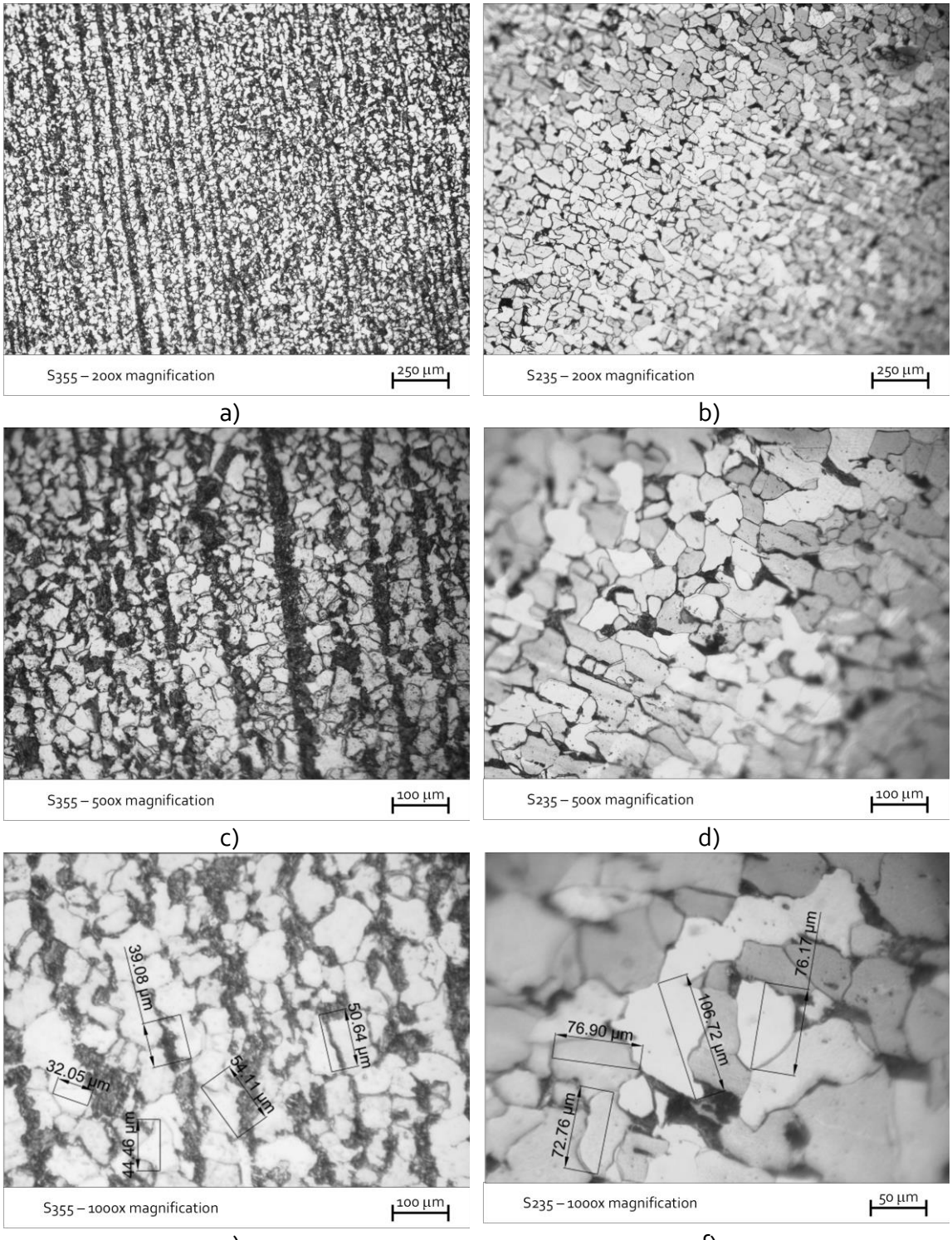

Figure 3.1 – Typical microstructures of the S355 and S235 structural steels: a) S355, 200x magnification; b) S235, 200x magnification; c) S355, 500x magnification; d) S235, 500x magnification; e) S355, 1000x magnification; f) S235, 1000x magnification.

a) b)

Figure 3.2 - Experimental setup: a) INSTRON 8801 servo-hydraulic machine; b) INSTRON clip gauge, model 2670-602.

3.3.1. Cyclic elastoplastic behaviour of the S355 steel

Concerning the S355 structural steel, a total of 13 smooth plane specimens were tested under strain-controlled conditions, according to the programme depicted in Table 3.1. This table includes the central section (gauge) dimensions, for each specimen. Figure 3.3a) shows the nominal dimensions of the flat dog-bone specimens and Figure 3.3b) exhibits a photo of such specimens. All specimens were manufactured from undamaged base material removed from a remote part of the welded specimens that will be presented in the next chapter.

Figure 3.4 presents the stabilized cyclic stress–strain hysteresis loops obtained for the S355 steel. Some relative scatter is observed in the Figure 3.4, mainly when the amount of cyclic plasticity decreases. These hysteresis loops allow the assessment of the Masing behaviour of the material [3]. The Masing behaviour is observed when the upper branches of the hysteresis loops are coincident. For a material obeying the Masing behaviour, the cyclic curve of the material may be used to describe the shape of the hysteresis loops.

Concerning the S355 steel, some degree of deviation from the Masing behaviour is observed. The material may be then characterized as a non-Masing material. The hysteresis loops presented in Figure 3.4 were determined using a half-life criterion. This criterion may coincide with a cyclic stabilized behaviour criterion, for those tests that showed stabilization. However, for this material some tests did not show cyclic stabilization and, therefore, this criterion represented a pseudo-stabilized behaviour. The evolution of the stress amplitude with the number of cycles is plotted in Figure 3.5, for the S355 steel. No clear stabilization of the cyclic behaviour is observed for the S355 steel grade. For the highest tested strain ranges, the material suffers some hardening after initial softening. In this case, the global response may be considered coarsely stable. For lower strain ranges, the material tends to soften. Some specimens experienced accentuated cyclic softening, showing an uncharacteristic cyclic behaviour.

Table 3.1 - Fatigue experimental program of smooth plane specimens made of S355 steel.

Specimens	$L1$	$L2$	S_t	R_ε	$\Delta\varepsilon$	$d\varepsilon/dt$	f
	[mm]	[mm]	[mm]	[-]	[%]	[%/s]	[Hz]
S355-200-01	6.19	5.03	31.14	0.01	1.00	0.80	0.40
S355-100-01	6.18	5.04	31.15	0.01	1.00	0.80	0.40
S355-200-02	6.13	5.03	30.83	0.01	2.00	0.80	0.20
S355-100-02	6.12	5.04	30.84	0.01	2.00	0.80	0.20
S355-0.50-01	6.15	5.04	31.00	0.01	0.50	0.80	0.80
S355-0.50-02	6.12	5.04	30.84	-0.01	0.50	0.80	0.80
S355-0.40-01	6.08	5.04	30.64	0.01	0.40	0.80	1.00
S355-0.40-02	6.07	5.04	30.59	0.01	0.40	0.80	1.00
S355-0.30-01	6.07	5.10	30.96	0.01	0.30	0.80	1.33
S355-0.30-02	6.21	5.04	31.30	0.01	0.40	0.80	1.00
S355-0.25-01	6.18	5.04	31.15	0.01	0.30	0.80	1.33
S355-0.75-01	6.10	5.04	30.74	0.01	0.25	0.80	1.60
S355-0.75-02	6.19	5.04	31.20	0.01	0.25	0.80	1.60

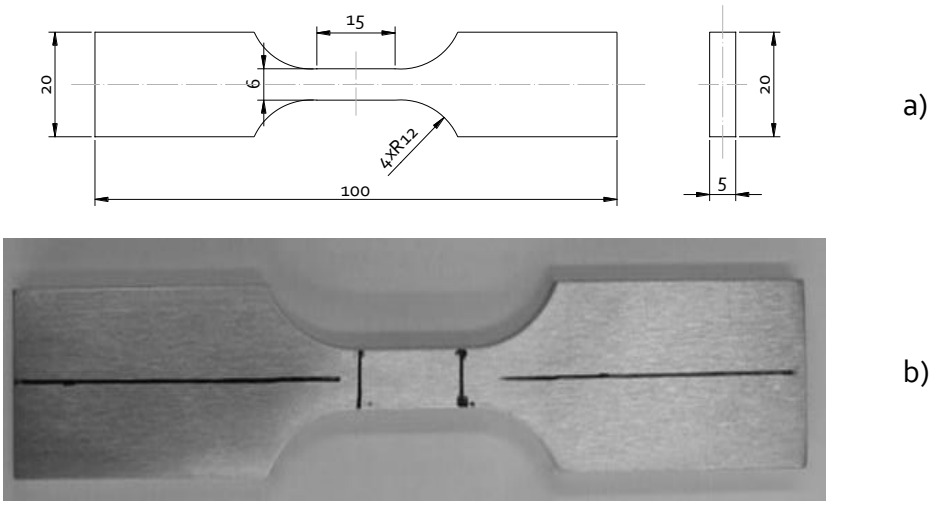

Figure 3.3 - Smooth plane fatigue specimen (S355 steel): a) dimension in mm; b) photo of a smooth plane specimen.

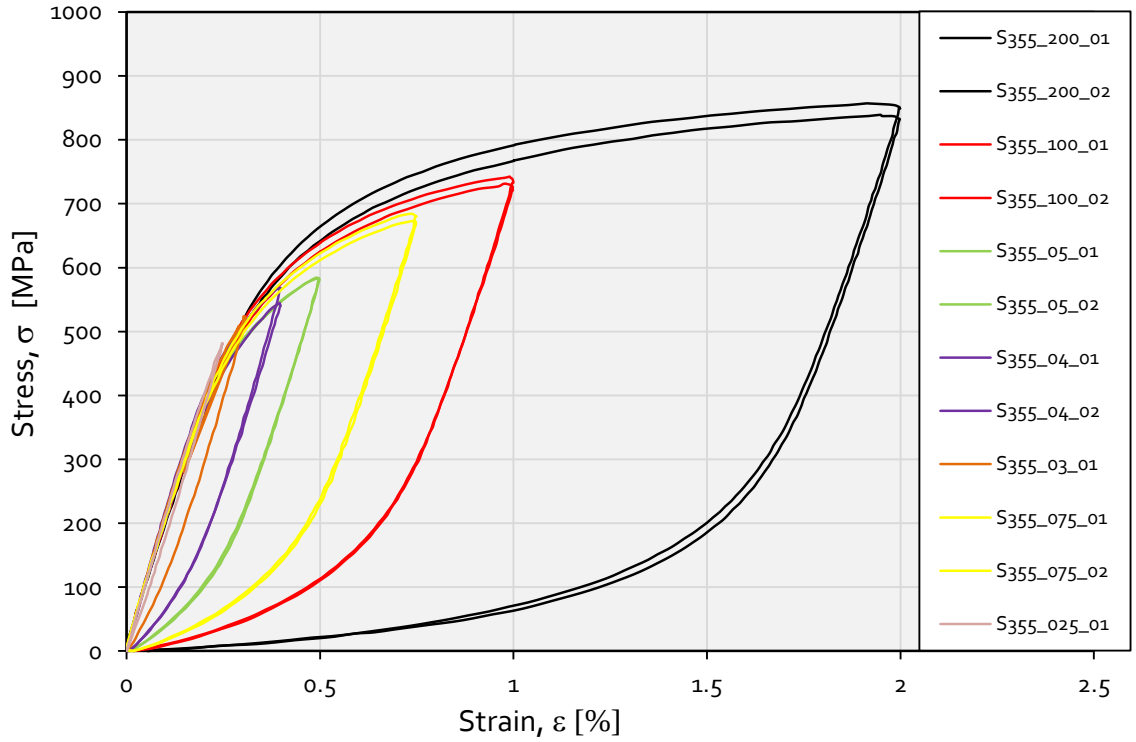

Figure 3.4 - Stabilized stress–strain hysteresis loops (S355 steel).

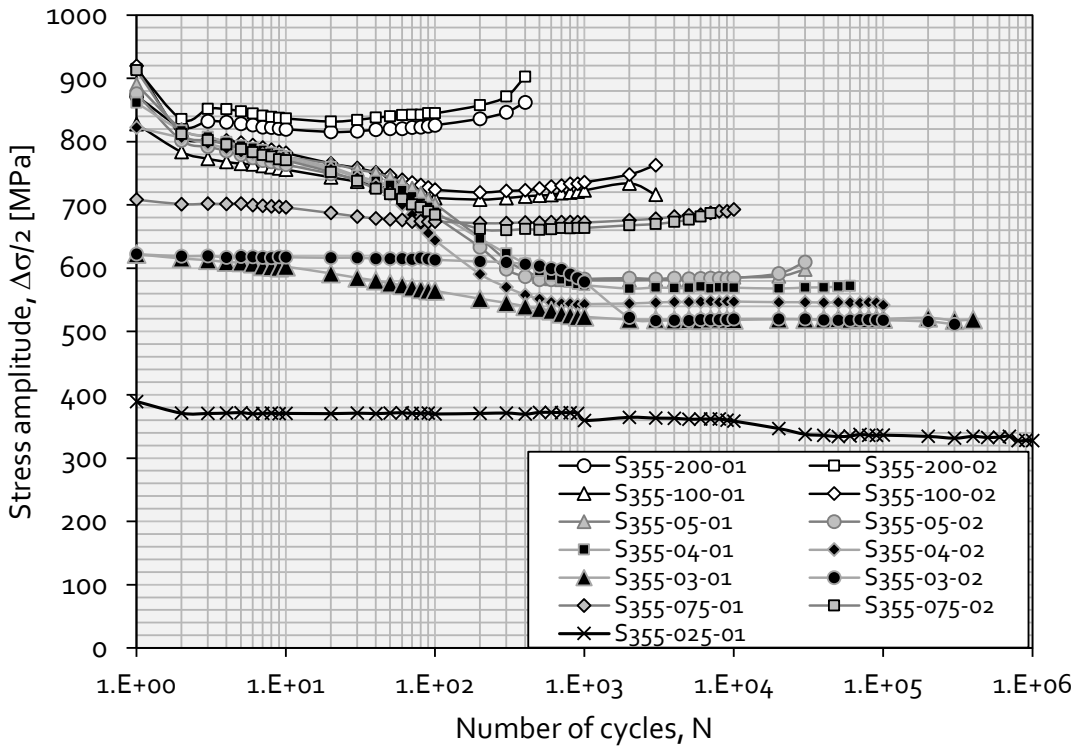

Figure 3.5 - Stress range evolution with the number of cycles (S355 steel grade).

Figure 3.6 presents the cyclic curve of the S355 steel, which relates the plastic strain amplitude with the stress amplitude of the (pseudo-)stabilized hysteresis loops. The cyclic curve was obtained with a relative low determination coefficient. A mathematic relation widely used to represent the cyclic curve was proposed by Ramberg and Osgood [4]. According to these authors, a linear relation between the plastic strain amplitude and the stress amplitude may be established if both data are plotted in a bi-logarithmic representation:

$$\frac{\Delta\sigma}{2} = K'\left(\frac{\Delta\varepsilon^P}{2}\right)^{n'} = 590.881\left(\frac{\Delta\varepsilon^P}{2}\right)^{0.089} \text{ (MPa)} \qquad (3.1)$$

where K' and n' are the cyclic strain hardening coefficient and exponent, respectively. Superposing the elastic strain amplitude with the plastic strain amplitude, given by Equation (3.1), results the following relation:

$$\frac{\Delta\varepsilon}{2}=\frac{\Delta\varepsilon^{E}}{2}+\frac{\Delta\varepsilon^{P}}{2}=\frac{\Delta\sigma}{2E}+\left(\frac{\Delta\sigma}{2K'}\right)^{1/n'}=\frac{\Delta\sigma}{2E}+\left(\frac{\Delta\sigma}{2\times 590.881}\right)^{1/0.089} \tag{3.2}$$

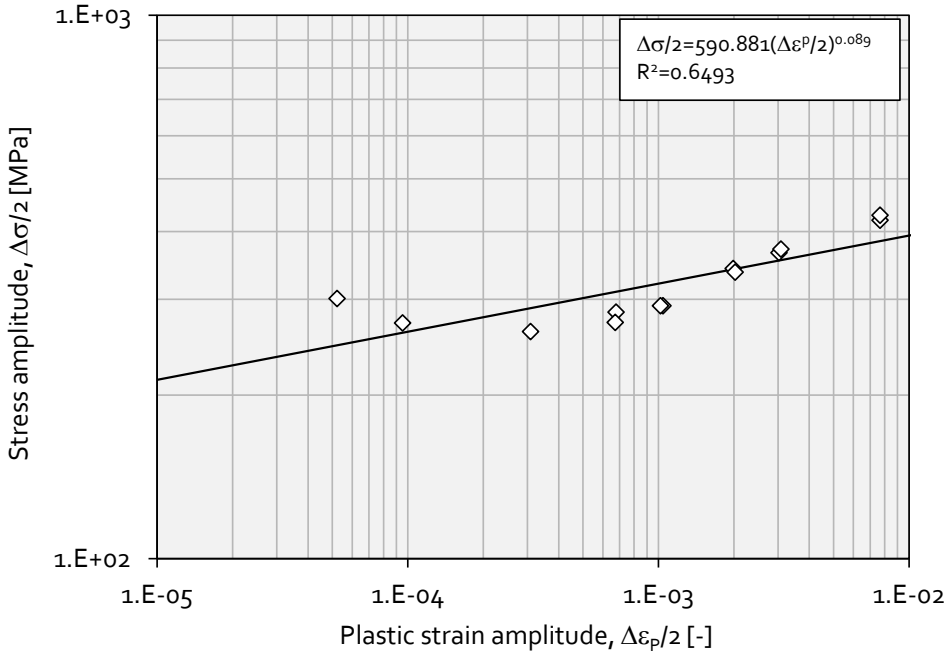

Figure 3.6 - Cyclic curve of the S355 steel grade.

3.3.2. Cyclic elastoplastic behaviour of the S235 steel

The cyclic elastoplatic behaviour of the S235 steel was also investigated using strain-controlled fatigue tests of smooth specimens. A total of 13 smooth plane specimens were fatigue tested, under a null strain ratio. Table 3.2 summarizes the strain-controlled fatigue tests performed on the S235 steel. Figure 3.7 shows the dimensions of the specimens. All these smooth plane specimens were manufactured from an undamaged part of a riveted beam (R1 series) which will be described in the next chapter. The Figure 3.8 presents the cyclic stress–strain hysteresis loops obtained for the S235 material, using a half-life criterion. This material shows higher scatter than observed for the S355 steel. Despite the scatter of the material may hinder the Masing behaviour assessment, it may also be claimed for this material a non-Masing behaviour.

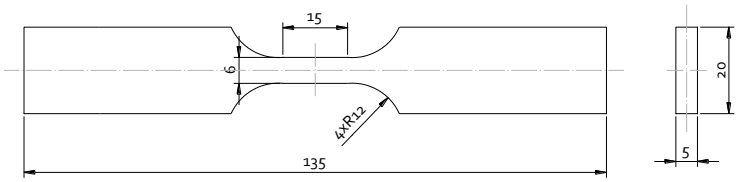

Figure 3.7 - Smooth plane fatigue specimen (S235 steel) (dimension in mm).

Table 3.2 - Fatigue experimental program of smooth plane specimens made of S235 steel.

Specimens	*L1*	*L2*	S_t	R_ε	$\Delta\varepsilon$	$d\varepsilon/dt$	*f*
	[mm]	*[mm]*	*[mm]*	*[-]*	*[%]*	*[%/s]*	*[Hz]*
S235-100-01	6.19	5.03	31.14	-1.00	1.00	0.80	0.40
S235-100-02	6.18	5.04	31.15	-1.00	1.00	0.80	0.40
S235-200-01	6.13	5.03	30.83	1.00	2.00	0.80	0.20
S235-200-02	6.12	5.04	30.84	-1.00	2.00	0.80	0.20
S235-050-01	6.15	5.04	31.00	-1.00	0.50	0.80	0.80
S235-050-02	6.12	5.04	30.84	-1.00	0.50	0.80	0.80
S235-040-01	6.08	5.04	30.64	-1.00	0.40	0.80	1.00
S235-040-02	6.07	5.04	30.59	-1.00	0.40	0.80	1.00
S235-030-01	6.07	5.10	30.96	-1.00	0.30	0.80	1.33
S235-040-03	6.21	5.04	31.30	-1.00	0.40	0.80	1.00
S235-030-02	6.18	5.04	31.15	-1.00	0.30	0.80	1.33
S235-025-01	6.10	5.04	30.74	-1.00	0.25	0.80	1.60
S235-025-02	6.19	5.04	31.20	-1.00	0.25	0.80	1.60

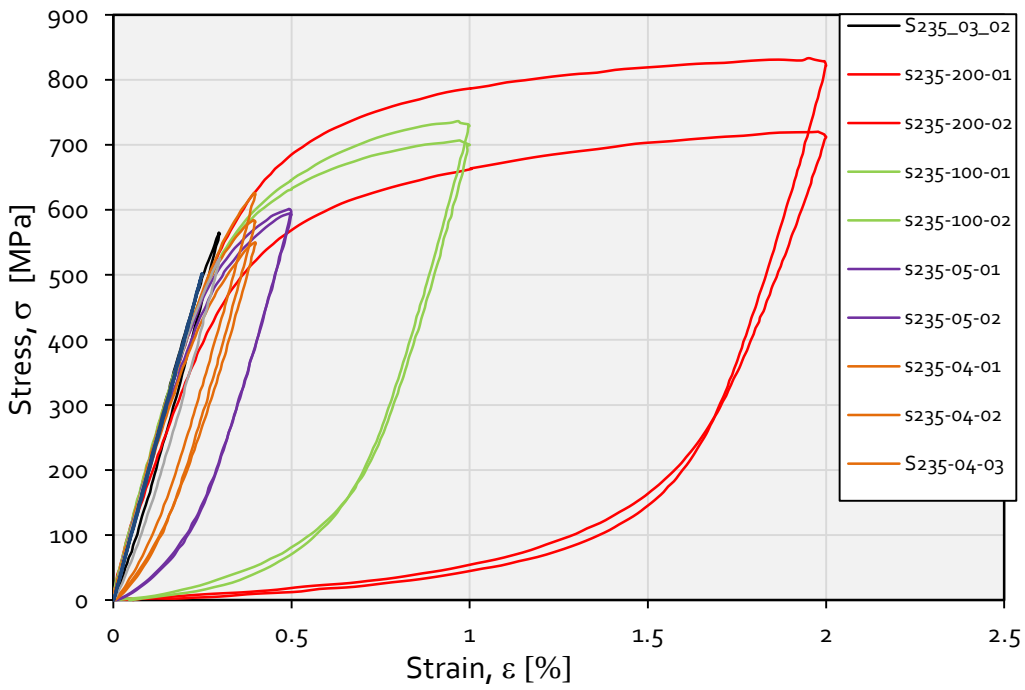

Figure 3.8 - Fatigue hysteresis loop of the S235 steel.

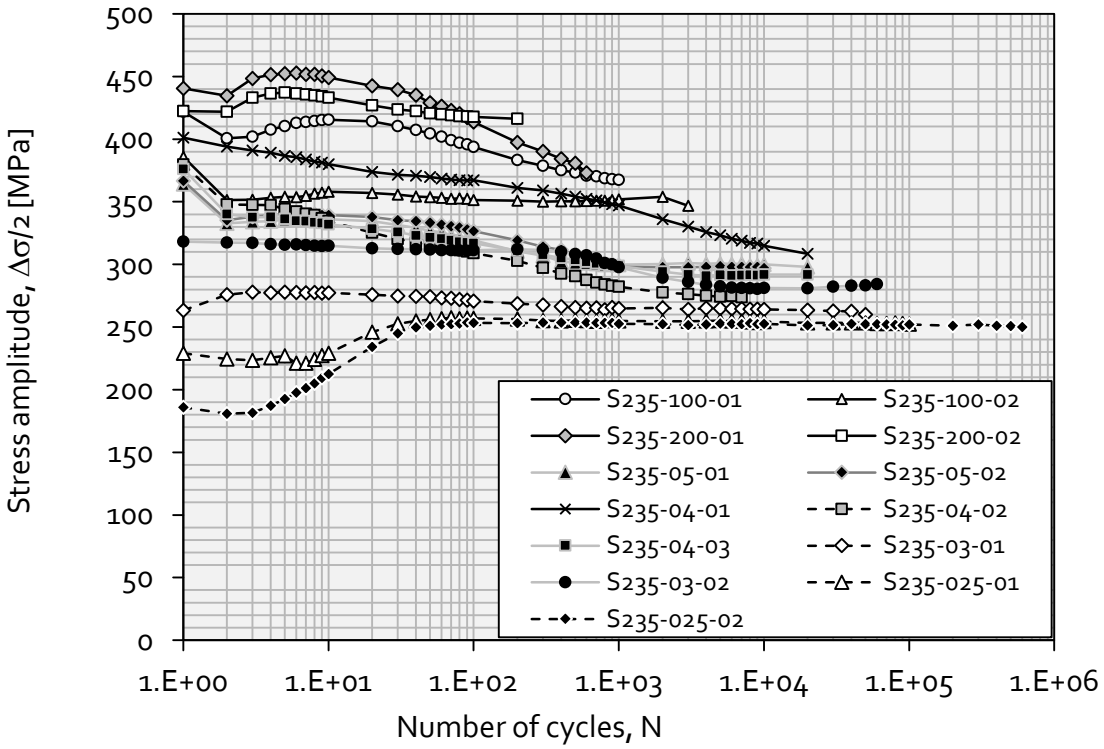

Figure 3.9 - Stress range evolution with the number of cycles (S235 steel).

Figure 3.9 presents the evolution of the stress amplitudes with the number of cycles for various strain ranges. It is clear that for some applied strain ranges, no stabilization of the cyclic behavior is observed. This material shows a general trend of progressive cyclic

softening. Only for low strain ranges, a cyclic stabilization is observed. There is also some instability at the first cycles of the cyclic behaviour which may be justified by some adjustments of the clip-gauge knives to the specimen's surface.

Figure 3.10 plots the cyclic curves of the S235 steel. The Ramberg-Osgood relationship [4] was adjusted to the experimental data with a determination coefficient of 0.7771, higher than obtained for the S355 steel:

$$\frac{\Delta\varepsilon}{2}=\frac{\Delta\varepsilon^{E}}{2}+\frac{\Delta\varepsilon^{P}}{2}=\frac{\Delta\sigma}{2E}+\left(\frac{\Delta\sigma}{2K'}\right)^{1/n'}=\frac{\Delta\sigma}{2E}+\left(\frac{\Delta\sigma}{2\times 555.520}\right)^{1/0.077} \tag{3.3}$$

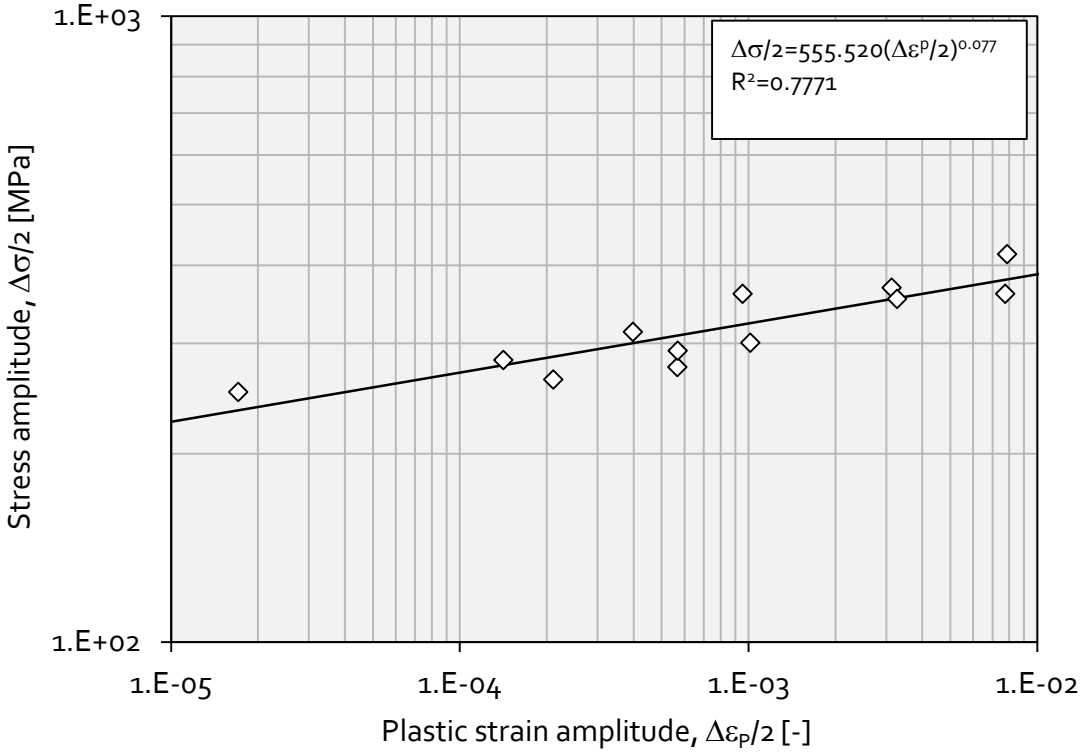

Figure 3.10 - Cyclic curve of the S235 steel grade.

3.3.3. Strain-life behaviour of the S355 steel

The strain-life behaviour of the S355 steel is presented in this section, using the results of the fatigue tests presented in the Section 3.3.1. Figures 3.11a) and 3.11b) presents, respectively, the evolution of the elastic and plastic strain amplitudes with the number of reversals to failure. The total strain-life data is shown in the Figure 3.11c). The Basquin [5]

and the Coffin-Manson [6, 7] relations were used, respectively, to fit the elastic and plastic strain-based experimental data. Combining the Basquin and Coffin-Manson relations results the Morrow relation [8], presented in the Figure 3.11c):

$$\frac{\Delta\varepsilon}{2}=\frac{\Delta\varepsilon^{E}}{2}+\frac{\Delta\varepsilon^{P}}{2}=\frac{\sigma_f{}'}{E}\left(2N_f\right)^{b}+\varepsilon_f{}'\left(2N_f\right)^{c} \tag{3.4}$$

where $\sigma_f{}'$ and *b* are, respectively, the fatigue strength coefficient and exponent; $\varepsilon_f{}'$ and *c* are, respectively, the fatigue ductility coefficient and exponent; $2N_f$ is the number of reversals to failure; $\Delta\varepsilon$, $\Delta\varepsilon^{E}$ and $\Delta\varepsilon^{P}$ are, respectively, the total, elastic and plastic strain ranges and *E* is the Young's modulus.

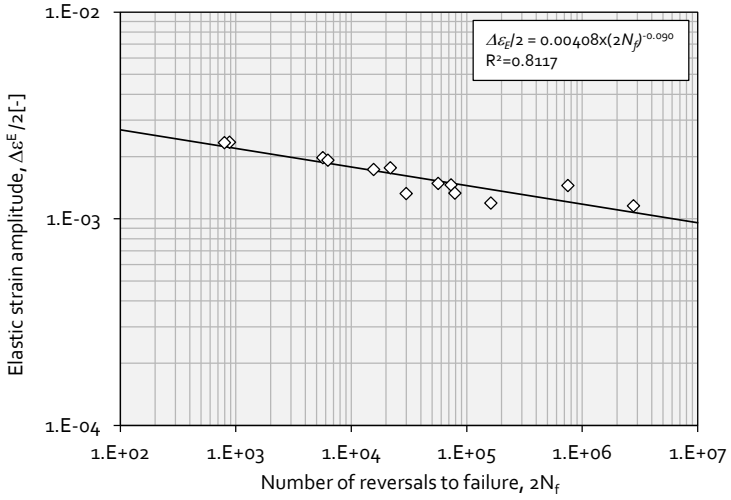

a)

Figure 3.11 - Strain-life data obtained for the S355 steel grade: a) elastic strain–life data; b) plastic strain–life data; c) total strain–life data (1/2).

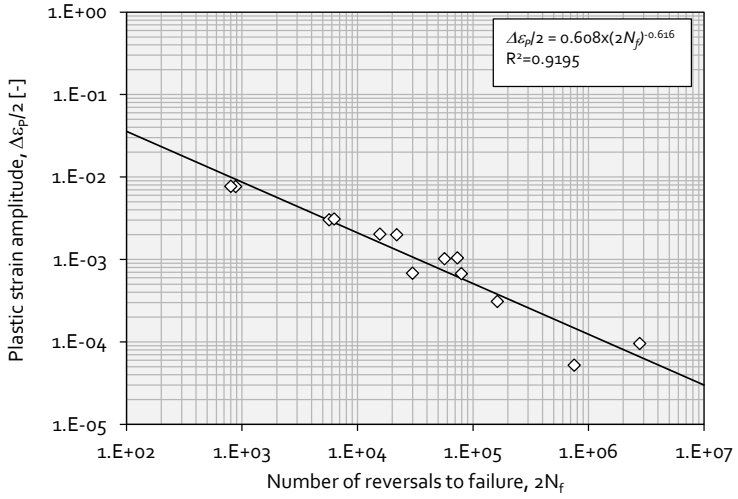

b)

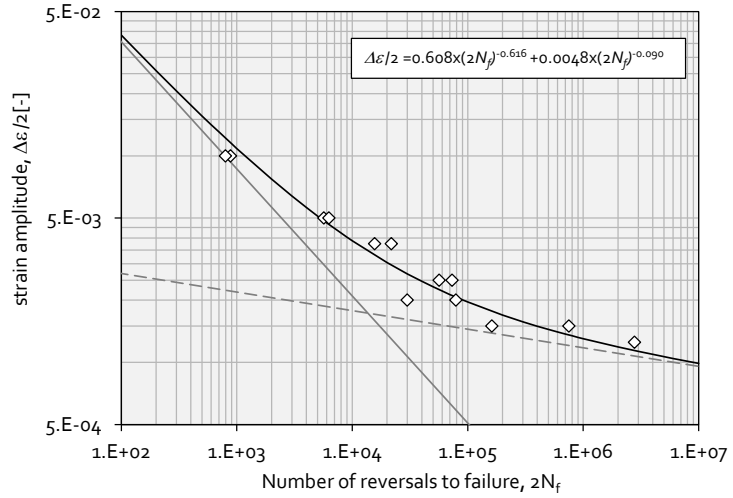

c)

Figure 3.11 - Strain-life data obtained for the S355 steel grade: a) elastic strain–life data; b) plastic strain–life data; c) total strain–life data (2/2).

3.3.4. Strain-life behaviour of the S235 steel

Regarding to the strain-life analysis of the S235 steel, Figures 3.12a) and 3.12b) present, respectively, the evolution of the elastic and plastic strain amplitudes with the number of reversals to failure. Figure 3.12c) represents the Morrow strain-life relation, which results from the superposition of the results from the elastic and plastic strain-life relations. The strain-life fatigue data presented in this section resulted from the cyclic tests performed on the smooth plane dog-bone specimens, as described in Section 3.3.2.

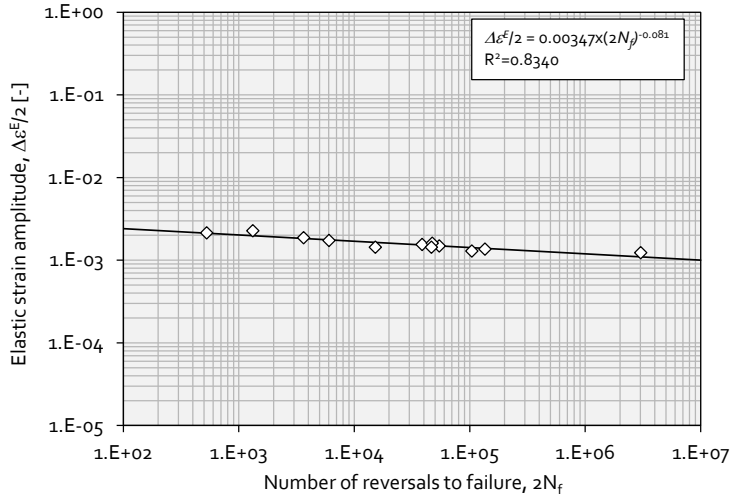

a)

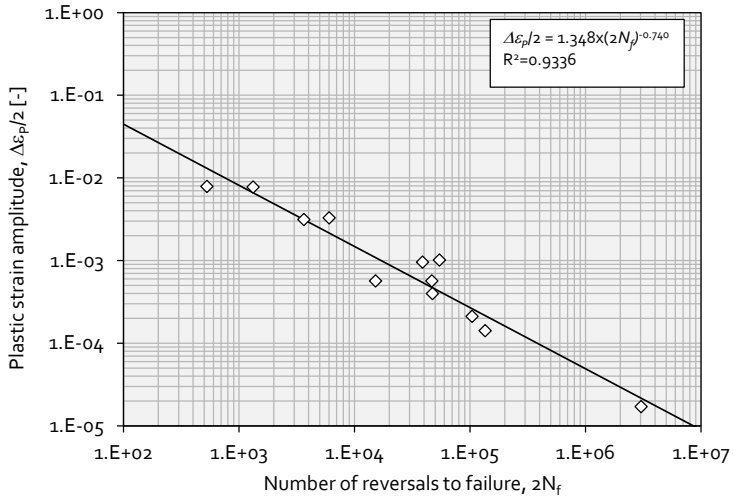

b)

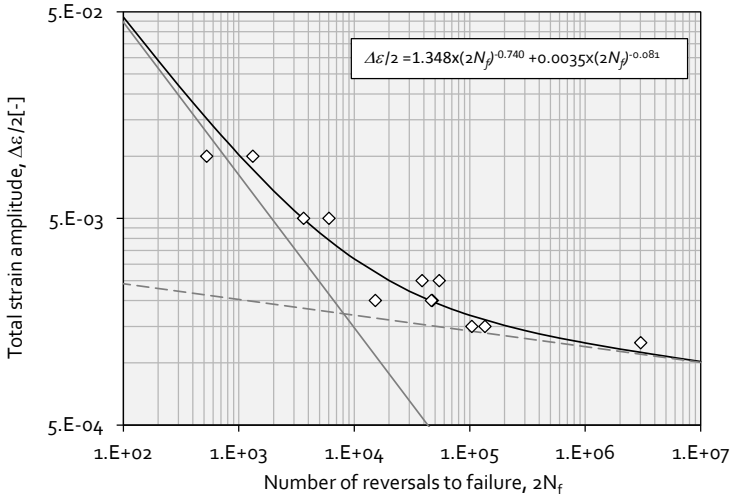

c)

Figure 3.12 - Strain-life data for the S235 steel grade: a) elastic strain–life data; b) plastic strain–life data; c) total strain–life data.

3.3.5. Comparison of the cyclic elastoplastic and fatigue behaviours of the tested structural steels

This section compares the cyclic curves and the strain-life behaviours of the S355 and S235 steel grades. Figure 3.13 compares the cyclic curves obtained for the S355 and S235 materials. The comparison of the two cyclic curves shows that materials exhibit very similar cyclic strain hardening behaviours (cyclic strain hardening coefficient). Concerning the slopes of the cyclic curves, they are essentially parallel, which means very similar slopes (cyclic strain hardening exponent).

Concerning the comparison of the strain-life relations, three distinct steel grades were considered: the S235 and S355 investigated in this work, and the S355 and S690 whose results were made available in reference [9]. Figure 3.14 compares the elastic, plastic and total strain amplitude *versus* reversals to failure, for all considered materials. Regarding to the elastic strain-life relations, the S690 steel grade shows significantly higher fatigue resistance, when compared with the other lower strength steel grades.

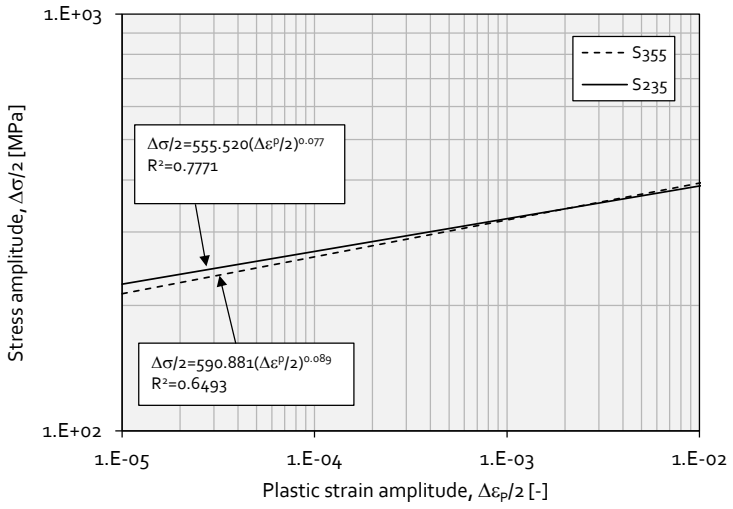

Figure 3.13 - Comparison of the cyclic curves obtained for the S235 and S355 steel grades.

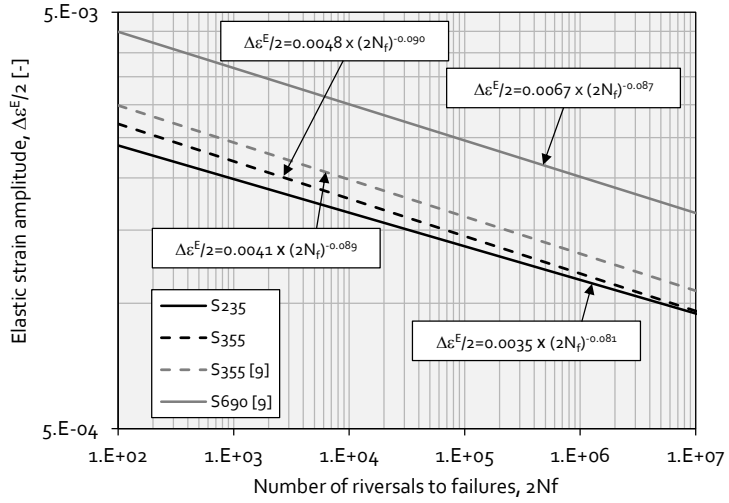

a)

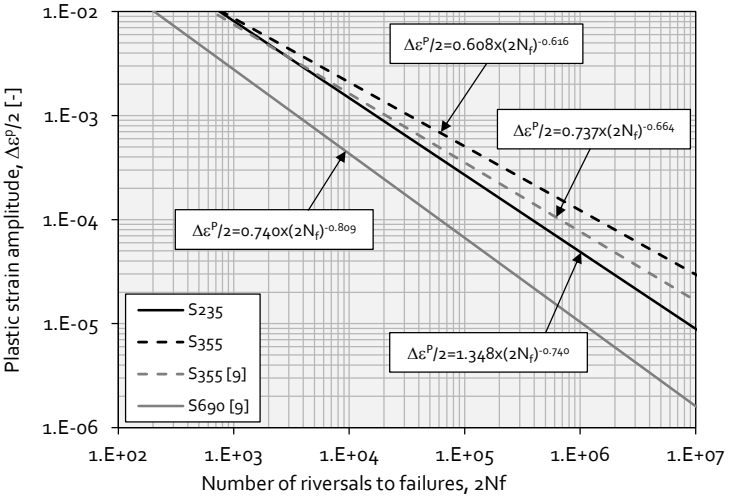

b)

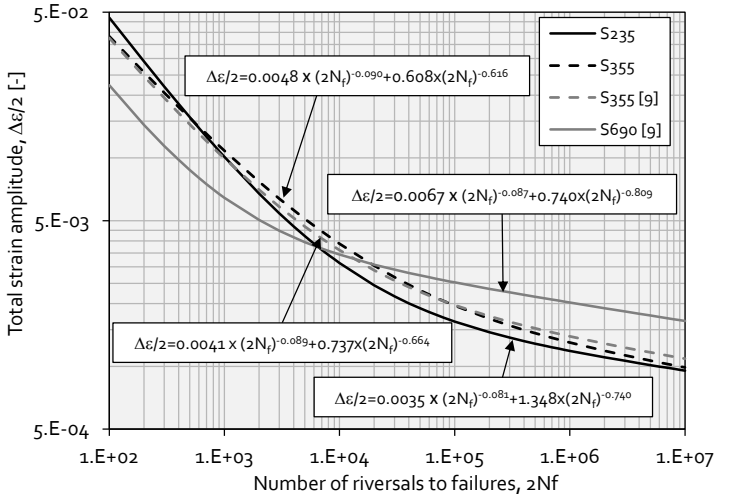

c)

Figure 3.14 - Comparison of strain-life data between S235, S355 and S690 steel grades: a) elastic strain–life data; b) plastic strain–life data; c) total strain–life data.

The fatigue resistance increases with the increasing static strength of the steel. Nevertheless, the slopes of the elastic strain-life relations remain similar for all steel grades. Considering the plastic strain-life relations, the S690 steel shows the lower fatigue ductility. An analysis of the total strain-life relations show that the S690 steel show better fatigue performance for high-cycle fatigue; however, for low-cycle fatigue the better fatigue performance is attributed to the lower strength steels. The fatigue curves rotate counter-clockwise around approximately 10^4 reversals, with the increase of the fatigue strength of the structural steels.

Table 3.3 summarizes the cyclic elastoplastic constants as well as the strain-life parameters for all investigated structural steels. Table 3.3 also presents the constants proposed for the S355 and S690 steel grades given in references [9] and [10], as well as for structural steels specified in ASTM standards [11]: a high performance steel (HPS 485W) and one carbon structural steel (A7).

Table 3.3 – Summary of cyclic elastoplastic and fatigue properties for structural steels.

Steel grade	*K´*	*n´*	σ_f'	*b*	ε_f'	*c*	$2N_T$
	[MPa]	*[-]*	*[MPa]*	*[-]*	*[-]*	*[-]*	*[reversals]*
S235	555.52	0.079	720	-0.076	1.348	-0.740	6822
S355	590.88	0.089	857	-0.090	0.608	-0.616	4054
S355 [9]	595.85	0.076	952	-0.089	0.737	-0.664	7095
S690 [9]	1282.65	0.092	1403	-0.087	0.740	-0.809	675
S690 [10]	-	-	1191	-0.090	0.911	-0.674	5809
HPS 485W [11]	956	0.113	851	-0.069	0.775	-0.701	3686
A7 [11]	1139	0.248	760	-0.121	0.196	-0.486	50119

3.4. ASSESSMENT OF FATIGUE CRACK GROWTH RATES OF THE S355 AND S235 STRUCTURAL STEELS

This section presents an investigation on fatigue crack growth behaviour of the S355 and S235 structural steels. Concerning the S355 steel, pure mode I fatigue crack growth tests

were performed according to the ASTM E647 [2] standard. Compact Tension (CT) specimen geometries were adopted and the effect of the thickness in the fatigue crack growth rates was investigated. For this purpose, two distinct thicknesses were considered: 4mm and 8mm. Regarding the S235 steel, pure mode I and mixed mode (mode I and mode II) fatigue crack growth behaviours were studied. Pure mode I fatigue tests were conducted according to the ASTM E647 [2] standard, using the CT geometry. Mixed mode crack propagation tests were performed using modified CT geometries. The experimental data assessment for the mixed mode tests was performed using Digital Image Correlation (DIC). DIC was used with two purposes: i) crack path evaluation and ii) stress intensity factors computation. A sequential two-steps approach was followed. The crack path is first assessed and then the stress intensity factors are computed.

The experimental crack propagation data was correlated using the power relation between the fatigue crack propagation rates and the stress intensity factor ranges, as proposed Paris and Erdogan [12]:

$$\frac{da}{dN} = C\Delta K^m \tag{3.5}$$

Equation (3.5) does not account for the stress ratio effects on fatigue crack growth rates. In order to allow stress ratio effects to be accounted conveniently on fatigue crack growths rates, the Walker model [13] was considered:

$$\frac{da}{dN} = C\left(\overline{\Delta K}\right)^m = C\left(\frac{\Delta K}{\left(1-R_\sigma\right)^{1-\gamma}}\right)^m \tag{3.6}$$

where *C* and *m* are the same constants as presented in the Paris law and γ is an additional material constant.

Concerning the pure mode I fatigue crack propagation tests, the fatigue crack growth rates were computed using the seven point incremental polynomial technique, as proposed in the ASTM E647 standard [2]. The stress intensity factor ranges were computed using the formulation also proposed in the ASTM E647 standard for CT specimens:

$$\Delta K = \frac{\Delta F}{t\sqrt{W}} \frac{(2+\alpha)}{(1-\alpha)^{3/2}} \left(0.886 + 4.64\alpha - 13.32\alpha^2 + 14.72\alpha^3 - 5.6\alpha^4\right) \quad (3.7)$$

where: $\alpha = a/W$, a is the fatigue crack size, t is the thickness of the CT specimen (t=4mm or t=8mm), W is the width of the specimen (W=40 mm for t=4mm; W=50 for t=8mm) and ΔF is the applied load range. For pure mode I fatigue crack propagation, the crack tip position was evaluated as the average value of two surface measurements performed on both faces of the CT specimens. These measurements were performed using two travelling microscopes with an accuracy of 0.001mm (Figure 3.15a)).

The crack tip measurement for modified CT specimens tested under mixed mode conditions was accomplished using two alternative systems: the previous referred optical microscope was used to inspect one surface of the CT specimens; and DIC method was considered to observe the other surface of the CT specimen (Figure 3.15b). Figure 3.15c) shows the experimental setup used for the mixed mode fatigue crack propagation tests. The direct optical observations performed on one face of the modified CT specimens were used for the calibration of the DIC technique which was applied on the other face of the modified CT specimen.

All fatigue crack propagation tests were carried out in load control, with constant amplitude loading and assuming a load ratio of 0.01. All tests were also performed in air condition, at room temperature, under sinusoidal waveform with a maximum frequency of 20 Hz.

3.4.1. Fatigue crack propagation rates of the S355 steel

The thickness effect on pure mode I fatigue crack propagation rates was investigated for the S355 steel grade. A total of 8 CT specimens were manufactured, from welded joints presented in the Chapter IV, according to the ASTM E647 standard [2] (see Figure 3.15). Table 3.4 presents the details of the fatigue crack growth testing program for the S355 steel, which includes the nomenclature adopted to identify each CT specimen, the main dimensions and the tested stress ratios, R_σ. Thicknesses of 4 mm and 8 mm were taken

into account. An initial stress intensity factor of 475.34 $Nmm^{1.5}$ was applied to all tested CT specimens. Since the tests were performed under constant load amplitude, stress intensity factors increased during the crack growth.

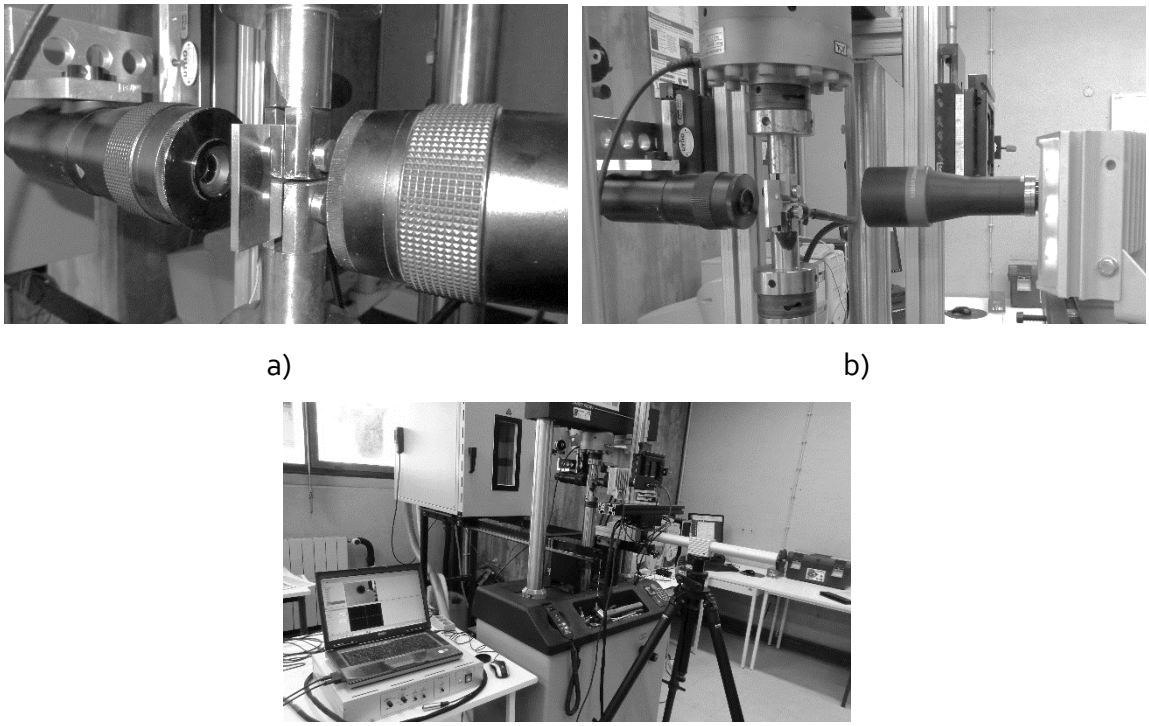

a) b)

c)

Figure 3.15 - Experimental setup used for fatigue crack growth testing: a) crack tip measurement using optical microscopes inspecting both surfaces of the CT specimen; b) crack tip measurement using both optical microscope and DIC inspecting opposite surfaces of the CT specimen; c) setup overview for mixed mode fatigue crack growth testing.

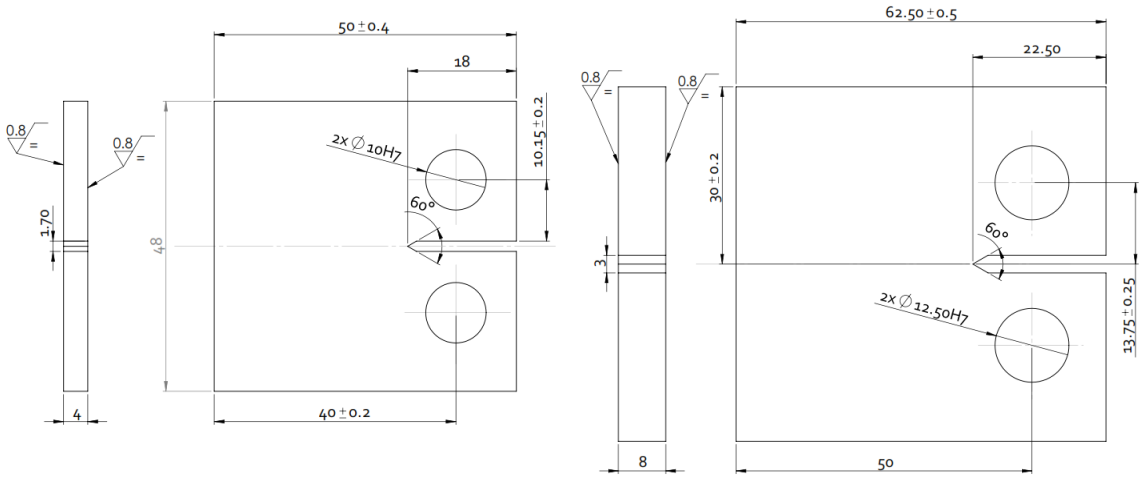

a) b)

Figure 3.16 – CT specimens made of S355 structural steel: a) thickness of 4mm; a) thickness of 8mm.

Table 3.4 – Overview of fatigue crack growth testing adopted for the S355 steel.

Specimens	*W*	*Thickness*	$R_\sigma=\sigma_{min}/\sigma_{max}$
	[mm]	[mm]	[-]
S355_T4_01_01	40	4	0.01
S355_T4_01_02	40	4	0.01
S355_T4_05_01	40	4	0.50
S355_T4_05_02	40	4	0.50
S355_T8_01_01	50	8	0.01
S355_T8_01_02	50	8	0.01
S355_T8_05_01	50	8	0.50
S355_T8_05_02	50	8	0.50

Figure 3.17 plots the experimental fatigue crack propagation rates measured for the S355 steel grade with a thickness of 4 mm tested for a stress ratio, R_σ=0.01 (see Figure 3.17a) and R_σ=0.5 (see Figure 3.17b). The fatigue crack growth rates, *da/dN*, are plotted as a function of the applied stress intensity factor ranges, ΔK. For each stress ratio, the Paris relation is fitted to the experimental data, a very high determination coefficient being found. Figure 3.17c) compares the Paris relation lines for each stress ratio and one may conclude that the material only exhibits a minor dependency on stress ratio. A slight increase of the crack propagation rate is observed with the increase in the stress ratio, which is a well-known behaviour in fatigue. Figure 3.17d) plots the experimental data for the two tested stress ratios and a global correlation is proposed using the Paris relation. A very high determination coefficient still is observed in this case.

Similarly, Figure 3.18 plots the experimental fatigue crack growth rates obtained for the S355 steel grade with a thickness of 8 mm, which were tested for a stress ratio, R_σ=0.01 (see Figure 3.18a) and R_σ=0.50 (see Figure 3.18b). Figure 3.18c) shows that for the thickness of 8 mm there is a slight increase of the stress ratio effects on the fatigue crack growth rates. Consequently, the overall correlation of the data using the Paris relation resulted in a reduction of the determination coefficient, when compared with the lower thicknesses.

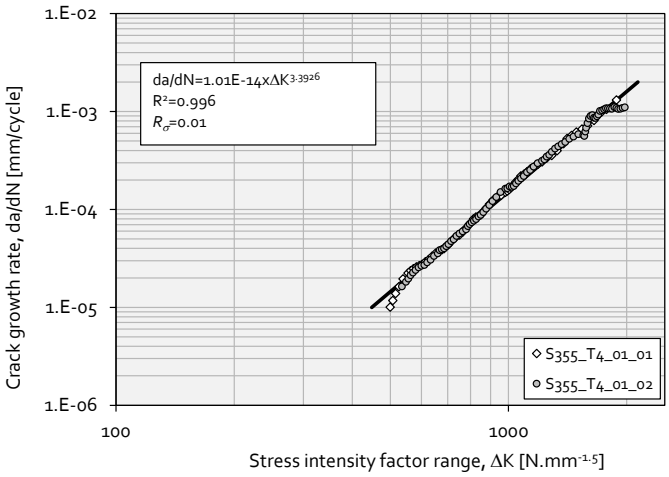

a)

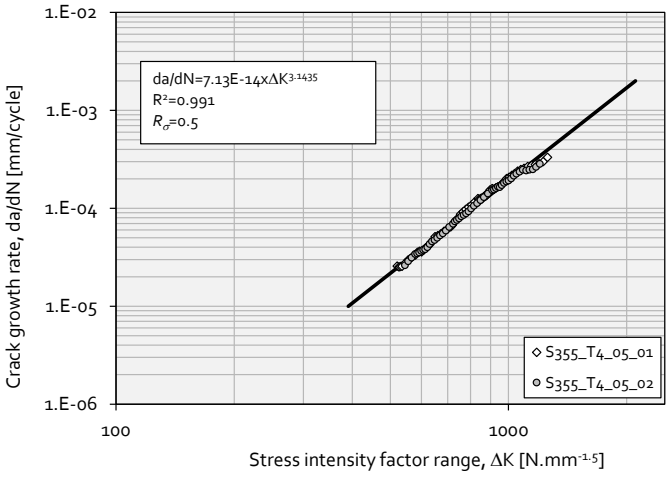

b)

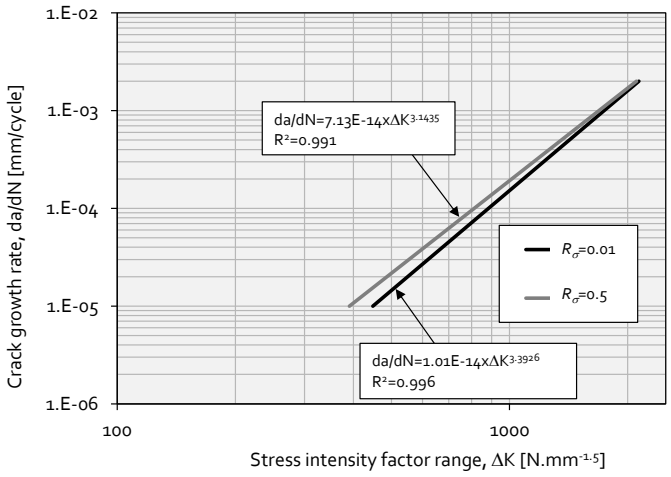

c)

Figure 3.17 - Experimental fatigue crack propagation rates obtained for the S355 steel grade, with a thickness of 4 mm and correlated using the Paris law: a) R_σ=0.01; b) R_σ=0.5; c) stress ratio effects; d) global correlation with the Paris relation. (1/2)

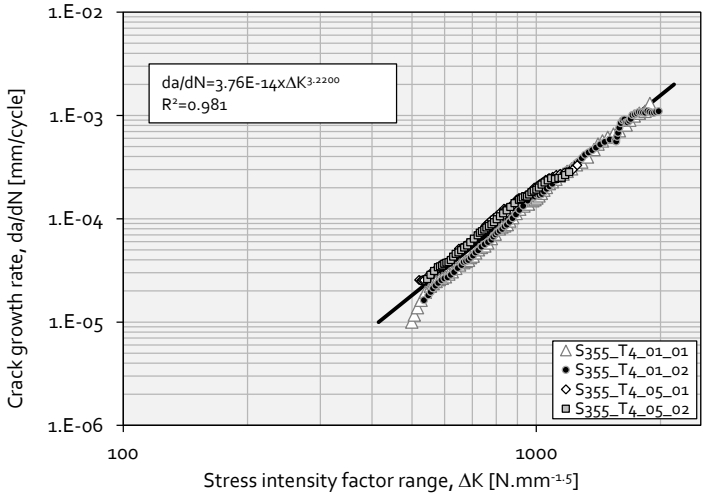

d)

Figure 3.17 - Experimental fatigue crack propagation rates obtained for the S355 steel grade, with a thickness of 4 mm and correlated using the Paris law: a) R_σ=0.01; b) R_σ=0.5; c) stress ratio effects; d) global correlation with the Paris relation. (2/2)

Figure 3.18a) compares the fatigue crack propagation rates (Paris trend lines) obtained with this study for the S355 steel grade, for thicknesses of 4 mm and 8 mm, and the fatigue crack propagation rates obtained by Albuquerque *et al.* [14], for the same material, but with a thickness of 30 mm. The trend lines for 4 and 8 mm correspond to the trend lines adjusted to both stress ratios considered in this study (see Figures 3.16d) and 3.17d)). One may conclude that thickness has a negligible influence on fatigue crack propagation results between 4 and 30 mm. Figure 3.18b) plots all the data derived in this study for the S355 steel (both thicknesses and stress ratios). All data was correlated with the Paris law and a significant determination coefficient was still observed. However, it was possible to increase this determination coefficient using the effective stress intensity factor as proposed by Walker [13] (see Figure 3.18c). The effective stress intensity factor proposed by Walker is suitable for modelling the mean stress effects in this material. Since thickness has a minor influence on fatigue crack propagation rates, the stress ratio has a relatively more impact on fatigue crack propagation rates, justifying the use of Walker model.

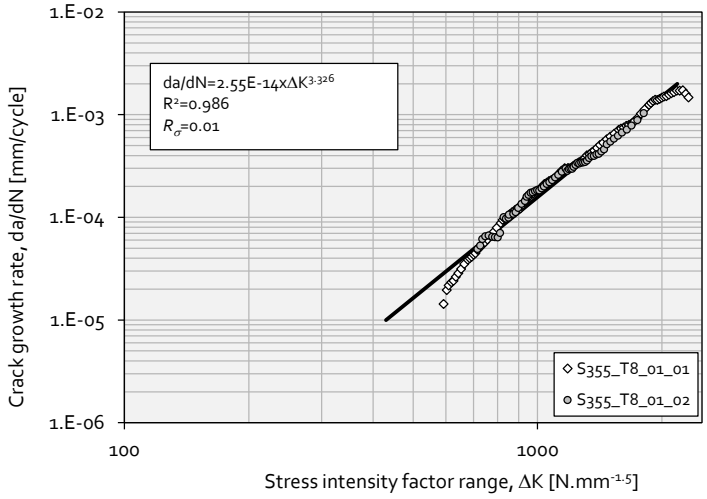

a)

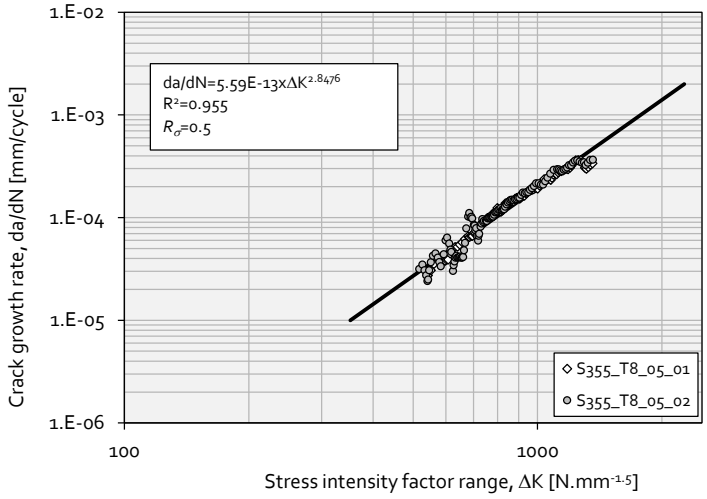

b)

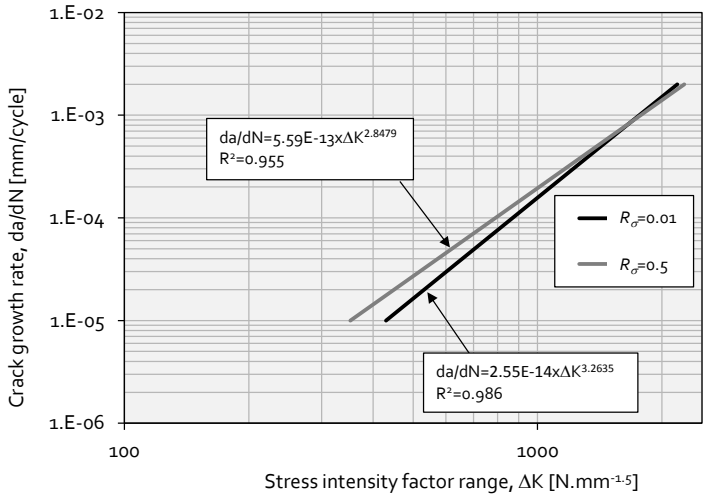

c)

Figure 3.18 - Experimental fatigue crack propagation rates obtained for the S355 steel grade, with a thickness of 8mm and correlated using the Paris law: a) R_σ=0.01; b) R_σ=0.5; c) stress ratio effects; d) global correlation with Paris relation. (1/2)

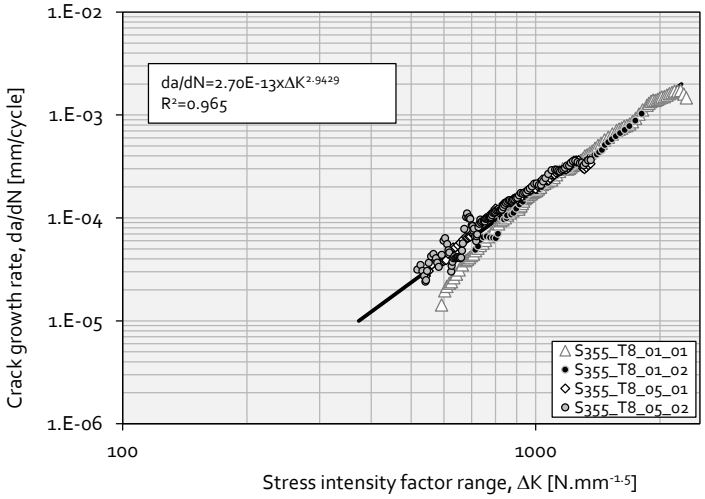

d)

Figure 3.18 - Experimental fatigue crack propagation rates obtained for the S355 steel grade, with a thickness of 8mm and correlated using the Paris law: a) R_σ=0.01; b) R_σ=0.5; c) stress ratio effects; d) global correlation with Paris relation. (2/2)

3.4.2. Fatigue crack propagation rates of the S235 steel

The S235 steel was tested under pure mode I and mixed mode (mode I and mode II) testing conditions. Figure 3.20 shows the geometry and dimensions of the CT specimens that were extracted from a beam used for riveted specimens (R1 series), that will be presented in Chapter IV. Figure 3.20a) exhibits the CT specimen which was manufactured to characterize the pure mode I fatigue crack propagation rates, according to the ASTM E647 standard [2]. In order to induce mixed mode fatigue crack propagation conditions, modified CT specimens were manufactured with a hole located at C_x and C_y coordinates, measured relatively to the V notch tip. Table 3.5 presents a summary of the fatigue crack propagation tests carried out for the S235 steel grade. A total of 4 CT specimens were considered for pure mode I testing and other 4 modified CT specimens with side hole were proposed for mixed mode testing. Regarding the mixed mode fatigue crack propagation tests, Table 3.5 also includes the diameter of the side holes as well as the coordinates of the side holes, C_x and C_y.

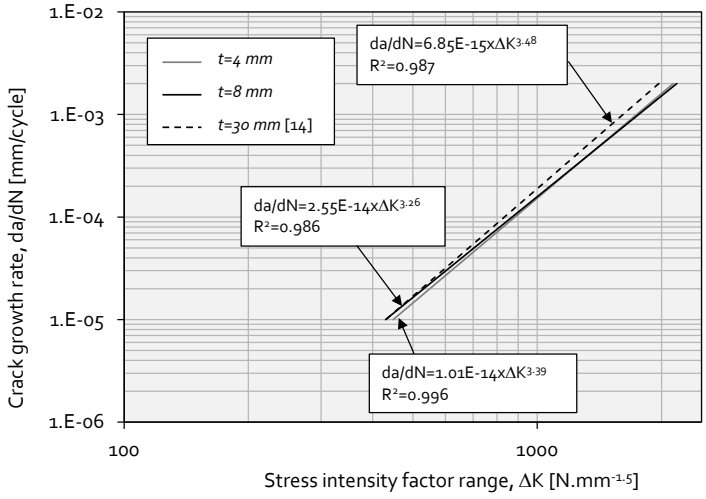

a)

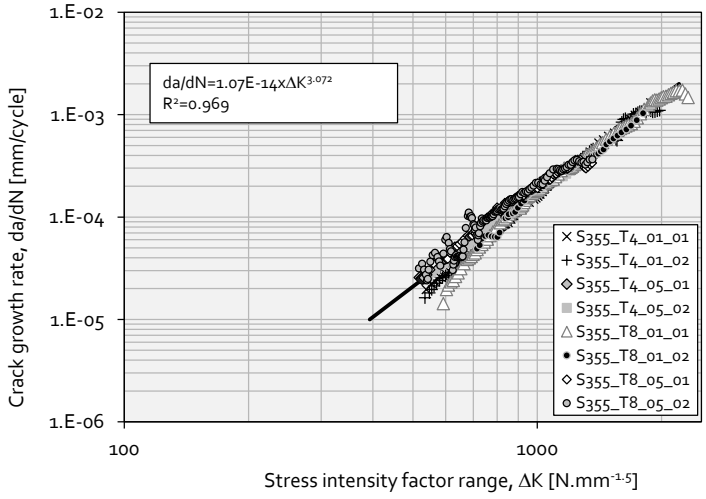

b)

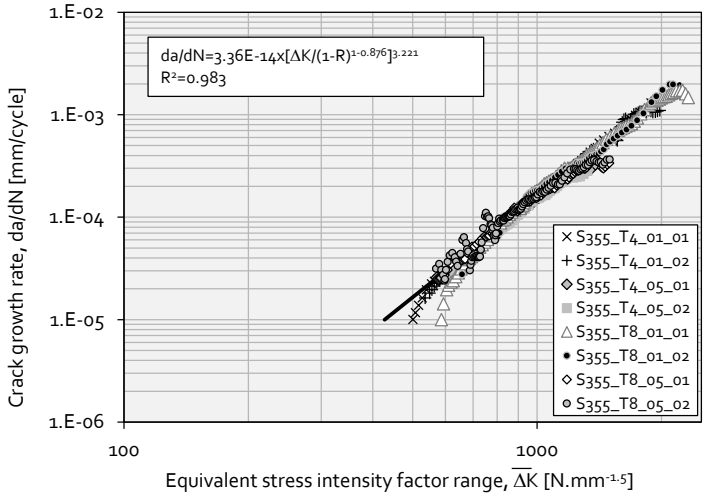

c)

Figure 3.19 - Experimental fatigue crack propagation rates for the S355 steel grade: a) thickness effects; b) global Paris correlation; c) global Walker correlation.

Table 3.5 - Overview of fatigue crack growth testing adopted for the S235 steel.

Specimens	R_σ	*Crack propagation mode*	*Hole location from notch tip*	*Hole diameter*	$\Delta K_{initial}$
	[-]		[mm]	[mm]	[Nmm$^{1.5}$]
S235_01_01	0.01	Pure mode I	-	-	474.34
S235_01_02	0.01	Pure mode I	-	-	474.34
S235_05_01	0.50	Pure mode I	-	-	474.34
S235_05_02	0.50	Pure mode I	-	-	474.34
S235_I+II_01_01	0.01	Mixed mode (I+II)	C_x=12.0 C_y=7.5	7.0	474.34
S235_I+II_01_02	0.01	Mixed mode (I+II)	C_x=12.0 C_y= 7.5	7.0	474.34
S235_I+II_01_03	0.01	Mixed mode (I+II)	C_x=12.0 C_y=8.0	7.5	474.34
S235_I+II_01_04	0.01	Mixed mode (I+II)	C_x= 10.0 C_y= 7.0	7.5	474.34

3.4.2.1. Pure mode I fatigue crack propagation data for the S235 steel

Figure 3.21 presents the experimental fatigue crack propagation rates obtained for the S235 steel tested under pure mode I fatigue crack propagation. Figure 3.21a) illustrates the fatigue crack growth data obtained for a stress ratio R_σ=0.01 and Figure 3.21b) plots the fatigue crack growth data for a stress ratio R_σ=0.50. The experimental data of Figures 3.21a) and 3.21b) were correlated with the power relation between the fatigue crack growth rate and the stress intensity factor range, proposed by Paris and Erdogan [12]. Figure 3.21c) compares the resulting Paris lines, a minor increase of the fatigue crack propagation rates being observed with the increase of the stress ratio. Figure 3.21d) shows a correlation of all pure mode I fatigue crack propagation data (both stress ratios included) using the Paris law. In order to increase the description of the fatigue crack propagation data, the Walker model was used as illustrated in Figure 3.22. An increase of the determination coefficient was observed.

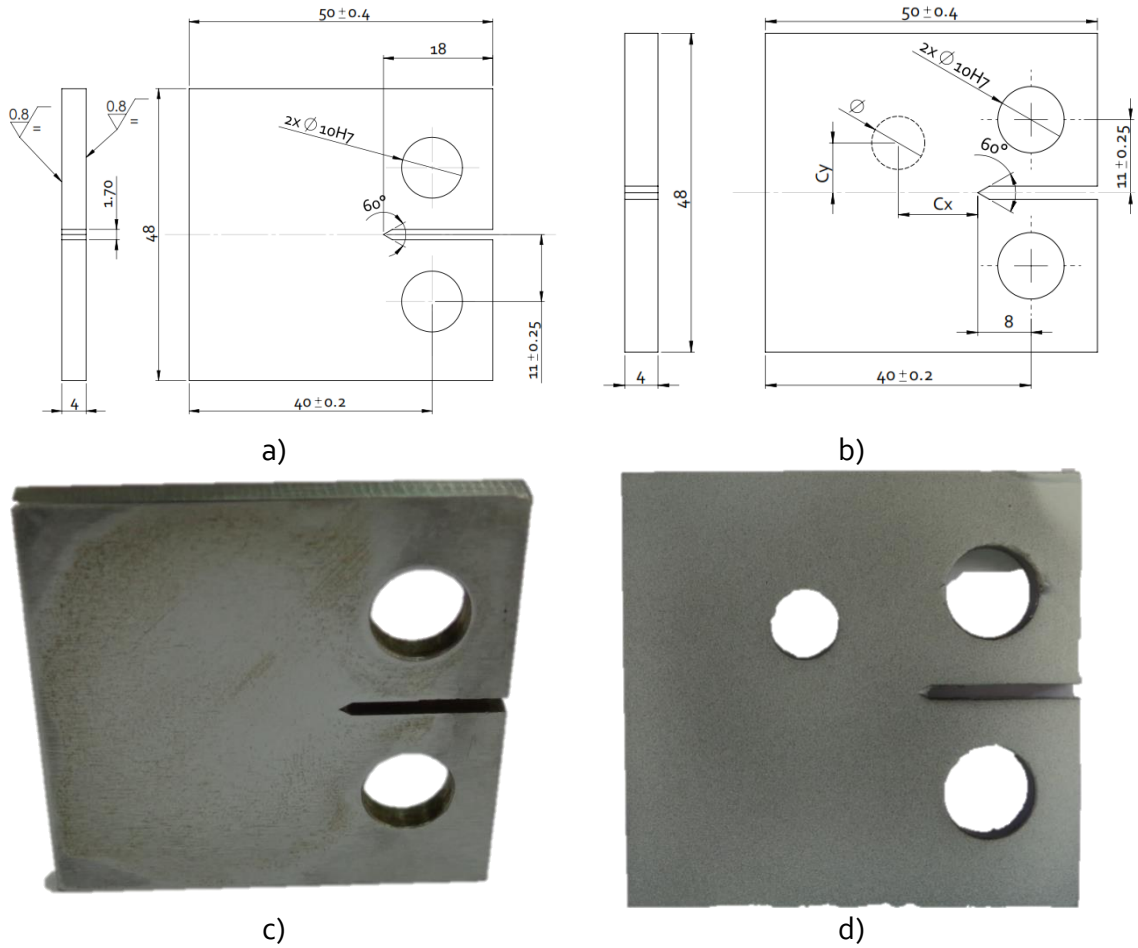

Figure 3.20 - Compact tension specimens made of S235 steel: a) geometry of CT specimens; b) geometry of modified CT specimens; c) photo of CT specimens; d) photo of modified CT specimens.

3.4.2.2. Mixed- mode (I and II) fatigue crack propagation rates of the S235 steel

Mixed-mode fatigue crack propagation data was derived for the S235 steel using a non-standardized modified CT specimen. This non-standardized specimen requires the application of techniques for data reduction analysis, in particular aiming the evaluation of the stress intensity factors evolution, for a measured crack path. For this purpose, a displacement based technique was followed in this section, using displacement fields obtained from DIC analysis. The DIC can also be used for the crack path assessment itself, resulting in this way an attractive tool for non-standardized mixed-mode fatigue crack propagation testing.

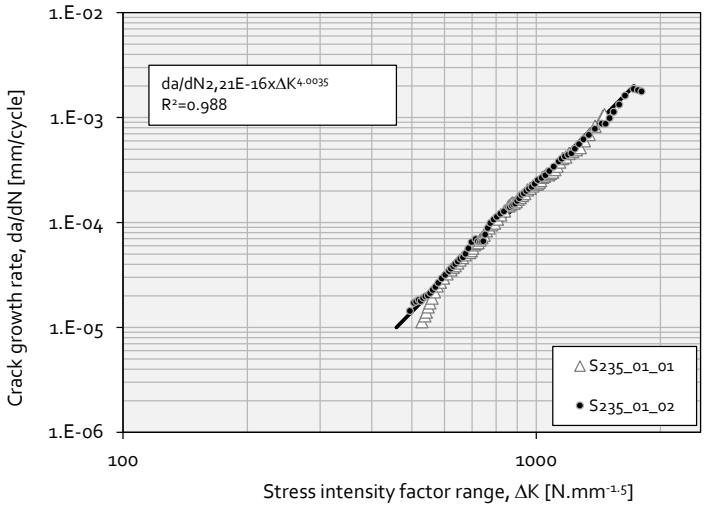

a)

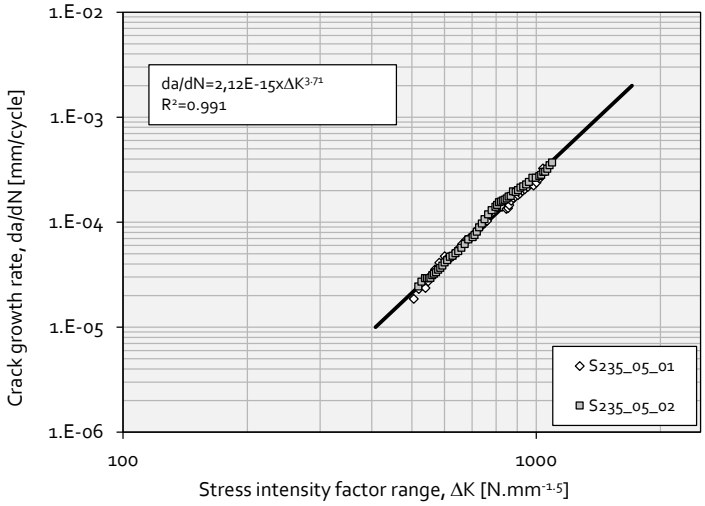

b)

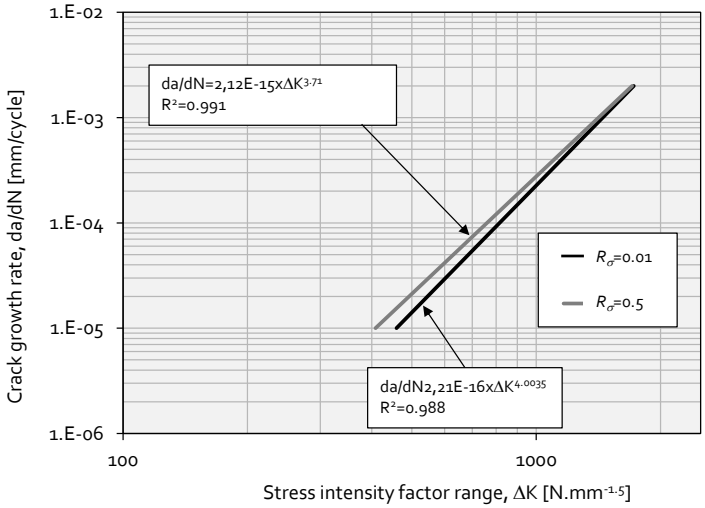

c)

Figure 3.21 - Pure mode I fatigue crack propagation rates obtained for the S235 steel and correlations with Paris relation: a) R_σ=0.01; b) R_σ=0.5; c) stress ratio effects; d) global correlation with the Paris relation. (1/2)

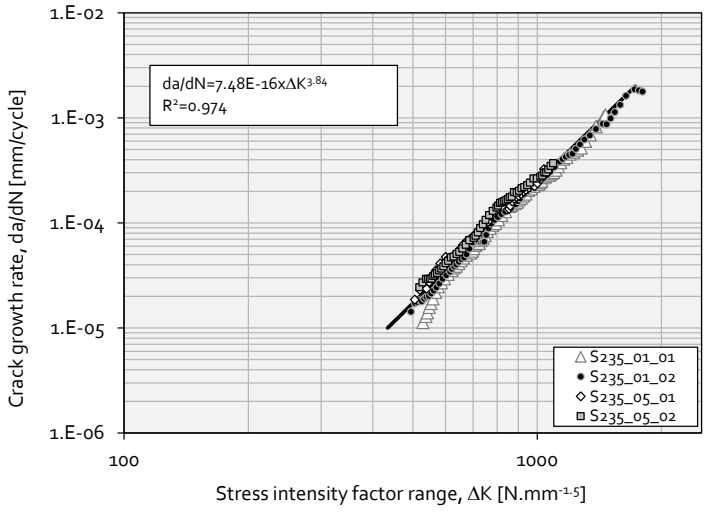

d)

Figure 3.21 - Pure mode I fatigue crack propagation rates obtained for the S235 steel and correlations with Paris relation: a) R_σ=0.01; b) R_σ=0.5; c) stress ratio effects; d) global correlation with the Paris relation. (2/2)

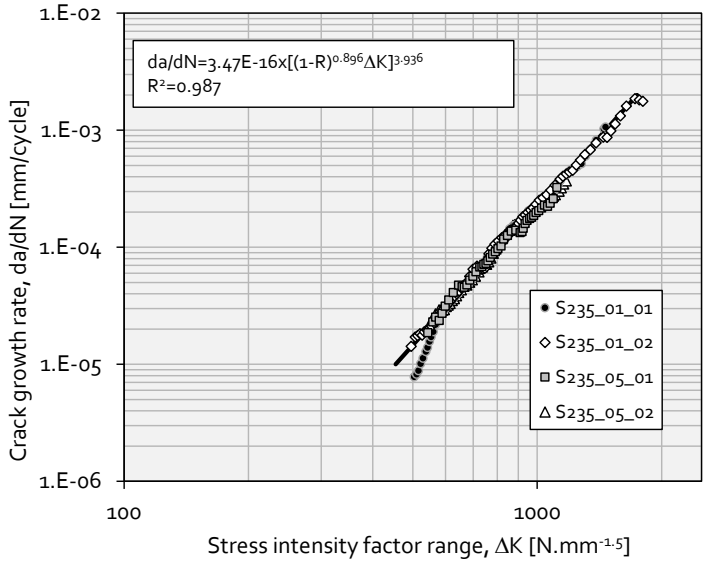

Figure 3.22 – Correlation of pure mode I fatigue crack propagation rate using the Walker relation.

The mode I and mode II stress intensity factors computation from experimental displacement fields may be a challenging task, since experimental displacement fields near the crack tip may contain measurement errors due to significant amount of plastic deformation, out-of-plane displacement and high displacement gradients [15]. However, works have been done in order to directly determine stress intensity factors from experimental displacement fields [16–18], using an extrapolation method. This

displacement extrapolation method is also frequently used with finite element analyses [19-20].

The least-squares regression method has been widely used to extract stress intensity factors using experimental full-field displacement data [21-26]. With this technique, analytical solutions for the displacement fields nearby the crack tip will be fitted to the experimental full-field displacement data. The set of parameters of the analytical solution to be identified by the least-squares technique will include the mode I and mode II stress intensity factors. Yoneyama [15] proposed a one-step method to assess both stress intensity factors and crack tip location. However, this methodology can be time consuming for a large displacement fields.

In this chapter, a two-step approach is followed, as follows: firstly the crack tip is located from the displacement field resulting from Digital Image Correlation (DIC). Once located the crack tip, the stress intensity factors will be estimated using linear least squares method to match the analytical solution for the displacement field and the experimental full-field DIC data.

3.4.2.2.1. Digital image correlation

The DIC technique was mainly developed by Sutton *et al.* [27-28]. The method allows the assessment of the full-field displacements for an object surface. It is assumed that the spatial distribution of pixel grey levels within each subset gives a distinctive fingerprint of the surface with suitable contrast and isotropy [29]. These image patterns, before and after deformation, are then digitized and stored in a computer. The digitized images are then compared and subsets are matched between one image and the other. The initial image representing the body before motion is a discrete function $f(x,y)$ that is transformed into another discrete function $f^*(x^*,y^*)$ after motion (deformation/distortion or displacement). The theoretical relation between the two discrete functions can be written as:

$$f^*(x^*, y^*) - f(x + u_x(x,y), y + u_y(x,y)) = 0 \tag{3.8}$$

where $u_x(x,y)$ and $u_y(x,y)$ represent the displacement field for a pattern. Since an independent value of displacement is measured per subset, the size of the subsets must be carefully defined and compromised between correlation and interpolation errors. A sub-pixel correlation algorithm calculates the position (centre) of each feature on the deformed configuration, therefore it is determined the displacement field across the region of interest.

In this study, the ARAMIS® 2D DIC system by GOM was used to store periodically a sequence of two images at maximum and minimum cycle loads (see setup represented in Figure 15). One face of each modified CT specimen was provided with a speckled-pattern, as illustrated in Figure 3.24. The size of the correlation windows used in the proposed method was 19x19 pixels, whilst the subset on the Aramis was defined as 15x15 pixels (with a step size of 15x15pixels). A telecentric lens TC 23 36 from Opto-Engineering, with a field of view of 26.3x22.1 mm^2 was used.

The proposed algorithm for the crack path assessment and stress intensity factors assessment was programmed in Matlab code. However, the GOM Aramis 2D DIC commercial software [30], v6.0.2, was also used to compute displacement fields for comparison purposes with the ones from Matlab code.

3.4.2.2.2. Crack tip location assessment

The algorithm used to identify the crack tip location in the CT specimens was proposed by Xavier *et al.* [31]. The method is based on the variation of the relative position among adjacent subsets [32-34], as illustrated in the Figure 3.23. A mapping scalar function $A(x,y)$ is introduced as the maximum norm of the relative position vectors:

$$A(x,y) = \max(\|u_i - u_k\|; \|u_j - u_l\|) \tag{3.9}$$

where u_β represents the displacement vector of data point (subsets) β (with β=*i*, *j*, *k* and *l*). A mapping mask is then defined assuming threshold segmentation according to the following inequalities:

$$\begin{cases} M(x,y)=1 \ \text{ if } \ A(x,y)\geq\alpha\bar{A} \\ M(x,y)=0 \ \text{ if } \ A(x,y)<\alpha\bar{A} \\ M(x,y)=-1 \ \text{ if } \ A(x,y)=\text{no data} \end{cases} \tag{3.10}$$

where $\bar{A}$ is the average of $A(x,y)$ and α is a scalar representing a threshold, as used for instance in image segmentation. This mask function *M(x,y)* (Equation 3.10) allows the classification of the measuring region according to the following description:

- *M(x,y)* = 1 represents the damaged region (assumed here as the region around the crack tip);
- *M(x,y)* = 0 corresponds to the region where the material is undamaged;
- *M(x,y)* = -1 represents the region where the material is completely damaged and no information is available using digital image correlation (boundary of discontinuities).

The crack tip is then estimated from the mask function for locations with *M(x,y)*=1. A key issue of this algorithm, however, is the calibration of the threshold α (Equation 3.10). In this work, the threshold parameter was calibrated crossing direct xy optical observations on one face of the specimens and the DIC results from the opposite face of the specimen. This calibration process is not the most accurate one is the crack deviates across the thickness.

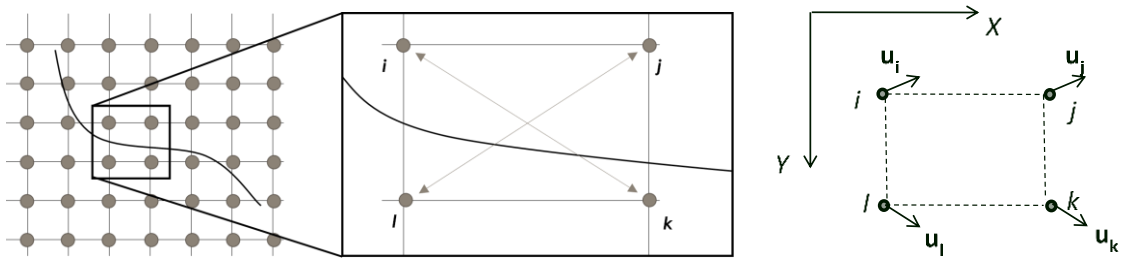

a) b)

Figure 3.23 - Schematic representation of the variation of relative position between adjacent subsets: a) subsets grid; b) adjacent subset displacements.

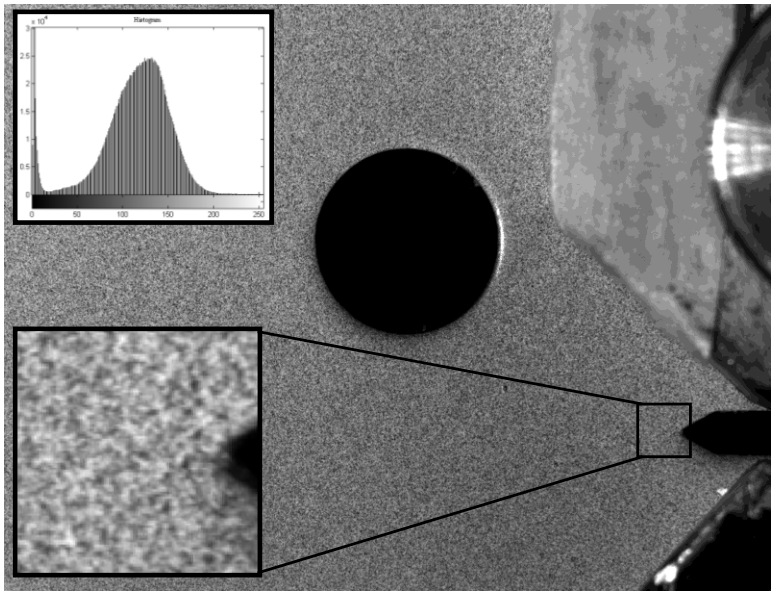

Figure 3.24 - Speckle pattern applied to one face of the modified CT specimen.

In order to illustrate the process for crack tip identification, Figure3.25 plots the scalar function *A(x,y)* for the S235_I+II_01_01 specimen, for two distinct stages of the crack propagation process (stage 20 and 40). This scalar function may be understood as a damage map. Once assessed the *A(x,y)* map, the crack geometry are then defined using a cut plane located at $\alpha\bar{A}$. Figure 3.26 plots the transformed map after the application of the cutting threshold, again for the S235_I+II_01_01 specimen, at stages 20 and 40.

The crack paths assessed for S235_I+II_01_01, S235_I+II_01_02, S235_I+II_01_03 and S235_I+II_01_04 specimens are plotted in Figures 3.27, 3.28, 3.29 and 3.30, respectively. The Figures 3.27a) and b) plot the comparison between the X coordinate (horizontal direction) (Figure 3.27a) and Y coordinate (vertical direction) (Figure 3.27b), both assessed along the number of cycles using both optical microscope observations and DIC approach, for the S235_I+II_01_01 modified CT specimen. Figure 3.27 shows that both approaches yield similar crack paths, mainly regarding the X coordinate of the crack tip evolution. The deviation between approaches was higher when the comparison was based on the Y coordinate (see Figure 3.27b)). Figure 3.27c) points out a maximum difference between the trajectories of the crack tip of about 0.5 mm for the S235_I+II_01_01 specimen. It is important to stress that direct optical observations and DIC approach were applied to opposite specimen faces which may result in distinct observations due to cracks non-perpendicular to the side faces.

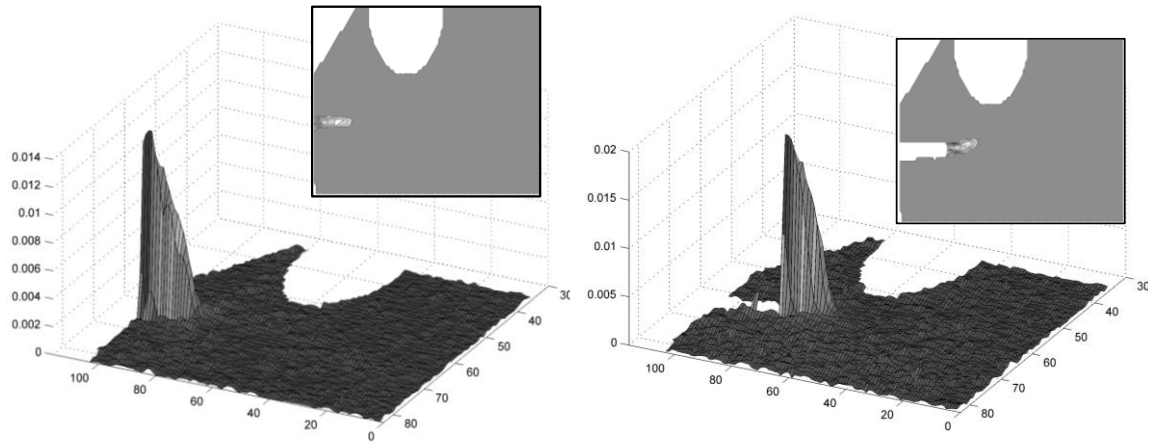

a) b)

Figure 3.25 - *A(x,y)* map for the cracked S235_I+II_01_01 specimen at distinct stages of the crack propagation: a) for measurement stage 20; b) for measurement stage 40.

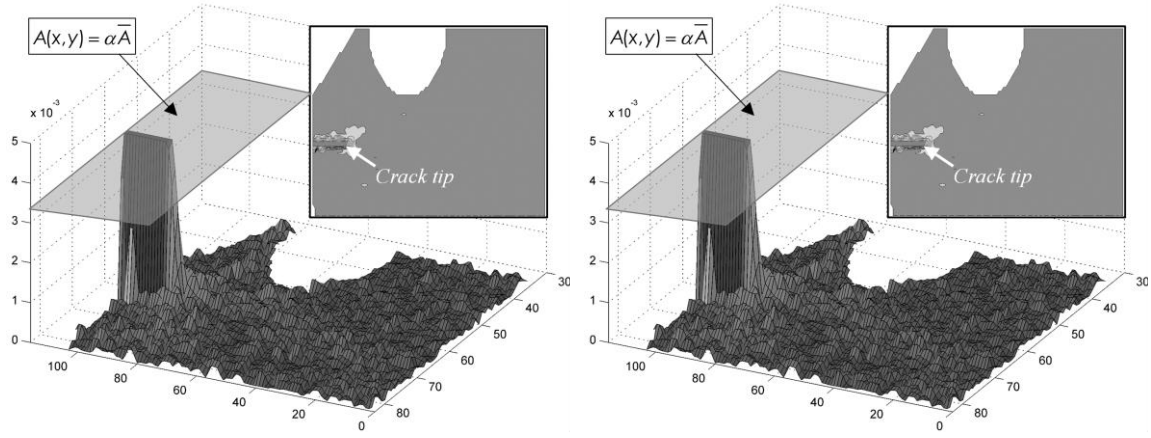

a) b)

Figure 3.26 - *A(x,y)* map for the cracked S235_I+II_01_01 specimen with the application of the threshold: a) for measurement stage 20; b) for measurement stage 40.

Regarding the analysis of the Figure 3.28, it is observed that the X coordinate measured between both approaches presents a very good match (Figure 3.28a). However, the comparison between the Y coordinates (Figure 3.28b) exhibits a maximum difference of about 1 mm between both approaches. The deviation between approaches tends to reduce when the Y coordinate is higher than 1 mm. Figure 3.28c) shows the global crack path of the fatigue crack observed for S235_I+II_01_02, resulting from both experimental measurements.

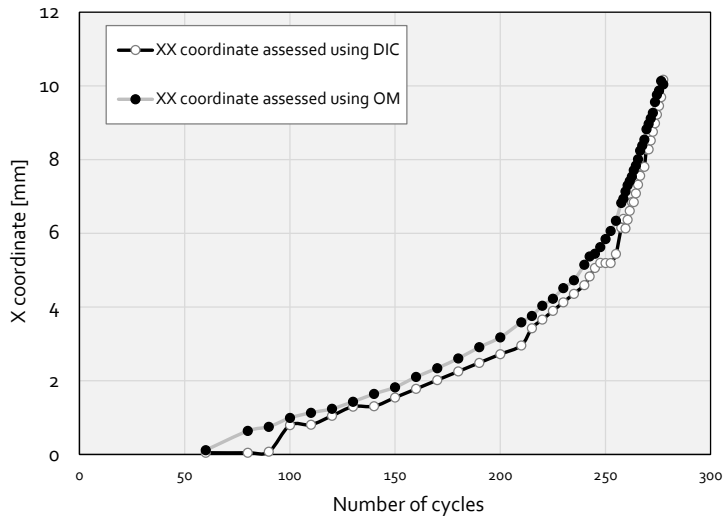

a)

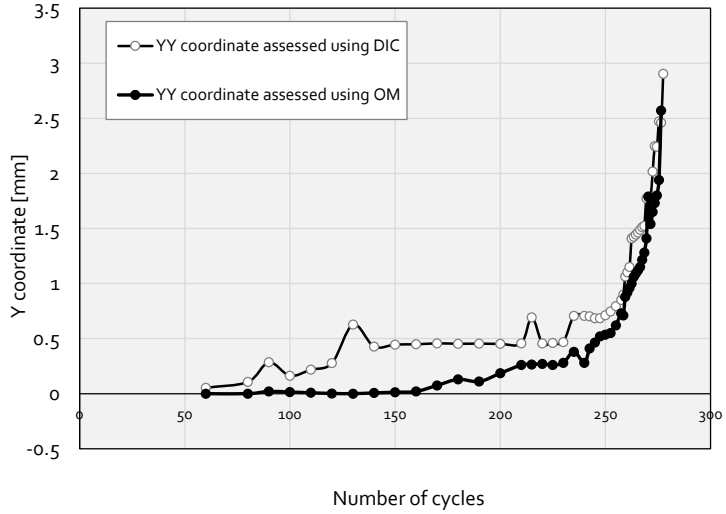

b)

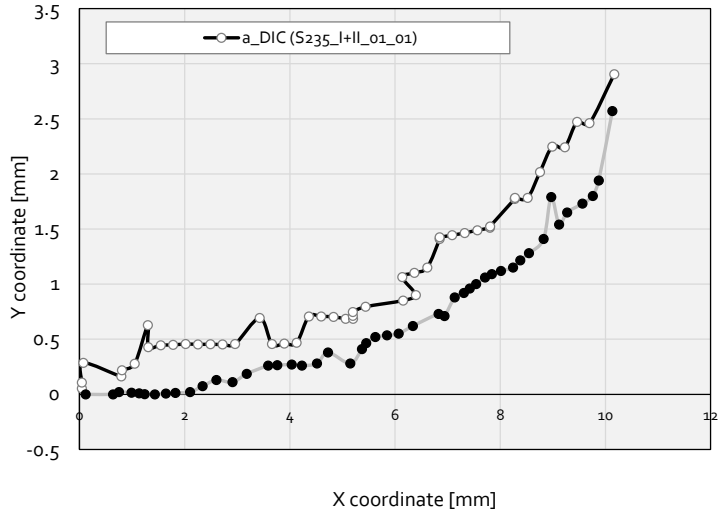

c)

Figure 3.27 – Comparison of assessed crack paths for S235_I+II_01_01 specimen: a) evolution of the X coordinate of the crack tip; b) evolution of the Y coordinate of the crack tip; c) crack path.

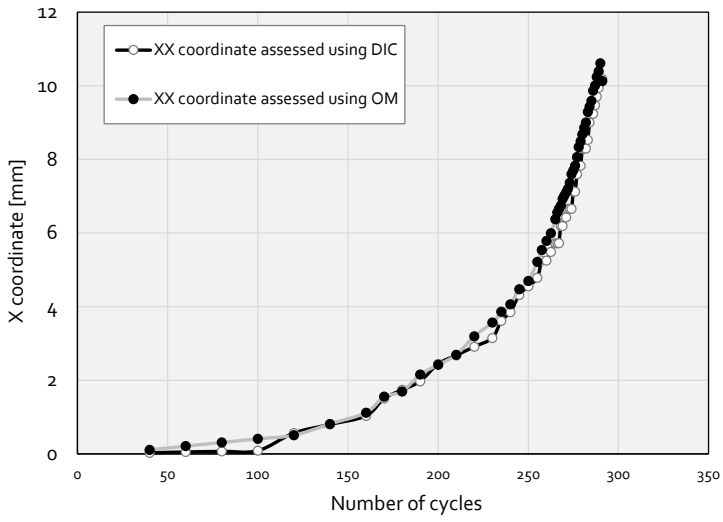

a)

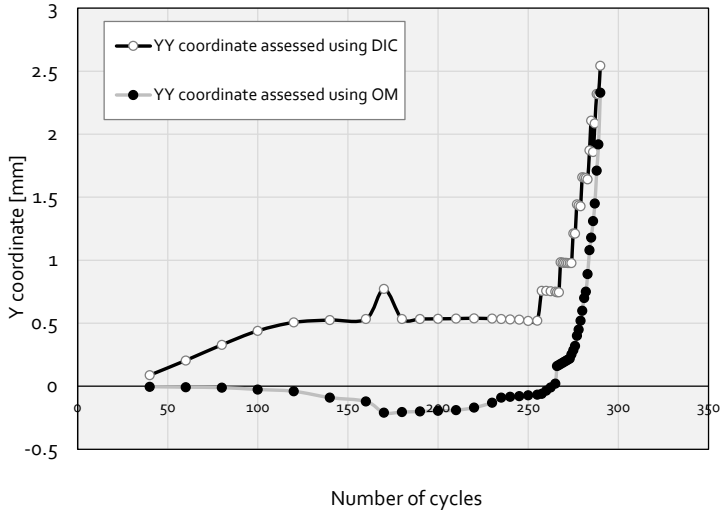

b)

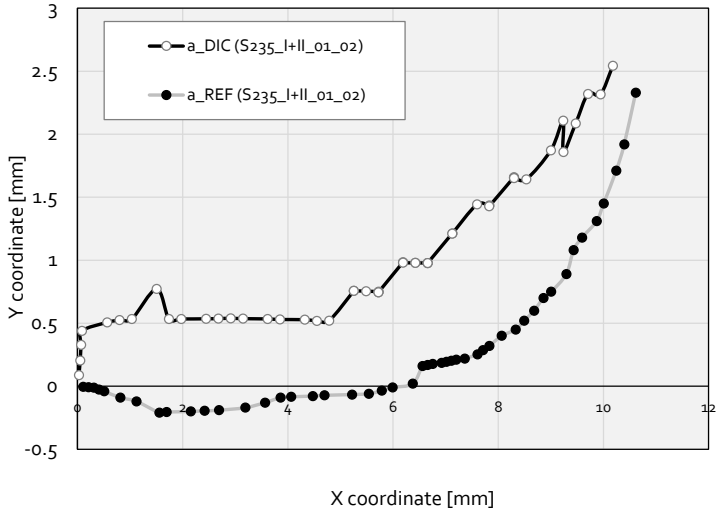

c)

Figure 3.28 – Comparison of assessed crack paths for S235_I+II_01_02 specimen: a) evolution of the X coordinate of the crack tip b) evolution of the Y coordinate of the crack tip; c) crack path.

The crack path assessments regarding the S235_I+II_01_03 specimen, using both applied methods, are plotted in Figure 3.29. Figure 3.29a) compares the evolution of the X coordinate evaluated using the proposed two approaches, a very good agreement between approaches being observed. However, the comparison of the evolution of the Y coordinate (Figure 3.29b) exhibits a maximum deviation of about 1mm between both methodologies. However this deviation tends to reduce as the Y coordinate increases to a value higher than 1mm. The fatigue crack path of the modified CT specimen (S235_I+II_01_03) is presented in Figure 3.29c). The Figure 3.30 plots the measured crack paths for the S235_I+II_01_04 specimen. Again the absolute deviations were registered for the Y coordinate computation. For this specimen the crack propagated horizontally for a few millimetres and only deviated latter when the measured fatigue crack length increased above 4mm (Figure 3.30b). The measured fatigue crack path of the S235_I+II_01_04 specimen is presented in Figure 3.30c).

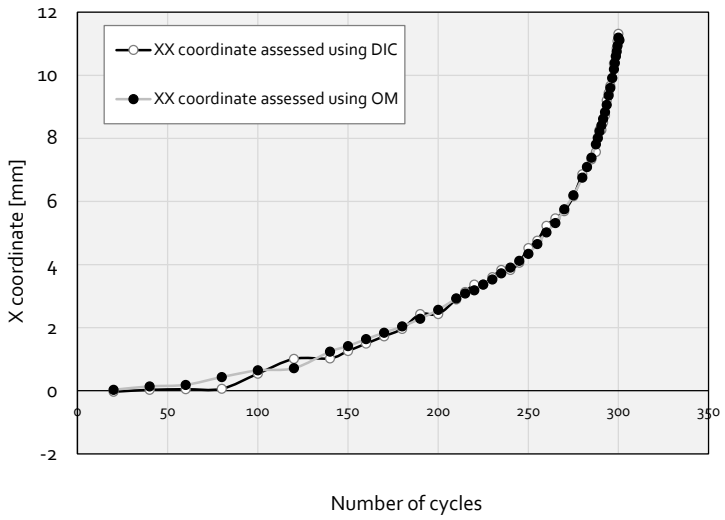

a)

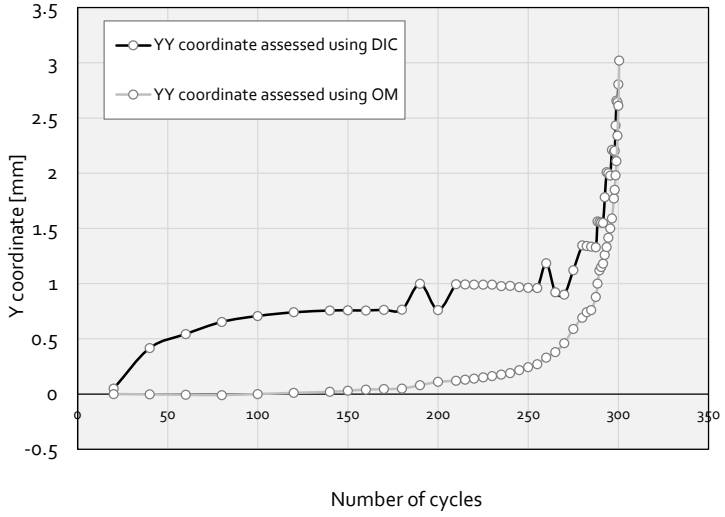

b)

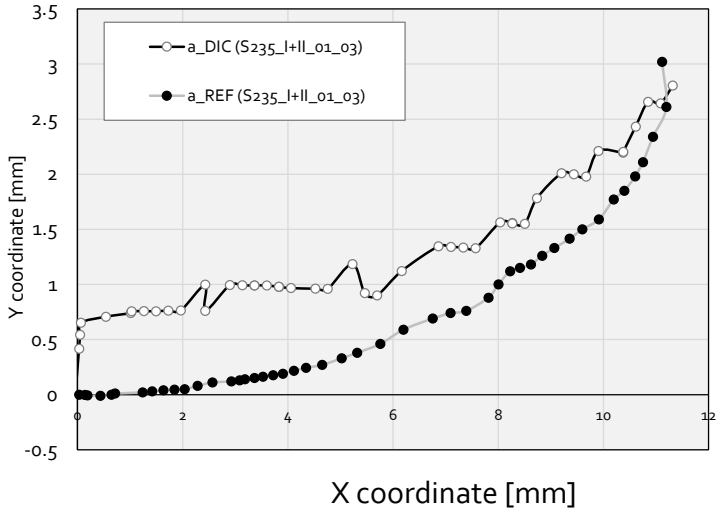

c)

Figure 3.29 - Comparison of assessed crack paths for S235_I+II_01_03 specimen: a) evolution of the X coordinate of the crack tip b) evolution of the Y coordinate of the crack tip; c) crack path.

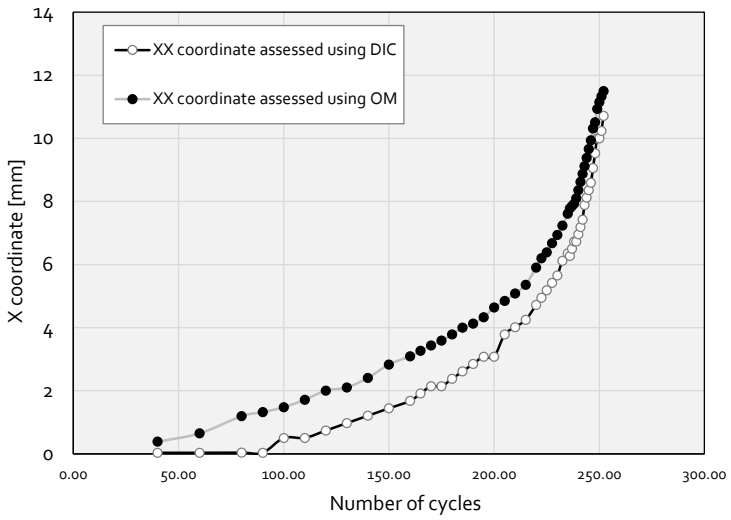

a)

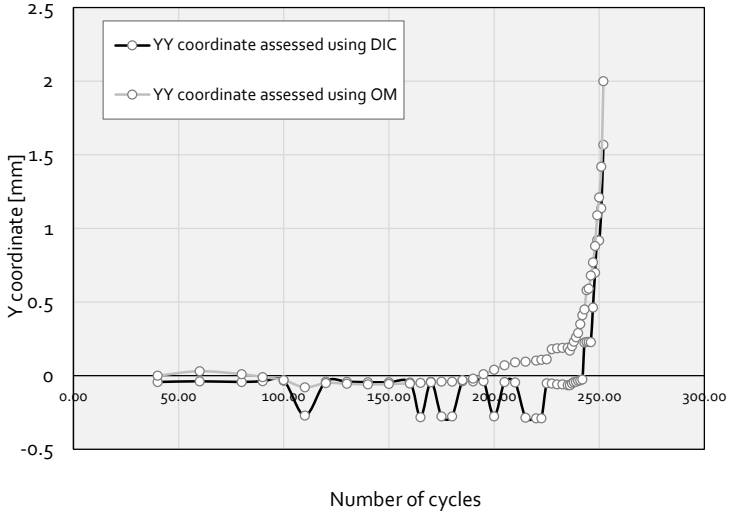

b)

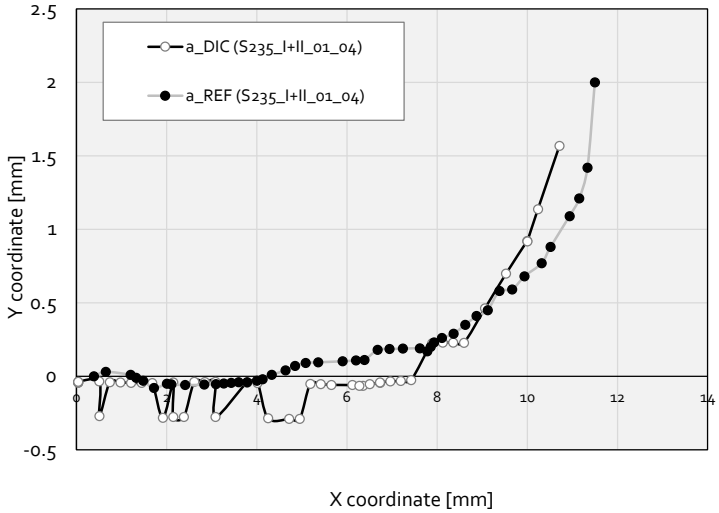

c)

Figure 3.30 - Comparison of assessed crack paths for S235_I+II_01_04 specimen: a) evolution of the X coordinate of the crack tip b) evolution of the Y coordinate of the crack tip; c) crack path.

In general, the crack path assessment using the DIC approach revealed higher scatter than resulted from the direct optical observations. Also, the DIC approach presented crack paths with higher Y coordinates than the one obtained from direct optical measurements. Only one partial exception was observed for the S235_I+II_01_04 specimen.

Figure 3.31 plots over the fractured specimen's surface background, the crack path geometries assessed using both approaches for the S235_I+II_01_01, S235_I+II_01_02, S235_I+II_01_03 and S235_I+II_01_04 specimens. A third degree polynomial function (red line) and an exponential function (green line) were fitted to the path computed from DIC approach. It can be observed that the crack path assessed using DIC data fits well the actual fatigue crack path. A slight mismatch is observed in Figures 3.31a) and 3. 31d), which may be very likely attributed to parasitic rigid body adjustments in the experimental setup.

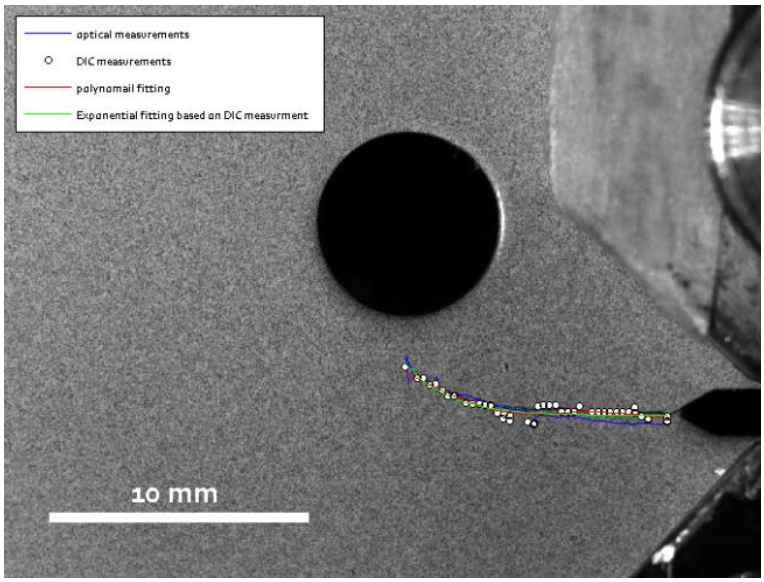

a)

Figure 3.31 – Comparison of crack paths evaluated from direct optical measurements, DIC computation and from polynomial and exponential fittings of DIC results: a) S235_I+II_01_01; b) S235_I+II_01_02; c) S235_I+II_01_03 and d) S235_I+II_01_04. (1/2)

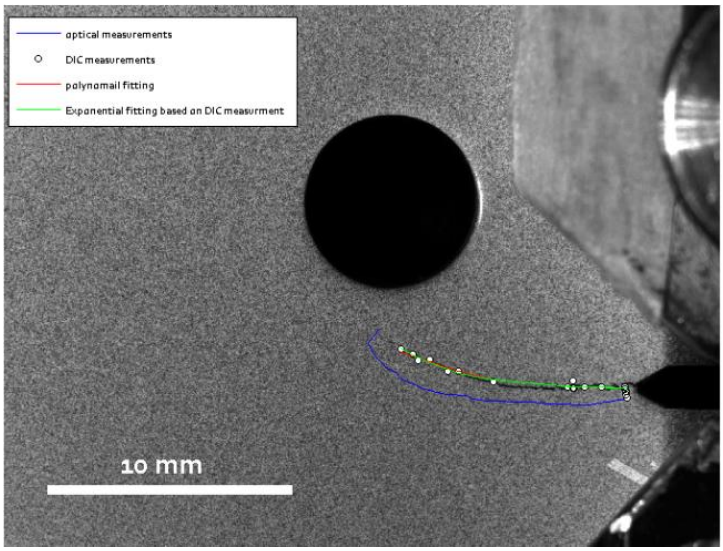

b)

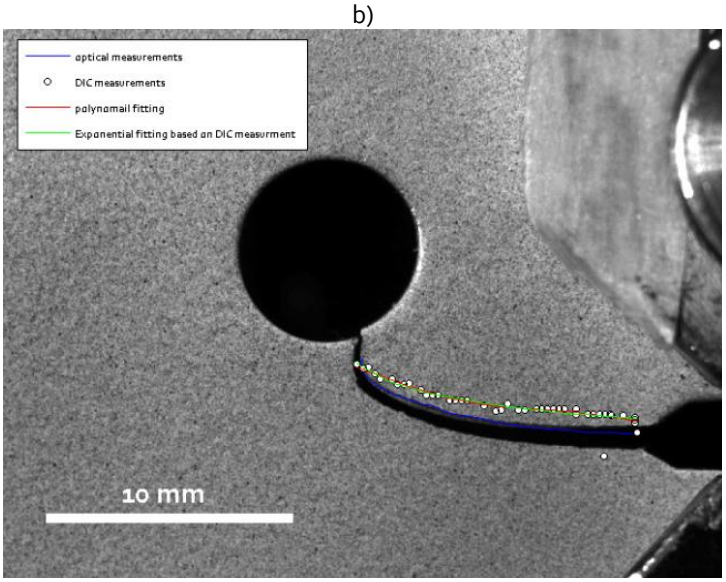

c)

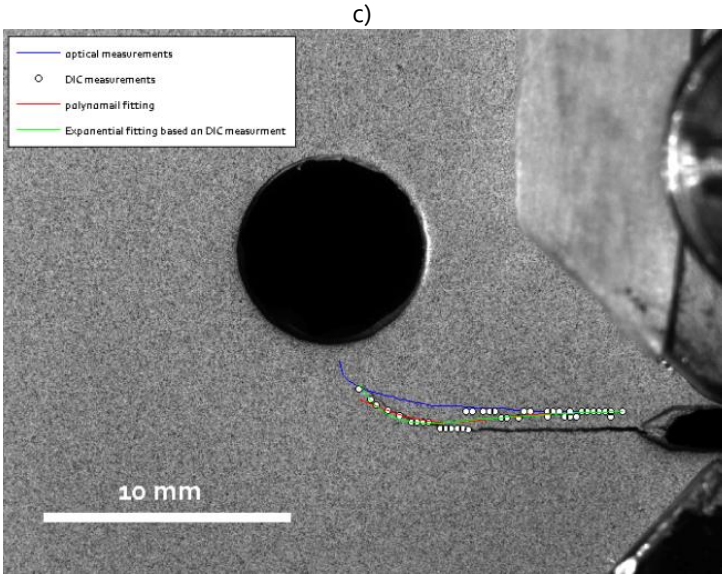

d)

Figure 3.31 – Comparison of crack paths evaluated from direct optical measurements, DIC computation and from polynomial and exponential fittings of DIC results: a) S235_I+II_01_01; b) S235_I+II_01_02; c) S235_I+II_01_03 and d) S235_I+II_01_04. (2/2)

In order to improve the discussion about the fatigue crack paths obtained in mixed-mode fatigue crack conditions, 2D finite element models of the modified CT specimens were built using the commercial software ANSYS®[35]. This model was used to simulate the fatigue crack growth from the initial notch root. The material was considered linear elastic and isotropic (E=210 GPa and ν=0.27). To model the pin loading on the CT specimens, all simulations were performed using the Augmented Lagrange contact algorithm, together with the Coulomb friction model (μ=0.3). Quadratic quadrilateral and triangular, with 8 and 6 nodes, respectively, were considered. Regular quadratic quadrilateral finite elements were applied around the crack tip (see Figure 3.32). Mode I and Mode II stress intensity factors were computed for this case using the modified Virtual Crack Closure Technique [36], using the displacements and nodal forces from the finite element model.

Numerical fatigue crack path predictions were performed using a crack branching criterion. For this case, three possibilities for the crack branching criterion were adopted: i) the Maximum Tangential Stress criteria (MTS) [37], ii) the Maximum Circumferential Stress criteria (MCS) [37] and iii) the Maximum Energy Release Rate (MERR) [37].

Figure 3.33 compares the simulated fatigue crack paths with the experimentally based fatigue crack paths. Two experimental based fatigue crack paths were considered in this comparison, namely based on direct optical observation (a_REF series) and based on DIC analysis (a_DIC series). Concerning the numerical predictions, the previous referred branching criteria were used.

Figure 3.33a) exhibits the experimental and numerical fatigue crack paths simulated for specimens S235_I+II_01_01 and S235_I+II_01_02. These specimens show the same nominal geometry, therefore only one crack path was simulated for each crack branching criterion. Figure 3.33a) reveals important scatter between experimental based crack paths, optical and DIC based ones. The numerical simulated crack paths using distinct crack branching criteria are almost coincident. The simulated crack paths fit in between both experimental based crack paths obtained for the S235_I+II_01_01 and S235_I+II_01_02 specimens, but a very close proximity of obtained with respect to the S235_I+II_01_01 specimen. The Figure 3.33b) presents the results concerning the S235_I+II_01_03 specimen, revealing that the predicted crack path is closer to the DIC

experimentally based crack path. In this case a small discrepancy in the simulated crack paths between the MCS and the other branching criteria was observed. Figure 3.33c) presents the analysis of the S235_I+II_01_04 and S235_I+II_01_05 specimens (two repetitions). Unfortunately, no experimental based DIC path was processed for the S235_I+II_01_05 specimen. A very good agreement between the numerical based crack paths and the optical observed crack path was observed for the S235_I+II_01_05 specimen. It can also be pointed out that the S235_I+II_01_04 specimen showed very distinct behaviour than S235_I+II_01_05 specimen. In this specimen, mixed-mode crack propagation conditions only started for a fatigue crack above 4 mm.

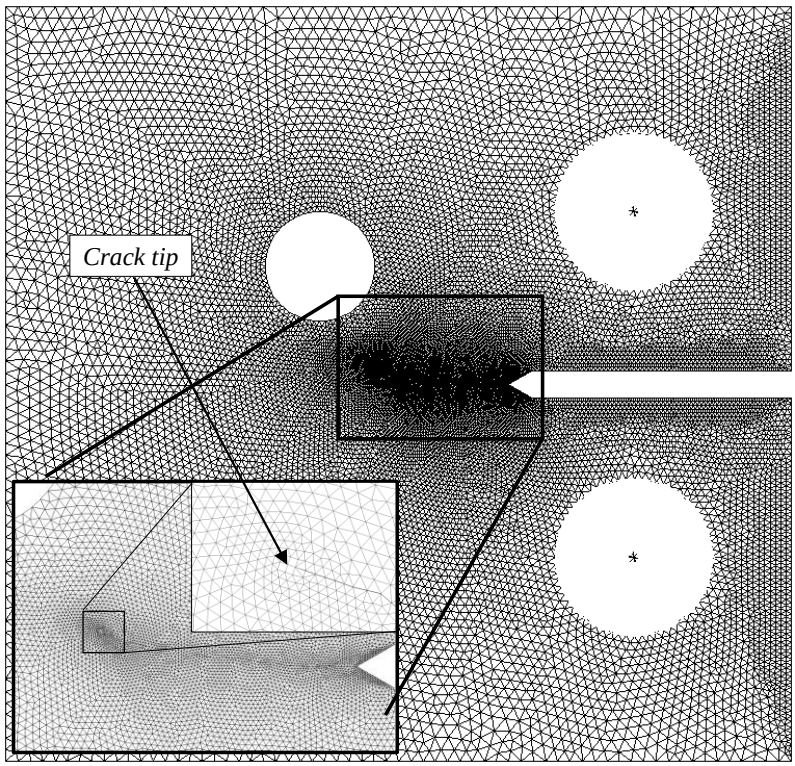

Figure 3.32 - Finite element mesh of a cracked modified CT specimen.

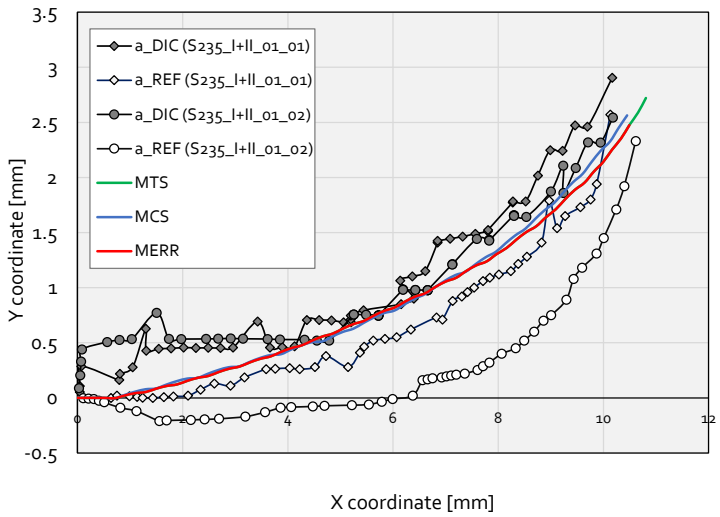

a)

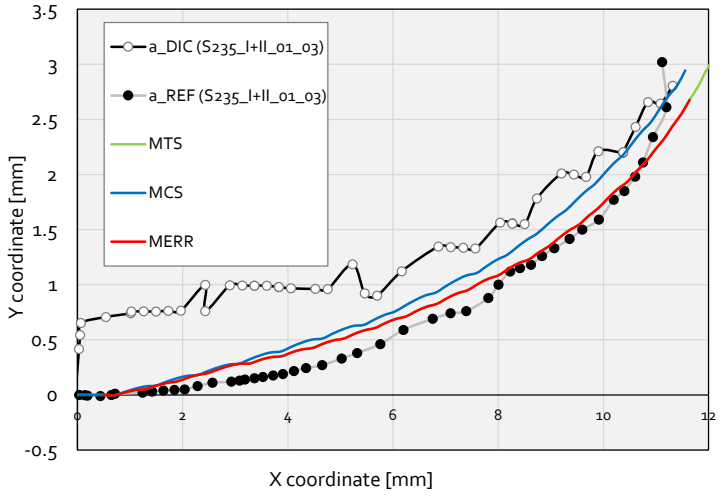

b)

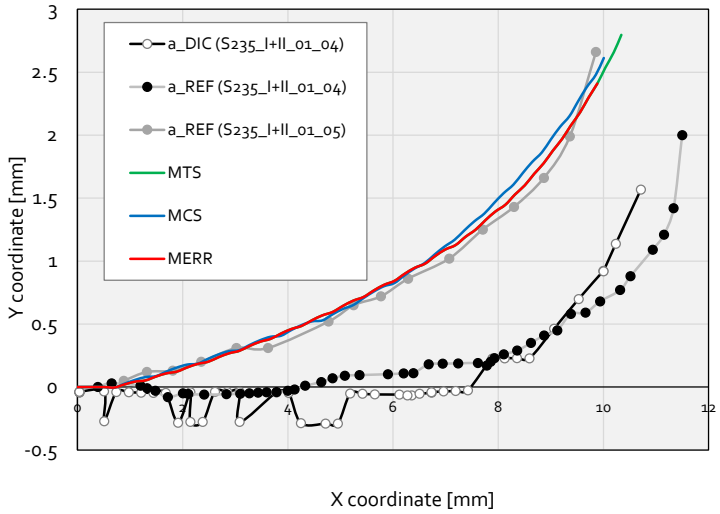

c)

Figure 3.33 - Comparison of fatigue crack path predictions and experimental based crack paths: a) S235_I+II_01_01 and S235_I+II_01_02 specimens; b) S235_I+II_01_03 specimen; c) S235_I+II_01_04 and S235_I+II_01_05 specimens.

The discrepancies in the experimentally based crack paths verified in some test repetitions may be attributed to geometric variations within general manufacturing tolerances. However, these specimens showed great sensitivity to the side hole position, therefore the tolerances respecting the side hole position and size should be reduced.

3.4.2.2.3. Stress intensity factors assessment for experimentally based crack paths

In this section, the mode I and mode II stress intensity factors were evaluated for the tested modified CT specimens, along the experimentally based crack paths. This task was performed using the displacement fields from the DIC (displacement based technique). In addition, a numerical approach was followed based on finite element analysis. In this second approach, the experimentally based crack paths (from DIC analysis) were introduced in the finite element model and the respective stress intensity factors were computed using the virtual crack closure technique and the displacement extrapolation techniques.

3.4.2.2.3.1. SIFs computation using full-field DIC displacements

DIC was applied previously to compute crack tip location. Once determined the crack tip location, the corresponding stress intensity factors are computed using a displacement based approach. For mixed-mode (mode I and mode II) loaded cracks, the analytical displacement fields around the crack tip are expressed using the Williams series, as follows [38]:

$$\begin{aligned} u_x = &\sum_{n=1}^{\infty} \frac{A_{In}}{2G} r^{n/2} \left\{ \kappa \cos\frac{n}{2}\theta - \frac{n}{2}\cos\left(\frac{n}{2}-2\right)\theta + \left[\frac{n}{2}+(-1)^n\right]\cos\frac{n}{2}\theta \right\} \\ &- \sum_{n=1}^{\infty} \frac{A_{IIn}}{2G} r^{n/2} \left\{ \kappa \sin\frac{n}{2}\theta - \frac{n}{2}\sin\left(\frac{n}{2}-2\right)\theta + \left[\frac{n}{2}-(-1)^n\right]\sin\frac{n}{2}\theta \right\} \end{aligned} \tag{3.11}$$

$$\begin{aligned} u_y = &\sum_{n=1}^{\infty} \frac{A_{In}}{2G} r^{n/2} \left\{ \kappa \sin\frac{n}{2}\theta + \frac{n}{2}\sin\left(\frac{n}{2}-2\right)\theta - \left[\frac{n}{2}+(-1)^n\right]\sin\frac{n}{2}\theta \right\} \\ &- \sum_{n=1}^{\infty} \frac{A_{IIn}}{2G} r^{n/2} \left\{ -\kappa \cos\frac{n}{2}\theta - \frac{n}{2}\cos\left(\frac{n}{2}-2\right)\theta + \left[\frac{n}{2}-(-1)^n\right]\cos\frac{n}{2}\theta \right\} \end{aligned} \tag{3.12}$$

where u_x and u_y are the displacement components, G represents the elastic shear modulus, κ is equal to $(3-\nu)/(1+\nu)$ for plane stress conditions and is equal to $3-4\nu$ for plane strain conditions, ν is the Poisson ratio and r and θ are respectively the polar coordinates cantered at crack tip. In the previous series the first terms A_{I1} and A_{II1} are relate to the mode I and mode II stress intensity factors, K_I and K_{II} according to the following relations:

$$A_{I1} = \frac{K_I}{\sqrt{2\pi}} \tag{3.13}$$

$$A_{II1} = -\frac{K_{II}}{\sqrt{2\pi}} \tag{3.14}$$

The dominant displacement component, concerning mixed-mode crack problems is unknown. Luo and Huang [25] and Yoneyama *et al.* [39] used the radial or circumferential displacement component on the polar coordinate system transformed from displacements on Cartesian coordinates. In the proposed method, both displacement components on the Cartesian coordinates are used simultaneously for the determination of the mixed-mode stress intensity factors. The displacement fields in Equation (3.11) and Equation (3.12) can be rewritten in the following compact form:

$$u_x = \sum_{n=1}^{\infty} A_{In} f_{In}(r,\theta) - \sum_{n=1}^{\infty} A_{IIn} f_{IIn}(r,\theta) \tag{3.15}$$

$$u_y = \sum_{n=1}^{\infty} A_{In} g_{In}(r,\theta) - \sum_{n=1}^{\infty} A_{IIn} g_{IIn}(r,\theta) \tag{3.16}$$

where f_I, f_{II}, g_I and g_{II} are known functions of the coordinates r and θ and characteristic properties of the material, as shown in Equations (3.11) and (3.12). Considering the possibility of rigid body displacements, the displacement field data obtained by experimental or numerical methods can be expressed as:

$$u_{xk} = \sum_{n=1}^{N} A_{In} f_{In}\left(r_k, \theta_k\right) - \sum_{n=1}^{N} A_{IIn} f_{IIn}\left(r_k, \theta_k\right) + T_x - R y_k \tag{3.17}$$

$$u_{yk} = \sum_{n=1}^{N} A_{In} g_{In}\left(r_k, \theta_k\right) - \sum_{n=1}^{N} A_{IIn} g_{IIn}\left(r_k, \theta_k\right) + T_y + R x_k \tag{3.18}$$

where T_x and T_y express the rigid body translation along the x and y directions, R is the rigid body rotation. In previous equations the series were truncated to a finite number of N terms. The subscript k (k =1,2,..., M, M: total number of displacement data points) represents a point with polar coordinates $\left(r_k, \theta_k\right)$ at which the displacement values u_{xk} and u_{yk} are expressed using the truncated series. The polar coordinates of a given point at crack tip vicinity can be computed using the following relations:

$$r_k = \sqrt{\left(x_k - x_0\right)^2 + \left(y_k - y_0\right)^2} \tag{3.19}$$

$$\theta_k = \tan^{-1}\left(\frac{y_k - y_o}{x_k - x_o}\right) \tag{3.20}$$

where x_o and y_o are the location of a crack tip relative to an arbitrary cartesian coordinate system and x_k and y_k are the Cartesian coordinates of the k point under consideration. As the crack tip coordinate is already known. The unknown coefficients A_{In}, A_{IIn}, T_x, T_y and R may be computed using a system of linear equations that results from the application of the least-squares technique to fit the analytical relations (3.17) and (3.18) to the experimental DIC displacement fields.

All experimental data points were considered leading to an over-determined set of simultaneous equations. In this work the Williams series were truncated to 10 terms. In this case, not only the coefficients of the Williams series were computed, including the stress intensity factors, but also the rigid body translations and rotation were estimated.

3.4.2.2.3.2. Stress intensity computation using FEM

Besides the simulation of the fatigue crack paths, finite element modelling was also used to compute the history of stress intensity factors for the experimentally-based crack paths. The same finite element models of the modified CT specimens described previously were also used to this purpose. The experimental fatigue crack paths assessed using the DIC approach were introduced into the finite element models of the modified CT specimens and the stress intensity factors afterwards computed using numerical approaches. The computed numerical stress intensity factors were then compared with the stress intensity factors computed from the full DIC approach.

A typical finite element mesh of a modified CT specimen was already presented in Figure 3.32. The mesh presented in this figure corresponds to the mesh proposed for the S235_I+II_01_01 specimen and the presented crack corresponds already to an imposed crack path from DIC evaluation. It is interesting to refer that regular quadratic quadrilateral finite elements were considered around the crack tip, in order to facilitate the stress intensity factors computation using the Virtual Crack Closure Technique, as proposed by Krueger [36]. A coordinate system was adopted at the crack tip, oriented along the crack tip faces direction, in order to allow the appropriate computation of the nodal displacements and forces. The displacement extrapolation procedure was also used to compute the stress intensity factors, as an alternative approach. The stress intensity factors computation may be achieved using several alternative techniques, as the referred Virtual Crack Closure Technique (VCCT) [36], the Displacement Extrapolation method (DE), the contour integral method [40], among others. However, it was decided to limit the study presented in this section to the referred two techniques.

The Virtual Crack Closure Technique

The virtual crack closure technique is based on the assumption that the energy E released when the crack is extended by Δa from $a+\Delta a$ (node i) to $a+2\Delta a$ (node k) is identical to the energy required to close the crack. A modified version of the virtual crack closure technique [36] considers both nodal forces and displacement for the same step, to obtain the energy release rate. On effect, it is assumed that a crack extension from $a+\Delta a$ to $a+2\Delta a$ does not significantly modify the state at the crack tip. Therefore the

displacements behind the crack tip are approximately equal to the displacements behind the original crack tip [36]. For 8-noded 2D elements (see Figure 3.34), the equations to calculate the mode I and mode II strain energy release rates are:

$$G_I = \frac{1}{2\Delta a}\left[Z_i \left(w_l - w_{l^*} \right) + Z_j \left(w_m - w_{m^*} \right) \right] \tag{3.21}$$

$$G_{II} = \frac{1}{2\Delta a}\left[X_i \left(u_l - u_{l^*} \right) + X_j \left(u_m - u_{m^*} \right) \right] \tag{3.22}$$

where: Δa is the length of the elements at the crack front; X and Z are nodal forces; u and w are nodal displacements. Previous relations were proposed for a unit thick plate. For a plate with thickness t, the relations must be divided by this parameter. The strain energy release rates can be converted into stress intensity factors using well-known fracture mechanics relations.

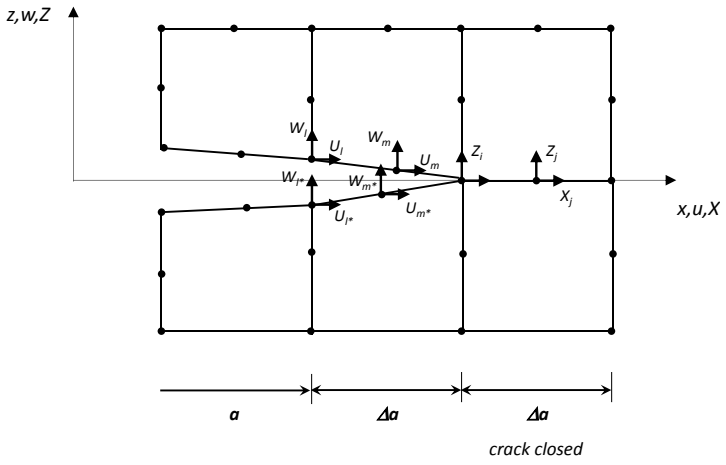

Figure 3.34 – Nomenclature for Virtual Crack Closure Technique applied to 8-noded plane finite elements.

Displacement extrapolation method

The displacement extrapolation method uses a fit of the nodal displacements in the vicinity of the crack tip. The actual displacements near the crack tip, for linear elastic materials, may be computed using the following relations, which correspond to the truncated Williams series [41]:

$$u_x = \frac{K_I}{4G}\sqrt{\frac{r}{2\pi}}\left((2\kappa-1)\cos\frac{\theta}{2}-\cos\frac{3\theta}{2}\right)-\frac{K_{II}}{4G}\sqrt{\frac{r}{2\pi}}\left((2\kappa+3)\sin\frac{\theta}{2}+\sin\frac{3\theta}{2}\right) \tag{3.23}$$

$$u_y = \frac{K_I}{4G}\sqrt{\frac{r}{2\pi}}\left((2\kappa-1)\sin\frac{\theta}{2}-\sin\frac{3\theta}{2}\right)-\frac{K_{II}}{4G}\sqrt{\frac{r}{2\pi}}\left((2\kappa+3)\cos\frac{\theta}{2}+\cos\frac{3\theta}{2}\right) \tag{3.24}$$

where u_x and u_y are the nodal displacements, assessed in a local Cartesian coordinate system located at the crack tip, r and θ are polar coordinates defined with respect to a origin at the crack tip, G is the shear modulus and κ is defined according to the following relation:

$$\kappa = \begin{cases} 3-4\nu \ \textit{if plane strain} \\ \dfrac{3-\nu}{1+\nu} \ \ \textit{if plane stress} \end{cases} \tag{3.25}$$

where ν is the Poisson's ratio. Considering $\theta = \pm 180^\circ$, Equations (3.23) and (3.24) result into the following expressions:

$$u_x = \frac{K_{II}}{2G}\sqrt{\frac{r}{2\pi}}\left(1+\kappa\right) \tag{3.26}$$

$$u_y = \frac{K_I}{2G}\sqrt{\frac{r}{2\pi}}\left(1+\kappa\right) \tag{3.27}$$

Equations (3.26) and (3.27) can be applied for some points at crack faces, located at distinct distances, r, from the crack tip. The stress intensity factors can then be computed by extrapolation the $K(r)$ results for r=0. By this process, the numerical and truncation errors of the proposed procedure are minimized.

Stress intensity factors values

Figure 3.35 plots the equivalent stress intensity factors range evolution with the fatigue crack size. The equivalent stress intensity factor was computed using the Tanaka relation

42 Four series were presented in the graphs of Figure 3.35. In one series, the stress intensity factors were computed using a full two-steps approach. Firstly the crack path was assessed using DIC and then the stress intensity factors were computed using full-field displacements from DIC. This original approach led to significant scatter in the data. In order to reduce this scatter, the crack path was then fitted using a third degree polynomial function and the stress intensity factors were afterwards computed using this smoothed crack path, which resulted in significantly less scatter.

Stress intensity factors computed with the numerical model, for the imposed experimental crack path, were also plotted in Figure 3.35. The smoothed crack path from DIC analysis was used as input in the numerical model for the stress intensity factors computation. Figure 3.35a) presents the experimental and numerical stress intensity factor results for the S235_I+II_01_01 modified CT specimen. Figure 3.35a) allows the observation of a good match between the experimental and numerical equivalent stress intensity factors, at least until a crack of 7 mm. The full DIC results, without crack path filtering, shows very oscillating responses. The numerical does not exhibits this kind of scatter because a smoothed crack path was used in the simulations. Both numerical techniques explored for stress intensity factors computation produced the same results. The same analysis was made for the S235_I+II_01_02 specimen (Figure 3.35b)) and a reasonable agreement between both numerical and experimental stress intensity evolution curves was also observed. The Figure 3.35c) presents the results for the S235_I+II_01_03 specimens. A very good agreement may be observed for crack sizes until 8 mm. Above this value, some deviations are found between the numerical approaches and the experimental approaches. Figure 3.35d) exhibits the comparisons of the numerical and experimental equivalent stress intensity factor evolutions for the S235_I+II_01_04 specimen. In this case, only above crack sizes of 8 mm, the numerical/experimental approaches deviate significantly.

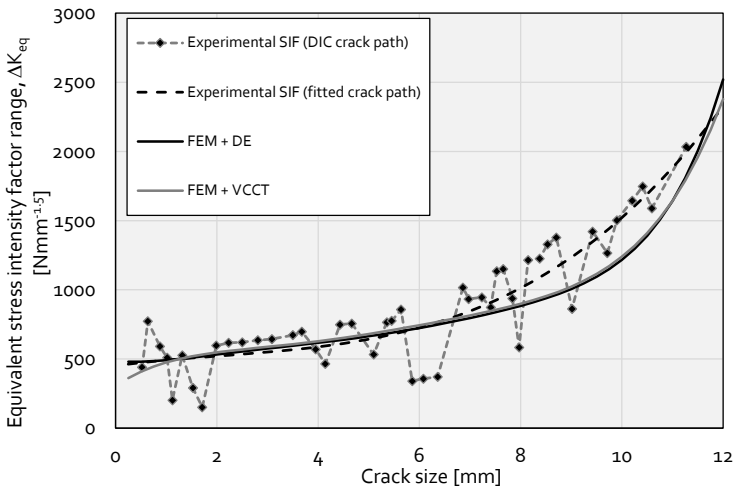

a)

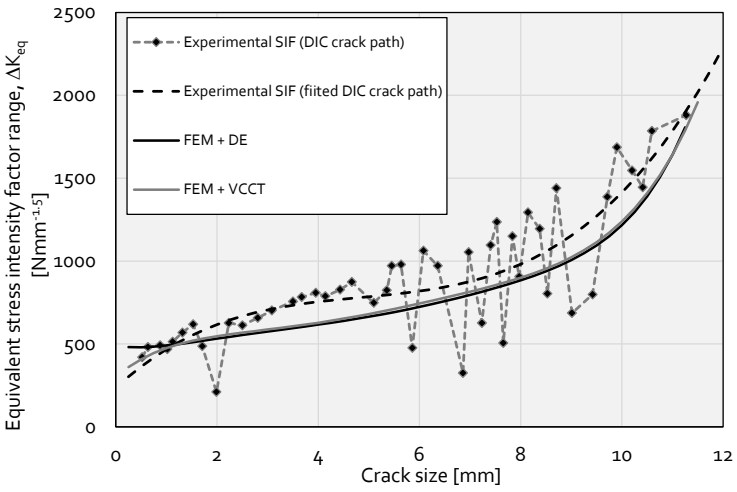

b)

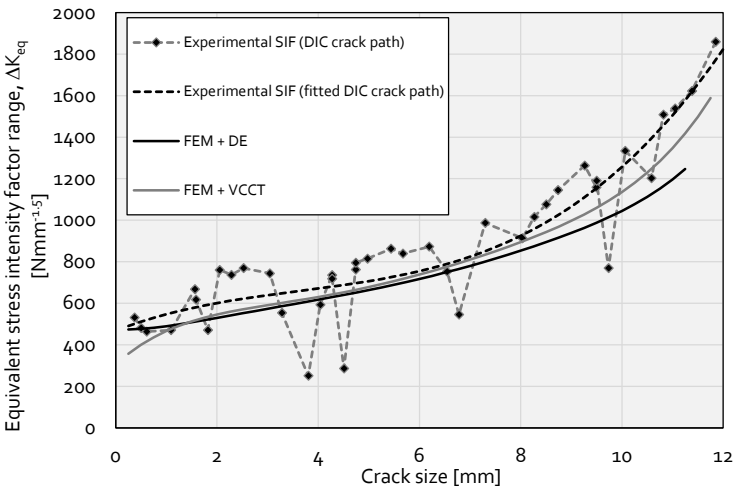

c)

Figure 3.35 - Comparison of equivalent stress intensity factor range evolutions with the fatigue crack size: a) S235_I+II_01_01; b) S235_I+II_01_02; c) S235_I+II_01_03; d) S235_I+II_01_04. (1/2)

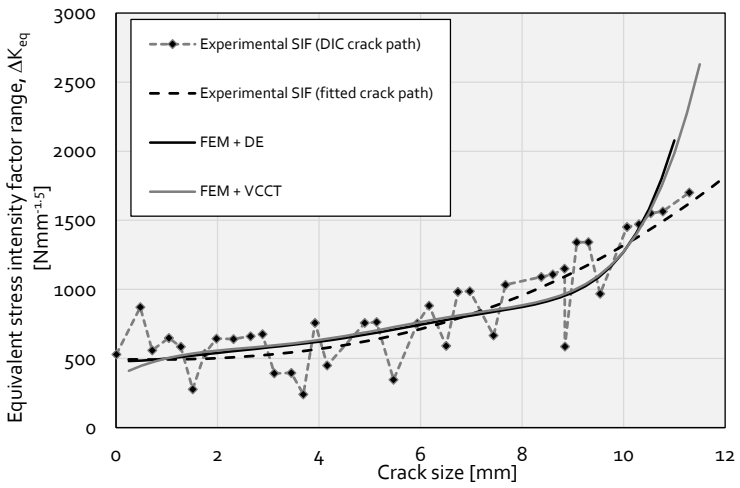

d)

Figure 3.35 - Comparison of equivalent stress intensity factor range evolutions with the fatigue crack size: a) S235_I+II_01_01; b) S235_I+II_01_02; c) S235_I+II_01_03; d) S235_I+II_01_04. (2/2)

3.4.2.2.4. Correlation of pure mode I and mixed mode crack propagation data

In this section, the pure mode I and mixed-mode fatigue crack propagation rates are correlated for the S235 steel. The mixed-mode fatigue crack propagation data used in this section came from DIC data reduction analysis applied to mixed-mode fatigue crack propagation tests, with the crack path fitted with a 3rd degree polynomial. Figure 3.36a) presents the fatigue crack growth rates obtained for the S235 steel grade, combining pure mode I fatigue crack growth data for a stress ratio R_σ=0.01, and mixed-mode (I+II) fatigue crack propagation data. The data is correlated using the Paris relation, a determination coefficient of 0.916 being observed, representing a satisfactory value, taking into account the distinct data sources. The equivalent stress intensity factor, as proposed by Tanaka [42], is demonstrated to be adequate to correlate mixed-mode fatigue crack propagation data.

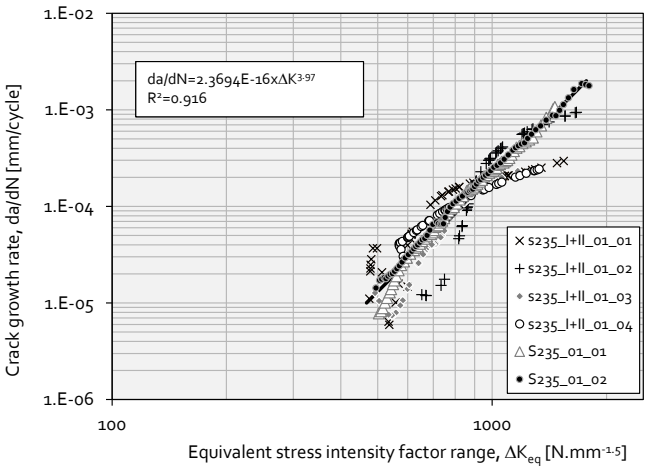

a)

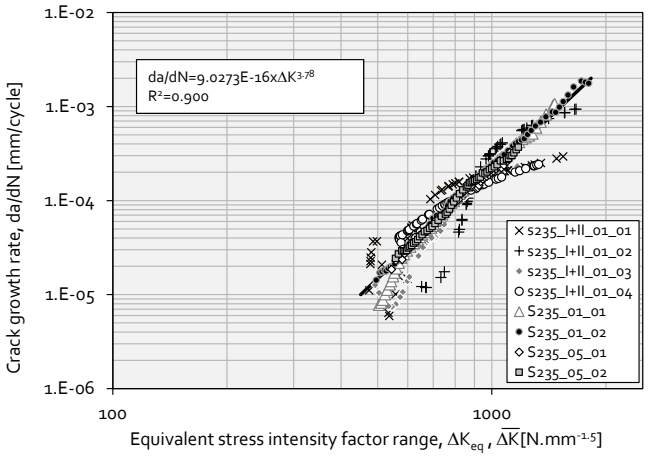

b)

Figure 3.36 - Mixed mode fatigue crack propagation rates measured for the S235 steel grade: combine pure mode I (R_σ=0) and Mixed mode fatigue crack growth rate data.

Figure 3.36b) plots together all pure mode I and mixed-mode fatigue crack propagation data, covering for pure mode I two distinct stress ratios. In this case the Walker equation is used, resulting a determination coefficient R^2=0.900.

3.4.3. Comparison of fatigue crack growth data of several structural steels

Figure 3.37 compares the global fatigue crack propagation trends for S235, S355 and S690 steels, tested in this study and tested by De Jesus *et al.* [9]. Only pure mode I data is presented. One interesting observation is the clear higher fatigue crack propagation rates observed for the S690 steel, independently of the stress ratio. With respect to the S355 and S235 steels, the comparison of their crack propagation rates is not so conclusive since contradictory results may be observed. For example, for R_σ=0.01, the S235 shows

higher fatigue crack propagation rates than the S355 steel; however, for R_σ=0.5 the S235 steel shows higher fatigue crack propagation rates than S355 steel tested in this study, but lower values than S355 steel tested by De Jesus *et al.* [9]. However, the differences between fatigue crack propagation rates for these two steels are lower than the one obtained for the S690 steel. Another important aspect is the stress ratio influence that is higher for the S690 steel than for the mild steels.

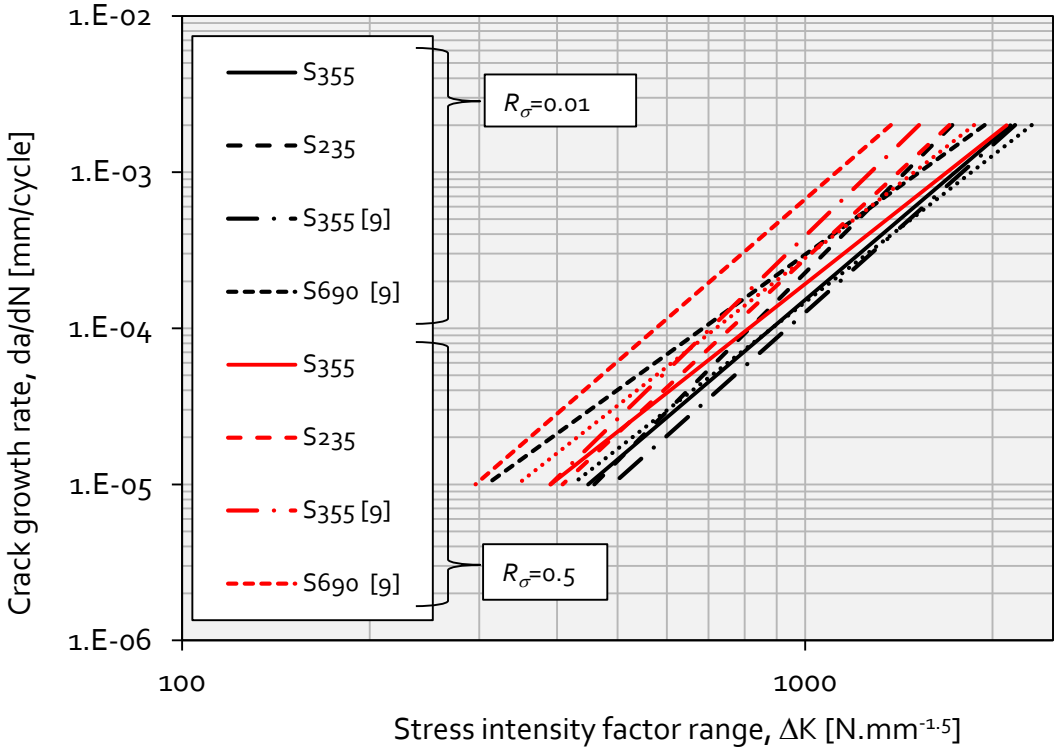

Figure 3.37 –-Comparison of pure mode I fatigue crack propagation rates for several structural steels.

3.4.4. Comparison of the fracture surfaces between S355 and S235 structural steels

In this section fracture surfaces from pure mode I fatigue crack propagation tests are presented and compared for the two structural steel grades. The fracture surfaces were obtained using scanning electron microscopy and are shown in Figure 3.38. These figures show typical fatigue striations that were observed at the final stage of the crack propagation tests. However, no distinctive features can be referred for these materials which is coherent with the fact that both materials showed relatively close fatigue crack propagation rates.

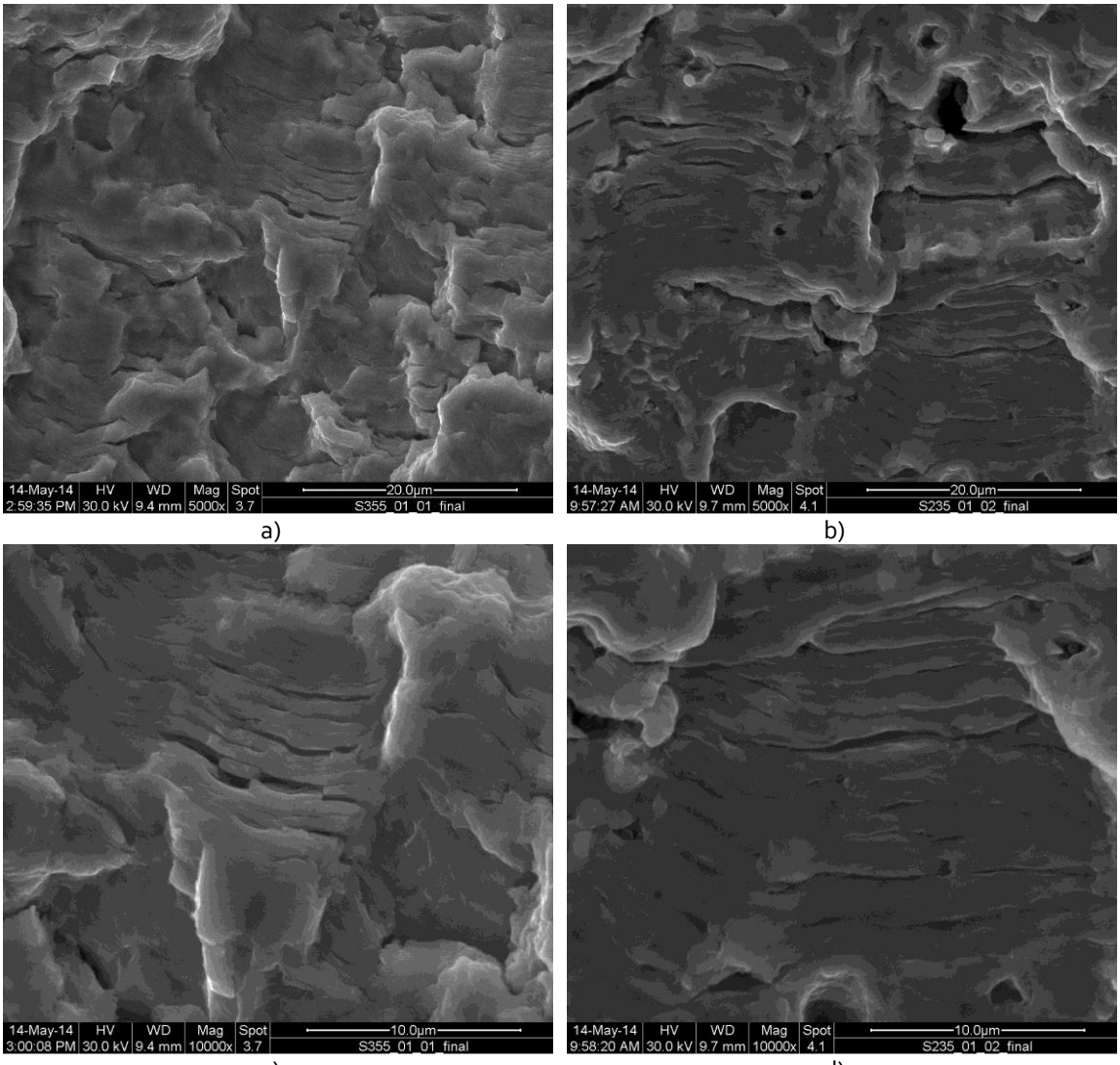

Figure 3.38 – Fracture surfaces of CT specimens tested under pure mode I fatigue loading, obtained from SEM: a) S355, 5000x magnification; b) S235, 5000x magnification; c) S355, 1000x magnification; d) S235, 1000x magnification.

3.5. CONCLUDING REMARKS

A fatigue characterization of two structural mild steels, the S355 and S235 steel grades, was presented in this chapter. The investigated materials were extracted from welded and riveted joints that are presented in the Chapter IV. Fatigue tests using smooth specimens were performed on these steels since this information is important to assess fatigue crack initiation on structural components. Also, fatigue crack propagation tests were performed in order to assess fatigue crack propagation rates that are required to

model fatigue crack propagation in structural components. Besides the Pure mode I fatigue crack propagation tests, mixed mode fatigue crack propagation tests were also considered for the S235 steel. Digital Image Correlation technique was used to measure the fatigue crack path and to compute stress intensity factors directly from field information.

Regarding cyclic elastoplastic analysis, the two investigated steels show similar cyclic elastoplastic and fatigue properties. The investigated materials were also compared with the S690 steel, which is considered a high strength structural steel. There is a clear distinction between the fatigue performance of the high strength and mild steels. The strain-life curve suffers a clock-wise rotation with the decrease of the static strength of the steel. This result makes the high strength steels more fatigue resistant for high-cycle fatigue regimes.

Concerning the fatigue crack growth results, the thickness effect on fatigue crack propagation was investigated for the S355 steel grade. It was observed that the fatigue crack growth rates do not change significantly when tested thicknesses range from 4 to 30 mm. Pure mode I and mixed mode (mode I + mode II) fatigue tests were performed for the S235 material. A two-step methodology to compute stress intensity factor using the displacement field from DIC data is proposed. It was observed that the two-steps approach was able to assess the fatigue crack paths and also to compute the stress intensity factors. Mixed mode and pure mode I data was conveniently assessed using the Tanaka equivalent stress intensity factor.

A comparison involving the fatigue crack propagation rates of the mild steels and the S690 high strength steel was also considered. A global analysis revealed that the mild steels show lower fatigue crack propagation rates than the high strength steel and the stress ratio effects were more relevant for the high strength steel than for the mild steels.

3.6. REFERENCES

[1] ASTM - American Society for Testing and Materials, "ASTM E606-92: Standard Practice for Strain Controlled Fatigue Testing", In Annual Book of ASTM Standards, Part 10, pp. 557-571, 1998.

[2] ASTM - American Society for Testing and Materials, "E647-9: Standard test method for measurement of fatigue crack growth rates", 03.01, West Conshohocken, PA, pp. 591-629, 1999.

[3] Abdel-Raouf, H.A., Plumtree A., "Cyclic stress–strain response and substructure", International Journal of Fatigue 23, pp.799-805, 2001.

[4] Ramberg, W., Osgood, W.R., "Description of stress-strain curves by threeparameters", NACA Tech. Note No. 902, 1943.

[5] Basquin, O.H., "The Exponential Law of Endurance Tests", Proceedings of the American Society for Testing and Materials. 10, pp. 625-630, 1910.

[6] Coffin, L.F., "A study of the effects of the cyclic thermal stresses on a ductile metal", Translations of the ASME. 76, pp. 931-950, 1954.

[7] Manson, S.S., "Behaviour of materials under conditions of thermal stress", NACA TN-2933, National Advisory Committee for Aeronautics, 1954.

[8] Morrow, J. D., "Cyclic plastic strain energy and fatigue of metals", Int. Friction, Damping and Cyclic Plasticity, ASTM, STP 378, pp. 45-87, 1965.

[9] de Jesus, A. M. P., Matos, R., Fontoura, F. C. B., Rebelo, C., da Silva, L.S., Veljkovic,. M., "A comparison of the fatigue behavior between S355 and S690 steel grades", Journal of Constructional Steel Research 79, pp. 140–150, 2012.

[10] Beretta, S., Bernasconi, A., Carboni, M., "Fatigue assessment of root failures in HSLA steel welded joints: a comparison among local approaches", International Journal of Fatigue 31, pp.102-10, 2009.

[11] Chen, H., Grondin, G.Y., "Driver RG. Characterization of fatigue properties of ASTM A709 high performance steel", J Constr Steel Res 63, pp.838-48, 2007.

[12] Paris, P.C., Erdogan, F., "A critical analysis of crack propagation laws", Transactions of the ASME Series E: Journal Basic Engineering 85, pp.528–34, 1963.

[13] Walker, E.K., "The effect of stress ratio during crack propagation and fatigue for 2024-T3 and 7076-T6 aluminum", In: Effect of environment and complex load history on fatigue life, ASTM STP 462. Philadelphia: American Society for Testing and Materials, pp.1–14, 1970.

[14] Albuquerque, C.M.C., Miranda, R., Richter-Trummer, V., Figueiredo, M., Calçada, R., De Castro, P.M.S.T., "Fatigue crack propagation behaviour in thick steel weldments", International Journal of Structural Integrity 3(2), pp. 184 – 203, 2012.

[15] Yoneyama, S., Ogawa, T., Kobayashi, Y., "Evaluating mixed-mode stress intensity factors from full-field displacement fields obtained by optical methods", Engineering Fracture Mechanics 74, pp.1399–1412, 2007.

[16] Nishioka T, Kurio K, Nakabayashi H., "An intelligent hybrid method to automatically detect and eliminate experimental measurement errors for linear elastic deformation fields", Exp Mech 40(2), pp.170–9, 2000.

[17] Réthoré J., Gravouil A., Morestin F., Combescure A., "Estimation of mixed-mode stress intensity factors using digital image correlation and an interaction integral", International Journal of Fracture,132(l), pp. 65–79, 2005.

[18] Hild F., Roux S., "Measuring stress intensity factors with a camera: integrated digital image correlation". Comptes Rendus Mecanique, 334(1), pp.8–12, 2006.

[19] Epstein, J. S., Jung, H. Y., Reuter, W. G., "Stress intensity factor extraction using moiré interferometry based on a two-parameter displacement eigenfunction – validity criteria and comparison with ASTM E399 K plane-strain test methods", Optics Lasers Engng 13(2), pp.167–80, 1990.

[20] MacKenzie, P. M., Walker, C.A., Giannettoni, R., "A technique for experimental evaluation of mixed mode stress intensity factors", International Journal of Fracture 62(2), pp.139–48, 1994.

[21] Chao, Y.J., Luo, P. F., Kalthoff, J. F., "An experimental study of the deformation fields around a propagating crack tip", Exp Mech, 38(2), pp.79–85, 1998.

[22] Barker, D. B., Sanford, R. J., Chona, R., "Determining K and related stress-field parameters from displacement fields", Exp Mech 25(4), pp.399–407, 1985.

[23] McNeill, S.R., Peters, W.H., Sutton, M.A., "Estimation of stress intensity factor by digital image correlation", Engng Fract Mech28(1), pp.101–12, 1987.

[24] Moore, A. J., Tyrer, J. R., "Phase-stepped EPSI and moiré interferometry for measuring stress-intensity factor and J integral" Exp Mech 35(4), pp.306–14, 1995.

[25] Luo, P. F., Huang, F. C., "Application of stereo vision to the study of mixed-mode crack-tip deformations", Optics Lasers Engng, 33(5), pp.349–68, 2000.

[26] Ju, S. H., Liu, S. H., Liu K. W., "Measurement of stress intensity factors by digital camera" Int J Solids Struct 43(5), pp.1009–22, 2006.

[27]Sutton, M., Orteu, J.J., Schreier, H., "Image correlation for shape, motion and deformation measurements: Basic concepts, theory and applications", Springer, 2009.

[28]Pan, B., Qian, K., Xie, H., Asundi, "A. Two-dimensional digital image correlation for in-plane displacement and strain measurement: a review", Measurement Science and Technology, 20, 062001, 2009.

[29] Xavier, J., Pereira, J.C. R., de Jesus, A. M.P., "Characterisation of steel components under monotonic loading by means of image-based methods", Optics and Lasers in Engineering 53, pp.142-151, 2014.

[30] ARAMIS comercial software. GOM (http://www.gom.com/)

[31] Xavier, J., Oliveira M., Monteiro P., Morais J.J.L., "Direct Evaluation of Cohesive Law in Mode I of Pinus pinaster by Digital Image Correlation, Experimental Mechanics (in press DOI: 10.1007/s11340_013-9838-y), 2010.

[32] Grégoir D., "Initiation, propagation, arrêt et redémarrage de fissures sous impact", PhD Thesis, LaMCoS-INSA de Lyon, 2002.

[33] Catalanotti G., Camanho P.P,. Xavier J., Dávila C.G., Marques A.T., "Measurment of resistance curve in the longitudinal failure of composites using digital images correlation, Compos, Sci Technol 70(13), pp.1986-1993, 2010.

[34] Nguyen T.L., Hall S., Vacher P., Viggiani G., "Fracture mechanisms in soft rock: identification and quantification of evolving displacement discontinuities by extended digital image correlation", Tectonophysics 503(1-2), pp.117-128, 2011.

[35] SAS, ANSYS, Version 12.0, Swanson Analysis Systems Inc., Houston, 2010.

[36] Krueger, R., "Virtual crack closure technique: History, approach, and applications", Applied Mechanics Reviews 57(2), pp.109-143, 2004.

[37] Stine V., "Numerical Simulation of Fatigue Crack Growth", Norwegian University of Science and Technology Department of Engineering Design and Materials, June 2012.

[38] Atluri, S.N., Kobayashi, A.S., "Mechanical responses of materials. In: Kobayashi AS, editor. Handbook on experimental mechanics. 2nd ed. VCH; pp. 1–37, 1993.

[39] Yoneyama, S., Morimoto, Y., Takashi, M., "Automatic determination method of stress intensity factor utilizing digital image correlation and nonlinear least squares", In: Wu Z, Abe M, editors. Structural health monitoring and intelligent infrastructure. Swets & Zeitlinger; pp. 1357–1367, 2003.

[40] Paris, P. C., Sih, G. C., "Stress Analysis of Cracks". Fracture Toughness and Testing and its Applications. American Society for Testing and Materials. Philadelphia, STP 381. pp. 30-83. 1965.

[41] Raju, I. S., "Calculation of Strain-Energy Release Rates With Higher Order And Singular Finite Elements", Eng. Fracture Mech., Vol. 28, pp. 251-274, 1987.

[42] Tanaka, K., "Fatigue Crack propagation from crack inclined to the cycle tensile axis", Engineering Fracture Mechanics 6, pp. 496-507, 1974.

Chapter IV

Fatigue behaviour of relevant riveted and welded details of railway bridges

4.1. INTRODUCTION

This chapter presents an experimental program of fatigue tests performed with riveted and welded connections. Three riveted connections were considered, namely one down-scale connection and two small-scale connections. The down-scale geometry is a beam-to-column connection that was motivated by a potential critical detail of the Trezói Railway Bridge. As referred previously (see Chapter I), one bridge potential critical detail consists of a cross girder-to-upper stringer riveted connection, located just over a pier of the bridge. Concerning the welded specimens, four welded specimens with small variations were considered. These welded specimens were motivated by welded joints present inside the steel box girder of the Alcácer do Sal Railway Bridge, at an internal reinforcing diaphragm, particularly in the welded joint between the diagonal of the diaphragm and the central hanger/gusset. It can be emphasized that the proposed welded joints aimed the investigation of the fillet welds geometry and the member thickness effects on fatigue strength of the welded joint. The original welded detail of the Alcácer do Sal Railway Bridge that was the motivation for the fatigue tests on welded joints, was not fully performed according to the current design rules, such as the ones foreseen in the Eurocode 3 (EC3) [1]. The actual and code recommended fillet welds were tested. Also the thicknesses of the members currently in the bridge are too high to allow laboratory testing with the same thicknesses. Therefore, welded specimens with reduced thicknesses were proposed for laboratory testing. Nevertheless, two distinct reduced thicknesses were investigated in order to assess any possible thickness effect on the fatigue strength of the riveted joints. This experimental campaign was performed by author and was a contribution for the FADLESS European project [2].

4.2. EXPERIMENTAL FATIGUE PROGRAM OF RIVETED DETAILS

In this section an experimental program of fatigue tests of riveted structural details is described. This experimental program includes fatigue tests of riveted details which are common in old bridges, which is the case of the Trezói Railway Bridge. The geometry of the selected structural details will be described in detail as well as the experimental details will be given. The testing results and their discussion will be presented.

4.2.1. Design of the riveted specimens and experimental details

Riveted specimens were motivated by fatigue studies performed on the Trezói Railway Bridge under the framework of the FALDLESS project [2]. Numerical studies performed under the FADLESS project using a classical S-N code-based approach, supported by a global beam finite element model of the bridge referred the structural node number six, located at the top of the west pier, as the most stressed nodes of the Trezói railway bridge (see Figure 4.1). Despite not showing visible damage, this node can be considered one of the most fatigue critical nodes of the bridge. Particularly, the riveted connection between the cross-girder and the upper stringer, shown in the Figure 4.2, has been indicated as a potential fatigue critical location. Therefore, the riveted connection between the cross girder and the structural node was investigated using a down-scale simplified riveted specimen which was fatigue tested at laboratory conditions. An experimental laboratory fatigue campaign was performed based on a series of beam-to-column riveted joints. In addition, two series of double shear riveted splices were investigated, one with a single row of rivets and the other with two rows of rivets. This type of riveted shear splices is very common in riveted bridges.

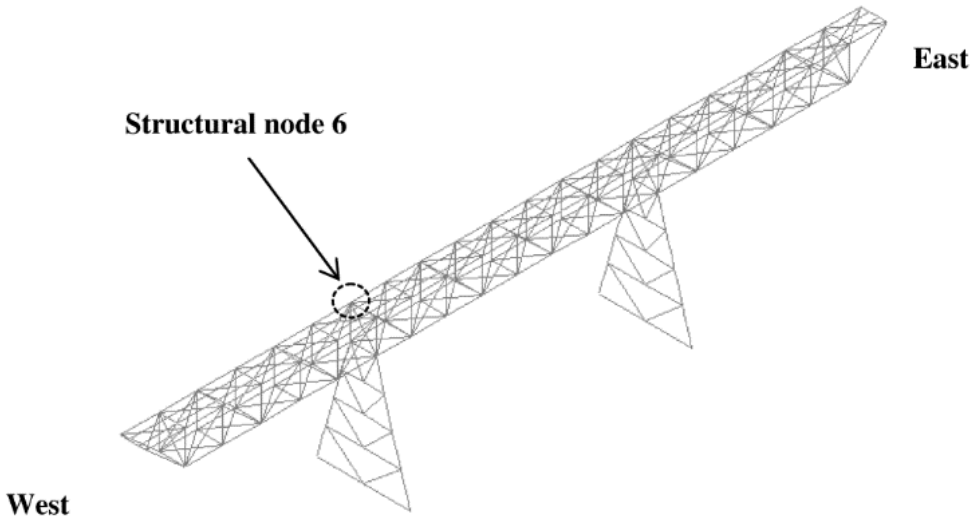

Figure 4.1 - Location of the potential fatigue critical node in the riveted Trezói railway bridge.

Figure 4.2 - Actual photo of the potential fatigue critical structural node of the Trezói railway bridge (node 6).

Taking into account the laboratory load capacities available in FEUP, the down-scale riveted specimen illustrated in the Figures 4.3 and 4.4 was produced for fatigue testing. These riveted specimens were composed of an IPN220 beam of 2000 mm in length, attached to a rigid column (HEB300 beam) by two angles (L120x120x12). Table 4.1 compares the down-scale riveted specimen with the actual structural node of the Trezói bridge. The connection between the I-shaped beam and the angle was achieved by rivets with original diameter of 17 mm applied in holes with diameter of 19 mm. The angles were attached to the rigid column via preloaded high strength bolts (M20-12.9). Despite similar, the bridge and laboratory riveted joints show distinct stifnesses. However, the same type of load distribution is promoted in the joint. Also, the distinct stiffnesses are not relevant since the tests were performed under load control. A total of eight down-scale R1 specimens were fatigue tested under cycling bending (simple bending). The rigid column was used for all specimens. In the current analysis, the down-scale riveted specimens were named as R1 series. The R1 series were fatigue tested using an INSTRON servo-hydraulic actuator rated to 100kN, mounted in a rigid steel frame, as illustrated in Figure 4.5. Strain gauges were applied near rivets as well as remotely in order to monitor local/remote strains (see strain gauge positions illustrated in Figure 4.6).

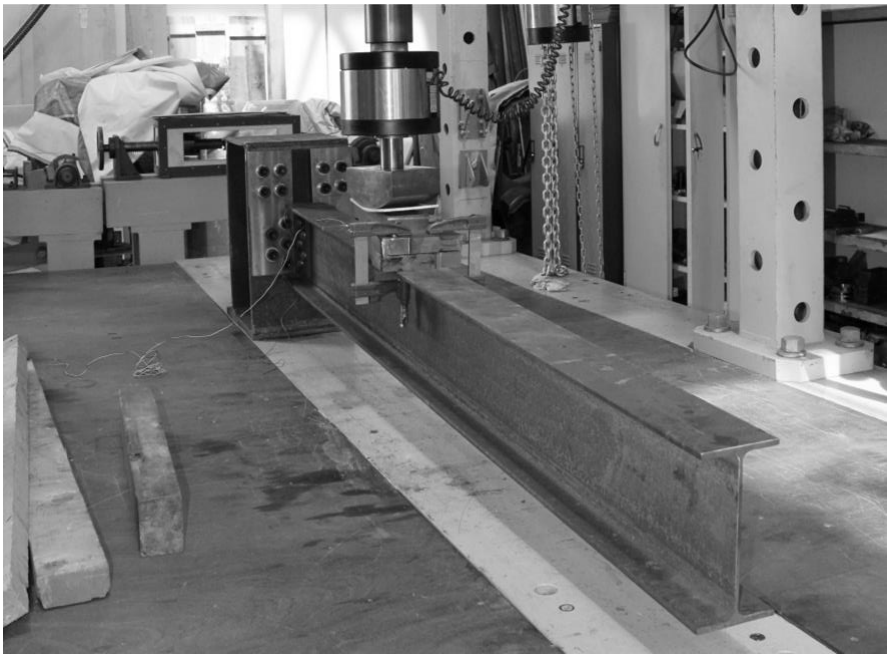

Figure 4.3 – Down-scale riveted specimen, R1 series.

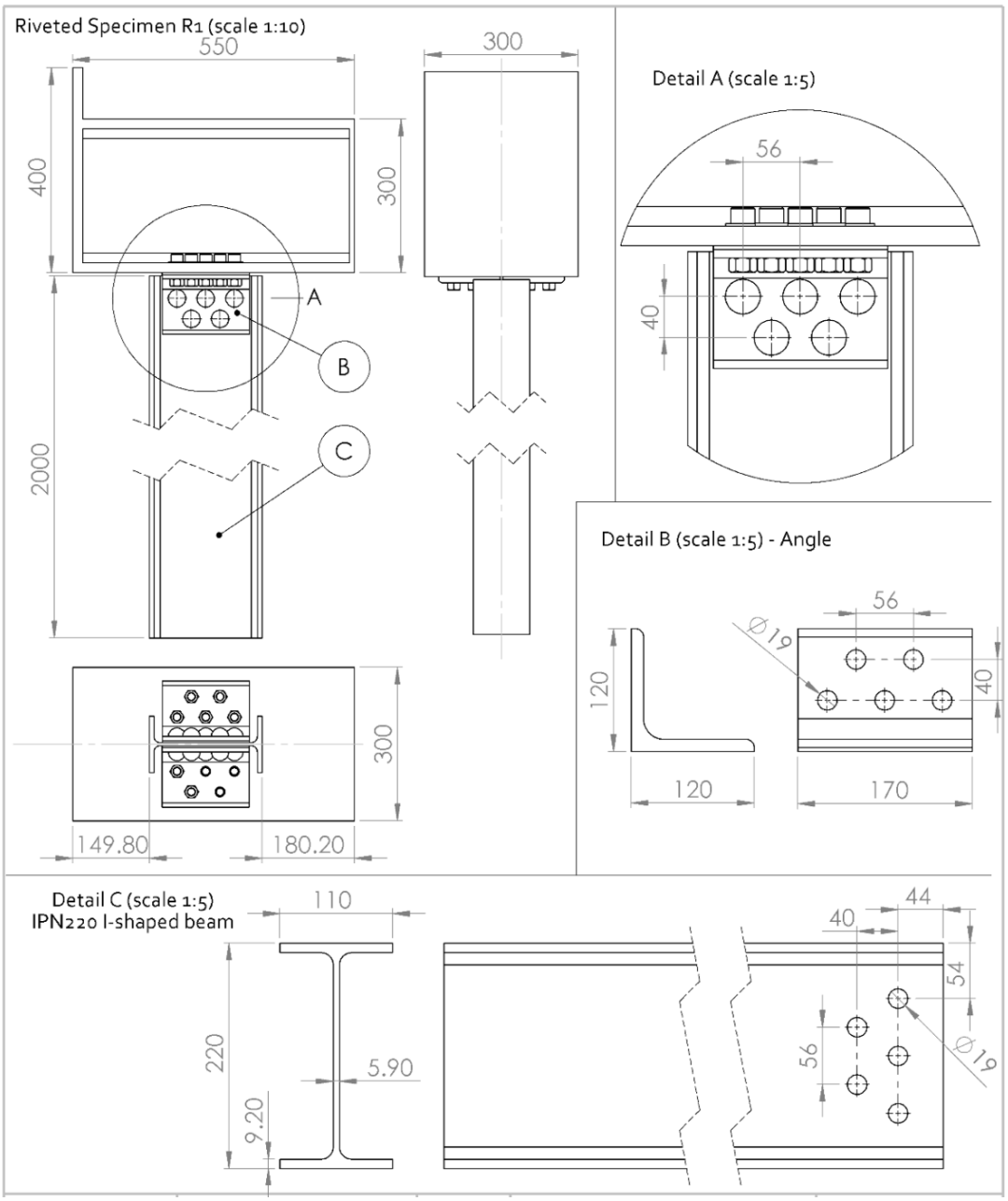

Figure 4.4 - Down-scale riveted specimen geometry (R1 series).

During the fatigue tests of the R1 riveted series, some premature fatigue failures were observed in bolts used to connect the angles to the column. Since the aim of these tests was to investigate the fatigue behaviour of the riveted connections, two reinforcing steel plates were used to cover the angle legs that are in direct contact with the flange of the column (see Figure 4.3). These plates promoted the load redistribution in a higher number of bolts, eliminating the fatigue weakness on the tensioned bolts.

The R1 riveted specimens were tested under cyclic bending loading (cantilever beam). Despite being prepared with 2000 mm in length, beams were tested with a load applied at 800 mm from the beam clamped end, in order to allow actuator displacement reduction during test and a testing frequency increasing. The load was applied thru a roller-type support.

Additionally to the down-scale specimens (R1 series), two series of small-scale specimens were prepared for fatigue testing in laboratory, as illustrated in the Figures 4.7 and 4.8. One of these series consisted of a double shear splice with one line of four rivets (see Figure 4.7). Strain gauges were placed between the first two rivets in order to generate data about the load transfer between the middle and side plates. These riveted specimens formed the R2 series. The R2 specimens were fatigue tested using an Instron 8801 servo-hydraulic machine, rated to 100kN (Figure 4.9 a)), with a load R-ratio equal to 0.01. Another small-scale riveted connection consisted of a double shear splice with two lines of four rivets each (see Figure 4.8). These double shear riveted splices formed the R3 series. Rivet centres were not aligned in the transverse direction, as illustrated in Figure 4.8. Strain gauges were also glued between rivets for the R3 series (see Figure 4.8c). The R3 series were fatigue tested in a MTS servo-hydraulic machine rated to 250kN (Figure 4.9 b)) with a load R-ratio equal to 0.1.

All riveted specimens were built with the same rivets. 17 mm diameter rivets were applied and expanded to adjust to 19 mm diameter holes.

Relevant components of the Trezói Bridge were made of St37 steel grade, corresponding to current S235JR structural steel grade, according to the current European standards (EN 10028). Consequently, the riveted specimens were built using the S235JR steel for the plates, beams and angles. The rivets were produced with low-carbon steel. Tables 4.2 and 4.3 show respectively the chemical composition and tensile properties for the S235JR steel and rivet material.

The experimental program of all riveted joints is summarized in Tables 4.4, 4.5 and 4.6 for the R1, R2 and R3 test series, respectively. Besides the applied loading conditions, these tables also include the observed fatigue lives for the tested specimens.

Table 4.1 - Comparison between the structural node of the Trezói Bridge and the suggested riveted down-scale simplified specimens.

Cross girder-to-stringer riveted connection	***Riveted down-scale specimens***
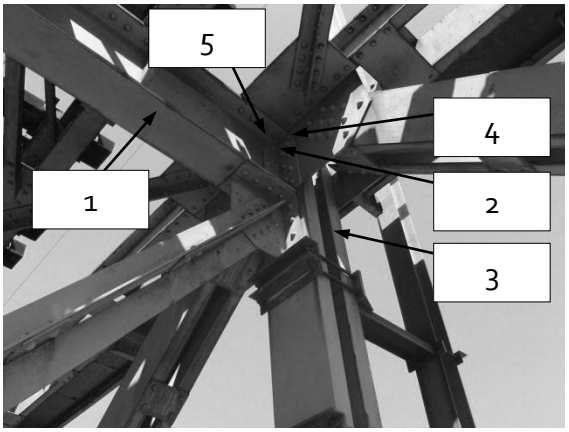	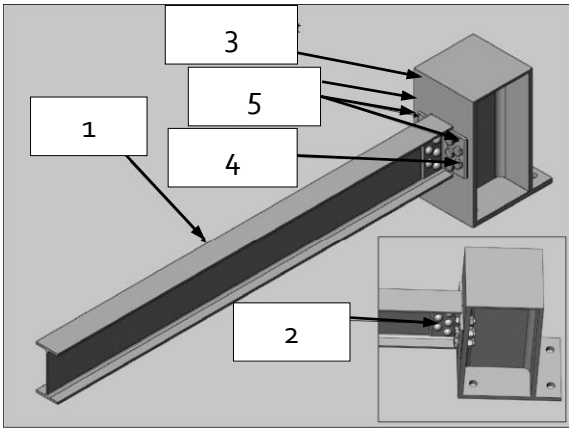
1 I-shape beam (height=690mm)	1 I-shape beam (height=220mm)
2 Riveted connection (7 rivets, ϕ12mm and expanded to ϕ24mm)	2 Riveted connection (5 rivets, ϕ17mm and expanded to ϕ19mm)
3 Column/pier (section height=400mm/section width=300mm: 2xC sections with 400x120 mm)	3 Column support (HEB300)
4 Rivets (ϕ22mm)	4 Preload high strength bolts (M20-12.9)
5 Angles (L126x126x14 mm)	5 Angles (L120x120x12 mm)

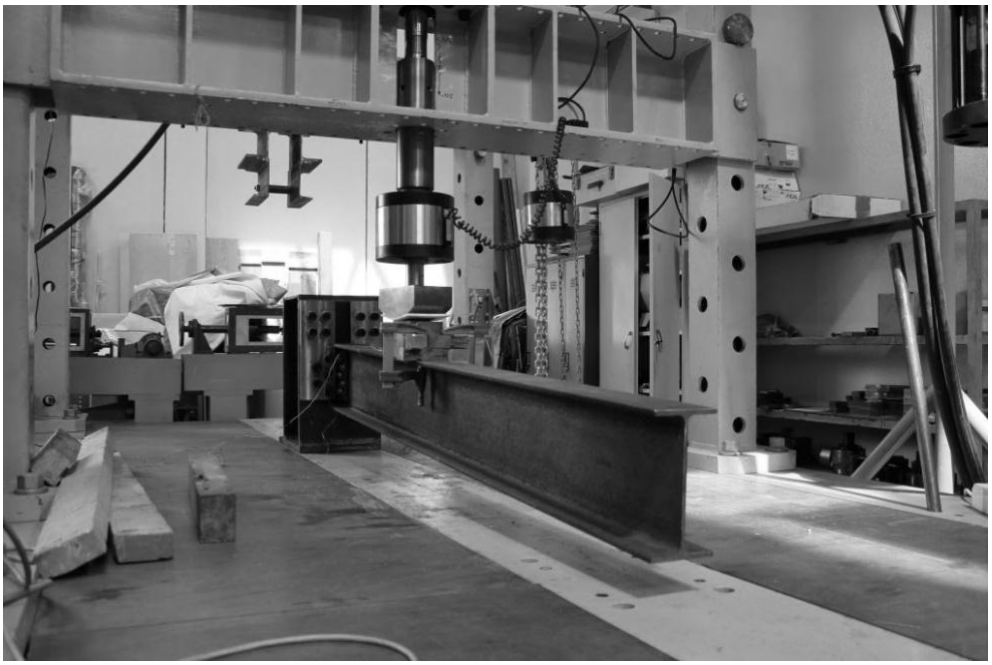

Figure 4.5 - Riveted down-scale specimen mounted in a rigid frame and 10 tons servo-hydraulic actuator.

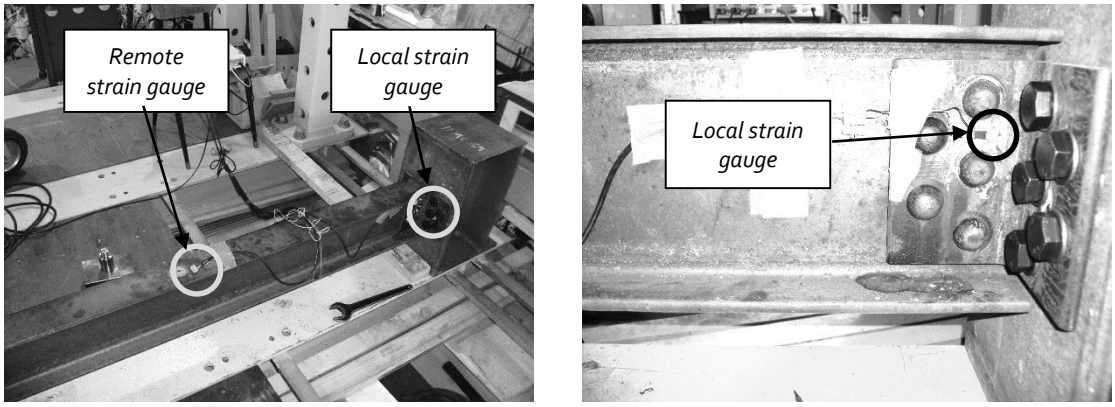

Figure 4.6 – Instrumentation of the riveted beams with strain gauges placed along the beam longitudinal direction, at remote position (flange of the beam) (CEA-06-250UW-350) and at local position in between the two top most rivets (CEA-06-062UW-350).

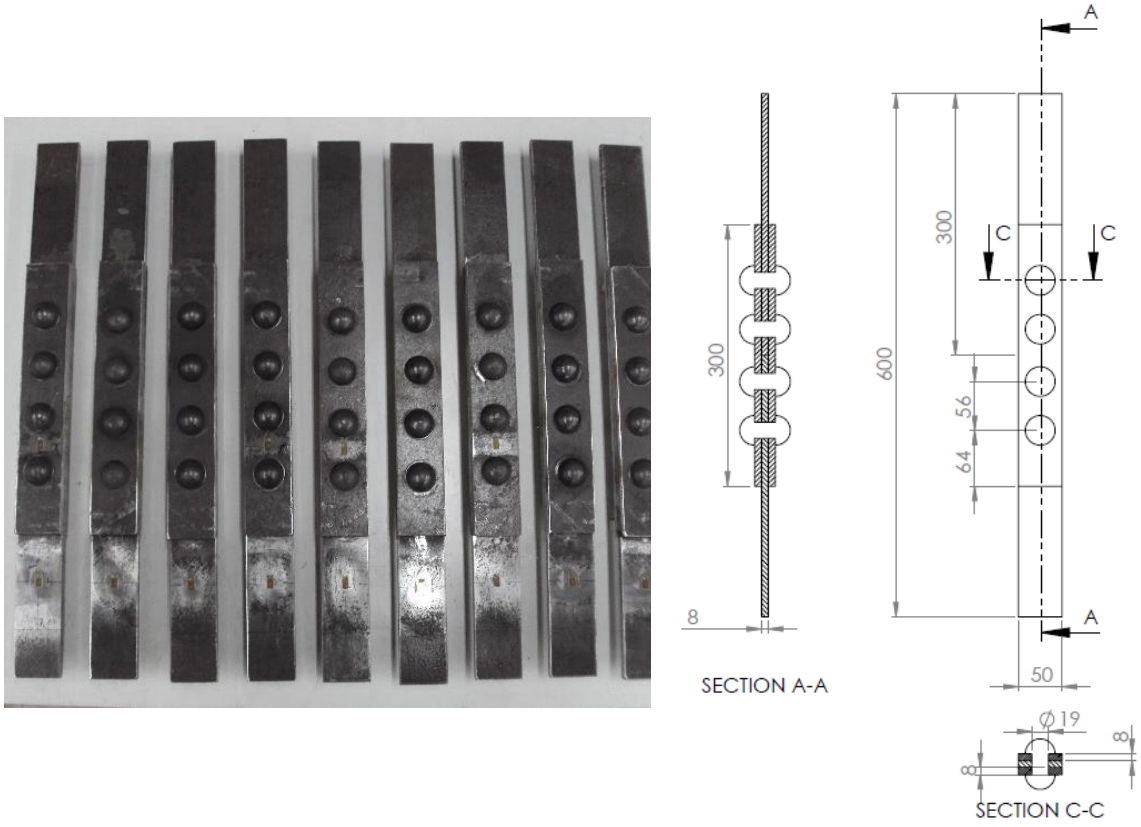

Figure 4.7 - Single line double shear riveted splices (R2 series), instrumented with strain gauges: 9 specimens with remote strain gauges (CEA-06-250UW-350) and 4 specimens with strain gauges placed in between first and second rivet (CEA-06-062UW-350).

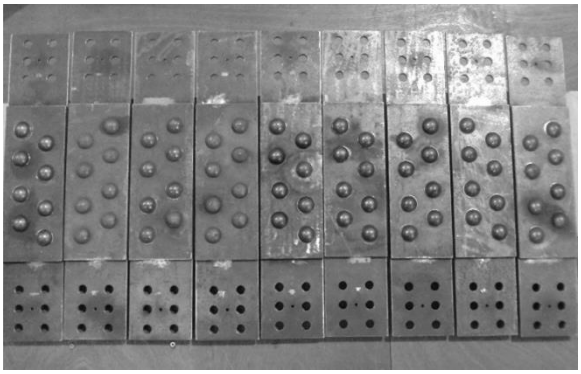

a)

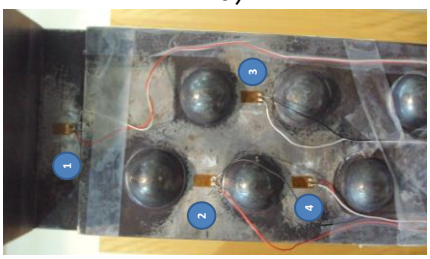

c)

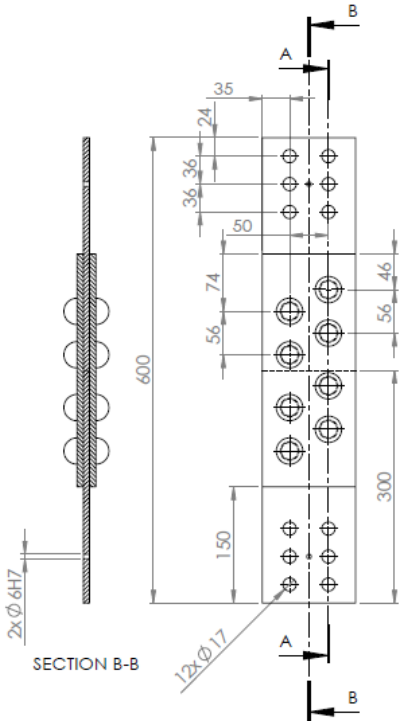

b)

Figure 4.8 - Double line double shear riveted splices, R3 series: a) photo of the complete series; b) geometry of the specimens (dimensions in mm); c) instrumentation of the specimen with strain gauges (3 specimens instrumented; remote strain gauge (1) (CEA-06-250UW-350) and local strain gauges (2), (3) and (4) (CEA-06-062UW-350).

a)

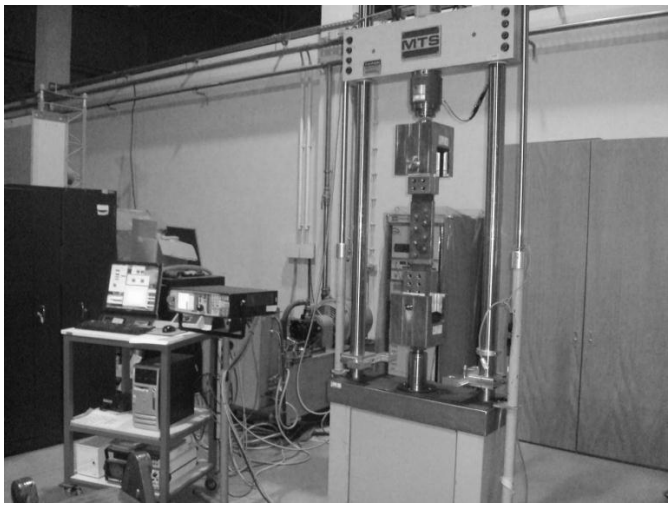

b)

Figure 4.9 – Servo-hydraulic machines used in the fatigue tests of the R2 and R3 riveted series: a) 10 tons Instron testing machine used in the R2 specimens; b) 25 tons MTS machine used in the R3 specimens.

Table 4.2 - Chemical composition of the S235JR steel and rivet material used in the fabrication of the riveted specimens (% weight).

Steel Grade	*C*	*Mn*	*Si*	*P*	*S*	*N*	*Mo*	*B*
	max	*max*	*max*	*max*	*max*	*max*	*max*	*max*
S235JR	0.190	1.500	0.030	0.045	0.045	0.014	-	-
Rivet	0.100	0.410	0.014	-	0.030	-	0.045	0.045

Table 4.3 - Tensile properties of the S235JR steel and rivet material used in the fabrication of the riveted specimens.

Steel Grade	*Rp*	*Rm*	*Elongation at fracture*
	[MPa]	*[MPa]*	*%*
S235JR	235	360-510	26
Rivets	-	-	26

Table 4.4 - Experimental fatigue test data of R1 riveted specimens.

Specimens	*Load R-ratio*	*Fmax [kN]*	*Fmin [kN]*	*ΔF [kN]*	N_f
R1-01	0.01	20	0.2	19.8	232376
R1-02	0.01	20	0.2	19.8	2569570
R1-03	0.01	25	0.25	24.75	78473
R1-04	0.01	25	0.25	24.75	89292
R1-05	0.01	20	0.2	19.8	286745
R1-06	0.01	15	0.15	14.85	1009059
R1-07	0.01	15	0.15	14.85	791476
R1-08	0.01	20	0.2	19.8	234015

Table 4.5 - Experimental fatigue test data of R2 riveted specimens.

Specimens	*Load R-ratio*	F_{max} *[kN]*	F_{min} *[kN]*	ΔF *[kN]*	$\Delta\sigma_{rem}$ *[MPa]*	$\Delta\sigma_{net}$ *[MPa]*	*Nf*
R2-01	0.01	50.00	0.50	49.5	122.6	198.0	391735
R2-10	0.01	95.95	0.96	94.99	235.3	379.9	77904
R2-02	0.01	95.95	0.96	94.99	232.8	375.7	28764
R2-03	0.01	95.00	0.95	94.05	234.9	379.6	18631
R2-04	0.01	80.00	0.80	79.20	194.8	314.2	361858
R2-05	0.01	65.00	0.65	64.35	160.2	258.9	807561
R2-06	0.01	80.00	0.80	79.20	198.1	320.2	47843
R2-07	0.01	60.00	0.60	59.40	147.7	238.3	1.13E+06
R2-08	0.01	80.00	0.80	79.20	196.7	317.7	127102
R2-09	0.01	70.00	0.70	69.30	171.9	277.8	868598

Table 4.6 - Experimental fatigue test data of R3 riveted specimens.

Specimens	*Load R-ratio*	F_{max} *[kN]*	F_{min} *[kN]*	ΔF *[kN]*	$\Delta\sigma_{rem}$ *[MPa]*	$\Delta\sigma_{net}$ *[MPa]*	N_f
R3-01	0.10	160.00	16	144	148.7	176.9	660121
R3-02	0.10	180.00	18	162	167.1	199.3	455794
R3-03	0.10	100.00	10	90	92.8	110.4	3125148
R3-04	0.10	120.00	12	108	112.4	133.9	1633734
R3-05	0.10	120.00	12	108	112.4	133.9	1146928
R3-06	0.10	200.00	20	180	187.1	222.7	208727
R3-07	0.10	120.00	12	108	112.3	133.7	1633734
R3-08	0.10	180.00	18	162	167.2	198.8	309294
R3-09	0.10	160.00	16	144	148.6	176.6	662938

One riveted specimen was sectioned after testing, for Vickers hardness measurements along the resulting cross section, which includes plate and rivet materials. Figure 4.10 presents several locations on a sample, were hardness measurements were performed for the R2 riveted specimens. Locations 1, 2 and 3 were aligned at the rivet axis. The other locations were placed at the mid thickness line of the plates. Figure 4.11 presents the individual hardness measurements. The analysis clearly distinguishes the hardness values measured at the rivet and plates. The results shown in Figure 4.11 indicated that the hardness values in the rivet are about 135-140 HV, which are quite below the values observed at the plates, which are about 145-155 HV. A low scatter can be observed in the graph of Figure 4.11.

Figure 4.12 shows a micrograph of a rivet/plate interface. It can be easily observed that the rivet material reveals a finer microstructure. Regarding the plate material - the S235JR steel grade, it exhibits a typical carbon steel microstructure, with perlite (dark zones) surrounded by a ferrite matrix (white zones).

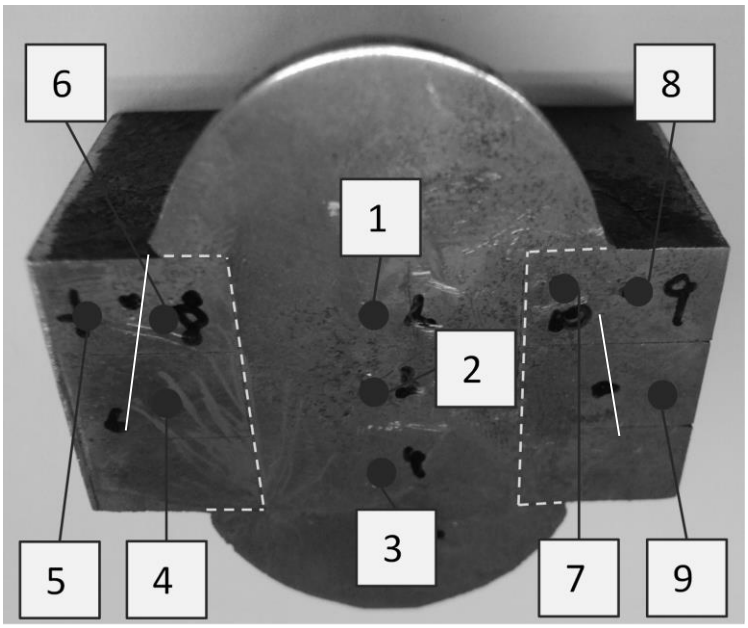

Figure 4.10 - Hardness measurement locations assessed on a cross section of a R2 riveted specimen.

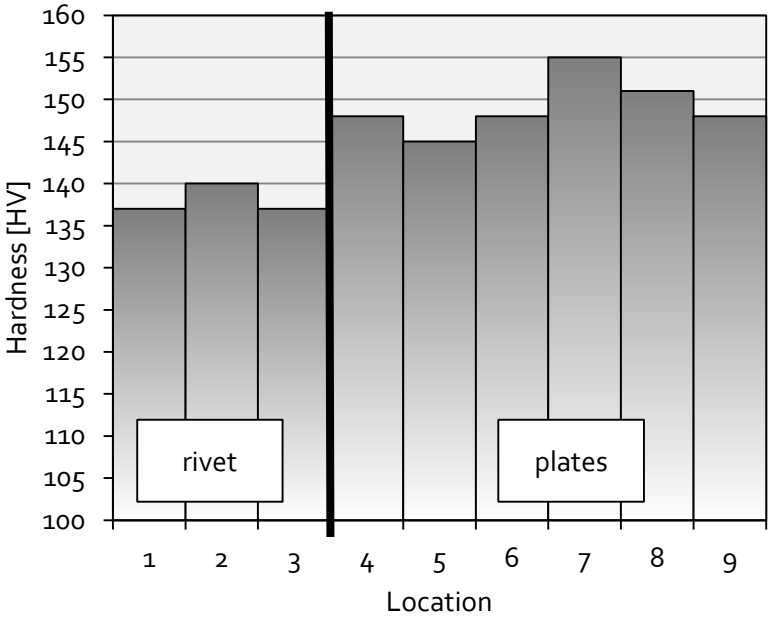

Figure 4.11 - Hardness values on a cross section of a R2 riveted specimen.

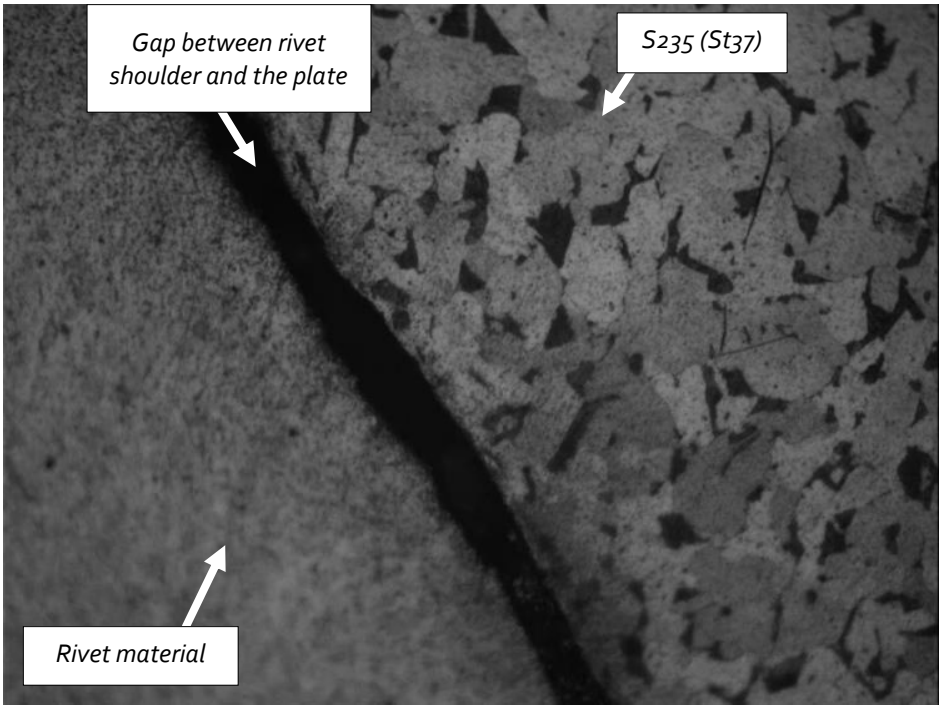

Figure 4.12 - Micrograph of the rivet/plate interface: rivet and plate (S235) microstructures.

4.2.2. S-N fatigue results obtained for riveted specimens

In this section, the fatigue results obtained with the experimental fatigue program performed on riveted joints, is presented and discussed. Fatigue test data are usually

plotted in form of S-N curves, which relate an applied stress range with the number of cycles to failure. In order to determine S-N curves from experimental data points, a linear regression analysis was performed according to the ASTM E739 standard [3]. In the next subsection a summary of the formulae for the regression analysis is briefly presented.

4.2.2.1. Statistical assessment of fatigue data aiming S-N curves definition

For each riveted tested series, a mean S-N curve will be derived using linear regression analysis as well as the respective scatter bands, using the statistical procedures proposed in the ASTM E739 standard [3]. Statistical parameters concerning the linear regression quality, are also presented.

The mean S-N curve may be described using the linear model, as:

$$Y = A + B \cdot X \tag{4.1}$$

with the dependent variable, Y, and independent variable, X, defined as:

$$Y = LogN_f \; ; \; X = Log\Delta\sigma \tag{4.2}$$

where $\Delta\sigma$ is the applied stress range and N_f is the number of cycles to failure. Based on Equations (4.1) and (4.2), it is possible to rewrite the S-N curve as follows:

$$\begin{cases} LogN_f = A + B \cdot Log\Delta\sigma \\ Log\Delta\sigma = {}^{A}\!/_{B} + {}^{1}\!/_{B} \cdot LogN_f \end{cases} \tag{4.3}$$

It is also common to express the S-N curves in design codes using the following form [1]:

$$\Delta\sigma^m N_f = C \tag{4.4}$$

where m and C are related with the regression parameters, A and B:

$$C = 10^A \; ; \; m = -B \tag{4.5}$$

It is assumed that the dependent variable *Y* follows a normal distribution with constant variance along whole range of the independent variable considered during the fatigue tests [3]. The parameters *A* and *B* can be computed as:

$$A = \overline{Y} + B \cdot \overline{X} \tag{4.6}$$

$$B = \frac{\sum_{i=1}^{k} (X_i - \overline{X})(Y_i - \overline{Y})}{\sum_{i=1}^{k} (X_i - \overline{X})^2} \tag{4.7}$$

where $\overline{X}$ and $\overline{Y}$ are mean values of the experimental data $X_i = Log\Delta\sigma_i$ and $Y_i = LogN_{fi}$ respectively, and *k* is the number of cracked specimens. The confidence intervals for the *A* and *B* parameters may be computed using the *t*-student distribution according to the following formulae:

$$A \pm t_{p,k-2} S \left[\frac{1}{k} + \frac{\overline{X}^2}{\sum_{i=1}^{k} \left(X_i - \overline{X} \right)^2} \right]^{0.5} \tag{4.8}$$

$$B \pm t_{p,k-2} S \left[\sum_{i=1}^{k} \left(X_i - \overline{X} \right)^2 \right]^{-0.5} \tag{4.9}$$

where $t_{p,k-2}$ are the value of the *t*-student distribution associated to a probability *p* and *k-2* degrees of freedom; *S* represents the standard deviation of the normal distribution associated to the *Y* variable, which may be computed using the following expression for the variance, S^2:

$$S^2 = \frac{\sum_{i=1}^{k} \left(Y_i - A + B \cdot X_i \right)^2}{k-2} \tag{4.10}$$

Linear scatter bands can be established for the S-N curve using the following relation:

$$Y = A + B \cdot X \pm \alpha \cdot S = \left(A \pm \alpha \cdot S\right) + B \cdot X \tag{4.11}$$

where α is usually a positive integer value. For the analysis presented in this chapter, α was assumed equal to α=2 and α=3, which represents bands with failure probabilities of 95.4% and 99%, respectively.

4.2.2.2. Experimental results

Experimental S-N data from the fatigue tests of riveted joints are plotted in Figures 4.13, 4.14 and 4.15 for R1, R2 and R3 specimens, respectively. The stresses used for the description of the S-N experimental data were defined as the uniform or linearized stresses at the net sections. For the R1 specimens, a linearization of stresses was performed at the net section of the web containing the line of 3 rivets. This procedure was based on an elastic stress analysis performed with a finite element model of the joint which takes into account friction and clamping stresses on rivets. The finite element model was described in Chapter VI, and a clamping stress on rivets of 30MPa was used with a friction coefficient of 0.3. The relevant stress for the R1 series was computed as the linearized stress at the critical location of the web, which is the 12 o'clock point at the upper rivet hole, where fatigue cracks were observed to initiate. For the R2 and R3 series, the stresses were computed simply dividing the load by the net section, which consisted of the plate section where cracks propagated, subtracted by the projected area of a rivet hole.

The mean S-N curves and scatter bands obtained with the mean S-N curve $\pm$2 and $\pm$3 standard deviations are plotted in the Figures 4.13, 4.14 and 4.15. The EC3 class 71 S-N curve is also plotted in each graph for comparison purposes with the experimental data. It can be observed that the class 71 S-N curve results in lower fatigue strength than obtained for all the three experimental S-N curves.

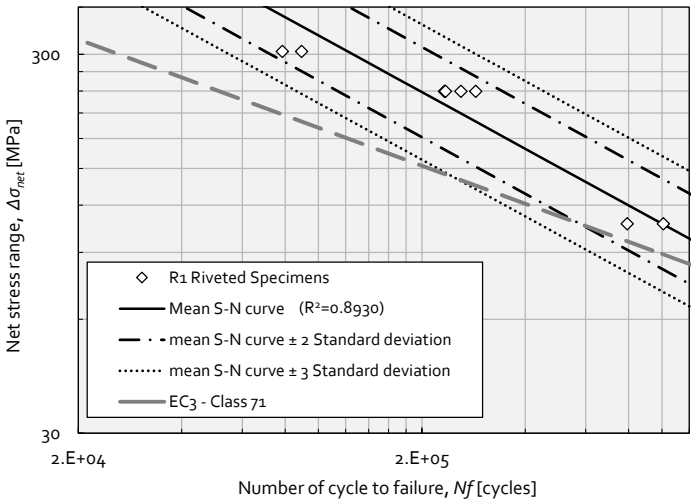

Figure 4.13 - S-N curves of riveted specimens: R1 series.

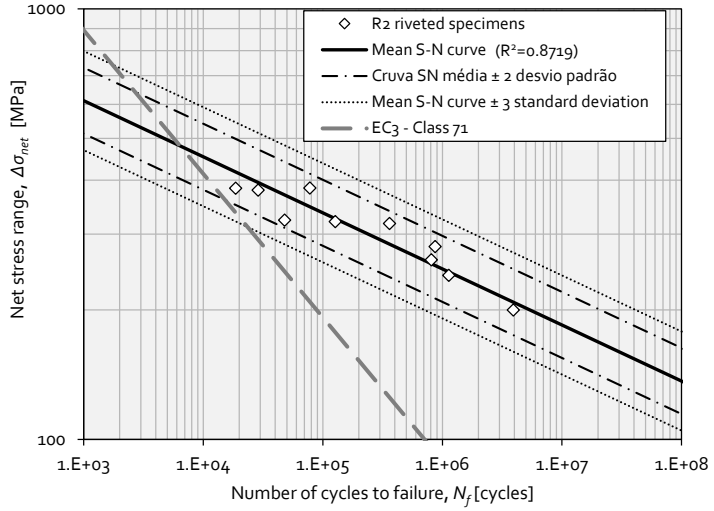

Figure 4.14 - S-N curves of riveted specimens: R2 series.

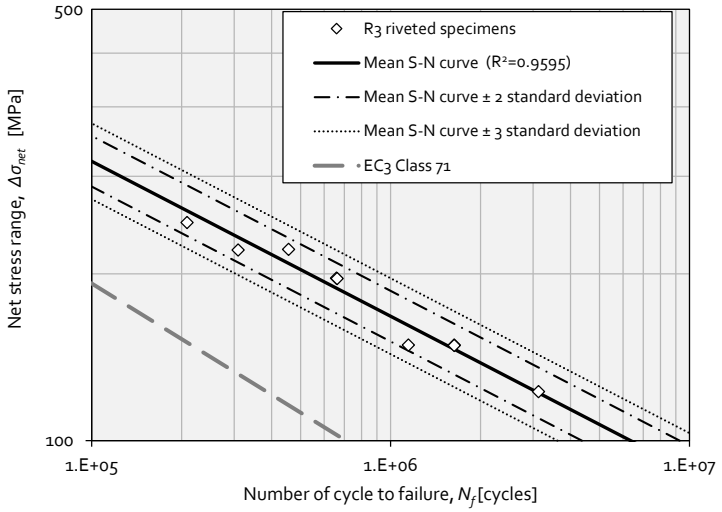

Figure 4.15 - S-N curves of riveted specimens: R3 series.

The analysis of the Figure 4.13, which plots the S-N data from R1 series, reveals that the experimental mean S-N curve slope is lower than the EC3 S-N curve slope (m=3). At this point it is worthwhile to refer that two failure modes of R1 riveted specimens occurred due to cracks that initiated and propagated at the corner of the angle (shorter fatigue lives), and the other specimens failed due to cracks emanating and propagating at the rivet holes. However, inspections made after tests and after removal of the angle and rivets for all R1 riveted specimens, showed that R1 riveted specimens that collapsed at the angle also exhibited fatigue cracks at the rivet holes. Figure 4.16 illustrates both failure modes for the R1 riveted specimens.

The AASHTO (class D) and AREA present S-N curves for riveted joints. However, in this work only EC3 S-N curves are plotted in order to have perceptible plots.

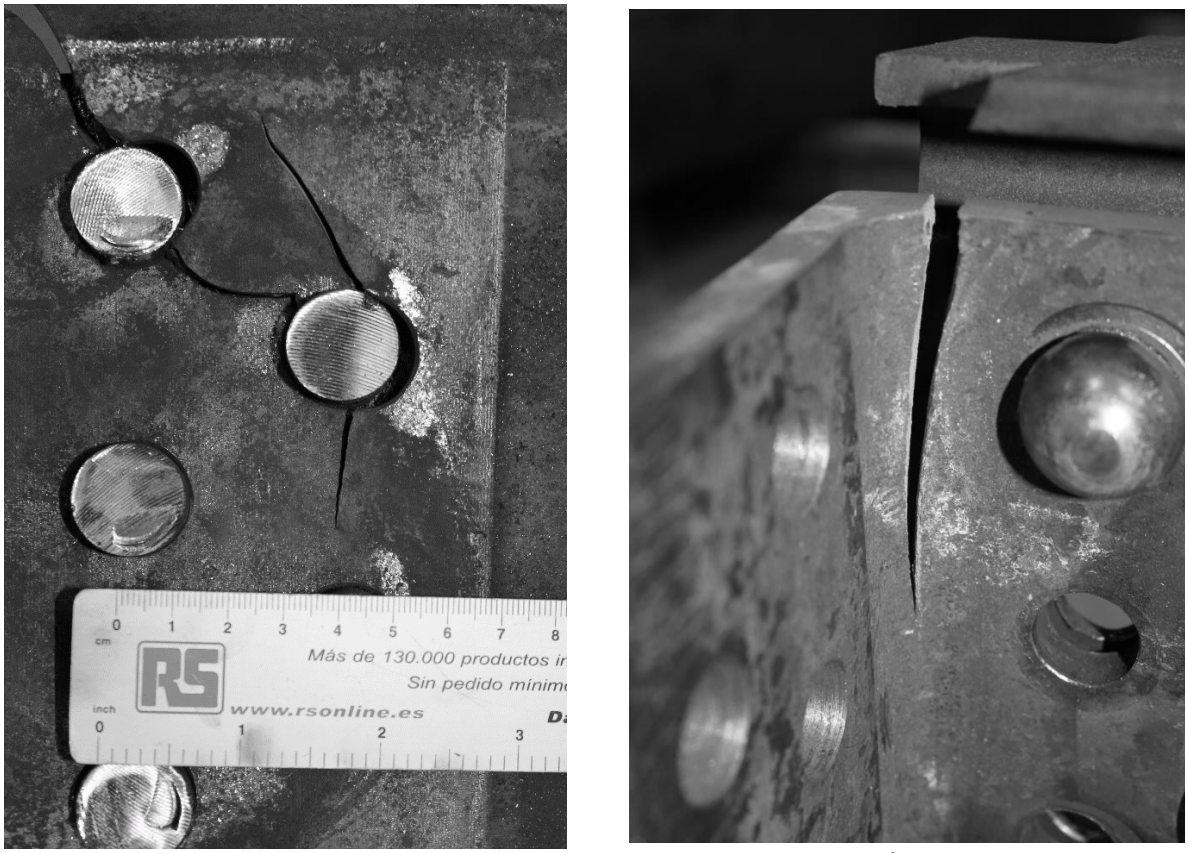

a) b)

Figure 4.16 - Typical failure modes of riveted specimens of R1 series: a) fatigue cracks propagated from riveted holes; b) fatigue crack propagated from corner of angles.

Concerning the R2 series, the experimental S-N curve slope is significantly higher than the class 71 S-N curve (see Figure 4.14). Finally, Figure 4.15 shows that the R3 series S-N curve exhibits a slope closer to the one proposed by the Eurocode 3. It is interesting to note that both R1 and R3 riveted series showed closer slope values, to the EC3 class 71 S-N curve, which is an indication that these geometries exhibit a significant crack propagation phase. The R2 series, due to their small net section, exhibits a dominant crack initiation fatigue process. Crack propagation phase was reduced for this joint. Figure 4.17 illustrates the failure surfaces of the R2 and R3 tested series. It is clear that the planar fracture surfaces were significantly higher for the R3 series, meaning a higher fatigue crack propagation phase. Figures 4.18 to 4.20 represent high magnification representations of the fracture surfaces of the R2 tested series. These figures show typical fatigue striations.

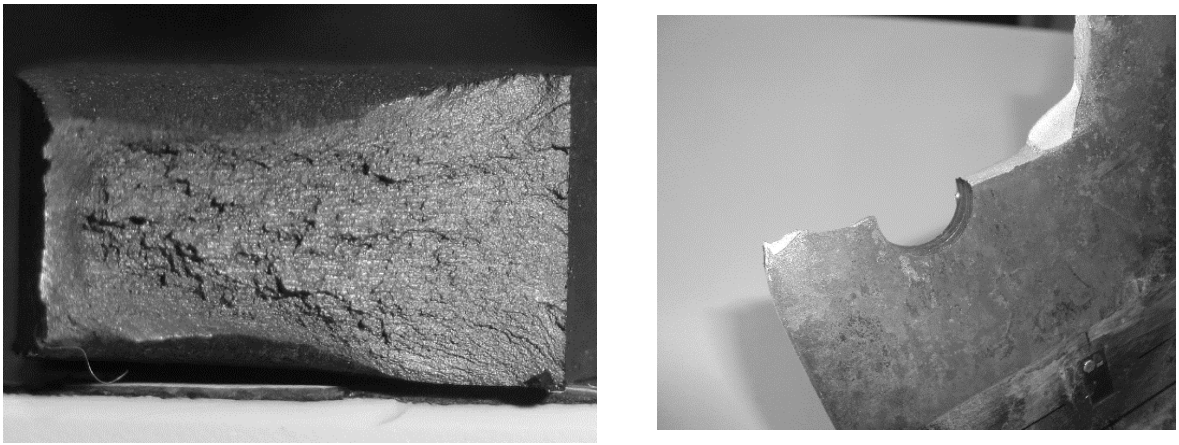

a) b)

Figure 4.17 - Typical failure surfaces of riveted tested series: a) R2 series; b) R3 series.

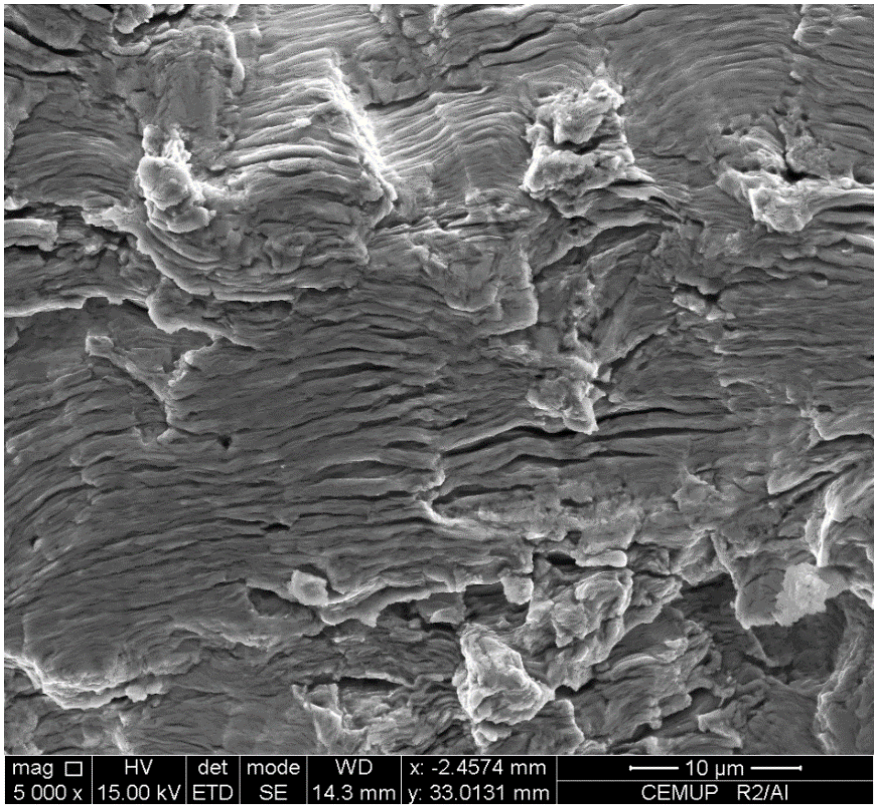

Figure 4.18 - Fatigue striations representative of the fracture surfaces of R2 riveted specimens observed with SEM (magnification 5000 x).

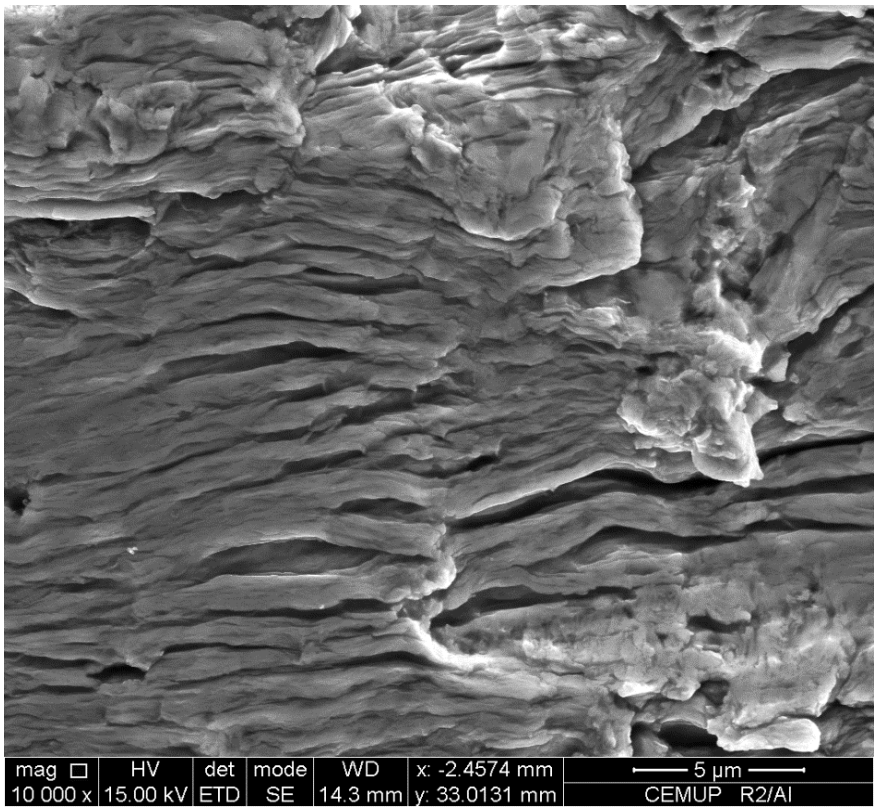

Figure 4.19 - Fatigue striations representative of the fracture surfaces of R2 riveted specimens observed with SEM (magnification 10000 x).

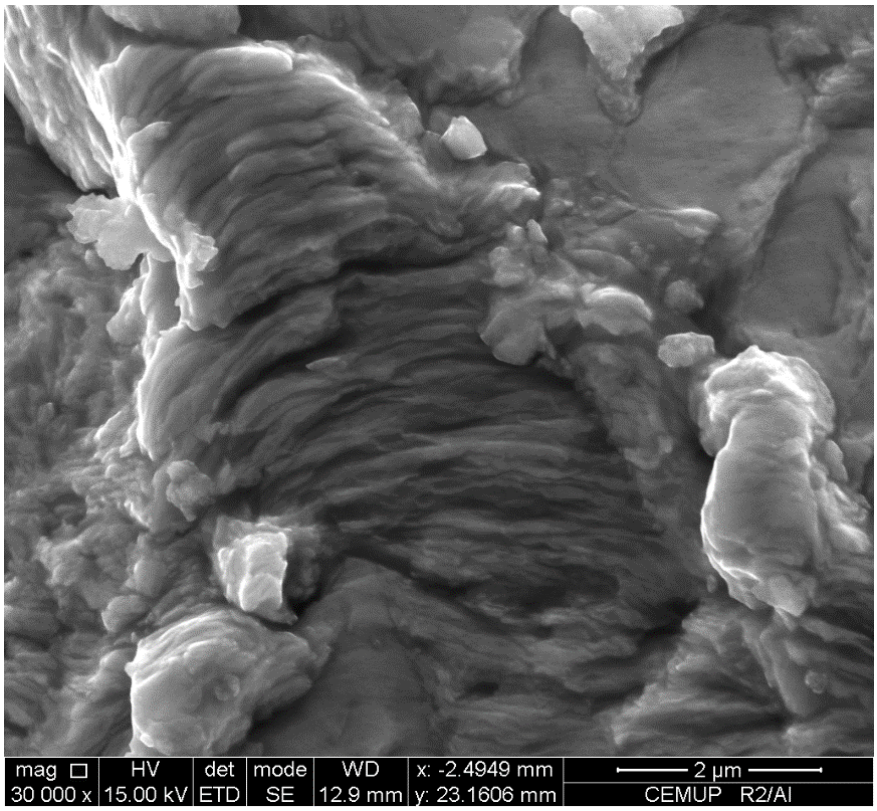

Figure 4.20 - Fatigue striations representative of the fracture surfaces of R2 riveted specimens observed with SEM (magnification 30000 x).

Table 4.7 - Summary of linear regression data for each tested riveted series.

Linear regression parameters	***R1***	***R2***	***R3***
Number of specimens, k	8	9	9
Mean value of the independent variable, $\overline{X}$	2.319	2.481	2.253
Mean value of the dependent variable, $\overline{Y}$	5.419	5.346	5.899
Slope, *B*	-2.013	-7.680	-3.578
Intercept, *A*	10.087	24.401	13.960
Variance, S^2	0.019	0.087	0.007
Standard deviation, *S*	0.138	0.295	0.082

Table 4.8 - Confidence intervals for regression parameters *A* and *B* given in Table 4.7.

Riveted series	*Confidence level of 95%*				*Confidence level of 99%*			
	A		*B*		*A*		*B*	
	Lower	*Upper*	*Lower*	*Upper*	*Lower*	*Upper*	*Lower*	*Upper*
R1	8.469	11.706	-2.709	-1.317	7.635	12.539	-3.068	-0.958
R2	18.444	30.359	-10.079	-5.280	15.733	33.070	-11.171	-4.188
R3	12.479	15.442	-4.235	-2.921	11.768	16.153	-4.551	-2.606

Table 4.7 summarizes the linear regression parameters. The R3 series showed the lower scatter which is demonstrated by the lowest standard deviation associated to the *Y* variable. Table 4.8 exhibits the confidence intervals of parameters A and B with associated confidence levels of 95 and 99%.

Figure 4.21 compares all fatigue test data obtained for the three riveted test series, in particular the S-N regression lines are compared in the figure. Concerning the R1 series, the S-N regression line excluded two experimental points that corresponded to failures at the angles, which is a failure mode that does not involve directly the riveted holes. The analysis of the figure shows that R1 and R3 series have very close S-N curves; the R2 S-N curve is clearly distinct from the other two (higher fatigue resistance). This result is consistent with the discussion referred previously about the fatigue crack initiation and propagation weights. It is important to refer that the Eurocode 3 S-N curve slope is based on a crack propagation behaviour, which is well suited for welded joints rather than for bolted or riveted joints, where crack initiation may play an important role. Based on the analysis of the Figure 4.21, new regression analyses of the fatigue data were proposed and presented in the Figure 4.22 and Figure 4.23. A regression using the joint data from R1 and R3 riveted series was proposed (Figure 4.22) and compared with the class 71 S-N curve. In addition, the regression analysis was extended to all experimental data from the three riveted series together (Figure 4.23). A very high correlation was observed for R1 and R3 test data presented together. Table 4.9 summarizes the regression data computed for the R1 and R3 riveted series together showing results consistent with the high correlation observed in Figure 4.22. Table 4.10 exhibits the confidence intervals for the respective *A* and *B* parameters. The correlation reduces significantly when all data

(R1, R2 and R3) is treated together, as plotted in Figure 4.23 and, which corroborates the need for riveted details categorization. The Table 4.11 outlines the linear regression data computed using all riveted specimens data together. The use of a unique fatigue curve for all riveted joints may lead to discrepancies. In both graphs of Figures 4.22 and 4.23, it is verified the conservatism of the class 71 EC3 S-N curve. The slope constant, *m*, of the experimental S-N curves is always greater than the value of 3 proposed for the class 71 S-N curve.

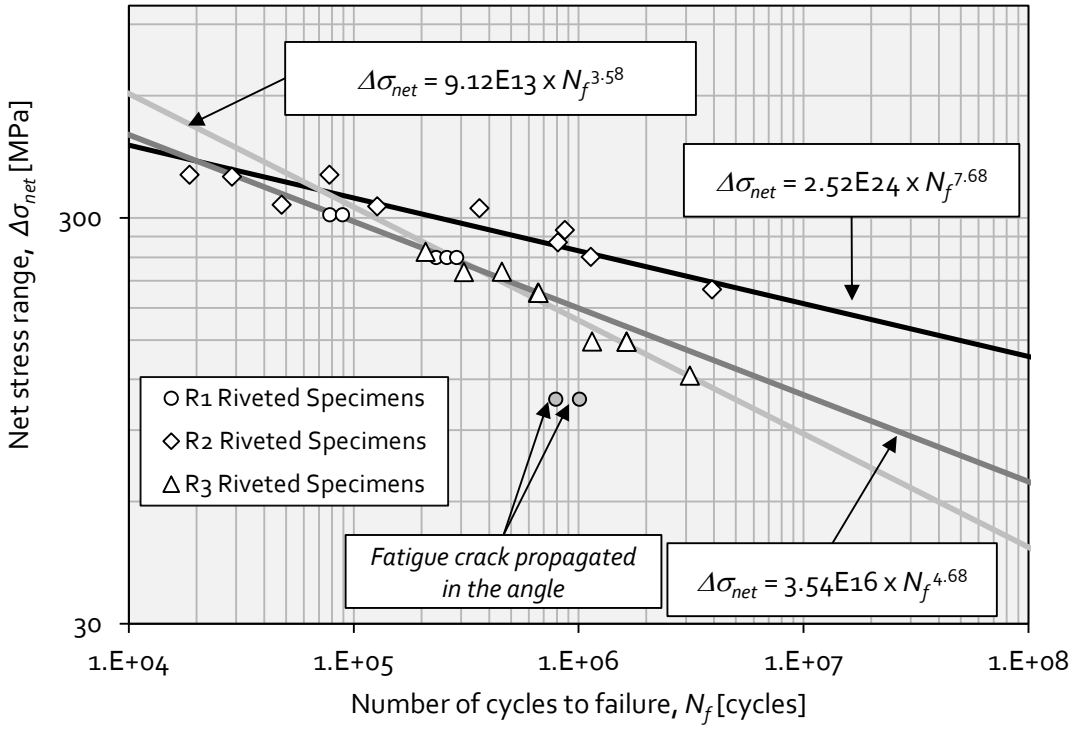

Figure 4.21 – Comparison of experimental S-N data of all tested riveted series.

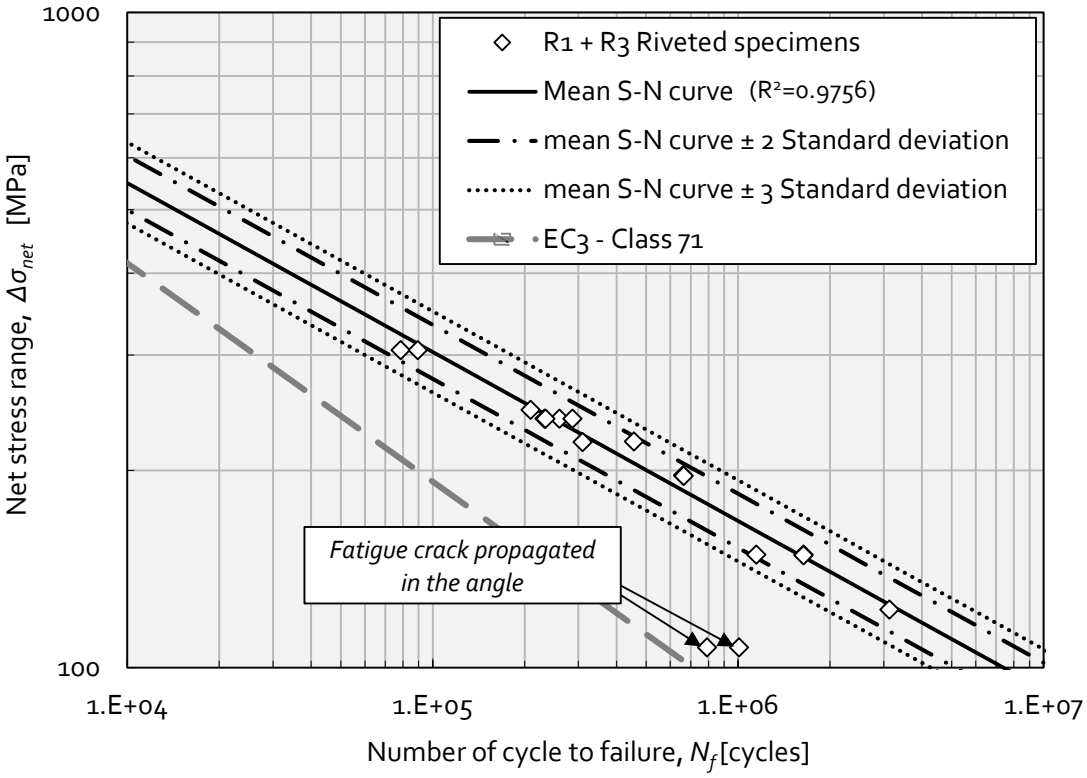

Figure 4.22 –S-N curves for R1 and R3 series jointed tested data.

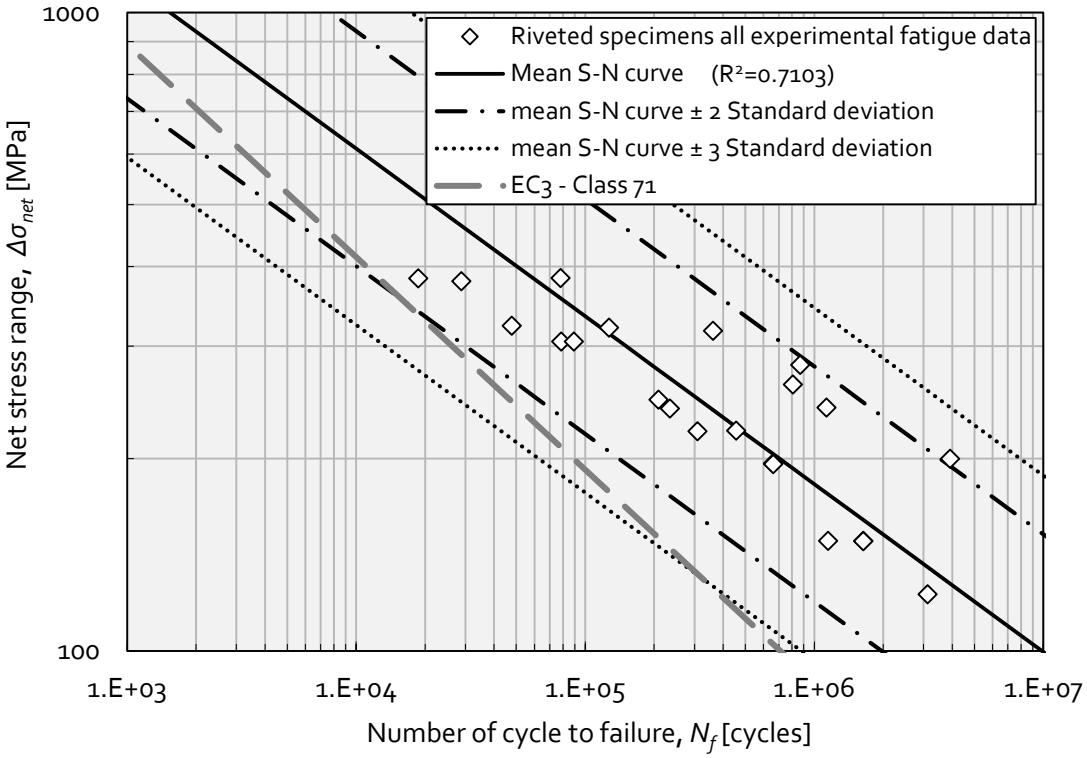

Figure 4.23 - S-N curves of jointed riveted test data.

Table 4.9 - Summary of linear regression data for joint data from R1 and R3 series.

***Number of specimens**, k*	14
***Mean value of the independent variable**, $\overline{X}$*	2.308
***Mean value of the dependent variable**, $\overline{Y}$*	5.674
***Slope**, B*	-3.878
***Intercept**, A*	14.625
***Variance**, S^2*	0.006
***Standard deviation**, S*	0.080

Table 4.10 - Confidence intervals for S-N curve parameters resulting from R1 and R3 series joint test data.

Confidence level of 95%				***Confidence level of 99%***			
A		***B***		***A***		***B***	
Lower	***Upper***	***Lower***	***Upper***	***Lower***	***Upper***	***Lower***	***Upper***
13.685	15.566	-4.285	-3.471	13.298	15.952	-4.453	-3.304

Table 4.11 - Summary of linear regression data for joint data from all test series.

***Number of specimens**, k*	23
***Mean value of the independent variable**, $\overline{X}$*	2.384
***Mean value of the dependent variable**, $\overline{Y}$*	5.535
***Slope**, B*	-3.806
***Intercept**, A*	14.607
***Variance**, S^2*	0.123
***Standard deviation**, S*	0.350

Table 4.12 - Confidence intervals for S-N curve parameters resulting from all joint test data.

Confidence level of 95%				***Confidence level of 99%***			
A		***B***		***A***		***B***	
Lower	***Upper***	***Lower***	***Upper***	***Lower***	***Upper***	***Lower***	***Upper***
11.900	17.315	-4.940	-2.673	10.914	18.301	-5.353	-2.260

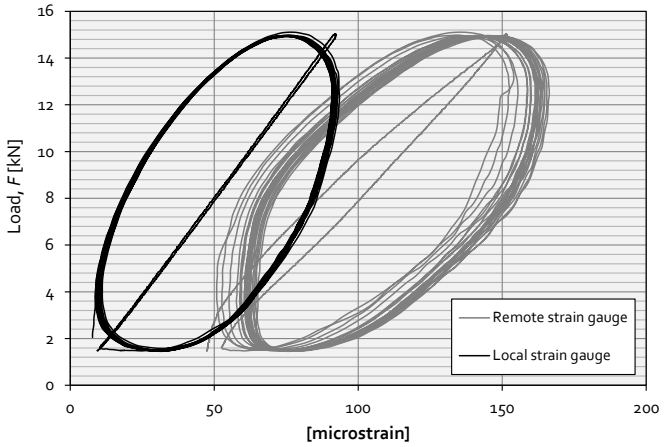

a)

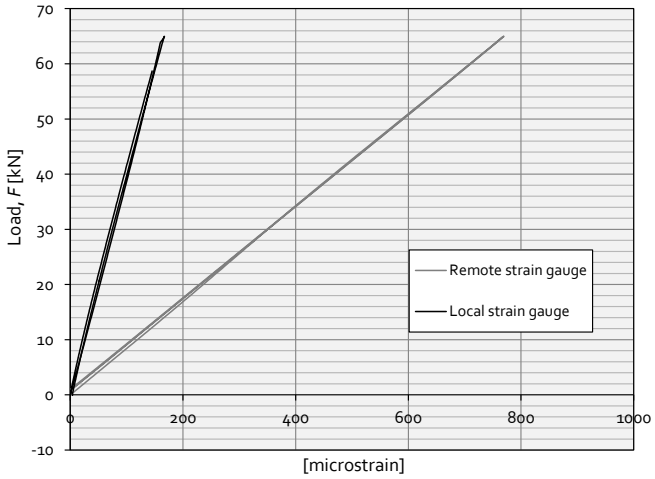

b)

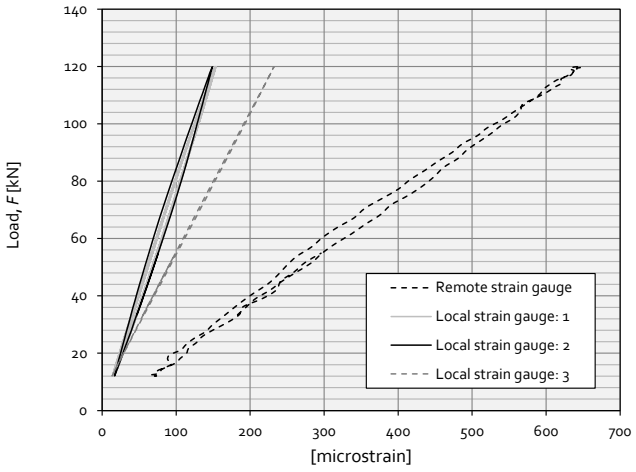

c)

Figure 4.24 - Typical strain measurements for riveted specimens: a) R1 series (R1-07); b) R2 series (R2-04); c) R3 series (R3-07).

Figure 4.24 represents some typical experimental strain records obtained for each riveted specimen. Both local and remote strain measurements are presented in the same graph. Figure 4.24a) presents the strain histories obtained for a riveted beam, particularly for a local and a remote location. The strain values were plotted against the loading history. The strain measurements were performed during the first cycle using quasi-static loading conditions; afterwards the load-strain records were obtained during some applied load cycles using the fatigue testing frequency. An approximately linear relation is observed for both remote and local load-stain records during the quasi-static loading. For the following cycles, a very significant hysteresis is observed which is due to slip and friction effects in the riveted joint. It is interesting to note that local strains are lower than remote ones, this fact being justified by the load distribution promoted by rivets.

For R2 series the load-strain records are linear. The stiffness associated to each monitored location is distinct, resulting distinct slopes and maximum strains at maximum loads.

For R3 series, load-strain measurements showed a linear trend. Local strain measurements were lower than remote one due to clamping effects of rivets and load redistribution between rivets. The local strain gauges, 2 and 3, showed the same measurements. These strain gauges are placed between the first and second rivets in each row (see Figure 4.8c)), so they are sensing the strain transferred between these rivets which is approximately the same. The strain gauge 4 senses approximately one third of the remote strain applied to the joint and measures an higher strain than the 2nd and 3rd strain gauges.

4.2.3. Fatigue classification of riveted joints

The Figure 4.25 compares experimental S-N data of riveted joints from several sources, including those from this research. EC3 class 71 S-N curve is plotted as well as the design S-N curve suggested by Taras and Greiner for riveted joints [4]. It is important to mention that the EC3 does not refer explicitly the riveted joints. However, literature has been suggesting the class 71 S-N curve as appropriate for fatigue design of riveted joints [4]. Taras and Greiner suggested that fatigue resistance of riveted details should be established according to distinct categories taking into consideration the loading

scenarios and joint configuration. Table 4.13 presents the description of the categories 2 and 3 proposed by these authors. Category 3 is more acceptable to describe the experimental data generated in this research. The category 3 S-N curve, suggested by Taras and Greiner, resulted from the analysis of a vast fatigue experimental data from old riveted joints. This curve was also plotted in the Figure 4.25. Observing the graph of the Figure 4.25, the S-N curve suggested by Taras and Greiner is the most conservative one. The slope of the referred S-N curve is higher than the slope of the S-N curve of EC3, but is more consistent with the experimental S-N data. Table 4.14 presents the constants of the S-N curve equations, for all riveted series plotted in Figure 4.25.

The Figure 4.25 also includes the data from another double riveted shear splice, made of original puddle iron from the Portuguese Fão bridge [5]. Also, the data of a single shear riveted splice made of original material from the Trezói bridge is included. This latter data from the original Trezói bridge riveted joints should be classed according to the detail category 2, as proposed by Taras and Greiner. On effect, this experimental data is very close to the design curve proposed by Taras and Greiner for detail category 3. Therefore, the safety margin is reduced for this experimental data, which justifies the use of a detail category with lower fatigue strength.

The analysis of results presented in Figure 4.25 consolidates the proposal by Taras and Greiner for riveted details categorization.

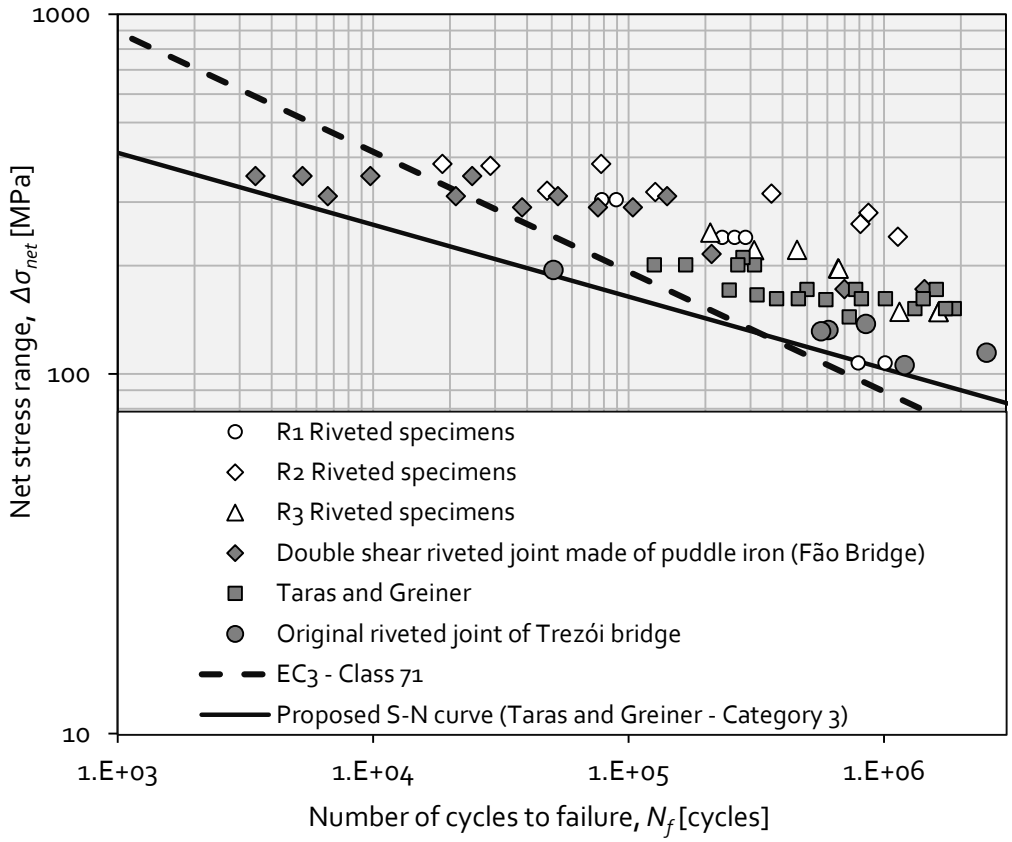

Figure 4.25 - Experimental S-N data for riveted joints from several sources.

Table 4.13 - Riveted connection categorization proposed by Taras & Greiner [4].

Detail Category	***Fatigue strength***	***Detail***	***Description and examples***	***Remarks***
Cat. 2	$\Delta\sigma_c$=71MPa m=5		One-shear joint with gusset plates	If the calculated shear force in the rivets is lower than the minimum value of slip resistance, $\Delta\sigma_c$=85MPa can be used.
Cat. 3	$\Delta\sigma_c$=90MPa m=5	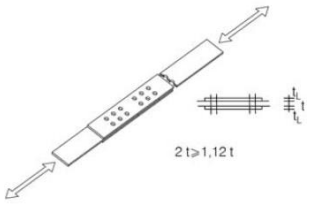	Symmetrical joint with splice plates - Middle plates in two-shear connections are to be verified with $\Delta\sigma_c$=90MPa - $\Delta\sigma_c$=80MPa applied for the splices plates themselves, so no verification is required when $2t_L$>1.12t	The ratio $\Delta\sigma_{bearing}$ to $\Delta\sigma_{net}$ must be smaller than 2. When rivets of steel grade St44 or higher were employed no corrosion protection coating must have been applied. If one of these conditions is not kept, $\Delta\sigma_c$=80MPa applies.

Table 4.14- S-N curves constants, referring to experimental data presented in Figure 4.25.

	$\Delta\sigma$@ 2E6	m	C
EC_3	71	3	7.10E+11
R1	154.95	4.679	3.54E+16
R2	227.44	7.68	1.20E+29
R_3	138.17	3.57	2.33E+14
Original Trezói riveted joint	113	6.6	7.20E+19
Taras & Greiner	109.3	4.74	1.70E+15
Fão riveted joint	168	6.9	4.50E+21
Proposed S-N curve (Taras & Greiner – Category 3)	**90**	**5**	**1.18E+16**

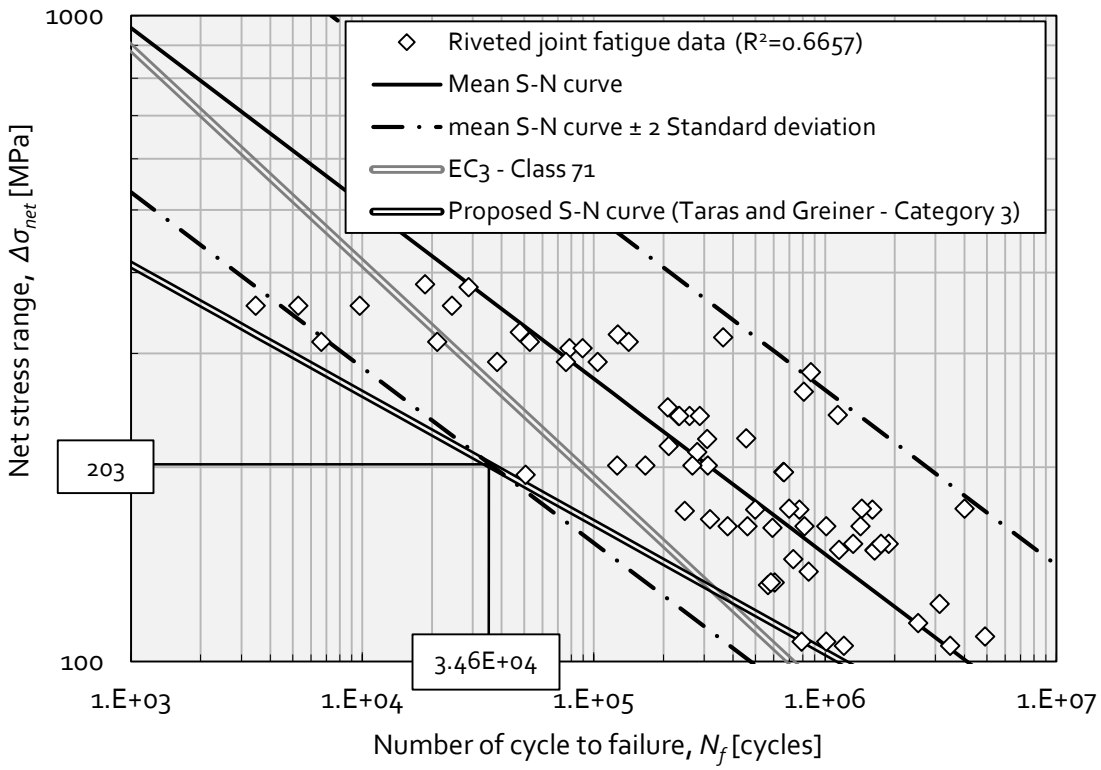

Figure 4.26 - Experimental S-N data for riveted joints from several sources.

Figure 4.26 plots the same experimental data as plotted in the Figure 4.25. However, the data was correlated together, resulting a mean S-N curve. Also, a confidence band is plotted based on the mean S-N curve ± 2 standard deviations. Only 2 data points fall

below this band. The Taras and Greiner S-N curve only shows one point below it, but at a very close distance of the S-N curve. Table 4.15 presents the linear regression data relative to the correlation performed in Figure 4.26 and Table 4.16 displays the confidence intervals for *A* and *B* constants for confidence levels of 95% and 99%.

Table 4.15 - Summary of linear regression parameters for S-N data of riveted joints from several sources illustrated in Figures 4.25 and 4.26.

***Number of specimens**, k*	53
***Mean value of the independent variable**, $\overline{X}$*	2.304
***Mean value of the dependent variable**, $\overline{Y}$*	5.494
***Slope**, B*	-3.683
***Intercept**, A*	13.979
***Variance**, S^2*	0.219
***Standard deviation**, S*	0.468

Table 4.16 - Confidence intervals for S-N curve parameters resulting from all joint test data shown in Figures 4.25 and 4.26.

Confidence level of 95%				***Confidence level of 99%***			
A		***B***		***A***		***B***	
Lower	***Upper***	***Lower***	***Upper***	***Lower***	***Upper***	***Lower***	***Upper***
12.509	15.448	-4.319	-3.047	15.733	33.070	-4.528	-2.838

4.3. EXPERIMENTAL FATIGUE PROGRAM OF WELDED DETAILS

In this section an experimental program of fatigue tests of welded structural details is described. The welded joints are common in current bridges, which is the case of the Alcácer do Sal Railway Bridge. This bridge is a composite steel/concrete bridge. A concrete slab is supported by a welded steel box girder. The geometry of the selected structural details will be described as well as the experimental details will be given and the testing results and discussion presented.

4.3.1. Design of welded specimens

In order to investigate the actual fatigue behaviour of the welded connection between the diagonal and the hanger gusset of the reinforcing diaphragms of the steel box girder (see Figure 4.27), welded specimens were prepared for fatigue testing in laboratory. These specimens presented fillet welded joints with load transfer through the weld. A Weld geometry similar to the one foreseen in the bridge was investigated. In addition, an alternative weld geometry following the specifications of the Eurocode 3 was prepared. Table 4.17 illustrates the EC3 recommendations for fillet weld lap joints. According to the EC3 procedures, the fillet welds should stop before the end of the plates, respecting a minimum distance of 10 mm. However, in the bridge, the fillet welds were made until the end of the plates, turning around the plate thickness a hole along the plate thickness (see Figure 4.27c)).

a) b) c)

Figure 4.27 - Alcácer do Sal bridge box girder: a) inside view with reinforcing diaphragms; b) local view of the connection between the diagonal and the hanger gusset; c) welded connection investigated between the gusset the diagonal.

Table 4.17 – Fillet weld lap joint configuration and respective strength according to the EC3.

Fatigue strength	*Detail*	*Description and examples*	*Remarks*
$\Delta\sigma_c$=45MPa m=3	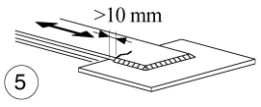	Fillet welded lap joint	- $\Delta\sigma$ to be calculated in the overlapping plates - Weld terminations more than 10 mm from plate edge

Figure 4.28 - Welded specimens designed according actual geometry used in the Alcácer do Sal bridge.

Figure 4.29 - Welded specimens designed according to EC3 [1].

Figures 4.28 and 4.29 show details of both welded geometries that were prepared for fatigue testing in laboratory. The welded joints consist of two perpendicular plates, a thick and a thin plate. The thin plate is provided with a slot to allow the assembly of the plates. A fillet weld is used to consolidate the connection of the two plates. In one case, the fillet weld goes until the end of the thick plate end turns around the thin plate thickness (see Figure 4.28). This is the weld configuration used in the bridge. In the other case, the fillet weld stops before the end of the thick plate (see Figure 4.29). This configuration is according to the EC3 procedure.

Table 4.18 gives a description of the welding specifications used in the fabrication of the welded specimens. Taking into account load capacity available in the laboratories, the

thickness of the plate, representing the diagonal (where fatigue cracks are expected to initiate and propagate) was reduced. The thickness of the plate representing the gusset (thicker plate) was kept as it is in the bridge. Two distinct thicknesses of the thin plate were fatigue tested (5 mm and 12 mm), which are lower than the actual thickness of the diagonal of the bridge (35mm). A total of 32 welded specimens were tested in laboratory: eight welded specimens with the same weld configuration of the bridge detail and a thickness of 5 (five) millimetres (W1 series) (Figure 4.30a)); eight welded specimens with a weld configuration according to EC3 and a thickness of 5 (five) millimetres (W2 series) (Figure 4.30b)); eight welded specimens with the same weld configuration of the bridge detail and a thickness of 12 (twelve) millimetres (W3 series) (Figure 4.30c)); eight welded specimens with a weld configuration according to EC3 and a thickness of 12 (twelve) millimetres (W4 series) (Figure 4.30d)). Tables 4.19, 4.20, 4.21 and 4.22 present, respectively, a summary of the testing fatigue data relative to W1, W2, W3 and W4 series. In the referred tables, the remote and net stresses were presented. The remote stresses were computed dividing the load by the remote cross section of the thinner plate; the net stresses were obtained diving the load by the cross section of the thinner plate containing the weld roots from which the fatigue cracks initiate and propagate.

Table 4.18 - Welding procedure specifications.

Standard		ISO 15609-1
Joint type		*Fillet welds*
Base material	Specification	S355 N2+J
Filler material	Process	MIG
	EN Standard - classification	EN 17635-A: T42 2 M M/c 1H5
	AWS Spec. - Classification	A5.18: E70C-6M/-6C
	Dimension ϕ	1.2 mm
	Deposit Weld Metal [mm]	3.5-7
Current	Type/Polarity	DC (+)
	Amperes [mA]	260 - 280
	Tension [V]	30 - 32
	Travel Speed [mm/min]	330 - 360
	Heat Input	< 1.49
Electrical characteristics	Electrode wire feed speed [m/min]	10 a 11

Table 4.19 - Experimental data of the fatigue tests of W1 welded specimens.

Specimens	a_{remot} [mm²]	a_{net} [mm²]	ΔF [kN]	*Fmax* [kN]	*Fmin* [kN]	*R*	$\Delta\sigma_{rem}$ [MPa]	$\Delta\sigma_{net}$ [MPa]	N_f
W1-01	498.75	300.00	45.00	50	5.00	0.10	90.2	150.0	92016
W1-02	506.58	306.03	76.50	85	8.50	0.10	151.0	250.0	24674
W1-03	500.00	301.00	22.50	25	2.50	0.10	45.0	74.8	1329750
W1-04	500.58	300.00	22.50	25	2.50	0.10	44.9	75.0	901107
W1-05	503.99	303.00	22.50	25	2.50	0.10	44.6	74.3	1120090
W1-06	499.83	302.00	18.00	20	2.00	0.10	36.0	59.6	4007718
W1-07	498.33	302.49	45.00	50	5.00	0.10	90.3	148.8	132095
W1-08	500.58	301.50	76.50	85	8.50	0.10	152.8	253.7	26812

Table 4.20 - Experimental data of the fatigue tests of W2 welded specimens.

Specimens	a_{remot} [mm²]	a_{net} [mm²]	ΔF [kN]	*Fmax* [kN]	*Fmin* [kN]	*R*	$\Delta\sigma_{rem}$ [MPa]	$\Delta\sigma_{net}$ [MPa]	N_f
W2-01	501.67	301.00	54.00	60	6.00	0.10	107.6	179.4	81238
W2-02	499.17	300.00	76.50	85	8.50	0.10	153.3	255.0	50369
W2-03	499.08	300.00	54.00	60	6.00	0.10	108.2	180.0	77293
W2-04	509.93	306.00	22.50	25	2.50	0.10	44.1	73.5	2039538
W2-05	499.33	300.00	22.50	25	2.50	0.10	45.1	75.0	4041419
W2-06	500.00	300.00	76.50	85	8.50	0.10	153.0	255.0	30609
W2-07	499.33	300.00	22.50	25	2.50	0.10	45.1	75.0	4348390
W2-08	499.67	300.00	54.00	60	6.00	0.10	108.1	180.0	73109
W2-09	499.67	300.00	76.50	85	8.50	0.10	153.1	255.0	38753

Table 4.21 - Experimental data of the fatigue tests of W3 welded specimens.

Specimens	a_{remot} *[mm²]*	a_{net} *[mm²]*	ΔF *[kN]*	*Fmax [kN]*	*Fmin [kN]*	*R*	$\Delta\sigma_{rem}$ *[MPa]*	$\Delta\sigma_{net}$ *[MPa]*	N_f
W3-01	1233.91	734.45	90	100.00	10.00	0.10	72.9	122.5	177283
W3-02	1225.29	729.57	153	170.00	17.00	0.10	124.9	209.7	37104
W3-03	1241.90	748.17	45	50.00	5.00	0.10	36.2	60.1	1969046
W3-04	1232.47	748.50	90	100.00	10.00	0.10	73.0	120.2	163344
W3-05	1253.38	751.27	45	50.00	5.00	0.10	35.9	59.9	2247175
W3-06	1229.21	738.03	45	50.00	5.00	0.10	36.6	61.0	1888763
W3-07	1223.25	737.55	153	170.00	17.00	0.10	125.1	207.4	37218
W3-08	1231.67	740.00	90	100.00	10.00	0.10	73.1	121.6	253039

Table 4.22 - Experimental data of the fatigue tests of W4 welded specimens.

Specimens	a_{remot} *[mm²]*	a_{net} *[mm²]*	ΔF *[kN]*	*Fmax [kN]*	*Fmin [kN]*	*R*	$\Delta\sigma_{rem}$ *[MPa]*	$\Delta\sigma_{net}$ *[MPa]*	N_f
W4-01	1238.83	733.61	153.00	170	17.00	0.10	123.5	208.6	63903
W4-02	1220.37	716.72	153.00	170	17.00	0.10	125.4	213.5	66411
W4-03	1233.70	739.47	45.00	50	5.00	0.10	36.5	60.9	4275055
W4-04	1227.55	738.03	45.00	50	5.00	0.10	36.7	61.0	4207489
W4-05	1215.65	726.18	90.00	100	10.00	0.10	74.0	123.9	327493
W4-06	1219.35	720.98	90.00	100	10.00	0.10	73.8	124.8	387780
W4-07	1229.82	730.28	67.50	75	7.50	0.10	54.9	92.4	882649
W4-08	1234.95	731.95	67.50	75	7.50	0.10	54.7	92.2	741613

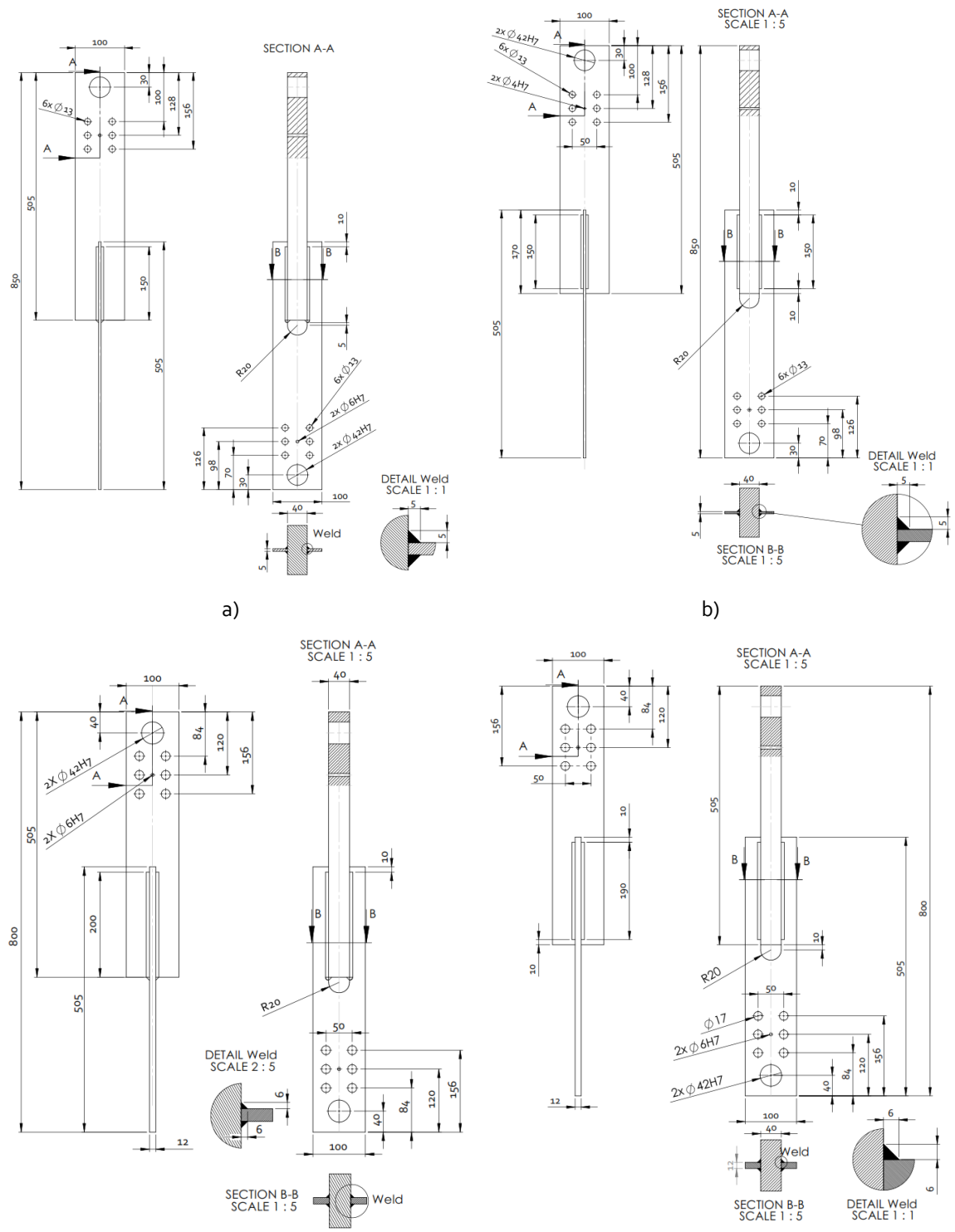

Figure 4.30 - Welded specimens geometries for laboratory fatigue tests: a) same weld configuration of the bridge detail and a 5 mm thickness (W1 series); b) weld configuration according to EC3 and a 5 mm thickness (W2 series); c) same weld configuration of the bridge detail and a 12 mm thickness (W3 series); d) weld configuration according to EC3 and a 12 mm thickness (W4 series).

Table 4.23 - Chemical composition of S355J2+N steel, S355NL1 and welded material (% weight).

Steel Grade	*C*	*Mn*	*Si*	*P*	*S*	*Al*
	max	*max*	*max*	*max*	*max*	*max*
S355J2+N	0.17	1.5	0.230	0.020	0.013	0.047
S355NL1	0.22	1.6	0.55	0.025	0.025	-
Welded material	0.073	1.51	0.49	0.011	0.015	-

Table 4.24 - Tensile strength properties of the S355 and welded materials.

Steel Grade	R_p	R_m	*Elongation at fracture*
	[MPa]	*[MPa]*	*%*
S355J2+N	389	510	26
S355NL1	400	525	26
Welded material	452	558	27

The steel box girder of the Alcácer do Sal bridge was built using the S355NL1 construction steel. This steel grade has special low temperature specifications. In particular, this material guarantees a Charpy energy of 27J at -50ºC. In the experimental fatigue campaign, the S355J2+N steel grade was adopted, which has a Charpy energy of 27J at -20ºC. This steel is less expensive than the actual bridge material, but is expected to exhibit similar fatigue behaviours than the original bridge material. Table 4.23 gives the chemical composition of the materials, including the welded material, according to the standard specifications. Table 4.24 summarizes the reference monotonic tensile strength properties.

Vickers hardness measurements were performed for some sections of the welded specimens. The main goal was to observe evolution of the hardness across the base, HAZ and welded materials. These measurements were performed on W1 and W3 specimens in order to cover the two distinct thicknesses of the thinner plate. Figure 4.31 shows the measurement locations for a W3 sample. It was measured several hardness values along a middle thickness straight line in the thinner plate. Figure 4.32 presents the hardness results at each point. A global analysis reveals two distinct hardness values, which

correspond to the base material and the weld metal. Figure 4.32 does not exhibit significant hardness differences between plates. However, the welded material exhibited significant higher hardness values. A Hardness range of 140-175 HV was measured at the base material plate, and 220-230 HV into the weld material. Concerning the W1 welded specimen (Figure 4.33), the same number of measuring points of the previous sample, was performed. Figure 4.34 shows the hardness results regarding the W1 specimen. It can be observed in this figure that the thinner plate presents higher hardness values than observed for the centre plate. Also higher scatter was observed for the thinner plate hardness values. The hardness values in the thinner plate increase with the proximity to the welded joint, approaching the hardness of the welded material itself.

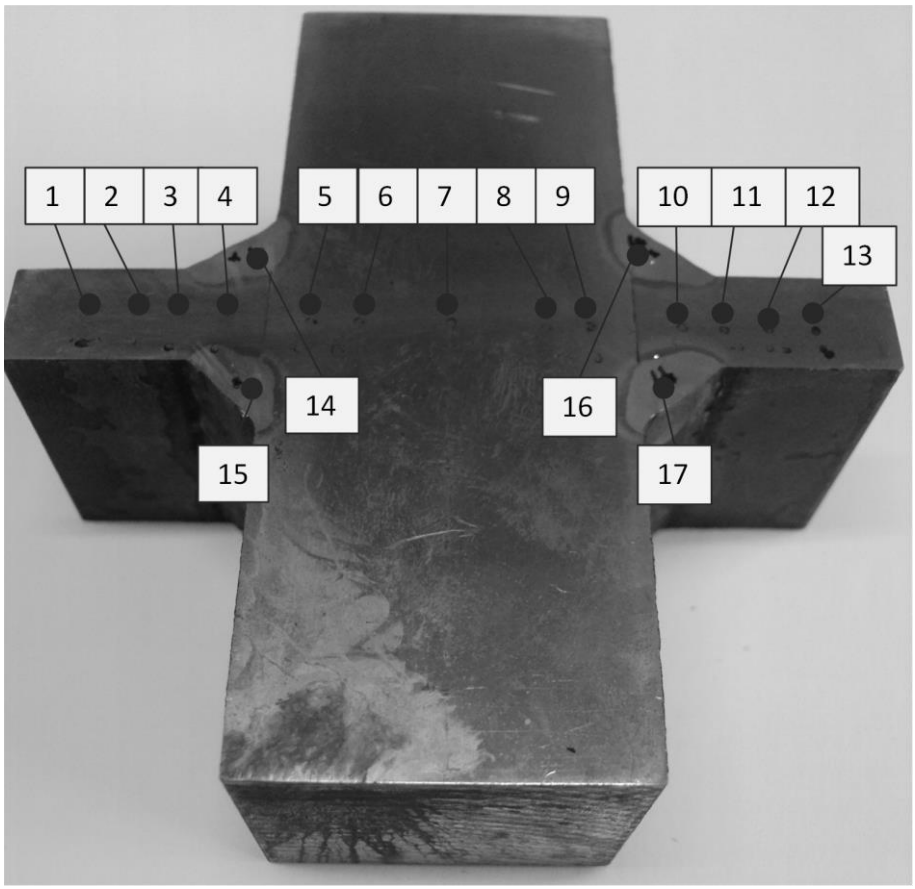

Figure 4.31 - Hardness measurements performed in a W3 welded specimens.

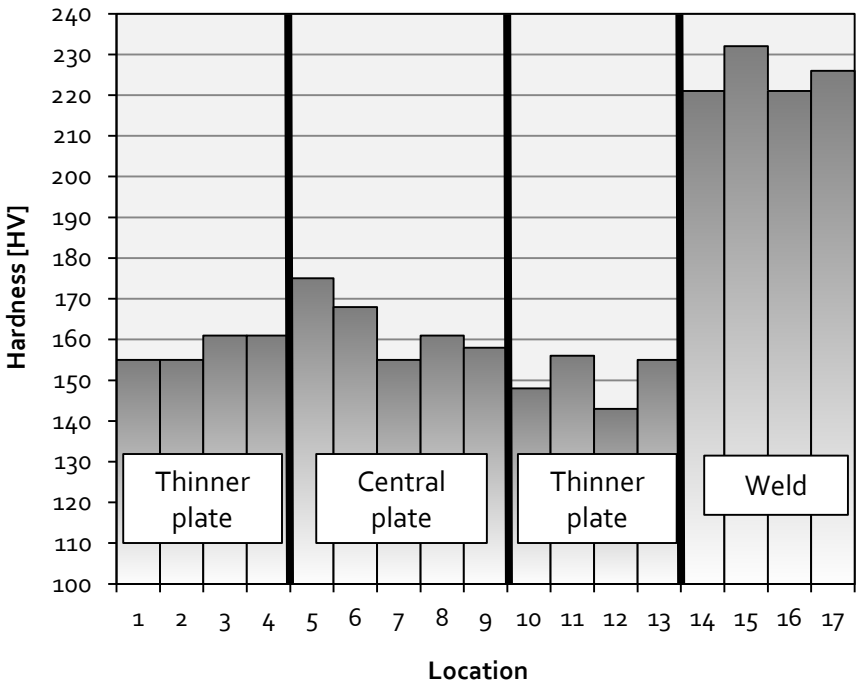

Figure 4.32 - Hardness values in the W3 welded specimens.

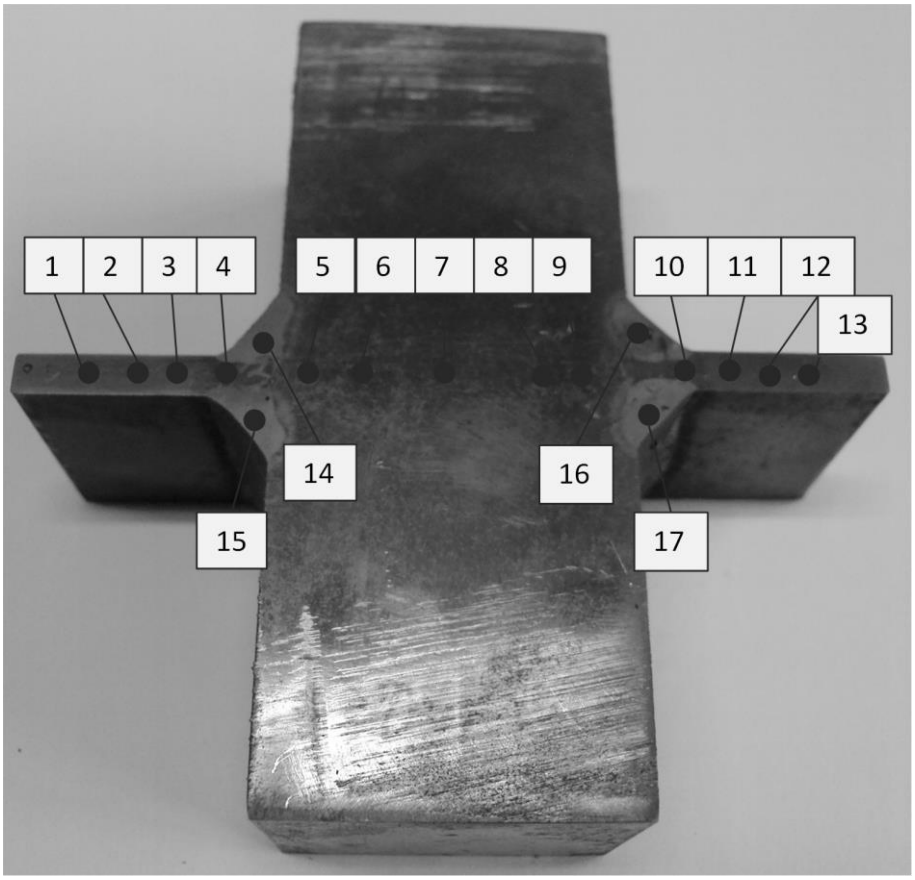

Figure 4.33 - Hardness measurements performed in a W1 welded specimen.

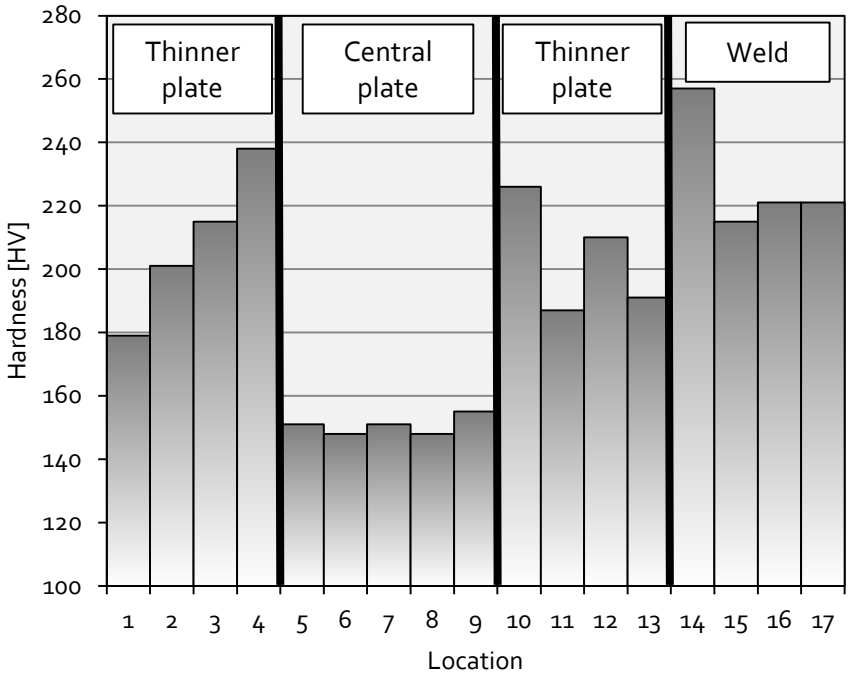

Figure 4.34 - Hardness values in the W1 welded specimens.

The microstructures of the welded joint materials were observed using an optical microscope. It was intended to observe three distinct materials, which is usual to detect near the weld toe, namely the base material (BM) the HAZ and the welded material (WM). Figure 4.35a) shows the BM zone. It is illustrated a typical hipoeutectoid carbon steel microstructure - an equilibrium microstructure of ferrite (white zones) and perlite (dark zones). The steel plates were made by a rolling process that explains the microstructure orientation illustrated in the Figure 4.35a). Figure 4.35b) shows the micrograph at the weld toe with a magnification factor of 10. It can be observed the WM and BM zones. Dark spots in the WM are observed, which correspond to weld slag inclusions. Figure 4.35c) illustrates the same material, but with a magnification of 20 times. In this figure is possible to distinct all three referred materials. Figure 4.35d) presents the weld toe with 50 times magnification. It is shown two zones, namely the WM and the HAZ. The current figure highlights the weld slag inclusions located at the WM.

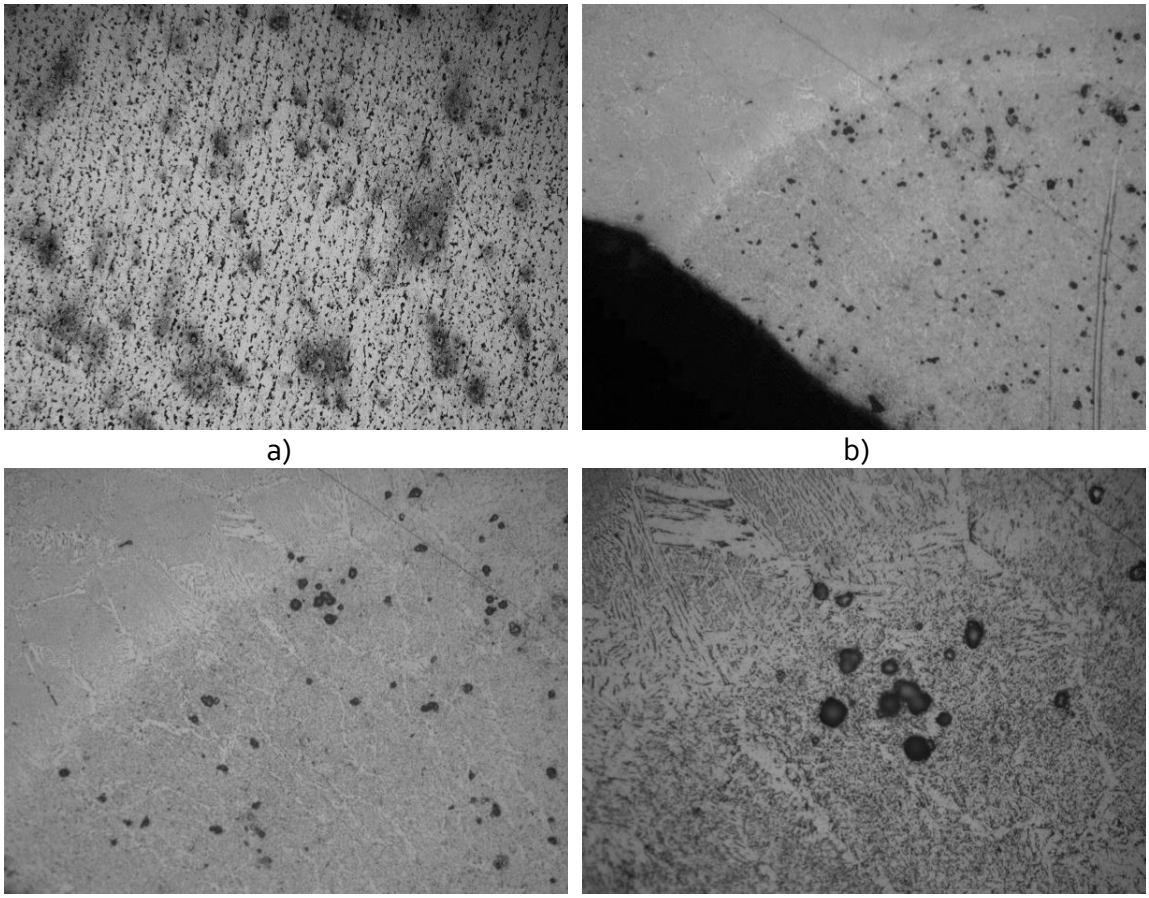

Figure 4.35 - Microstructures of the steel: a) microstructure of the BM zone; b) microstructure of the weld toe (10x); c) microstructure of the weld toe (20x);d) microstructure of the weld toe (50x).

4.3.2. Experimental results

Experimental S-N curves resulting from the fatigue tests of the welded joints are plotted in Figures 4.36, 4.37, 4.38 and 4.39 respectively, for W1, W2, W3 and W4 welded series. The experimental results are plotted together with scatter bands based on two and three standard deviations. In the referred S-N curves, the number of cycles to failure is related with the remote stress range. The EC3 class 45 S-N curve is also plotted for comparison purposes. A statistical analysis was also presented for the welded specimen, similar to the one proposed for the riveted specimens. The Table 4.25 shows the linear regression data for all welded joints. The Table 4.26 exhibits the confidence intervals associated to 95% and 99% confidence levels for the parameters *A* and *B* used in the definition of the mean S-N curve. In general, all fatigue tested welded series exhibit low scatter. The EC3 class 45 S-N curve did not produce the desired conservative predictions for the W1 and W3 welded series that were the tested series prepared using the weld joint according the

actual bridge configuration. For W2 and W4 welded series, the class 45 S-N curve produced conservative predictions for high-cycle fatigue domain. It is important to emphasize that this comparison was based on experimental data computed using a remote stress definition. When a nominal/net stress definition is used (load/net section), the EC3 rules are conservative in all cases. These stresses were computed at the thinner plate, as a uniform stress applied at the minimum cross section that excludes the plate slot cut. Figures 4.40 to 4.43 show the experimental S-N data using the nominal/net stress definition. In contrast to the S-N curves resulting from a remote stress definition, it is observed that the EC3 S-N curves are conservative for all welded series. The respective linear regression data are presented in Table 4.27, concerning the welded series W1, W2, W3 and W4. Table 4.28 presents the confidence intervals for 95% and 99% confidence levels for parameters *A* and *B*.

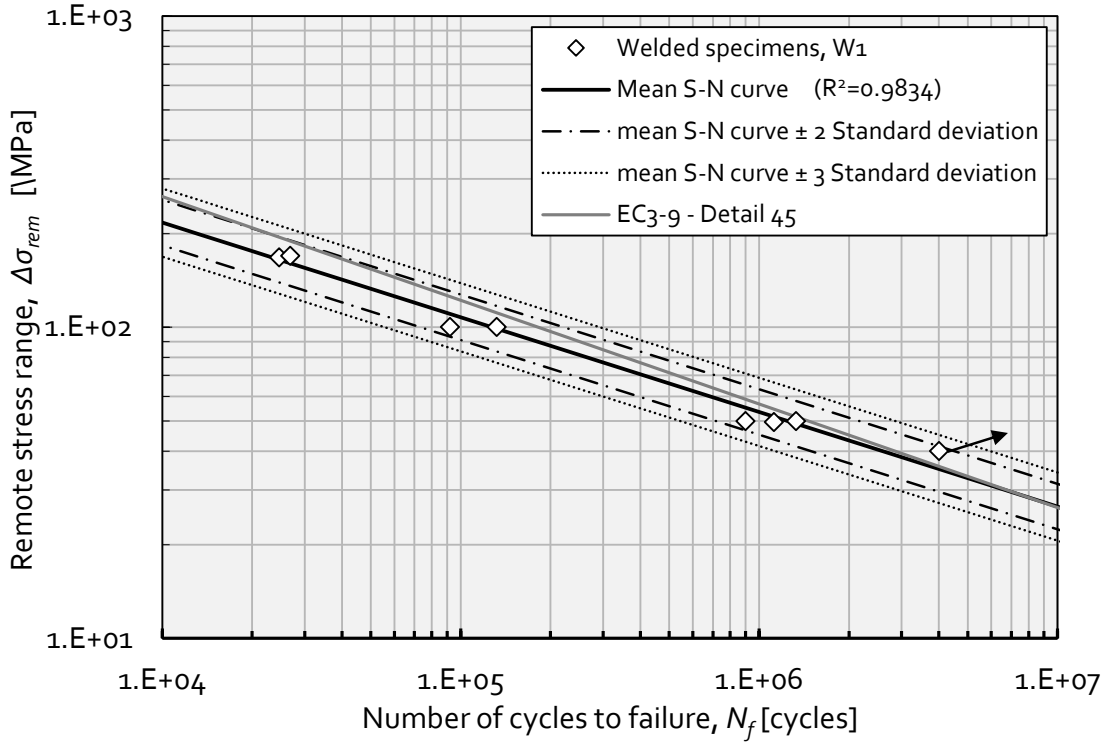

Figure 4.36 - Experimental S-N curves of W1 welded series, using remote stress definition.

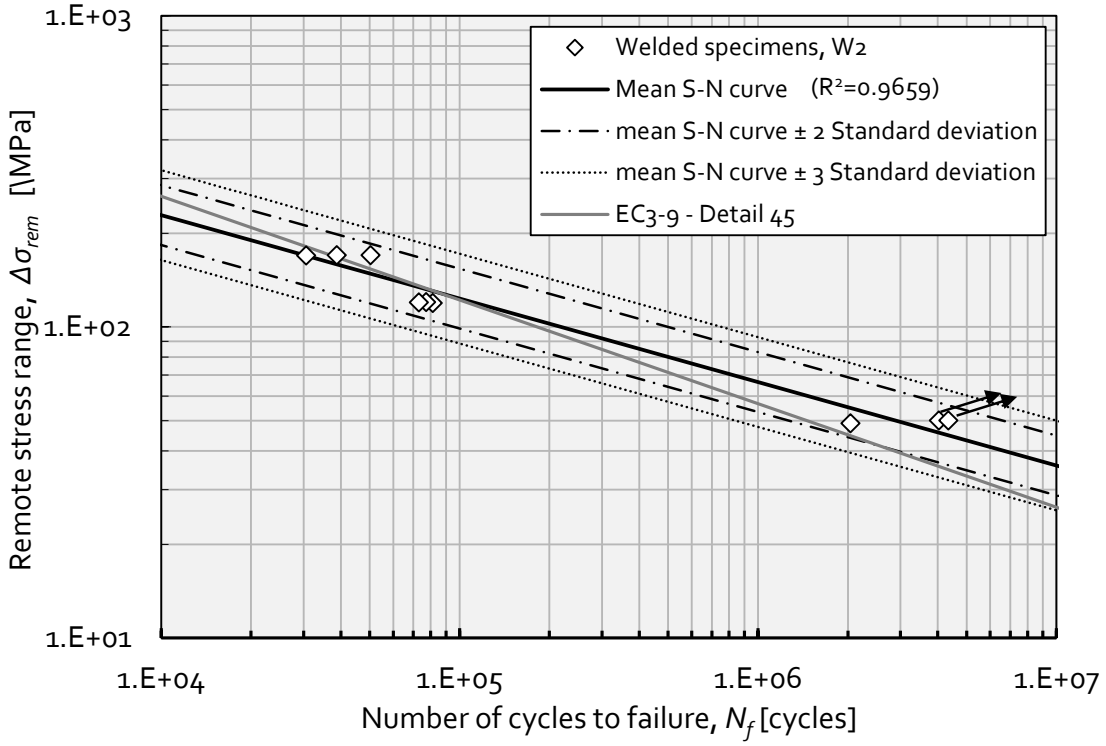

Figure 4.37 - Experimental S-N curves of W2 welded series, using remote stress definition.

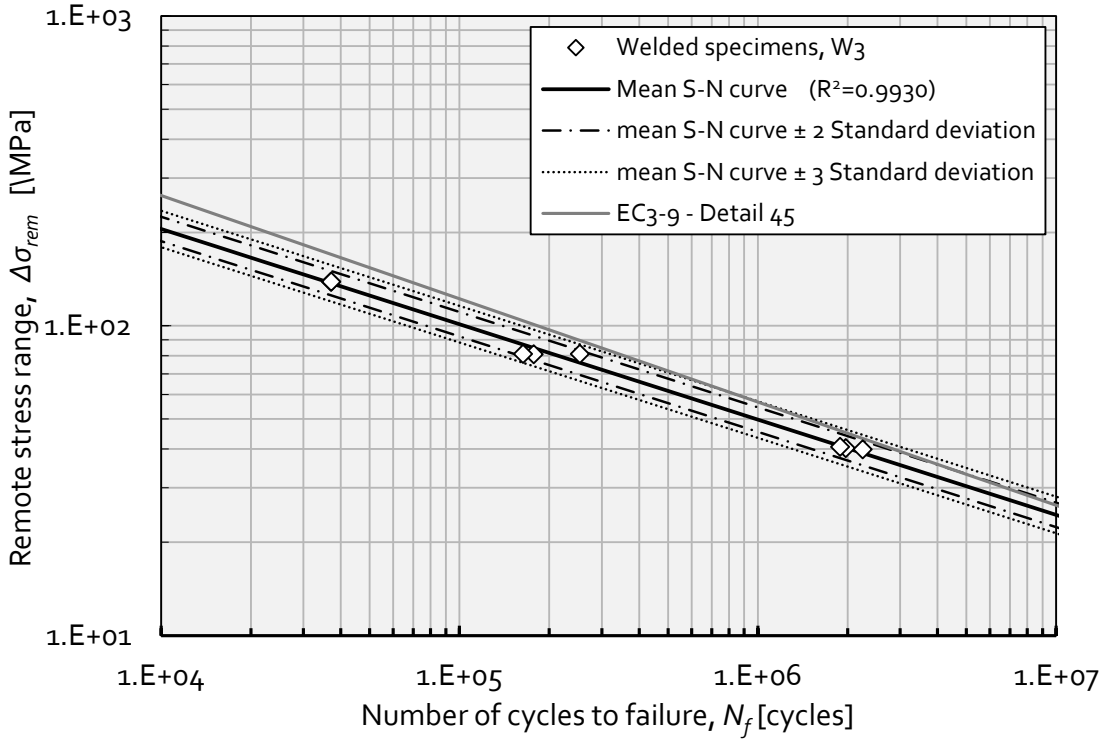

Figure 4.38 - Experimental S-N curves of W3 welded series, using remote stress definition.

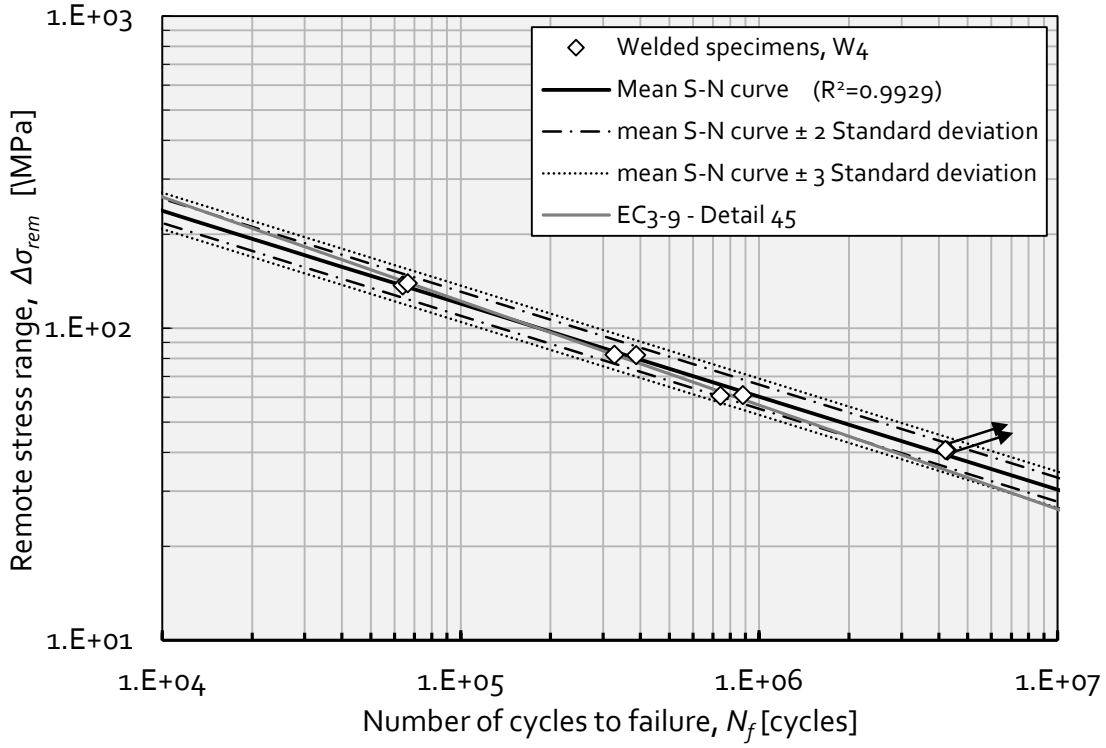

Figure 4.39 - Experimental S-N curves of W4 welded series, using remote stress definition.

Table 4.25 - Summary of linear regression parameters for all welded series (using of remote stresses).

Welded series	W1	W2	W3	W4
Number of specimens, *k*	8	8	8	8
Mean value of the independent variable, $\overline{X}$	2.114	2.224	2.075	2.088
Mean value of the dependent variable, $\overline{Y}$	5.455	5.333	5.491	5.725
Slope, *B*	-3.295	-3.728	-3.242	-3.315
Intercept, *A*	12.420	13.622	12.219	12.648
Variance, S^2	0.014	0.032	0.004	0.004
Standard deviation, *S*	0.117	0.179	0.067	0.063

Table 4.26 - Confidence intervals for regression parameters *A* and *B* given in Table 4.25.

Welded series	*Confidence level of 95%*				*Confidence level of 99%*			
	A		*B*		*A*		*B*	
	Lower	*Upper*	*Lower*	*Upper*	*Lower*	*Upper*	*Lower*	*Upper*
W1	11.509	13.331	-3.723	-2.867	11.040	13.800	-3.944	-2.646
W2	12.222	15.022	-4.354	-3.102	11.550	15.694	-4.655	-2.801
W3	11.651	12.786	-3.514	-2.970	11.358	13.079	-3.655	-2.830
W4	12.062	13.233	-3.594	-3.036	11.760	13.535	-3.738	-2.892

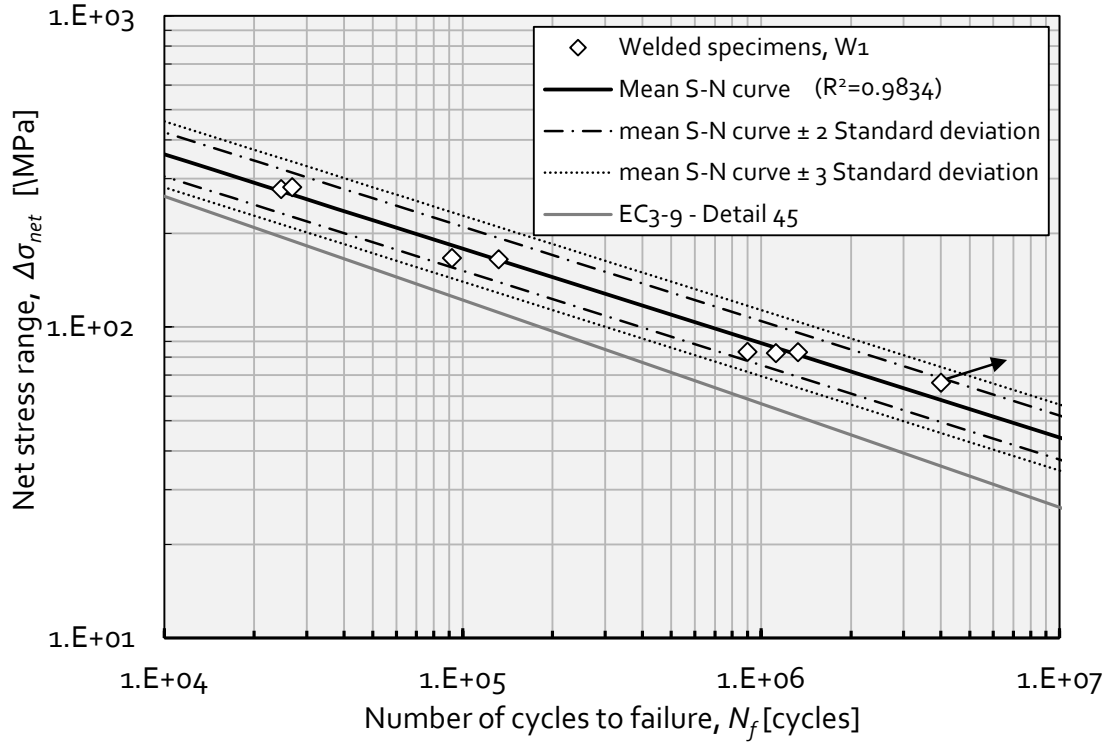

Figure 4.40 - Experimental S-N curves of W1 welded series, using net stress definition.

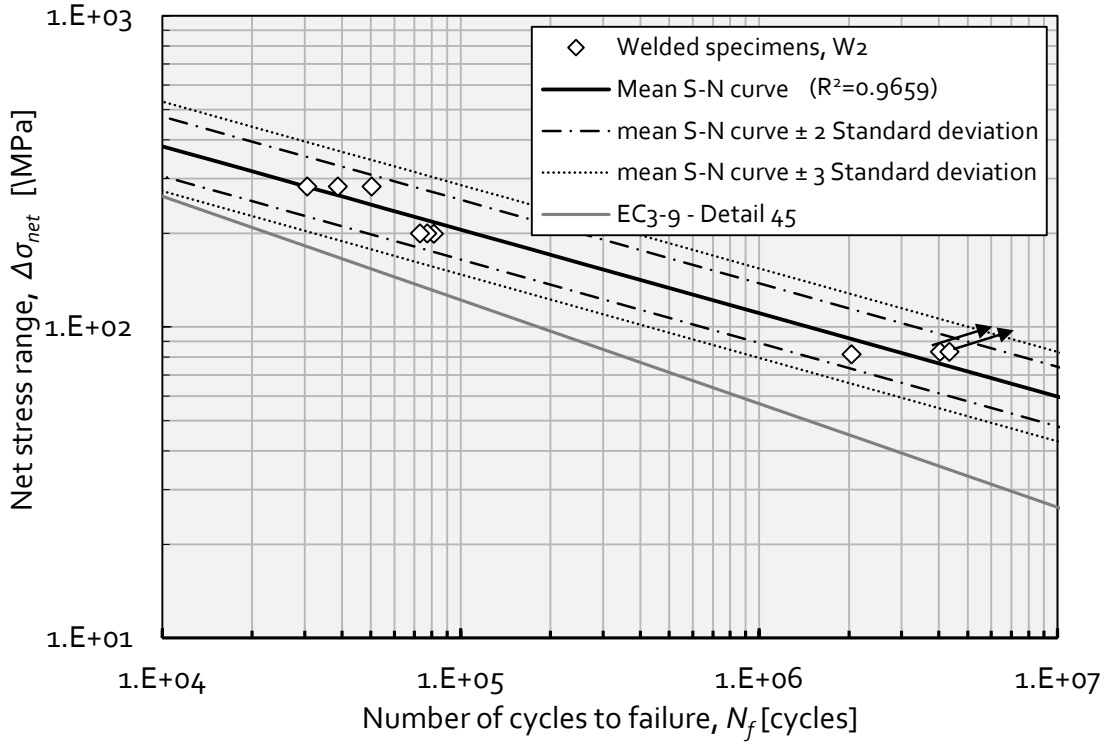

Figure 4.41 - Experimental S-N curves of W2 welded series, using net stress definition.

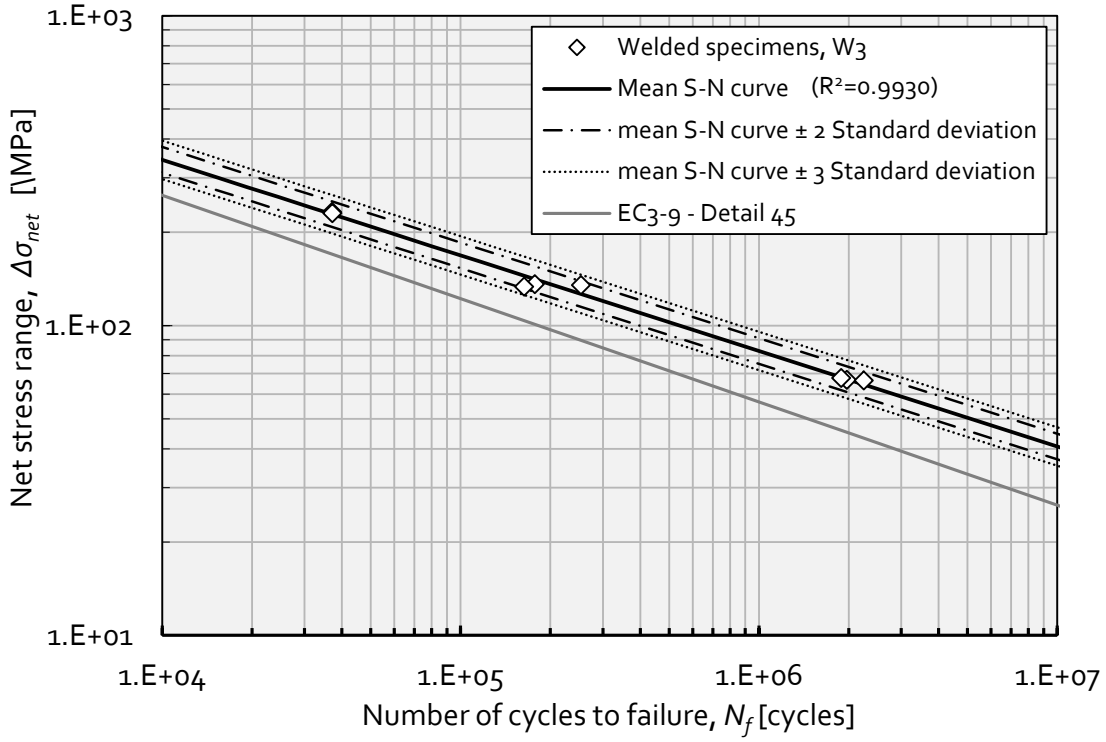

Figure 4.42 - Experimental S-N curves of W3 welded series, using net stress definition.

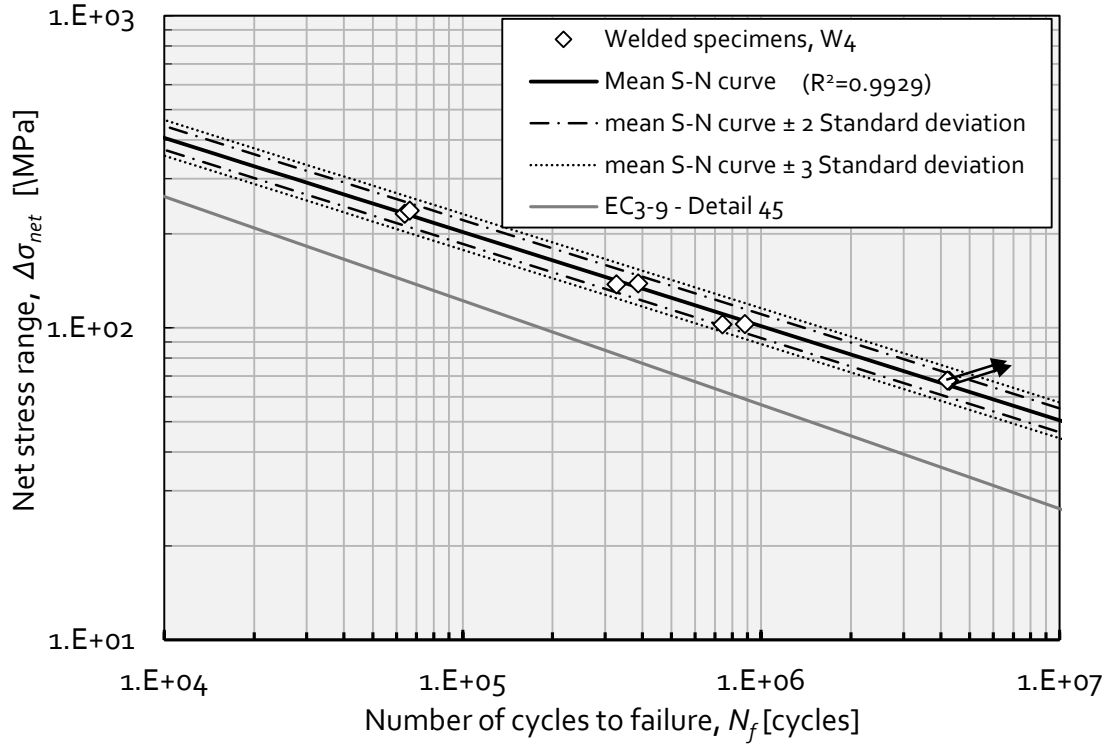

Figure 4.43 - Experimental S-N curves of W4 welded series, using net stress definition.

Table 4.27 - Summary of linear regression parameters for all welded series (using of net stresses).

Welded series	W1	W2	W3	W4
Number of specimens, *k*	8	8	8	8
Mean value of the independent variable, $\overline{X}$	1.894	2.002	1.853	1.862
Mean value of the dependent variable, $\overline{Y}$	5.455	5.333	5.491	5.725
Slope, *B*	-3.286	-3.728	-3.249	-3.358
Intercept, *A*	11.679	12.796	11.513	11.979
Variance, S^2	0.014	0.032	0.004	0.004
Standard deviation, *S*	0.120	0.179	0.064	0.065

Table 4.28 - Confidence intervals for regression parameters *A* and *B* given in Table 4.27.

Welded series	*Confidence level of 95%*				*Confidence level of 99%*			
	A		*B*		*A*		*B*	
	Lower	*Upper*	*Lower*	*Upper*	*Lower*	*Upper*	*Lower*	*Upper*
W1	10.839	12.519	-3.726	-2.846	10.406	12.951	-3.953	-2.620
W2	11.530	14.062	-4.356	-3.099	10.923	14.670	-4.658	-2.798
W3	11.027	11.998	-3.509	-2.989	10.777	12.249	-3.643	-2.855
W4	11.437	12.521	-3.648	-3.069	11.157	12.801	-3.797	-2.920

Figure 4.44 compares the experimental S-N curves of W1 and W2 welded series. This figure illustrates the influence of the fillet weld extension effect on the fatigue strength, for welded specimens with a thinner plate of 5mm. Analyzing the Figure 4.44, it is clear that a very small influence of the fillet weld extension can be observed on the mean S-N curve. However, a comparison of the S-N curves for $2x10^6$ cycles shows that welds made according to EC3 standard ([1]) have higher fatigue strength (about 9.12% higher). Figure 4.45 compares the experimental S-N curves of the welded specimens W3 and W4 (thickness of the thinner plate of 12mm). In this case, an almost perfect superposition of the mean S-N curves is observed. The comparison of the fatigue strength for $2x10^6$ cycles reveals only a minor 0.9% increase of fatigue strength when the code recommendations are followed for the fillet weld extension.

Figure 4.46 presents the experimental S-N curves for the welded specimen series with a weld configuration according to the current bridge detail (W1 and W3). A high determination coefficient (R^2=0.9838) was obtained for the mean S-N curve. Table 4.29 presents the linear regression data resulting from the correlation of both W1 and W3 series. Table 4.30 shows the respective confidence intervals for the *A* and *B* parameters, with 95% and 99% confidence levels.

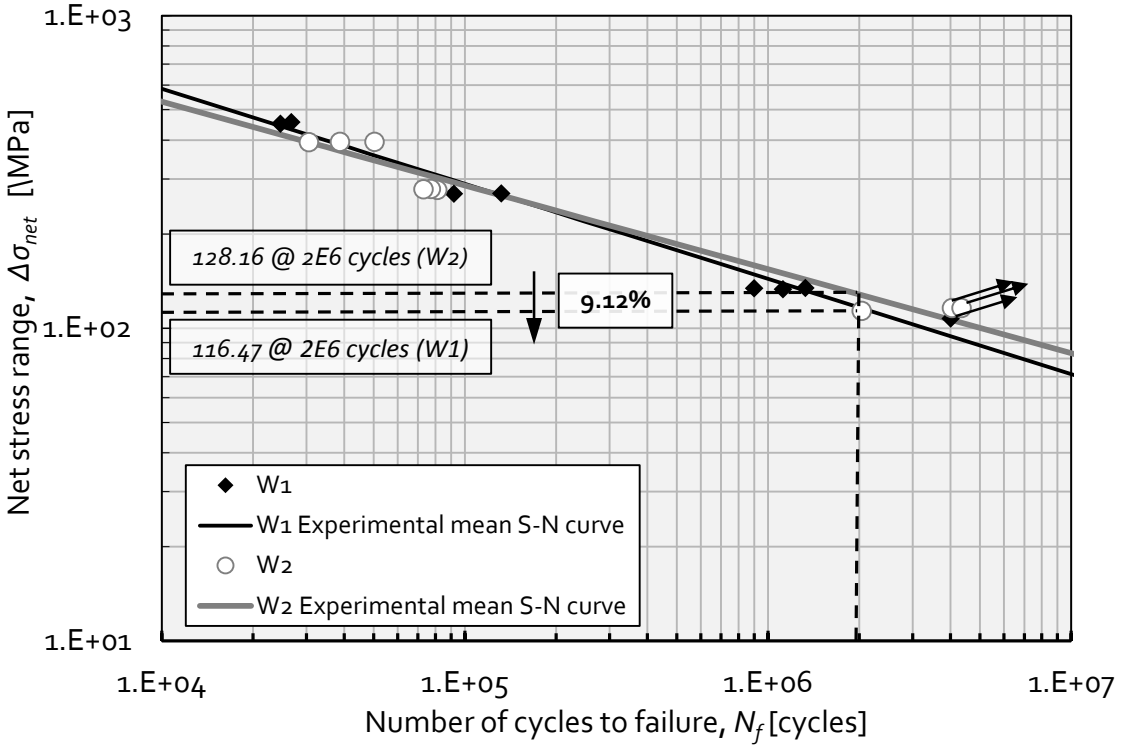

Figure 4.44 - Comparison of S-N curves for welded series W1 and W2 (thin plate thickness of 5 mm).

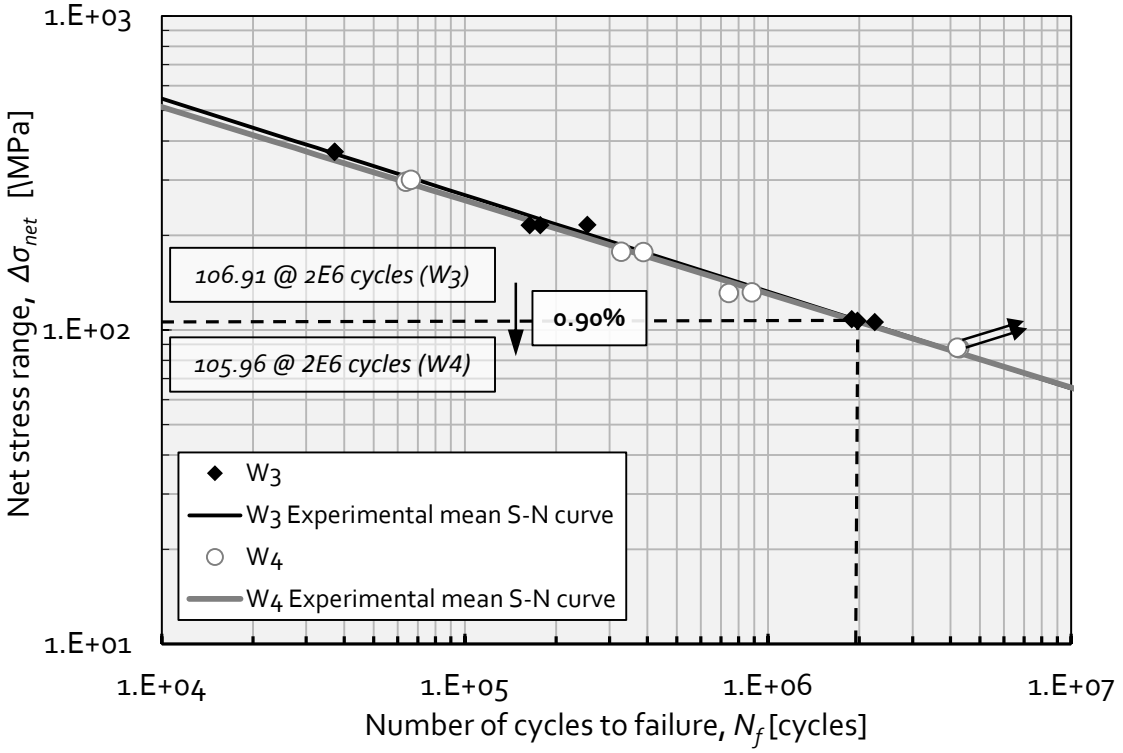

Figure 4.45 - Comparison of S-N curves for welded series W3 and W4 (thin plate thickness of 12 mm).

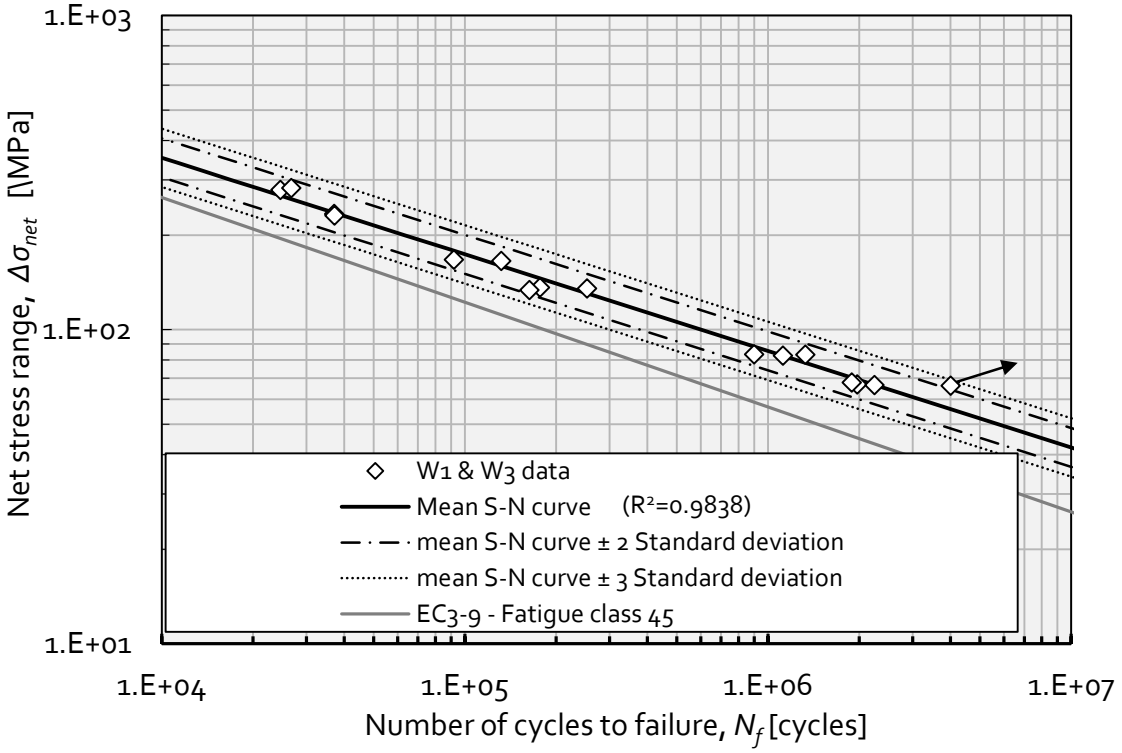

Figure 4.46 - Experimental S-N data for W1 and W3 welded series joined together.

Table 4.29 – Summary of linear regression parameters resulting from W1 and W3 welded data analyzed together.

***Number of specimens**, k*	16
***Mean value of the independent variable**, $\overline{X}$*	2.094
***Mean value of the dependent variable**, $\overline{Y}$*	5.473
***Slope**, B*	-3.254
***Intercept**, A*	12.288
***Variance**, S^2*	0.010
***Standard deviation**, S*	0.101

Table 4.30 - Confidence intervals for regression parameters *A* and *B* given in Table 4.29.

Confidence Level at 95%				***Confidence Level at 99%***			
A		***B***		***A***		***B***	
Lower	***Upper***	***Lower***	***Upper***	***Lower***	***Upper***	***Lower***	***Upper***
11.783	12.792	-3.493	-3.014	11.587	12.988	-3.586	-2.921

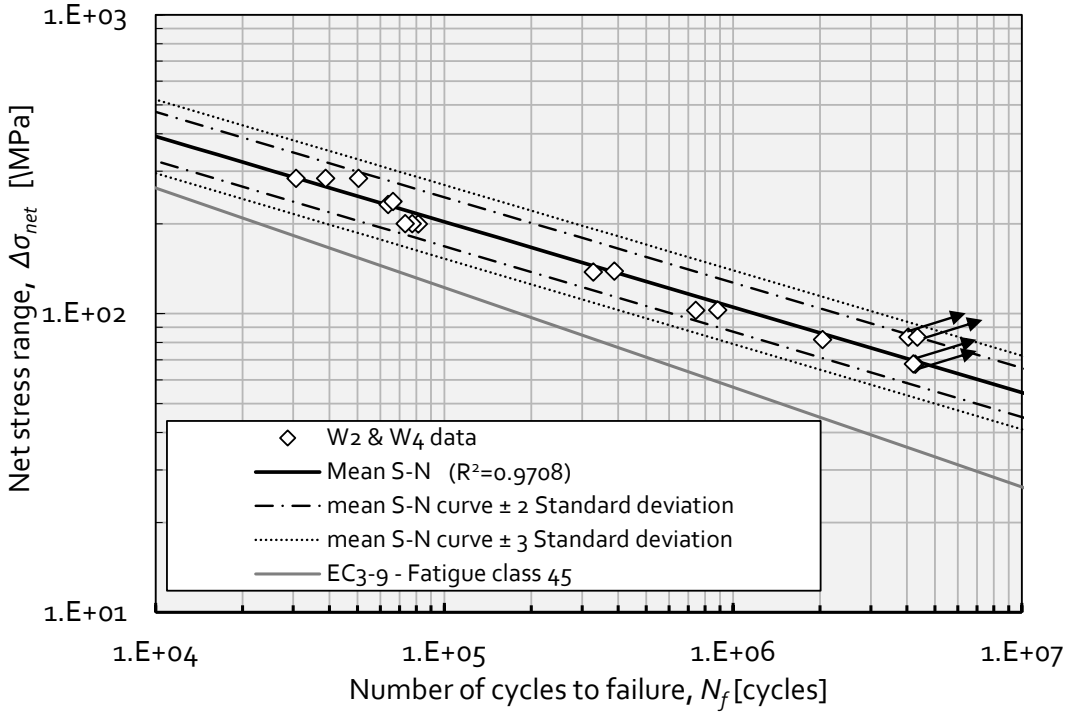

Figure 4.47 - Experimental S-N data for W2 and W4 welded series joined together.

The Figure 4.47 presents the experimental S-N curves resulting from welded specimens with a fillet weld configuration according to standard recommendations [1] (W2 and W4). For this case a high determination coefficient was also observed for the mean S-N curve, meaning low scatter of fatigue data. The Table 4.31 presents the linear regression data resulting from the analysis of the W2 and W4 series data. The Table 4.32 shows the confidence intervals at 95% and 99% confidence levels for *A* and *B* parameters.

Table 4.31 - Summary of linear regression parameters resulting from W2 and W4 welded data analyzed together.

***Number of specimens**, k*	17
***Mean value of the independent variable**, $\overline{X}$*	2.160
***Mean value of the dependent variable**, $\overline{Y}$*	5.517
***Slope**, B*	-3.500
***Intercept**, A*	13.076
***Variance**, S^2*	0.021
***Standard deviation**, S*	0.144

Table 4.32 - Confidence intervals for regression parameters *A* and *B* given in Table 4.31.

Confidence Level at 95%				***Confidence Level at 99%***			
A		***B***		***A***		***B***	
Lower	***Upper***	***Lower***	***Upper***	***Lower***	***Upper***	***Lower***	***Upper***
12.35111	13.801	-3.834	-3.166	12.073	14.078	-3.961	-3.038

Figure 4.48 presents the S-N curves obtained with the combination of all welded series with the thinner plate thickness of 5mm (W1 and W2) using the nominal/net stress definition. The class 45 EC3 S-N curve is plotted as well. The class 45 S-N curve is observed to be conservative since it fits below the lower limit represented for the S-N band. The respective linear regression data is presented in Table 4.33 and the confidence intervals at 95% and 99% confidence level for parameters *A* and *B*, are shown in Table 4.34.

Figure 4.49 presents the S-N curves obtained with the junction of the W3 and W4 welded data (thickness of thin plate equal to 12 mm). The class 45 EC3 S-N curve is also plotted. The class 45 S-N curve still is conservative for the joined welded series. Table 4.35 and Table 4.36 present the parameters of the linear regression analysis for this last data set.

Table 4.33 - Summary of linear regression parameters resulting from W1 and W2 welded data analyzed together (5 mm thick plates).

***Number of specimens**, k*	17
***Mean value of the independent variable**, $\overline{X}$*	2.172
***Mean value of the dependent variable**, $\overline{Y}$*	5.390
***Slope**, B*	-3.385
***Intercept**, A*	12.743
***Variance**, S^2*	0.042
***Standard deviation**, S*	0.204

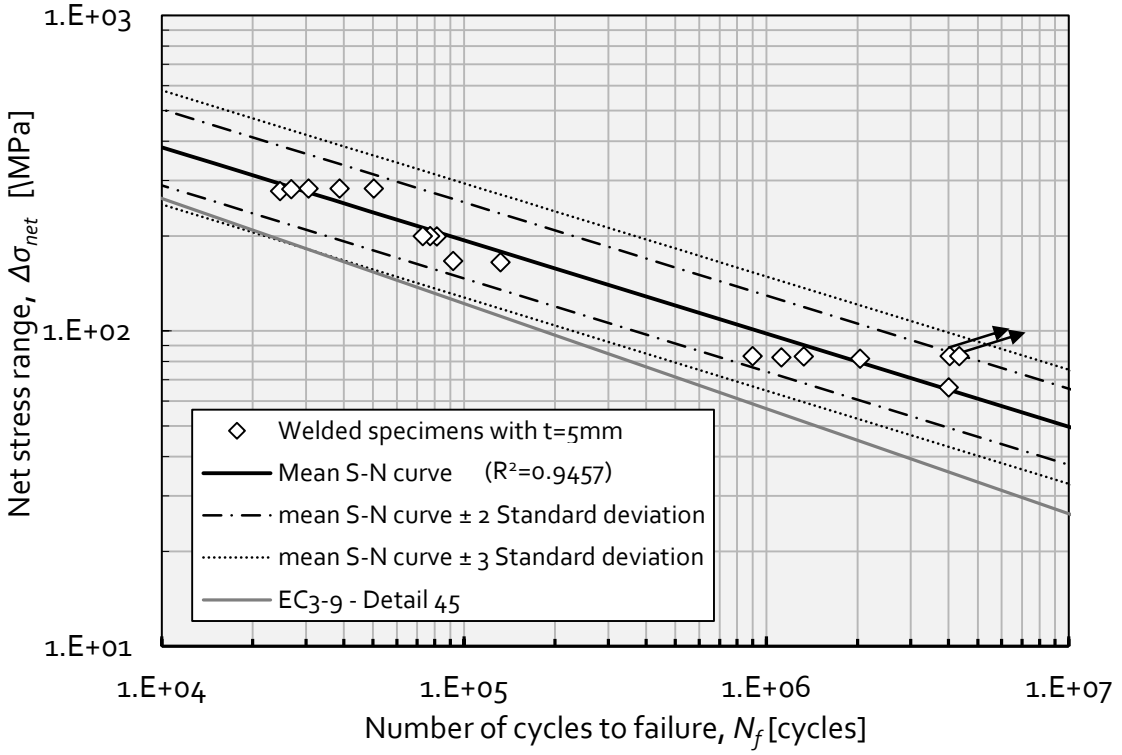

Figure 4.48 - Experimental S-N data for welded series with the thinner plate of 5mm thick (W1 and W2).

Table 4.34 - Confidence intervals for regression parameters *A* and *B* given in Table 4.33.

Confidence Level at 95%				***Confidence Level at 99%***			
A		***B***		***A***		***B***	
Lower	***Upper***	***Lower***	***Upper***	***Lower***	***Upper***	***Lower***	***Upper***
11.768	13.718	-3.832	-2.939	11.395	14.091	-4.002	-2.768

Figure 4.50 plots an experimental mean S-N curve obtained by the combination of all welded specimens fatigue data tested in the current experimental campaign. The experimental mean S-N curve was assessed using the nominal/net stress definition. Figure 4.50 compares the class 45 EC3 S-N curve with the experimental data showing a conservative code-based curve. The nominal stress at 2E6 cycles, for the experimental mean S-N curve, is 76.5 MPa, contrasting with the 45 MPa as foreseen in the code.

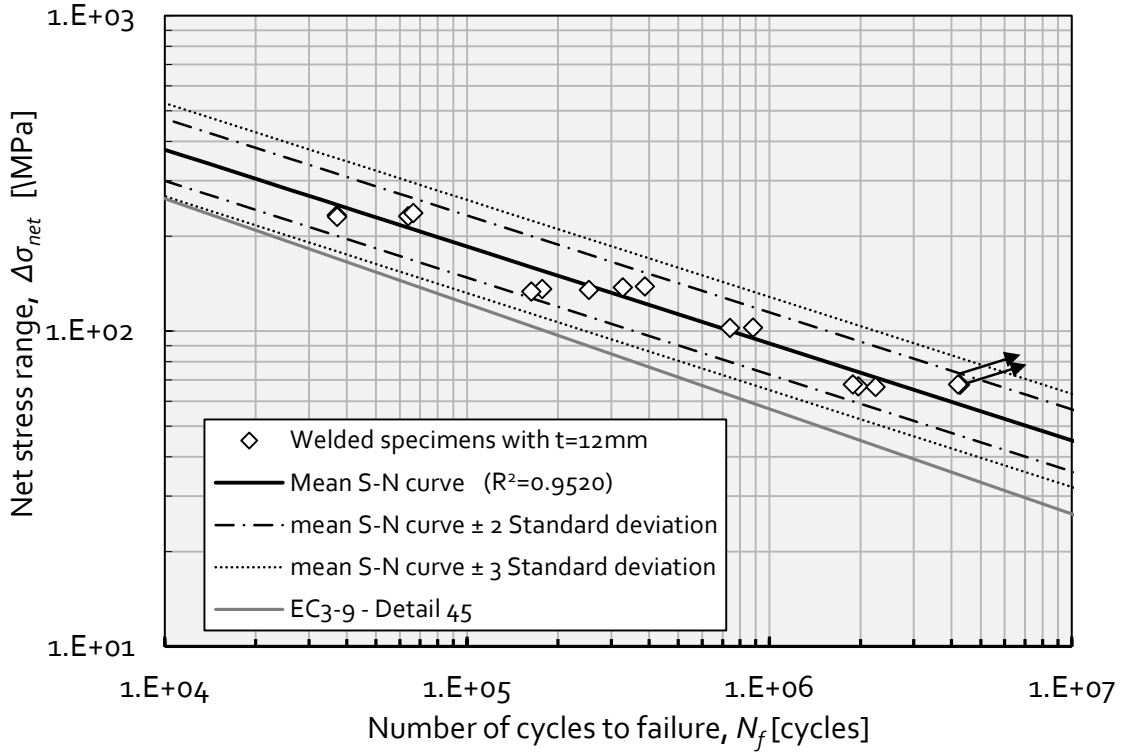

Figure 4.49 - Experimental S-N data for welded series with the thinner plate of 12mm thick (W3 and W4).

Table 4.35 - Summary of linear regression parameters resulting from W3 and W4 welded data analyzed together (12 mm thick plates).

***Number of specimens**, k*	16
***Mean value of the independent variable**, $\overline{X}$*	2.081
***Mean value of the dependent variable**, $\overline{Y}$*	5.608
***Slope**, B*	-3.254
***Intercept**, A*	12.382
***Variance**, S^2*	0.026
***Standard deviation**, S*	0.160

Table 4.36 - Confidence intervals for regression parameters *A* and *B* given in Table 4.35.

Confidence Level at 95%				***Confidence Level at 99%***			
A		***B***		***A***		***B***	
Lower	***Upper***	***Lower***	***Upper***	***Lower***	***Upper***	***Lower***	***Upper***
11.506	13.258	-3.673	-2.836	11.166	13.598	-3.836	-2.673

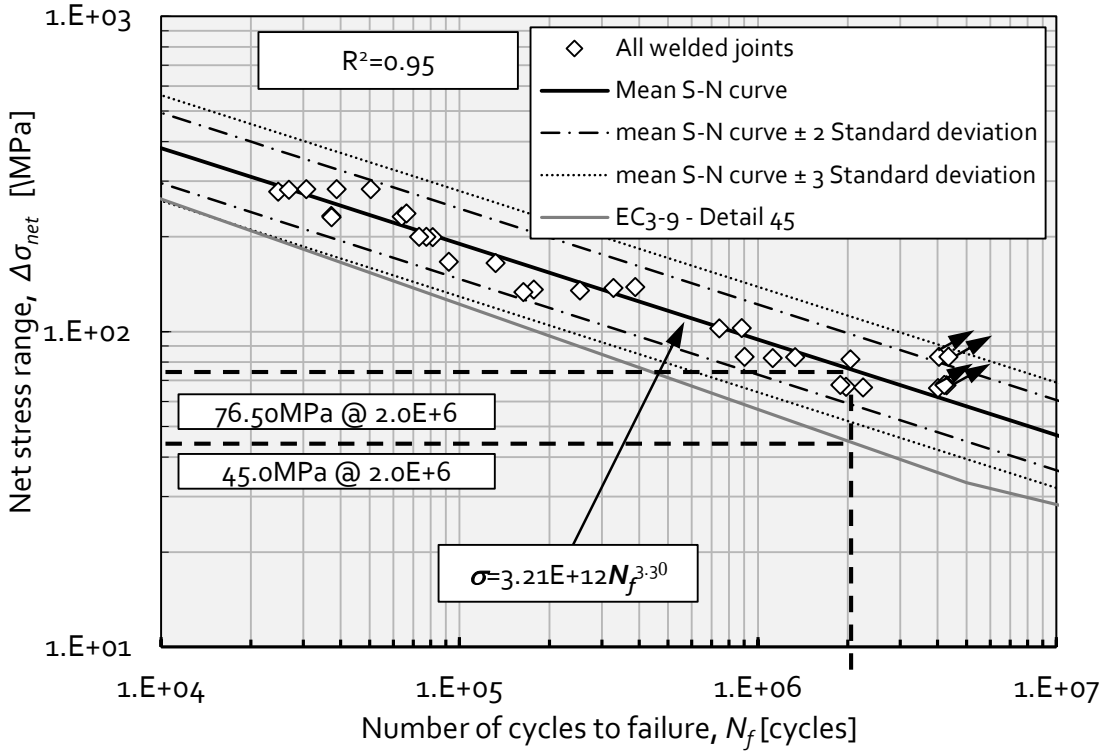

Figure 4.50 - Comparison of experimental S-N data of all welded specimens with EC3 class 45 S-N curve using the net stress definition.

4.3.2.1. Fracture surfaces of welded specimens

Fracture surfaces of W3 welded specimens are illustrated in Figure 5.51. Two fatigue cracks initiated at weld toes and propagated transversely to the loading direction. The final crack lengths were not the same on both sides of the specimen due to distinct crack growth rates and or crack initiation duration.

Fracture surfaces of some welded specimens were observed and fatigue crack striations were identified. Figure 4.52 exhibits fatigue crack striations with 50000 times magnification, where is possible to observe fatigue crack striations with less than 1μm spacing. Figure 4.53 illustrates fatigue crack striations smaller than 100nm spacing.

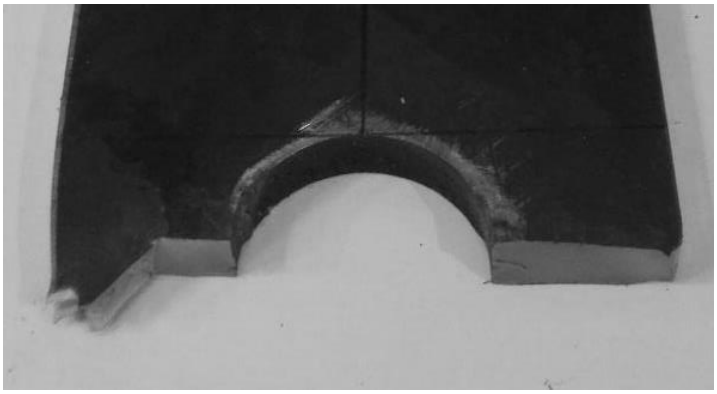

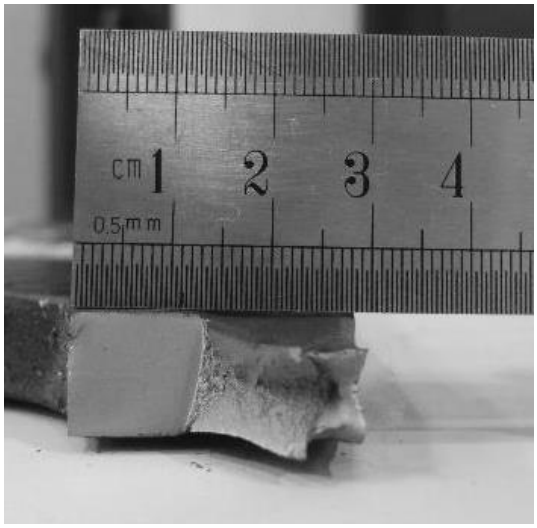

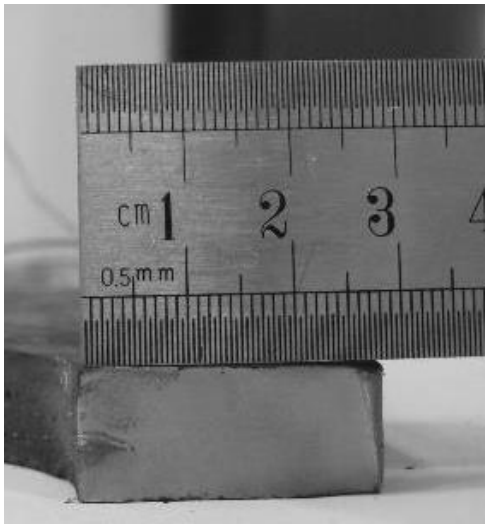

Figure 4.51 - Fracture surfaces of welded specimens (W3 specimen).

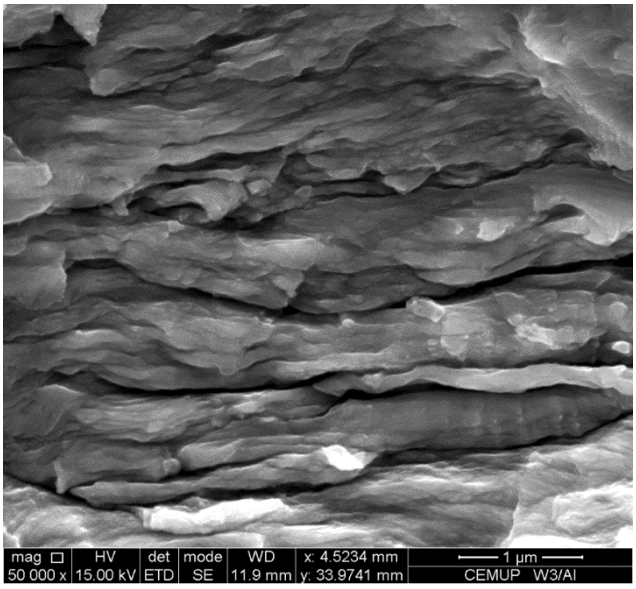

Figure 4.52 - Fatigue crack striations observed with a Scan Electron Microscopy (SEM) on fracture surface of W3 welded specimens (magnification: 50 000x).

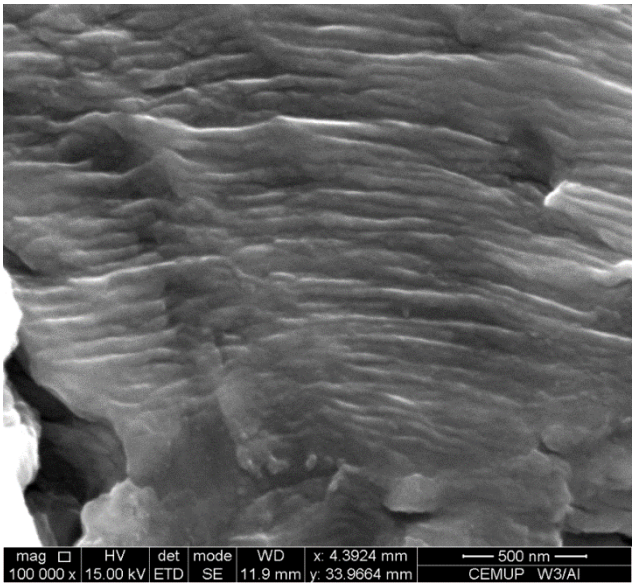

Figure 4.53 - Fatigue crack striations observed with a SEM on fracture surface of a W3 welded specimen (magnification: 100 000 x).

4.3.2.2. Digital image correlation performed on welded specimens

In this section an experimental stress analysis is performed on some welded specimens using digital image correlation (DIC). The region around the fillet weld end, on the thin plate surface is investigated. DIC allows the displacement field computation whose derivation results in the strain field. From linear elasticity equations, the stress field is computed.

Figure 4.54 shows results from the analysis of the W1-05 specimen. Figure 4.54a) presents the speckle pattern created on the welded W1-05 specimen surface around the hot spot where fatigue cracks were observed to start. The Figure 4.54b) illustrates the stress field assessed using DIC results. The overlapping of Figures 4.54a) and 4.54b) is in Figure 4.54c). The Figure 4.55 compares the *x* strain evolution resulting from a strain gauge (CEA-06-062UW-350) and from the DIC data for a specific location on the region assessed using DIC. The strain from the DIC was the average value computed at the area of the strain gauge. A good match can be observed between both strain results, for two load cycles ranging between 0 and 25kN.

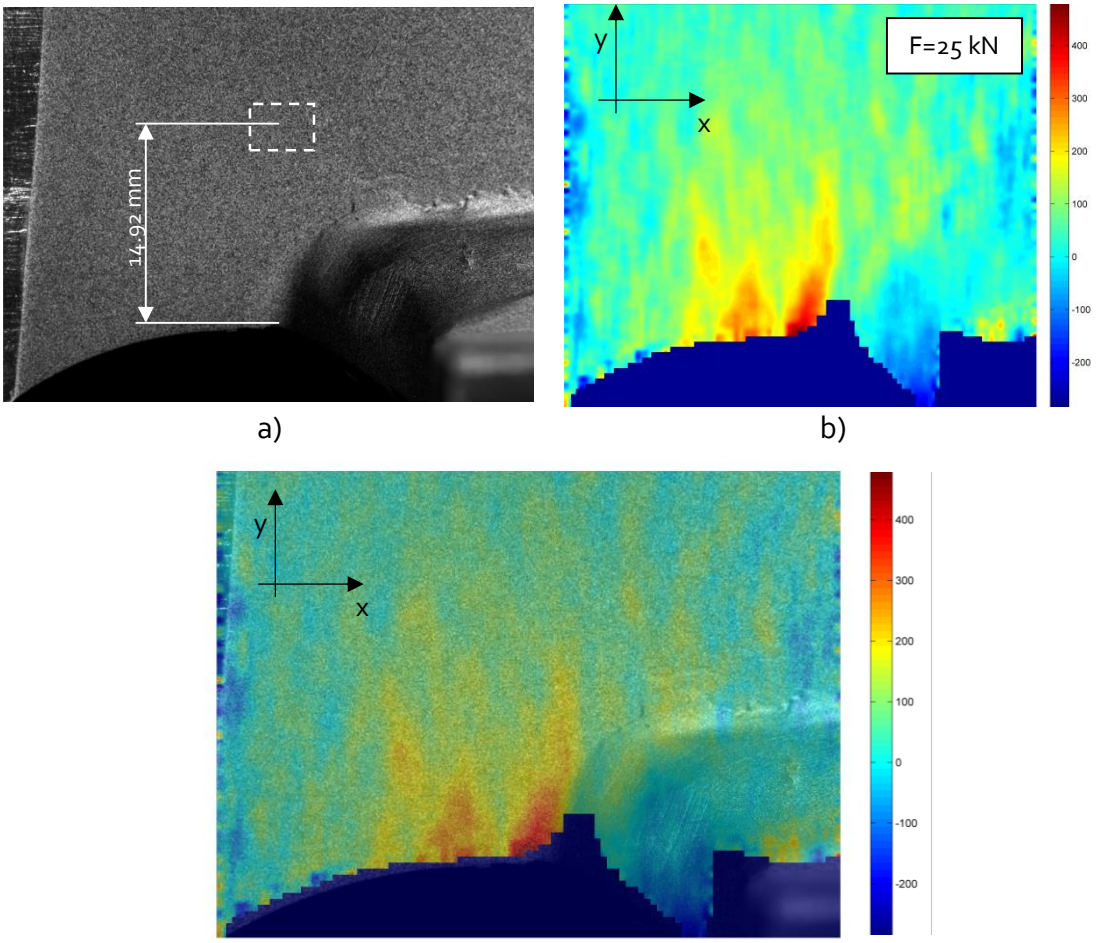

Figure 4.54 - Experimental stress field computation using DIC on W1-05 welded specimen: a) speckled specimen surface and strain gauge location defined by a dashed rectangle; b) computed *x* stress field (MPa); c) overlapping of figures (a) and (b).

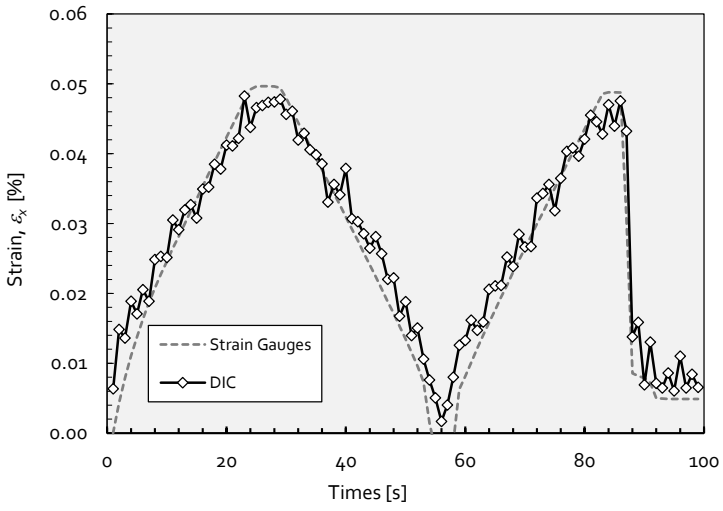

Figure 4.55 - Comparison of x strain evolution given by both strain gauge and DIC measurements (W1-05 welded specimen).

The Figure 4.56 presents the experimental (DIC) stress analysis performed for the W1-07 specimen. Figure 4.56 a) exhibits the speckle pattern painted to the welded W1-07 specimen surface. Figure 4.56 b) plots the resulting x stress field computed using DIC data for an applied load of 50kN. Figure 4.56 c) superimposes the computed stress field on the real specimen surface. The analysis of the figure shows clearly the hot spots ahead of the weld toe. Figure 4.57 compares the strain history for two load cycles, computed using both strain gauges and DIC. In order to compare DIC data and strain gauges measurements, a mean strain value was computed with DIC data on the same area and location of the used strain gauge.

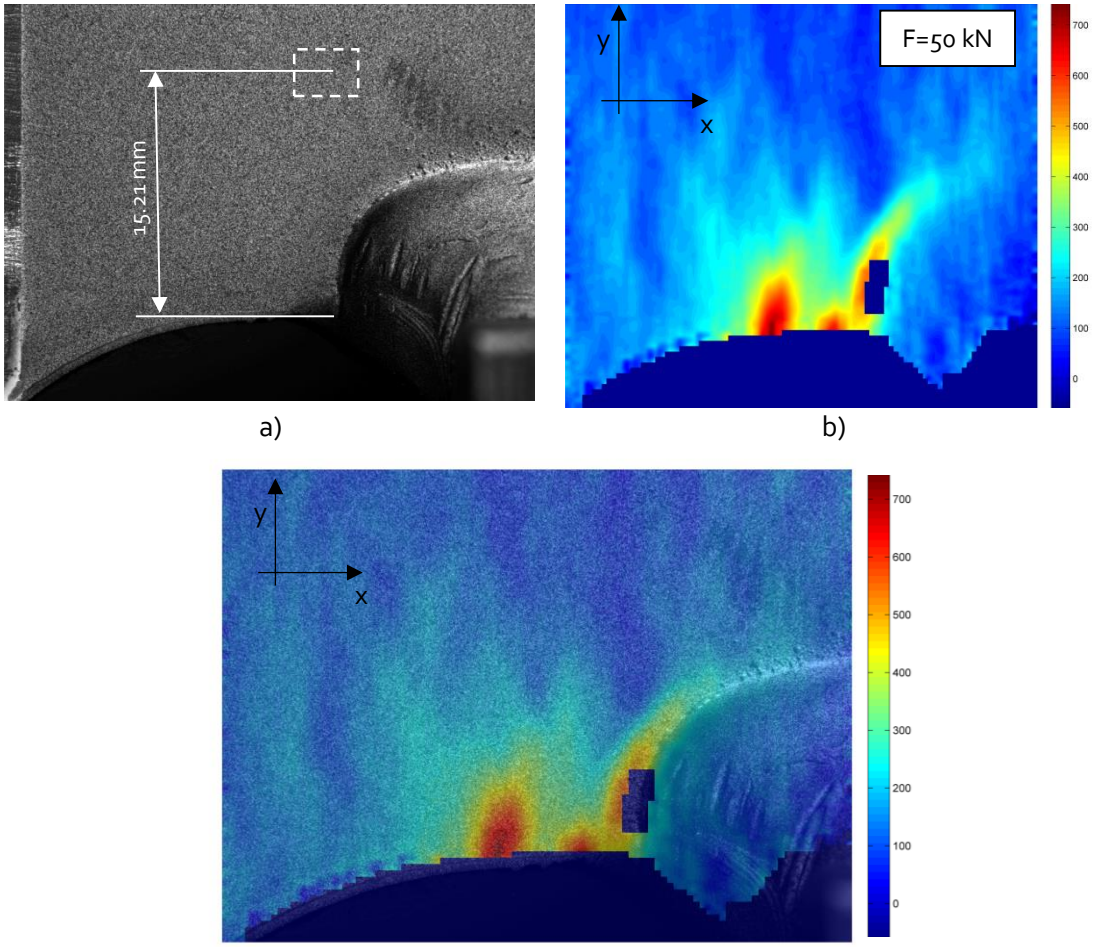

Figure 4.56 - Experimental stress field computation using DIC on W1-07 welded specimen: a) speckled specimen surface and strain gauge location defined by a dashed rectangle; b) computed *x* stress field (MPa); c) overlapping of figures (a) and (b).

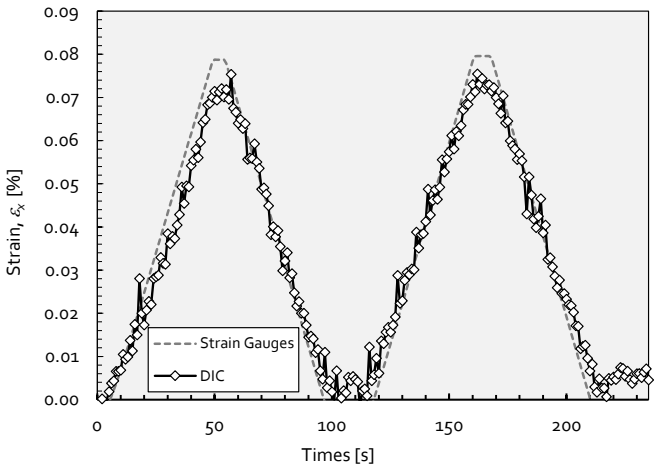

Figure 4.57 - Comparison of x strain evolution given by both strain gauge and DIC measurements (W1-07 welded specimen).

The Figure 4.58 presents the DIC post-processing results concerning the W2-02 welded specimen. Figure 4.58a) shows the speckle pattern attached to the specimen surface. Figure 4.58b) plots the x stress field resulting from DIC analysis. It can be observed that this welded specimen presents high stress values. The maximum applied load was 85kN, which probability resulted into local plastic strains. The stress values were computed using the Hooke's law of elasticity which in the case of plastic strains are no longer valid, resulting higher stress values than actual. The Figure 4.58c) illustrates the W2-02 welded specimen hot spot. Figure 4.59 compares the strain evolutions measured using both a strain gauge and DIC methodology. For this case some deviation between the two measurements was observed mainly for the lower peak strain.

The Figure 4.60 presents DIC post-processing results for the specimen W2-05 specimen. The speckle pattern linked to the specimen surface is shown in Figure 4.60a). Figure 4.60b) plots the strain field resulting by DIC assessment and the Figure 4.60c) presents the hot spot location. The Figure 4.61 compares the strain evolution computed using both strain gauge and DIC.

In general a very good agreement was found in the four reported cases between the DIC strains and the single strain gauge measurements. Using the DIC stress field, an analysis of the stress evolution along a net cross section of the assessed welded specimens is performed in the next paragraphs in order to derive structural stresses (membrane plus bending). In this case, the structural stresses were computed as the linearized stresses computed for the loading direction, along the crack path.

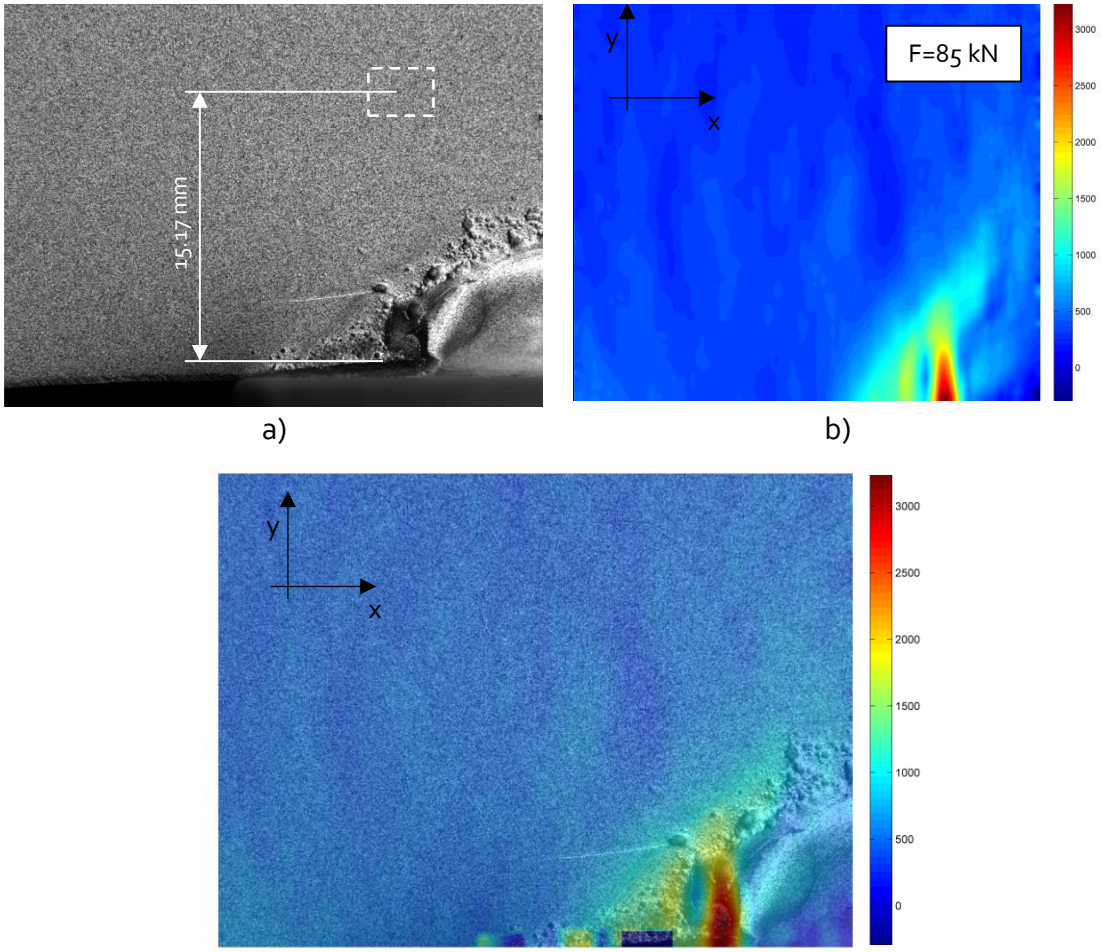

Figure 4.58 - Experimental stress field computation using DIC on W2-02 welded specimen: a) speckled specimen surface and strain gauge location defined by a dashed rectangle; b) computed x stress field (MPa); c) overlapping of figures (a) and (b).

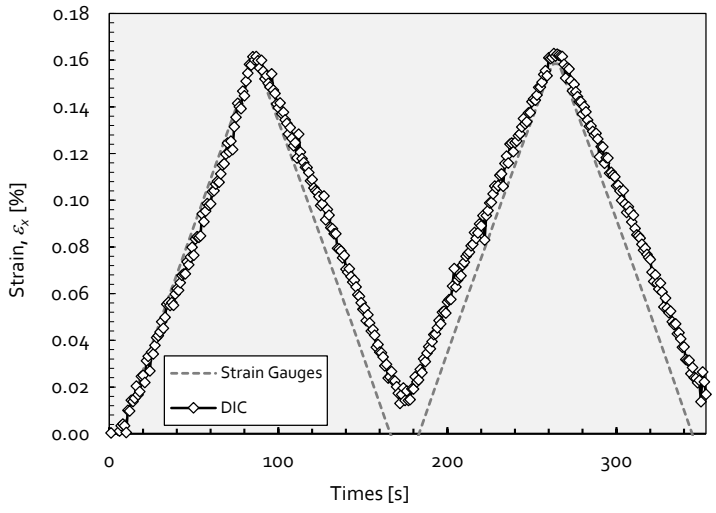

Figure 4.59 - Comparison of x strain evolution given by both strain gauge and DIC measurements (W2-02 welded specimen).

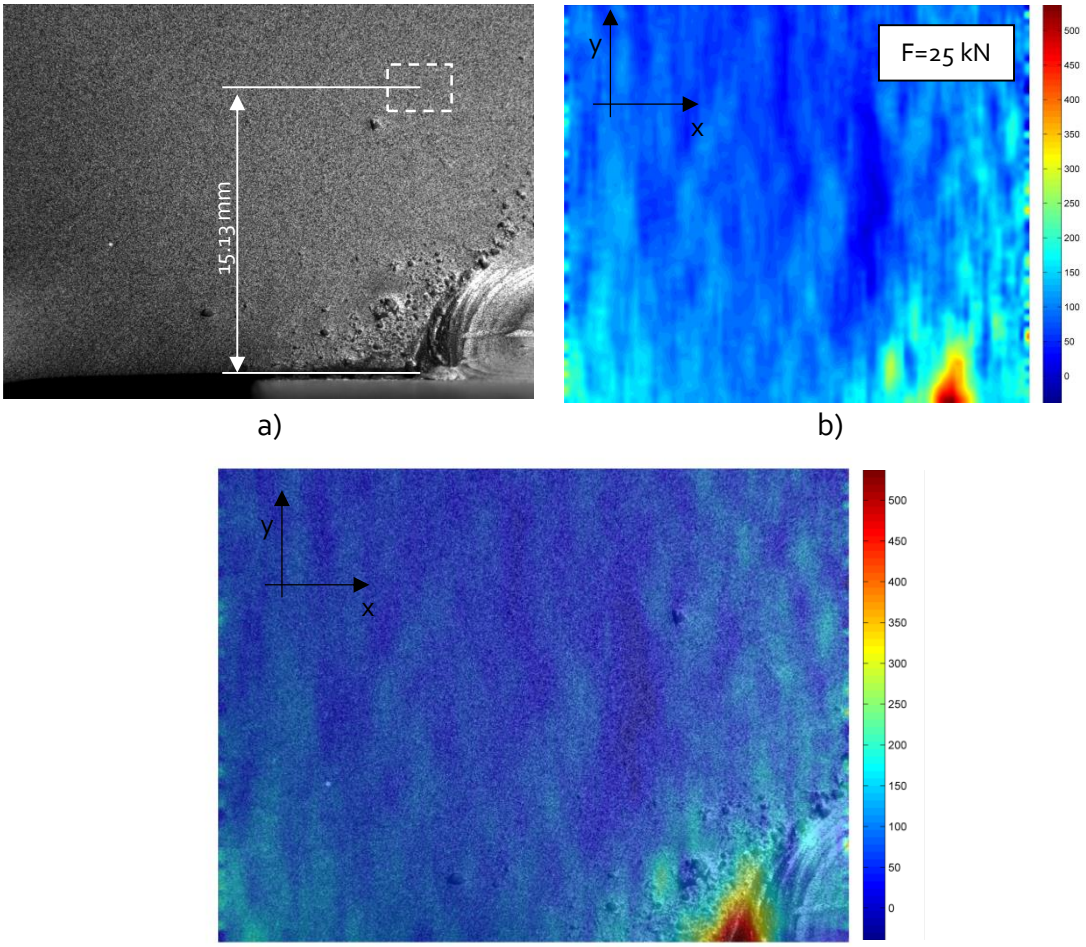

Figure 4.60 – Experimental stress field computation using DIC on W2-05 welded specimen: a) speckled specimen surface and strain gauge location defined by a dashed rectangle; b) computed x stress field (MPa); c) overlapping of figures (a) and (b).

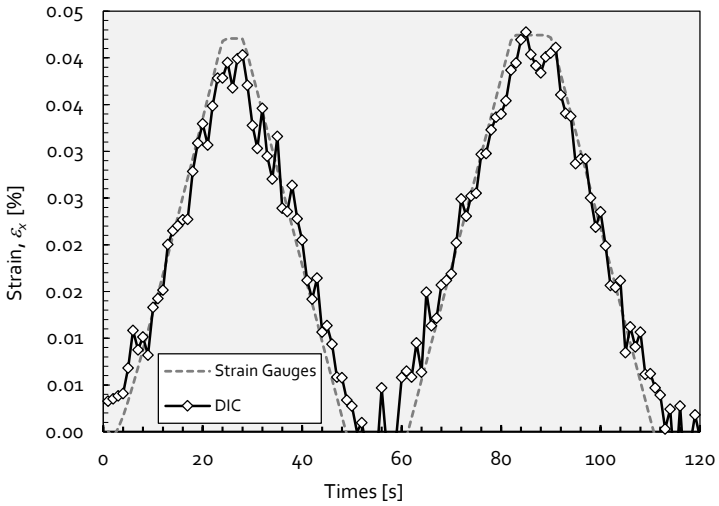

Figure 4.61 - Comparison of x strain evolution given by both strain gauge and DIC measurements (W2-05 welded specimen).

The DIC technique only allowed the monitoring of a partial area of the welded specimens around the welded hot spot. Therefore the stress field was only computed for a subdomain of the base plate of the welded specimen. In order to reproduce the stress field along the complete crack path, an extrapolation technique was proposed, based on the following considerations:

- A third order polynomial was fitted to the available CDI data (direct stresses along the loading direction). The CDI data covered the crack initiation spot until approximately mid distance of one side ligament (approximately 15 mm extension)
- A second order polynomial was proposed for the remaining hypothetical crack propagation path. The coefficients of this polynomial were computed using the following information:
    - Continuity between the third and second order polynomials;
    - Continuity of the slopes between the third and second order polynomials;
    - Load resultant of the complete stress distribution equal to the half load applied to the specimen.

Having obtained the two polynomials, a unique polynomial is then fitted to the entire crack path. With this polynomial the membrane (uniform) stress, σ_m, and bending moment, σ_b, are computed using the following relations (refers to Figure 4.60 for the axis orientation), obtained by stress linearization procedures [6]:

$$\sigma_m = \frac{1}{B}\int_0^B \sigma_x(y)dy \tag{4.12}$$

$$\sigma_b = \frac{6}{B^2}\int_0^B \sigma_x(y)\left(\frac{t}{2}-y\right)dy = \frac{6}{B^2}\left[\frac{B^2\sigma_m}{2}-\int_0^B \sigma_x(y)\,y\,dy\right] \tag{4.13}$$

where B (=30 mm, aprox.) is the width of the side plate ligament, on the thinner plate.

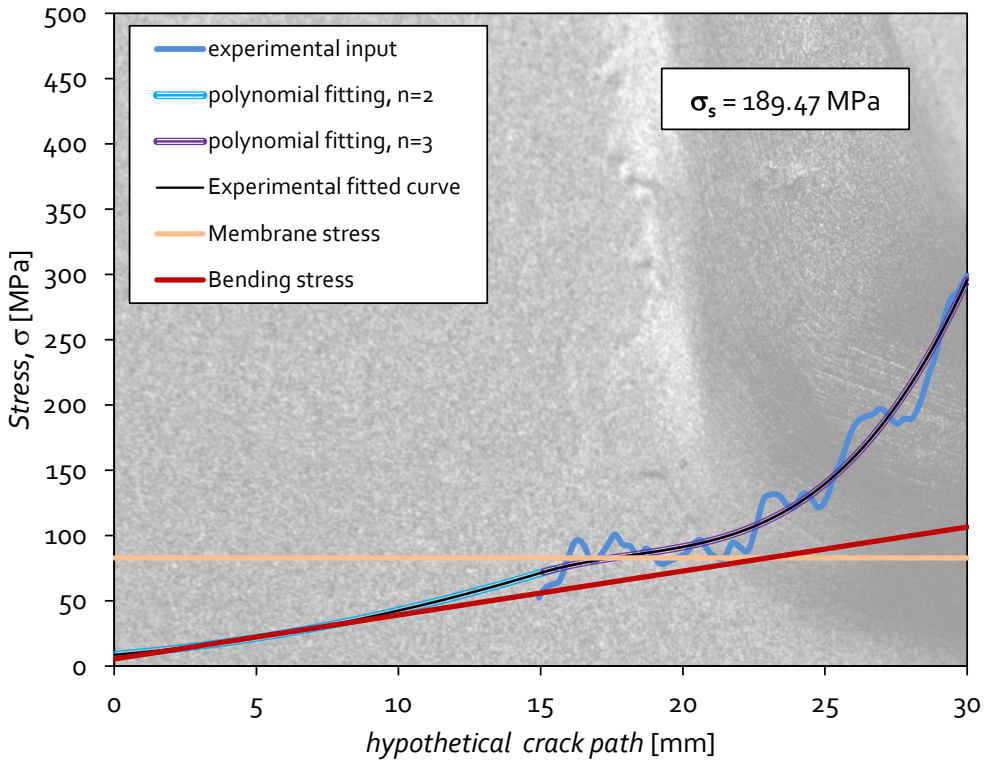

Figure 4.62 - Structural stress computation using DIC (W1-05) (F=22.5 kN).

Figure 4.62 to 4.65 plot the stress distributions along the hypothetical crack path, respectively for the W1-05, W1-07, W2-02 and W2-05 welded specimens. The figures include the stress results from the DIC analysis ("experimental input") for a limited extension of the crack path. Also polynomials for the total stress distribution are presented, namely for the subdomain of the available CDI results ("polynomial fitting, n=3"), for the remaining subdomain ("polynomial fitting, n=2") and for the complete domain ("experimental fitted curve", black curve). The figures also show the membrane and bending stresses that result from the application of the formulae (4.12) and (4.13). The structural stress was defined as the membrane and bending stress at the crack initiation spot. For some cases the peak and structural stresses revealed very high which may be justified by the fact that some plastic deformation may occur at the crack initiation site. The CDI strain data was used to compute the stresses assuming a linear elastic behaviour of the material which, for the presence of plastic deformation, leads to significant stresses.

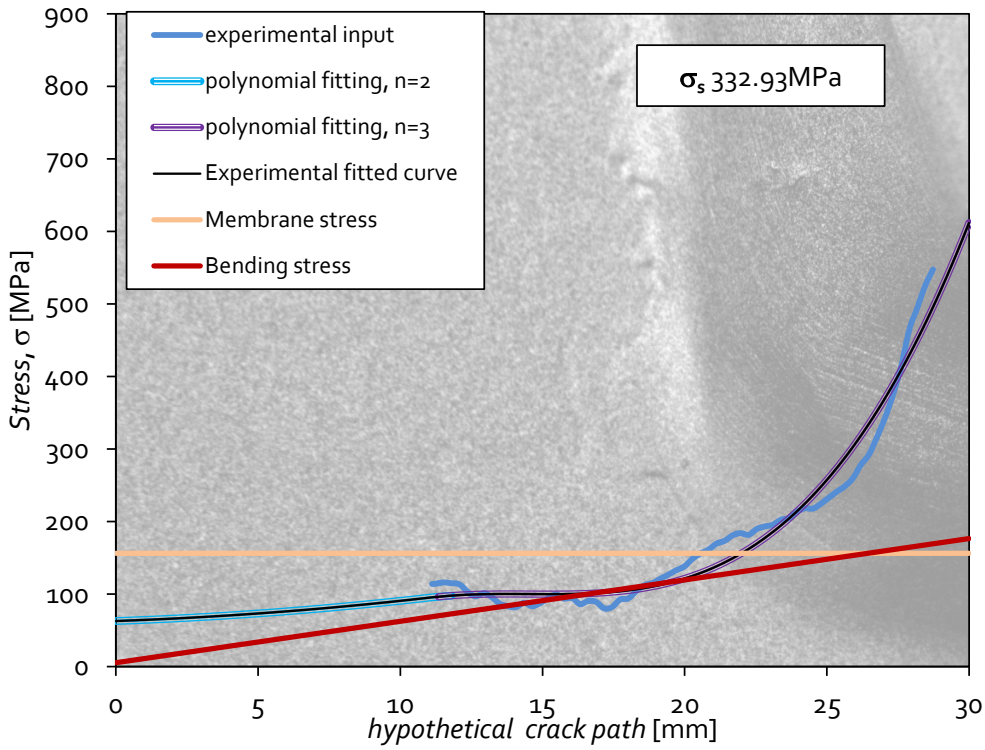

Figure 4.63 - Structural stress computation using DIC (W1-07) (F=50 kN).

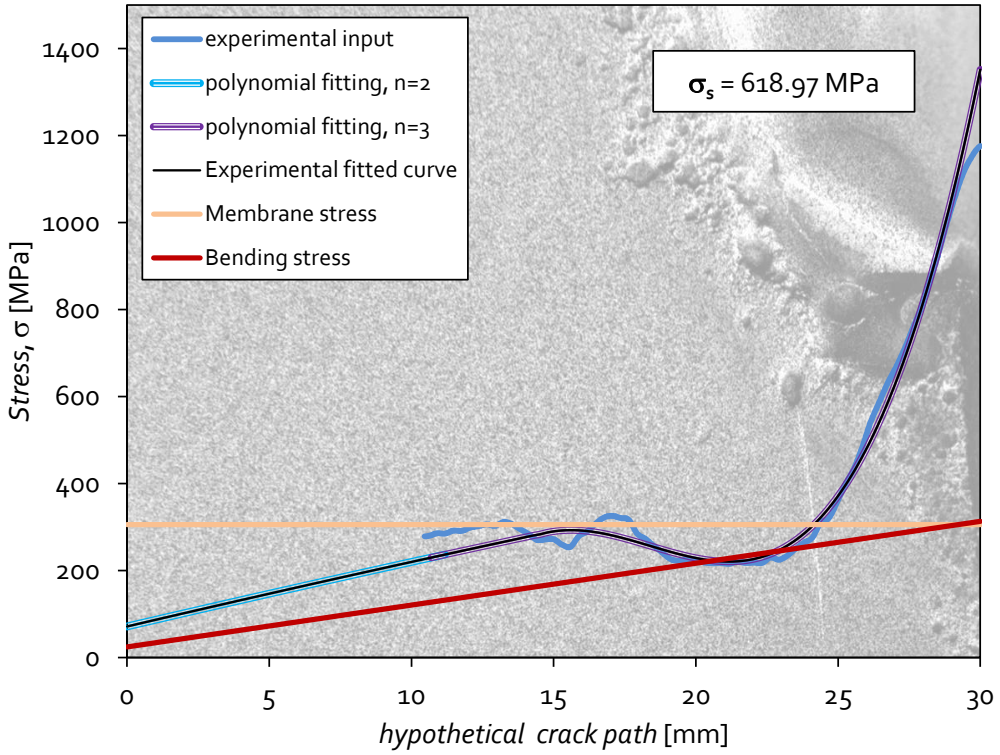

Figure 4.64 - Structural stress computation using DIC (W2-02) (F=85 kN).

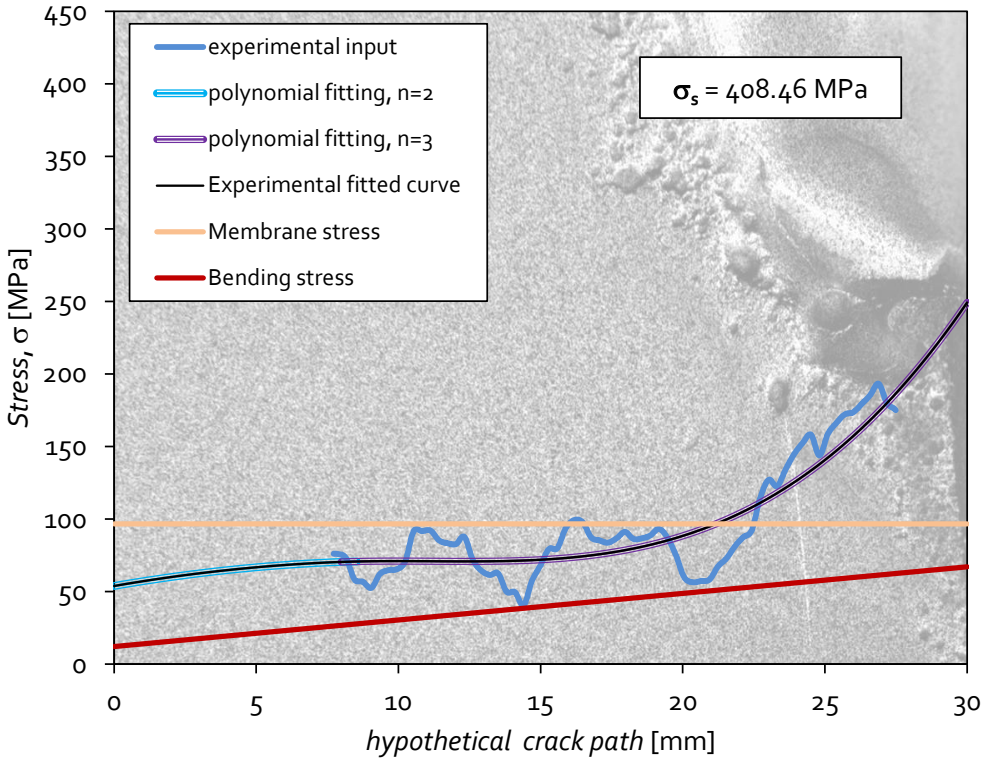

Figure 4.65 - Structural stress computation using DIC (W2-05) (F=25 kN).

4.4. CONCLUDING REMARKS

An experimental campaign of fatigue tests was performed on riveted and welded connections and results presented and discussed in this chapter. Each type of the connections was motivated by distinct bridge construction aiming different purposes. The riveted series R1, R2 and R3 were fatigue tested in order to validate S-N curves for riveted joints, as the ones proposed in EC3 and also by Taras and Greiner. It is important to refer that the EC3 does not mention explicitly the riveted joints, but literature suggests the class 71 S-N curve as appropriate for fatigue design of riveted joints. Taras and Greiner suggested riveted details categorization and the use of distinct S-N slopes in opposition to the universal value proposed in the EC3.

The experimental results of the R1 riveted specimens showed two failure modes: some specimens collapsed due to a fatigue crack growing from the rivet hole and other specimens collapsed due to a fatigue crack propagating at angle corner. In the first case

a mixed-mode fatigue crack propagation is likely to occur; in the second failure mode, a pure mode I fatigue crack propagation is very likely to occur. The failure modes for the R2 and R3 riveted specimens were characterized by a fatigue crack starting at the first rivet hole, perpendicularly to the loading direction. The R1 and R3 riveted series exhibited S-N slopes that are relatively closer to the EC3 class 71 S-N curve, which is an indication that these geometries exhibit a significant crack propagation phase. The R2 series, due to their small net section, exhibits a dominant crack initiation fatigue process. The R1 and R3 riveted series exhibited similar mean S-N curves. The R2 series exhibited a distinct mean S-N curve with higher fatigue resistance when compared with the other riveted series. The analysis of the S-N data generated in this study in conjunction with the S-N fatigue data gathered by Taras and Greiner for riveted joints of the same category showed that the Taras and Greiner design S-N curve is more consistent than the EC3 S-N curve. The slope of the S-N curve, m=5, seems more appropriate to describe the global trend of the fatigue data.

Regarding the welded joints, the experimental campaign was planned in order to allow the assessment of a deviation, with respect to the EC3 recommendations, of a local geometric feature of a welded detail of the Alcácer do Sal bridge. In addition, a welded plate thickness effect was also investigated. The experimental results showed that the fatigue strength at $2x10^6$ cycles decreases approximately 10% due to the use of a non-standardized geometric weld feature. Concerning the thickness effect, no significant influence of this parameter on the S-N curves was verified, for the range of investigated thicknesses. The S-N data from all tested series was correlated together with a high determination coefficient, R^2=0.85, which is a clear indication that the geometric variations characterizing the distinct welded series, did not show a very significant influence on the S-N curves. Concerning the slopes of the individual S-N curves they exhibited very similar values and they are similar to the EC3 S-N curve. The EC3 class 45 S-N curve showed to be conservative as expected for this kind of fillet welded joints. This curve fits below the global mean S-N curve minus 3 times the standard deviation which demonstrated the suitability of the design curve. All welded specimens exhibited similar failure modes that resulted from fatigue cracks that initiated at weld toes and propagated perpendicularly to the loading direction.

Digital image correlation was used to assess the strain and stress field at the hot spot vicinity area. A hybrid technique was proposed for structural stress computation for the welded specimens.

4.5. REFERENCES

[1] Eurocode 3: Design of steel structures, Part 1-9: Fatigue, CEN: Brussels, Belgium, 2004.

[2] F. Lippi , W. Salvatore, Braconi, A., Finetto, M., Wenzel, H., De Roeck, G., Peeters, B., Könke, C., Zabel, V., Cunha, A., "Fatigue damage control and assessment for railway bridge", Research Fund for Coal and Steel, Directorate-General for Research and Innovation, Grant Agreement RFSR-CT-2009-00027, 1 July 2009 to 30 June 2012.

[3] American Society for Testing and Materials, "ASTM E739-91: Standard Practice for Statistical Analysis of Linear or Linearized Stress-Life (S-N) and Strain Life (ε-N) Fatigue Data", Annual Book of ASTM Standards, pgs. 597-603, 1991.

[4] Taras, A., Greiner, R., "Development and Application of a Fatigue Class Catalogue for Riveted Bridge Components", Institute for Steel Structure and Shell Structure, Graz, August 2009.

[5] de Jesus A.M.P., da Silva A.L.L., Correia J.A.F.O., "Fatigue of Riveted and Bolted Joints Made of Puddle Iron-An Experimental Approach", Journal of Constructional Steel Research 104, pp. 81-90, 2015.

[6] Dong, P., "A Structural Stress Definition and Numerical Implementation for Fatigue Analysis of Welded Joints", International Journal of Fatigue 23, pp.865-876, 2001.

Chapter V

Welded joint fatigue behaviour assessment using mesh insensitive procedures and S-N master curve concepts

5.1. INTRODUCTION

Although existing alternatives for fatigue life prediction of welded joints based on local stresses or crack initiation-based fatigue approaches available in the literature [1-2], current code-based fatigue assessment procedures for welded structures are mainly based on nominal or hot spot stress approaches, both requiring a family of S-N curves each one corresponding to groups of details with similar characteristics [3-6].

The nominal stress approach can be categorized as a global fatigue approach. The stress computation is based primarily on the cross-section properties and does not include the effects of geometric including weld stress concentrations. These effects are implicitly accounted for using a fatigue classification of common structural details. This classification and the corresponding strength curves are based on statistical evaluation of fatigue test data of typical details. The nominal stress approach is computationally less expensive but its accuracy decreases as the details become increasingly more complex. Due to its relative ease of application for simple details, the nominal stress approach has been adopted in many fatigue design guidelines [6-11].

The hot spot or structural stress approach considers gross geometrical discontinuities in the stress analysis and therefore does not need so many detail categories as required by the nominal stress approach. This approach should lead to more accurate fatigue assessments than the nominal approach. The hot spot stress approach accounts for the stress field at the vicinity of the weld hot spot resulting from gross geometric discontinuities, but ignores the local weld notch effects that lead to non-linear stress distributions across thickness. These local effects are implicitly included in the definition of a family of fatigue strength curves. Generally, more than one S-N curve is required to represent different weld conditions. The approach often involves the use of finite element method to evaluate the hot spot stress, which makes the approach computationally more expensive than the nominal approach. This approach was initially

developed for fatigue assessment of offshore tubular structures [12-14]. Its application to plate structures, particularly bridge details, has been more limited.

With the advances in computing, finite element method became a very popular numerical tool. Efforts are being made to extend the hot spot stress approach to plate structures [15] very often supported by finite element analysis. Various societies offer guidelines to perform such analyses for plate structures [16-18]. However, this methodology exhibits one important disadvantage that results from mesh sensitive stresses.

Despite several methods to assess hot spot (structural) stresses are available in the current literature, the following chapter will discuss the recent approach by Dong [19] that will be applied and assessed using welded results derived in this investigation. Dong proposed a methodology to compute structural stresses claimed as mesh insensitive. At least, the mesh sensitivity drawback from standard finite element procedures for structural stress computations is minimized with the methodology by Dong. This author also proposed a master S-N curve for welded joints valid for any welded geometry, using a modified version of the structural stress. This methodology has been verified for tubular welded details as for example the ones typical of pressure vessels [20]. As a consequence of these studies, the methodology has been incorporated in the recent revision of the ASME VIII-Div. 2 [21]. Its verification for plate welded joints should be intensified in order to promote its extension for other construction codes.

This chapter firstly presents an overview of the methodology for the computation of mesh insensitive structural stresses. Afterward, the methodology will be assessed using several 2D and 3D benchmark examples. Then, the Dong method is applied to the welded joints fatigue data presented in the Chapter IV, combining the mesh insensitive structural stresses with the master curve concept.

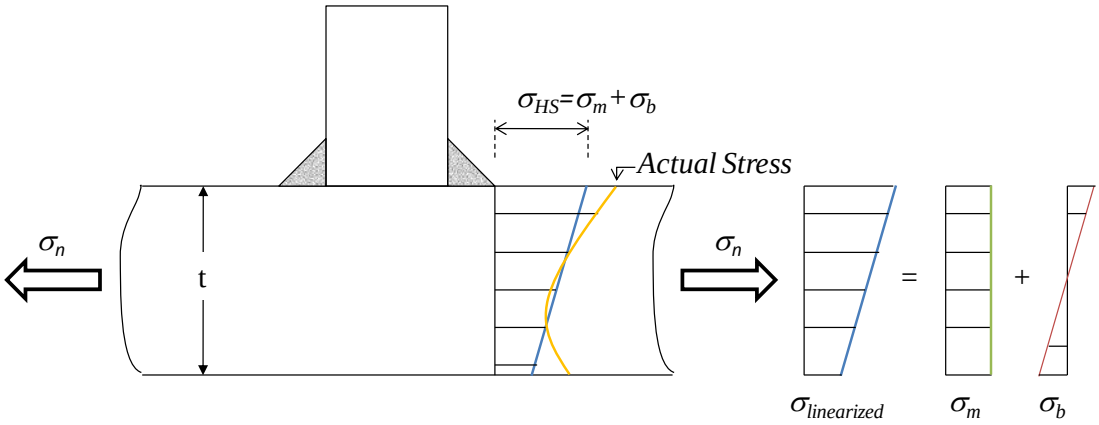

Figure 5.1 - Through thickness stress linearization [19].

5.2. MESH INSENSITIVE PROCEDURE TO COMPUTE STRUCTURAL STRESSES ON WELDED JOINTS

Radaj [5] proposed the linearization concept of the stresses across the member thickness (crack path) to compute the structural stresses, as illustrated in the Figure 5.1. However, the linearization of the stresses computed directly from a finite element analysis may suffer of objectivity due to the mesh dependency of those stress finite element stress distributions. This method was modified by Dong [19-24], using elementary structural mechanics principles, such as force and moment balances between two sections through the plate thickness, reducing in this way the mesh sensitivity of the structural stresses. Associated to the structural stress definition, Dong also proposed a Master S–N curve concept that will be also described latter on this chapter.

According to Dong [19] the structural stress may be established based on the following assumptions:

a) For a given local through thickness stress distribution, as illustrated in Figure 5.2 a), there exists an equivalent structural stress distribution as shown in Figure 5.2 b), composed of membrane and bending stress components, which are equilibrium-equivalent with the local stress distributions of Figure 5.2a).

b) The structural stress distribution must satisfy equilibrium conditions, based on the context of elementary structural mechanics theory, between the hypothetical crack planes, define as section A-A in Figure 5.3, and a nearby reference plane, distanced δ from section A-A, where the local stress distributions are known from finite element computation (section B-B in Figure 5.3).

c) The local stresses at the notch are mesh-size sensitive, mainly due to the asymptotic stress behaviour as the singularity (e.g. weld toe) is approached. The imposition of the equilibrium conditions in the context of elementary structural mechanics with respect to this regime should eliminate or minimize the mesh-size sensitivity in the structural stress calculations [19]. This is due to the fact that the local stress concentration close to a notch is dominated by self-equilibrating stress distribution, as discussed by Niemi [18].

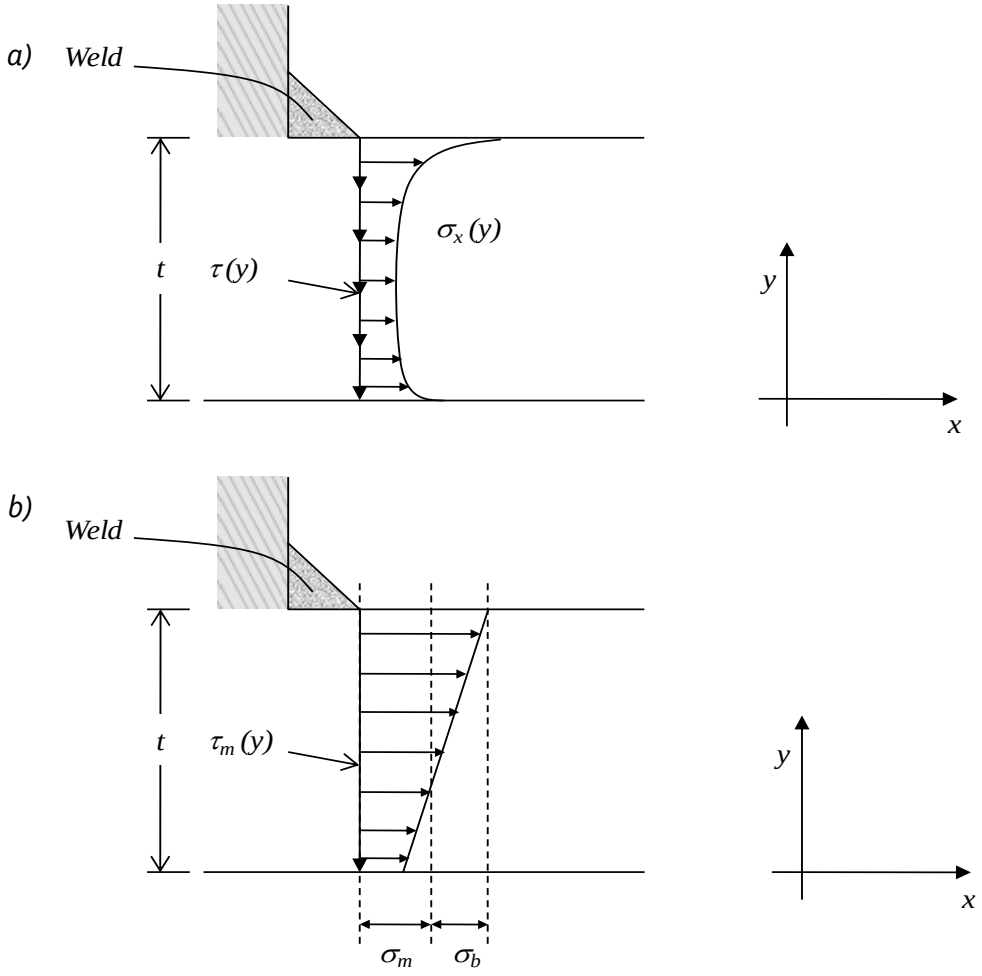

Figure 5.2 - Structural stresses definition for through-thickness fatigue crack: a) local through-thickness normal and shear stress at weld toe; b) structural stress definition at weld toe [22].

As shown in Figure 5.2a), the stress distribution along a hypothetical crack path containing the weld toe is assumed to exhibit a peak stress around the weld toe. It should be noted that in typical finite element analysis, the stress values within some distance from the weld toe can significantly change, as the finite element mesh size changes [19], referred as mesh-size sensitivity [19, 23]. The corresponding statically equivalent structural stress distribution illustrated in Figure 5.2b) is composed of membrane (σ_m) and bending (σ_b) stress components, consistent with elementary structural mechanics definition:

$$\sigma_s = \sigma_m + \sigma_b \tag{5.1}$$

where the membrane and bending stress components may be computed by a stress linearization according to the following relations [23]:

$$\sigma_m = \frac{1}{t}\int_0^t \sigma_x(y)dy \tag{5.2}$$

$$\sigma_b = \frac{6}{t^2}\int_0^t \sigma_x(y)\left(\frac{t}{2}-y\right)dy = \frac{6}{t^2}\left[\frac{t^2\sigma_m}{2} - \int_0^t \sigma_x(y)\,y dy\right] \tag{5.3}$$

In the above discussion, the transverse shear, τ_m, was not accounted for in the structural stress calculation. However, in practice the transverse shear component can be significant. In order to account for the transverse shear effects on structural stress definition, a second reference plane is defined at the B-B section parallel to the hypothetical crack path A-A section (see Figure 5.3), with δ representing the distance between A-A and B-B sections. For convenience, a single row of finite elements with size δ may be used to represent the material between A-A and B-B sections. Imposing equilibrium conditions between A-A and B-B sections results the following alternative equations for the membrane and bending stresses:

$$\sigma_m = \frac{1}{t}\int_0^t \sigma_x(y)\cdot \mathbf{d}y \tag{5.4}$$

$$\sigma_m \frac{t^2}{2} + \sigma_b \frac{t^2}{6} = \int_0^t \sigma_x(y)\cdot y \cdot \mathbf{d}y + \delta\int_0^t \tau_{xy}(y)\cdot \mathbf{d}y \tag{5.5}$$

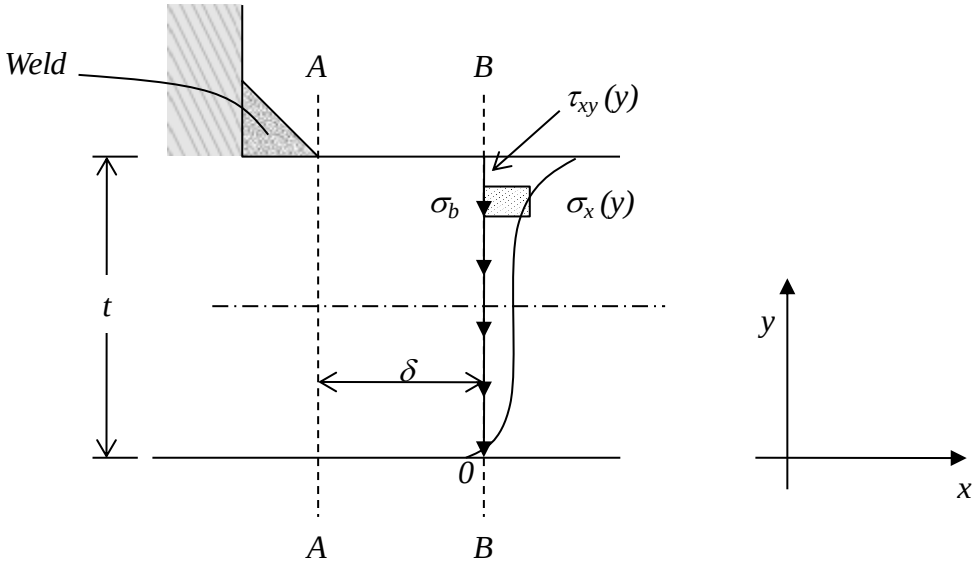

Figure 5.3 - Structural stresses calculation procedure for through-thickness fatigue crack [8].

Equation (5.4) represents the force balances along the x direction, using the normal stress distribution at section B-B. Equation (5.5) characterises the moment balance with respect to y=0, at section A-A. The integral term on the right-hand side of Equation (5.5), represents the transverse shear force as an important component of the structural stress definition. If element size (δ) is small or transverse shear is negligible, the integral representations of σ_b and σ_m in Equations (5.4) and (5.5) can be directly calculated at Section A-A of Figure 5.3.

Dong [19] recommended the use of nodal forces to assess the structural stresses from finite element models. This procedure revealed to be more robust concerning the computation of the structural stresses than using the stress distribution [19]. Instead of using the local stress outputs in the integration of Equations (5.4) and (5.5), the nodal forces can be used for all nodes located at plane A-A of Figure 5.3. Considering the nodal forces, both membrane and bending stress components, referred in Equations (5.4) and (5.5), can be rewritten as:

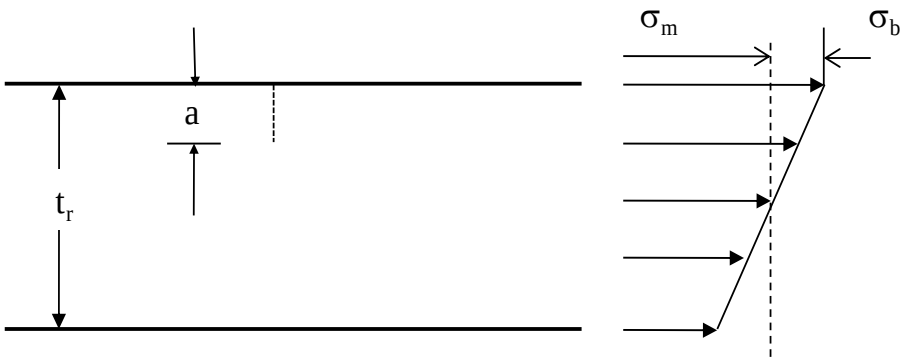

Figure 5.4 - Fracture mechanics interpretation of the structural stress. Fatigue damage interpreted as a fatigue crack propagation process.

$$\sigma_m \cdot w \cdot t = \sum_{i=1}^{n} F_{xi} \tag{5.6}$$

$$\sigma_b \cdot w \cdot \frac{t^2}{6} + \sigma_m \cdot w \cdot \frac{t^2}{2} = \sum_{i=1}^{n} F_{xi} \cdot y_i \tag{5.7}$$

where the above summation is carried out over all the nodes (*n*) located in the A-A plane and y_i is the coordinate of the node *i*, measured from the local reference coordinate system in Figure 5.3.

5.2.1. Equivalent structural stress compatible with a S-N Master Curve

Once a structural stress is assessed in terms of σ_m plus σ_b stress components, the structural stress transforms the actual loaded geometry (e.g. a given weld detail) into a simple plate geometry, as shown in Figure 5.4, where a represents a fatigue crack length and t_r corresponds to a reference length, concerning the final crack depth at failure. The two structural stress components are understood as an equivalent remote loading applied to a plate with a hypothetical crack spanning from a=0 to a=t_r. For such a simple cracked geometry presented in Figure 5.4 stress intensity factor solutions are available in the literature [25]. It can be shown, that the Mode I stress intensity factor range, for the crack geometry in Figure 5.4, can be expressed as a function of the ranges of the structural stress components using superposition principle [19]:

$$\Delta K = \Delta K_m + \Delta K_b = \sqrt{t_r}\left[\Delta\sigma_m f_m\left(\frac{a}{t_r}\right) + \Delta\sigma_b f_b\left(\frac{a}{t_r}\right)\right] \tag{5.8}$$

where $f_m\left(a/t_r\right)$ and $f_b\left(a/t_r\right)$ are dimensionless functions of a/t_r for membrane and bending components, expressed by:

$$f_m\left(\frac{a}{t_r}\right) = \left[0.752 + 2.02\left(\frac{a}{t_r}\right) + 0.37\left(1 - \sin\frac{\pi a}{2t_r}\right)^3\right]\frac{\sqrt{2\tan\frac{\pi a}{2t_r}}}{\cos\frac{\pi a}{2t_r}} \tag{5.9}$$

$$f_b\left(\frac{a}{t_r}\right) = \left[0.923 + 0.1997\left(1 - \sin\frac{\pi a}{2t_r}\right)^4\right]\frac{\sqrt{2\tan\frac{\pi a}{2t_r}}}{\cos\frac{\pi a}{2t_r}} \tag{5.10}$$

It has to be referred that the previous solution for the stress intensity factor, based on Equations (5.8) to (5.10) are exclusive for welded joints where no symmetry is observed with respect to the midplane of the horizontal member. A more appropriate approach is given by Dong *et al.* [19], for joints with horizontal symmetry.

Taking into account Equation (5.1), one may rewrite Equation (5.8) as

$$\Delta K_s = \Delta\sigma_s\sqrt{t_r}\left[f_m - r\left(f_m - f_b\right)\right] \tag{5.11}$$

where $\Delta\sigma_s$ is the structural stress range and *r* is the ratio between the bending stress range and the structural stress:

$$r = \frac{\Delta\sigma_b}{\Delta\sigma_s} \tag{5.12}$$

The fatigue crack growth is directly affected by the welded toe vicinity. However, this effect is not considered in the structural stress intensity factor definition, as given in the

Equation (5.11). In order to consider the welded toe vicinity effect on fatigue crack growth, Dong [19] suggested a modification of the Paris law, including the magnification stress intensity factor concept:

$$\frac{da}{dN} = C(M_{kn})^n(\Delta K_n)^m \tag{5.13}$$

where M_{kn} is the magnification stress intensity factor parameter. Details about the magnification stress intensity factor parameter may be read in literature [19]. Figure 5.5 illustrate the magnification stress intensity factor parameter effect on fatigue crack growth. Figure 5.5 a) exhibits fatigue crack growth data from different sources without considering the magnification stress intensity factor parameter. Figure 5.5 b) plots the fatigue crack growth, when M_{kn} is considered. All fatigue data collapsed into one narrow band.

The number of cycles to failure can be assessed integrating Equation (5.13), between $a \to 0$ and $a = t_r$:

$$N = \int_{a\to 0}^{a=t_r} \frac{da}{C(M_{kn})^n(K_n)^m} = \int_{a/t_r \to 0}^{a/t_r=1} \frac{t_r d\left(a/t_r\right)}{C(M_{kn})^n(K_n)^m} \tag{5.14}$$

Equation (5.14) may be rewritten as:

$$N = \frac{1}{C} t_r^{1-(m/2)} \cdot \left(\Delta\sigma_s\right)^{-m} I\left(r\right) \tag{5.15}$$

where $I\left(r\right)$ is a dimensionless function of r, defined as:

$$I(r) = \int_{a/t_r \to 0}^{a/t_r=1} \frac{d\left(a/t_r\right)}{(M_{kn})^n(f_m - r(f_m - f_b))^m} \tag{5.16}$$

Dong proposed a dimensionless polynomial function of the bending ratio r (under load controlled conditions) [19]:

$$I(r) = 0.294r^2 + 0.846r + 25.815 \tag{5.17}$$

Finally, the Equation (5.15) allows the definition of an equivalent structural stress which can be used to define a universal/ master S-N curve valid for any welded detail:

$$\Delta S_s = \frac{\Delta \sigma_s}{t_r^{(2-m)/2m} \cdot I(r)^{1/m}} \tag{5.18}$$

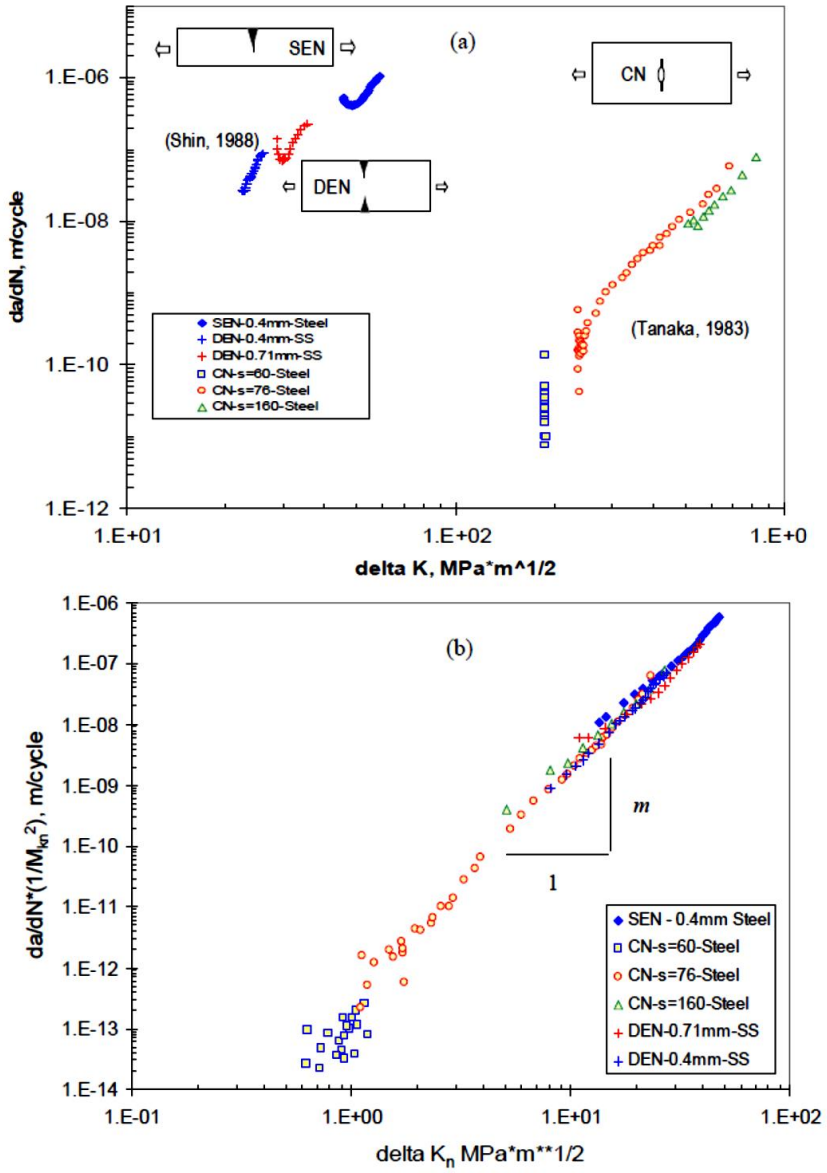

Figure 5.5 - Comparison of fatigue crack propagation data resulting from various fatigue tests: a) data presented without M_{kn} effect; b) data represented using M_{kn} effect with n=2 [19].

5.3. MESH INSENSITIVE APPROACH – VERIFICATION EXAMPLES

In this section, numerical simulations aiming the assessment of structural stresses according to the method proposed by Dong [19] will be performed. In particular, the mesh sensitivity of the computed structural stresses is assessed for some proposed verification examples. Nodal forces and stress distribution integration approaches were both applied to 2D and 3D geometries. Several mesh refinements were simulated for each example, in order to test the mesh insensitive approaches. Linear elastic stress analyses were performed in all verification examples. Linear finite elements were applied with full integration scheme.

5.3.1. Verification example 1: 2D tensile problem

The first verification example consists of a welded T-joint with fillet welds, as represented in Figure 5.6. A uniform tensile stress applied to the horizontal plate was considered. Several finite element meshes were modelled. Figure 5.7 plots all finite element meshes considered in this analysis. Table 5.1 presents the finite element size as well as the distance δ from the weld toe (see Figure 5.6). Structural stress was computed using both nodal forces (Equations (5.6) and (5.7)) and through thickness stress integration (Equations (5.4) and (5.5)). Both approaches were then compared with local notch stresses computed for all finite element meshes.

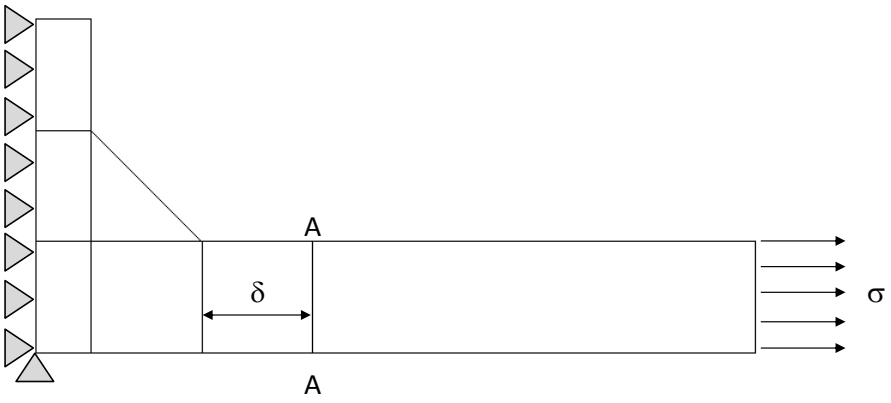

Figure 5.6 - Verification example 1: 2D tensile problem.

Table 5.1 - Finite element details for the verification example 1.

Model	FE size [mmxmm]	δ [mm]
Mesh 1	20x20	20
Mesh 2	10x10	10
Mesh 3	5x5	5
Mesh 4	2x2	2
Mesh 5	1.5x1.5	1.5
Mesh 6	1x1	1

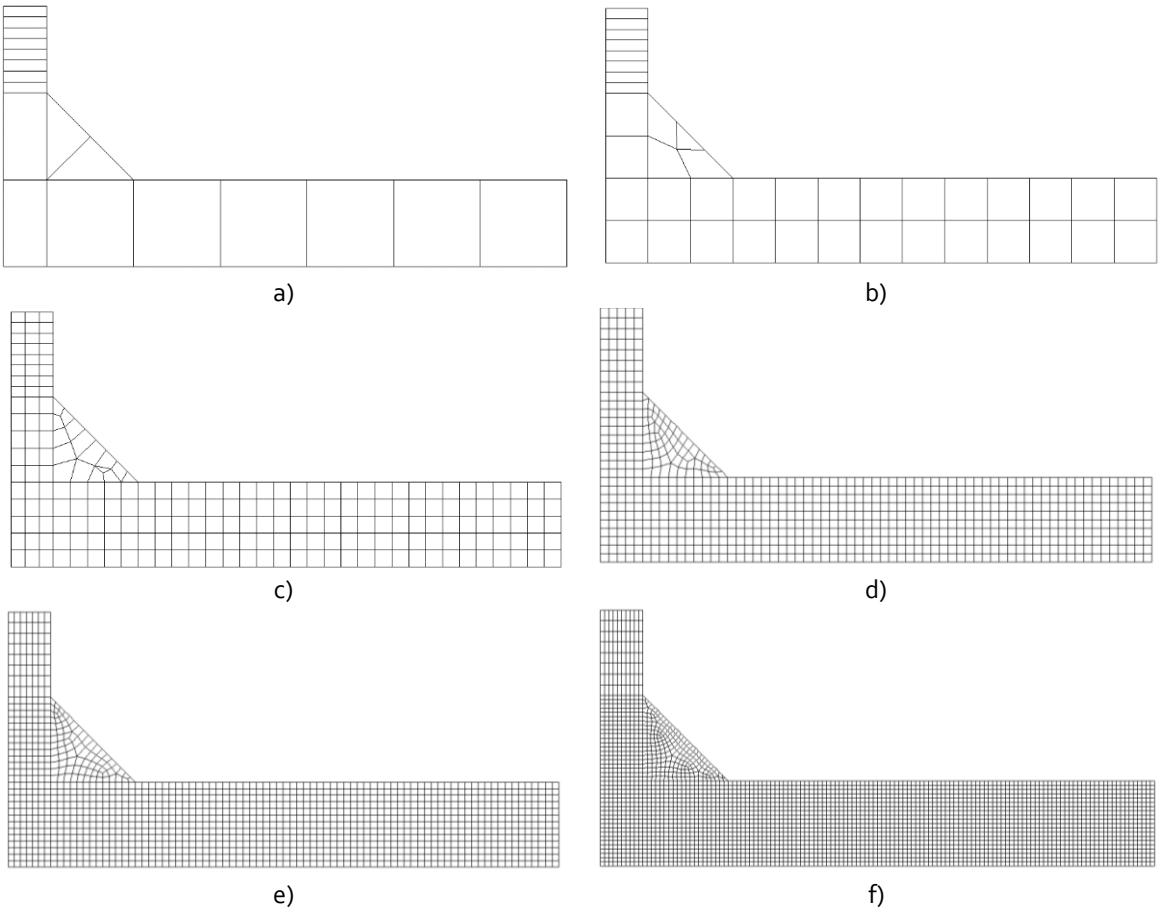

Figure 5.7 - Finite element meshes simulated for verification example 1: a) mesh 1; b) mesh 2; c) mesh 3; d) mesh 4; e) mesh 5; f) mesh 6.

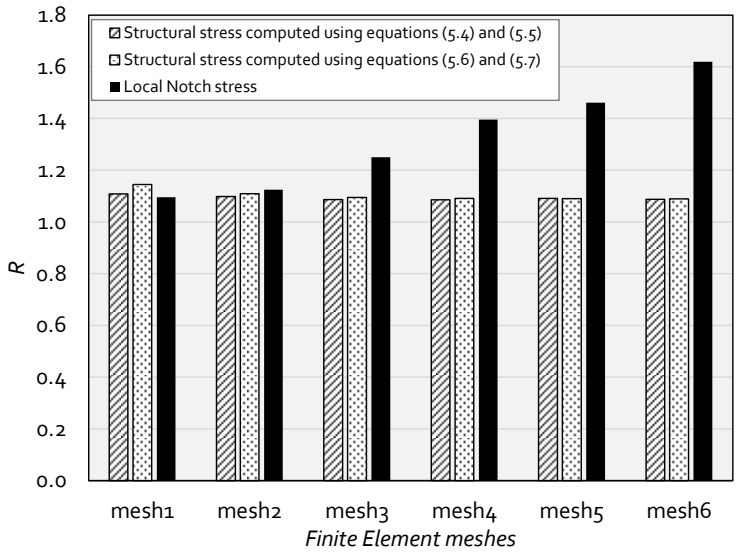

Figure 5.8 - Local notch and structural stresses (stress concentration factors) computed using distinct finite element sizes (verification example 1).

Figure 5.8 plots the structural and local notch stresses computed for distinct mesh sizes. For the structural stresses, the two computation alternatives were used: *i*) through thickness stress integration and *ii*) nodal forces approach. Both structural and local

notch stresses were normalized using the applied remote stress (σ in Figure 5.6) leading to a stress ratio, *R*. The analysis of the figure reveals that the local notch stresses are very sensitive to the mesh size and no stabilization was found in the local notch stresses, for the range of mesh densities considered. Concerning the structural stresses, it is observed a stabilization of the stress values in the transition from mesh 1 to mesh 2. One may conclude that for predominantly tensile loading both structural stress computation approaches are equivalent and the mesh insensitivity is achieved if the mesh refinement is not extremely coarse.

5.3.2. Verification example 2: 2D bending problem

The verification example 2 comprised the same filled welded T-joint presented in Figure 5.6. However, in this case, a transverse load F is applied, as shown in Figure 5.9, leading to transverse shear and bending moment dominant loading. Finite element meshes plotted in Figure 5.7, were also considered in this analysis. Finite element sizes and distances δ from the weld toe, presented in Table 5.1, were also considered in the analysis. Similarly to what was considered in the verification example 1, two structural stress definitions were computed, in addition to the local notch stresses.

Figure 5.10 exhibits the structural stresses computed using both through thickness stress integration and nodal forces approaches as well as the local notch stresses. These stresses were normalized by the theoretical bending stress value at the weld toe, computed using structural mechanics principles, i.e., the bending moment at that section and the Euler-Bernoulli bending theory. The structural stresses computed using the nodal forces approach was completely mesh insensitive. However, the structural stresses based on stress integration approach showed mesh sensitivity, but a quick monotonic convergence to the stable value similar to the one obtained using the nodal forces approach was verified. The relative mesh sensitivity of the structural stress based on cross section stress integration is due to the inability of a gross finite element mesh to capture accurately the shear stress distribution across the plate thickness. Figure 5.11 show the stress distributions (normal and shear) across the thickness and one realize that for the first mesh an inaccurate linear shear stress distribution is observed.

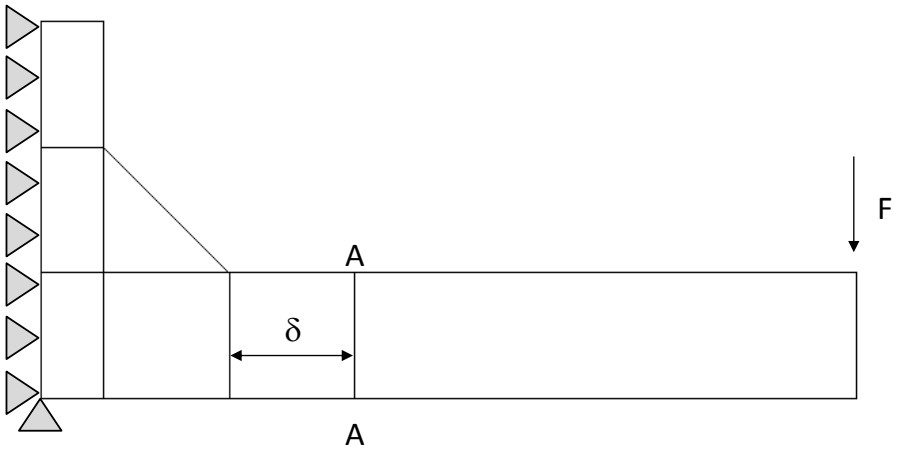

Figure 5.9 - Verification example 2: 2D bending problem.

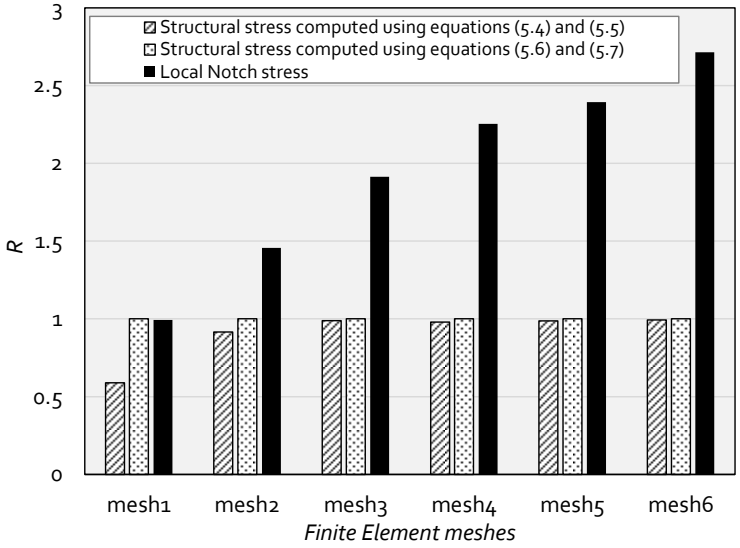

Figure 5.10 - Local notch and structural stresses (stress concentration factors) computed using distinct finite element mesh sizes (verification example 2).

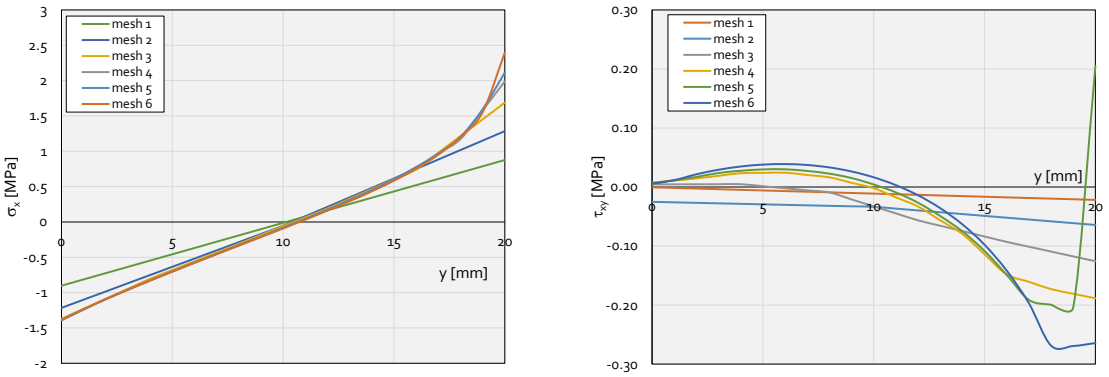

a) b)

Figure 5.11 – Through stress Stress evolution: a) normal stress (σ_x); b) shear stress (τ_{xy}).

5.3.3. Verification example 3: 3D tensile problem

The third verification example consists of a 3D welded geometry, similar to the 2D problem of the verification example 1, under a uniform remote tensile stress. The finite element meshes are illustrated in Figure 5.12. The mesh size details are the same of the previous verification cases (see Table 5.1), with cubic shaped finite elements being used. The width of the plates (*w*) was 3 times the thickness of the plate.

Figure 5.13 plots the ratio between the structural stress and the remote stress. The structural stresses were computed by means of through thickness stress integration and nodal forces approaches. The local notch stresses are also shown in Figure 5.13 for each finite element mesh. Both the local notch stresses and structural stresses computed using the through thickness stress integration method were obtained at a mid-width plane. Therefore, the referred structural stress was computed using Equations (5.4) and (5.5), with the integration performed along a mid-width and across thickness line. The alternative procedure for the computation of the structural stresses based on nodal forces was based on Equations (5.6) and (5.7) using all nodal forces at the complete hypothetical crack plane, considering a constant depth crack.

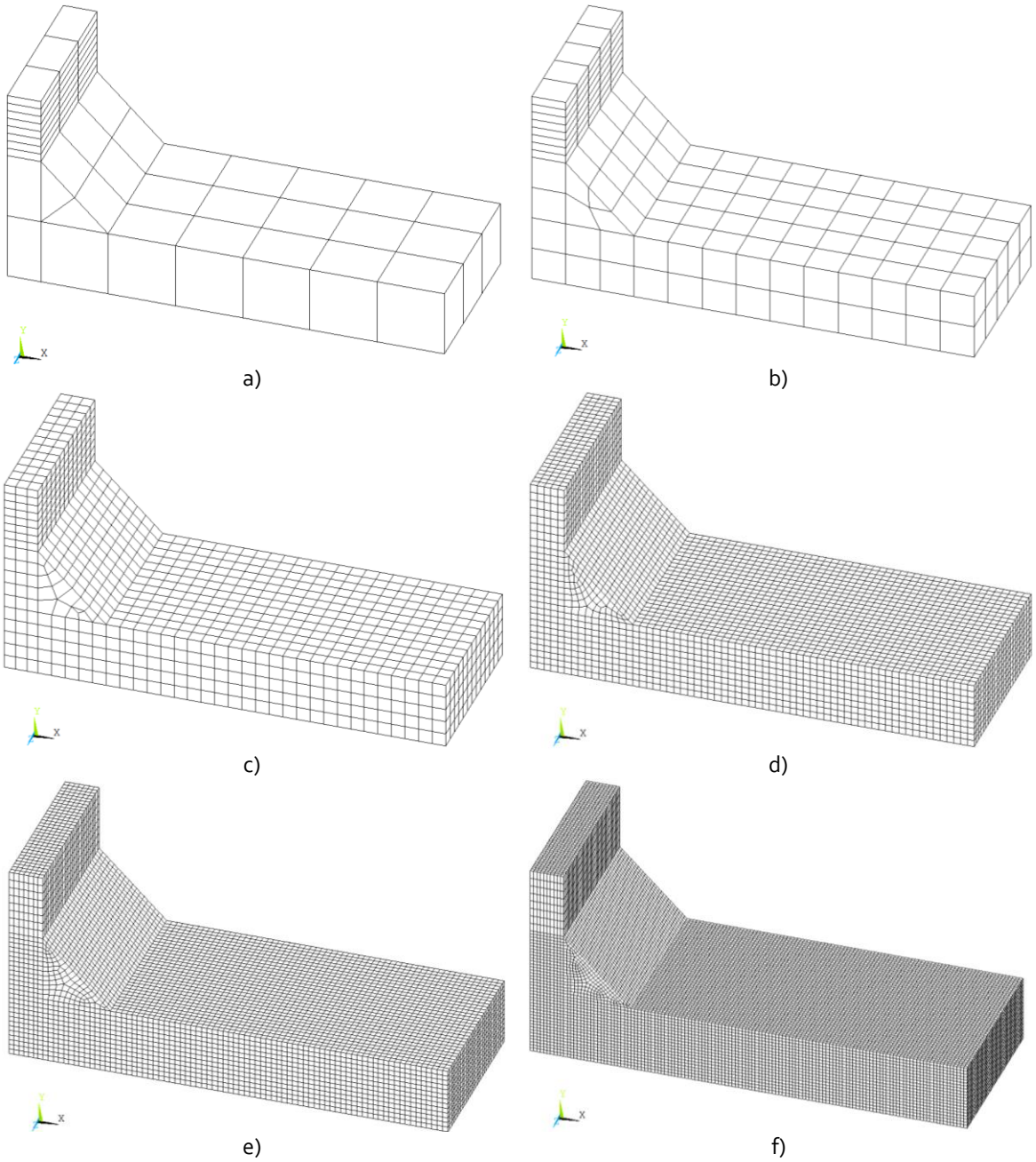

Figure 5.12 - Finite element meshes simulated for verification example 3: a) mesh 1; b) mesh 2; c) mesh 3; d) mesh 4; e) mesh 5; f) mesh 6 (elements with cubic shape).

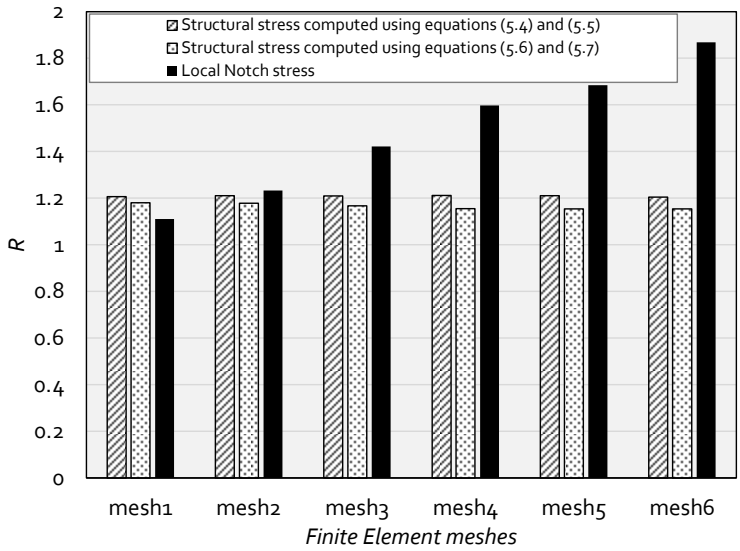

Figure 5.13 - Local notch and structural stresses (stress concentration factors) computed using distinct finite element sizes (verification example 3).

The analysis of Figure 5.13 shows that both approaches for the computation of the structural stresses are roughly insensitive to the mesh size. However, higher deviation between the two approaches is observed, if a comparison with the 2D example 1 is established. The approach based on stress distribution integration shows slightly higher values for the structural stresses. The structural stresses computed using the 3D example 3 were observed to be lower than values computed using the corresponding 2D example 1. Contrasting to the structural stresses, significant mesh sensitivity is observed in the local notch stresses.

5.4. MESH INSENSITIVE APPROACH APPLIED TO TESTED WELDED SPECIMENS

In this section the mesh insensitive structural stresses and the master curve concept are applied to the welded connections tested in this research and whose results were presented in Chapter IV. These welded joints were modelled using the finite element method using linear solid elements with full integration.

The mesh insensitive procedure proposed by Dong [19] to assess the structural stresses, assumes fatigue cracks propagating along the plate thickness direction. However, the crack propagation path in the tested welded specimens was verified along the plate width direction. Figures 5.14 and 5.15 plot the fatigue crack paths used to compute structural stresses, where *L* is the crack path maximum dimension. Therefore parameter *t* (defined as the thickness of the member in Equations (5.4), (5.5), (5.6) and (5.7) will be replaced by *L* in the computations aiming the structural stresses evaluation. The width w in Equations (5.6) and (5.7) are in this example the plate thickness.

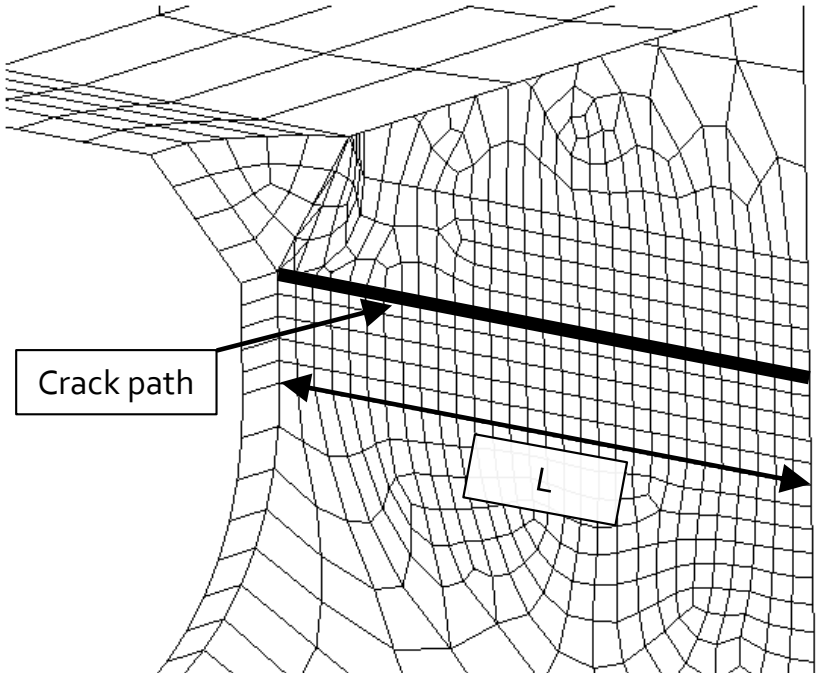

Figure 5.14 - Crack path definition based on experimental observation for W1 and W3 welded specimens.

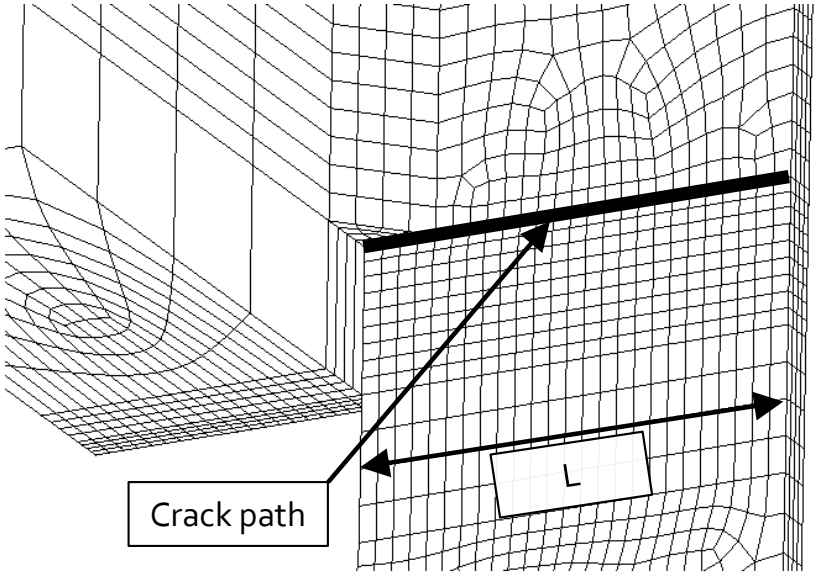

Figure 5.15 - Crack path definition based on experimental observation for W2 and W4 welded specimens.

Finite elements models of the investigated welded joints were prepared with several finite element mesh sizes. Figure 5.16 plots three distinct finite element meshes which were used to model the W1 and W3 welded specimens. Figure 5.16 a) exhibits the coarse mesh, where the size of the finite element at the crack path section is equal to the plate thickness (t=5 mm for W1 welded specimens and t=12mm for W3 welded specimens). The intermediate finite element size was defined as 1/4 of the plate thickness (Figure 5.16 b). The fine mesh was based on elements with a size of 1/8 of the plate thickness (Figure 5.16 c). Figure 5.17 illustrates the finite element meshes considered to model the W2 and W4 welded specimens. Figure 5.17 a) exhibits the coarse mesh, where the size of the finite element at the crack path section is equal to the plate thickness (t=5 mm for W2 welded specimens and t=12 mm for W4 welded specimens). The intermediate finite element size was defined with elements of 1/4 of the plate thickness (Figure 5.17 b).The finer mesh used elements placed at the crack path with a size of 1/8 of the plate thickness (Figure 5.17 c).

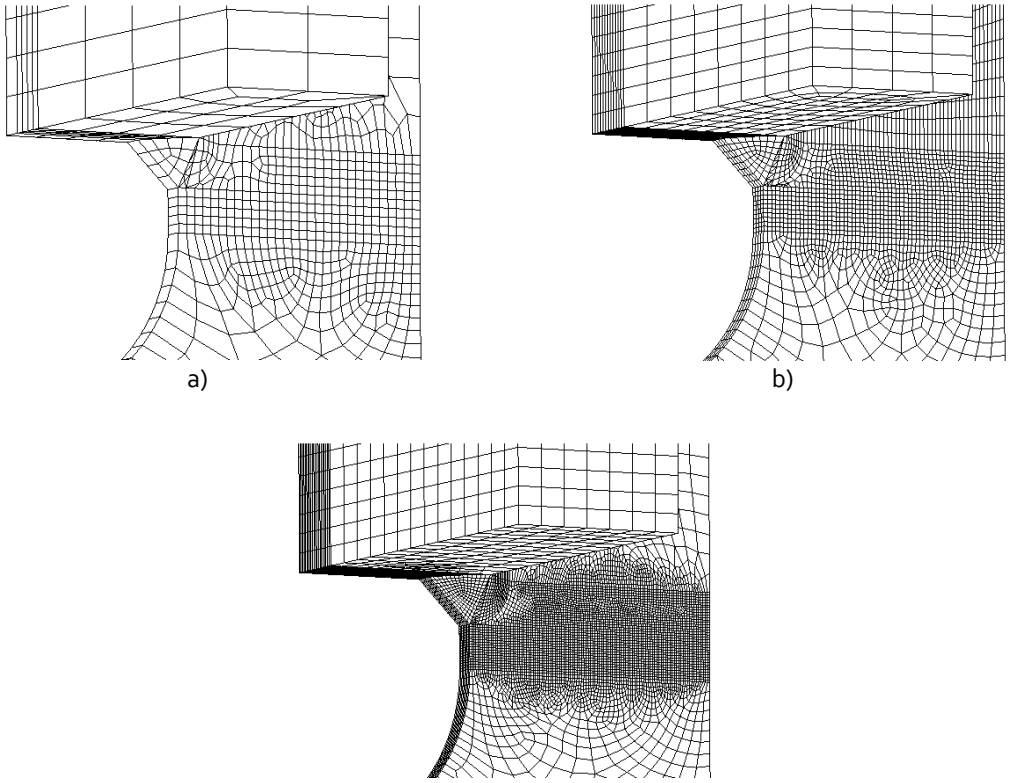

a) b)

c)

Figure 5.16 - Finite element meshes used to model the W1 and W3 welded specimens: a) coarse mesh (element size equal to plate thickness); b) intermediate mesh (element size equal to 1/4 of the plate thickness); c) finer mesh (element size equal to 1/8 of the plate thickness).

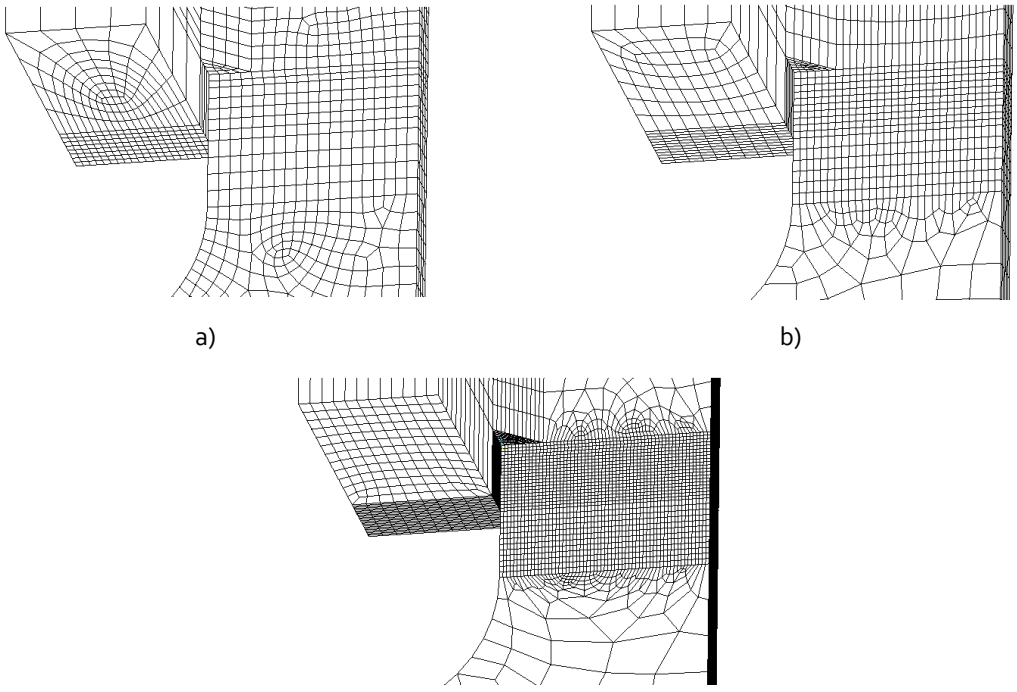

a) b)

c)

Figure 5.17 - Finite element meshes used to model the W2 and W4 welded specimens: a) coarse mesh (element size equal to plate thickness); b) intermediate mesh (element size equal to 1/4 of the plate thickness); c) finer mesh (element size equal to 1/8 of the plate thickness).

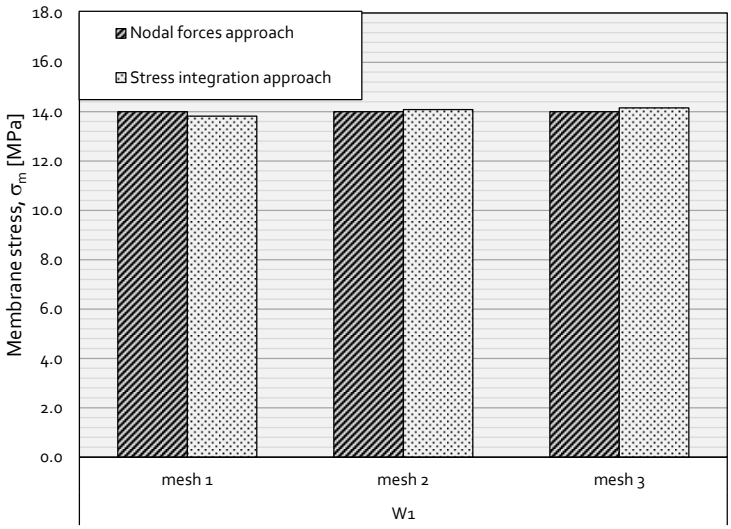

a)

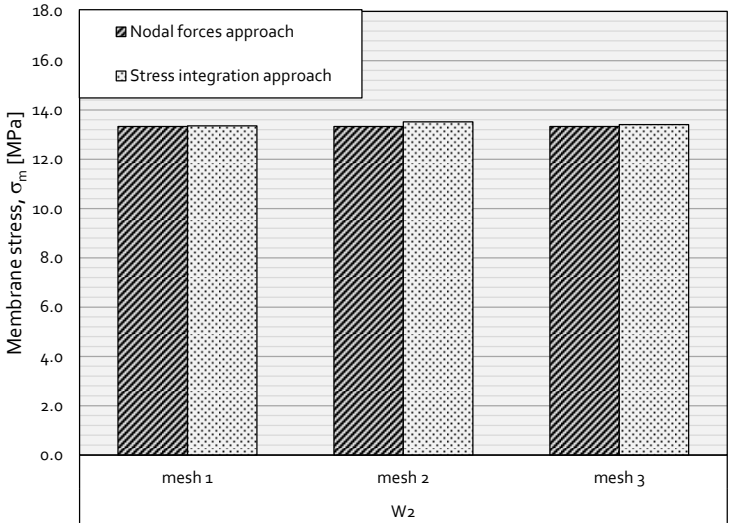

b)

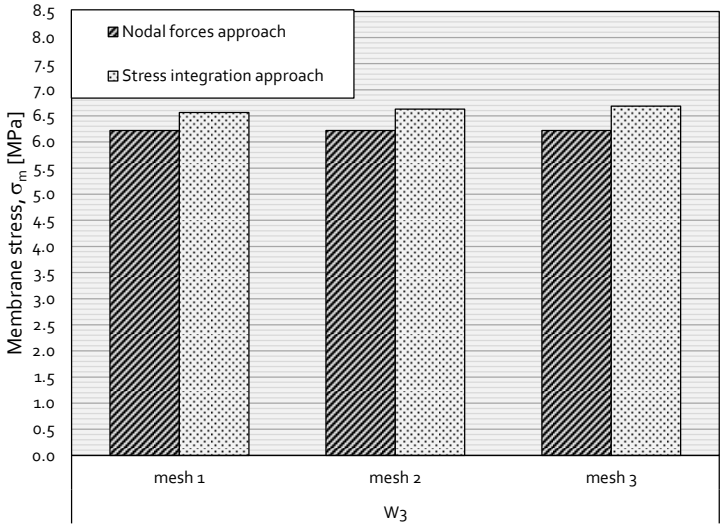

c)

Figure 5.18 - Membrane stress assessment using nodal forces approach and stress integration procedure for: a) W1 welded specimen; b) W2 welded specimen; c) W3 welded specimen and d) W4 welded specimen (1MPa applied remotely in the thicker plate). (1/2)

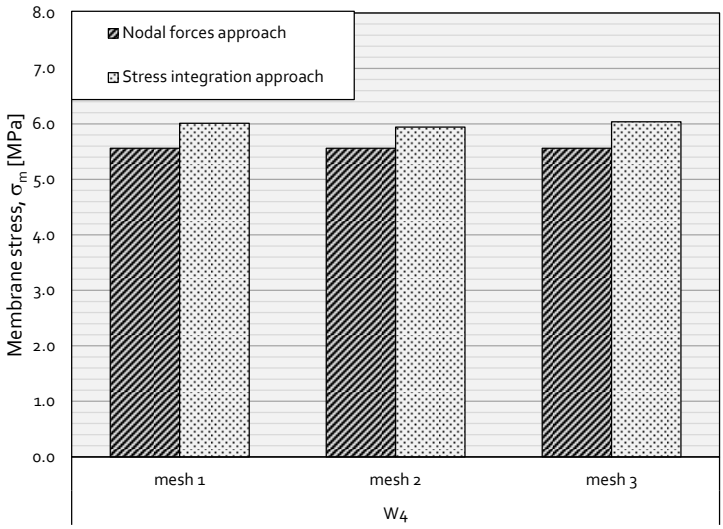

d)

Figure 5.18 - Membrane stress assessment using nodal forces approach and stress integration procedure for: a) W1 welded specimen; b) W2 welded specimen; c) W3 welded specimen and d) W4 welded specimen (1MPa applied remotely in the thicker plate). (2/2)

Membrane and bending stresses were computed using both stress integration and nodal forces approaches, considering an applied uniform remote stress of 1 MPa in the thicker plate of the specimens. The stress integration was performed along the crack path direction at plate mid-thickness line. Figure 5.18 plots the membrane stress using the nodal forces approach and stress integration procedure for W1 welded specimen (Figure 5.18a), for W2 welded specimen (Figure 5.1 b), for W3 welded specimen (Figure 5.18c) and for W4 welded specimen (Figure 5.18d). A global analysis of the Figure 5.18 allows concluding that both procedures to compute the membrane stress components yield similar results, with the stress integration approach resulting in slightly higher structural stress values. However the deviations between approaches used to compute the membrane stresses increase slightly for the thicker specimens (W3 and W4).

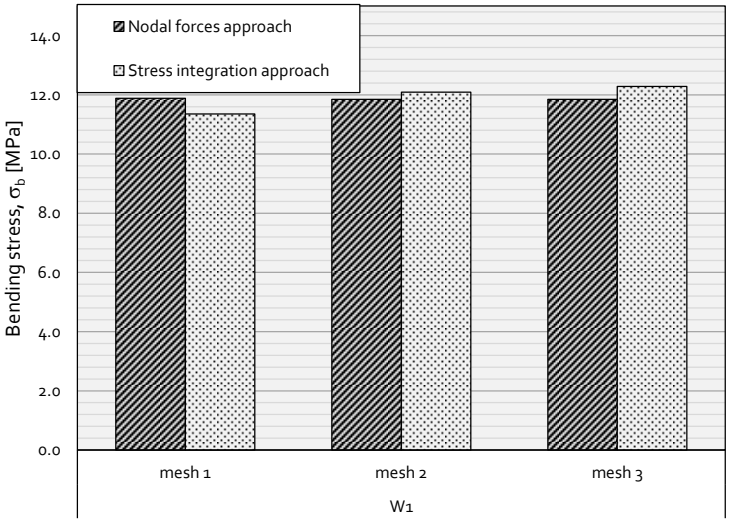

a)

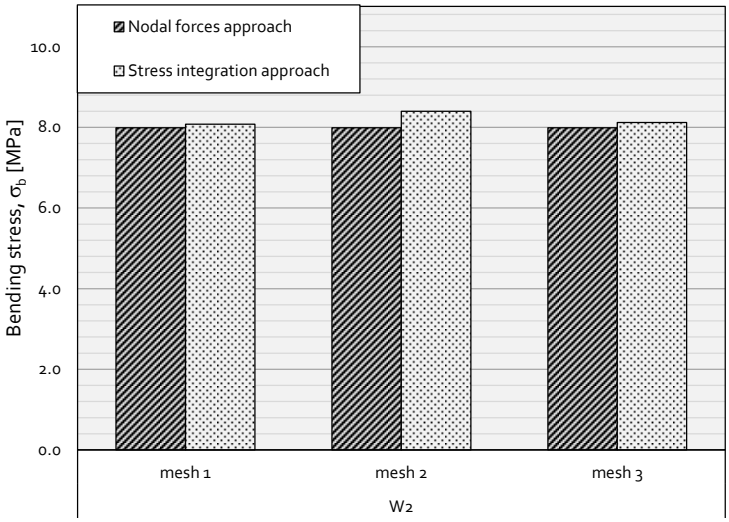

b)

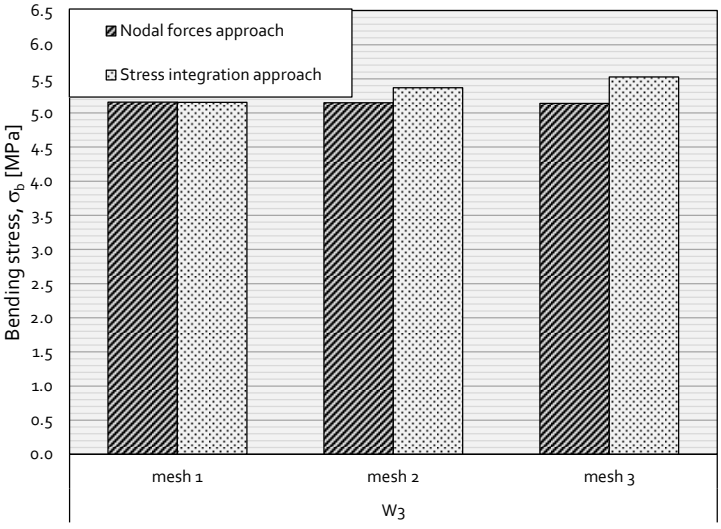

c)

Figure 5.19 - Bending stress assessment using nodal forces approach and through thickness stress integration approach procedure for: a) W1 welded specimen; b) W2 welded specimen; c) W3 welded specimen and d) W4 welded specimen (1MPa applied remotely in the thicker plate). (1/2)

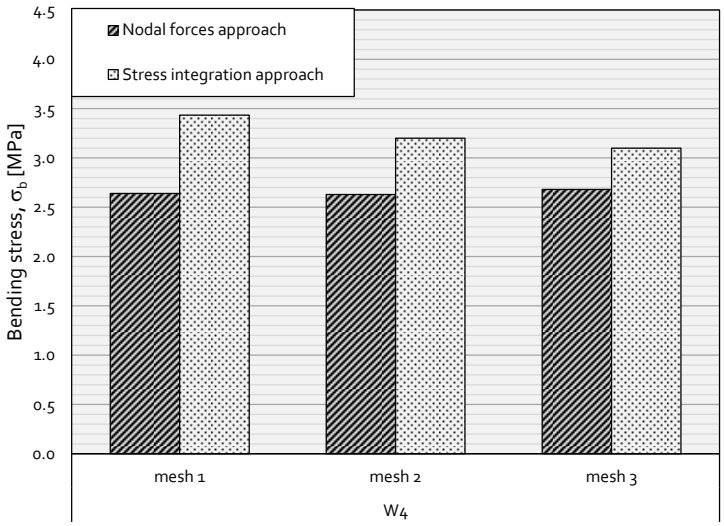

d)

Figure 5.19 - Bending stress assessment using nodal forces approach and through thickness stress integration approach procedure for: a) W1 welded specimen; b) W2 welded specimen; c) W3 welded specimen and d) W4 welded specimen (1MPa applied remotely in the thicker plate). (2/2)

Figure 5.19 plots the bending stress results for W1 welded specimens (Figure 5.19a), for W2 welded specimens (Figure 5.19b), for W3 welded specimens (Figure 5.19c) and for W4 welded specimens (Figure 5.19d). Both investigated procedures yield similar results for the thinner specimens. However for the thicker specimens both approaches yield distinct results, the stress integration approach yielding the higher values. This observation may be explained by the fact that the stress integration was performed along the mid-thickness plate line. With this process it is assumed that the stress distribution is uniform across the plate thickness which could not correspond to the reality. Structural stresses from the nodal forces approach showed greater mesh size insensitivity.

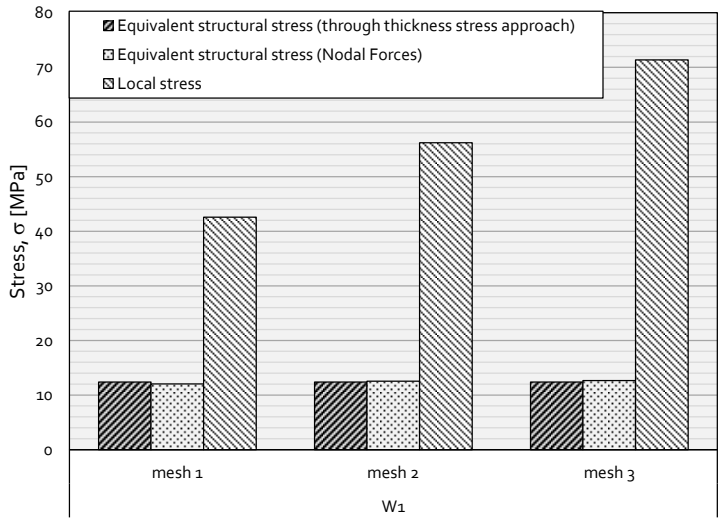

a)

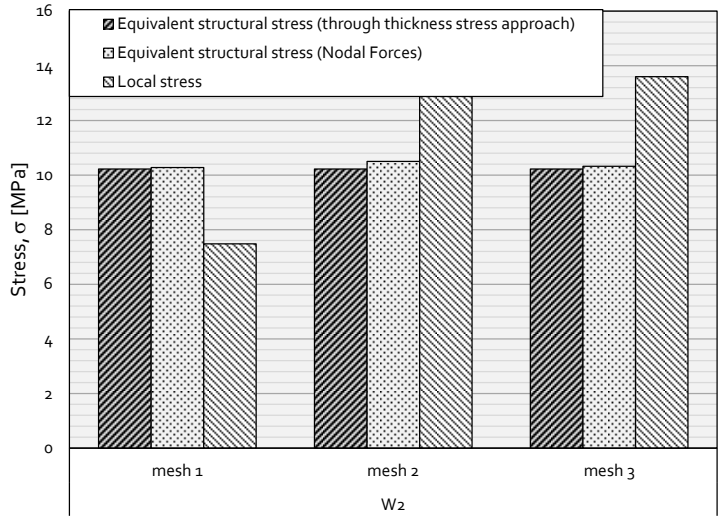

b)

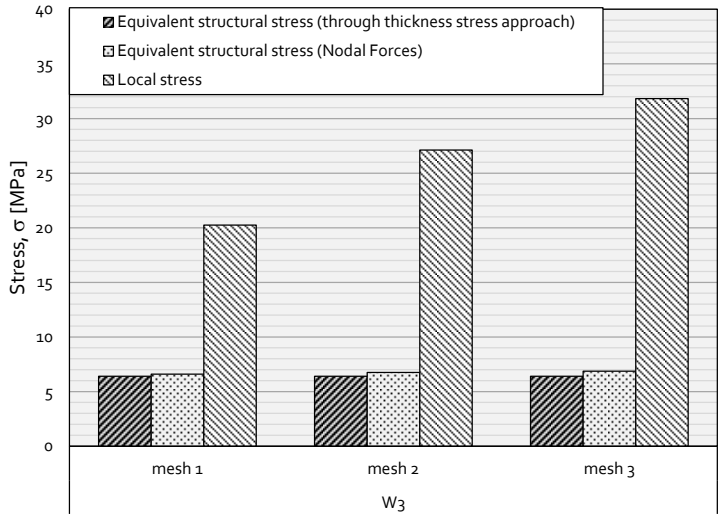

c)

Figure 5.20 - Comparison between structural stresses computed using through thickness stress integration and nodal forces approaches and notch stress (1MPa applied remotely in the thicker plate). (1/2)

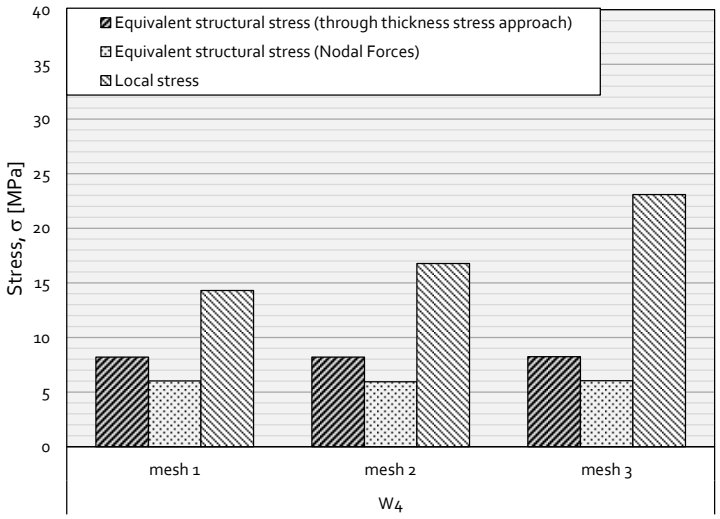

d)

Figure 5.20 - Comparison between structural stresses computed using through thickness stress integration and nodal forces approaches and notch stress (1MPa applied remotely in the thicker plate). (2/2)

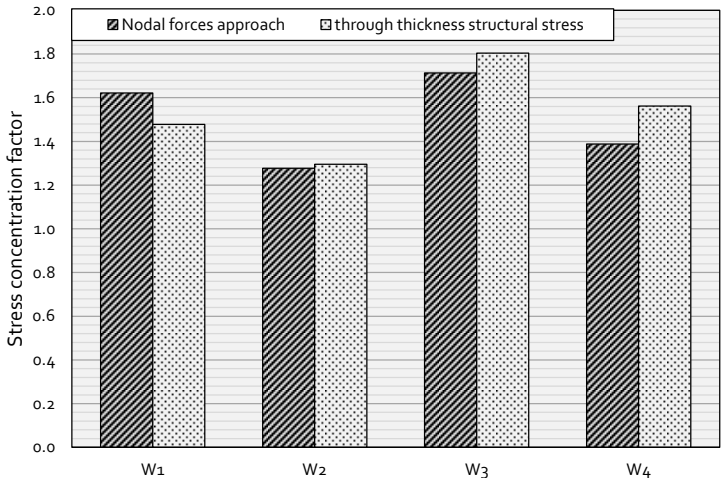

Figure 5.21 - Stress concentration factors resulting from the ratio between the equivalent structural stress computations, based on Equation (5.18), and the remote uniform applied stress.

Figure 5.20 compares the structural stress assessed using both aforementioned approaches and the local notch stresses. Figure 5.20 illustrates that the structural stress assessment is insensitive to the mesh size change, unlike the local notch stresses. Both structural stress approaches provide similar results, except for the W4 welded specimen, mainly due to differences in the bending stress components.

Figure 5.21 presents the stress concentration factor resulting from the ratio between the equivalent structural stress computations, based on Equation (5.18), and the remote applied stress. This information is important since it allows the computation of the equivalent structural stress for the welded specimens taking into account the distinct

tested remote stresses. The structural stresses were based on the mean results from all considered FEM meshes.

Figure 5.22 shows the individual experimental S-N curves, assessed for all welded specimens using the equivalent structural stresses based on through thickness stress integration approach. Figure 5.23 gives the S-N curves based on structural stresses computed using the nodal forces approach. Comparing the S-N curves resulting from both approaches, the main difference lies on *C* parameter, which means a translation of the S-N curves. The slope of the S-N curves remains the same for both approaches.

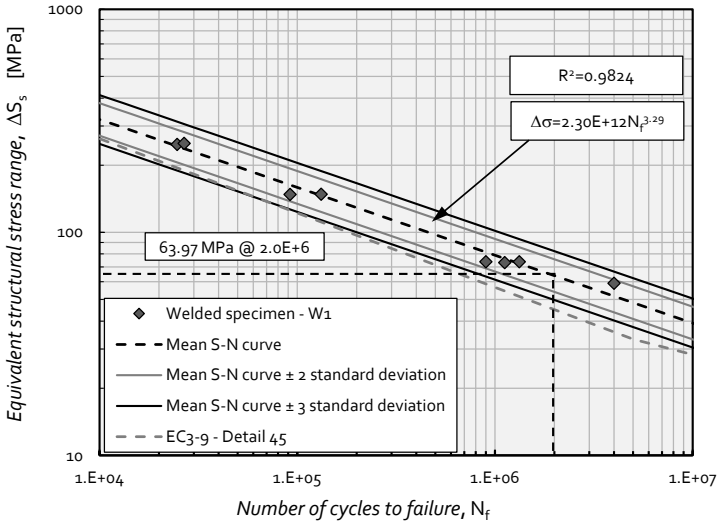

a)

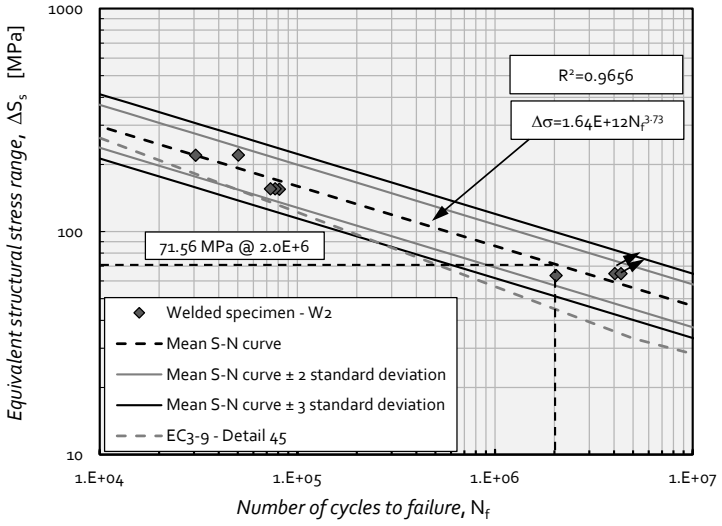

b)

Figure 5.22 - Experimental S-N curves assessed using through thickness structural stress procedure for welded specimens: a) W1; b) W2; c) W3 and d) W4. (1/2)

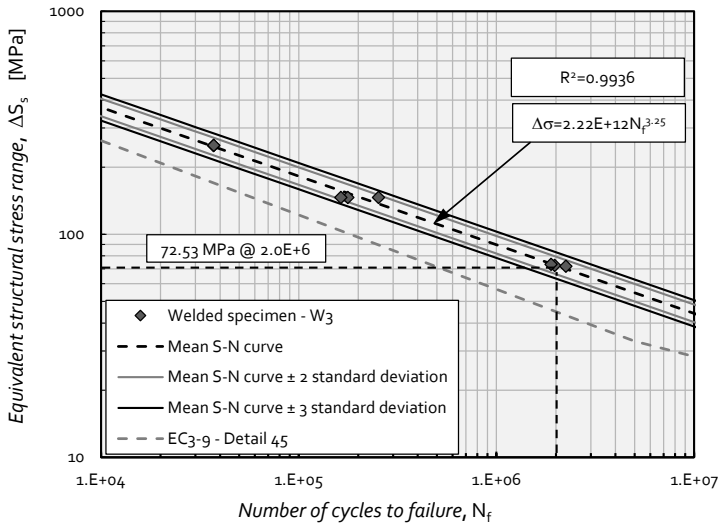

c)

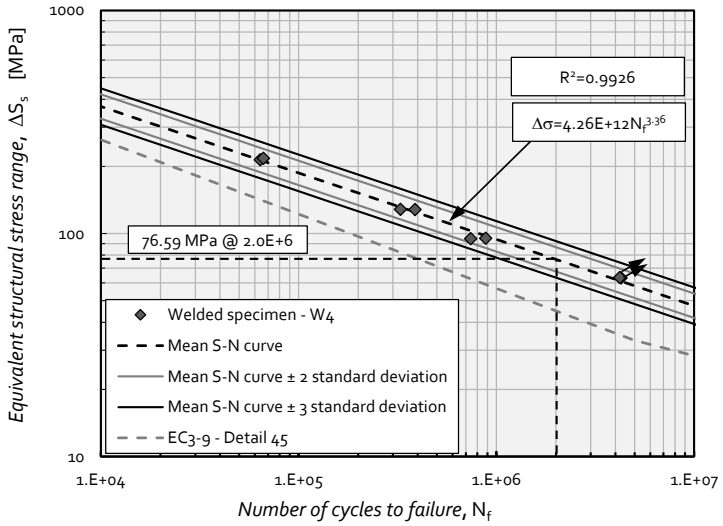

d)

Figure 5.22 - Experimental S-N curves assessed using through thickness structural stress procedure for welded specimens: a) W1; b) W2; c) W3 and d) W4. (2/2)

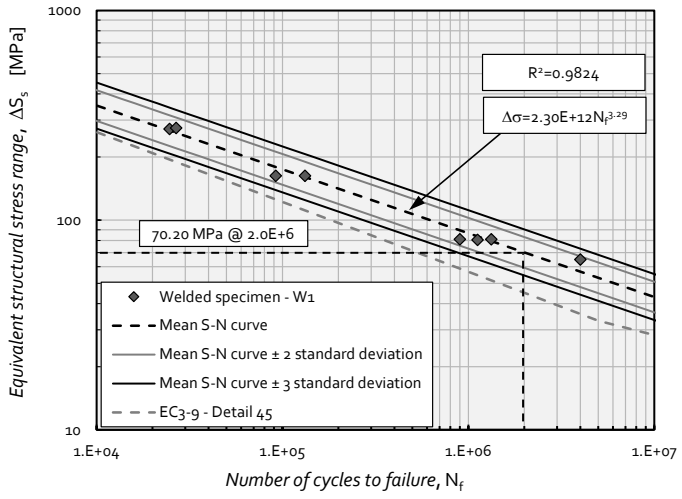

a)

Figure 5.23 - Experimental S-N curve assessed using nodal forces assessment for welded specimens: a) W1; b) W2; c) W3 and d) W4. (1/2)

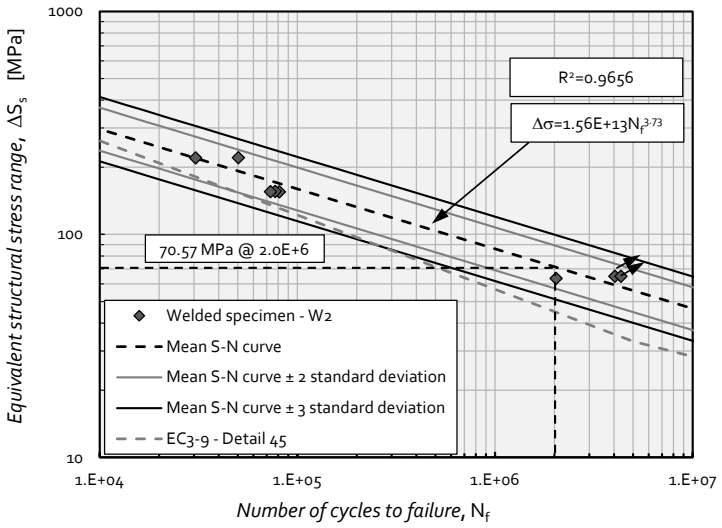

b)

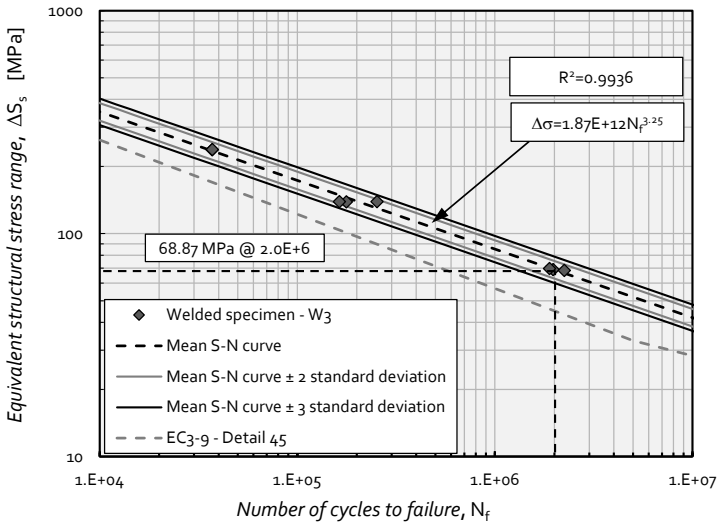

c)

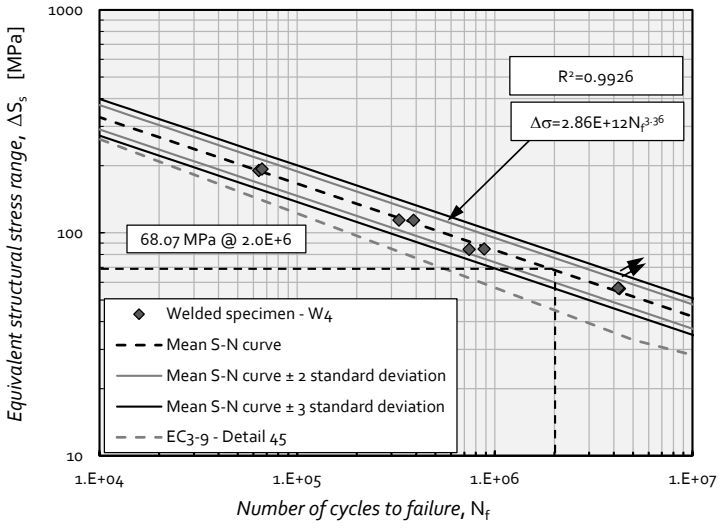

d)

Figure 5.23 - Experimental S-N curve assessed using nodal forces assessment for welded specimens: a) W1; b) W2; c) W3 and d) W4. (2/2)

Figure 5.24 shows the master S-N curve that results from the combination of all welded specimens fatigue tested in this work. The master S-N curve was assessed using the equivalent structural stress parameters, computed using the through thickness stress integration approach. Figure 5.24 plots the master S-N curve for all welded specimens, using the equivalent structural stress based on nodal force based approach. Correlations of Figures 5.24 and 5.25 show a higher determination coefficient, than observed in Figure 4.50 for the S-N curve based on nominal stress definition. However, the S-N curve assessed using the nominal stress definition yield a higher stress range value for a life of 2E6 cycles as summarized in Table 5.2.

Table 5.2 - Stress range values at 2E6 cycles.

Stress definition	**Δσ [MPa]**
Nominal stress	76.50
Equivalent structural stress (through thickness stress integration approach)	71.09
Equivalent structural stress (nodal forces approach)	69.37

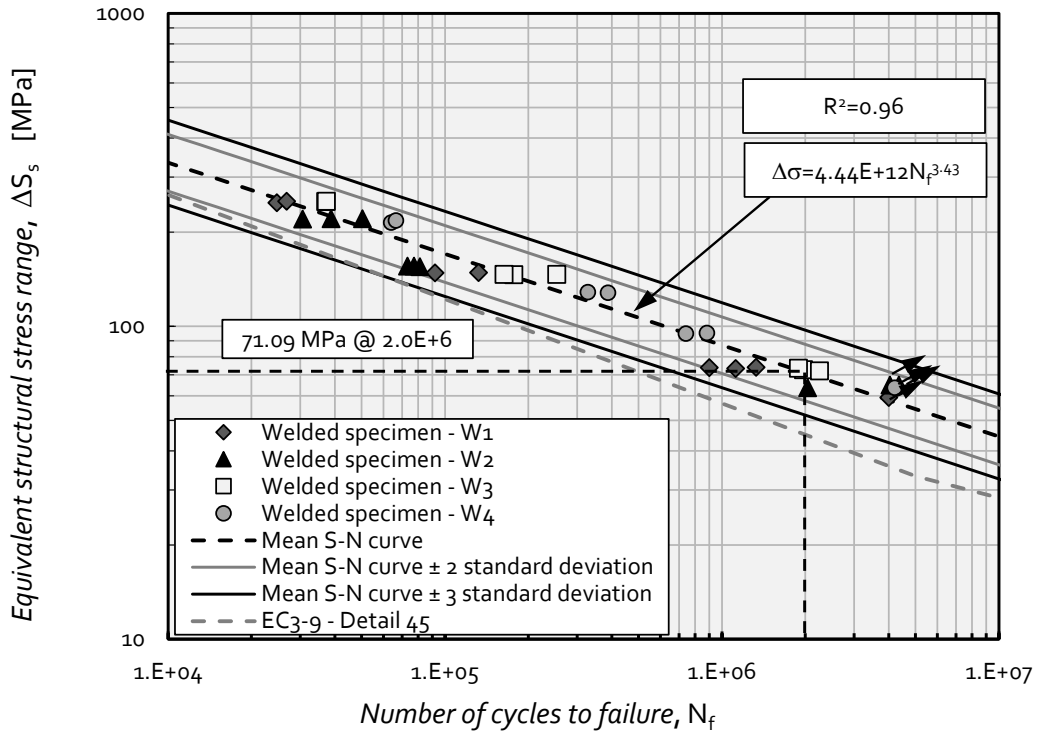

Figure 5.24 - S-N master curve assessed using through thickness structural stress procedure of welded specimens.

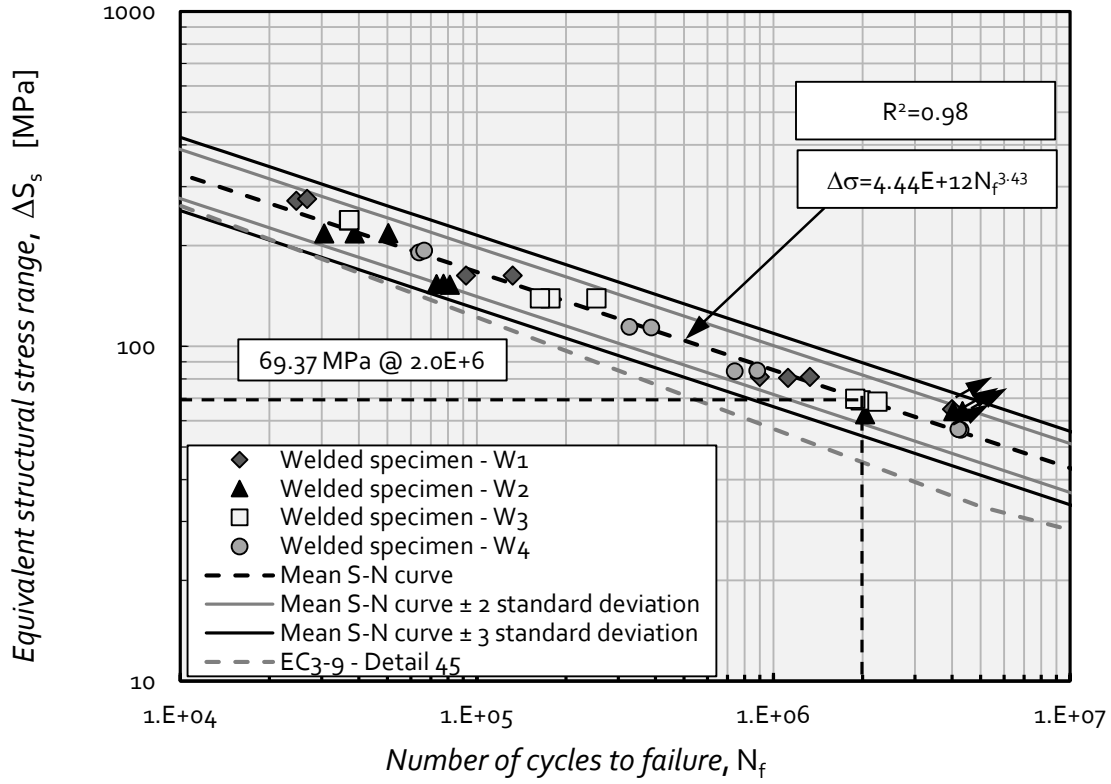

Figure 5.25 - S-N master curve assessed using nodal forces data, for all welded specimens fatigue tested.

Figures 5.26 and 5.27 compares the S-N fatigue data from this research with the fatigue data from several literature sources. The objective is to validate the S-N master curve concept for a wider range of fatigue data. Figure 5.25 includes the fatigue data from this research assessed using the through thickness stress integration approach. Figure 5.26 includes the fatigue data from this research assessed using the nodal forces approach. In both cases a very significant determination coefficient was observed. However, this determination coefficient was marginally higher in Figure 5.25 that resulted from the through thickness integration approach. These graphs illustrate clearly the validity of the S-N master curve concept, given the diversity of data sources and the high determination coefficients observed in the correlations.

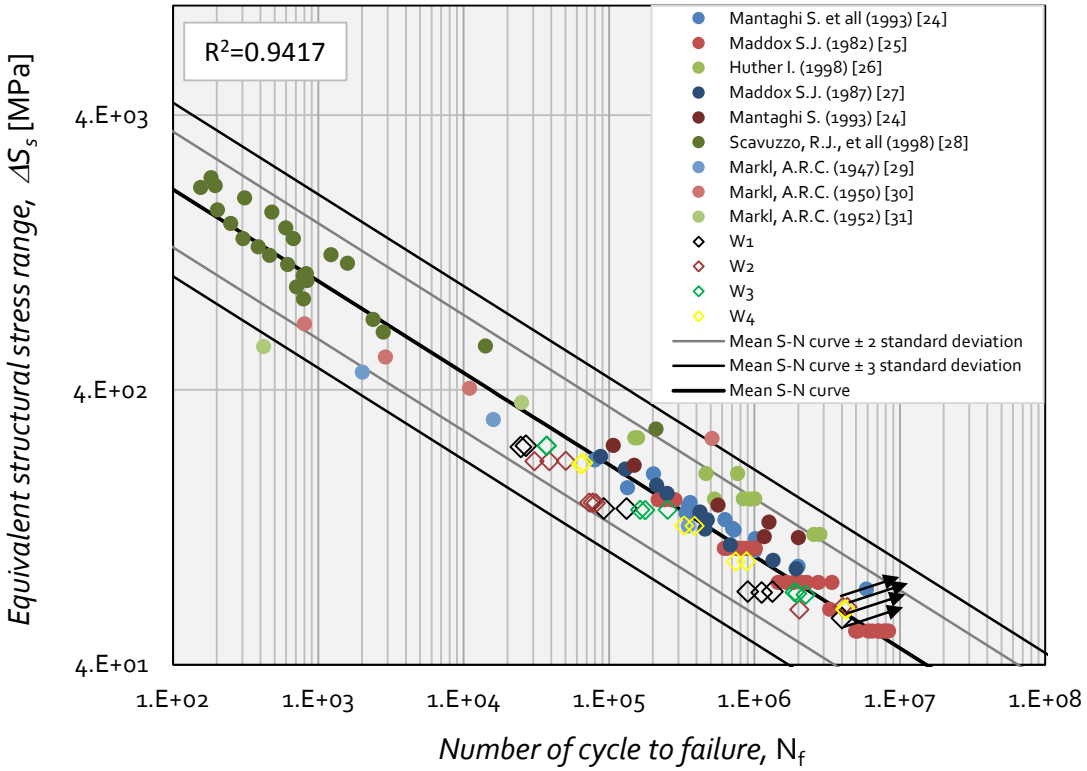

Figure 5.26 - S-N master curve resulting from literature data and the welded fatigue data from this work: S-N master curve validation using through thickness stress integration approach.

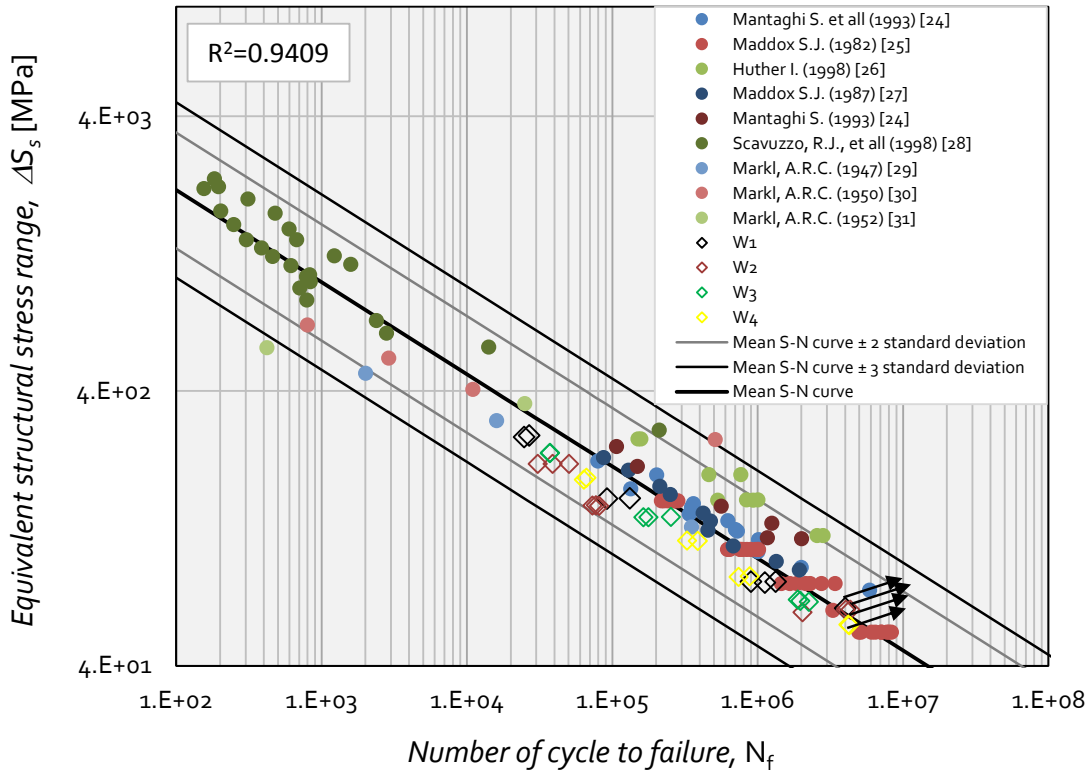

Figure 5.27 - S-N master curve resulting from literature data and the welded fatigue data from this work: S-N master curve validation using nodal forces approach.

5.5. CONCLUDING REMARKS

A methodology to compute structural stress in welded joints showing some degree of insensitivity to the mesh size was tested in this chapter. Two approaches to compute structural stress were investigated in this chapter: the through thickness stress integration approach and the nodal forces balance approach. Three finite elements models were built in order to investigated the robustness of the methodology proposed by Dong [19]. It was observed that the procedure is rather mesh insensitive, for both 2D and 3D problems if a predominantly tensile loading is applied. In cases of predominantly bending loading, small discrepancies were verified between approaches, the nodal force based approach being completely mesh insensitive. In this case the through thickness stress distribution integration approach shows mesh insensitive results but a quick monotonic convergence to the final values is observed.

The methodology was applied to the welded specimens tested in this research. Both approaches to compute the structural stresses were considered. The current work showed that the structural stress component - the bending stress and the membrane stress, shows similar results for through stress or nodal forces approaches.

A stress concentration factor was computed in order to relate the applied remote stress to the equivalent structural stress parameter. This parameter allowed the computation of the equivalent structural stress parameter of the welded specimens. The S-N master curve was then presented and correlated with other welded joints data from literature. It was observed the validity of the S-N master curve concept since all fatigue test data was correlated with a high determination coefficient.

5.6. REFERENCES

[1] Radaj, D., "Review of fatigue strength assessment of non-welded and welded structures based on local parameters", International Journal of Fatigue 18(3), pp.153–70, 1996.

[2] Lawrence, F.V., Mattos R.J., Higashida, Y., Burk, J.D., "Estimating the fatigue crack initiation life of welds", ASTM STP 648, pp.134–58, 1978.

[3] Hobbacher, A., "Fatigue design of welded joints and components: Recommendations of IIW Joint Working Group XIII–XV", Abington, Cambridge: Abington Publishing, 1996.

[4] Hobbacher, A., "Basic philosophy of the new IIW recommendations on fatigue design of welded joints and components", Welding in the World, 39(5):272–8, 1997.

[5] Code of practice for fatigue design and assessment of steel structures. BS7608, British Standards Institution, 1993.

[6] Eurocode 3: Design of steel structures, Part 1-9: Fatigue, CEN: Brussels, Belgium, 2004.

[7] American Association of State Highway and Transportation Officials (AASHTO). AASHTO LRFD Bridge Design Specifications. Washington, DC, 2007

[8] American Welding Society (AWS). Structural Welding Code - Steel: ANSI/AWS D1.1-94, Miami, 1994.

[9] American Association of State Highway and Transportation Officials (AASHTO). Guide Specification for Fatigue Evaluation of Existing Steel Bridges, Washington, DC, 1990.

[10] American Institute of Steel Construction (AISC). Specification for Structural Steel Buildings, Chicago, IL, 2005.

[11] British Standards Institution (BSI). Eurocode No. 3: Design of Steel Structures-Part 1.1: General Rules and Rules for Buildings, London, U.K, 1992.

[12] Gurney, T.R., "Some Comments on Fatigue Design Rules for Offshore Structures. in Second International Symposium on Integrity of Offshore Structures", Glasgow, UK: Applied Science Publishers, Englewood, N.J, July 1-3, 1981.

[13] Marshall, P.W., Toprac, A.A., "Basis for Tubular Joint Design. Welding Journal", Research Supplement: pp. 192s-201s, 1974.

[14] Reynolds, A.G., Sharp, J.V., "The Fatigue Performance of Tubular Joints – An Overview of Recent Work to Revise Department of Energy Guidance", Fourth Conference on Integrity of Offshore Structures, Glasgow, UK: Applied Science Publishers, Englewood, N.J, July 2-3, 1990.

[15] Maddox, S.L., "Hot-Spot Stress Design Curves for Fatigue Assessment of Welded Structures", International Journal of Offshore and Polar Engineering 12(2), pp. 134-141, 2002.

[16] American Bureau of Shipping (ABS). Fatigue Assessment of Offshore Structures, Houston, TX, 2003

[17] Det Norske Veritas (DNV). Recommended Practice (DNV-RP-C203): Fatigue Design of Offshore Steel Structures, Hovik, Norway, 2005.

[18] Niemi, E., Fricke, W., Maddox, S.J., "Fatigue Analysis of Welded Components", IIW-1430-00. International Institute of Welding, Cambridge, England, 2006.

[19] Dong, P., Zhang, J., Hong, J.K., "Structural stress calculation scheme", Battelle's Patent Application, 2000.

[20] Dong, P., "A structural stress definition and numerical implementation for fatigue analysis of welded joints", International Journal of Fatigue 23, pp. 865-876, 2001.

[21] Dong, P., Hong, J.K., Jesus, A.M.P., "Analysis of Recent Fatigue Data Using the Structural Stress Procedure in ASME Div 2 Rewrite", Journal of Pressure Vessel Technology 129, pp. 355-362, 2007.

[22] American Society for Testing and Materials, "ASTM E739-91: Standard Practice for Statistical Analysis of Linear or Linearized Stress-Life (S-N) and Strain Life (ε-N) Fatigue Data", Annual Book of ASTM Standards, pp. 597-603, 1991.

[23] Dong, P., Hong, J.K., "Analysis of hot spot stress and alternative structural stress methods", the 22nd international conference on offshore mechanics and artic engineering 3, pp. 213-224, 2003.

[24] Dong, P., Hong, J.K., Cao, Z., "Structural stress based master S- N curve for welded joints", IIW Doc. XIII -1930-02/XV-1119-02, p. 24, 2002.

[25] Tada, H., Paris, P., Irwin, G., "The stress analysis of cracks handbook". 2nd ed. St Louis, MO: Paris Productions, 1985.

Chapter VI

Finite element modelling of experimental details

6.1. INTRODUCTION

This chapter presents numerical models for the connection details presented in the Chapter IV. Several numerical approaches were considered in order to perform fatigue life predictions. Two main finite element tools were used: the standard Finite Element Method (FEM) and the eXtended Finite Element Method (XFEM). However, the XFEM approach was mainly limited to the welded joints simulation since the XFEM available in the ABAQUS® code [1] used for this purpose, did not allow the use of contact elements simultaneously with XFEM. Thus, the riveted specimens were essentially modelled using the FEM and the welded specimens were modelled using both FEM and XFEM approaches. The aim of the simulations was to derive numerical S-N curves for the joints. Fatigue life predictions were performed taking into account both fatigue crack initiation and fatigue crack propagation phases. The number of cycles to initiate a fatigue crack was computed using local notch strain approach and the number of cycles to propagate the fatigue crack was computed using a Fracture Mechanics based approach. To assist the Fracture Mechanics approach, both ANSYS® and ABAQUS® commercial codes were used to build numerical models in order to assess the stress intensity factor range. Contour integral method using a 3D XFEM (implemented in ABAQUS®), as well as the virtual crack closure technique (VCCT), as described by Krueger [2], with standard FEM (implemented in ANSYS®) were considered. The fatigue crack growth was modelled using Linear Elastic Fracture Mechanics (LEFM) together with the Paris Law [3].
Numerical S-N curves were simulated including both fatigue crack initiation and fatigue crack propagation phases, for riveted joints, and considering the crack propagation phase, for the welded joints.

6.2. CRACK INITIATION ASSESSMENT

The number of cycles to initiate a fatigue crack was computed using a local notch strain approach. The required cyclic elastoplastic strains were computed using the Neuber [4] and Ramberg-Osgood [5] relations, which may be combined in the following system of simultaneous equations:

$$\begin{cases} \dfrac{\left(k_t \Delta\sigma_{nom}\right)^2}{E} = \dfrac{\Delta\sigma_{loc}{}^2}{E} + 2\Delta\sigma_{loc}\left(\dfrac{\Delta\sigma_{loc}}{2K'}\right)^{1/n'} \\ \Delta\varepsilon_{loc} = \dfrac{\Delta\sigma_{loc}}{E} + 2\left(\dfrac{\Delta\sigma_{loc}}{2K'}\right)^{1/n'} \end{cases} \tag{6.1}$$

where k_t is the elastic stress concentration factor, K' and n' are, respectively, the cyclic strain hardening coefficient and exponent; $\Delta\sigma_{nom}$ is the nominal stress range computed at the net area near the hot spot; $\Delta\varepsilon_{loc}$ and $\Delta\sigma_{loc}$ are respectively the local strain and stress ranges. The stress concentration factor was computed using the finite element model of the riveted joint. The number of cycles for crack initiation was computed thru the Morrow relation [6]:

$$\frac{\Delta\varepsilon_{loc}}{2} = \frac{\sigma'_f}{E}\left(2N_i\right)^b + \varepsilon'_f\left(2N_i\right)^c \tag{6.2}$$

where $\Delta\varepsilon_{loc}$ is the local elastoplastic strain range; σ'_f and b are, respectively, the cyclic fatigue strength coefficient and exponent; ε'_f and c are, respectively, the fatigue ductility coefficient and exponent; E is the Young modulus.

6.3. FATIGUE CRACK PROPAGATION ASSESSMENT

Once assessed the number of cycles to start a fatigue crack, the number of cycles to propagate the respective fatigue crack is performed using a Linear Elastic Fracture Mechanics (LEFM) based approach. The stress intensity factor (*K*) is a key parameter to compute the number of cycles to propagate a fatigue crack. In this section, two techniques available in the literature for the computation of the stress intensity factors, namely the contour integral method and the Virtual Crack Closure Technique will be described.

6.3.1. Fatigue crack growth simulation

A well-established approach for fatigue crack propagation simulation consists of relating the fatigue crack growth with stress intensity factor range ΔK at the crack tip. One can find many approaches in the literature for the relationship between the crack growth rate and the stress intensity factor range [7]. In this work, the well-known Paris law will be used due to the availability of experimental data [3]:

$$\frac{da}{dN} = C\left(\Delta K\right)^m \tag{6.3}$$

where *C* and *m* are material constants. Despite mode I fatigue crack propagation is dominant for almost all modelled specimens, for some models a mixed mode fatigue crack growth criterion was considered, therefore both K_I and K_{II} stress intensity factors were computed. A crack branching procedure was then considered [8], with the new crack increment angle computed using the maximum hoop stress criterion:

$$\theta = \cos^{-1}\left(\frac{3K_{II}^2 + \sqrt{K_I^4 + 8K_I^2K_{II}^2}}{K_I^2 + 9K_{II}^2}\right) \tag{6.4}$$

In order to allow the application of the Paris relation for mixed mode conditions, an equivalent stress intensity factor was computed using the relation proposed by Tanaka [9]:

$$K_{eq} = \sqrt[4]{K_I^4 + 8K_{II}^4} \tag{6.5}$$

The number of cycles spent during the fatigue crack propagation may be computed thru the integration of the Paris crack propagation relation [3].

6.3.2. Stress intensity factor computation

Irwin [10-12] developed a method for the evaluation of the amount of energy available for the crack propagation. It is worthy to introduce the three basic crack deformation/loading modes, which are the mode I, mode II and mode III, as illustrated in Figure 6.1. The mode I fatigue crack propagation is the opening mode, which corresponds to the opening of the crack faces under a tensile load. Mode II is the in-plane shear/sliding loading mode. The applied shear stresses act parallel to the plane of the crack and perpendicular to the crack front. Mode III is classified as out of plane tearing mode. Loads are applied parallel to both the plane of the crack and the crack front.

The method evaluates the energy release rate based on the loading and geometry conditions. The stress field for a linear elastic solid in the neighbourhood of crack tip, in its generic form, is given as:

$$\sigma = K_I \boldsymbol{f_I}(r,\alpha) + K_{II} \boldsymbol{f_{II}}(r,\alpha) + K_{III} \boldsymbol{f_{III}}(r,\alpha) + \boldsymbol{\sigma_o} \tag{6.6}$$

where K_I, K_{II} and K_{III} are the stress intensity factors for the respective modes I, II and III, $\boldsymbol{\sigma_o}$ is a finite stress, r is the distance from the crack tip and α is the angle from the crack tip and f_I, f_{II}, and f_{III} are functions of α and r, being proportional to $\frac{1}{\sqrt{r}}$ (see Equations (6.7) and (6.8)).

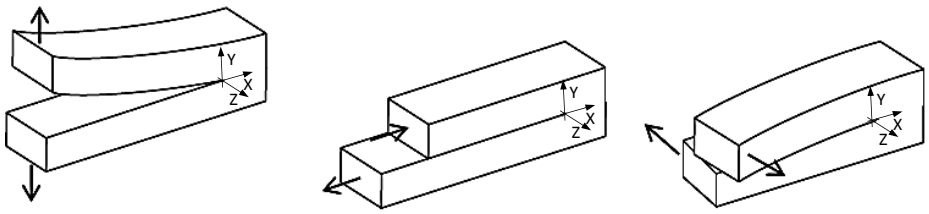

Figure 6.1 - Three pure crack loading modes: a) mode I; b) mode II and c) mode III.

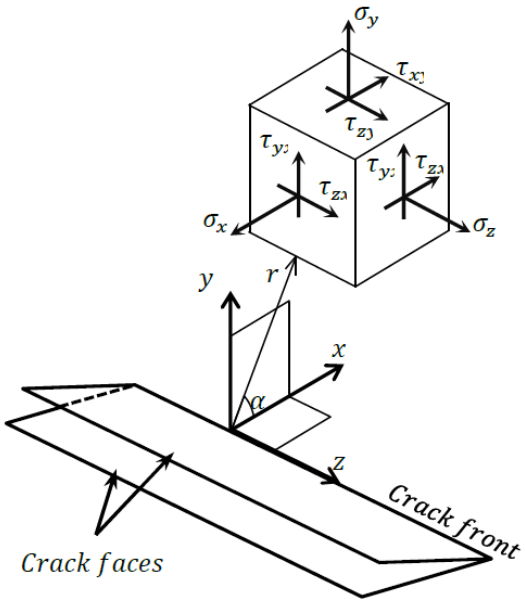

Figure 6.2 - A three-dimensional coordinate system describing the stresses near the crack front.

$$(f_I)_{xx} = \frac{1}{\sqrt{2\pi r}}\cos\left(\frac{a}{2}\right)\cdot\left(1-\sin\left(\frac{a}{2}\right)\sin\left(\frac{3a}{2}\right)\right) \tag{6.7}$$

$$(f_I)_{yy} = \frac{1}{\sqrt{2\pi r}}\cos\left(\frac{a}{2}\right)\cdot\left(1+\sin\left(\frac{a}{2}\right)\sin\left(\frac{3a}{2}\right)\right) \tag{6.8}$$

The terms represented in Equations (6.7) and (6.8) are singular when *r* tends to zero. Other terms may be included in the series which can be found in reference [13]. A schematic definition of the stress field near the crack tip can be observed in Figure 6.2. The stress intensity factors, for the three loading modes, are defined as:

$$K_I = \lim_{r\to 0}\sqrt{2\pi r}\,\sigma_{yy}(r,0) \tag{6.9}$$

$$K_{II} = \lim_{r \to 0} \sqrt{2\pi r}\, \sigma_{yx}(r,0) \tag{6.10}$$

$$K_{III} = \lim_{r \to 0} \sqrt{2\pi r}\, \sigma_{yz}(r,0) \tag{6.11}$$

where σ_{ij} is a particular stress component.

6.3.2.1. Contour integral evaluation

A way used in this work to compute the stress intensity factors considers the J-integral together with the so-called interaction integral method [14]. The J-integral is a contour integral that allows the assessment of the strain energy release rate during a fracture process [15]. This parameter is important in Fracture Mechanics since the energy can be related to the crack growth. The interaction integral method is an extension of the J-integral that allows the computation of the energy release rates for modes I and II, where the J-integral only allows pure modes.

6.3.2.2. J-integral

The J-integral is originally defined for a two dimensional contour integral, as shown in Figure 6.3a), but it can also be used, for computational purposes, considering a closed two dimensional contour integral, as exhibited in Figure 6.3b). This method can be extended to a 3D problem, which is currently linked to the interaction integral method to extract the stress intensity factors [14].
For a two dimensional quasi-static analysis, the J-integral may be defined as [14]:

$$J = \lim_{\Gamma \to 0} \int_{\Gamma} \boldsymbol{n} \cdot \boldsymbol{H} \cdot \boldsymbol{q}\, d\Gamma \tag{6.12}$$

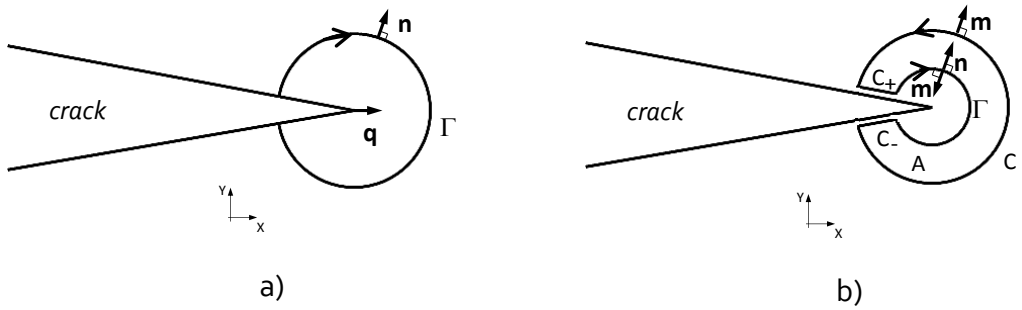

Figure 6.3 - Contour Integral definitions: a) 2D contour integral (open contour); b) 2D closed contour integral.

where Γ is the contour around the crack tip, $d\Gamma$ is the arc increment on Γ, $\boldsymbol{n}$ is the outwards normal of the contour, $\boldsymbol{q}$ is the unit vector in the virtual crack extension direction. Adopting the contour integral illustrated in Figure 6.3a), it is assumed that the contour Γ is connected to the two crack faces sealing the crack tip. The contour is reduced so that it only includes the crack tip ($\Gamma \to 0$ in Equation (6.12)). The outwards pointing normal is located along the whole contour and the unit vector in the virtual crack extension direction $\boldsymbol{q}$ is located at the crack tip. The contour does not have to shrink until the crack tip, but can be specified anywhere enclosing the crack tip, since the J-integral is path-independent for elastic material in the absence of body forces and tractions on the crack surfaces [14].

A regular 2D contour integral can be rewritten as a 2D closed contour integral [14]:

$$J = \oint_{C+C_+ +\Gamma+C_-} \boldsymbol{m} \cdot \boldsymbol{H} \cdot \bar{\boldsymbol{q}} \, d\Gamma \tag{6.13}$$

where the integral segments are defined as a closed contour that is extended from Γ, (see Figure 6.3b), C_+ and C_- are contours along the crack faces respectively and encloses the contour from and over the crack tip, $\boldsymbol{m}$ is a unit outwards-pointing normal defined as $\boldsymbol{m}$=-$\boldsymbol{n}$. The weighting function $\bar{q}$ has been introduced as the unit vector in the virtual crack extension direction, $\bar{q} = q$ on Γ and vanishes on C. The J-integral can now be transformed into a domain integral with the divergence theorem [14]:

$$J = \int_A \left(\frac{\partial}{\partial x} \right) \cdot \left(\boldsymbol{H} \cdot \bar{\boldsymbol{q}} \right) dA \tag{6.14}$$

where *A* is the area domain enclosed by the closed contour, and *dA* the infinitesimal area segment.

Considering the equilibrium equation, the gradient of the strain energy for a homogenous material with constant material parameters, the 2D J-integral can be rewritten in its final form [14]:

$$J = -\int_A \left[\boldsymbol{H} : \frac{\partial \bar{\boldsymbol{q}}}{\partial x} + \boldsymbol{f} \frac{\partial \boldsymbol{u}}{\partial x} \cdot \bar{\boldsymbol{q}} \right] dA \tag{6.15}$$

where $\boldsymbol{f}$ is the body force per volume unit. Thermal influence is neglected here.

The two dimensional J-integral procedure (Equation (6.15)) can be extended to a three dimensional crack front where the J-integral is a function of the variable *s* along the crack front, *J(s)*, as illustrated in Figure 6.4a) [14]. The three dimensional calculations are performed in a similar manner as the two dimensional case, but the energy release rate is calculated with respect to a finite segment of the crack front, denoted as $\bar{J}$. This is then used to obtain energy release rate *J(s)* for each node located along the crack tip.

This procedure is done by defining a parametric variable *s* along the crack front with a local coordinate system, as represented in Figure 6.4a). The axis, *z*, runs tangentially to the crack, *y* is defined perpendicular to the crack plane, and *x* normal to the crack front.

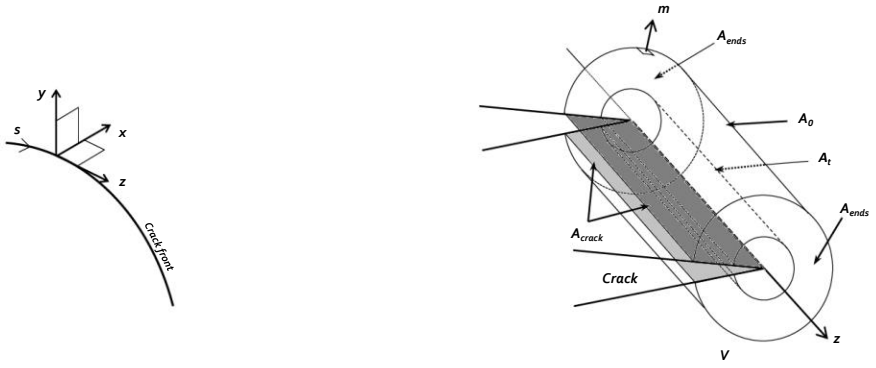

a) b)

Figure 6.4 - A three-dimensional coordinate system (a) used to define the 3D domain integral at the crack front (b).

In three dimension analysis, the energy release for a unit crack advance over a finite segment of the crack front, $\bar{J}$, is defined as [14]:

$$\bar{J} = -\int_V \left[\boldsymbol{H} : \frac{\partial \bar{\boldsymbol{q}}}{\partial x} + \boldsymbol{f} \frac{\partial \boldsymbol{u}}{\partial x} \cdot \bar{\boldsymbol{q}} \right] dV \tag{6.16}$$

The three dimensional case is a volume integral for the domain *V* shown in Figure 6.4b). This is a tubular domain for a closed contour along a finite segment of the crack front. The three dimensional integral presents the inner tube surface, A_t, the outer tube surface, A_o, the two surfaces along the crack face, A_{crack} and lastly the two surfaces at the ends, A_{ends}, in accordance with the closed contour domain. Noting that still $\Gamma \to 0$ which means that $A_t \to 0$. The two dimensional area domain along the crack front in the *x y*-plane is called contour domain in this document.

6.3.2.3. Stress intensity factor computation

For linear elastic materials, the J-integral is related to the stress intensity factors by the following relationship [16]:

$$J = \frac{1}{8\pi} \boldsymbol{K}^T \cdot \boldsymbol{B}^{-1} \cdot \boldsymbol{K} \tag{6.17}$$

where $\boldsymbol{K} = \begin{bmatrix} K_I & K_{II} & K_{III} \end{bmatrix}^T$ and $\boldsymbol{B}$ is the pre-logarithmic energy factor. For a homogeneous and isotropic material, the equation can be rewritten as:

$$J = \frac{1}{\bar{E}} \left(K_I^2 + K_{II}^2 \right) + \frac{1}{2G} K_{III}^2 \tag{6.18}$$

where $\bar{E} = E$ for plane stress and $\bar{E} = \frac{E}{1-\nu^2}$ for plane strain, axisymmetric and three dimensional problems. Furthermore, under pure mode I loading, the relation between the J-integral and K_I for three dimensions is:

$$J_1 = K_I^2\left(\frac{1-\nu^2}{E}\right) \tag{6.19}$$

To evaluate mixed-mode stress intensity factors, the interaction integral method can be used. The interaction integral method uses auxiliary fields superimposed to the actual fields. The auxiliary field consists of stresses or strains fields applied around the crack tip. The J-integral of the actual field is denoted as *J*, the J-integral related to the auxiliary field as J_{aux} and the J-integral from the interaction integral as J_{int}. These three terms joined together define the total J-integral, J_{tot}, that is:

$$J_{tot} = J + J_{aux} + J_{\text{int}} \tag{6.19}$$

By choosing the auxiliary fields wisely, the interaction integral for mode α (α =I, II and III) can be expressed as $J_{\text{int}}^{\alpha} = J_{tot}^{\alpha} - J_{aux}^{\alpha} - J$, which is used to extract the individual stress intensity factors.

The stress intensity factor extraction for mode I is obtained expanding equation (6.17). The relation between the J-integral and the stress intensity factors is given as:

$$J = \frac{1}{8\pi}\left(K_I B_{11}^{-1} K_I + 2K_I B_{12}^{-1} K_{II} + 2K_I B_{13}^{-1} K_{III}\right) + \left[\text{terms without } K_I\right] \tag{6.20}$$

The J-integral for an auxiliary field, mode I crack tip field with k_1 as stress intensity factor, is chosen as:

$$J_{aux}^{I} = \frac{1}{8\pi}\left(k_I \cdot B_{11}^{-1} \cdot k_I\right) \tag{6.21}$$

Superposition of the auxiliary field and the real field gives:

$$J_{tot}^{I} = \frac{1}{8\pi}\left(\left[K_I + k_I\right]B_{11}^{-1}\left[K_I + k_I\right] + 2\left[K_I + k_I\right]B_{12}^{-1}K_{II} + 2\left[K_I + k_I\right]B_{13}^{-1}K_{III}\right) + \left[\text{terms without } K_I \text{ and } k_I\right] \tag{6.22}$$

Since the terms without K_I and K_{II} are the same for J and J'_{tot}, the interaction integral can be expressed as:

$$J^I_{\text{int}} = J^I_{tot} - J^I_{aux} - J = \frac{k_I}{4\pi}\left(B^{-1}_{11}K_I + B^{-1}_{12}K_{II} + B^{-1}_{13}K_{III}\right) \tag{6.23}$$

The same procedure is done for mode II and mode III. The equations for the three modes can be written as:

$$J^{\alpha}_{\text{int}} = \frac{k_{\alpha}}{4\pi} B^{-1}_{\alpha\beta} K_{\beta} \tag{6.24}$$

Choosing unit values for k_{α}, the stress intensity factors are expressed in terms of the interaction integral as

$$\boldsymbol{K} = 4\pi \boldsymbol{B} \cdot \boldsymbol{J}_{\text{int}} \tag{6.25}$$

where $J_{\text{int}} = \left[J^I_{\text{int}} \quad J^{II}_{\text{int}} \quad J^{III}_{\text{int}}\right]^T$.

6.3.3. Virtual Crack Closure Technique

Besides the contour integral method, discussed above, there exist methods to compute the strain energy release rate based on results from finite element analysis. Two alternatives are discussed by Krueger [2]. Both approaches are based on the energy release rate, resulting from nodal forces at the crack tip, which are multiplied by the nodal displacements, computed at a local coordinate system, located at the crack tip. The finite crack extension method [2] is a two steps approach that is applied to evaluate the nodal forces at the nodes located at the crack tip in the first step, and then the displacements of both nodes that are split in the second step. The virtual crack closure method [2] considers both nodal forces and displacements at the same step to obtain the energy release rate. The current study only considers the one step method applied to quadratic (20-noded) 3D finite elements.

The virtual crack closure technique is based on the assumption that the energy released when the crack is extended by Δa from $a+\Delta a$ (node i) to $a+2\Delta a$ (node k) is identical to the energy required to close the crack between location of the node i and node l (see Figure 6.5). It is also assumed that a crack extension from $a+\Delta a$ (node i) to $a+2\Delta a$ (node k) does not significantly alter the state at the crack tip. Therefore, the displacements behind the crack tip at node i are approximately equal to the displacements behind the original crack tip at node l [2].

For 20-noded 3D elements, the equations to calculate the mode I and mode II strain energy release rate, at the element corner nodes (location L_i) (refer to Figure 6.5) are given by:

$$G_I = \frac{1}{2\Delta A_L}\left[\frac{1}{2}Z_{Ki}\left(w_{Kl}-w_{Kl^*}\right)+Z_{Li}\left(w_{Ll}-w_{Ll^*}\right)+Z_{Lj}\left(w_{Lm}-w_{Lm^*}\right)+\frac{1}{2}Z_{Mi}\left(w_{Ml}-w_{Ml^*}\right)\right] \quad (6.25)$$

$$G_{II} = \frac{1}{2\Delta A_L}\left[\frac{1}{2}X_{Ki}\left(u_{Kl}-u_{Kl^*}\right)+X_{Li}\left(u_{Ll}-u_{Ll^*}\right)+X_{Lj}\left(u_{Lm}-u_{Lm^*}\right)+\frac{1}{2}X_{Mi}\left(u_{Ml}-u_{Ml^*}\right)\right] \quad (6.26)$$

where $\Delta A_L=\Delta a.b$ as shown in Figure 6.5 [2]. Here X_{Ki} and Z_{Ki} denote the nodal forces at the delamination front in column K and row i. The relative displacements at the corresponding column K are calculated from the displacements behind the delamination at the lower face node, row l^*, as $u_K{}^*$ and $w_K{}^*$ and at the top face node, row l, as u_K and w_K (Figure 6.5). Similar definitions are applicable to column M for the forces at node row i and displacements at node row l and to column L for the forces at node row i and j and displacements at node row l and m, respectively. Only one half of the forces at locations K_i and M_i contribute to the energy required to virtually close the area ΔA_L. Half of the forces at location K_i contribute to the closure of the adjacent area ΔA_J and half of the forces at location M_i contribute to the closure of the adjacent area ΔA_N.

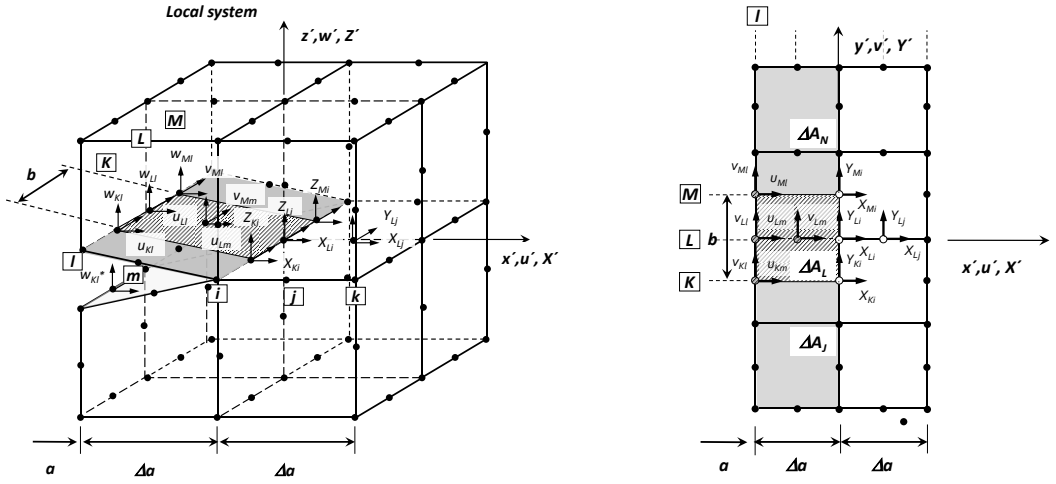

Figure 6.5 - Virtual Crack Closure Technique. Nomenclature for the computation of the energy release rate at corner nodes of a 20-noded solid mesh.

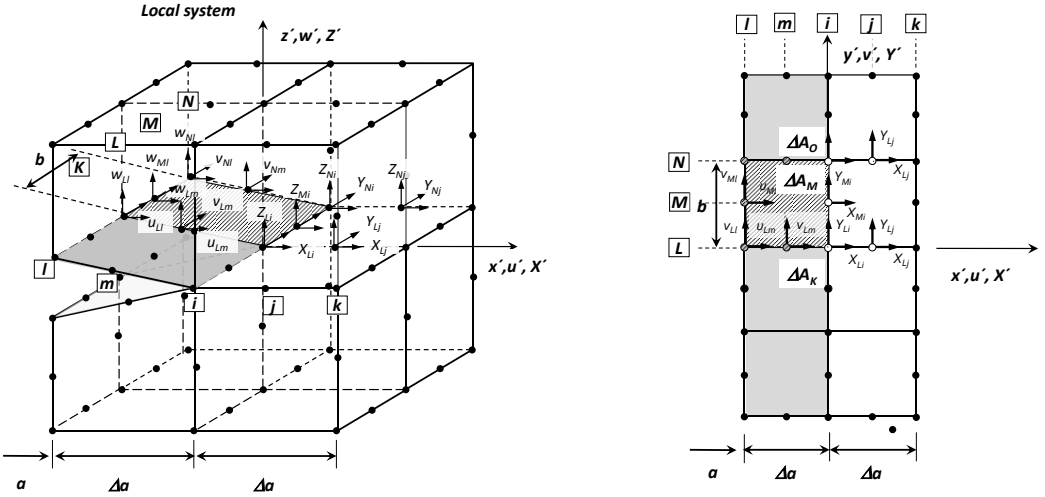

Figure 6.6 - Virtual Crack Closure Technique. Nomenclature for the computation of the energy release rate at mid-side nodes of a 20-noded solid mesh.

The equations to calculate the strain energy release rate components at the mid-side node (location M_i), as shown in Figure 6.6, are as follows [2]:

$$G_I = \frac{1}{2\Delta A_M}\left[\frac{1}{2}Z_{Li}\left(w_{Ll}-w_{Ll^*}\right)+\frac{1}{2}Z_{Lj}\left(w_{Lm}-w_{Lm^*}\right)+Z_{Mi}\left(w_{Ml}-w_{Ml^*}\right)+\right.$$
$$\left.+\frac{1}{2}Z_{Ni}\left(w_{Nl}-w_{Nl^*}\right)+\frac{1}{2}Z_{Nj}\left(w_{Nm}-w_{Nm^*}\right)\right] \tag{6.27}$$

$$G_{II} = \frac{1}{2\Delta A_M}\left[\frac{1}{2}X_{Li}\left(u_{Ll}-u_{Ll^*}\right)+\frac{1}{2}X_{Lj}\left(u_{Lm}-u_{Lm^*}\right)+X_{Mi}\left(u_{Ml}-u_{Ml^*}\right)+\right.$$
$$\left.+\frac{1}{2}X_{Ni}\left(u_{Nl}-u_{Nl^*}\right)+\frac{1}{2}X_{Nj}\left(u_{Nm}-u_{Nm^*}\right)\right] \tag{6.28}$$

where only one half of the forces at locations L_i, L_j and N_i, N_j contribute to the energy required to virtually close the area ΔA_M. Half of the forces at locations L_i and L_j contribute to the closure of the adjacent area ΔA_K and half of the forces at locations N_i and N_j contribute to the closure of the adjacent area ΔA_O.

6.4. THE STANDARD FINITE ELEMENT METHOD APPLIED TO FRACTURED SOLIDS

Solving three-dimensional fracture/fatigue engineering problems by standard finite element method can be quite a challenge, since the need to generate a suitable mesh which conforms to both the propagating crack surfaces and the surfaces of the component constitutes a cumbersome task. The crack surface must be aligned with the element boundaries, as illustrated in Figure 6.7. When a pure mode I fatigue crack is assumed, the crack path may be defined perpendicularly to the applied load and the crack increment, Δa, may be defined as the finite element length (see Figure 6.7). The crack length is defined as unmerged nodes between finite elements.

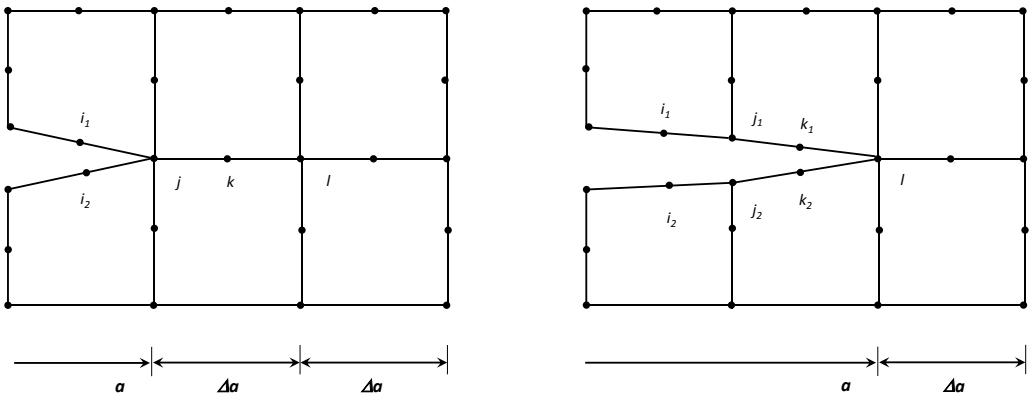

a) b)

Figure 6.7 - Fatigue crack propagation simulation using standard FEM: a) before crack increment; b) after crack increment.

Furthermore, for standard finite elements, the mesh must be built substantially more refined around the crack than in the remainder of the model. The difficulty increases when crack growth modelling is intended, because in this analysis, the finite element mesh must be re-meshed in the vicinity of the crack.

If the crack surface is not aligned with the element boundaries, the displacement discontinuity and the traction conditions on the crack surface cannot be treated as usual in a standard finite element analysis.

6.5. THE EXTENDED FINITE ELEMENT METHOD APPLIED TO FRACTURED SOLIDS

The eXtended Finite Element Method (XFEM) [17-18] presents several advantages regarding the crack growth modelling, because no remeshing procedures are required. The XFEM approach uses a displacement field approximation able of modelling an arbitrary discontinuity and near crack tip asymptotic crack fields [17]. The methodology was first presented by Belytschko [17] and Moës [19]. A finite element approach with additional enrichment functions coupled to the partition of unity concept [19], introduced by Babuška and Melenk [20] is used in this work. The resulting approximation can be used to treat cracks that are arbitrarily aligned in the finite element mesh, with great accuracy.

The eXtended finite element method is an extension of the standard finite element method that allows the simulation of discontinuities, as a crack, independently of the mesh [17, 21]. Once it is not necessary to update the mesh in order to match the current geometry of the discontinuity and the crack, this method is very attractive to simulate crack propagation in a solution-dependent path. Enrichment functions linked to additional degrees of freedom are added to the standard finite element approximation in the region where the crack is located. These enrichment functions involve the asymptotic crack tip functions that capture the singularity at the crack tip and a discontinuous function to represent the gap between the crack surfaces. These functions will be described in more detail in following subsections.

6.5.1. Enrichment functions

To model a crack in two-dimensional problems, two different forms of enrichment functions are required:

The Heaviside function

The Heaviside function, *H(x)*, is employed to enrich those elements that are completely cut by the crack. The domain cut by the crack suffers a jump in the displacement field and the Heaviside function provides a mathematical tool to model such behaviour. Figure 6.8 shows how the position of the arbitrary point *x* is characterized with respect to the crack location, represented as a continuous curve Γ, in a deformable body, Ω. The main goal is to define the closest point belonging to Γ, denoted by $\bar{x}$ (x,y) and the outward normal vector to Γ in $\bar{x}$ by $\vec{n}$. The Heaviside function may be written as:

$$H(x,y)=\begin{cases} 1 \quad for \quad \overrightarrow{\left(x-\bar{x}\right)}\cdot\vec{n}>0 \\ -1 \quad for \quad \overrightarrow{\left(x-\bar{x}\right)}\cdot\vec{n}<0 \end{cases} \tag{6.29}$$

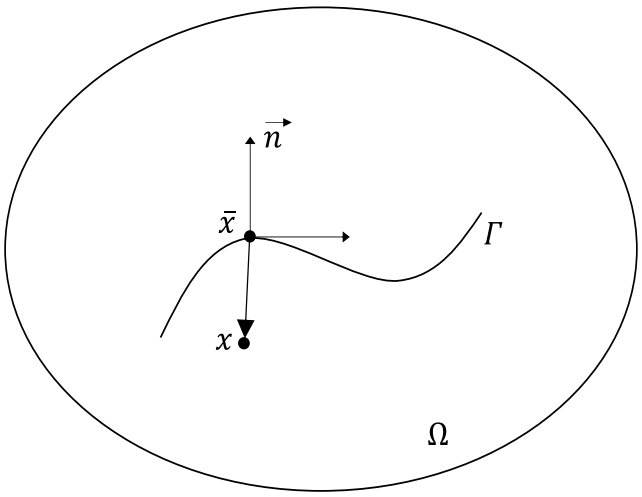

Figure 6.8 - Evaluation of the Heaviside function.

Asymptotic near crack tip functions

When the finite element is not completely cut by the crack, the Heaviside function cannot be used to approximate the displacement field over the entire element domain, since the element contains the crack tip. Fleming *et al.* [22] proved that the displacement field from LEFM theory is included within the span of the following four functions, expressed in terms of the local crack tip coordinate system (r, θ):

$$\left\{F_i(r,\theta)\right\}_{i=1}^{4} = \left\{\sqrt{r}\cos\left(\frac{\theta}{2}\right) \quad \sqrt{r}\sin\left(\frac{\theta}{2}\right) \quad \sqrt{r}\sin\left(\frac{\theta}{2}\right)\sin(\theta) \quad \sqrt{r}\cos\left(\frac{\theta}{2}\right)\sin(\theta)\right\} \tag{6.30}$$

These enrichment functions are added together with four degrees of freedom in each direction, for each node, in addition to those related with the standard finite element discretization.

Based on the two types of enrichment functions presented above, the following expression for the XFEM displacements approximation can be formulated:

$$\begin{aligned} &u^h(x) = u_{FEM}(x) + u_{ENRICHED}(x) = \\ &= \sum_{i\in I} N_i(x)u_i + \sum_{j\in J} N_j\left[H(x)\right]a_j + \sum_{k\in K_1} N_k(x)\left[\sum_{l=1}^{4} b_k^{l_1} F_l^1(x)\right] + \sum_{k\in K_2} N_k(x)\left[\sum_{l=1}^{4} b_k^{l_2} F_l^2(x)\right] \end{aligned} \tag{6.31}$$

where, J indicates the set of nodes belonging to the domain which is completely cut by the crack and enriched with the Heaviside function $H(x)$, K_1 and K_2 are the sets of nodes associated with the crack tips 1 and 2, and respectively enriched with the $F_l^1(x)$ and $F_l^2(x)$ functions. Moreover, u_i are the standard degrees of freedom, while a_j, $b_k^{l_1}$ and $b_k^{l_2}$ represent the additional nodal degrees of freedom introduced for modelling crack faces and two crack tips, respectively.

6.5.2. Level set method for modelling discontinuities

The modelling and tracking of time-varying objects, such as a fatigue propagating crack, is particularly cumbersome. The Level Set Method [23] is a numerical technique that

allows overcoming these difficulties. This method represents the crack as a zero level set function and to fully characterize a crack, two different level set functions are required:

- A normal level set function $\phi(x)$;
- A tangential level set function $\varphi(x)$.

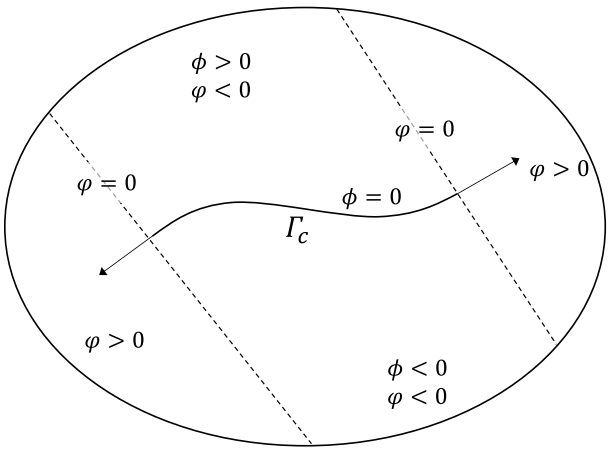

Figure 6.9 - Level set functions used for crack definition (crack path and crack tip).

In order to evaluated the $\phi(x)$ function, the signed distance functions that define the location of any point *x* to the crack, has to be assess. Consider the crack surface, Γ_c, of the Figure 6.9. In the same manner of what was achieved in the previous subsection, the normal level set function might be defined as:

$$\phi(x) = \overrightarrow{\left(x - \bar{x}\right)} \cdot \vec{n} \tag{6.32}$$

The tangential level set function $\varphi(x)$ is computed by finding the minimum signed distance to the normal at the crack tip; in case of an interior crack, two different functions can be formulated, but a unique tangential level set function can be defined as:

$$\varphi(x) = \max\left\{\varphi_1(x) \quad \varphi_2(x)\right\} \tag{6.33}$$

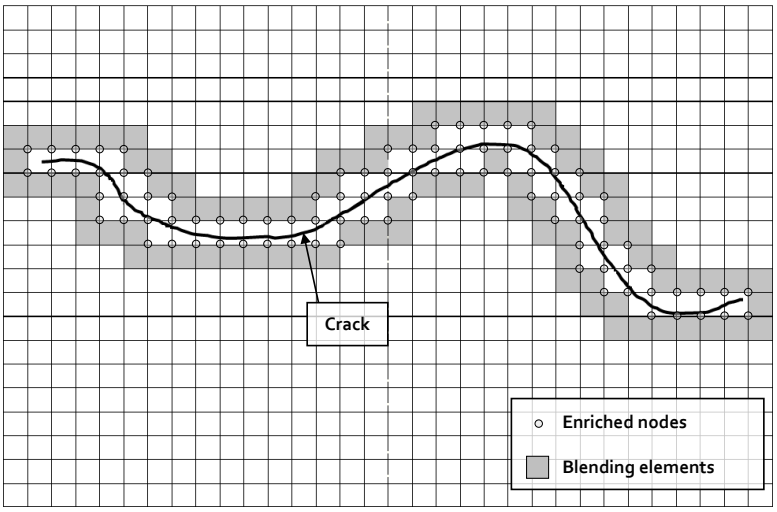

Figure 6.10 - Standard, enriched and blending elements in a XFEM domain discretization.

6.5.3. Blending elements

The finite elements having all nodes enriched may be named as reproducing elements since they reproduce the enrichment functions exactly. The blending elements allow to blend the enriched sub-domain with the rest of the domain, where standard finite elements are employed. Only some of the nodes in blending elements are enriched. Enriched finite elements, blending elements and standard finite elements defines the whole domain in three different parts, namely an enriched domain, a blending domain and finally a standard domain, as illustrated in Figure 6.10.

It is worthwhile to refer that two important drawbacks affect blending elements [24]:

- Enrichment functions cannot be reproduced exactly in blending elements, since the partition of unity property is not satisfied within them. These elements produce unwanted terms in the approximation, which cannot be compensated by the finite element part. For instance, if the enrichment introduces non-linear terms, a linear function can no longer be approximated within blending elements.
- A significant reduction of the convergence rate for general enrichment functions [25] is observed. Thus, suboptimal rate of convergence in XFEM may be caused by problems in blending elements [26].

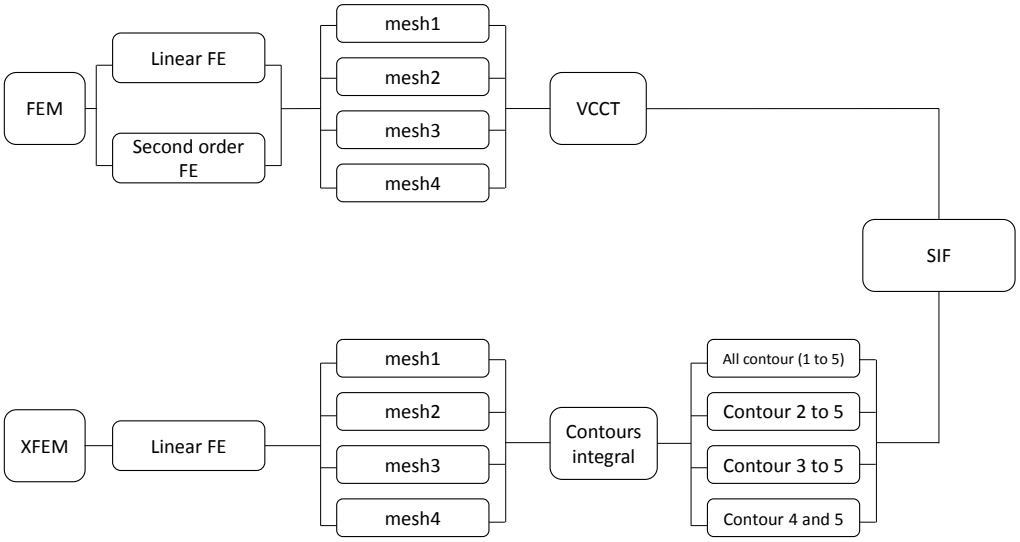

Figure 6.11 – Summary of the proposed simulations for each verification example, for stress intensity factors computation.

6.6. VERIFICATION EXAMPLES OF STRESS INTENSITY FACTORS COMPUTATION

This section presents some verification examples concerning the computation of the stress intensity factors using the XFEM procedure, combined with the contour integral method. The resulting stress intensity factors are compared with stress intensity factors computed using the VCCT approach, as well as using available analytical solutions (benchmark solutions). Several finite element mesh refinements are considered in order to observe the mesh sensitivity of the adopted approaches. Figure 6.11 presents an overview of the performed simulations for each verification example. Only thru thickness (constant depth) cracks were considered.

Concerning the standard finite element modelling (FEM), the ANSYS® program [27] was used to model 3D geometries using parametric models. Linear and quadratic finite elements were considered. A special care was dedicated to the model construction in order to control the mesh size at the crack tip. A refined mesh was built at the crack tip. The sensitivity of the stress intensity factors to the mesh size was evaluated, using four mesh refinements (mesh 1 to 4).

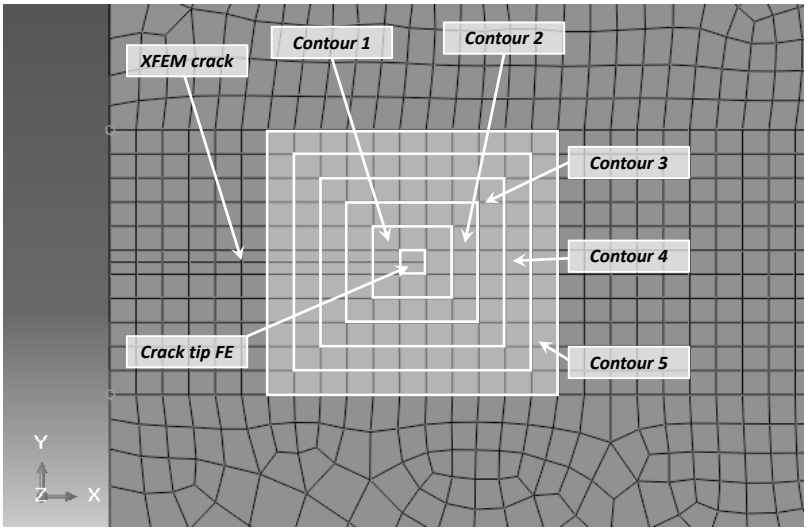

Figure 6.12 - Contours used in the computation of the stress intensity factors with the XFEM approach.

The XFEM is a methodology incorporated in the ABAQUS® software [1]. Stress intensity factors were computed using the contour integral method available in ABAQUS®. In order to evaluate accurately stress intensity factors, several contours were used (see Figure 6.12). As a first approach, five contours around the crack tip element were used to compute the stress intensity factors. The second approach to assess the stress intensity factors did not consider contour 1. The third approach only used contours 3, 4 and 5 to compute stress intensity factors and the last approach only considered contours 4 and 5. In order to allow more accurate computations of the stress intensity factors, the initial crack was considered long enough to assure the contours to be moved away from the plate edge. In order to investigate the mesh size effect on the numerical results, several finite element meshes were considered, referred in Figure 6.11 as mesh 1, 2, 3, and 4. Only linear finite element was considered in the analyses, since second order finite elements are not allowed to be used with the XFEM methodology in ABAQUS® [1].

6.6.1. Verification example 1

The first verification example consists of a central through-thickness crack located in a finite rectangular plate, as illustrated in Figure 6.12. As referred above, stress intensity factors were computed according to procedures depicted in Figure 6.11. The numerical results were then compared with analytical solutions available in BS 7910 standard [28]:

$$K_I = P\sqrt{\pi a}\left\{1-0.01\left(\frac{a}{W}\right)^2+0.96\left(\frac{a}{W}\right)^4\right\}\left[\sec\left(\pi\left(\frac{a}{W}\right)\right)\right]^{1/2} \tag{6.34}$$

where P is the applied load (equivalent to a uniformly distributed stress), $2a$ is the crack length and W a geometrical parameter (refer to Figure 6.13). Only ¼ of the geometry was modelled. Figure 6.14 illustrates the FEM model and plots three distinct mesh refinements modelled around the crack tip. For a fixed volume around the crack tip (box), the number of finite elements is progressively increased. Also, the element size through the thickness direction was also progressively increased. The information regarding the mesh refinement is summarized in Table 6.1, for the FEM model.

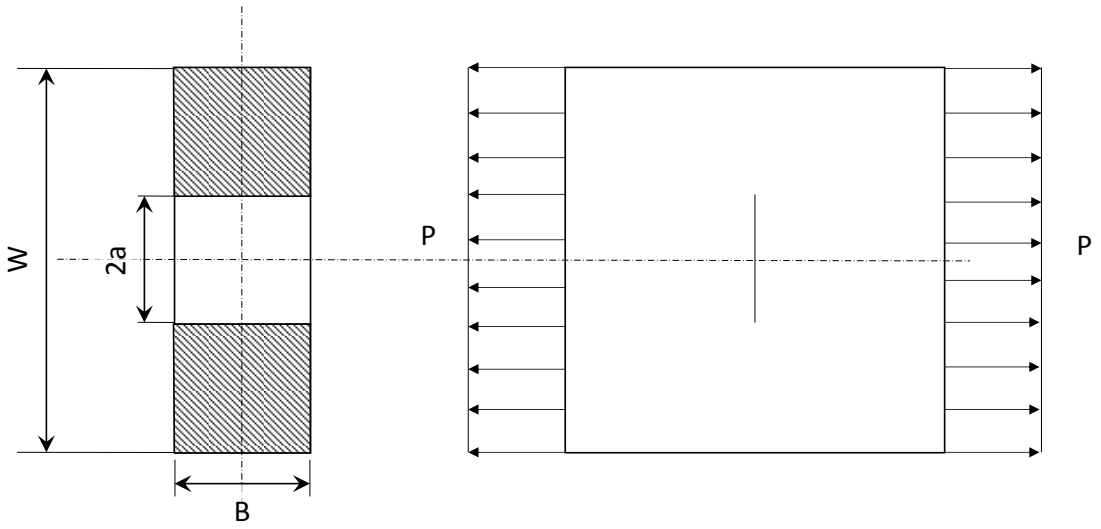

Figure 6.13 - Central through-thickness crack located in a finite plate.

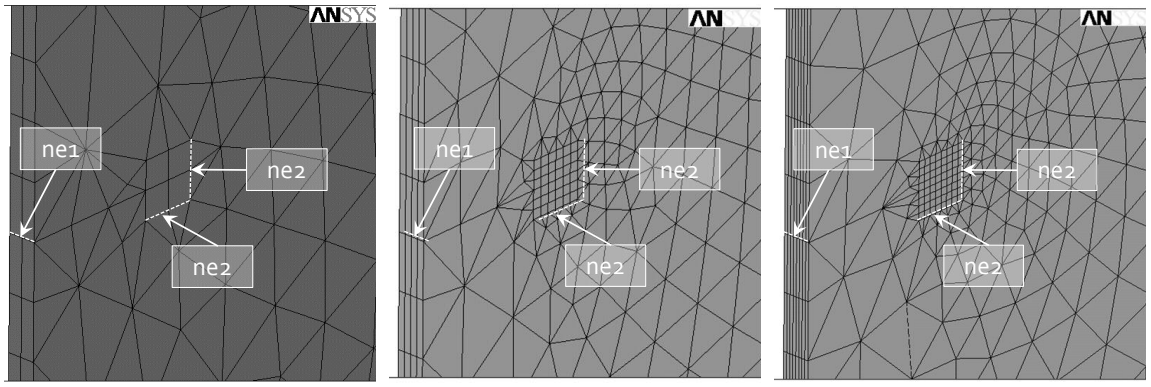

Figure 6.14 - Finite element meshes for the verification example 1: a) coarse FE mesh; b) intermediate FE mesh; c) fine FE mesh.

Table 6.1 - Finite element refinement used for the verification example 1 (FEM approach).

	ne1 – Number of FE	*ne2 – Number of FE*
mesh1	3	2
	4	
	8	
mesh2	3	3
	4	
	8	
mesh3	3	4
	4	
	8	
mesh4	3	8
	4	
	8	

Figure 6.15 illustrates the enriched finite elements zone used in the XFEM approach with two distinct mesh refinements. Table 6.2 summarizes the number of elements used in four distinct mesh refinements.

Figure 6.16 to 6.19 plot the ratio between the numerical stress intensity factors and the analytical stress intensity factors for distinct crack lengths. In particular, a) figures present the results from finite element computation and VCCT approach; b) figures show the results from the XFEM approach with the contour integral method.

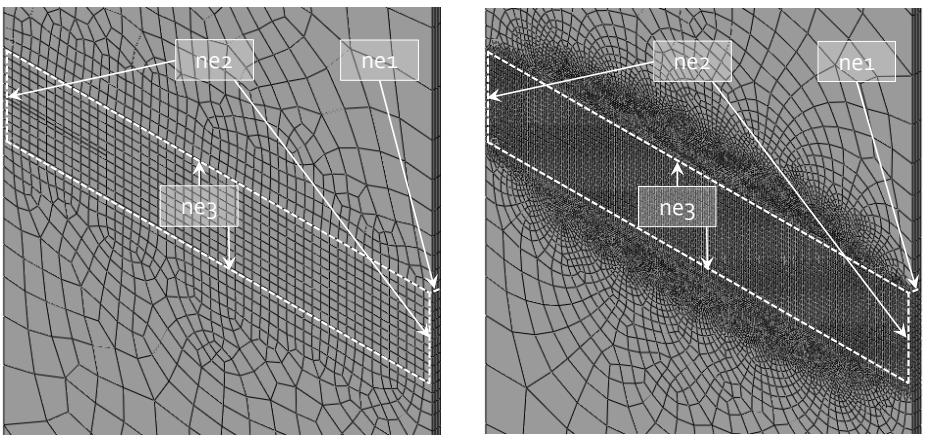

a) b)

Figure 6.15 – Examples of enriched finite elements area used in the computation of the stress intensity factors with the XFEM approach, for verification example 1: a) coarse FE mesh; b) fine FE mesh.

Table 6.2 - Finite element refinement used for the verification example 1 (FEM approach).

	ne1 – Number of FE	*ne2 – Number of FE*	*ne3 – Size of FE [mm]*
mesh1	3	5	1
	4		
	8		
mesh2	3	5	0.2
	4		
	8		
mesh3	3	50	1
	4		
	8		
mesh4	3	50	0.2
	4		
	8		

Analyzing the stress intensity values computed using XFEM (Figure 6.16 b), Figure 6.17 b), Figure 6.18 b) and Figure 6.19 b)), the numerical/analytical ratio was always greater than unity, which means that the computed numerical stress intensity factors are higher than the analytical stress intensity factors. The VCCT plus FEM results (Figure 6.16 a), Figure 6.17 a), Figure 6.18 a) and Figure 6.19 a)) are, in general, more close to the analytical results than XFEM approach and the accuracy of the first method increases with the increase of the crack length. For higher crack sizes, the VCCT method produces very accurate results. Concerning the VCCT approach, the higher refined mesh combined with quadratic elements produced less accurate results. For this approach, the use of quadratic elements did not result in more accurate predictions.

The XFEM with the contour integral approach gives better results if contour 1 is excluded from the analysis. We observe that the mesh refinement in the plate plane did not impact significantly the convergence of the numerical solution to the analytical solution. However the mesh refinement in the thickness direction showed important effect on stress intensity factors, mainly for smaller crack sizes.

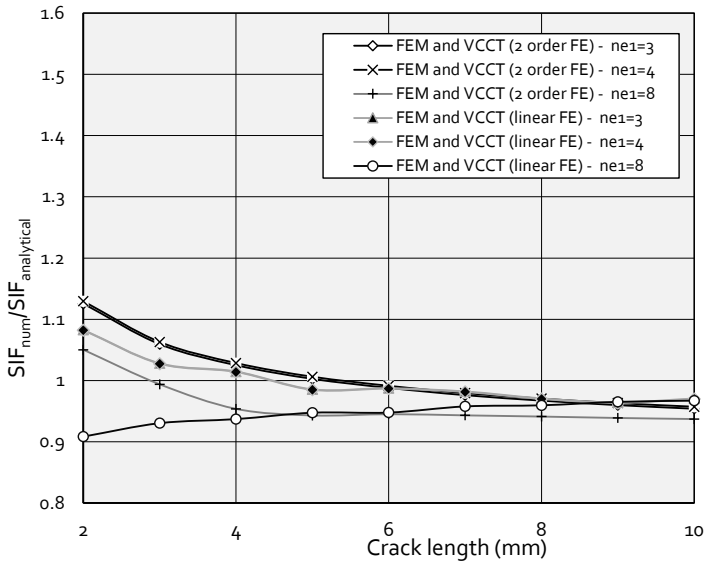

a)

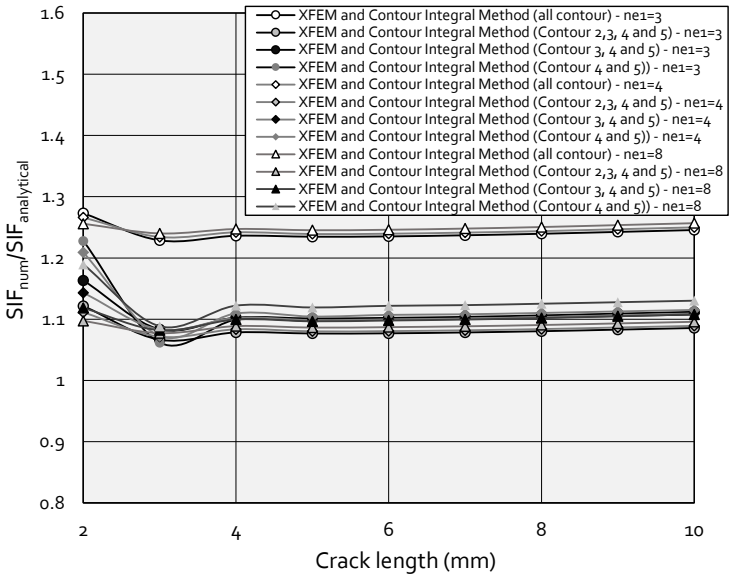

b)

Figure 6.16 - Ratio between the numerical stress intensity factor and analytical stress intensity factor versus the crack length computed for the mesh 1 (verification example 1): a) FEM analysis; b) XFEM analysis.

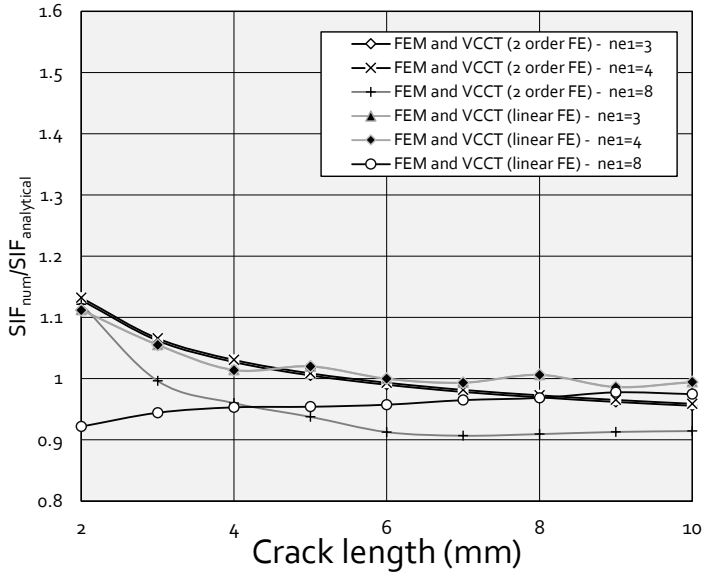

a)

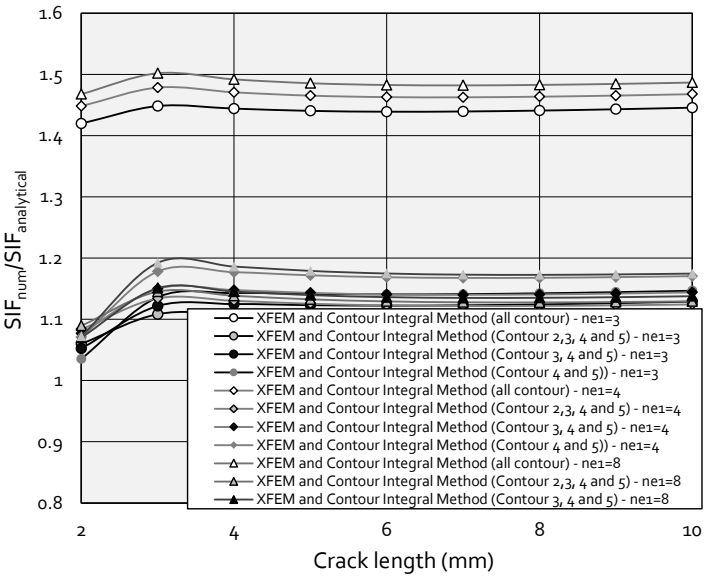

b)

Figure 6.17 - Ratio between the numerical stress intensity factor and analytical stress intensity factor versus the crack length computed for the mesh 2 (verification example 1): a) FEM analysis; b) XFEM analysis.

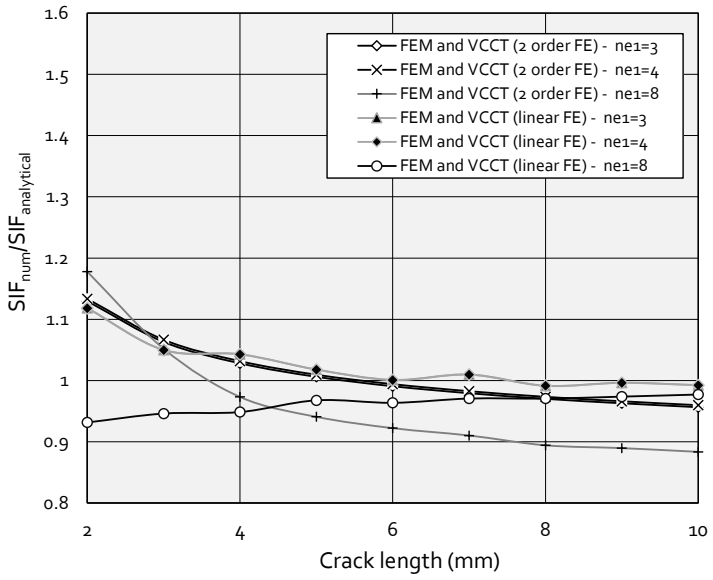

a)

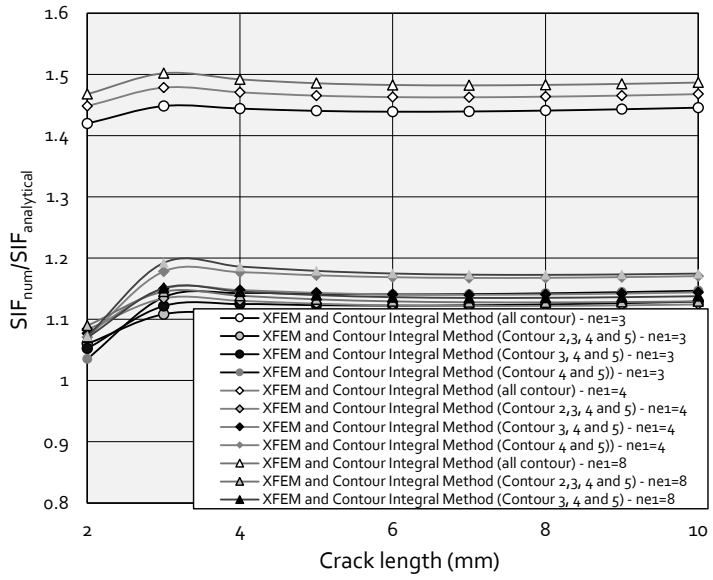

b)

Figure 6.18 - Ratio between the numerical stress intensity factor and analytical stress intensity factor versus the crack length computed for the mesh 3 (verification example 1): a) FEM analysis; b) XFEM analysis.

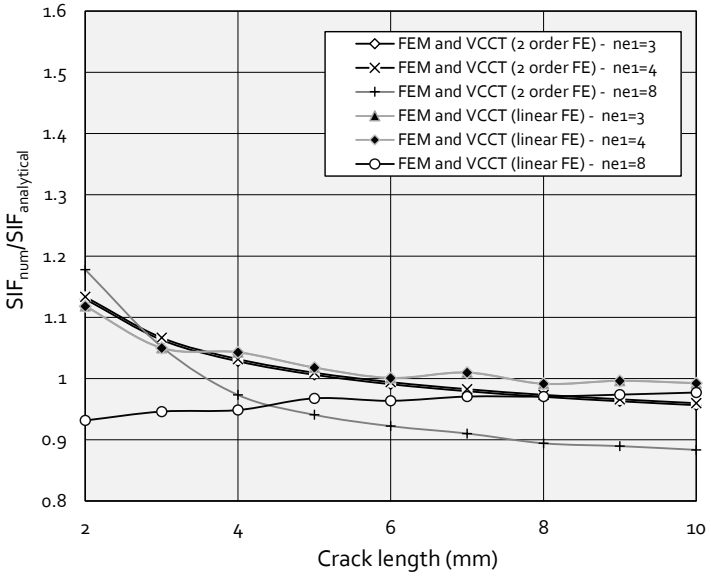

a)

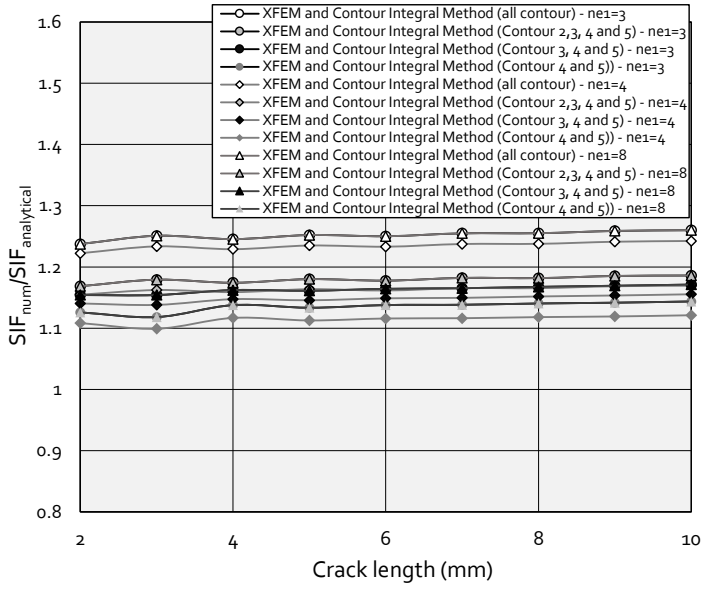

b)

Figure 6.19 - Ratio between the numerical stress intensity factor and analytical stress intensity factor versus the crack length computed for the mesh 4 (verification example 1): a) FEM analysis; b) XFEM analysis.

6.6.2. Verification example 2

The verification example 2 consists of a single edge notched bending specimen (see Figure 6.20). The stress intensity factor solution of a single edge notch bending specimen is given by the following analytical solution [29]:

$$K_I = \frac{P}{B}\sqrt{\frac{\pi}{W}}\left[1.6\left(\frac{a}{W}\right)^{1/2} - 2.6\left(\frac{a}{W}\right)^{3/2} + 12.3\left(\frac{a}{W}\right)^{5/2} - 21.2\left(\frac{a}{W}\right)^{7/2} + 21.8\left(\frac{a}{W}\right)^{9/2}\right] \tag{6.35}$$

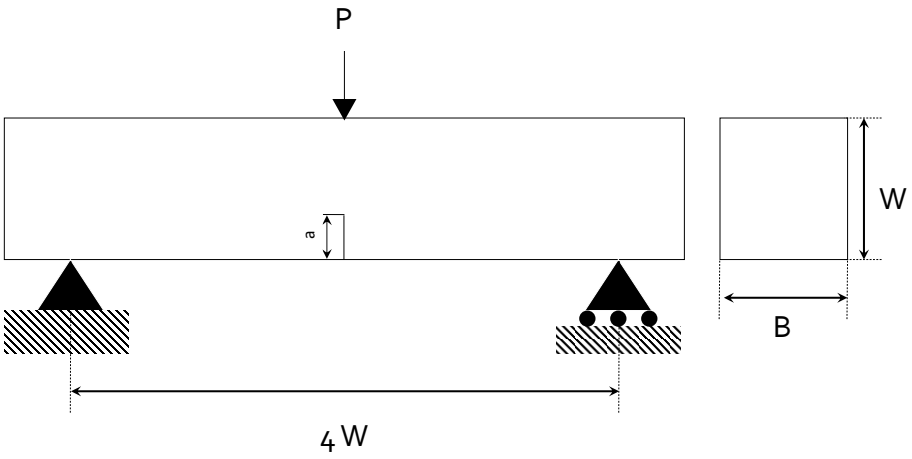

Figure 6.20 - Single edge notched bending specimen.

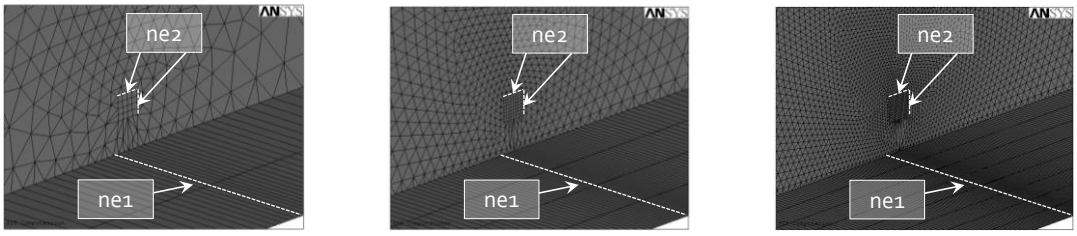

a) b) c)

Figure 6.21 - Finite element mesh sensitivity analysis (FEM): a) coarse FE mesh; b) intermediate FE mesh; c) fine FE mesh.

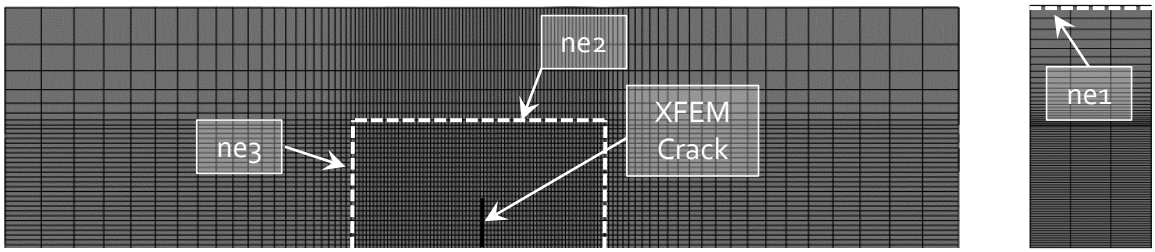

Figure 6.22 - Finite element mesh sensitivity analysis (XFEM).

where *P* is the applied load, *a* is the crack length and *W* the beam height (see Figure 6.20). The beam span is assumed equal to 4W.

About the FEM approach, a similar mesh sensitivity analysis to the one adopted for the verification example 1, was performed again in this verification example 2 (see Table 6.1). Figure 6.21 plots three distinct mesh refinements considered in the FEM analysis. Figure 6.22 presents three distinct finite element mesh densities used for XFEM numerical cracked models. Table 6.3 summarizes the distinct mesh densities tested in the XFEM simulations.

Figures 6.23, 6.24, 6.25 and 6.26 show the ratio between the numerical stress intensity factor and the analytical stress intensity factor computed for the verification example 2, using meshes 1, 2, 3 and 4, respectively, against the crack length. A global analysis of Figures 6.23 to 6.26 reveals that the XFEM stress intensity factor values based on all contours exhibit spurious behaviour. Analysing Figures 6.23 to 6.26 it can be pointed out that the deviation between numerical and analytical stress intensity factors is less than 10%. Concerning the XFEM approach and excluding the five contour values, the results are very accurate for intermediate mesh refinements. For higher mesh refinements, seems that the numerical results get worst since the crack path interacts with the finite element boundaries creating some instability in the results. Concerning the VCCT approach, the method based on linear finite elements with a good mesh refinement yields satisfactory results; the quadratic elements showed better performance in the VCCT approach, which is contradictory with the results obtained in the verification example 1.

Table 6.3 - Finite element size used for the verification example 2 using XFEM approach.

	ne1 – Number of FE	*ne2 – Number of FE*	*ne3 – Size of FE [mm]*
mesh1	3	0.1	0.05
	4		
	8		
mesh2	3	0.1	0.1
	4		
	8		
mesh3	3	0.1	0.2
	4		
	8		
mesh4	3	0.05	0.1
	4		
	8		

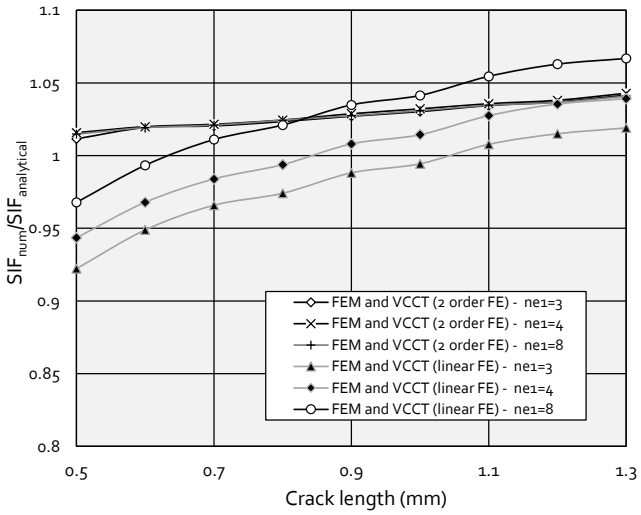

a)

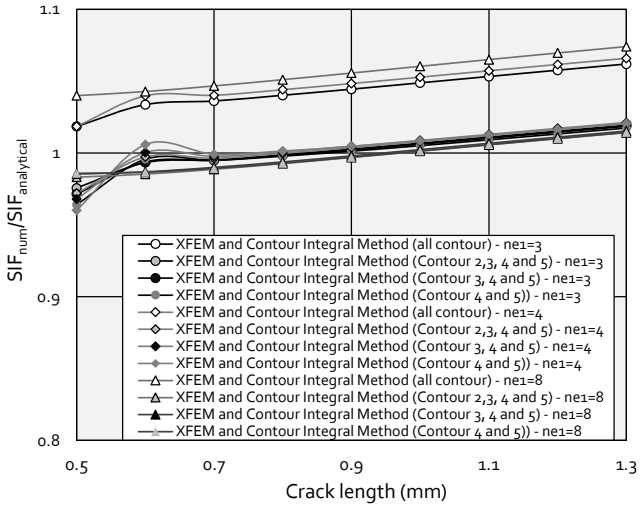

b)

Figure 6.23 - Ratio between the numerical stress intensity factor and analytical stress intensity factor versus the crack length computed for the mesh 1 (verification example 2): a) FEM analysis; b) XFEM analysis.

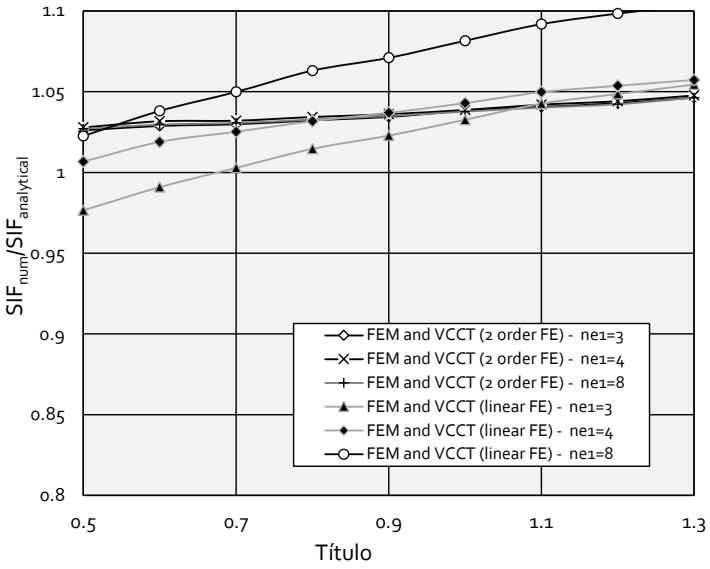

a)

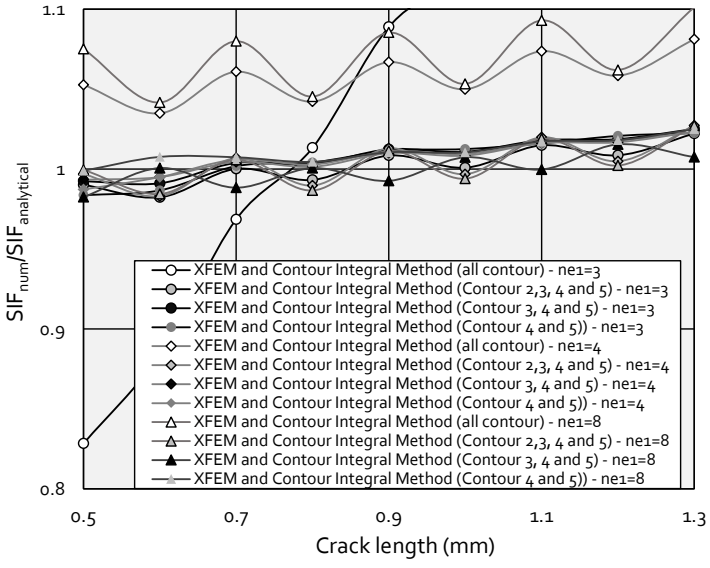

b)

Figure 6.24 - Ratio between the numerical stress intensity factor and analytical stress intensity factor versus the crack length computed for the mesh 2 (verification example 2): a) FEM analysis; b) XFEM analysis.

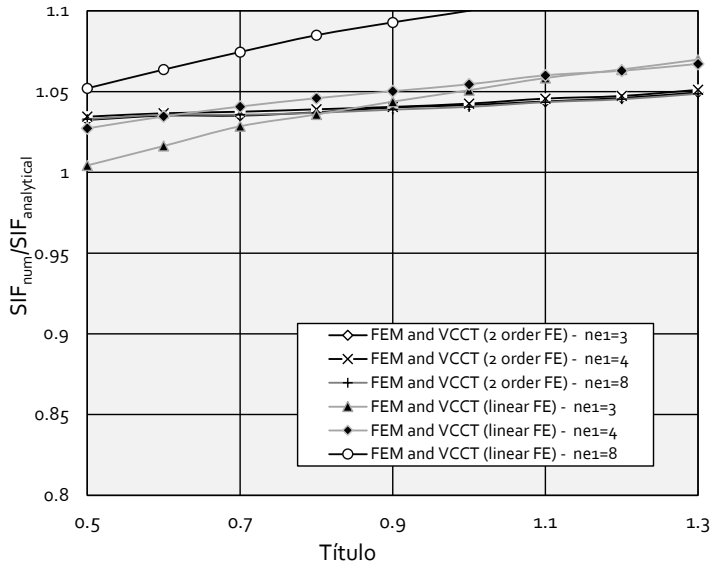

a)

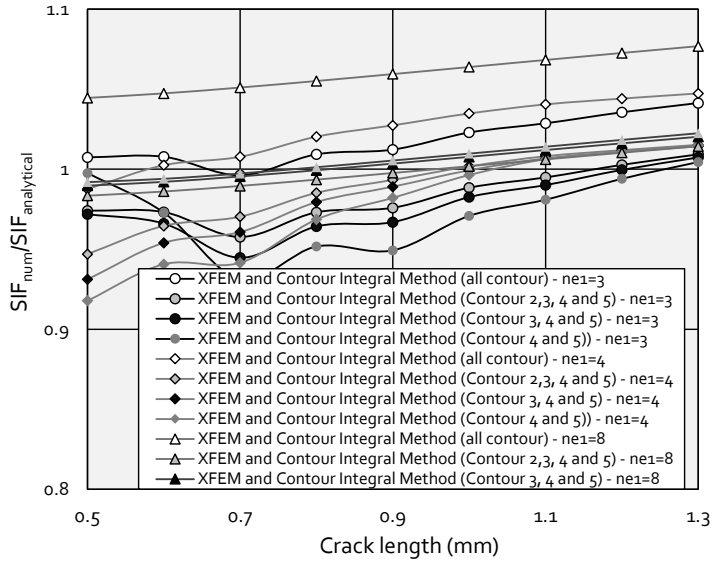

b)

Figure 6.25 - Ratio between the numerical stress intensity factor and analytical stress intensity factor versus the crack length computed for the mesh 3 (verification example 2): a) FEM analysis; b) XFEM analysis.

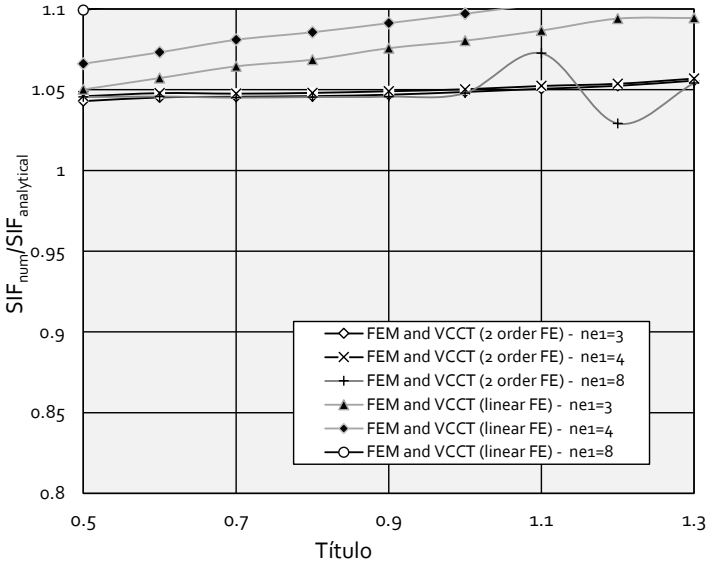

a)

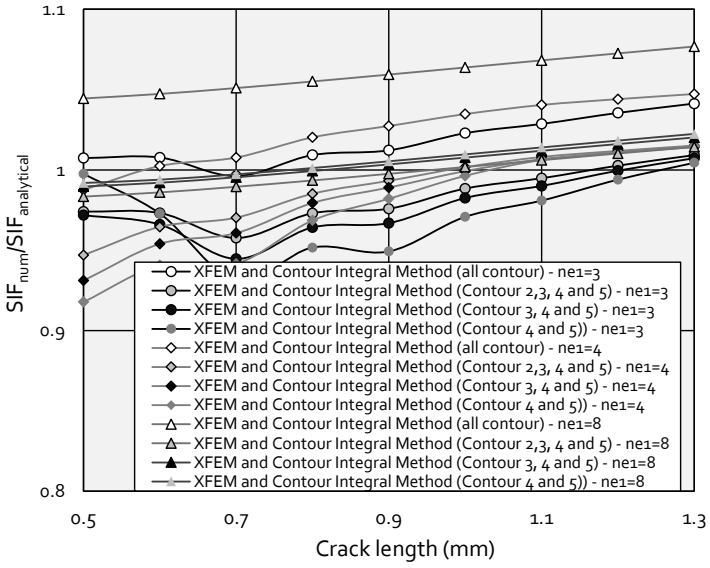

b)

Figure 6.26 - Ratio between the numerical stress intensity factor and analytical stress intensity factor versus the crack length computed for the mesh 4 (verification example 2): a) FEM analysis; b) XFEM analysis.

6.7. NUMERICAL SIMULATION OF WELDED SPECIMENS

This section presents a numerical investigation aiming the assessment of S-N curves for the welded specimens presented in the Chapter IV. The proposed assessment was performed considering both standard finite element method and extended finite element method. Numerical S-N curves were computed considering the contribution of fatigue crack growth (LEFM based approach). There is a generally accepted understanding that fatigue crack propagation is the major damage mechanism in welded joints. Existing code based design curves are supported by this assumption, their slopes being established from the fatigue crack propagation data. Fatigue crack initiation may be surpassed by existing defects in the welds.

Concerning the standard FE models, performed in ANSYS®, only ¼ of specimen geometries were modelled, taking into account existing symmetries (see Figure 6.27). Materials were considered linear elastic and isotropic (E=210 GPa; ν=0.27). Hexahedral 20-noded finite elements were used. The crack path was defined during the finite element mesh generation phase. Both the initial crack length and the crack increments were defined with 0.5mm. Stress intensity factor ranges were computed using the Virtual Crack Closure Technique, as proposed by Krueger [1]. The applied loading conditions result in dominant pure mode I, which means that only mode I stress intensity factors were computed at the crack tip. Figure 6.27 shows the finite element meshes of W1 welded specimens (Figure 6.27a), W2 welded specimens (Figure 6.27b), W3 welded specimens (Figure 6.27c) and W4 welded specimens (Figure 6.27d). Figure 6.27 also exhibits σ_y (y=loading direction) stress field for an arbitrary crack.

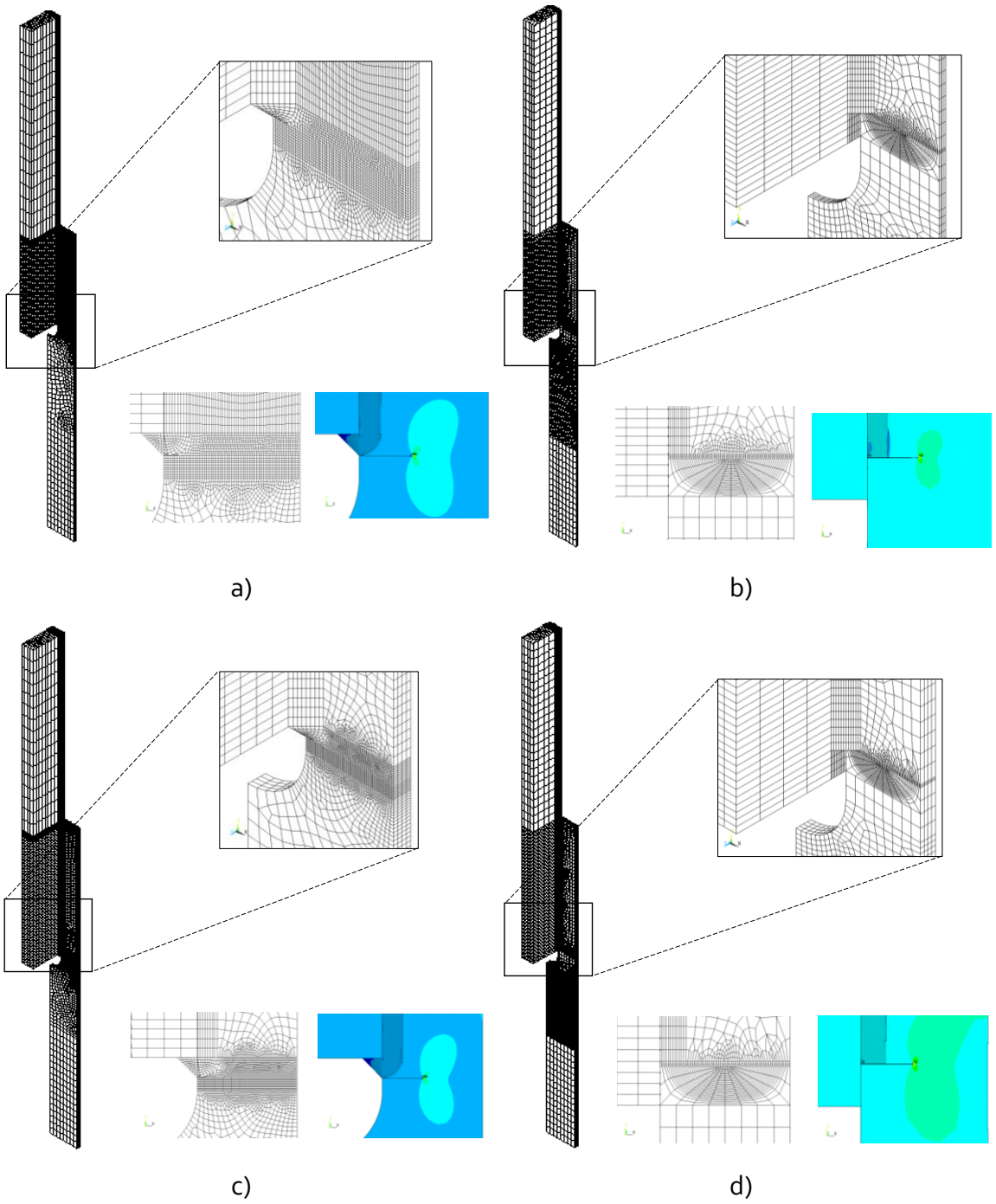

Figure 6.27 - FE models of welded specimens obtained using ANSYS® and σ_y stress field illustration for an arbitrary crack: a) W1 series; b) W2 series; c) W3 series; d) W4 series.

Finite element models were also built using ABAQUS® code aiming the application of the XFEM approach, implemented in ABAQUS®. As referred for standard FEM analysis, only ¼ of specimen geometries were modelled. Linear hexahedral 8-noded finite elements were used. Finite element formulation with reduced integration method was considered. Figure 6.28 illustrates the finite element model of the W1 welded specimen. The finite

element mesh used may be observed in Figures 6.28a) and b). Figure 6.28 b) illustrates the mesh region where finite elements were enriched with additional degrees of freedom. Figure 6.28 c) plots the σ_y stress field at the fatigue crack domain, for an arbitrary applied load. It is clear the asymptotic stress field introduced by the crack. Figures 6.28 d) and f) exhibit the ϕ and φ level set functions given by ABAQUS® for a given generic crack. Stress intensity factors were computed using the contour integral method available in ABAQUS®, several contours being considered. Stress intensity factors were computed considering 3 contours, namely contours 3, 4 and 5. Contours 1 and 2 were excluded since they led to instabilities and deviation from the expected theoretical solution as illustrated in the verification examples presented before.

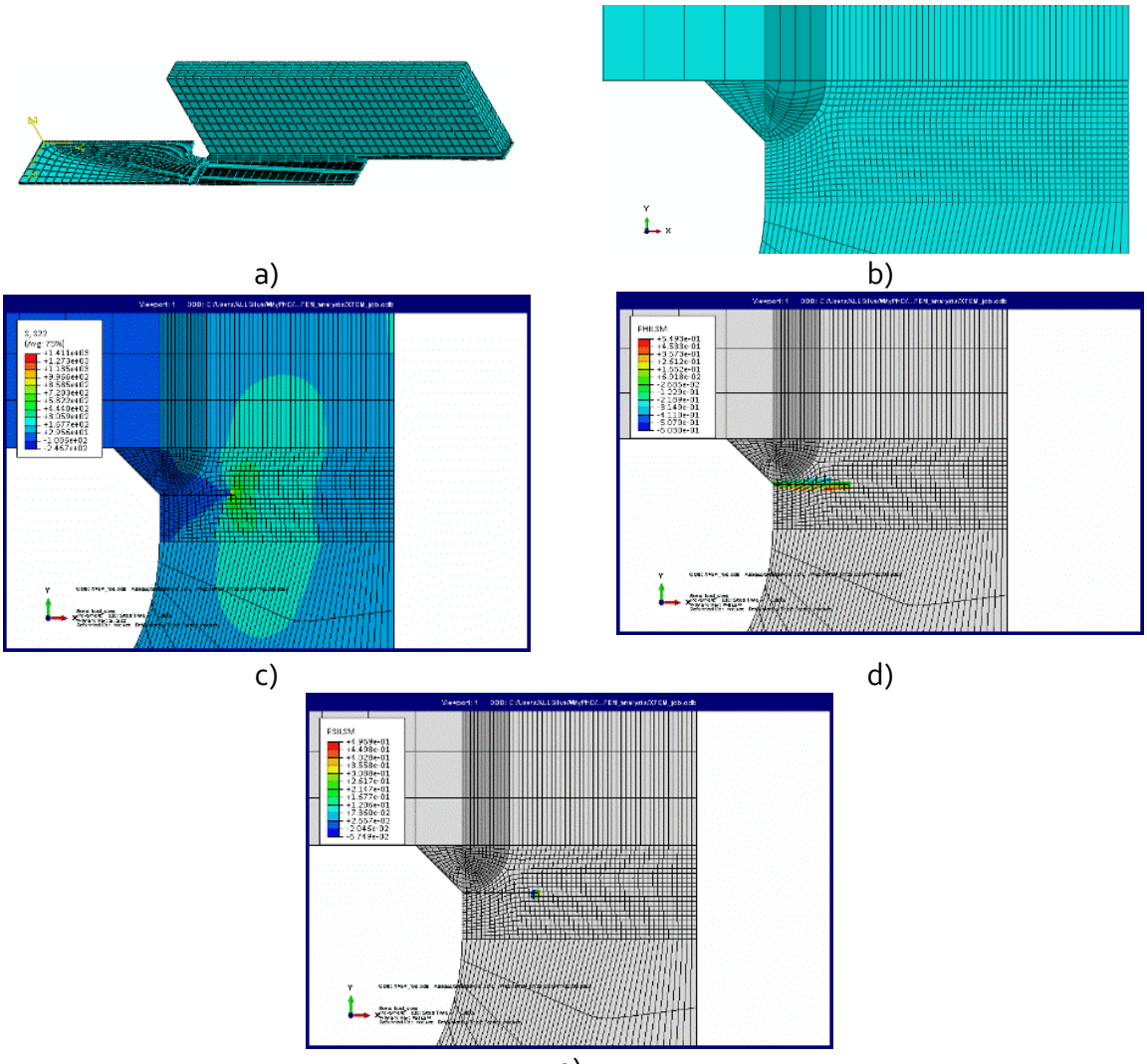

a) b) c) d) e)

Figure 6.28 - W1 welded specimen modelled using 3D XFEM: a) overview of the welded specimen finite element mesh; b) detail of the enriched finite elements; c) illustration of σ_{yy} stress field for an arbitrary crack; d) ϕ level set function; e) φ level set function.

Table 6.4 – Paris law material constant for the S355 steel considering thicknesses of 4mm and 8mm (R=0.01).

Welded specimens	*C**	*m*
W1 (t=4mm)	1.01E-14	3.39
W2 (t=4mm)		
W3 (t=8mm)	2.55E-14	3.33
W4 (t=8mm)		

*da/dN in mm/cycle and ΔK in $N.mm^{-3.5}$

Stress intensity factors range computed using FEM plus VCCT and X-FEM plus Contour Integral, for W1, W2, W3 and W4 welded specimens, are plotted, respectively, in Figures 6.29a), b), c) and d). Figure 6.29a) presents the stress intensity factors computed for W1 welded specimens loaded to 50kN (R=0.01). Figure 6.29 b) exhibits the stress intensity factors computed for a crack propagating in W2 welded specimens, loaded at 25kN (R=0.01). Figure 6.29 c) shows the stress intensity factors resulting from a crack propagating at the W3 welded specimens, loaded by 50kN load (R=0.1), and the Figure 6.29 d) illustrates the stress intensity factor history computed for a crack growing in the W4 welded specimens, loaded by a 75kN load (R=0.1). The grey curve corresponds to the numerical stress intensity factors results from ANSYS® plus VCCT computations (pure mode I). The other curve (black) was derived by means of the XFEM method together with the contour integral method, computed using several contours. The stress intensity factor computed using the XFEM method was elaborated considering both K_I and K_{II} stress intensity factors. An equivalent stress intensity factor was thus computed in order to compare both numerical approaches. The maximum crack size was defined by the maximum stress intensity factor registered in the small-scale fatigue crack propagation tests, using compact tension specimens, tested for the same stress ratio (see Chapter III). The analysis of Figure 6.29 reveals that the FEM procedure gives always higher stress intensity factors, than the X-FEM procedure. It is important to refer that the finite element mesh used in FEM analysis was coarser than in X-FEM models, which may justify some discrepancies in the stress intensity values. The deviation between the two approaches is small for specimens W1 and W4. A higher deviation between FEM and XFEM results was observed for the W2 and W4 specimens that are characterized by a significant discontinuity due to the fillet weld end. The XFEM plus contour integral

approach has more difficulties to simulate the stress intensity factors for small cracks since the proximity of the contours around the crack tip to the boundaries of the plate or geometric discontinuities may lead to spurious values. This was particularly the case of the W_3 and W_4 series, where some instability was observed as well as some divergent results.

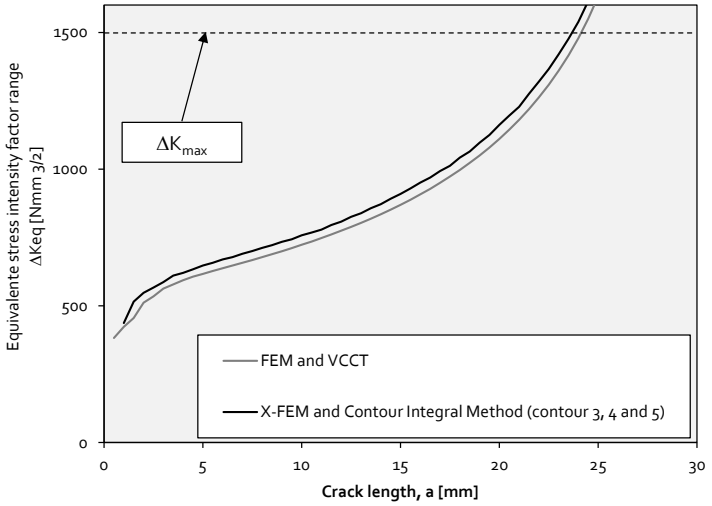

a)

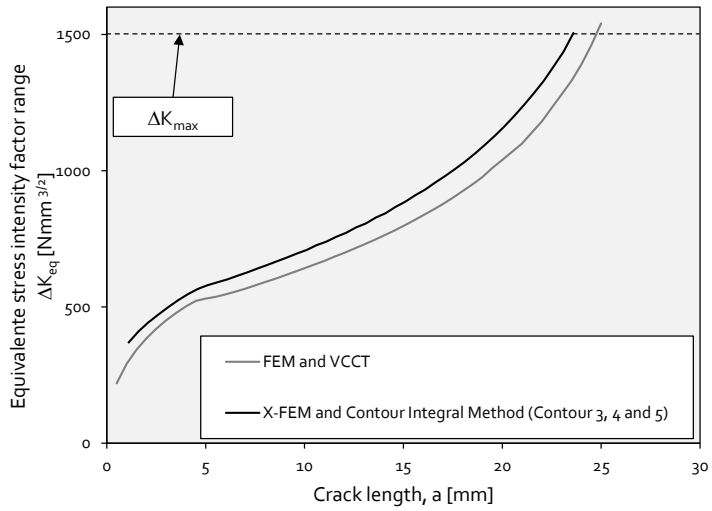

b)

Figure 6.29 - Stress intensity factors range computed using FEM/VCCT and XFEM approaches: a) W1 welded specimens loaded at 50kN; b) W2 welded specimens loaded at 25kN; c) W3 welded specimens loaded at 50kN; d) W4 welded specimens loaded at 75kN. (1/2)

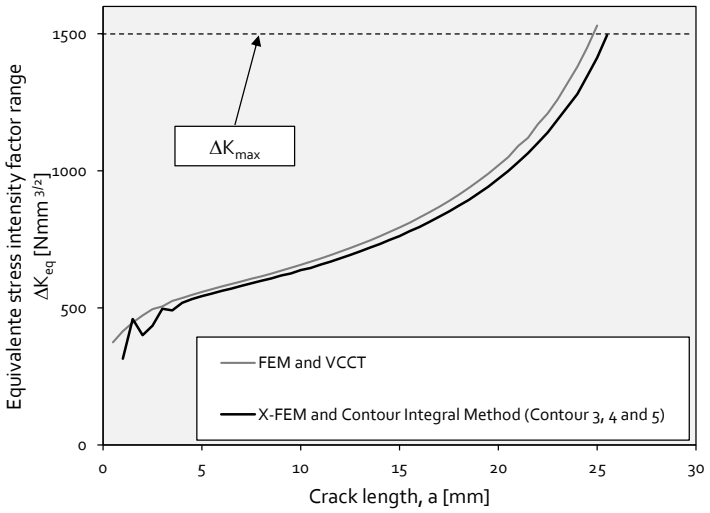

c)

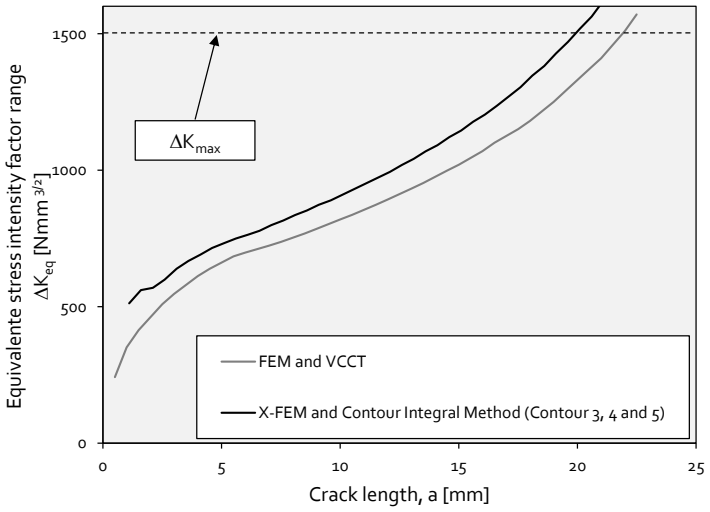

d)

Figure 6.29 - Stress intensity factors range computed using FEM/VCCT and XFEM approaches: a) W1 welded specimens loaded at 50kN; b) W2 welded specimens loaded at 25kN; c) W3 welded specimens loaded at 50kN; d) W4 welded specimens loaded at 75kN. (2/2)

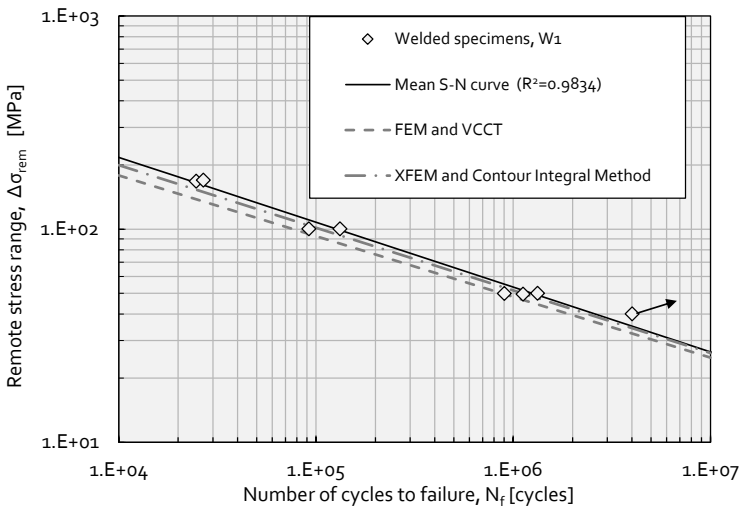

a)

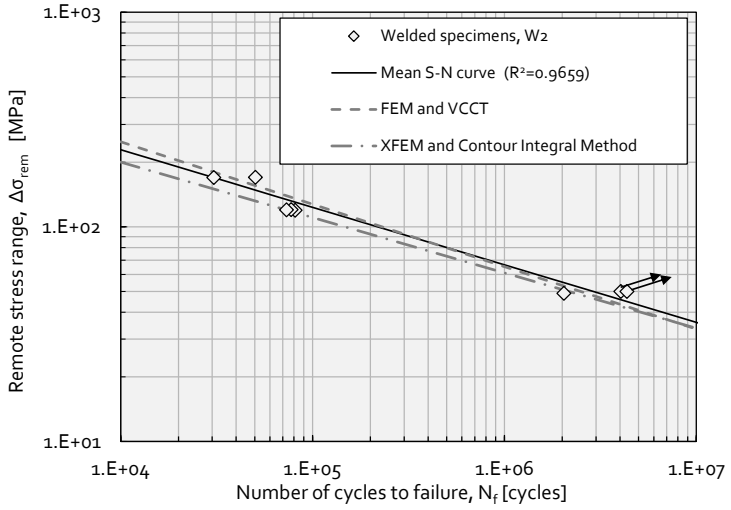

b)

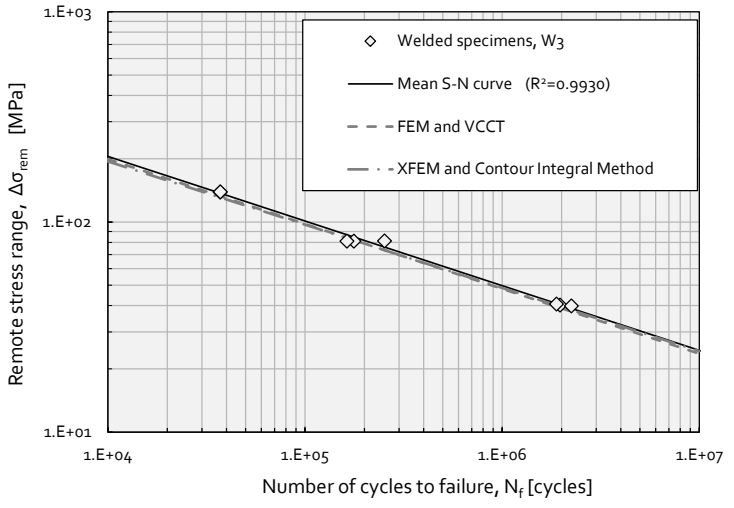

c)

Figure 6.30 - Comparison between experimental S-N data and numerical S-N curves computed using FEM/VCCT and XFEM analysis: a) W1 series; b) W2 series; c) W3 series; d) W4 series. (1/2)

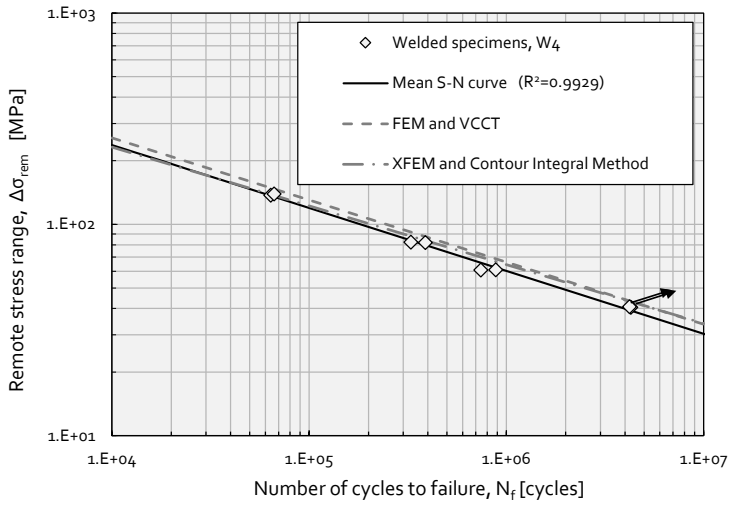

d)

Figure 6.30 - Comparison between experimental S-N data and numerical S-N curves computed using FEM/VCCT and XFEM analysis: a) W1 series; b) W2 series; c) W3 series; d) W4 series. (2/2)

Figure 6.30 compares the experimental S-N data with numerical S-N curves resulting from crack initiation and propagation modelling, supported by FEM/VCCT and XFEM analysis. The analysis of the Figure 6.30 reveals a very good agreement between the numerical S-N curves and the experimental fatigue data for all welded specimens. Also, it is visible a very good agreement between the two proposed numerical S-N curves. The discrepancy in the observed stress intensity factors did not result in significant discrepancies in the predicted S-N curves. The slopes of the simulated S-N curves were very similar to the slope of the mean experimental S-N curve, which is justified by the fact that the crack propagation curves were correlated with a Paris relation with an exponent that is in very close agreement with the slope of the experimental S-N curve.

The crack was propagated according constant increments of 0.5 mm for both FEM/VCCT and XFEM/J Integral approaches. For the first case, an initial crack of 0.5 mm was simulated. For the second case, if a similar initial crack size was simulated and taking into account the higher stress intensity factors that were simulated, lower fatigue lives would result from the XFEM approach. The similar values presented in the Figure 6.30 where obtained with an initial crack size of 0.8 mm for the XFEM simulation. Both values of possible initial crack sizes of 0.5 and 0.8 mm are within the usual range adopted in welded joints simulation (0.1-1.0mm).

6.8. NUMERICAL SIMULATION OF RIVETED SPECIMENS

Finite element models of the riveted specimens tested in this work, whose experimental results were presented in Chapter IV, were built in ANSYS® and ABAQUS®. Concerning the developed models, existing symmetry planes were considered in order to reduce their size. This resulted in a model of ½ of the geometry for the R1 series, ¼ of the geometry for the R2 series and ½ of the geometry for the R3 riveted series. Materials were assumed linear elastic and isotropic (E=210 GPa; ν=0.27).

The fatigue life of the riveted joints was simulated considering the fatigue crack initiation and propagation phases. Concerning the simulation of the fatigue crack initiation, the Morrow [5] relation (Equation (6.2)) was used with material constants identified for the base materials (see Table 6.5). In order to allow the fatigue crack initiation simulation, elastic finite element analyses were performed using the base finite element models without cracks (ANSYS® or ABAQUS® models). Then, the elastic stress field was transformed into elastoplastic strains, using the Neuber's approach [3].

The fatigue crack propagation was simulated through the integration of the Paris law, identified for the current S235 steel (see constants on Table 6.6). The crack was propagated according constant crack increments of 1.0 mm.

Table 6.5 – Constants of the strain-life Morrow relation for S235 steel.

Material	σ'_f/E	ε'_f	c	b
S235 steel	0.004	1.348	-0.740	-0.081

Table 6.6 – Constants of the Paris equation for S235 steel.

Material	C^*	M
S235 steel	2.36E-16	3.97

*da/dN in mm/cycle and ΔK in $N.mm^{-3.5}$

The ANSYS® code was used whenever the fatigue crack opropagation was simulated using the VCCT approach, for stress intensity factors computation. ABAQUS® was used with the XFEM approach and J-integral for stress intensity factors computation. Since the simulation of riveted joints requires the use of contact finite elements, and the XFEM approach in ABAQUS® [1] does not supported contact finite element elements, the XFEM approach was limited to a specific situation where contact elements were avoided. This was the case of the R1 riveted series, with a fatigue crack propagating at the corner of the angle.

The contacts between plates and between the rivet and plates were modelled using contact finite elements available in ANSYS®, using a surface-to-surface option. In particular, the CONTA174 and TARGE170 elements were used to model, respectively, the contact and target surfaces, forming the so-called contact pairs. Both surfaces in contact were assumed flexible. Due to the contact simulation, the finite element model becomes non-linear. Therefore an incremental solution analysis was required. The contact simulation was carried out using the Augmented Lagrange algorithm available in the ANSYS®, together with the Coulomb friction model (friction coefficient equal to 0.3 [30]). The Augmented Lagrange method requires the definition of the normal contact stiffness. The amount of penetration between the contact and target surfaces depends on the normal stiffness. Higher stiffness values decrease the amount of penetration, but can lead to ill-conditioning of the global stiffness matrix and to convergence difficulties. Lower stiffness values can lead to a certain amount of penetration and produce an inaccurate solution. Ideally, it is desirable a high enough stiffness that the penetration is acceptably small, but a low enough stiffness that the problem will be well-behaved in terms of convergence. On effect, a stiffness relationship between two bodies must be established for contact to occur. Without contact stiffness, bodies will pass through one another. The relationship is established through an 'elastic spring' that is put between the two bodies, where the contact force is equal to the product of the contact stiffness (κ) and the penetration (δ). The amount of penetration (δ), or incompatibility, between the two bodies is therefore dependent of the stiffness (κ). Ideally, there should be no penetration, but this implies that $\kappa=\infty$, which will lead to numerical instabilities. The value of κ that is computed by ANSYS®, depends on the relative stiffness of the contacting

bodies. There is the possibility of scaling κ through the FKN factor, usually called the normal penalty stiffness factor. The usual factor range is from 0.01 to 1.0, with a default of 1.0. The default value is appropriate for bulk deformation. Another relevant contact parameter to be used in conjunction with the augmented Lagrange method is FTOLN. FTOLN is a tolerance factor to be applied in the direction of the surface normal. The range for this factor is less than 1.0 (usually less than 0.2), with a default of 0.1, and is based on the depth of the underlying solid element. This factor is used to determine if penetration compatibility is satisfied. Contact compatibility is satisfied if penetration is within an allowable tolerance (FTOLN times the depth of underlying elements). The depth is defined by the average depth of each individual contact elements in the pair. If ANSYS® detects any penetration larger than this tolerance, the global solution is still considered unconverged, even though the residual forces and displacement increments have met convergence criteria. Default values of FTOLN and FKN were considered in this study [27]. Null clearance between the riveted holes was considered, as this is a characteristic of riveted connections.

Two distinct fatigue failure modes were observed for the riveted specimens R1 (see Chapter IV). Some failure modes were characterized by fatigue cracks that initiated at the upper most rivet hole and propagated towards the flange/web end section corner. The other failure mode consisted of a fatigue crack that initiated and propagated at the corner of the angle according to a direction perpendicular to the beam longitudinal axis direction. Three fatigue crack propagation models were built. In the first one, a constant depth crack, emanating from the rivet hole (see Figure 6.31) was simulated using a fatigue crack branching criteria (mixed-mode fatigue crack propagation conditions assumed). The second and third models considered a fatigue crack starting at the corner of the angle and propagating along the vertical direction (pure mode I approach adopted) (see Figures 6.32 and 6.33). The latter two cases were simulated using FEM with VCCT approach (Figure 6.32) and using XFEM (Figure 6.33). The first two models proposed for the R1 series were built in ANSYS® and the latter model was built in ABAQUS®.

The first crack propagation model proposed for the R1 specimens was built considering prismatic shaped (10 nodes) and pyramidal shaped (13 nodes) quadratic finite elements in the expected crack propagation region to allow easy remeshing during mixed-mode crack propagation and using of quadratic 20-noded finite elements elsewhere. An initial

crack length of 0.5 mm was considered. The numerical model allowed mixed mode I+II stress intensity factors computation. In order to define the crack path, a fatigue crack branching criterion was defined and the kink angle was computed from the K_I and K_{II} stress intensity factors, according to the maximum hoop stress criterion [8]. Contact finite elements, between plates and rivets, were considered. The number of cycles required to propagate the crack was computed using an effective stress intensity factor and the integration of the Paris relation. The R1 riveted specimens were loaded at the free end of the beam. A clamping stress of 30MPa was applied to the rivets.

The second finite element model proposed for the simulation of the fatigue crack propagation for the R1 riveted series also assumed a constant depth crack. However, this numerical model postulate a fatigue crack located at the corner of the angle, which is another failure mode observed for the R1 riveted joint (see Chapter IV). The finite element model was build using quadratic 20-noded finite elements. Pure mode I crack propagation was considered in this analysis. Also, contact finite elements were considered for all components in contact. Clamping stresses of 30MPa were also considered. Both previous finite element models were built using the commercial software ANSYS®.

The third numerical model proposed to simulate the fatigue crack propagation phase for R1 riveted specimens was built using the commercial software ABAQUS®. A XFEM crack was assumed at the corner angle, as observed experimentally in Chapter IV. Linear 8-noded finite elements was used to model the cracked beam, since the XFEM methodology available in ABAQUS® does not allow high order finite elements. The XFEM methodology also does not allow the use of contact methodology, therefore no clamping stress were considered in the rivets. Continuity between rivets and beam/angle was assumed. However, angle and beam were respectively build as two components linked only at rivets. The initial crack depth postulated for this simulation was of 0.8 mm. For the other previous models, the initial postulated crack was 0.5 mm. These distinct initial crack criteria was motivated by a difficulty of using XFEM to simulate small cracks without using not too much refined meshes. However the two values are within the usual range proposed in the literature for the initial cracks in the two-stage (initiation plus propagation) fatigue damage simulations.

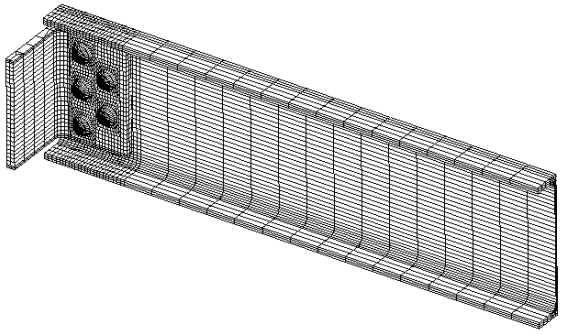

a)

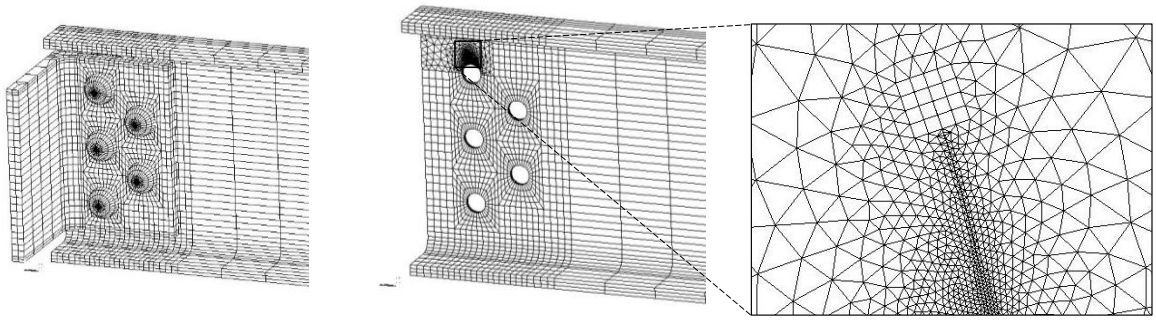

b)

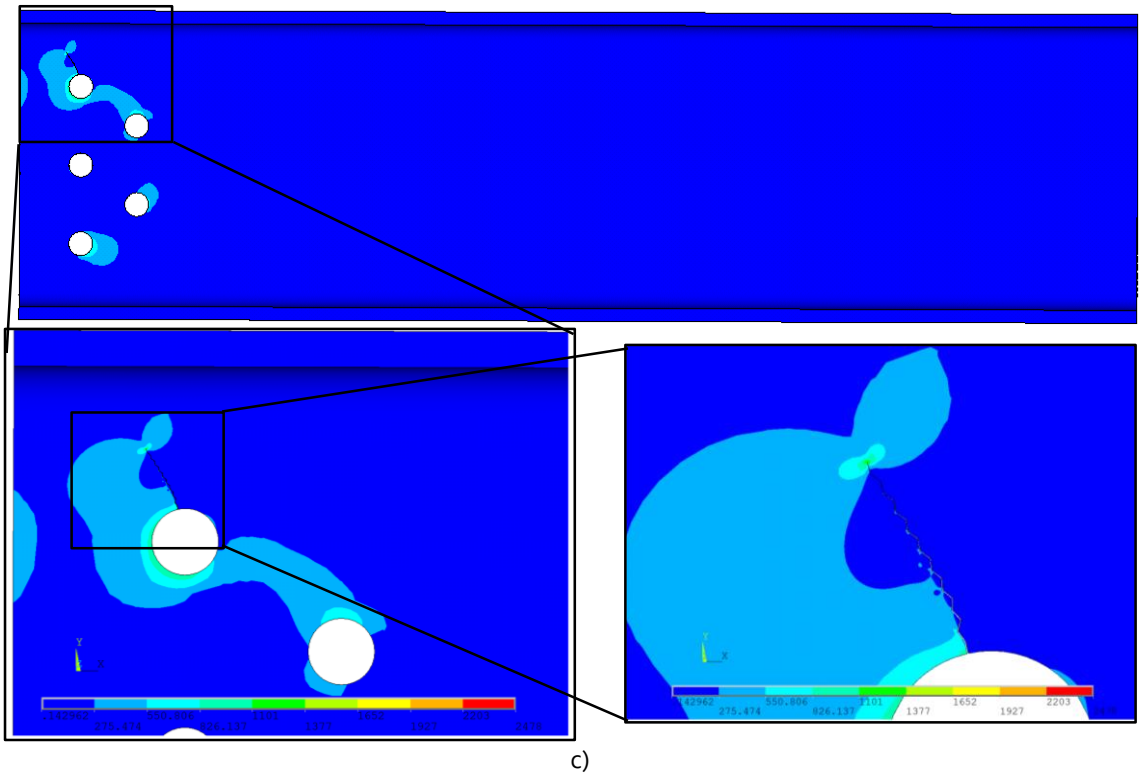

c)

Figure 6.31 – Finite element model for the R1 specimen with a crack emanating from the upper most rivet hole: a) global finite element mesh; b) local finite element mesh; c) Von Mises stress field for a particular crack size.

Regarding the simulation of the fatigue crack propagation phase for the R2 specimens, a symmetrical fatigue crack, growing from the rivet hole, was simulated (Figure 6.34a)). For this numerical model, a pure mode I fatigue crack propagation was assumed with a

crack path perpendicular to the loading direction (Figure 6.34b)). Quadratic 20-noded finite elements were used. Contact finite elements were defined between all structural components, such as the plates and rivets. Figure 6.34c) plots the σ_y stress map for a particular fatigue crack size.

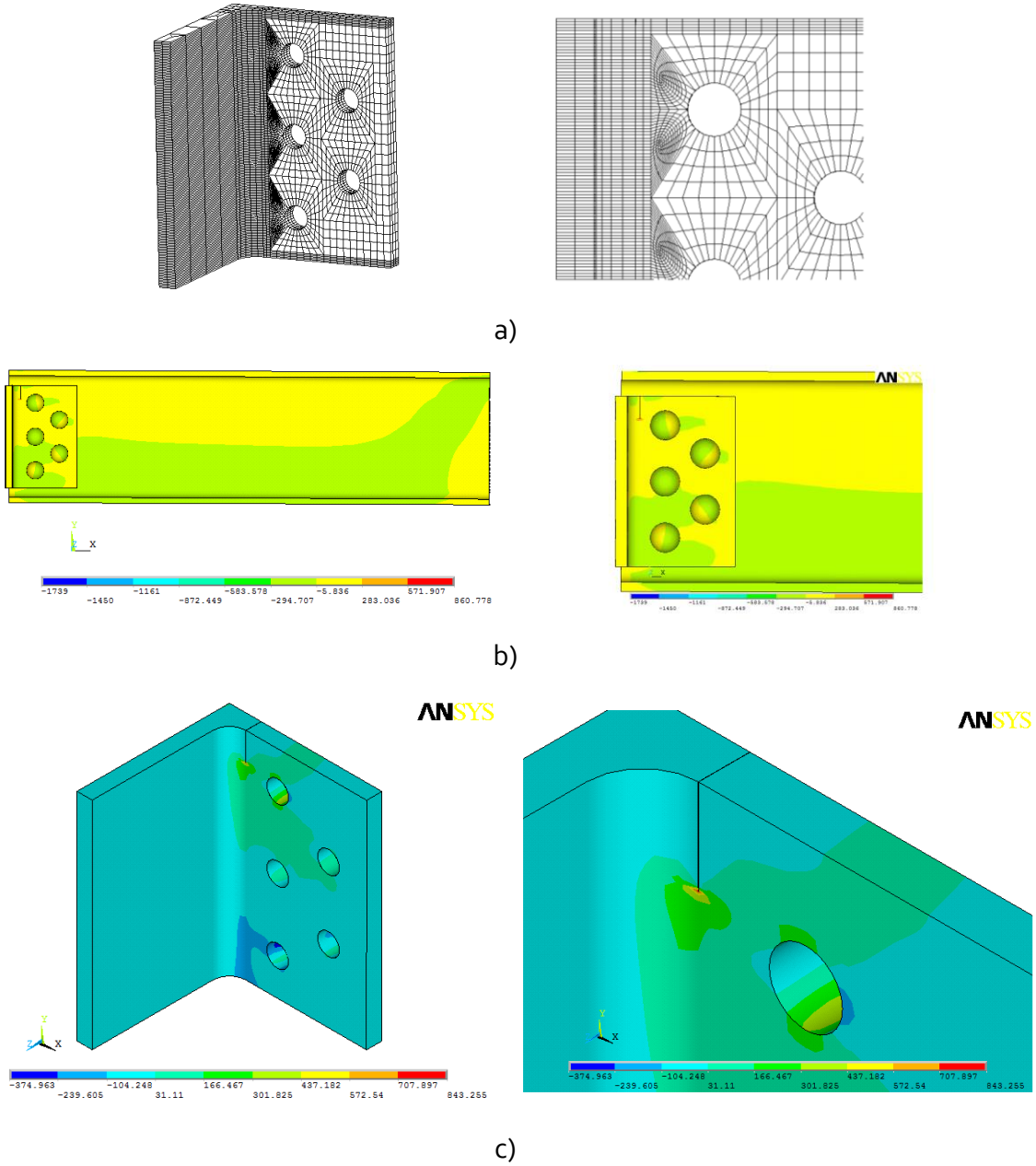

Figure 6.32 – Finite element model for the R1 riveted specimen with crack propagating at the angle corner): a) finite element mesh of the angle; b) illustration of σ_x stress field for a particular crack; c) detail of the σ_x stress field.

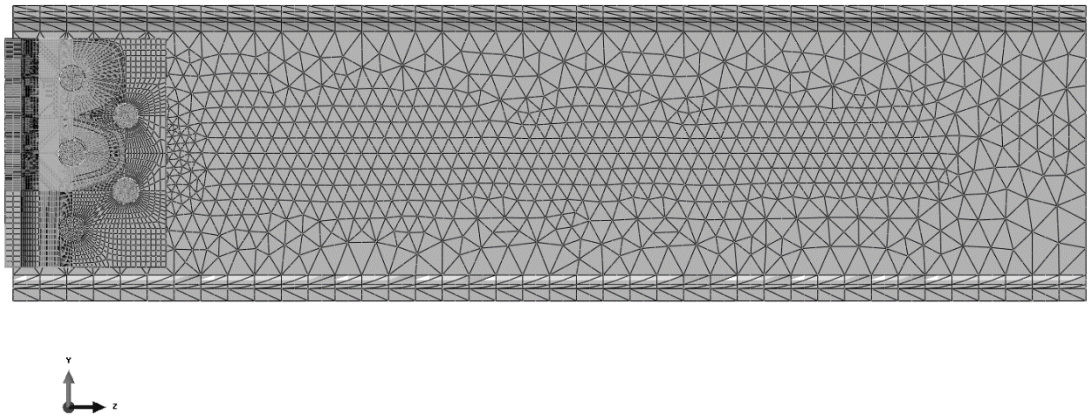

a)

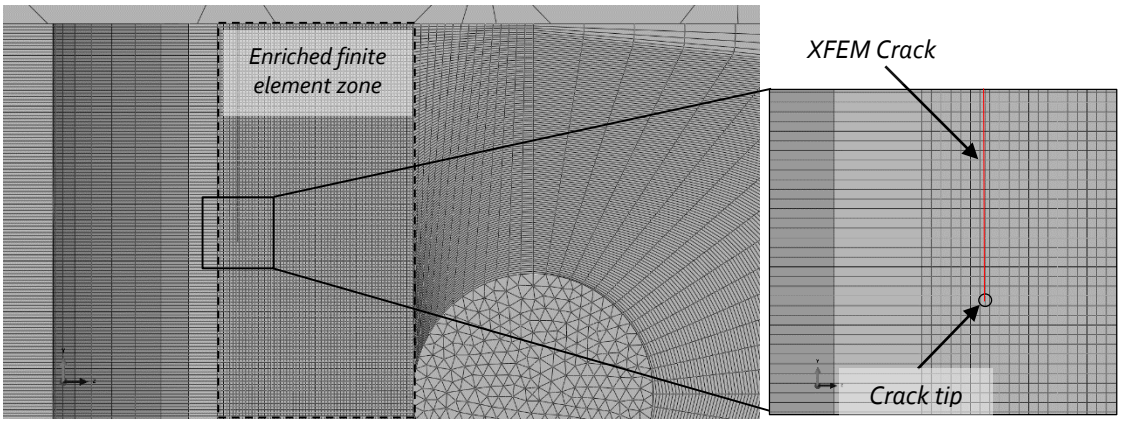

b)

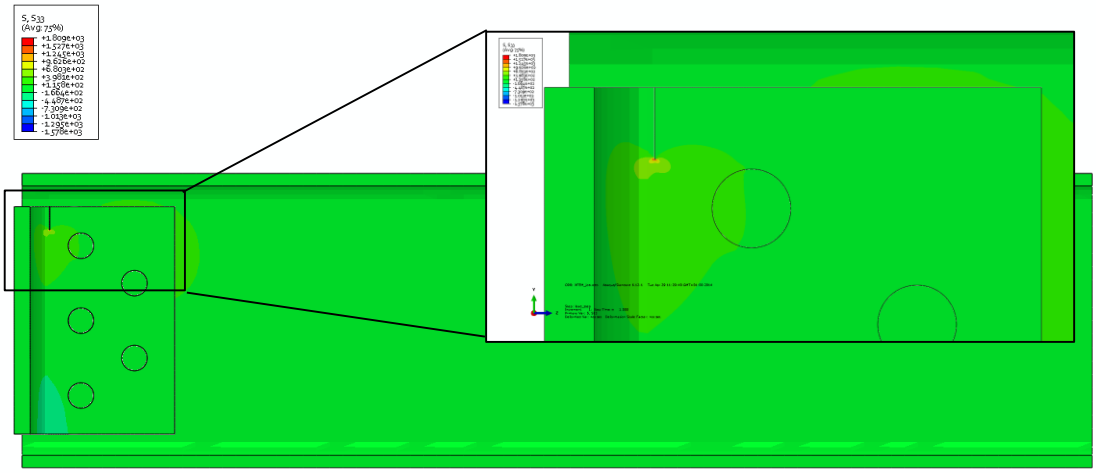

c)

Figure 6.33 - R1 riveted specimen modelled with XFEM and crack emanating from angle corner: a) global finite element mesh; b) local finite element mesh and XFEM crack location; c) σ_z stress field

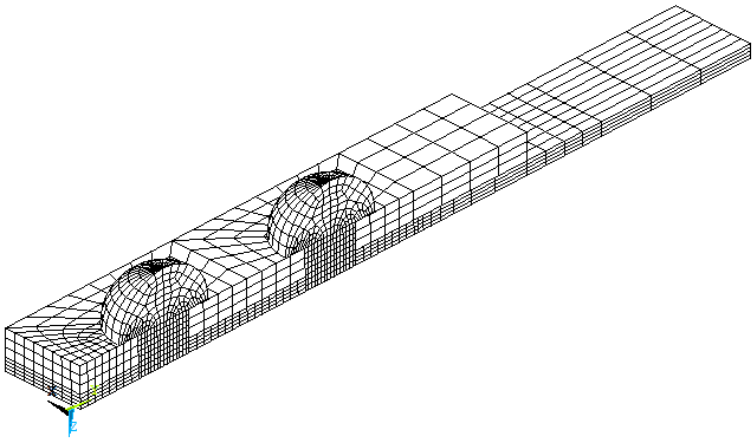

a)

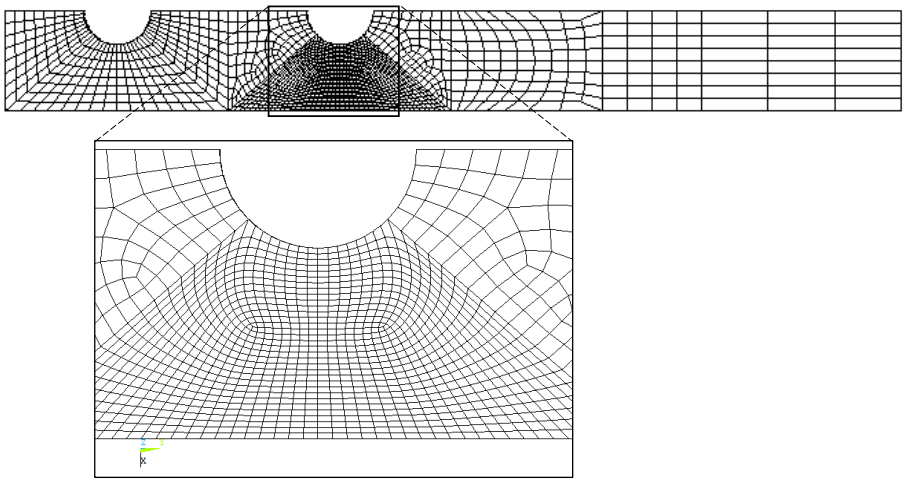

b)

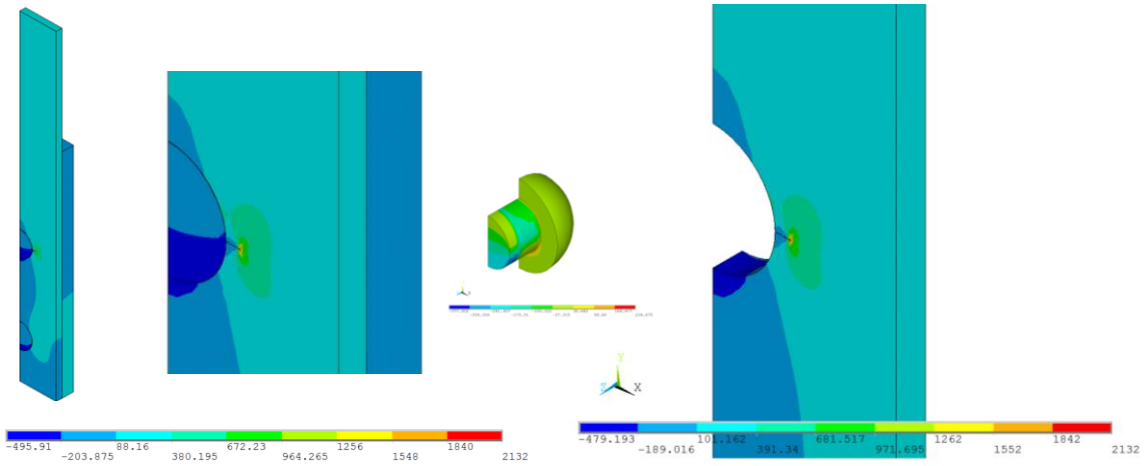

c)

Figure 6.34 – Finite element model of the R2 riveted specimen: a) global finite element mesh; b) local finite element mesh; c) σ_y stress field for a particular fatigue crack.

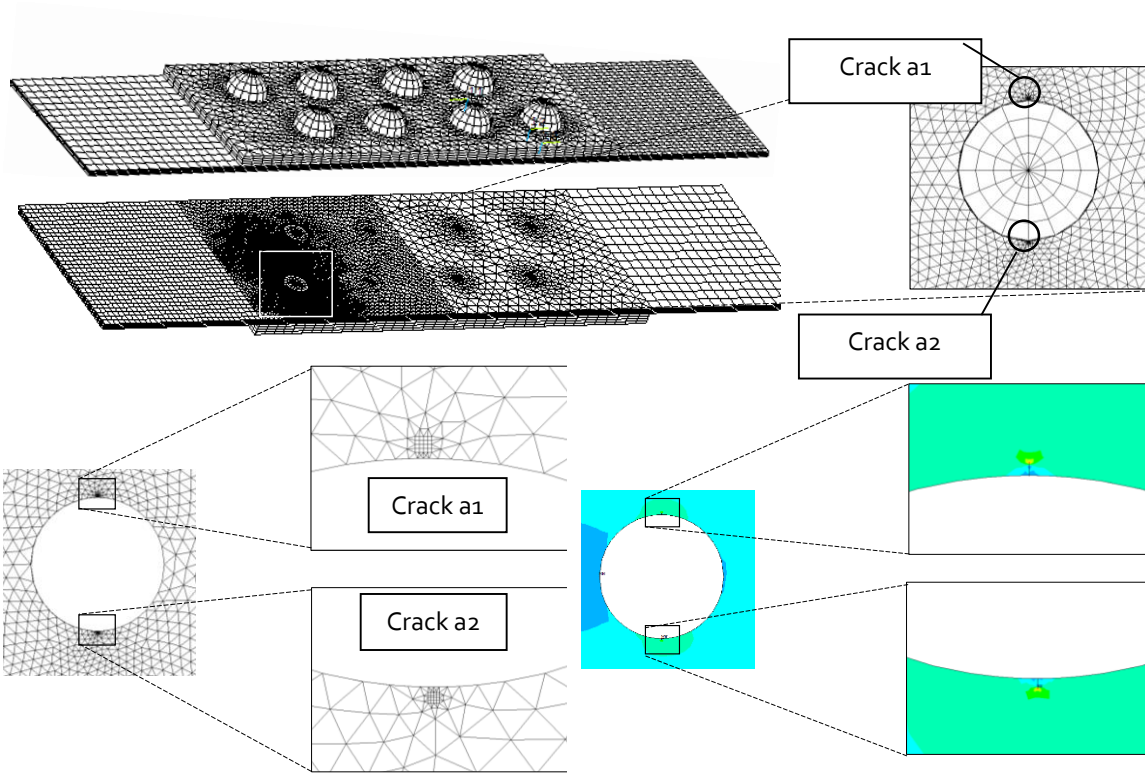

Figure 6.35 - Finite element model for the R3 riveted specimen.

The R3 riveted specimens were modelled considering two cracks (a1 and a2) emanating from the first rivet hole, as observed in the experimental tests (Figure 6.35). The crack a1 propagated towards the half width of the plate. The crack a2 also started at the rivet hole however it propagated towards the plate edge of the riveted specimen model. Mixed-mode fatigue crack propagation conditions were assumed. A fatigue crack branching criterion was selected (maximum tangential stress criteria) and the kink angle assessed from computed K_I and K_{II}, using the Tanaka [9] crack branching criterion. The crack increment was imposed to the crack a1 being equal to 0.5mm. Given this crack increment, the corresponding number of cycles was assessed using an effective stress intensity factor and the Paris's law [2]. With these cycles, the crack increment for the crack a2 was computed taking into account the effective stress intensity factor computed with K_I and K_{II} assessed at the a2 crack tip.

The fatigue life predictions were based on a procedure that accounts separately the crack initiation and crack propagation phases. The number of cycles to failure was, therefore, computed as the summation of the number of cycles required to initiate a crack and the number of cycles to propagate the crack until the failure of the component. The criterion for the crack initiation was the development of a macroscopic crack of 0.5 mm depth. The

crack initiation was modelled using the Morrow's relation [5] which requires the local elastoplastic strains at the crack initiation site, which were computed using the Neuber's approach. Since the stress concentration at the two crack initiation spots considered in this example were very close to each other, both initial cracks were postulated at the beginning of the crack simulation process.

Figures 6.36 compares the experimental mean S-N curves with numerical fatigue life predictions obtained for the R1 riveted specimens using the finite element model simulating a fatigue crack emanating from the rivet hole. The number of cycles required to initiate a fatigue crack (black line), the number of cycles required for the fatigue crack propagation (dashed black line) and the total number of cycles to failure (grey continuous line) are plotted in the figure. The experimental mean S-N curve is also presented as a dotted line. The simulations confirmed a dominant fatigue crack propagation phase. The simulations overestimated the total fatigue lives and the mean experimental S-N curve for medium to high cycle fatigue. The numerical S-N curve slope, *m*, is higher than the experimental S-N curve slope. However, the experimental slope is not characteristic of the failure mode characterised by the crack propagation from the rivet hole. If the two experimental points tested at the lowest stress ranges, corresponding to another failure mode (failure at the angle corner), are removed from the analysis, the resulting experimental mean S-N curve will show a slope very similar to the simulated S-N curve. The overestimation of the simulation S-N curve will be lower if the consistent failure mode is considered. It is very likely that the crack initiation simulation was overestimated in this process. In fact, the surface quality of the rivet holes was not controlled during the manufacturing process; a poor quality is expectable which may justify lower crack initiation lives. It must be emphasized that crack initiation was simulated using smooth/polished specimens fatigue data.

Figures 6.37 compares the experimental mean S-N curve with numerical S-N curves computed for R1 riveted specimens, assuming a fatigue crack propagating at the angle corner. Numerical results from standard finite element method and extended finite element models are presented. It can be observed that the total predicted fatigue life computed using the XEFM model provides a numerical S-N curve (grey continuous line) similar to the experimental S-N curve and only slightly above of the two experimental data points corresponding to the angle cracking failure mode. Figure 6.37 also illustrates

that the two numerical approaches resulted in a similar fatigue crack propagation curves. However the number of cycles computed using both numerical approaches to predict the fatigue crack initiation was very distinct. This is only justified by distinct stress estimates at the uncracked angle corner. The assumptions adopted for the finite element models to be used with XFEM included continuity between the rivets shoulders and the hole surfaces, at the angle leg and at the beam web. This condition led to higher stresses at uncracked angle corners, resulting significantly lower fatigue lives, but significantly more consistent with the experimental data. This result emphasizes an overestimation of the load transfer by friction (preload/friction coefficient not fully tuned) in the multi-body approach using contact finite elements (FEM approach). As observed in Figure 6.36, the propagating phase is not dominant as observed before for the failure mode consisting of a fatigue crack emanating from the rivet hole (see Figure 6.35).

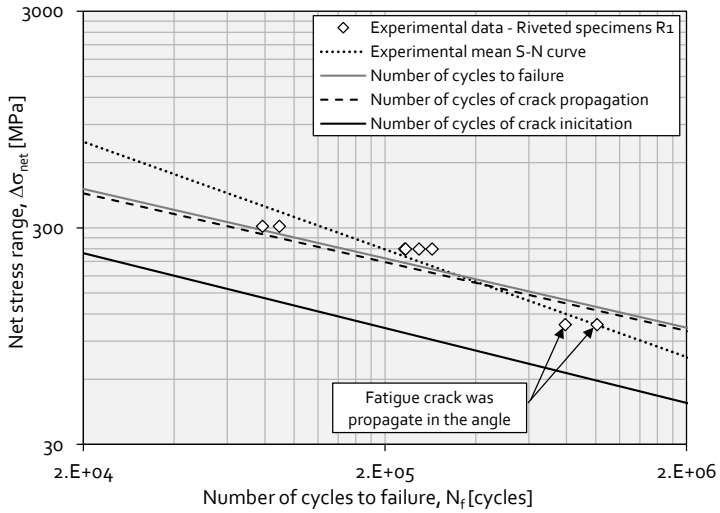

Figure 6.36 - Comparison between R1 riveted specimen experimental S-N curve with numerical results of the model with a crack propagating at the web, from a rivet hole.

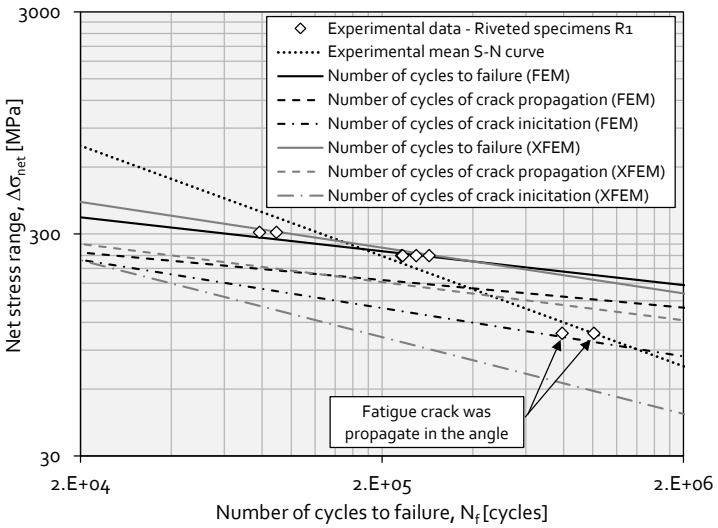

Figure 6.37 - Comparison between R1 riveted specimen experimental S-N curve and the numerical results obtained with the FEM model and XFEM with a crack propagating at angle corner.

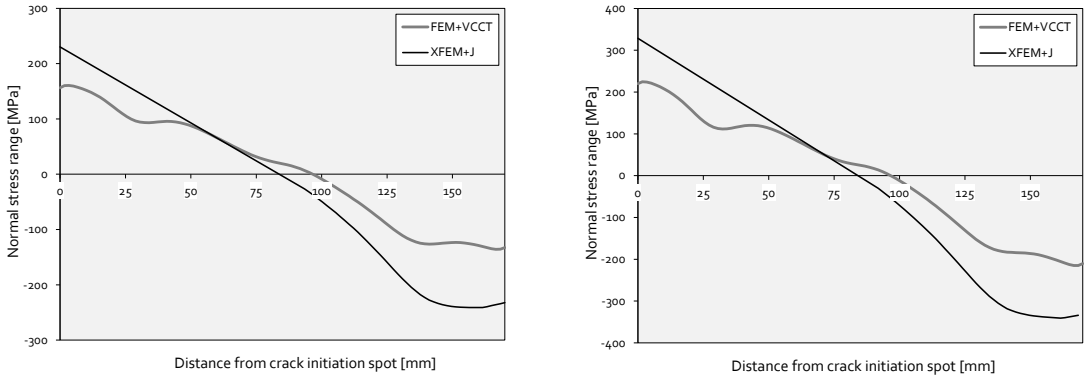

Figure 6.38 - Normal stress range evolution at the net section of the angle: a) applied load of 18kN; b) applied load of 25kN.

In order to get a clear indication of the effects of the two modelling assumptions on stress fields, Figure 6.38 plots the normal to the crack surface stress evolution for both numerical models used to simulate the crack propagation at the angle corner. It is shown that the numerical model built using the XFEM methodology exhibits higher stress values at the crack initiation spot, which is consistent with the above-mentioned crack initiation predictions. The model used to implement the XFEM approach gives a stress distribution that is compatible with a higher moment transferred thru the angles. Figure 6.39 compares the effective stress intensity range evolution, computed using contour integral method (XFEM) and VCCT (FEM) for an applied load range of 18 kN and load ratio of 0.1. Figure 6.39 exhibits that both simulation approaches yield similar stress intensity factors, with the XFEM slightly

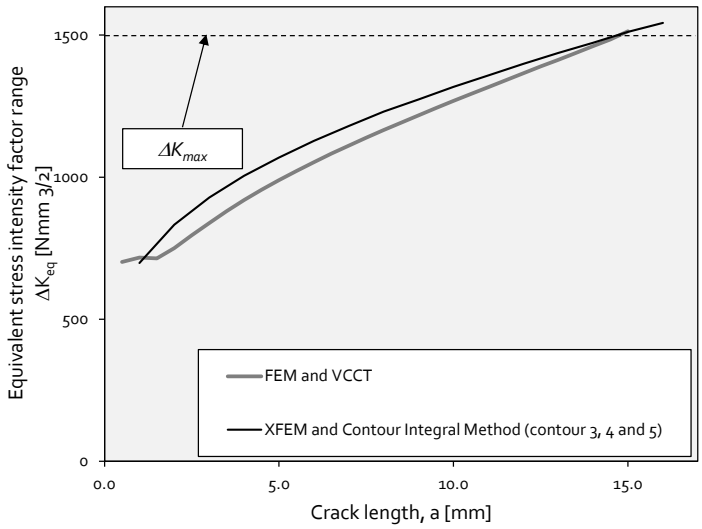

Figure 6.39 - Effective stress intensity factor range evolution computed using FEM plus VCCT and XFEM plus contour integral method, for a propagating crack at the angle corner (ΔP=18 kN).

Figure 6.40 shows numerical S-N results for the R2 riveted specimens which were simulated using two distinct clamping stresses, namely 30MPa and 80MPa. In both cases the predictions were conservative, i.e., fatigue lives were underestimated for the complete range of tested stresses. The simulated crack initiation and propagation phases demonstrated to be more balanced, without a significant domination of one phenomenon over the other. The clamping stresses have a significant effect on predictions. The consideration of a higher clamping stress in the rivets enhanced the fatigue predictions, including the slope of the resulting numerical S-N curve. The actual values on riveted specimens are not known, the simulations suggesting clamping stresses even higher than 80MPa. The numerical model of the R2 specimens was based on the ideal geometry of the joint, which leads consequently to a symmetrical crack propagation, which was not fully observed in the tests due to small misalignments. A two cracks (multi-site damage) model would be preferable, but it would lead to similar results if the ideal specimen geometry still is considered. A way to introduce random asymmetries in the specimens would be required.

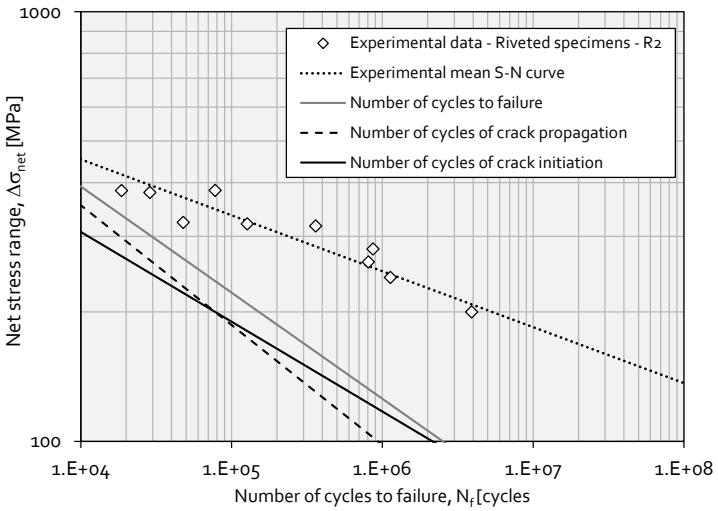

a)

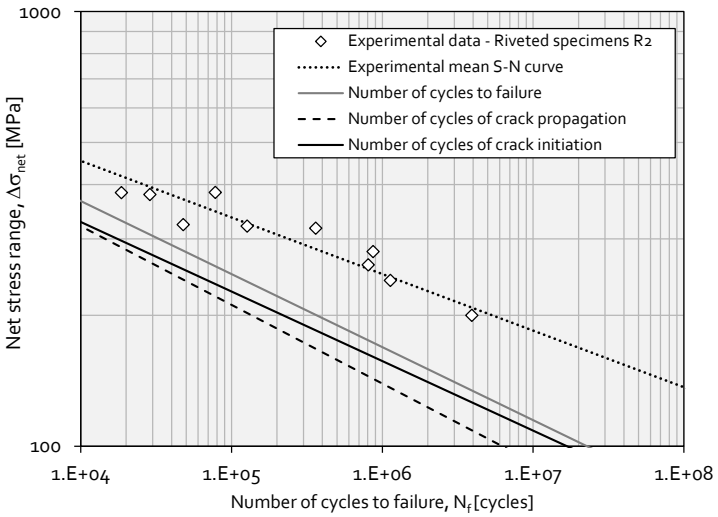

b)

Figure 6.40 - Comparison between R2 riveted specimen experimental S-N data and simulation results: a) clamping stress of 30MPa; b) clamping stress of 80MPa.

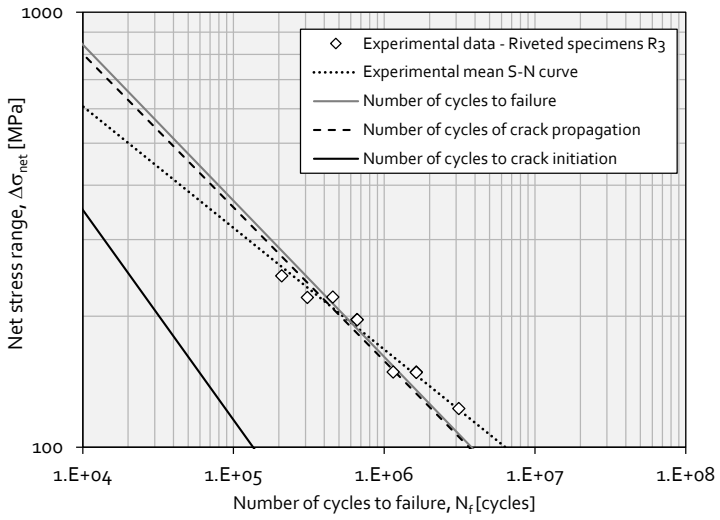

a)

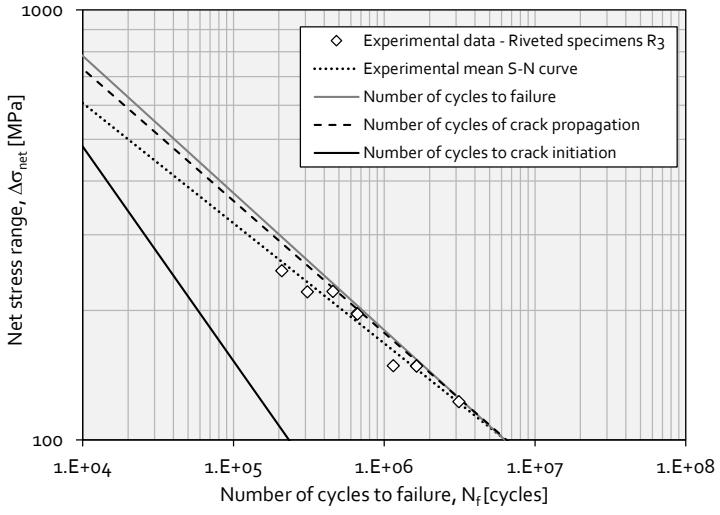

b)

Figure 6.41 - Comparison between R3 riveted specimen experimental S-N data and simulation results: a) clamping stress of 30MPa; b) clamping stress of 80MPa.

Figures 6.41a) and b) plot the numerical S-N curves vs. experimental S-N data for the R3 riveted specimens. The same two clamping stresses used for the R2 specimens, were also adopted for this series. The computed number of cycles corresponding to the fatigue crack propagation is significantly higher than the number of cycles necessary to initiate a fatigue crack. The analysis of the global predictions illustrated in the Figure 6.41 shows very accurate predictions for the R3 riveted joints, including a fair description of the S-N slopes. In is interesting to note that the clamping stress variation did not resulted in significant variation in the predicted S-N curves as observed for the R2 riveted series.

6.9. CONCLUDING REMARKS

This chapter presented the fatigue simulation results for the welded and riveted specimens tested in the present research. For the riveted specimens, a fatigue model based exclusively on the fatigue crack propagation phase produced very consistent results. In the simulation of the riveted specimens, both crack initiation and crack propagation phases were considered since for non-welded material fatigue crack initiation could represent an important contribution to the total fatigue life. Well established approaches were used for both fatigue crack initiation and fatigue crack propagation simulations, respectively the local strain approach and the fracture mechanics-based Paris propagation law.

Concerning the welded specimens, the required stress intensity factors for fatigue crack propagation simulation were computed based on two alternative techniques. A standard finite element method was considered with the VCCT technique. However, this could represent a cumbersome approach to apply in 3D problems with complex geometries, once the crack path must be compatible with the finite element mesh. An alternative method to compute the stress intensity factors, using the extended finite element method, was adopted. This method allows the fatigue crack modelling, independently of the finite element mesh. Both methods were applied to compute the stress intensity evolution, and slight differences were verified in the stress intensity values but these

differences did not resulted in significantly distinct fatigue life predictions for the welded joints. The predicted fatigue S-N curves were very consistent with available experimental data, which validates both proposed fatigue model as well as the techniques for stress intensity factors computation. It is clear that the crack propagation phase was the controlling damage mechanism for the riveted joints.

Concerning the simulation of the riveted specimens, the XFEM method was only applied to the R1 series with a crack propagating at the corner angle. Contact elements were not used in this case, and surprisingly it resulted in better total fatigue life predictions than using contact elements between the connection parts. The use of contact finite elements required the definition of the friction coefficient and clamping stresses on rivets which are usually an unknown, calibration procedures being required. The use of the same clamping stresses and friction coefficients resulted in distinct simulation results. The use of a clamping stress of 30MPa in the R1 series conducted to an overestimation of the fatigue lives (unsafe predictions). For the R2 tested series it was demonstrated that the clamping stress of 30MPa led to an underestimation of the fatigue lives. The increase in the clamping stresses to 80MPa reduced the discrepancy in the simulations, but the deviations still observed suggested even higher clamping stresses for the R2 series. Finally, for the R3 series the predictions were very accurate and the clamping stress variation between 30 and 80MPa did not resulted in significant change in the predicted results. This overview of the predictions suggests that the clamping stresses were not uniform in the manufacturing of the riveted series. For more simple details seems that the process of riveting is more controllable and higher clamping stresses are consequently obtained. For the more complex details as the R1 series the clamping stresses should be negligible. This is strengthened by the fact that the XFEM model (no clamping stresses simulated) yielded the better results for the R1 series.

This chapter also assessed the performances of the FEM plus VCCT and XFEM plus Interaction Integral approaches in the computation of stress intensity factors for some simple verification examples. Concerning the XFEM plus Interaction Integral approach it was verified that several contours should be considered, but the first contour closest to the crack tip should be avoided, otherwise spurious results will be obtained. Also it was verified that when a XFEM crack appears close the finite element boundaries it may cause some instability in the FEM results. The simulation of very small cracks may also

constitute a difficulty for the XFEM approach since it would require refined meshes in order to allow reliable information at the contours established around the crack tip. Concerning the mesh convergence studies, it was demonstrated that progressive mesh refinements did not produced monotonic convergence of the computed stress intensities. An average mesh refinement in general produces satisfactory results. Comparing the two approaches it was not possible to establish a definite conclusion about the better approach in terms of accuracy for the stress intensity factor computation.

6.10. REFERENCES

[1] Abaqus Analysis User's Manual, Version 6.12-1, Dassault Systémes Simulia Corp., Providence, RI

[2] Krueger, R., "Virtual crack closure technique: History, approach, and applications", Applied Mechanics Reviews, pp. 109-143, 2004.

[3] Paris, P., Erdogan, F., "A critical analysis of crack propagation laws", Journal of Basic Engineering 85, pp. 528-534, 1963.

[4] Neuber, H., "Theory of Stress Concentration for Shear-Strain Prismatic Bodies with Arbitrary Nonlinear Stress-Strain Law", Translation of the ASME, Journal of Applied Mechanics. 28, pp. 544-550, 1961.

[5] Ramberg, W., Osgood, W.R., "Description of stress-strain curve by three parameters. National Advisory Committee for Aeronautics", Tech. Note No. 902, 1943.

[6] Morrow, J.D., "Cyclic plastic strain energy and fatigue of metals", International Friction, Damping and Cyclic Plasticity, ASTM, STP 378, pp. 45-87, 1965.

[7] Beden, S.M., Abdullah, S., Ariffin, A.K., "Review of Fatigue Crack Propagation Models for Metallic Components," European Journal of Scientific Research, 28: 364-397, 2009.

[8] Erdogan F., Sih, G.C., "On the Crack Extension in Plates Under Plane Loading and Transverse Shear", Journal Basic Eng. Trans. ASME, pp. 519-527, 1963.

[9] Tanaka, K., "Fatigue crack propagation from a crack inclined to the cycle tensile axis", Engineering Fracture Mechanics 6(3), pp.493-507, 1974.

[10] Irwin, G.R., "Fracture", Handbuch der Physik, S. Flügge, editor. 6, pp. 551-590, 1958.

[11] Irwin, G.R., "Analysis of stresses and strains near the end of a crack traversing a plate", Journal of Applied Mechanics. 24, pp. 361-364, 1957.

[12] Irwin, G.R., "A continuum-mechanics view of crack propagation", Metallurgical Reviews. 10, No. 38, pp. 223-270, 1965.

[13] Miannay, Dominique, P., "Fracture Mechanics", Springer-Verlag New York Inc., New York, 1997.

[14] Shih, C.F., Moran, B., Nakamura, T., "Energy release rate along a three-dimensional crack front in a thermally stressed body", International Journal of Fracture 30, No. 2, 1986, pp. 79-102, 1985.

[15] Rice, J.R. "A path independent integral and the approximate analysis of strain concentrations by notches and cracks", Journal of Applied Mechanics. 35, No 2, 1968, pp. 379-386, 1968.

[16] Shih, C.F., Asaro, R.J., "Elastic-Plastic Analysis of Cracks on Bimaterial Interfaces: Part I - Small Scale Yielding", Journal of Applied Mechanics 55, pp. 299-316, 1988.

[17] Belytschko, T., Black, T., "Elastic crack growth in finite elements with minimal remeshing", International Journal for Numerical Methods in Engineering, pp 602-620, 1999.

[18] Moës, N., Belytschko, T., "Extended finite element method for cohesive crack growth", Engineering Fracture Mechanics, pp 813–833, 1999.

[19] Moës, N., Dolbow, J., Belytschko, T., "A finite element method for crack growth without remeshing", International Journal for Numerical Methods in Engineering, pp 131-150, 1999.

[20] Babuška, I., Melenk, J., "The Partition of Unity Method. International Journal for Numerical Methods in Engineering, pp. 727-758, 1997.

[21] Michael, L., Daniel, R., "Stationary 3D crack analysis with Abaqus XFEM for integrity assessment of subsea equipment", Department of Applied Mechanics, Division of Material and Computational Mechanics, Chalmers University of Technology, Göteborg, Sweden, 2012

[22] Fleming, M., Chu, Y.A., Moran, B., Belytschko, T., "Enriched element-free Galerkin methods for crack tip fields", International journal for numerical methods in engineeringb40(8), pp. 1483-1504, 1997.

[23] Osher, S., Sethian, J., "Fronts propagating with curvature dependent speed: algorithms based on Hamilton-Jacobi formulations", Journal of Computational Physics 89(1), pp. 12-49, 1988.

[24] Stine, V., "Numerical Simulation of Fatigue Crack Growth", NTNU- Trondheim, Norwegian University of Science and Technology, Product Design and Manufacturing, June, 2012.

[25] Laborde, P., Pommier, J., Renard, Y., Salaun, M., "High-order finite element method for cracked domains", International Journal for Numerical Methods in Engineering 64, pp.354-381, 2005.

[26] Stazi, F.L., Budyn, E., Chessa, J., Belytschko, T., "An extended finite element method for crack problems with curvature", Computational Mechanics 31, pp.38-48, 2003.

[27] SAS, ANSYS, Version 12.0, Swanson Analysis Systems Inc., Houston, 2010.

[28] BS 7910, 'Guide on methods for assessing the acceptability of flaws in metallic structures', BSI, 2005.

[29] Bower, A.F., "Applied mechanics of solids", CRC Press, 2009.

[30] de Jesus, A.M.P., da Silva A.L.L., Correia, J.A.F.O., "Fatigue of Riveted and Bolted Joints Made of Puddle Iron-An Experimental Approach", Journal of Constructional Steel Research, 2014

Chapter VII

Fatigue modelling of a relevant detail from the Trezói bridge

7.1. INTRODUCTION

This chapter presents a fatigue analysis of a representative detail from the Trezói riveted railway bridge. This bridge has been selected as a case study for some research projects in the last decade [1-2]. Also, several academic studies about the fatigue behaviour of the bridge has been published [3-4].Therefore, there is available significant information about the bridge, particularly about the mechanical properties of their materials and also about the typical load spectra the bridge has been subjected. In addition, global finite element models of the bridge were developed aiming dynamic simulation of the bridge [2].

Due to the available information about the bridge and also due to the collaboration of the author on the FADLESS European project, it was decided to develop a detailed local numerical model of a selected node of the bridge that was assumed as a potential critical node of the bridge [2].This local model was subjected to typical boundary condition histories obtained from global numerical models of the bridge. Also actual experimental strain data obtained from the bridge monitoring was used to validate both the local model and the boundary conditions. Finally, the fatigue damage assessment of the node was performed testing distinct levels of approaches. Since the bridge is a riveted bridge (no welds used), and no visible damage (cracks) on the bridge were observed during inspections performed to the bridge [2], it was decided to apply a local notch approach for fatigue crack initiation simulation. It is assumed that the crack initiation phase is a significant fatigue damage mechanism for riveted construction in opposition to the classical assumption for welded construction, where crack initiation may be neglected with respect to the fatigue crack propagation.

7.2. OVERVIEW OF THE PROPOSED APPROACH

A numerical finite element approach for the stress analysis of a representative detail (node) of the Trezói bridge is proposed in this chapter. Several levels of approximation will be simulated for the node, all involving 3D solid modelling. The node experiences a complex loading history, which results in complex multiaxial stress/strain histories. In particular non-proportional time-history stresses are expected. The principal stress directions rotate with time and there is not a clearly defined cycle (random stress spectra). The topic of non-proportional fatigue has deserved a lot of attention by scientists concerning the study of mechanical components [5]. However, the use of non-proportional multiaxial fatigue damage theories for the analysis of bridge details may be considered an innovative aspect of this work. The topic of non-proportional random fatigue is not completely solved, despite some available attempts, some of them being followed in this chapter. The main difficulty is concerned with the cycle counting (cycle definition) under non-proportional loading conditions, i.e., for situations that both the principal stress directions and their intensities vary with the time. For mechanical components these conditions have been investigated assuming that the loading history is formed by the repetition of small variable amplitude blocks. For these small blocks one equivalent cycle is extracted. For bridges, the block corresponds to a train crossing that may be repeated along the bridge life. The application of standard approaches for non-proportional fatigue would lead to one stress cycle for each train crossing which could be a non-conservative approach since other damaging cycles are most likely being disregarded.

Typically non-proportional multiaxial fatigue damage approaches try to identify the critical planes were fatigue cracking (damage) is most likely to occur. This is the base of the critical plane models, one of the important approaches in multiaxial fatigue, aside with the energy based approaches. For arbitrary multiaxial stress fields and complex details, the critical plane models application would require the scanning over an

important number of planes, at every point of the structure. Also the stress analysis has to be performed for each load step considered in the simulation of the train crossing. If several distinct train crossings are to be considered in the fatigue analysis, this task concerning a fatigue assessment of a real bridge detail could reach quickly a practical impossibility. Finally an important aspect of riveted joints simulation is the interaction of rivets with the plates, which must account for clamping effects and friction between elements. These interaction effects are responsible for non-linear finite element analyses.

For the aforementioned reasons, the fatigue damage assessment of real riveted bridge details is very time consuming, requiring a strategy for mitigating the computational costs. Therefore, a preliminary fatigue damage assessment of the structural node based on Von Mises equivalent stress is proposed to identify the most fatigue critical locations that will be subjected to a subsequent more refined non-proportional multiaxial fatigue damage assessment. In this simplified approach, the principal stress histories are derived at each node. The cycle counting is performed using the first principal stress, to establish the stress cycles ($\Delta\sigma_{1,i}$, n_i). The Rainflow cycle counting was considered in this investigation [6]. Assuming an approximation of proportional loading, the other principal stress ranges ($\Delta\sigma_{2,i}$, $\Delta\sigma_{3,i}$) are also defined by means of the same times (load steps) used to extract the first principal stress ranges. Then, equivalent stress ranges are computed using the Von Mises criterion as given by the following equation:

$$\Delta\sigma_{eq,i} = \frac{1}{\sqrt{2}}\sqrt{\left(\Delta\sigma_{1,i} - \Delta\sigma_{2,i}\right)^2 + \left(\Delta\sigma_{1,i} - \Delta\sigma_{3,i}\right)^2 + \left(\Delta\sigma_{2,i} - \Delta\sigma_{3,i}\right)^2} \tag{7.1}$$

Once the bridge detail is expected to show an elastic behaviour, one may apply the Basquin relation to derive the number of cycles to failure, N_i, for each equivalent Von Mises stress range, $\Delta\sigma_{eq,i}$:

$$\frac{\Delta\sigma_{eq,i}}{2} = \sigma'_f (2N_i)^b \tag{7.2}$$

A linear fatigue damage accumulation model, known as Miner's relation [7] may be considered to account for the different stress cycles:

$$D = \sum \frac{n_i}{N_i} \tag{7.3}$$

After the preliminary fatigue assessment is performed and most critical locations identified, a more refined non-proportional multiaxial fatigue assessment approach is proposed [5]. In the current work five distinct approaches are considered. A crucial problem regarding non-proportional multiaxial fatigue analysis is the cycle counting procedure definition. It is crucial to define the cycle counting strategy to be used for each approach. The first three approaches are strain-based models, namely the Smith-Watson-Topper (SWT) model, the Fatemi and Socie model and the Bannantine and Socie models. The Findley model, which corresponds to a stress-based approach [8], was also used following two formulations, particularly the original Findley and a modified Findley approach.

Smith *et al.* [9] proposed a fatigue damage parameter that relates the cyclic strain amplitude with the maximum stress. This parameter, commonly referred to as SWT parameter, was originally developed for uniaxial loading conditions to account for mean stress effects [8]. The SWT parameter has also being used in the analysis of both proportionally and non-proportionally loaded components constructed from materials that fail primarily due to mode I, tensile cracking [9]. The damage relation assumes the following form:

$$\sigma_{n,\max} \frac{\Delta\varepsilon_1}{2} = \frac{\sigma'^{\,2}_f}{E} (2N_f)^{2b} + \sigma'_f \varepsilon'_f (2N_f)^{b+c} \tag{7.4}$$

where $\Delta\varepsilon_1$ is the maximum principal strain range and $\sigma_{n,\max}$ is the maximum direct stress acting on the first principal strain range plane assessed during principal strain cycle counting procedure; σ'_f and b are respectively the tensile cyclic fatigue strength

coefficient and exponent; ε'_f and c are respectively the tensile cyclic fatigue ductility coefficient and exponent; E is the Young modulus and $2N_f$ is number of cycles to failure. Fatemi and Socie (FS) [10] suggested a damage parameter that results from the combination of the shear strain range and the normal stress:

$$\frac{\Delta\gamma}{2}\left(1+k\frac{\sigma_{n,\max}}{\sigma_y}\right)=\frac{\tau'_f}{G}(2N_f)^{b_\gamma}+\gamma'_f(2N_f)^{c_\gamma} \tag{7.5}$$

where, for a given plane, $\Delta\gamma$ is the shear strain range, $\sigma_{n,\max}$ is the maximum normal stress value assessed during the cycle counting procedure applied to the shear strain; τ'_f and b_γ are respectively the torsional cyclic fatigue strength coefficient and exponent; γ'_f and c_γ are respectively the torsional cyclic fatigue ductility coefficient and exponent; G is the shear modulus. This model assumes that mode II shear cracking is the dominant fatigue damage process. During shear loading, the irregularly shaped crack surface results in friction forces that will reduce crack tip stresses, thus hindering crack growth and increasing the fatigue life [8]. Tensile stresses and strains will separate the crack surfaces reducing the frictional forces.

Bannantine and Socie (BS) [8] proposed a multiaxial cumulative damage criterion based on the combination of critical plane damage parameters, rainflow cycle counting method and Miner's rule. The main concept behind BS criterion is to assess both the FS and SWT parameters for each plane. For this purpose the rainflow cycle counting technique is applied separately to the axial (normal) and shear strains. Then the FS and SWT damage parameters are computed independently and the damage associated to a specific plane is established as the greatest value given by the two alternative criteria (see Figure 7.1).

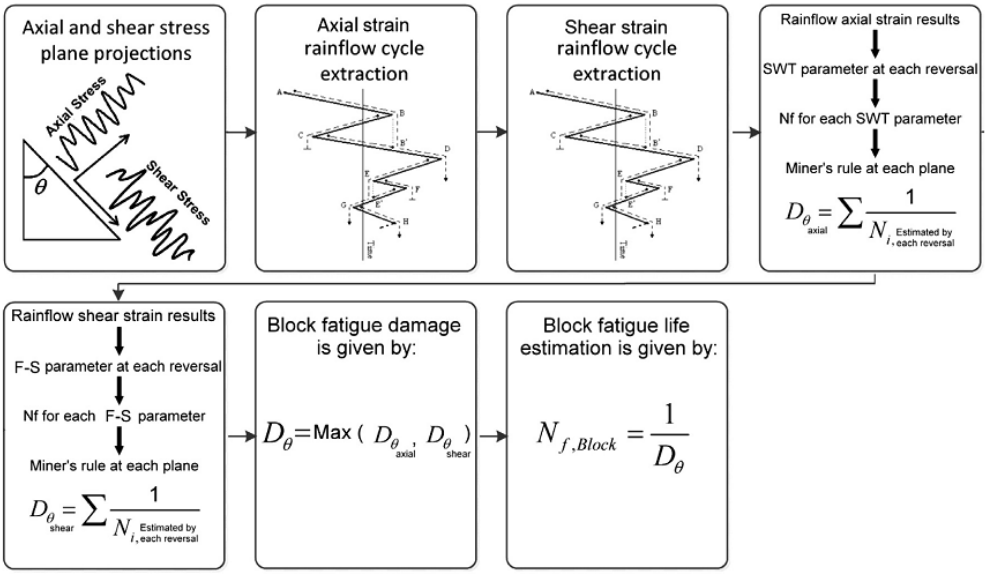

Figure 7.1 - Bannantine and Socie methodology [5].

Findley [11-14] criterion was also used in this investigation. This criteria was one of the first critical plane criteria being proposed. It considers that the shear stress amplitude $\Delta\tau/2$ is one of the most damaging parameters acting on a certain plane. The normal stress to that plain, $\sigma_{n,\max}$, has a secondary but not negligible effect on the fatigue damage. The Findley relation may be represented by the following equation [8]:

$$\frac{\Delta\tau}{2}+k\sigma_{n,\max}=\tau_f^*(N_f)^b \tag{7.3}$$

where k is a constant computed as $\sqrt{1+k^2}=1.04$, τ_f^* is computed from the torsional fatigue strength coefficient $\tau_f^*=\sqrt{1+k^2}\tau_f'$. The maximum normal stress value, $\sigma_{n,\max}$ is computed from the maximum of two load points (load steps) that were used to define the shear stress range, when the Rainflow procedure is applied. Another version of the Findley approach also considered in this work consisted in the definition of an equivalent shear stress parameter, $\tau_{eq}=\frac{\tau}{2}+k\sigma_{n,\max}$, that is computed for a specific plane along the time history. Then the cycle counting is applied directly to this equivalent shear stress parameter. This latter procedure is name here as modified Findley model.

7.3. FINITE ELEMENT MODEL OF A STRUCTURAL DETAIL FROM TREZÓI BRIDGE

Preliminary fatigue studies performed on Trezói bridge [2-3] pointed out the node 6 (see Figures 7.2 and 7.3) as one of the most fatigue critical detail of the bridge. In the previous fatigue studies, the S-N approach combined with 3D beam models of the bridge have been used. These global approaches are useful to identify in an efficient way the potential critical details of the bridge. However, they do not provide detailed information about the damage mechanisms. Also, the application of the global S-N approach to complex details such as the one selected in this work is not a straightforward task since the required nominal stresses may be not easily defined. Existing code based S-N curves for riveted details are mainly based on tensile stresses on members. Therefore, secondary bending dynamic effects that are frequent in bridges are not properly accounted using such a global S-N approach.

A local detailed finite element model of the structural node 6 was proposed using 3D solid quadratic finite elements. Materials were assumed linear elastic and isotropic (E=210 GPa; ν=0.27). The members connected in the node were modelled with 900 mm in length (see Figure 7.4). Two versions of the local model were constructed. The first model was built assuming full continuity between the components forming the node (Figure 7.5). The second finite element model was built assuming contact between the cross-girder and the remaining of the structural (Figure 7.6). Rivets were modelled between the cross-girder flange and the horizontal gusset (12 rivets) and between the cross-girder web and the angles (7 rivets). For the remaining components, full continuity is assumed. The model represented in Figure 7.5 has the same geometry of the model of Figure 7.6, including some rivets. However, in the model of Figure 7.5 the volumes were merged before meshing; when performing the mesh, a fully continuous model is obtained.

The simulation of all rivets actually used in the joint it is not possible since the model becomes too large for the simulation of a complete train crossing. Therefore, the

following strategy may be used to mitigate the high computational cost associated to a model with all rivets: several models can be developed, each one to assess a specific riveted part of a complex riveted detail, assuming continuity elsewhere. It is assumed that the behaviour of a specific riveted location is not influenced by the type of modelling approach used for other adjacent parts (riveting or continuity).

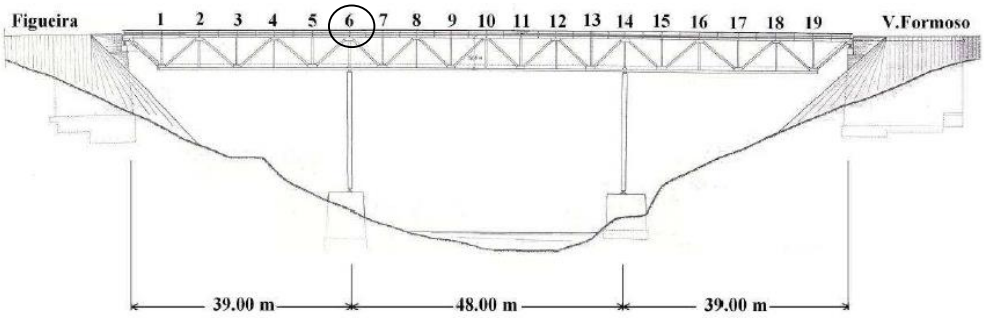

Figure 7.2 - Location of the potential critical node of the Trezói bridge to be fatigue assessed using a detailed local model (node 6).

Figure 7.3 - Potential critical node (node 6): actual photograph.

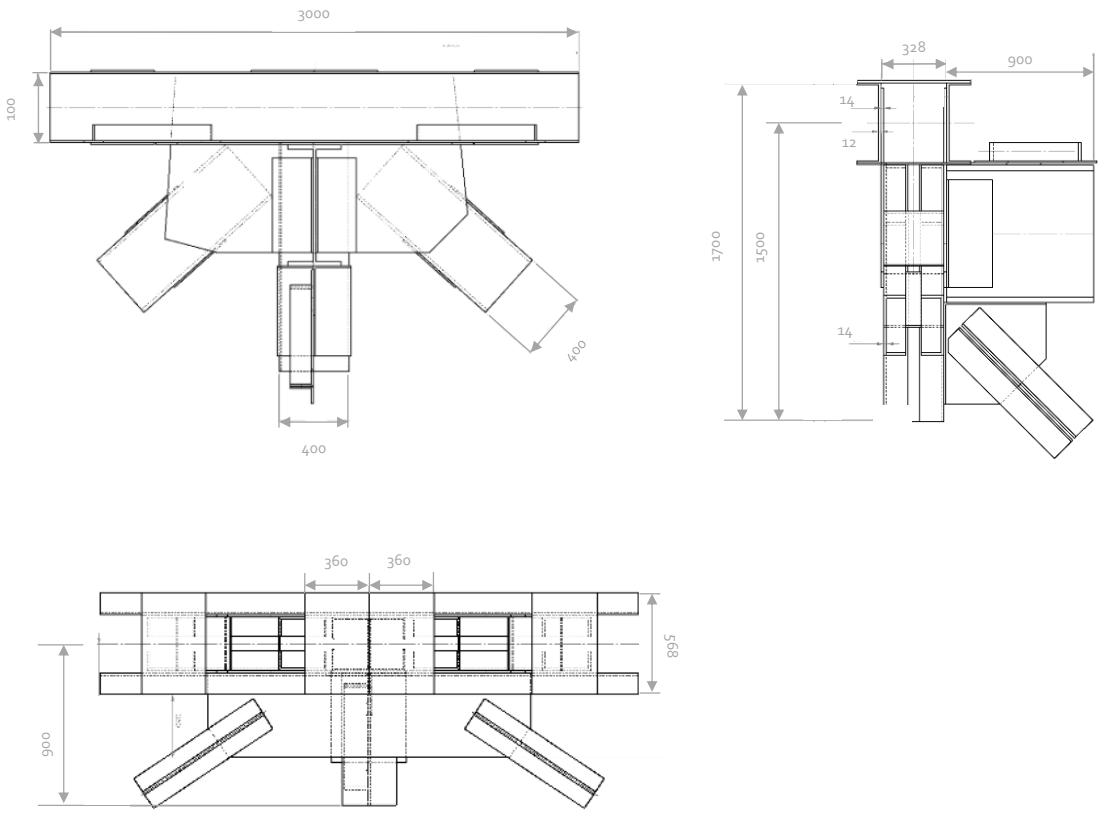

Figure 7.4 – Geometry and dimensions of node 6 of the Trezói bridge.

Local models of node 6 were constructed using the ANSYS® code. The contact between plates and rivets was modelled using contact finite elements available in ANSYS®, using a surface-to-surface option. In particular, the CONTA174 and TARGE170 elements were used to model, respectively, the contact and target surfaces, forming the so-called contact pairs. Both surfaces in contact were assumed flexible. The contact simulation was carried out using the augmented Lagrange algorithm available in the ANSYS®, together with the Coulomb friction model. A similar approach that was applied for the riveted specimens simulated in Chapter VI was also followed for this local node.

One key aspect of the numerical simulation using local models is the accurate definition of the boundary conditions to apply at the ends of the members. Multi-point constraints (MPC's) were used to impose the boundary conditions. With this technique, pilot nodes (reference points) were placed at the end of each member, at the centroid position of the cross section of the members.

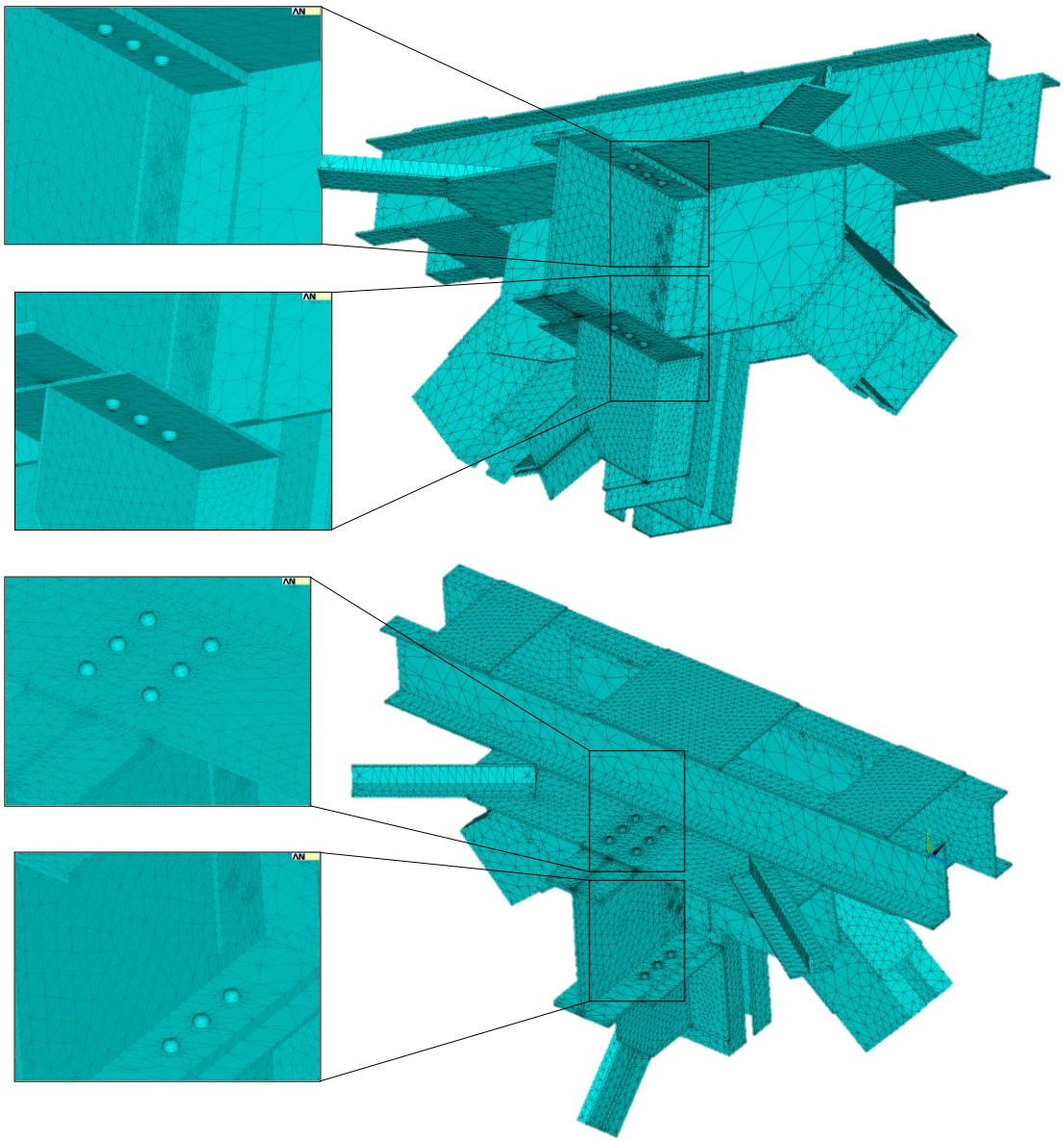

Figure 7.5 - Local finite element models: continuous model.

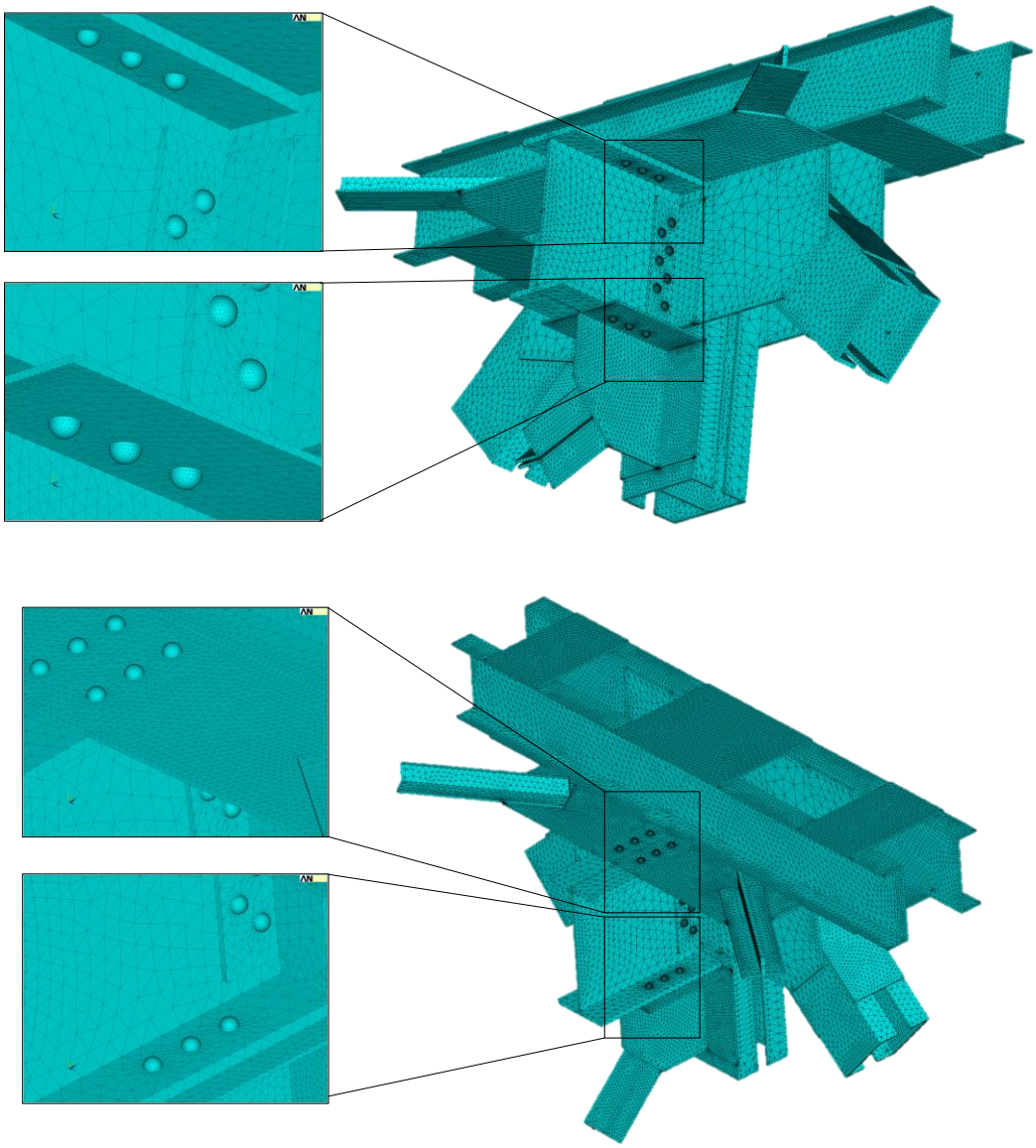

Figure 7.6 - Local finite element model: combined riveted and continuous model.

The displacements and rotations, obtained from a global dynamic analysis of the bridge, were applied directly to these pilot nodes which were later transformed into translations applied directly to the nodes of the respective cross sections (refer to Figure 7.7 for the cross sections identification). The global dynamic analysis of the Trezói bridge was performed in the framework of the FADLESS project, using global models of the bridge based on 3D beam finite element models [15].

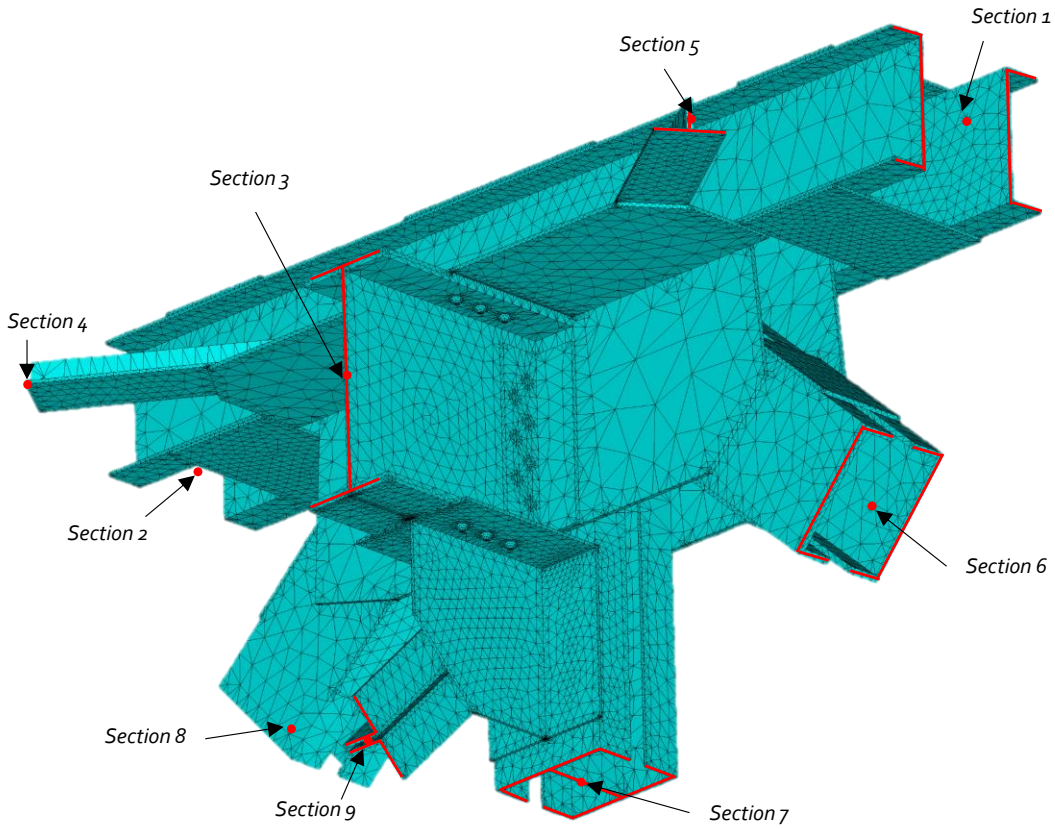

Figure 7.7 – Cross sections of the local models where boundary conditions were applied.

A locomotive-hauled passenger train as illustrated in Figure 7.8 was considered in this analysis, with a weight of 21.5 tons per axle for the locomotive and 11.7 tons per axle, for the passenger cars. Also it was considered that the train passage over the bridge took 14.652 seconds (~ train speed of 30 km/hour). The train passage was simulated using the global beam model of the bridge taking into account dynamic effects, using a total of 7326 steps (time increment of 0.002 seconds) [2]. Figures 7.9 and 7.10 illustrate the resulting displacements and rotations histories, for each section. We realize that some sections experience a vibrating patter that results from the dynamic response of the bridge. This vibration may contribute to additional fatigue cycles. The displacement/rotation spectra obtained from the bridge simulation using the global model were filtered in order to reduce the number of load steps to be applied in the local model. A total of 74 load steps were applied to the local model sections, in particular to the respective pilot nodes. The stress histories were evaluated at several fatigue potential critical locations for fatigue damage analysis.

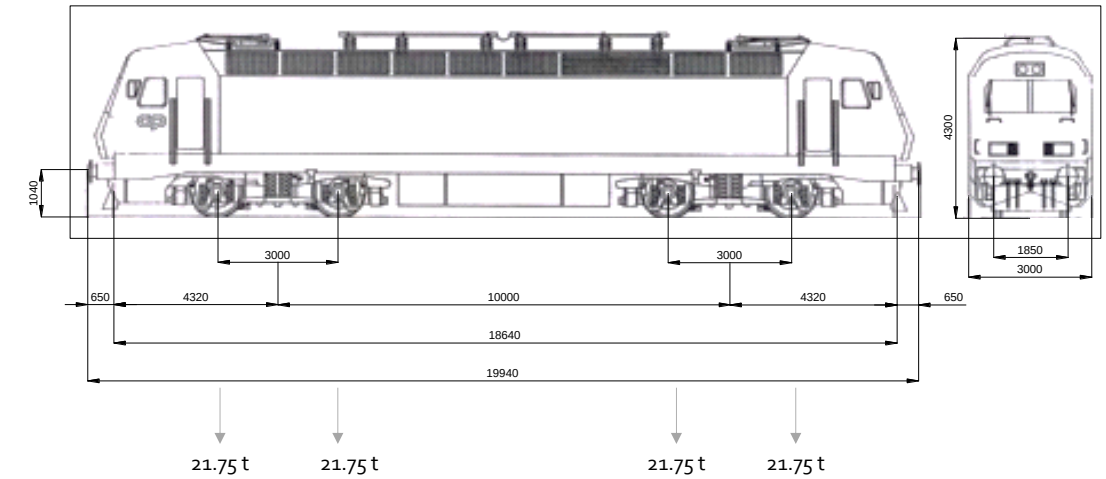

Figure 7.8 - Locomotive-hauled passenger train.

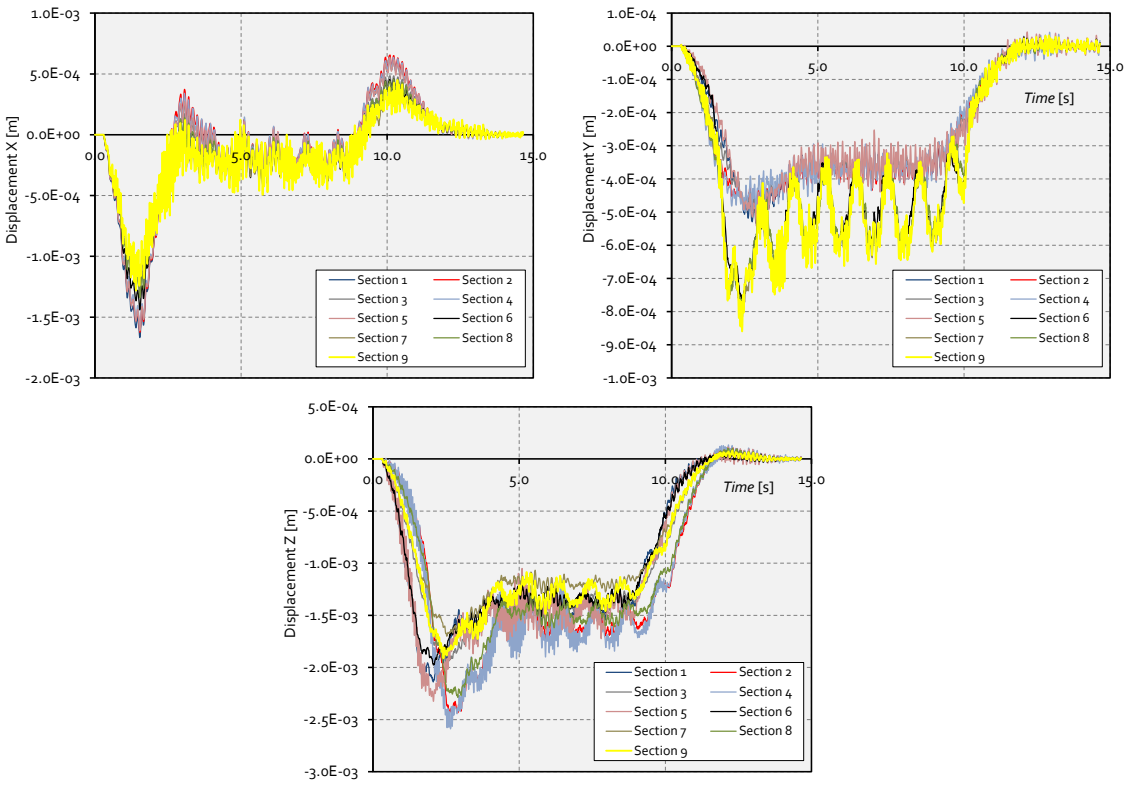

Figure 7.9 - Displacements histories at sections 1 to 9 of node 6 from Trezói bridge.

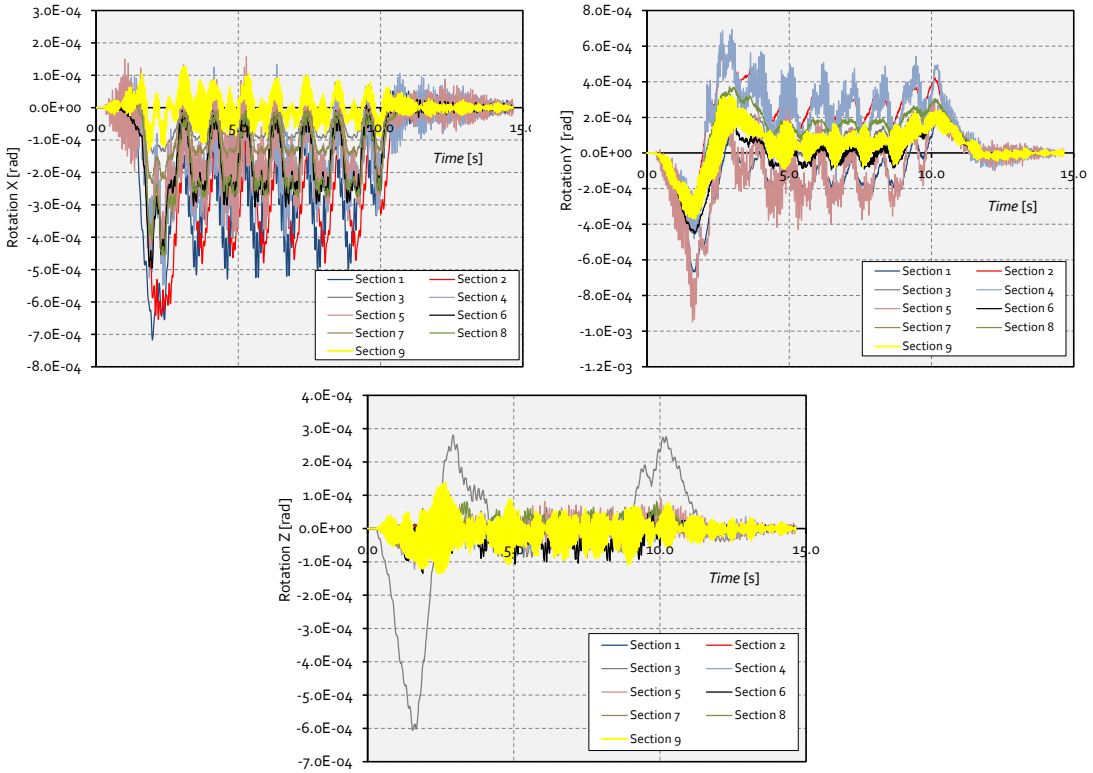

Figure 7.10 - Rotations histories at sections 1 to 9 of node 6 from Trezói bridge.

7.4. RESULTS AND DISCUSSION

Complex loading histories as illustrated in Figures 7.9 and 7.10 were applied to the local finite element model. The first aspect investigated was the multiaxiality nature the stresses experienced by the node material and the proportionality or non-proportionality of their time histories. Figure 7.11 a) plots the evolution of the principal stresses for a selected node (see Figure 7.12) of the finite element model of the Trezói detail. Figure 7.11 b) plots the evolution of the direction cosines of the first principal stress σ_1 during the train crossing the bridge. The analysis of Figure 7.11 reveals that the selected node exhibits a multiaxial stress field and that a non-proportional stress history is verified since the direction cosines are not constant with time. The results from Figure 11 were obtained using the continuous finite element model of the node 6.

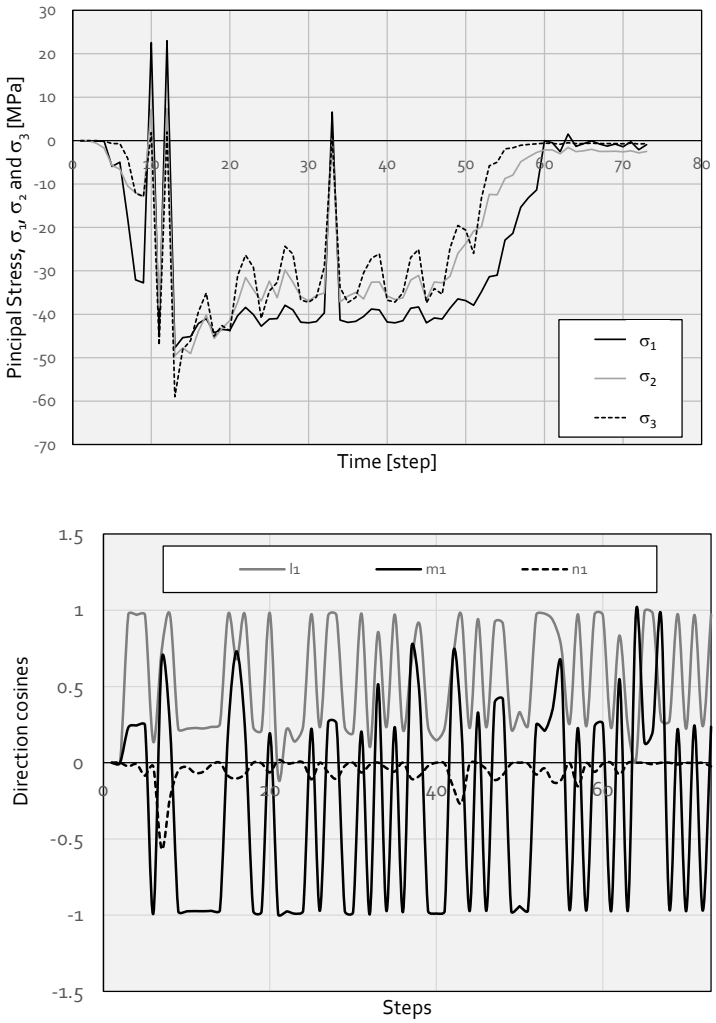

Figure 7.11 - Verification of the multiaxiality of the stress-time history: a) principal stresses evolution; b) direction cosines of the first principal stress direction.

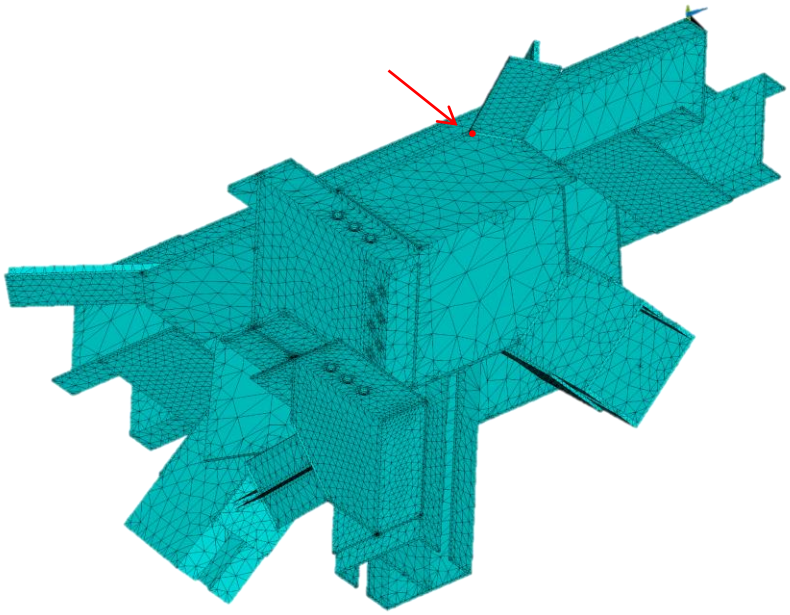

Figure 7.12 – Selected node for the verification of the multiaxiality of the stress-time history (full continuous model).

In order to validate the global finite element model of the bridge as well as the proposed local finite element of the node, experimental strain measurements were performed. Strain gauges were applied at the flange of the cross-girder (see Figure 7.13) and measurements were performed for the aforementioned train and crossing conditions. Strains were transformed into stresses using the Young modulus of the material. Figure 7.14 compares the experimental stress evolution, from three strain gauge measurements, with numerical stress results given by the continuous and combined continuous/riveted local finite element models. Figure 7.14 shows that the continuous finite element model presents higher peak stresses. The continuous numerical model has higher stiffness than the combined continuous/riveted model. The strain gauges were located near the connection between the cross-girder and the horizontal gusset, which justify the higher stress values simulated by a model that assumes continuity between the cross-girder and the horizontal gusset. Nevertheless, the finite model with contact elements between the cross-girder and the rest of the node would result in more accurate predictions.

7.4.1. Continuous finite element model of the structural detail of the Trezói bridge: results analysis

In this section, fatigue assessment results are presented using the nodal stress histories from the continuous finite element model of the structural node of the bridge. Only surface nodes of the structural joint were analysed since fatigue damage is commonly associated to surface crack initiation. In order to select a limited set of nodes most susceptive to fatigue damage, Equations (7.1) to (7.3) were applied to all surface nodes. The required material constants were obtained from Table 6.5 for the S235 steel grade. Figure 7.15 presents the fatigue damage calculated for each surface node, resulting from the above referred passenger train (refer to Figure 7.8) crossing the bridge. Figure 7.15 also presents a cut-off line used to select the set of 10 most damaged nodes. Those 10 nodes belong to three distinct locations (see Figure 7.16), that will be further investigated using multiaxial fatigue damage theories presented in Section 7.2. The number of train crossings until failure (D=1) using the Von Mises criterion are also presented in Figure 7.16. The Von Mises criterion suggested that the most critical locations are between the cross-girder and node connection parts. Damage levels for the simulated train crossing are very small which is consistent with the type of traffic considered (type of train/train speed).

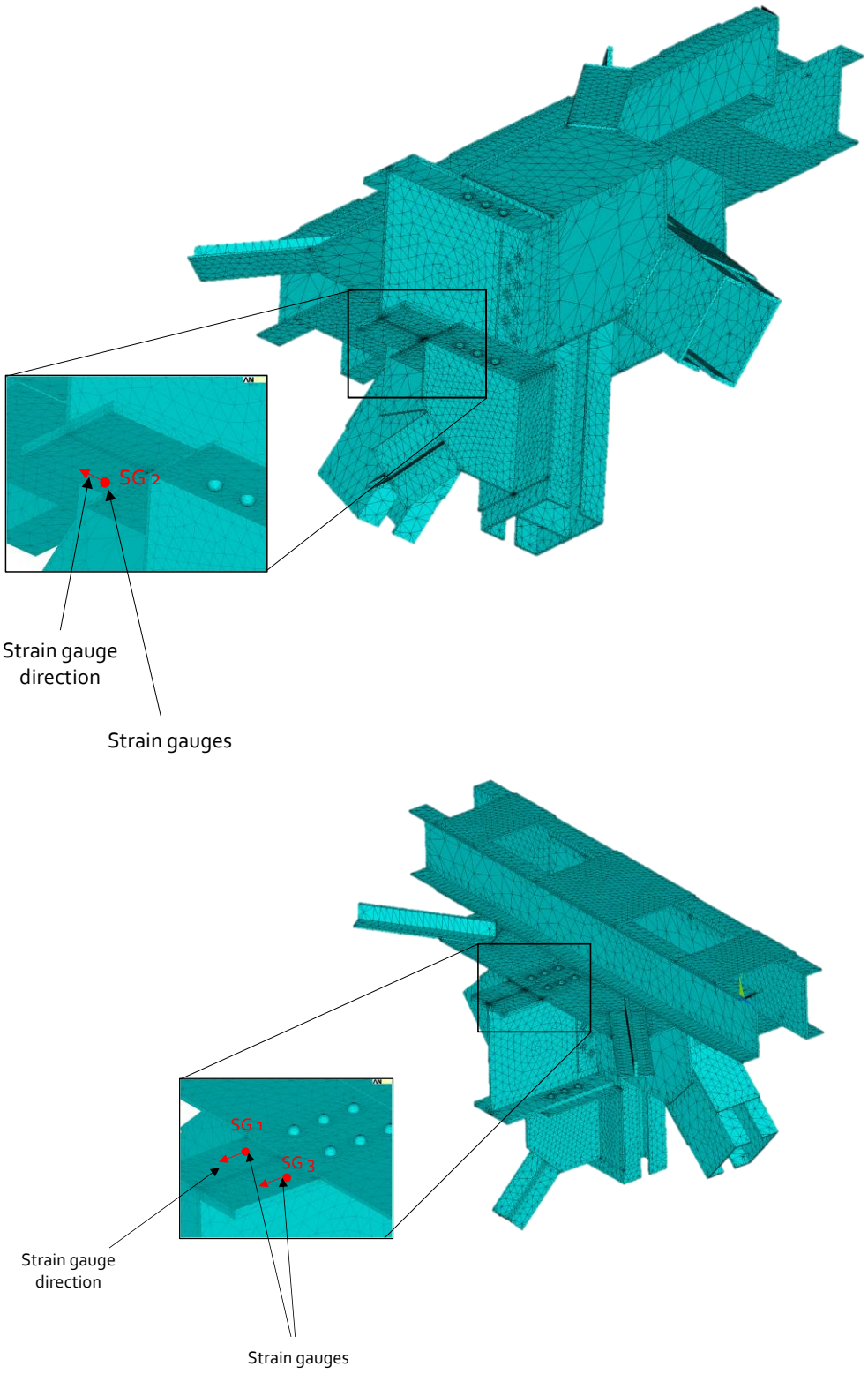

Figure 7.13 – Location of strain gauges used to monitor the strains at the node 6 of the bridge model.

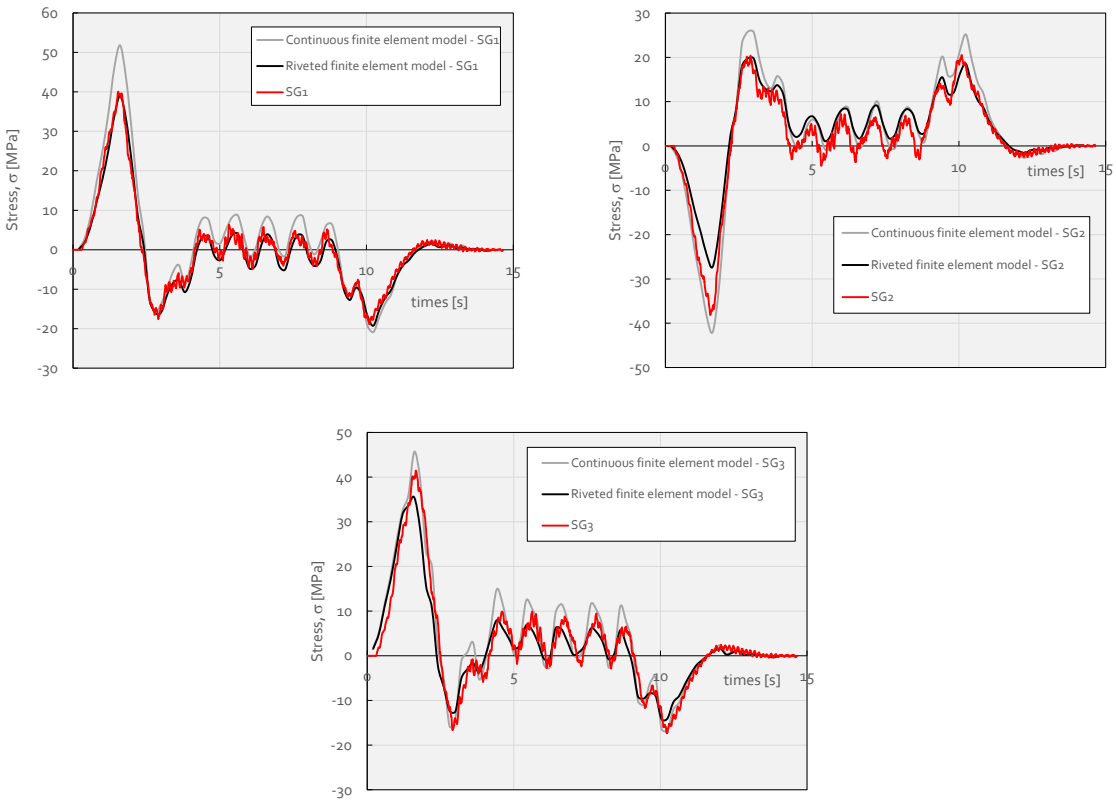

Figure 7.14 - Experimental vs numerical stress measurements at locations illustrated in Figure 7.13.

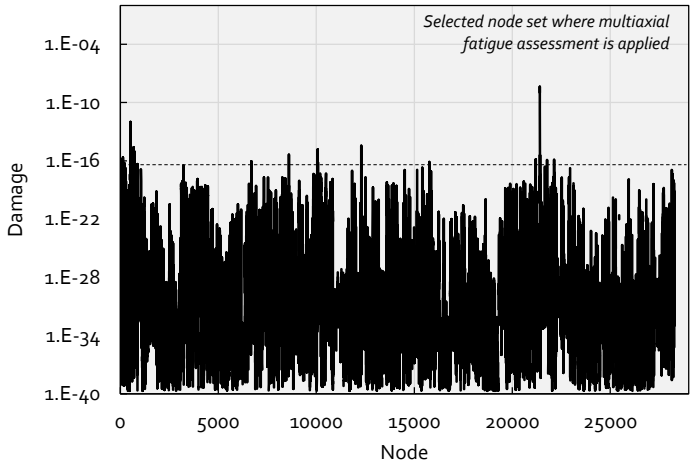

Figure 7.15 – Damage computed at each surface FE node of the local continuous model, for each passenger train crossing, using the Von Mises equivalent stress criterion.

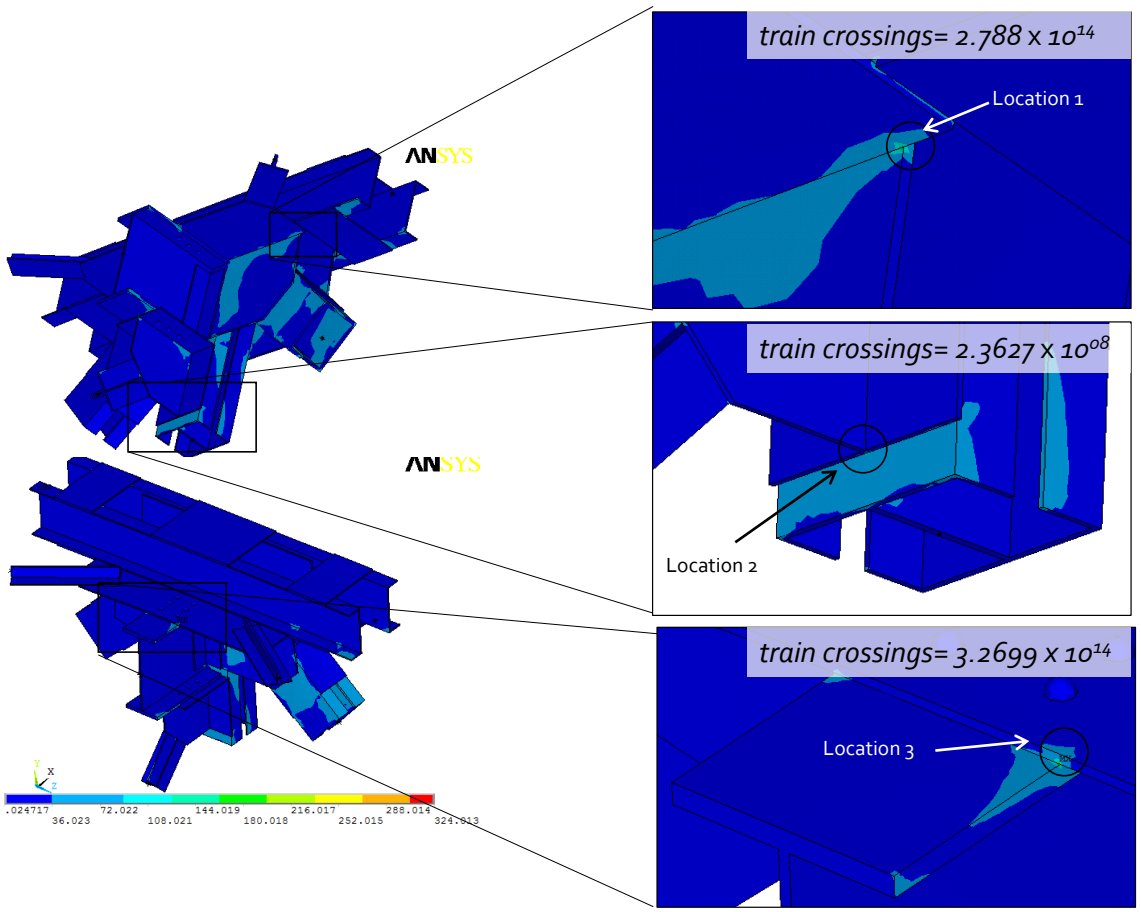

Figure 7.16 – Von Mises stress distribution (continuous model) (step 10).

The multiaxial fatigue criteria presented in Section 7.2, particularly the Bannantine and Socie, Fatemi and Socie, Smith-Watson-Topper, Findley and the modified Findley proposals were applied to the three most stressed locations identified previously (see locations 1 to 3 in Figure 7.16). For each location, the most stressed node was selected. Since the referred multiaxial damage criteria are critical plane based approaches, the critical plane was searched thru the variation of two angular coordinates (θ, ϕ) as illustrated in Figure 7.17. Tables 6.5, 7.1 and 7.2 summarize the constants required for the multiaxial damage models. Constants of Tables 7.1 and 7.2 resulted from empirical approximations instead of being computed using actual multiaxial fatigue data from materials testing. Multiaxial fatigue testing was considered out of scope of this research, but in future it should be considered for bridge materials.

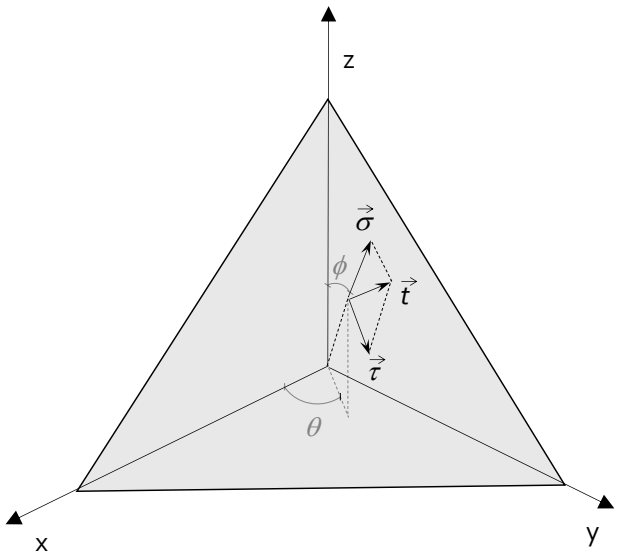

Figure 7.17 – Angular coordinates defining an arbitrary plane thru its normal.

Table 7.1 – Fatemi and Socie model constants [8].

$\tau'_f = \frac{\sigma'_f}{\sqrt{3}}$ [MPa]	$b_\gamma = b$	$\gamma'_f = \varepsilon'_f \times \sqrt{3}$	$c_\gamma = c$	G [GPa]	k
415.9	-0.081	2.335	-0.74	80	1

Table 7.2 – Findley model constants [8].

$k\ (\sqrt{1+k^2} = 1.04)$	$\tau^*_f = \sqrt{1+k^2}\,\tau'_f$ [MPa]
0.286	432.5

Figures 7.18 to 7.20 present for the three locations identified in the previous Von Mises fatigue analysis, a map of the damage as a function of the plane orientation. The damage map was firstly computed for one single passenger train crossing. Then, the damage was linearly accumulated using the same train crossing until damage reaches the unity in a specific plane (critical plane). When this condition is verified, the corresponding number of train crossings required to failure is obtained and the respective value is plotted over the damage maps of the Figures 7.18 to 7.20. In

particular, Figure 7.18 presents the damage map computed for the planes at the location between the horizontal gusset and the vertical gusset (location 1). Figure 7.18a) presents the fatigue damage map assessed using the Bannantine and Socie relation; the Fatemi and Socie relation produced the damage map of Figure 7.18b); the Smith-Watson-Topper relation is responsible for the damage map of Figure 7.18c); the Findley and modified Findley relations resulted in the damage maps of Figures 7.18d) and e), respectively. The analysis of the Figure 7.18 reveals that the strain-based approaches result in more conservative results than the stress-based methods. In particular, the BS approach leads to the lower fatigue live values. Figure 7.19 presents the results corresponding to the node located between the column and the lower support of cross girder (location 2), using the same approaches that were considered for the previous location. As observed in Figure 7.18, the strain-based approach results into the more conservative fatigue lives. Finally, Figure 7.20 presents the accumulated fatigue damage for the node located at the cross-girder/ horizontal gusset junction (location 3). The strain-based approach also produced more conservative results. Table 7.3 summarizes the fatigue life computed using the continuous finite element model. It can be observed that the stress-based approaches such as Findley and modified Findley approaches result in the less conservative solutions. It is interesting to note that all critical plane approaches led to less conservative predictions than resulted with the application of the Von Mises criterion, which makes the last criterion for this kind of structures which are not fatigue critical.

In all the cases the number of train crossings required to start a fatigue crack is very high as a result of a very low damage induced by a single passengers train crossing. The actual structure does not exhibit any signal of fatigue damage. Therefore, the results shown are consistent with the observations performed over the bridge. The proposed methodology can be also applied to more damaging traffic as the one from freight trains crossing the bridge at higher velocities, as soon as the respective global analysis of the bridge is performed to derive the local sections displacements histories. The selection of a passengers train was motivated by the available experimental strain measurements at the node of the bridge.

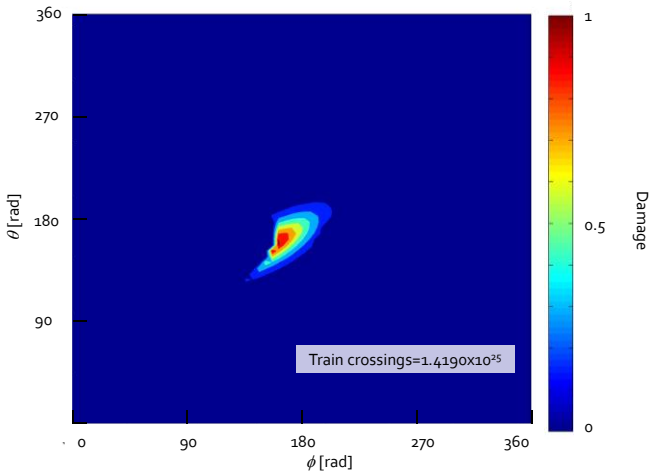

a)

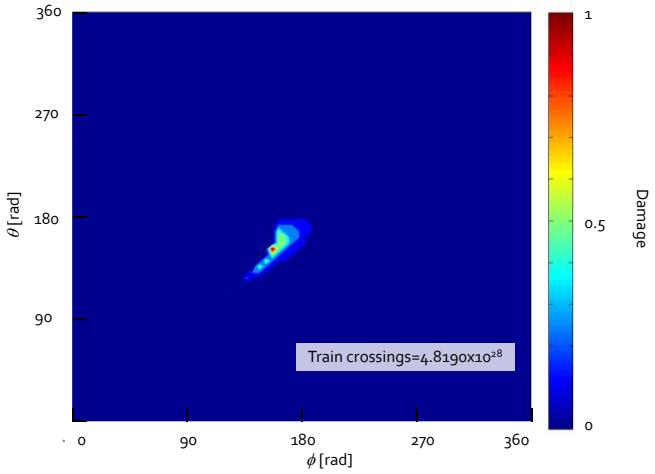

b)

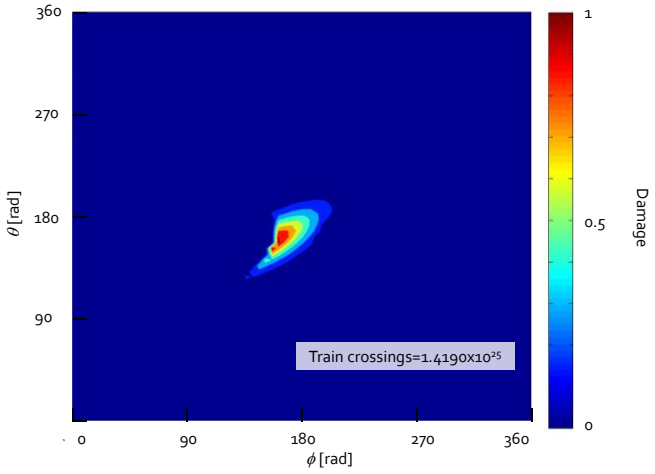

c)

Figure 7.18 – Critical plane assessment for the node located at location 1 (continuous FEM model): a) BS approach; b) FS approach; c) SWT approach; d) Findley approach and e) modified Findley approach. (1/2)

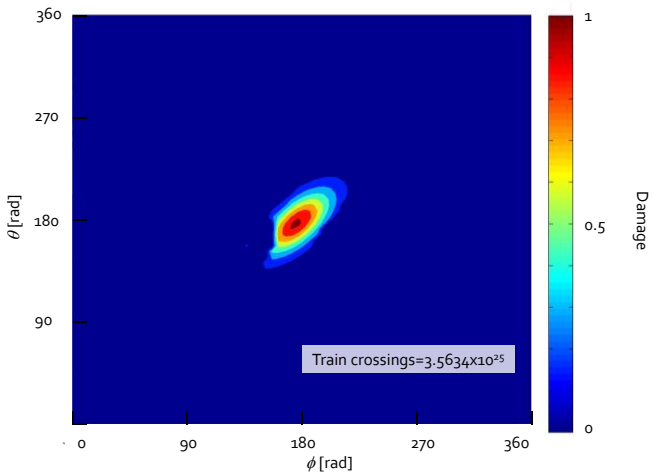

d)

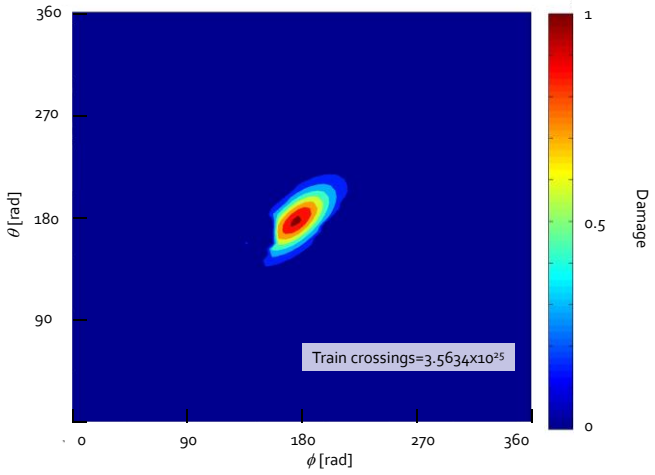

e)

Figure 7.18 – Critical plane assessment for the node located at location 1 (continuous FEM model): a) BS approach; b) FS approach; c) SWT approach; d) Findley approach and e) modified Findley approach. (2/2)

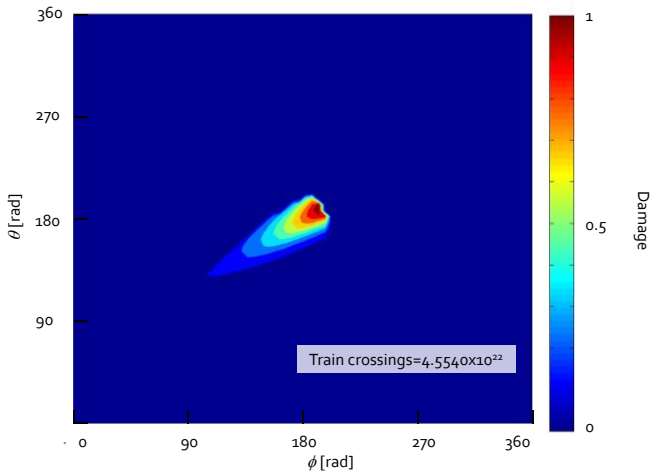

a)

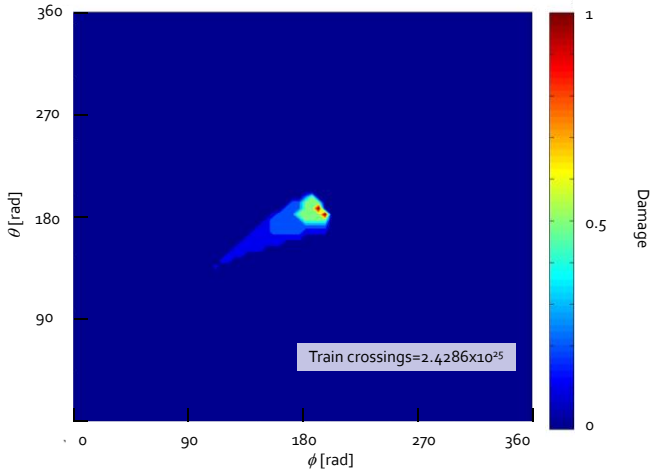

b)

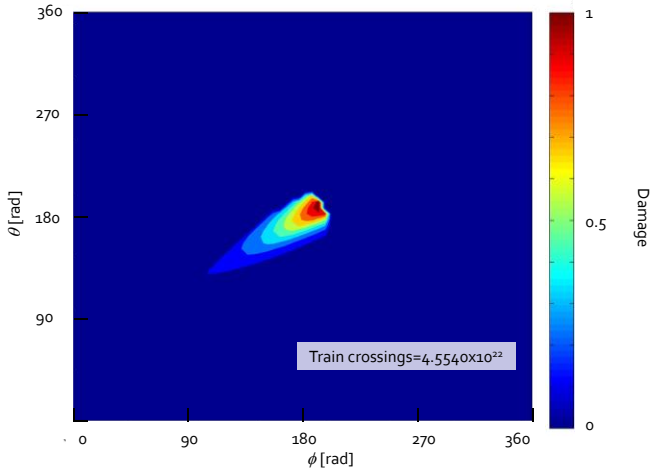

c)

Figure 7.19 – Critical plane assessment for the node located at location 2 (continuous FEM model): a) BS approach; b) FS approach; c) SWT approach; d) Findley approach and e) modified Findley approach. (1/2)

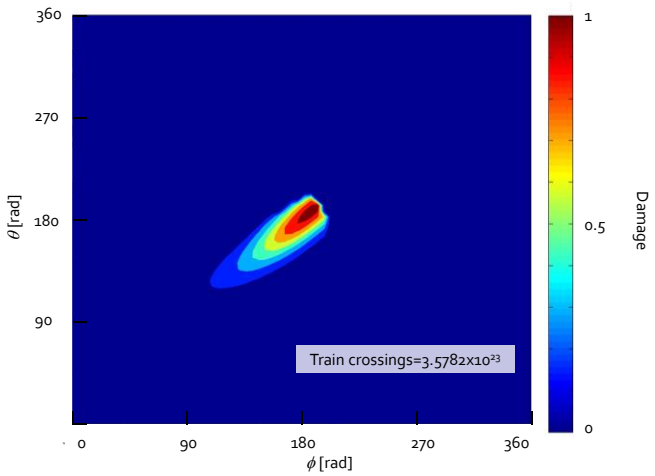

d)

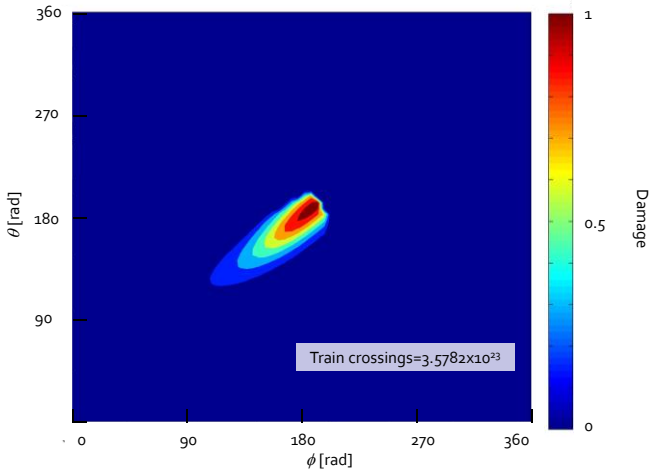

e)

Figure 7.19 – Critical plane assessment for the node located at location 2 (continuous FEM model): a) BS approach; b) FS approach; c) SWT approach; d) Findley approach and e) modified Findley approach. (2/2)

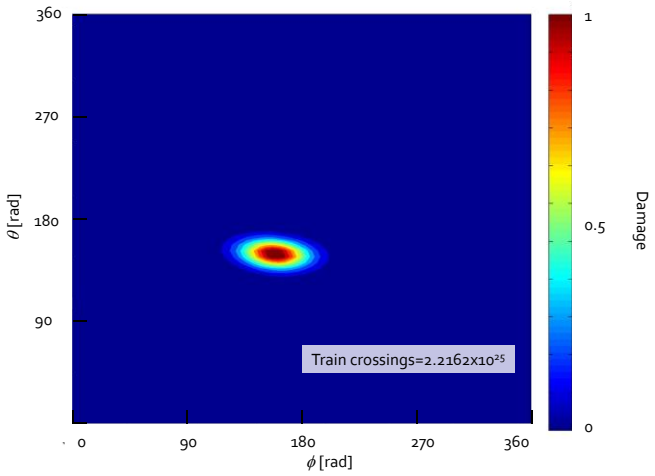

a)

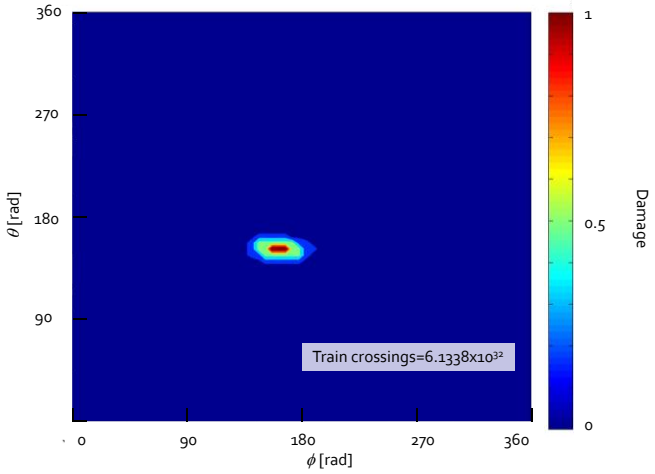

b)

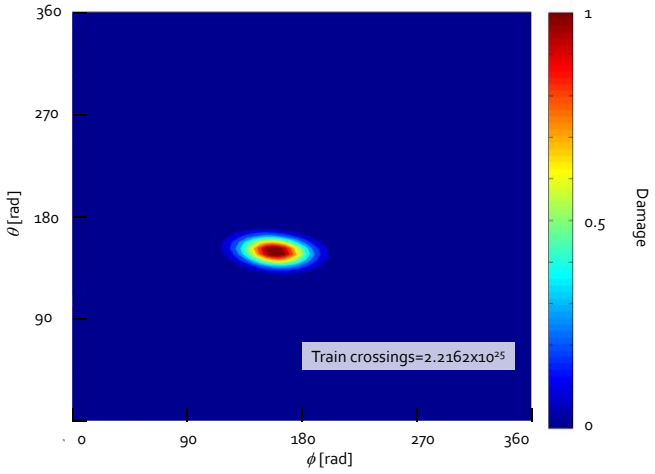

c)

Figure 7.20 – Critical plane assessment for the node located at location 3 (continuous FEM model): a) BS approach; b) FS approach; c) SWT approach; d) Findley approach and e) modified Findley approach. (1/2)

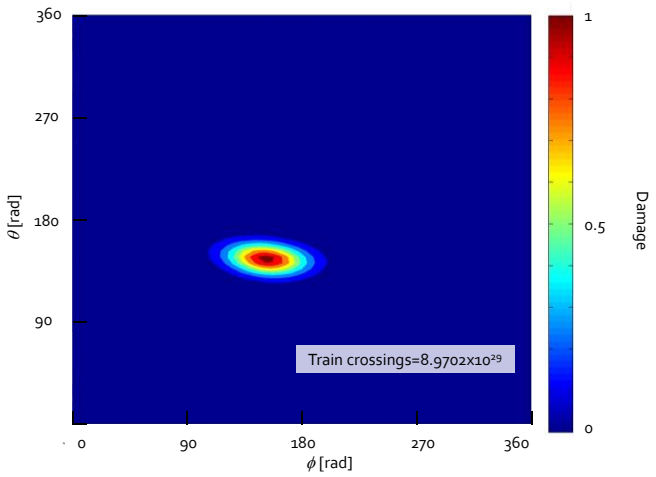

d)

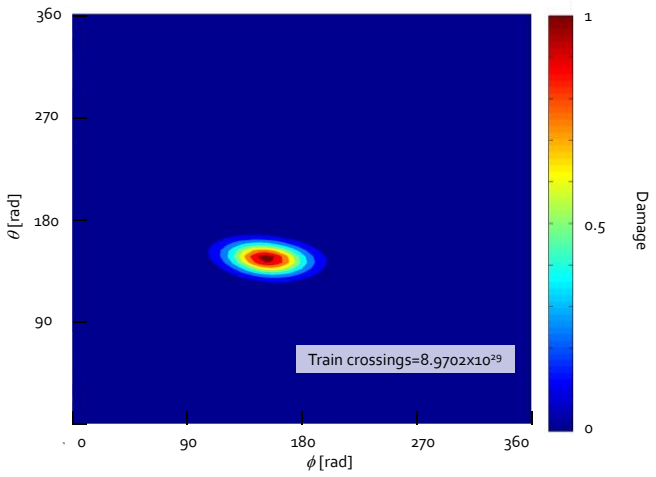

e)

Figure 7.20 – Critical plane assessment for the node located at location 3 (continuous FEM model): a) BS approach; b) FS approach; c) SWT approach; d) Findley approach and e) modified Findley approach. (2/2)

Table 7.3 – Summary of the number of passenger train crossings until failure, computed using several fatigue assessment models, based on a continuous finite element model.

Node location	***Von Mises***	***BS approach***	***FS approach***	***SWT approach***	***Findley***	***Modified Findley***
Vertical gusset/ horizontal gusset (location 1)	$2.9x10^{14}$	$1.4x10^{25}$	$4.8x10^{28}$	$1.4x10^{25}$	$3.6x10^{25}$	$3.6x10^{25}$
Column/lower support of cross-girder (location 2)	$2.3x10^{08}$	$4.6x10^{22}$	$2.4x10^{25}$	$4.6x10^{22}$	$3.6x10^{23}$	$3.6x10^{23}$
Horizontal gusset/ Cross-girder (location 3)	$3.3x10^{14}$	$2.2x10^{25}$	$6.1x10^{32}$	$2.2x10^{25}$	$9.0x10^{39}$	$9.0x10^{39}$

7.4.2. Riveted finite element model of a structural detail of the Trezói bridge: results analysis

Figure 7.21 presents the fatigue damage calculation for the surface nodes using the Von Mises stress criterion, for the passenger train crossing the bridge. Figure 7.21 also presents an arbitrary cut-off line used to select the locations where multiaxial fatigue assessment criteria will be applied. Contrarily to the observed for the continuous finite element model (see Figure 7.15), a significant number of nodes show similar damage values (damage close to the cut-off line). It was verified that nodes located at the rivet holes surfaces present similar damage levels. Figure 7.22 presents the three most critical locations. The number of train crossings to failure (D=1) are also presented in Figure 7.22. The Von Mises stress criterion indicated that the most critical locations of the finite element model are at the first riveted hole, located in the top left beam flange.

Figures 7.23 to 7.26 plot the accumulated fatigue damage for three selected locations of the rivet holes, with the plane variation (θ and ϕ). Figure 7.23 presents the accumulated fatigue damage computed at the critical location 1, indicated in Figure 7.22.The number of train crossings to failure computed using the FS and BS relations are illustrated in Figures 7.23a) and b), respectively. The SWT results are plotted in Figure 7.23c), the Findley results in Figure 7.23d) and finally the modified Findley results in Figure 7.23e). The analysis of the Figure 7.23 indicated that the SWT approach (strain-based approach) resulted in more conservative results than the stress based approaches or the FS approach. The FS approach was the less conservative approach.

Figure 7.24 presents the results corresponding to the node at the location 2. As observed in Figure 7.23, the SWT approach results into more conservative fatigue life predictions. Finally, Figure 7.25 presents the accumulated fatigue damage for the location 3. As concluded with results shown in Figures 7.23 and 7.24, the SWT based approach is the more conservative one.

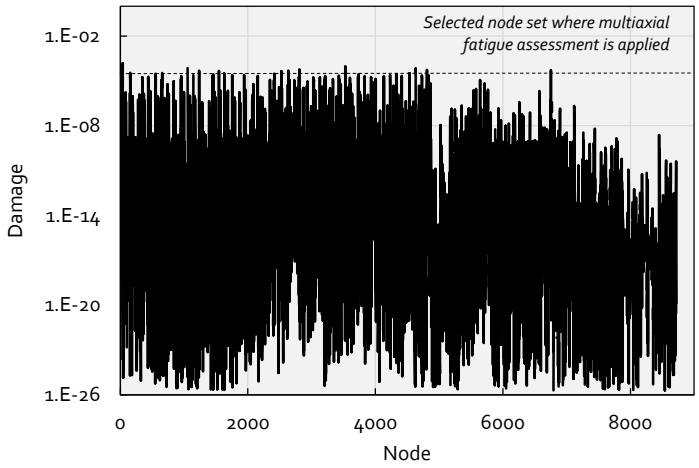

Figure 7.21 – Fatigue damage computed at each surface FE node of the local combined continuous/riveted model, for each passenger train crossing.

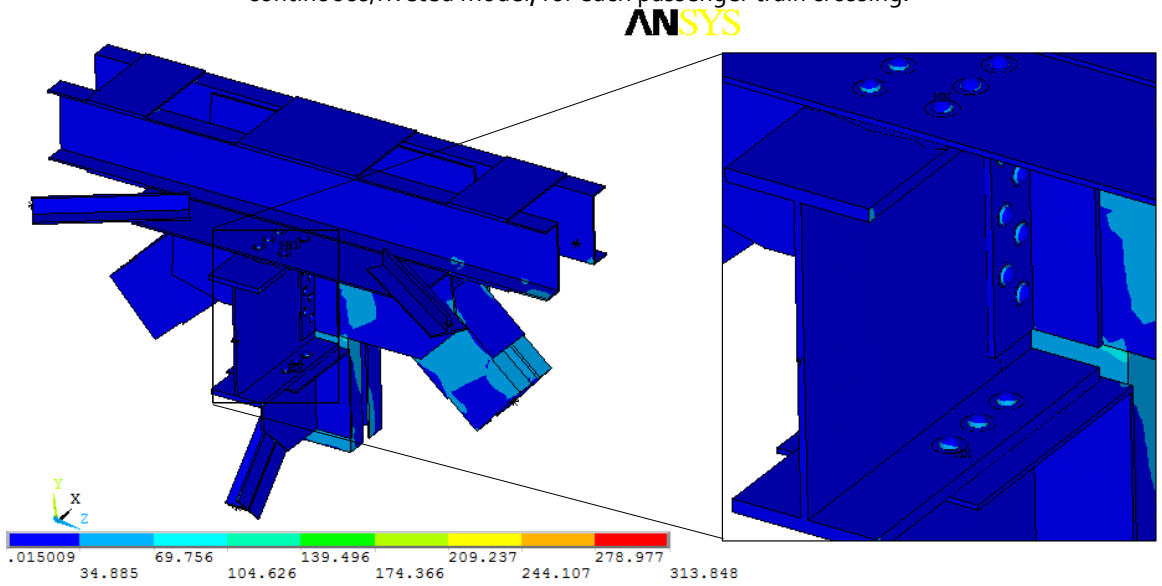

a)

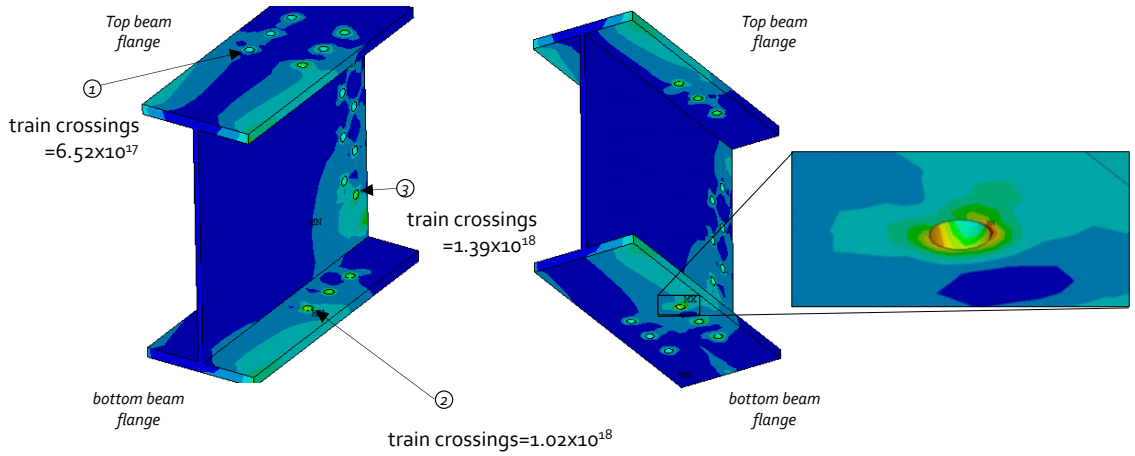

b)

Figure 7.22 - Von Mises stress distribution (combined continuous/riveted model) (step 10): a) local model overview; b) detail of riveted cross girder with some highlighted hot spot locations at rivet holes.

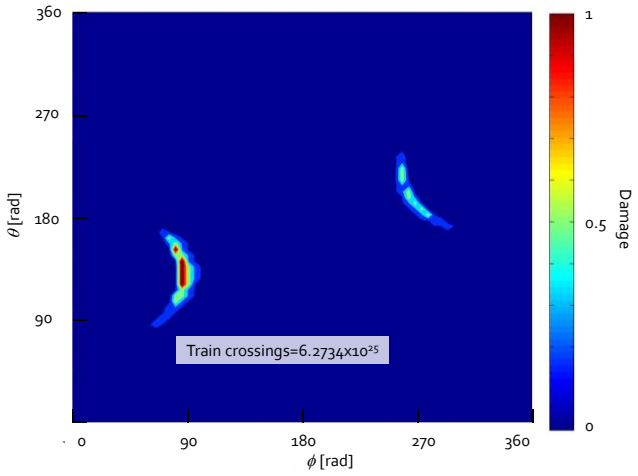

a)

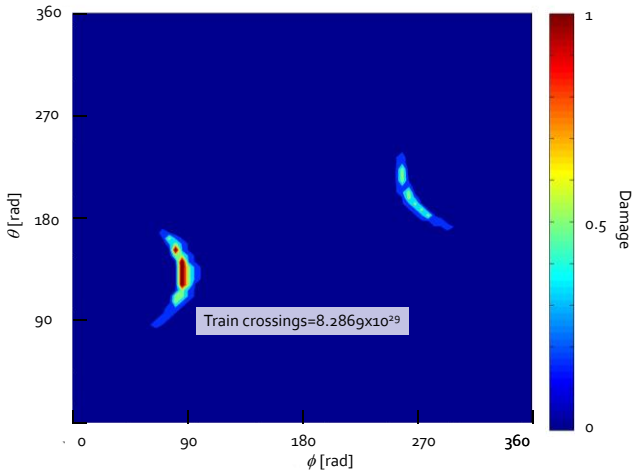

b)

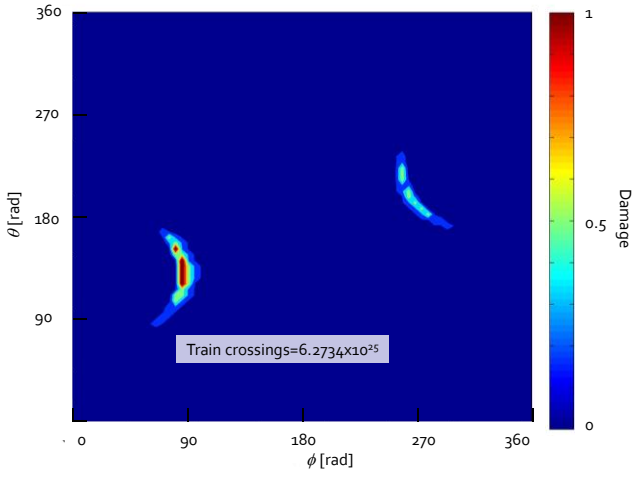

c)

Figure 7.23 – Critical plane fatigue damage assessment for the location 1 (combined continuous/riveted model): a) BS approach; b) FS approach; c) SWT approach; d) Findley approach and e) modified Findley approach.

(1/2)

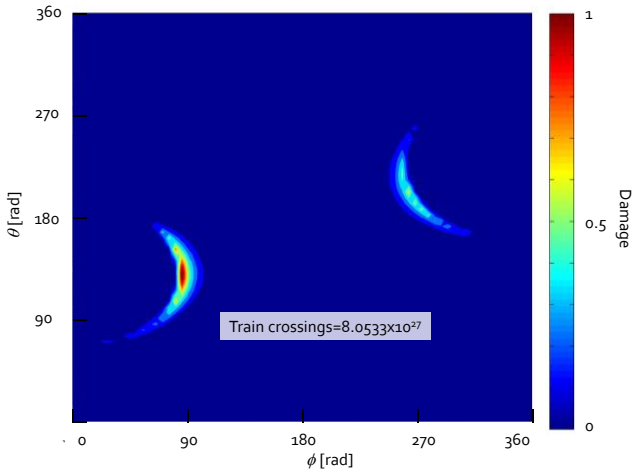

d)

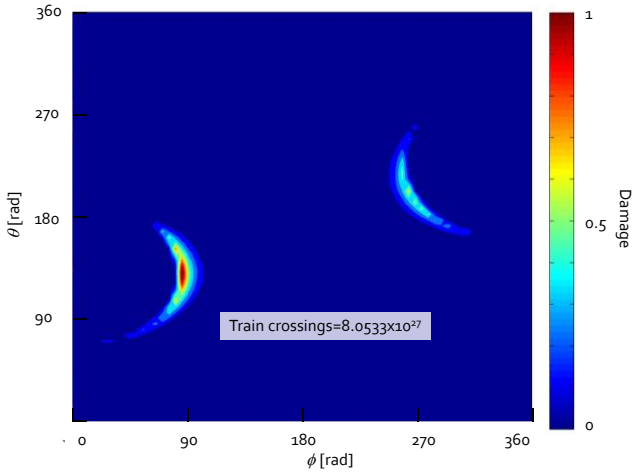

e)

Figure 7.23 – Critical plane fatigue damage assessment for the location 1 (combined continuous/riveted model): a) BS approach; b) FS approach; c) SWT approach; d) Findley approach and e) modified Findley approach.
(2/2)

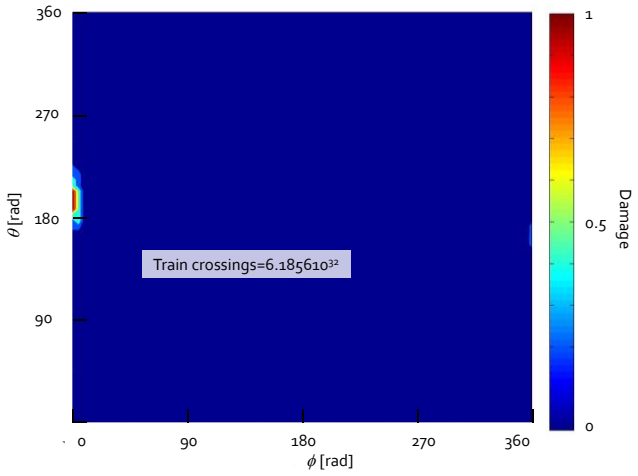

a)

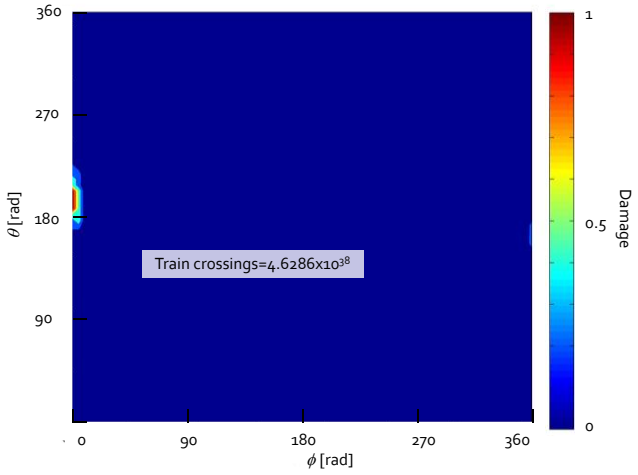

b)

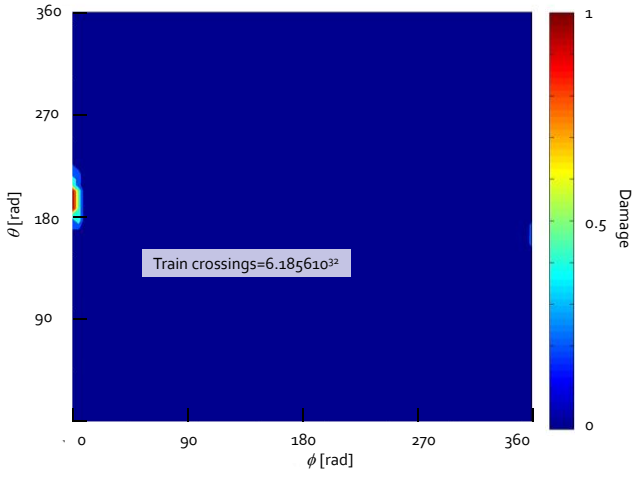

c)

Figure 7.24 – Critical plane fatigue damage assessment for the location 2 (combined continuous/riveted model): a) BS approach; b) FS approach; c) SWT approach; d) Findley approach and e) modified Findley approach.

(1/2)

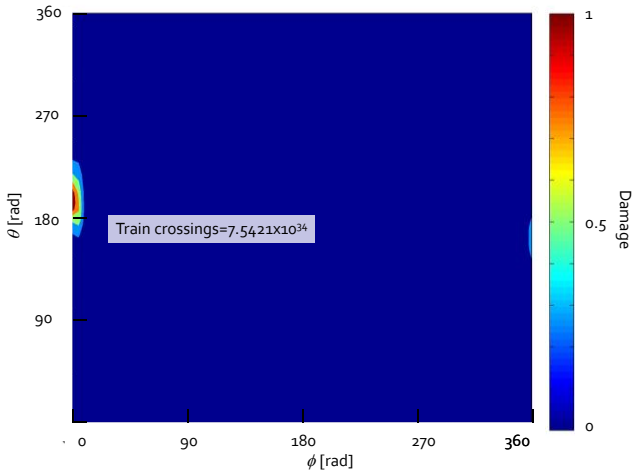

d)

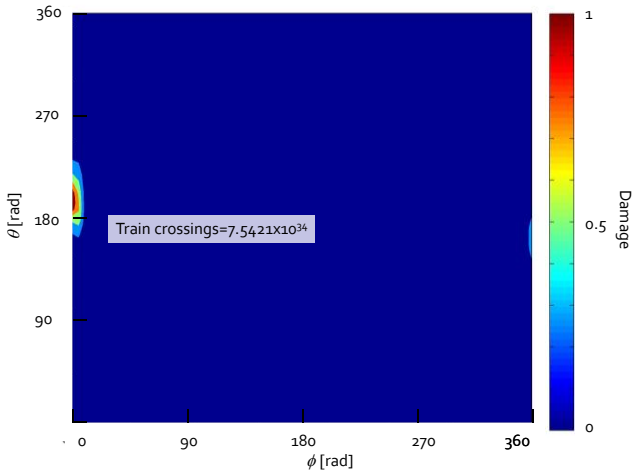

e)

Figure 7.24 – Critical plane fatigue damage assessment for the location 2 (combined continuous/riveted model): a) BS approach; b) FS approach; c) SWT approach; d) Findley approach and e) modified Findley approach.

(2/2)

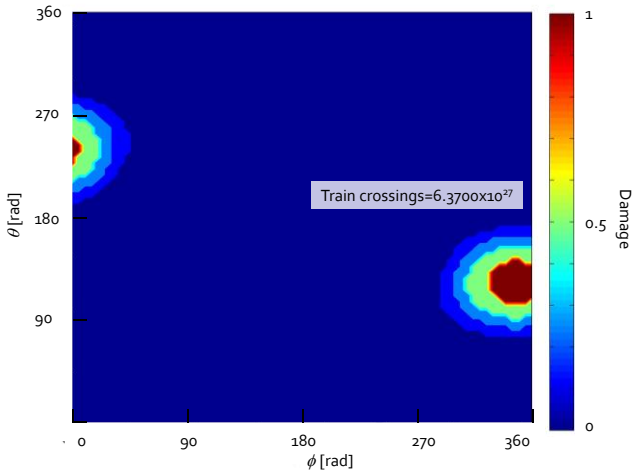

a)

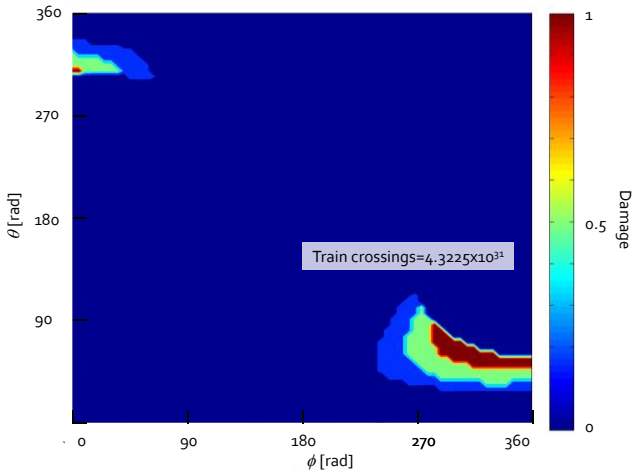

b)

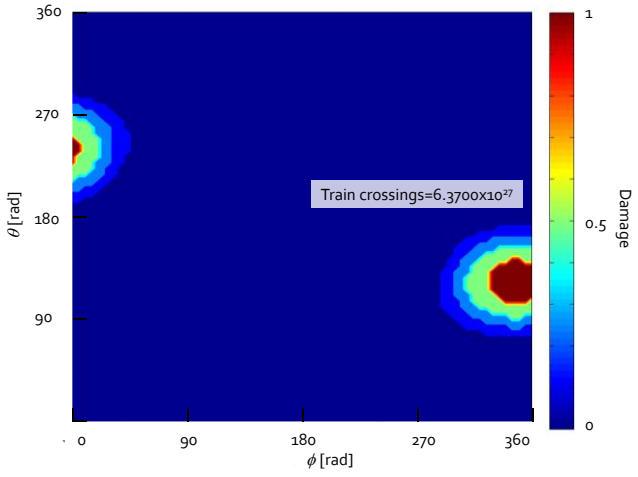

c)

Figure 7.25 – Critical plane fatigue damage assessment for the location 3 (combined continuous/riveted model): a) BS approach; b) FS approach; c) SWT approach; d) Findley approach and e) modified Findley approach.
(1/2)

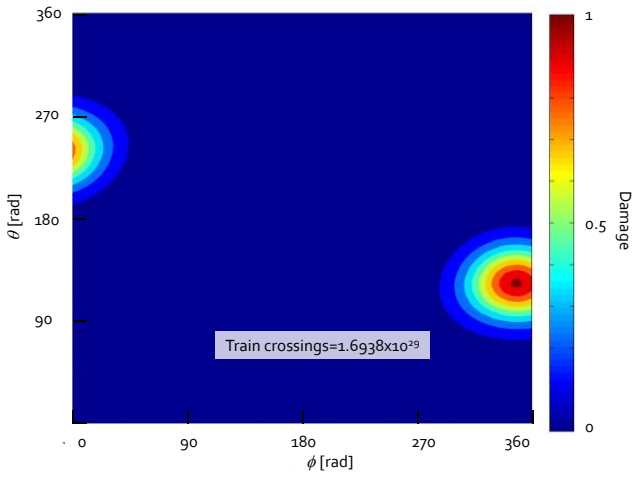

e)

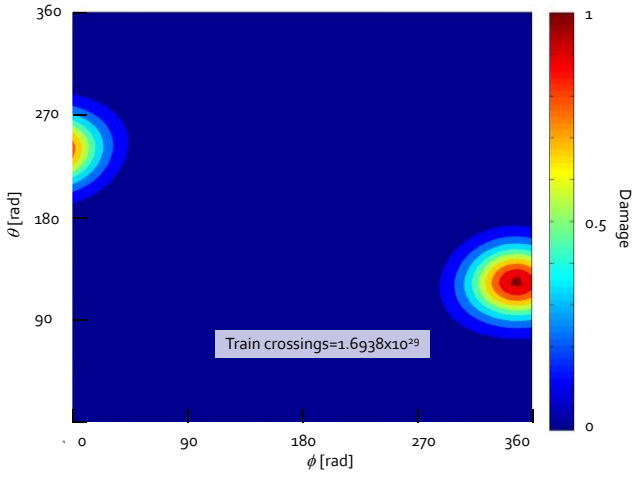

f)

Figure 7.25 – Critical plane fatigue damage assessment for the location 3 (combined continuous/riveted model): a) BS approach; b) FS approach; c) SWT approach; d) Findley approach and e) modified Findley approach.
(2/2)

Table 7.4 summarises the fatigue life results computed for the selected three locations identified in the riveted cross-girder. It can be observed that Von Mises approach was the most conservative one. Considering the critical plane approaches, significantly higher fatigue lives were obtained. The SWT approach was consistently the less conservative approach among the critical plane models, followed by Findley approaches and finally the FS approach, which was the less conservative one.

The comparison of Tables 7.3 and 7.4 shows that the fully continuous model produces lower fatigue lives (more conservative estimations of $2.3\text{x}10^{08}$ *vs.* $3.5\text{x}10^{17}$ train

crossings), which is an indication of the higher stress estimations using the continuous model. In fact, the continuous model introduces more severe geometric discontinuities than the riveted model.

Table 7.4 – Summary of the number of passenger train crossings to failure computed using several fatigue assessment models, based on a combined continuous/riveted finite element model.

Node location	*Von Mises*	*BS approach*	*FS approach*	*SWT approach*	*Findley*	*Modified Findley*
Location 1	$6.5x10^{17}$	$6.3x10^{25}$	$8.3\ x10^{29}$	$6.3x10^{25}$	$8.1x10^{27}$	$8.1x10^{27}$
Location 2	$1.0x10^{18}$	$6.2x10^{32}$	$4.6x10^{38}$	$6.2x10^{32}$	$7.5x10^{34}$	$7.5x10^{34}$
Location 3	$1.39x10^{18}$	$6.4x10^{27}$	$4.3x10^{31}$	$6.4x10^{27}$	$1.7x10^{29}$	$1.7x10^{29}$

7.5. CONCLUDING REMARKS

In this chapter a numerical strategy for the fatigue analysis of riveted details from bridges was proposed and illustrated for a node of the Trezói Bridge. The proposed strategy mitigates the very high computational costs that a local fatigue analysis of real complex details may demand. The application of local approaches to fatigue in real bridge details leads to a multi-scale problem that, taking into account the state-of-the art computational resources, cannot be solved with a unique model that encompasses both scales. Therefore, the proposed methodology suggested a multi model approach to overcome the multi-scale problem, according the following sequence:

- Creation of global models of the bridge using beam elements where dynamic effects of traffic should be conveniently accounted. With this model a prior selection of potential critical details is performed using an S-N approach.
- Development of local models of the selected potential critical location, using solid elements. This model will be simulated using a quasi-static analysis but with displacement histories from the global dynamic analysis of the bridge that will be applied with sub-modelling techniques (e.g. multi-point constraints).

- If the details are riveted ones, it would be impossible to simulate all the rivets that for real bridge nodes could reach the value of hundreds. Therefore, various local models can be proposed to simulate specific riveted parts interaction from the whole detail. This was the case of the problem presented in this chapter to investigate the fatigue behaviour of the riveted connection between the cross-girder and the node.

The study presented in this chapter demonstrated that the use of full continuous models to simulate the fatigue behaviour of riveted details leads to distinct potential failure locations of the ones obtained using riveted models, with contact finite elements. In the latter case, the rivet holes revealed as the most critical locations. The use of rivets in the numerical modelling also allowed a better correlation of the available experimental strain-life data, which is a clear indication of the advantage of the proposed local model.

The analysis of the stress histories for a real traffic stress history revealed that the stress states are multiaxial and the stress histories are non-proportional at the nodes of the local model. Therefore, it was recommended the use of non-proportional multiaxial fatigue approaches for the model. This is actually an open problem for variable amplitude (random) load spectra, but some existing literature approaches were applied in the fatigue analysis of the node. The critical planes approaches are very popular approaches in multiaxial fatigue but they are very time consuming since they require the scanning of the multiplicity of damage planes. This represents a difficulty for 3D problems, which is the case of the complex bridge details, since the number of planes to be search is very high. In order to mitigate the increased computational cost resulting from the critical plane approaches, a preliminary assessment based on Von Mises stresses was proposed to identify the most critical locations at the local model for further analysis using the more accurate damage models.

Despite the multiaxial fatigue models requires constants to be identified with specific multiaxial material fatigue tests, in this chapter empirical approximations were adopted. The critical plane damage models were less conservative than the Von Mises approach, resulting in higher number of train crossings. Therefore the Von Mises approach could be a valuable approach for the prior identification of critical locations.

The different critical plane damage models resulted in some cases in very distinct life results. This is justified by the fact that only empirical estimations of their parameters were used and the model reliability depends greatly on these parameters. In addition, since the damage levels of one train crossing is very low, the models are working in the fatigue endurance limit domain. Therefore, small perturbations in the computed fatigue damage parameters or on model constants may lead to significant distinct results. The SWT damage approach was the one leading to less conservative approaches within the critical planes approaches. It is worth mentioning that the data required for this model was assessed using fatigue tests performed in this work with tension/compression smooth specimens.

7.6. REFERENCES

[1] Cunha, A., "Avaliação da Integridade Estrutural de Pontes Metálicas Ferroviárias/ Assessment of the Structural Integrity of Metalic Railway Bridges", POCTI/ECM/57286/2004, FEUP, 2005-2008.
[2] Lippi, F., Salvatore, W., Braconi, A., Finetto, M., Wenzel, H., De Roeck, G., Peeters, B., Könke C., Zabel, V., Cunha, A.,"Fatigue damage control and assessment for railway bridge", Research Fund for Coal and Steel, Directorate-General for Research and Innovation, 2009-2012.
[3] Marques, F.M., "Avaliação do comportamento estrutural e análise de fadiga em pontes metálicas ferroviárias", Dissertação de mestrado, FEUP, 2006.
[4] Correia, J.A.F.O., "Desenvolvimento de Modelos de Previsão da Vida à Fadiga de Ligações Rebitadas", Dissertação de mestrado, UTAD, 2008.
[5] Anes, V., Reis, L., Li, B., Fonte, M., de Freitas, M., "New Approach for Analysis of Complex Multiaxial Loading Paths", International Journal of Fatigue 62, pp. 21–33, 2014.
[6] ASTM - American Society for Testing and Materials, "E1049-85: Standard Practices for Cycle Counting in Fatigue Analysis", Vol. 03.01, West Conshohocken, PA, pp. 5-8, 1999.
[7] Miner, M.A., "Cumulative Damage in Fatigue", Journal of Applied Mechanics 67, pp. A159-A169, 1945.
[8] Socie, D.F., Marquis, G.B., "Multiaxial Fatigue", Society of Automotive Engineers, Inc. Warrendale, Pa., ISBN 0-7680-0453-5, 2000.

[9] Smith, R.N., Watson, P., Topper, T.H., "A Stress-Strain Parameter for the Fatigue of Metals", Journal of Materials 5 (4), pp. 767-778, 1970.
[10] Socie, D.F., Shield, T.W., "Mean Stress Effects in Biaxial Fatigue of Inconel 718", ASME Journal of Engineering Materials and Technology 106, pp. 227-232, 1983.
[11] Findley, W.N., "Combined Fatigue Strength of 76S-T61 Aluminum Alloy with Superimposed Mean Stresses and Correction for Yielding", NACATN 3934, National Advisory Committee for Aeronautics, Washington, DC, p. 90, 1953.
[12] Findley, W.N., "A Theory for the Effect of Mean Stress on Fatigue Metals Under Combined Torsion and Axial Load or Bending", Journal of Engineering Industry, pp. 301-306, 1959.
[13] Findley, W.N., "Modified Theories of Fatigue Failure Under Combined Stress", Proceedings of the Society of Experimental Stress Analysis 14(1), pp. 35-46, 1956.
[14] Findley, W.N., Coleman, J.J., Hanley, B.C., "Theory for Combined Bending and Torsion Fatigue with Data for SAE 4340 Steel", Proceedings of the International Conference on Fatigue of Metals, Institute of Mechanical Engineers, London, pp. 150-156, 1956.
[15] Marques, F., Cunha, A., Fernandes, A.A., Caetano, E., Magalhães, F., "Evaluation of dynamic effects and fatigue assessment of a metallic railway bridge", Structure and Infrastructure Engineering: Maintenance, Management, Life-Cycle Design and Performance 6(5), pp. 635–646, 2009.

Chapter VIII

Finite element modelling of a relevant detail of the Alcácer do Sal Bridge

8.1. INTRODUCTION

Fatigue is a cause of progressive damage of bridges. Particularly the steel and the composite steel/concrete railway bridges are the most susceptive to this damage phenomenon [1-4]. The increasing number of numerical and experimental fatigue damage assessments being performed on railway bridges [5-12] is a clear indication of the relevance of this topic in structural engineering.

Local models to fatigue have gained popularity with respect to the classical nominal S-N approaches [13-16]. Local approaches to fatigue recognize the localized nature of fatigue damage process; however they require reliable models and local time-history data, such as local stress and strain histories, stress intensity factors histories at fatigue crack tips, in order to permit trustworthy fatigue assessments, including residual life assessments.

The local nature of the fatigue problem raises important challenges concerning the fatigue analysis of large structures using local fatigue models, which is the case of the bridges subjected to an important diversity of traffic characteristics. Theoretically, a global computational model of the bridge is required - generally a finite element model - which must include the critical location modelled in fine detail to allow the accurate assessment of the fatigue damage. That level of refinement at the details cannot be extended to the global structure [17]. This kind of modelling requirement corresponds to a multi-scale modelling problem [18], which inevitably leads to heavy computational models, demanding huge computational resources and time for the fatigue analyses. This situation could become impracticable, if a significant diversity of traffic has to be modelled and their dynamic effects to be accounted.

This chapter will present an accurate and computationally efficient method for the fatigue assessment of bridge details, using Fracture Mechanics and including the numerical simulation of fatigue crack growth. The local time-history data needed for the fatigue damage assessment is generated using the new concept of modal stress

intensity factors and modal superposition method. This procedure was firstly presented for the computation of stress intensity factors a simple structural problem [19]. In this chapter the proposed procedure is applied to a complex problem, the Portuguese Alcácer do Sal Composite Railway Bridge, for which experimental data concerning both traffic and bridge local response are available [20]. An hypothetical scenario of fatigue residual life assessment, based on Fracture Mechanics concepts, is presented, to illustrate the efficiency of the proposed method.

Since the bridge was made of welded construction, the proposed approach could be also used to model the total fatigue life. Also, the proposed approach can be also extended for the application of local approaches aiming the crack initiation simulation. Nevertheless the chosen problem shows higher complexity since the crack is allowed to propagated under mixed-mode conditions and taking into account a significant sample of distinct trains, that were obtained from monitoring information.

8.2. THEORETICAL BACKGROUND

This section contains the theoretical background supporting the methodology that will be discussed in this chapter. Subsection 8.2.1 gives an overview of the modal superposition method and its importance for the dynamic analysis of railway bridges are briefly presented. The fatigue model adopted, which is based on Linear Elastic Fracture Mechanics, is detailed in Section 8.2.2 and Section 8.2.3 describes how the modal superposition can be applied to compute the stress intensity factors.

8.2.1. Dynamic analysis using modal superposition

A train crossing a railway bridge originates a dynamic response/vibration of the structure. If the traffic loads are known, the dynamic response can be simulated numerically using a finite element model of the bridge, trains being simulated as moving loads. Two common numerical methods employed to perform that dynamic

analysis are the direct integration and the modal superposition methods [21]. For finite element models with a large number of degrees-of-freedom (*N*), the direct integration method becomes highly time-consuming, as it requires solution of the following equation, without additional assumptions:

$$\mathbf{M}\cdot\ddot{u}(t)+\mathbf{D}\cdot\dot{u}(t)+\mathbf{K}\cdot u(t)=F(t) \tag{8.1}$$

where, **M**, **D** and **K** are the mass, damping and stiffness matrices, respectively, and have a $N\times N$ dimension, each. $F(t)$ is the $N\times 1$ matrix of the nodal forces acting in the structure for a certain time-step and $u(t)$, $\dot{u}(t)$ and $\ddot{u}(t)$ are $N\times 1$ matrices of the displacements, velocities and accelerations at the same time step.

The modal superposition method can be used for the dynamic analysis and could be computationally more efficient if the global dynamic response of the structure can be accurately reproduced by superimposing a limited number (*J*) of modes of vibration. That is the case of flexible structures with elastic behaviour, such as composite railway bridges [22].

Applying modal superposition, the full $N\times N$ system of equations is converted into N uncoupled single-variable equations that can be solved independently:

$$\ddot{Y}_j(t)+2\omega_j\cdot\xi_j\cdot\dot{Y}_j(t)+\omega_j^2\cdot Y_j(t)=f_j(t) \tag{8.2}$$

where Y_j is the modal coordinate, ω_j is the natural frequency, ξ_j is the modal damping ratio and f_j represents the modal forces, for the j^{th} mode of vibration. The efficiency of the modal superposition technique is twofold: i) uncoupling of the system of equations; ii) the total number of modes of vibration needed to accurately reproduce the dynamic response of the flexible structure, J, is usually significantly lower than the total number of degrees of freedom $\left(J\ll N\right)$ [22].

8.2.2. Fatigue model

In order to demonstrate the proposed methodology, a fatigue model was selected to simulate the crack propagation at a selected welded detail of the Alcácer do Sal bridge. Since initial cracks are normally present in welded joints, their fatigue behaviour is usually well characterized by Fracture Mechanics approaches [16], the initiation phase being disregarded. This was demonstrated in the Chapter 6, where such approach was demonstrated to produce very consistent S-N predictions for the laboratory welded details tested in this work. Moreover, when the dimension of the plastic zone at the crack tip is small when compared with the crack length, Linear Elastic Fracture Mechanics (LEFM) can be assumed. This latter assumption is representative of metallic bridges since it is expected they exhibit low stress levels and an elastic dominant mechanical behaviour is expected.

In the linear elastic domain, the stress fields around the crack tip are controlled by the stress intensity factor (SIF), K [23]. The fatigue crack propagation rate, on the other hand, is related with the ranges of cycles of K, which is commonly represented as ΔK. A variety of crack propagation laws are available in the literature, with more or less complexity depending on the number of variables considered [24]. In the current work, the well-known Paris Law (Equation (8.3)) was adopted [25]:

$$\frac{da}{dN} = C\Delta K^m \tag{8.3}$$

where da/dN is the crack propagation rate and C and m are material-dependent properties. In spite of its known limitations, Paris's law has been widely used (e.g. in design codes) due to its simplicity. It should be stressed that it is only valid for the fatigue crack propagation in Region II.

Fatigue cracks in complex details of railway bridges subjected to real traffic conditions, may experience mixed mode (I+II) growth conditions. Mixed mode crack propagation was therefore assumed, in the current work. Therefore, an equivalent stress intensity factor was computed using the relation proposed by Tanaka [26]:

$$K_{eq}(t) = \sqrt[4]{K_I^4(t) + 8K_{II}^4(t)} \tag{8.4}$$

where K_I is the mode I stress intensity factor and K_{II} is the mode II stress intensity factor. Since traffic loads generate random/variable amplitude stress histories, the rainflow method [27] was selected to extract the histogram of equivalent stress intensity factor ranges ($\Delta K_{eq,i}$, n_i). The fatigue crack increment corresponding to the application of the histogram can be computed by the direct integration of the Paris's law, neglecting interaction effects:

$$\Delta a = \sum_i n_i \cdot C\left(\Delta K_{eq,i}\right)^m \tag{8.5}$$

Under mixed mode conditions, the crack path is no longer straight, and a crack branching criteria is required. A methodology based on the maximum tangential stress criteria [28] was adopted. The first step of this methodology consisted in the computation of the time history of the kink angle, θ:

$$\theta(t) = \cos^{-1}\left(\frac{3K_{II}^2(t) + \sqrt{K_I^4(t) + 8K_I^2(t)K_{II}^2(t)}}{K_I^2(t) + 9K_{II}^2(t)}\right) \tag{8.6}$$

For an histogram of stress intensity factors, e.g. corresponding to a train crossing, the equivalent kink angle can be computed, using the following weighted average [29]:

$$\overline{\theta} = \frac{\sum_{i=1}^{n} \frac{da}{dN}\left(\Delta K_{eq,i}\right) \times \theta_i\left(K_I, K_{II}\right)}{\sum_{i=1}^{n} \frac{da}{dN}\left(\Delta K_{eq,i}\right)} \tag{8.7}$$

8.2.3. Modal superposition of stress intensity factors

As described in [19], the utilization of the modal superposition method allows the computation of the stress intensity factor time histories, $K_{total}(t)$, with a low computational cost. *K* can be defined generically as follows:

$$K(t) = C\sqrt{\pi a}\cdot\sigma \tag{8.8}$$

where *C* is a function of the crack dimensions, the geometry of the structure and the loading configuration, σ is the remote stress acting on the detail and a is the crack dimension. Static loading acting on the structure (*e.g.* structure's self-weight) induces a certain stress state on it, σ_{sta}. If the structure contains a crack of dimension a_n, the corresponding stress intensity factor, K_{sta}, through the crack front, is:

$$K_{sta} = C_n\sqrt{\pi a_n}\cdot\sigma_{sta} \tag{8.9}$$

If the same structure is subjected to a dynamic loading, the corresponding stress field, variable in time, is $\sigma_{dyn}(t)$. Assuming that, during each dynamic loading event, the crack remains with approximately constant dimensions, a_n, then:

$$K_{dyn}(t) = C_n\sqrt{\pi a_n}\cdot\sigma_{dyn}(t) \tag{8.10}$$

Considering the contribution of both the static and dynamic loadings and considering that the static load is usually constant over time, the total stress intensity factor at the crack front becomes:

$$K^{*}_{total}(t) = K_{sta} + K_{dyn}(t) \tag{8.11}$$

Nevertheless, K^*_{total} is not yet the final total stress intensity factor, as it requires a "signal" correction to be performed. This correction is detailed in later paragraphs.
By applying the modal superposition method, $\sigma_{dyn}(t)$ can be expressed as:

$$\sigma_{dyn}(t) = \sum_j \sigma_j \cdot Y_j(t) \tag{8.12}$$

In Equation (8.12), the j subscript refers to the number of each mode of vibration, σ_j is the nominal stress in the j^{th} mode shape and $Y_j(t)$ is the modal coordinate of the j^{th} mode of vibration [21]. Replacing Equation (8.12), in Equation (8.10), the SIF due to the dynamic loading becomes:

$$K_{dyn}(t) = C_n\sqrt{\pi a_n} \cdot \sum_j \sigma_j \cdot Y_j(t) = \sum_j C_n\sqrt{\pi a_n} \cdot \sigma_j \cdot Y_j(t) = \sum_j K_j \cdot Y_j(t) \tag{8.13}$$

where K_j is the modal stress intensity factor, or in other words, the stress intensity factor obtained with the configuration of the j^{th} mode shape. Finally, the total stress intensity factor can be expressed as:

$$K^*_{total}(t) = K_{sta} + \sum_j K_j \cdot Y_j(t) \tag{8.14}$$

As detailed in [19], the computed $K^*_{total}(t)$ can have a negative sign during some periods of time. In the opening mode that situation would correspond to crack closure. From a practical perspective, when the computed $K^*_{total}(t)$ assumes negative values it will be converted to a null value to represent a closed crack. Thus, the final expression for mode I stress intensity factor computation becomes:

$$K_I(t) = \begin{cases} K_{I,sta} + \sum_j K_{I,j} \cdot Y_j(t) & \Leftarrow K_{I,sta} + \sum_j K_{I,j} \cdot Y_j(t) \geq 0 \\ 0 & \Leftarrow K_{I,sta} + \sum_j K_{I,j} \cdot Y_j(t) < 0 \end{cases} \tag{8.15}$$

If mixed mode crack propagation is assumed, besides K_I also K_{II} needs to be computed. That is done, in a similar way, using the following equation:

$$K_{II}(t) = K_{II,sta} + \sum_j K_{II,j} \cdot Y_j(t) \tag{8.16}$$

In the case of mode II, negative values of stress intensity factor are allowed. The change of signal of K_{II} corresponds to the reversal of sliding movement between the faces of the crack with consequence change in direction propagation.

As defined by Equations (8.14) to (8.16), the mode I and mode II stress intensity factors time histories may be obtained if the modal stress intensity factors for an adequate number of vibration modes, K_j, plus the stress intensity factor regarding to the static load (e.g. self-weight), K_{sta} are known in advance. Also the modal coordinates $Y_j(t)$ associated to each mode of vibration are also required.

8.3. Proposed workflow for residual fatigue life assessment of bridge details

Based on the methodology and fatigue model described previously, a workflow was developed aiming the simulation of the fatigue crack propagation in critical details of bridges, subjected to a diversity of traffic. The workflow is divided in two main steps. The first step (Figure 8.1) consists of pre-processing activities involving the following inputs:

global numerical model of the bridge;

local numerical model of the detail under analyses;

traffic information, such as axle loads, axles spacing and trains speed. The traffic scenario may come from monitoring systems or from other sources such as design codes.

The modal analysis performed on the global numerical model of the structure allows the computation of the modal displacement fields, Φ_j, and dynamic properties, ω_j and m_j. The required modal damping ratios, ξ_j, can be estimated based on design codes or field measurements [22]. On the other hand, the displacement field originated by the static loading, Φ_{stat}, is obtained after a static analysis using the same model.

The above mentioned displacement fields are then extrapolated to the boundary nodes of the local numerical model of the detail, through a submodelling process. The boundary nodal displacements associated to the static loading are stored in the file $BDCO_{sta}$. Additionally, the displacements associated to each j^{th} mode of vibration are stored in the file $BDCO_j$.

Finally, the traffic information available in the monitoring system database (trains speeds, axle loads and axles spacing) is combined with the dynamic properties (Φ_j, ξ_j, ω_j and m_j) of the global model in order to obtain the modal coordinates time histories, $Y_j(t)$. That is achieved by solving Equation (8.2) for each traffic event and for each mode of vibration [22].

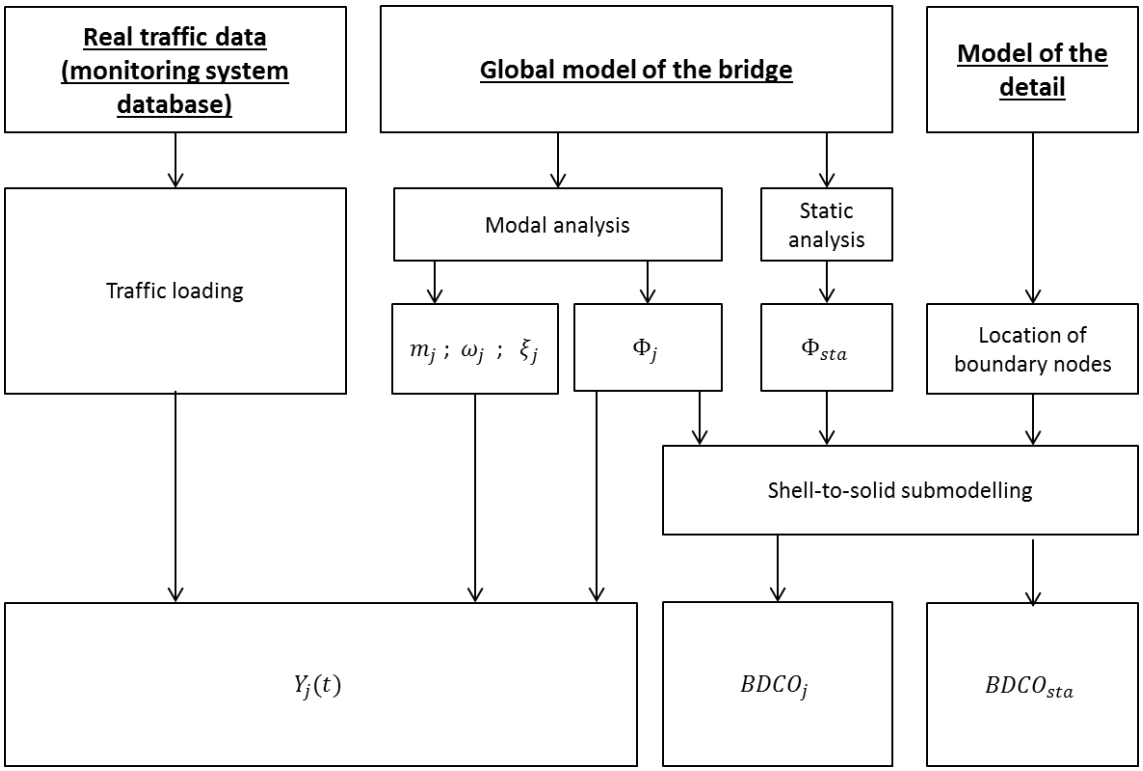

Figure 8.1 – Workflow of the proposed analysis: pre-processing of the input data (1st step).

Therefore, the outputs of the first step of the workflow (pre-processing of the input data) will be:

- the time history of the modal coordinates, for each mode of vibration of the structure and for each traffic event considered;
- the nodal displacements to be applied to the boundaries of the local model of the detail in order to replicate the static and modal displacement fields.

One key advantage of the proposed method is that the referred outputs only need to be computed once. They then become the only inputs needed for the second step of the workflow (Figure 8.2), which consists on the crack propagation simulation.

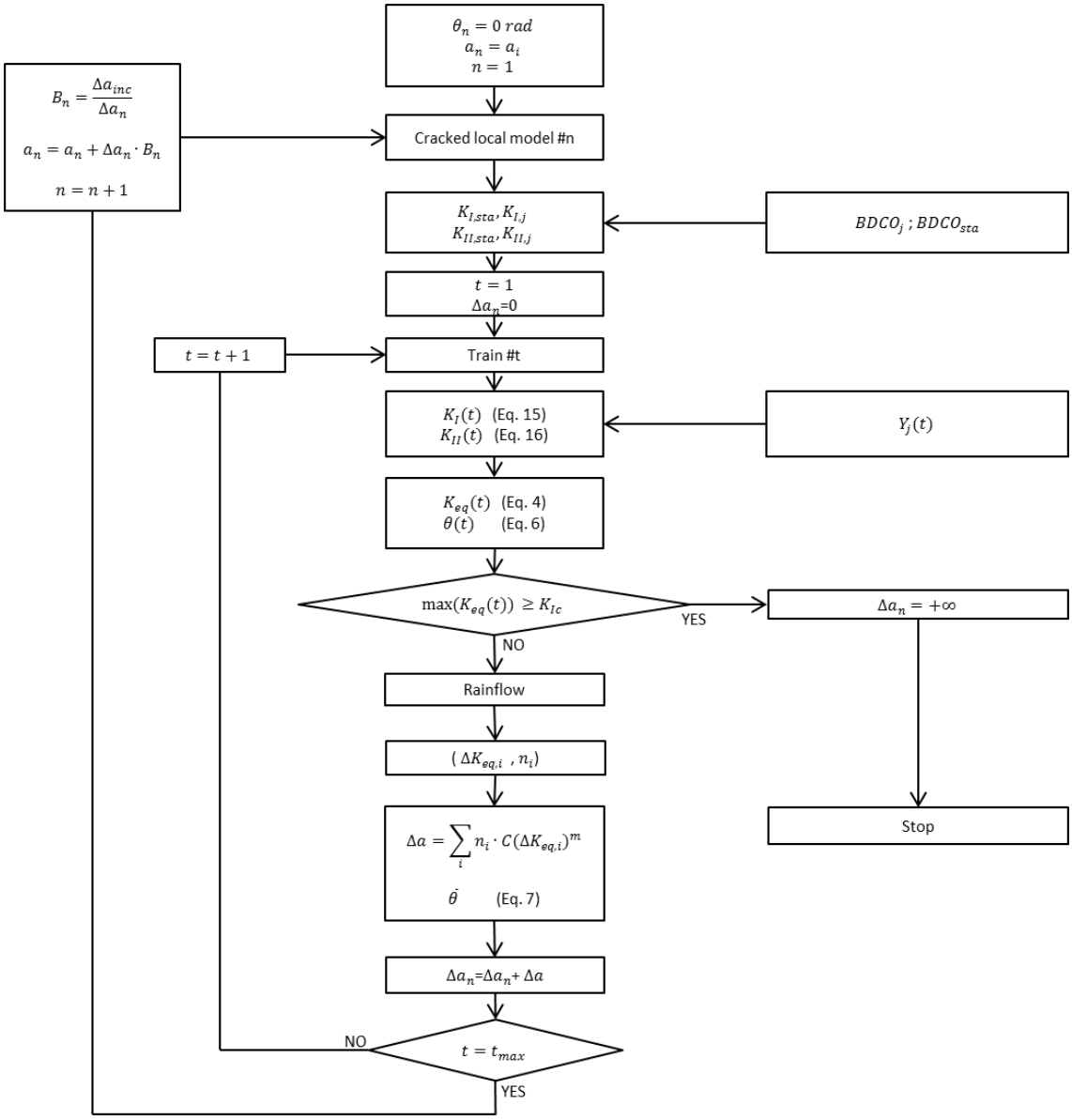

Figure 8.2 – Workflow of the proposed analysis: crack propagation simulation (2nd step).

The simulation starts with an initial crack in the local model of the detail. Applying the previously stored boundary conditions ($BDCO_{sta}$ and $BDCO_j$), the static and modal stress intensity factors, K_{sta} and K_j are computed, using an appropriate numerical technique, such as the virtual crack closure technique (VCCT) [30], the J-integral [31] or the displacements extrapolation (DE) methods [32].

For each train stored in the monitoring system database, the corresponding modal coordinates are loaded allowing to compute K_I(t) and K_{II}(t), by application of Equation (8.15) and (8.16), respectively. Equivalent stress intensity factors, K_{eq}(t) (Equation (8.4)), and the kink angle $\theta(t)$ (Equation (8.6)) are computed next. At this point, if the maximum observed value of K_{eq}(t) exceeds the material toughness, K_{Ic}, that means the crack would propagate in an instable way, the simulation stops and current crack length is considered the final crack length before the failure of the detail. Otherwise, if the maximum observed value of K_{eq}(t) does not surpass the adopted material toughness, the crack propagation associated to the train passage is computed. The rainflow method is applied to the K_{eq}(t) time history to obtain the histogram of stress intensity factor ranges. Then, Equations (8.5) and (8.7) are applied to compute the fatigue crack increment , Δa, and corresponding direction for that train passage. The contribution of all trains of an existing database is summed up to obtain a final crack increment, Δa_n. For computational efficiency reasons, it is useful to adopt constant crack length increments, Δa_{inc}. In this case, the crack increment corresponding to a loading block needs to be scaled by $B_n=\Delta a_{inc}/\Delta a_n$. B_n represents the number of loading blocks, i.e. the number of the trains database need to be applied in order to achieve the Δa_{inc} increment.

After computing the crack increment for all the trains of the monitoring system database, the total crack length and direction is updated in the local model and the process is repeated.

In the next section, the proposed approach is demonstrated for a welded detail from the Alcácer do Sal railway bridge.

Figure 8.3 – New Alcácer do Sal railway bridge.

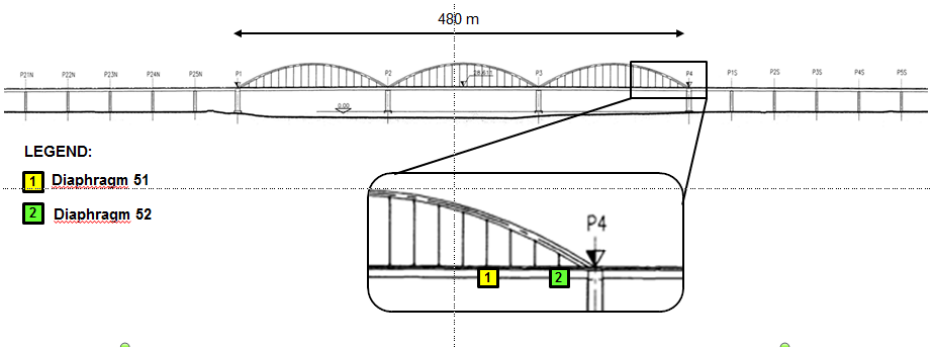

Figure 8.4 – Location of diaphragms 51 and 54 on bridge.

8.4. APPLICATION OF THE PROPOSED METHODOLOGY TO A CASE STUDY

The case study selected to demonstrate and validate the proposed methodology was a welded detail of the composite bridge of the new railway crossing of river Sado, which is located in the Lisboa-Algarve connection, in Portugal (Figure 8.3).

8.4.1. Monitoring system

Due to the paramount relevance of this structure, a monitoring system was installed to allow the real time traffic characterization and structural behaviour evaluation [20].

The structural behaviour was assessed by means of strain gauges installed at the diagonals of diaphragm 51 and 54 (Figure 8.4). In addition, diaphragm 51 was monitored

with 5 additional strain gauges that were installed at the top of the diagonal in order to better assess the stress field near the detail (local strain gauges) (Figure 8.5).

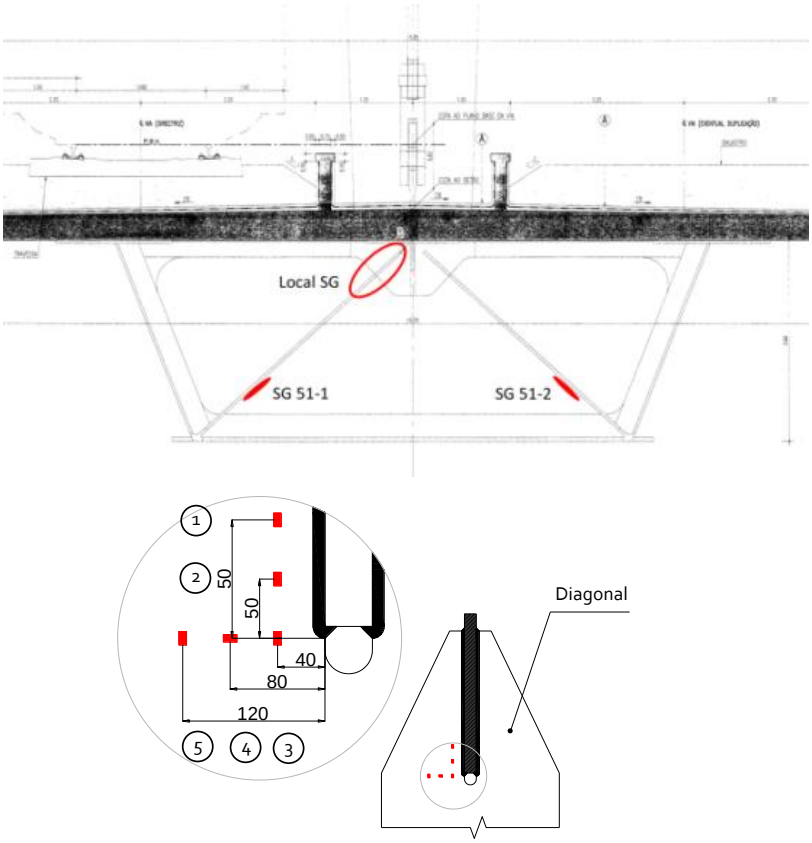

Figure 8.5 – Location of strain gauges at diaphragm 51: a) global and local strain gauges locations; b) detail of local strain locations.

The traffic was characterized using shear strain gauges welded to the rails and instrumented rail pad sensors. Each train crossing the bridge is totally characterized (train speed and direction, axle loads and axles spacing), through routines developed for that purpose, in MATLAB®, and the corresponding information stored in a database also in MATLAB® format. The information has been sent, through a 3G connection, to a server at the Faculty of Engineering of University of Porto. Therefore, an extensive database, including real strain measurements and trains characteristics is available and was used in the present work. The monitoring system development was out of scope of the current dissertation, therefore the respective details can be found elsewhere [33, 34]. Only the local strain gauges instrumentation was performed with the works leading to this document.

8.4.2. The global numerical model of the bridge

The global numerical model of the bridge was developed using the ANSYS® code [35] and its ANSYS® Parametric Design Language (APDL). This was performed within the context of FADLESS project and only general information will be given in this chapter for the sake of completeness [22-34].

The concrete slab and the steel box girder were modelled using linear 4-noded shell elements (SHELL63 of ANSYS® library) while most of the diaphragms and diagonals, the arches and the hangers were modelled with linear beam elements (BEAM44 of ANSYS® library [32]). The connection between the concrete slab and the upper flanges of the steel box was achieved by means of multipoint constraint procedures, assuming rigid connections (MPC184 of ANSYS® library).

The diaphragms 51 and 54 and corresponding diagonals were modelled with a fine mesh of shell elements, with maximum dimension of 0.1m, in order to facilitate the comparison of the numerical results with the strain gauge measurements captured with the permanent monitoring system [33]). The rest of the deck used a mesh size of 2m, as per the results of a sensitivity analysis. The numerical model was calibrated, based on the results of an Ambient Vibration Test and a load test performed in the bridge [36]. After calibration of the global numerical model, a modal analysis was performed and the corresponding modal properties (Φ_j , ξ_j, ω_j and m_j) were computed and exported to MATLAB®. In MATLAB®, those modal properties are combined with the traffic information already stored in the database, $F(t)$, and the dynamic response of the structure is simulated, using the modal superposition technique (Equation 8.2) and adopting a total of 1500 modes of vibration. At this stage, the modal coordinates, $Y_j(t)$, are computed and stored.

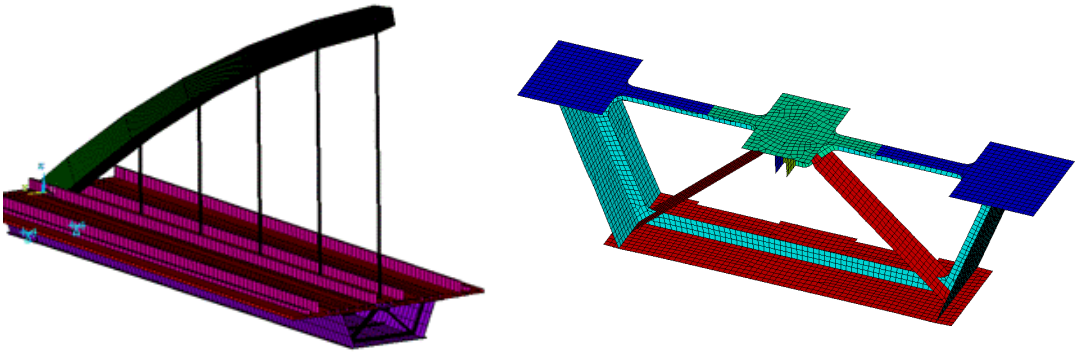

a) b)

Figure 8.6 – Some details of the global numerical modal of the bridge: a) deck, hangers and arch; b) diaphragm 51 and corresponding diagonals.

8.4.3. The local numerical model of the selected detail and shell-to-solid sub-modelling technique

A local finite element model of a selected welded detail was built. Its geometry was defined using the commercial software SOLIDWORKS® and then exported to the finite element software ANSYS®. All the properties of the finite element model were defined in a parametric format, using ANSYS® APDL language. The parametric code was prepared for the simulation of a fatigue crack with curved generic crack path or to simulate an uncracked detail.

An uncracked geometry was considered first, aiming the validation of the submodelling process and the submodel itself, by comparing numerical results with the experimental data from the local strain gauges placed near the welded joint (Figure 8.5). Furthermore, the uncracked finite element model allowed detecting potential fatigue cracking hot spots. It must be emphasized that the bridge does not show any visible signal of fatigue damage, in particular fatigue cracks. Therefore, the monitoring system gives information regarding the uncracked bridge. Also, the bridge was inaugurated very recently which means that it could be considered in virgin state.

Once the potential cracking location was defined, the APDL routine developed allowed the simulation of an initial postulated crack explicitly in the finite element model of the welded detail. Moreover, the APDL routine was also used to update the fatigue crack path after each running of the workflow.

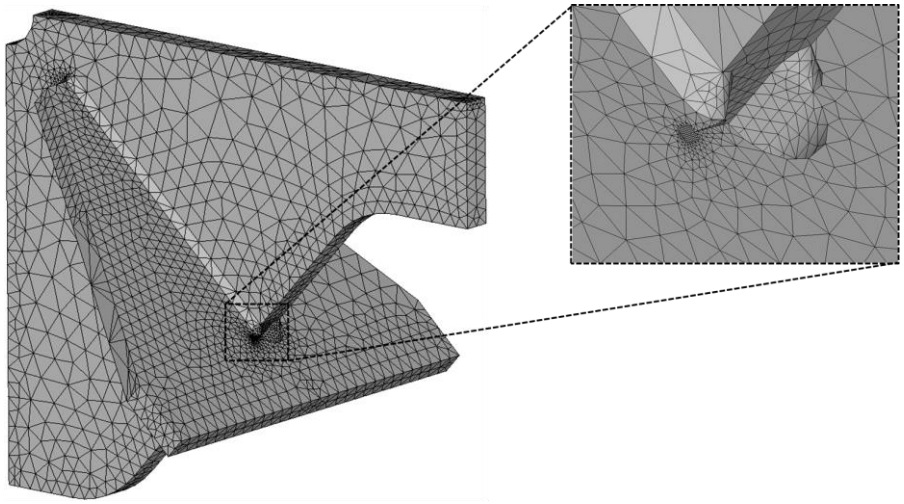

Figure 8.7 – Local finite element model of the welded joint of the Alcácer do Sal bridge.

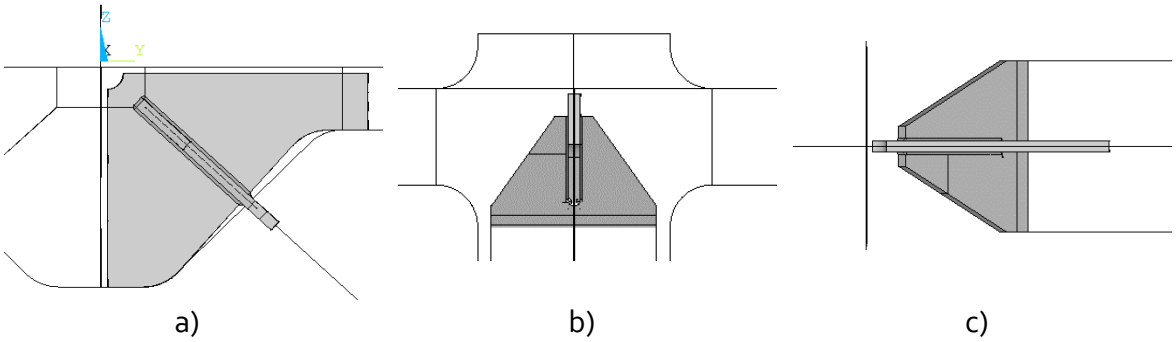

Figure 8.8 – Shell-to-solid sub-modelling, location of the local FE model with respect the shell model: a) front view; b) side view; c) top view.

Figure 8.7 shows the local finite element model with an initial crack. The bulk of the welded detail was modelled using tetrahedral quadratic finite elements. However, at the crack tip, a refined region was modelled with hexahedral quadratic finite elements, in order to accurately assess the stress intensity factors. The transition between the refined and coarse regions is achieved by means of pyramidal finite elements.

In order to compute the boundary conditions to be applied to the local finite element model of the detail, displacements resulting from the global finite element model of the bridge were interpolated for the whole set of boundary nodes of the local finite element model. This was accomplished using the shell-to-solid submodeling procedure which was an automatic procedure available in ANSYS® [32]. In order this procedure work properly, the shell planes of the global model should fit the mid thickness of the plates of the local model. That was achieved in this case, as illustrated in Figure 8.8.

By applying the shell-to-solid submodeling procedure, the computation of the static and modal stress intensity factors using the local numerical model of the selected detail, can be uncoupled from the analysis of the global numerical model of the structure, reducing drastically the computation cost, is such a way that this local fatigue analysis are now feasible for significant variety of traffic conditions [19]. The virtual crack closure technique, as described by Krueger [30], as well as the displacement extrapolation (DE) method were implemented in APDL code for the stress intensity factors computation.

8.4.4. Fatigue model assumptions

The implementation of the adopted fatigue model requires the definition of the appropriate Fracture Mechanics parameters and the fatigue crack propagation data. The Paris law material dependent constants, *C* and *m*, were determined by fatigue crack propagation tests conducted using compact tension (CT) specimens built on the same material used in the bridge and with similar thickness (35 mm) [37]. Since fracture toughness tests were not specifically performed, the material toughness (K_c= 1434 $MPa\sqrt{mm}$) was estimated as the minimum value of the maximum stress intensity factors measured at failure, during a set of fatigue tests performed on CT specimens of the same material [38]. Fatigue crack propagation was simulated until $K_{eq}(t)$ reached the estimated, K_C. An initial crack length, a_i, equal to 15 mm was imposed. This value is considered a high value for an intrinsic material defect. It was proposed aiming the demonstration of a residual life computation from a known macro defect, instead of performing a full fatigue life computation, which typically would require a fatigue crack bellow 1 mm. The assumption of a 1 mm crack would require the simulation of a non-constant depth crack. Taking into account the high thickness of the diagonal, a crack of 1 mm depth will be very likely well simulated with a curved crack front. This type of crack front does not represent a limitation of the proposed method, only a change in the local numerical model being required.

At the end of each run of the 2nd step of the proposed workflow, the crack length is incremented by 5mm (Δa_{inc}). As the traffic loading block originates a much lower crack

progression, Δa_n, the equivalent number of traffic loading blocks, B_n, has to be computed. Table 8.1 summarizes the Fracture Mechanics and fatigue parameters considered in the analysis. Since the stress levels experienced by the bridge details for real traffic conditions were very small, the real fatigue crack propagation threshold of the material was not applied otherwise the postulated fatigue crack would not propagate. A residual propagation threshold was selected in order to allow filtering very small stress cycles.

Table 8.1 – Adopted fracture mechanics and fatigue parameters for the fatigue analysis performed using the welded model of the Alcácer do Sal bridge.

ΔK_{th}	K_{IC}	C	m	a_i	a_{inc}	$a_{\max}$
$MPa\sqrt{mm}$	$MPa\sqrt{mm}$	$MPa\sqrt{mm}$	$MPa\sqrt{mm}$	mm	mm	mm
63*	1434 [16]	9.93e-14 [15]	3.14 [15]	15	5	200

**Since no crack propagation was observed, the authors adopted K_{th} =0.1 $MPa\sqrt{mm}$ in order to promoted crack propagation*

8.5. Results

8.5.1. Experimental Validation

In order to validate the adopted submodeling procedure, the experimental local strain gauge data from the monitoring system was compared with the numerical simulation results obtained at the same locations, in the uncracked submodel. The numerical simulation was performed in MATLAB® using the modal superposition technique. An example of that comparison, for a freight train crossing (Figure 8.13c), is shown in Figure 8.9.

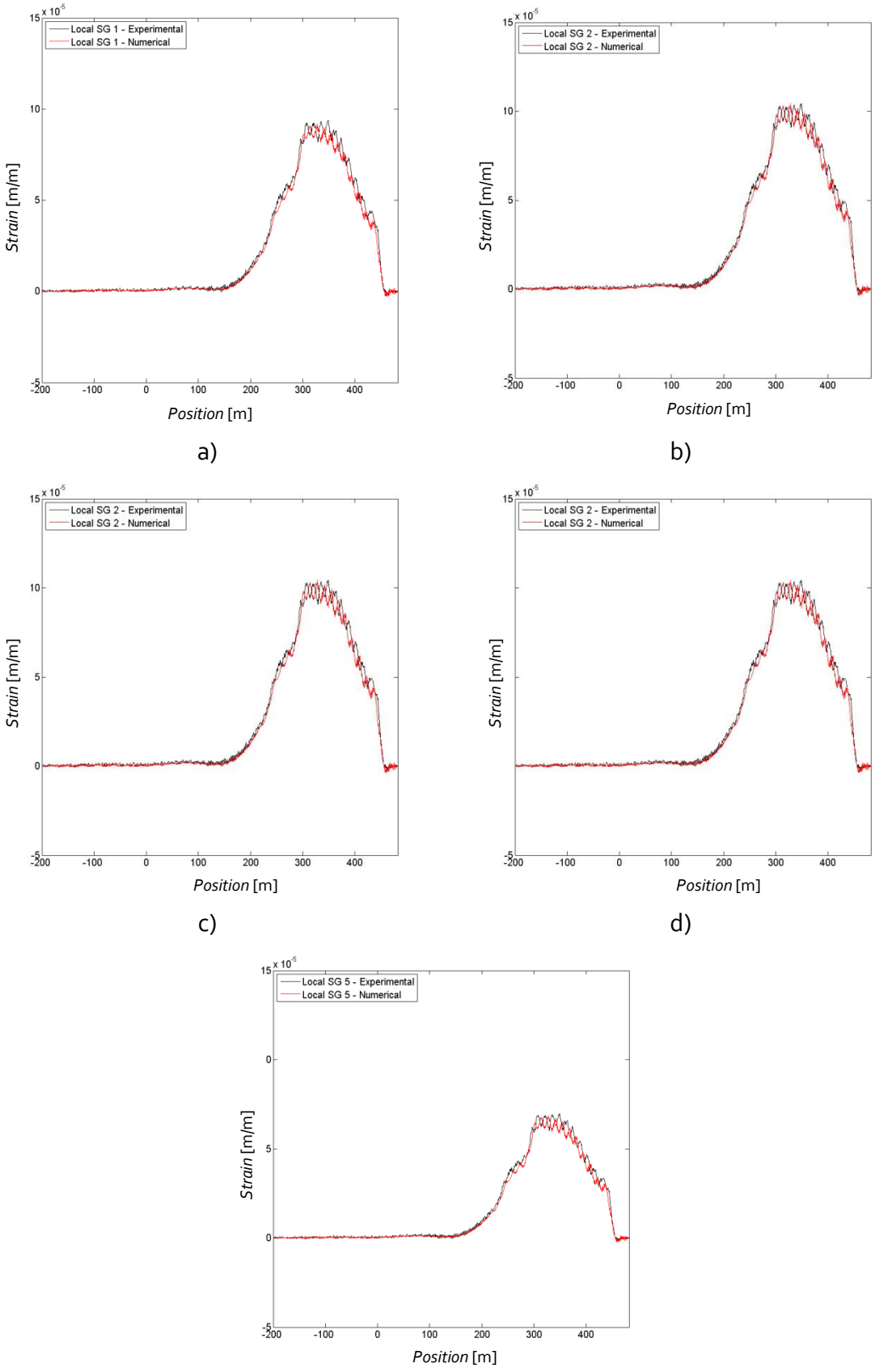

Figure 8.9 – Experimental vs. numerical strain measurements: a) strain gauge 1; b) strain gauge 2; c) strain gauge 3; d) strain gauge 4; e) strain gauge 5.

A very good agreement can be observed between the experimental and the numerical results, which confirms the adequacy of the complete proposed procedure including the submodeling techniques employed.

After validation of the submodeling procedure, the uncracked local model was used to determine the most probable crack initiation spot. For several train crossing simulations, the maximum normal stresses at the diagonal confirmed the same location, which is at the weld toe of the joint between the diagonal and the gusset plate (Figure 8.10a). This location is coincident with the crack initiation location observed at the experimental tests performed using small-scale replicas of this welded joint [39] (Figure 8.10b). This location was therefore used for the crack localization in the local model. It must be stressed that even if experimental observations pointed out the formation of 2 symmetrical fatigue cracks (Figure 8.10b), only one fatigue crack propagation was modelled. That allowed reducing the complexity of the model without jeopardizing the validation of the proposed methodology.

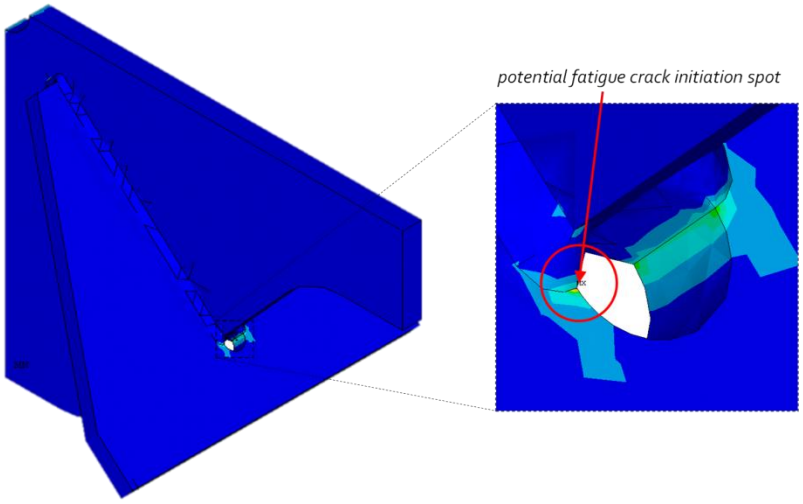

a)

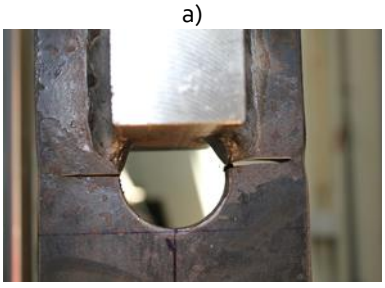

b)

Figure 8.10 – Fatigue crack initiation spot: a) numerical simulation of real detail; b) experimental evidence from fatigue tests of small-scale fatigue tests.

8.5.2. Comparison of stress intensity factors computation techniques

Different numerical methods are available for the numerical computation of stress intensity factors. In the current work, two different methods were used for cross-validation: the virtual crack closure technique [14] and the displacements extrapolation method [18]. The stress intensity factors were computed in ANSYS® using both methods, for the same freight train presented before and an initial crack dimension of 15mm. The results are presented in Figure 8.11. The difference between both methods is less than 10%. Therefore, the DE method was adopted as the reference being selected as the basis for the numerical results presented in the rest of this paper. The analysis of the results presented in Figure 8.11 shows that, for the initial crack, mode I stress intensity factor, K_I, is one order of magnitude higher than Mode II stress intensity factor, K_{II}.

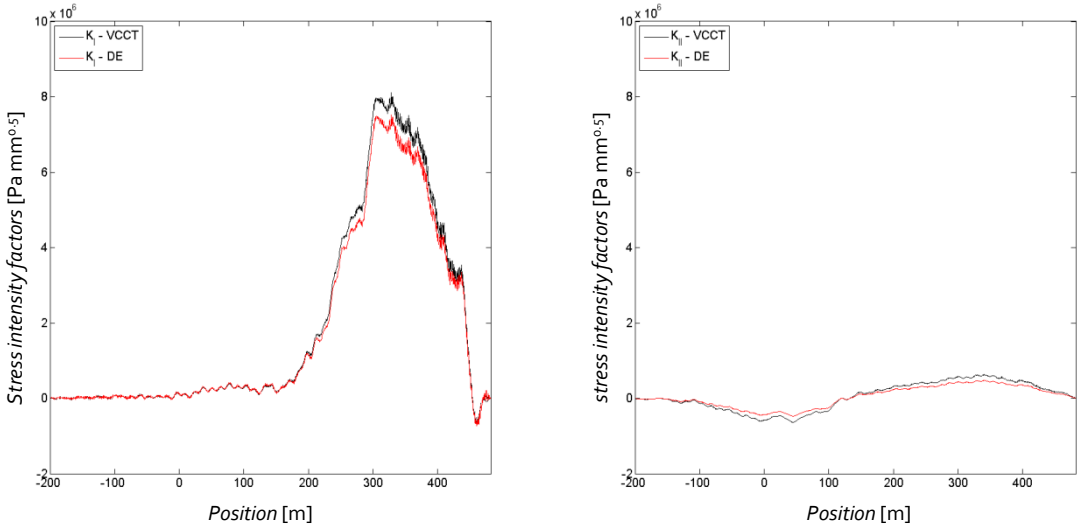

Figure 8.11 – VCCT vs. DE: a) K_I; b) K_{II}.

8.5.3. Residual fatigue life computation

Once all the different techniques applied were validated, the entire workflow was run (Figures 8.1 and 8.2), in order to assess the remaining fatigue life of the structure.

The crack propagation occurred, as expected, in a direction perpendicular to the principal stresses, which underlined the importance of considering a crack branching

criteria. The crack propagation stopped at iteration number 33, when the maximum computed stress intensity factor reached the adopted material toughness. The entire crack propagation path (a=175mm) is illustrated in Figure 8.12.

The crack propagation simulation, which comprised blocks of 565 trains, 33 crack increments and 1500 modes of vibration, was accomplished in approximately 3.5 days, confirming the high computational efficiency of the proposed methodology. A personal computer with a 3.2 GHz i7 processor and 24 GB RAM memory was used. Each traffic block included 565 trains corresponding to a total traffic load of 0.52 MMt. The equivalent annual traffic volume is 3.1 MM t/year. The trains are freight and passenger trains (Figure 8.13), with a variety of weights, speeds and lengths, as illustrated in Figure 8.14.

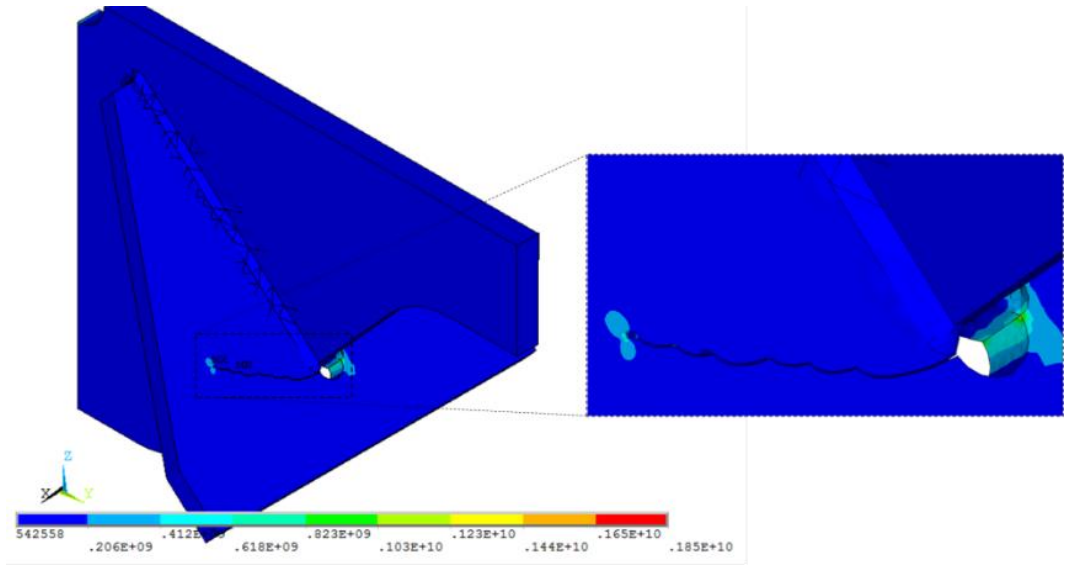

Figure 8.12 – Fatigue crack propagation path simulated for the welded detail of the Alcácer do Sal bridge.

a) b) c)

Figure 8.13 – Types of trains crossing the bridge: a) Alfa Pendular passengers train; b) intercity passengers train; c) freight train.

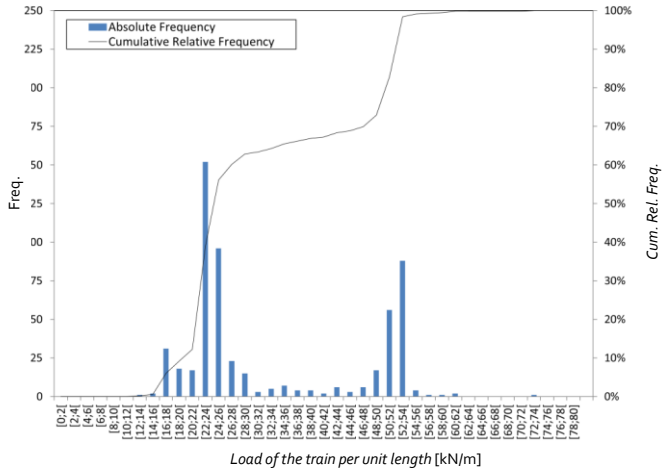

a)

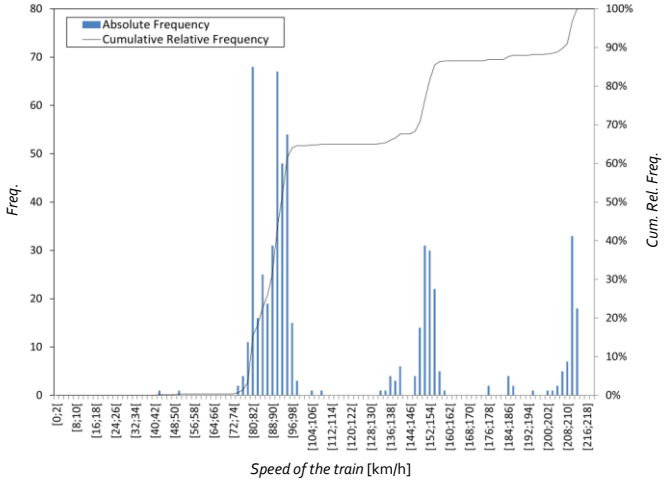

b)

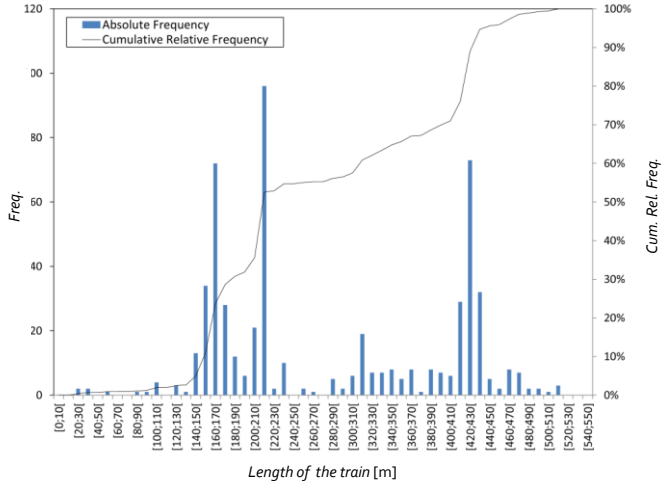

c)

Figure 8.14 – Characteristics of simulated trains: a) Trains loads per unit length: b) Trains speeds; c) Trains lengths.

The evolution of the total crack length as a function of the cumulative traffic volume is shown in Figure 8.15. It should be noted that the changes in crack propagation rates and in the crack path observed over time are affected by the length of the finite crack increments adopted for the crack simulation (Δa_{inc}=5mm). Smaller crack increments would provide more accurate results, but with associated costs in terms of computational time.

If the current traffic volumes on the bridge were kept stable in the remaining life of the bridge, the hypothetical crack would propagate during approximately 95 years (see Figure 8.16). Nevertheless, it should be noted that the fatigue traffic mixes present in the standards usually assume higher traffic volumes. In the Eurocodes, for instance, an annual traffic volume of 25 MM t is considered as reference. Therefore, a scenario of 25 MM t per year was also included in the analysis. In that case, the simulated crack would take approximately 12 years to propagate (Figure 8.16).

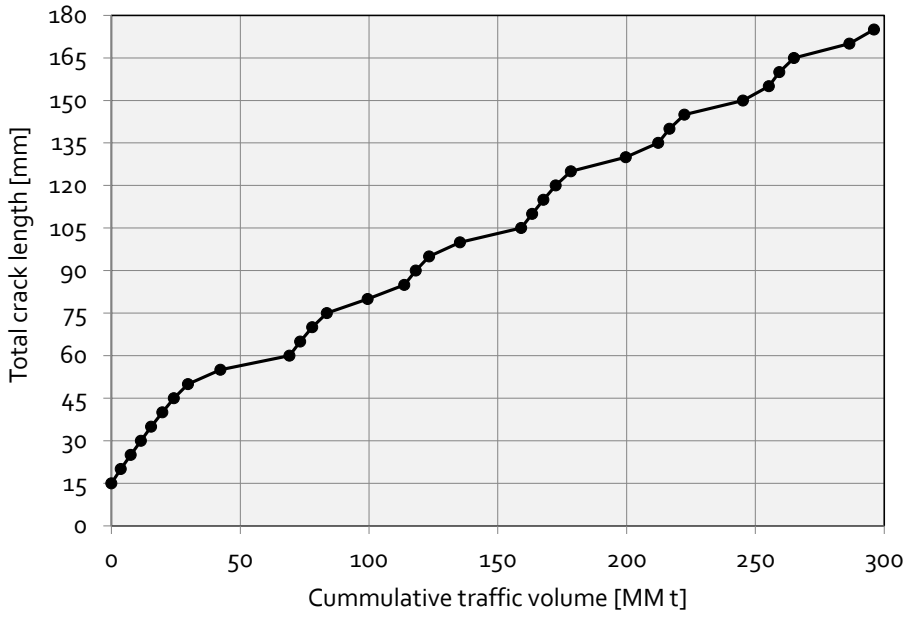

Figure 8.15 – Crack propagation length as a function of cumulative traffic for current traffic volumes.

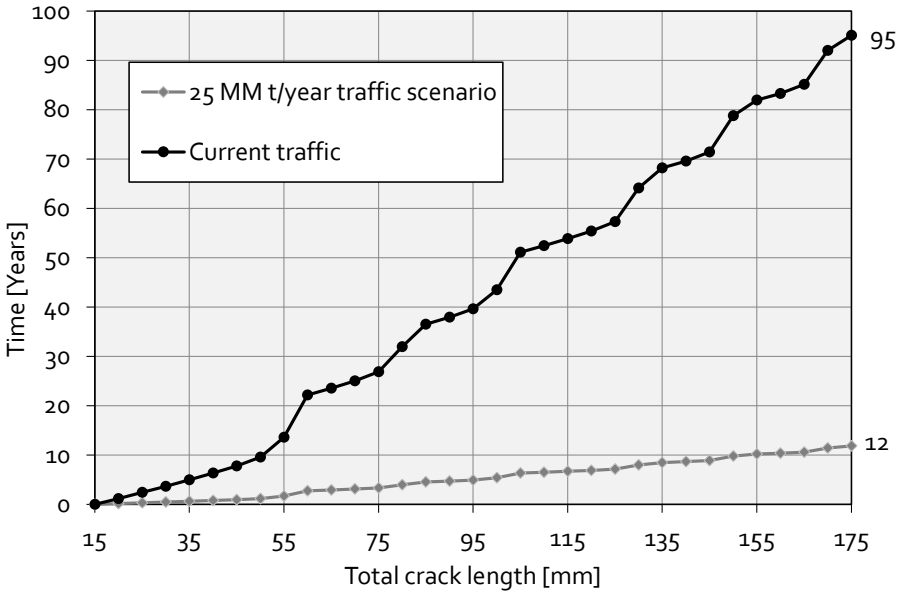

Figure 8.16 – Comparison of crack propagation for distinct traffic scenarios.

It should also be noted that these results were achieved with a highly conservative assumption on the initial crack dimension (15mm). The hypothetical crack initiation period and/or propagation period up to that 15mm crack dimension have been therefore disregarded.

The employment of the Paris Law is also considered a conservative assumption for the range of stress intensity factors observed in this analysis, since almost no crack propagation threshold ΔK_{th} was adopted.

8.6. CONCLUDING REMARKS

This chapter presented a new efficient method for the fatigue assessment of railway bridges. This method was validated by application to a case study, the bridge of the new railway crossing of river Sado. The main conclusions withdrawn from the current work are as follow:

- The simulation of fatigue crack propagation in critical details can be achieved using minimal computational resources;

- Shell-to-solid submodelling proves to be an effective way to address multiple-scale structural problems, such as localized fatigue crack propagation in large structures;
- Modal superposition of stress intensity factors confirms to be an adequate and efficient method when multiple and complex load histories are considered, such as multiple traffic events on bridges;
- For the current case study and selected detail, the assumption of mixed mode fatigue crack propagation has impact on crack propagation path;
- The proposed methodology allows the quick assessment of different traffic scenarios, e.g, the consideration of an increase of annual traffic volume over time.

Finally, it should be underlined that the simulation can be optimized, by the implementation of parallel computing, further increasing the computational efficiency. In that case it will be possible to incorporate more complex fatigue crack propagation models, for example to foreseen complex geometries for the fatigue cracks.

8.7. REFERENCES

[1] Kühn, B., Lukić, M., Nussbaumer, A., Günther, H.P., Helmerich, R., Herion, S., Kolstein, M.H., Walbridge, S., Androic, B., Dijkstra, O., Bucak, Ö., "Assessment of Existing Steel Structures: Recommendations for Estimation of Remaining Fatigue Life", in: G. Sedlacek, F. Bijlaard, M. Géradin, A. Pinto, S. Dimova (Eds.) JRC Scientific and Technical Reports, European Commission, Joint Research Centre, 2008.

[2] Haghani, R., Al-Emrani, M., Heshmati, M., "Fatigue-Prone Details in Steel Bridges", Buildings 2, pp.456-476, 2012.

[3] Miki, C., "Retrofitting Engineering for Fatigue Damaged Steel Structures", International Institute of Welding, pp. 70, 2010.

[4] Fisher, W., Roy, S., "Fatigue of steel bridge infrastructure", Structure and Infrastructure Engineering 7, pp.457-475, 2010.

[5] Zhou, H., Liu, K., Shi, G., Wang, Y.Q., Shi, Y.J., De Roeck, G., "Fatigue assessment of a composite railway bridge for high speed trains. Part I: Modeling and fatigue critical details", Journal of Constructional Steel Research 82, pp.234-245, 2013.

[6] Guo, T., Chen, Y.W., "Fatigue reliability analysis of steel bridge details based on field-monitored data and linear elastic fracture mechanics", Structure and Infrastructure Engineering 9, pp.496-505, 2013.

[7] Cremona, C., Eichler, B., Johansson, B., Larsson, T., "Improved Assessment Methods for Static and Fatigue Resistance of Old Metallic Railway Bridges", Journal of Bridge Engineering 18, pp.1164-1173, 2013.

[8] Vincenzi, L., Savoia, M., Salvatore, W., "Experimental modal analysis and fatigue assessment on the Lagoscuro viaduct", Crc Press-Taylor & Francis Group, Boca Raton, 2012.

[9] Lippi, F.V., Orlando, M., Salvatore, W., "Assessment of the dynamic and fatigue behaviour of the Panaro railway steel bridge", Structure and Infrastructure Engineering 9, pp.834-848, 2011.

[10] Caglayan, B., O., Ozakgul, K., Tezer, O., "Fatigue life evaluation of a through-girder steel railway bridge, Engineering Failure Analysis", 16, pp. 765-774, 2009.

[11] Zhou, Y., "Assessment of Bridge Remaining Fatigue Life through Field Strain Measurement", Journal of Bridge Engineering 11, pp. 737-744, 2006.

[12] Marques, F., Cunha, Á., Fernandes, A.A., Caetano, E., Magalhães, F., "Evaluation of dynamic effects and fatigue assessment of a metallic railway bridge", Structure and Infrastructure Engineering 6, pp.635-646, 2009.

[13] Righiniotis, T.D., Chryssanthopoulos, M.K., "Fatigue and fracture simulation of welded bridge details through a bi-linear crack growth law", Structural Safety 26, pp. 141-158, 2004.

[14] Imam, B.M., Righiniotis, T.D., Chryssanthopoulos, M.K.," Numerical modelling of riveted railway bridge connections for fatigue evaluation", Engineering Structures 29, pp. 3071-3081, 2007.

[15] Righiniotis, T.D., Imam, B.M., Chryssanthopoulos, M.K., "Fatigue analysis of riveted railway bridge connections using the theory of critical distances", Engineering Structures 30, pp.2707-2715, 2008.

[16] Radaj, D., Sonsino, C.M., Fricke, W., "Recent developments in local concepts of fatigue assessment of welded joints", International Journal of Fatigue 31, pp.2-11, 2009.

[17] Chan, T.H.T., Guo, L., Li, Z.X., "Finite element modelling for fatigue stress analysis of large suspension bridges, Journal of Sound and Vibration", 261, pp.443-464, 2003.

[18] Li, Z.X., Zhou, T.Q., Chan, T.H.T., Yu, Y., "Multi-scale numerical analysis on dynamic response and local damage in long-span bridges", Engineering Structures 29, pp. 1507-1524, 2007.

[19] Albuquerque, C., de Castro, P.M.S.T., Calçada, R., "Efficient crack analysis of dynamically loaded structures using a modal superposition of stress intensity factors", Engineering Fracture Mechanics 93, pp.75-91, 2012.

[20] Albuquerque, C., Calçada, R., de Castro, P.M.S.T., "Fatigue assessment of a bowstring railway bridge", P.B.H.V. Topping (Ed.) CST 2012, Civil-Comp Press, Dubrovnik, Croatia, 2012.

[21] Clough, R., W., Penzien, J., "Dynamics of structures", McGraw-Hill, 1975.

[22] Albuquerque, C., da Silva, A.L.L., de Jesus, A.M.P., Calçada, R., "An Efficient Methodology for Fatigue Damage Assessment of Bridge Details Using Modal Superposition of Stress Intensity Factors", International Journal of Fatigue, 2014.

[23] Broek, D., "Elementary engineering fracture mechanics", 4th rev. ed., Martinus Nijhoff Publishers, Dordrecht, 1987.

[24] Tada, H., Paris, P.C., Irwin, G.R,. "The stress analysis of cracks handbook", 3rd ed ed., ASME Press Professional Engineering Publishing, New York, 2000.

[25] Paris, P.C., Gomez, M.P., Anderson, W.E., "A Rational Theory of Fatigue", The Trend in Engineering 13, pp.9-14, 1961.

[26] Tanaka, K., "Fatigue crack propagation from a crack inclined to the cyclic tensile axis", Engineering Fracture Mechanics 6, pp.493-507, 1974.

[27] Matsuishi, M., Endo, T., "Fatigue of metals subjected to varying stress", Japan Society of Mechanical Engineers, 1968.

[28] Erdogan, F., Sih, G.C., "On the Crack Extension in Plates Under Plane Loading and Transverse Shear", Journal of Fluids Engineering 85, pp.519-525, 1963.

[29] I. Fracture Analysis Consultants, Franc3D Reference Manual, in, New York, 2011.

[30] Krueger, R., "The Virtual Crack Closure Technique: History, Approach and Applications", NASA, Hampton, Virginia, USA, 2002.

[31] Rice, J.R., "A Path Independent Integral and the Approximate Analysis of Strain Concentration by Notches and Cracks", Journal of Applied Mechanics 35, pp.379-386, 1968.

[32] I. Advanced Analysis Techniques Guide, in: Release 12.0 Documentation for ANSYS, ANSYS, Inc., 2009.

[33] Albuquerque, C., "Advanced methodologies for the assessment of the fatigue behaviour of railway bridges", ongoing.

[34] Lippi, F., Salvatore, W., Braconi, A., Finetto, M., Wenzel, H., De Roeck, G., Peeters, B., Könke C., Zabel, V., Cunha, A.,"Fatigue damage control and assessment for railway bridge", Research Fund for Coal and Steel, Directorate-General for Research and Innovation, 2009-2012.

[35] SAS, ANSYS, Version 12.0, Swanson Analysis Systems Inc., Houston, 2010.

[36] Albuquerque, C.M.C., Pinto, N.M.P., Calçada, R.A.B., Gabriel, J., "Experimental characterization of the dynamic behaviour of the new railway bridge over the river Sado", U.o. L'Aquila, P.d. Milano (Eds.) EVACES 2011, University of L'Aquila, Politecnico di Milano, Varenna, Italy, 2011.

[37] Albuquerque, C.M.C., Miranda, R.M.C., Richter-Trummer, V., Figueiredo, M.A.V.d, Calçada, R., "Fatigue crack propagation behaviour in thick steel weldments", International Journal of Structural Integrity, 2012.

[38] Carvalho, D., da Silva, A.L.L., Jesus, A.M.P., Fernandes, A.A., "Fatigue Behaviour of Structural Steels. Comparison of Strain-Life And Fatigue Crack Propagation Data", in: 9º Congresso Nacional de Mecânica Experimental, Aveiro, Portugal, 2014.

[39] da Silva, A.L.L., Jesus, A.M.P., Fernandes, A.A., Figueiredo, M., Calçada, R., "Análise do comportamento à fadiga de ligações soldadas com base no conceito das tensões estruturais", 3º Congresso Nacional sobre Segurança e Conservação de Pontes - ASCP'2013, Porto, 2013.

Chapter IX

Final conclusions and future works

9.1. OVERVIEW OF MAIN CONCLUSIONS

Fatigue is a cause of progressive damage of bridges, particularly of steel and composite steel/concrete railway bridges [1-4]. The increasing number of numerical and experimental fatigue damage assessments being performed on railway bridges [5-12] is a clear indication of the relevance of this topic in structural engineering. A number of projects covering this topic have been performed in the last years. This was the case of the FADLESS European project, entitled *Fatigue Damage Control and Assessment for Railways Bridges* [13], which was the background for the research performed within this PhD work. The referred European project aimed the development of methodologies for the fatigue assessment of critical details, to be demonstrated for several European railway bridges, selected as case studies. Regarding the Portuguese case studies, two railway bridges were selected, namely the Trezói Railway Bridge and the new Alcácer do Sal Railway Bridge.

The presented dissertation presented contributions towards the development of advanced methodologies to be applied in the fatigue assessment of structural details from metallic bridges, including welded and riveted joints. Local models for the fatigue analysis were preferably followed in the proposed research, in alternative to traditional global S-N approaches. Strategies were proposed to overcome the difficulties introduced by the multi-scale problem that this kind of local fatigue models introduces. In the following paragraphs, the main conclusions of the performed work are presented, following the chapters structure of the thesis.

Chapter II presented an overview of important works in the field of experimental fatigue testing and numerical simulation of bridge details. Both fields need further developments, but the field of numerical simulation of bridge details (riveted and welded) seems to be the one that needs substantial work in order to provide reliable alternative tools to the conventional blind and over conservative S-N approaches.

A fatigue characterization of two structural mild steels, the S235 and S355 steel grades, was presented in Chapter III. These materials are common options for bridge construction. The investigated materials were extracted from welded and riveted joints that were fatigue tested in the Chapter IV. Fatigue tests using smooth specimens were performed on these steels since this data is important to assess fatigue crack initiation on structural components. Additionally, fatigue crack propagation tests were performed in order to measure fatigue crack propagation rates that were used to model the fatigue crack propagation in structural components. Besides the pure mode I fatigue crack propagation tests, mixed mode fatigue crack propagation tests were also considered for the S235 steel. Digital Image Correlation technique was used to measure the fatigue crack path and to compute stress intensity factors directly from field information. The following set of conclusions can be formulated:

i) The two investigated steels show similar cyclic elastoplastic and fatigue properties.

ii) Both investigated materials were compared to the S690 high strength structural steel. Clear distinct behaviours between both steel categories were observed.

iii) Mild steels showed lower fatigue crack propagation rates than the high strength steel and the stress ratio effects were more relevant for the high strength steel than for the mild steels.

iv) The thickness effect on fatigue crack propagation was investigated for the S355 steel grade. Similar fatigue crack growth rates were observed, when tested thicknesses range from 4 to 30 mm.

v) Pure mode I and mixed mode (mode I + mode II) fatigue tests were performed for the S235 steel. A two-step methodology to compute stress intensity factors using the displacements fields from DIC data was proposed. The approach allowed the assessment of the fatigue crack paths and the stress intensity factors. Further algorithm developments may be required to reduce scatter in the experimental data.

vi) Mixed-mode fatigue crack propagation data was satisfactorily correlated with pure mode I fatigue crack propagation data using the effective stress intensity factor range as proposed by Tanaka for the S235 steel.

Chapter IV presented the results of an experimental campaign performed on riveted and welded connections. Each type of connections was motivated by distinct bridge construction aiming different purposes. Three distinct riveted geometries (R1, R2 and R3) were fatigue tested in order to validate S-N curves for riveted joints (EC_3 [14] and Taras/Greiner [15]). The following conclusions concerning the riveted specimens testing were formulated:

i) The experimental results of the R1 riveted specimens showed two distinct failure modes: some specimens collapsed due to a fatigue crack growing from the rivet hole and other specimens collapsed due to a fatigue crack propagating at angle corner. In the first case, mixed-mode fatigue crack propagation was likely to occur; in the second failure mode, a pure mode I fatigue crack propagation was observed. The failure modes for the R2 and R3 riveted specimens was characterized by a fatigue crack starting at the first rivet hole, perpendicularly to the loading direction.

ii) The R1 and R3 riveted series exhibited S-N slopes that are relatively closer to the EC_3 class 71 S-N curve. The R2 series, due to their small net section, exhibits a dominant crack initiation fatigue process. The analysis of the S-N data generated in this study in conjunction with the S-N fatigue data gathered by Taras and Greiner for riveted joints of the same category showed that the Taras and Greiner design S-N curve is more consistent than the EC_3 S-N curve. The slope of the S-N curve, m=5, seems more appropriate to describe the global trend of the fatigue data.

Regarding the welded joints, the experimental campaign was planned in order to allow the assessment of a deviation, with respect to the EC_3 recommendations, of a local geometric feature of a welded detail of the Alcácer do Sal bridge. In addition, the welded plate thickness effect was also investigated. Two main conclusions were derived concerning the welded joints testing:

i) The experimental results showed that the fatigue strength at 2e6 cycles decreases approximately 10% due to the use of a non-standardized geometric weld feature.

ii) Concerning the thickness effect, no significant influence of this parameter on the S-N curves was verified, for the range of investigated thicknesses.

Chapter V tested a methodology to compute structural stresses in welded joints using finite element analysis, which is claimed as mesh size insensitive. Two approaches for the structural stresses computation were investigated, namely the through thickness stress distribution integration and using nodal forces from the finite elements models, the latter being known as Dong's approach [16]. Three verification examples were proposed to investigate the robustness of the methodologies. It was observed the mesh insensitivity for 2D and 3D problems. . Two approaches for the structural stresses computation were investigated, namely the through thickness stress distribution integration and using nodal forces from the finite elements models, the latter being known as Dong's approach [16]. The structural stress methodology proposed by Dong was also applied to the welded specimens presented in Chapter IV and was demonstrated its compatibility with a master S-N curve concept. Fatigue data from various literature sources was correlated. It was observed that the Master S-N curve concept did collapse all fatigue tested data into one S-N curve.

Numerical S-N curves for all experimental specimens presented on Chapter IV were modelled in Chapter VI. For the welded specimens, a fatigue model based exclusively on the fatigue crack propagation phase produced very consistent results. In the simulation of the riveted specimens, both crack initiation and crack propagation phases were considered since for non-welded material fatigue crack initiation could represent an important contribution to the total fatigue life. The local strain approach and the Fracture Mechanics-based Paris propagation law were used for both fatigue crack initiation and fatigue crack propagation simulations. Concerning the welded specimens, the required stress intensity factors for fatigue crack propagation simulation were computed based on two alternative techniques. A standard finite element method was considered with the VCCT technique. However, this could represent a cumbersome approach to apply in 3D problems with complex geometries, once the crack path must be compatible with the finite element mesh. An alternative method to compute the stress intensity factors, using the extended finite element method, was adopted. The predicted fatigue S-N curves were very consistent with available experimental data, which validates both proposed fatigue model as well as the techniques for stress intensity factors computation. Concerning the simulation of the riveted specimens, the XFEM method was only applied to the R1 series with a crack propagating at the corner

angle. Contact elements were not used in this case, and resulted in better total fatigue life predictions than using contact elements between the connection parts. The use of contact finite elements required the definition of the friction coefficient and clamping stresses on rivets which are usually an unknown, calibration procedures being required. The use of the same clamping stresses and friction coefficients resulted in distinct simulation results. The use of a clamping stress of 30MPa in the R1 series conducted to an overestimation of the fatigue lives (unsafe predictions). For the R2 tested series it was demonstrated that the clamping stress of 30MPa led to an underestimation of the fatigue lives. The increase in the clamping stresses to 80MPa reduced the discrepancy in the simulations, but the deviations still observed suggested even higher clamping stresses for the R2 series. Finally, for the R3 series the predictions were very accurate and the clamping stress variation between 30 and 80MPa did not resulted in significant change in the predicted results. This overview of the predictions suggests that the clamping stresses were not uniform in the manufacturing of the riveted series. This chapter also assessed the performances of the FEM plus VCCT and XFEM plus Interaction Integral approaches in the computation of stress intensity factors for some simple verification examples. The following conclusions were drawn:

i) Concerning the XFEM plus Interaction Integral approach it was verified that several contours should be considered, but the first contour closest to the crack tip should be avoided, otherwise spurious results will be obtained.

ii) Also it was verified that when a XFEM crack appears close the finite element boundaries it may cause some instability in the results.

iii) The simulation of very small cracks may also constitute a difficulty for the XFEM approach since it would require refined meshes in order to allow reliable information at the contours established around the crack tip.

iv) Concerning the mesh convergence studies, it was demonstrated that progressive mesh refinements did not produced monotonic convergence of the computed stress intensities.

In Chapter VII a numerical strategy for the fatigue analysis of riveted details from bridges was proposed and illustrated for a node of the Trezói Bridge. The proposed strategy mitigates the very high computational costs that a local fatigue analysis of real complex details may demand. The application of local approaches to fatigue in real

bridge details leads to a multi-scale problem that, taking into account the state-of-the art computational resources, cannot be solved with a unique model that encompasses both scales. The following specific conclusions were obtained:

i) The used of full continuous models to simulate the fatigue behaviour of riveted details leads to distinct failure locations of the ones obtained using riveted models with contact finite elements. In the latter case, the rivet holes revealed as the most critical locations.

ii) The analysis of the stress histories for a real traffic stress history revealed that the stress states are multiaxial and the stress histories are non-proportional at the nodes of the local model. Therefore, it is recommended the use of non-proportional multiaxial fatigue approaches such as the critical plane approaches. This represents a difficulty for 3D problems, which is the case of the complex bridge details, since the number of planes to be search is very high.

iii) In order to mitigate the increased computational costs resulting from an application of fatigue critical plane approaches to complex structural details, a preliminary fatigue assessment based on Von Mises stresses is proposed to identify the most critical locations at the local model, for further analysis using the more accurate damage models. The Von Mises stress fatigue approach revealed more conservative than critical plane approaches.

iv) The fatigue analysis performed to the Trezói node revealed negligible damage levels for the selected train. Inspections on the bridge did not detect visible fatigue cracks; therefore the analysis is coherent with the observations. Nevertheless without visible damage the aptitude of the proposed approach to simulate crack initiation in real bridge details needs further validation. However the proposed methodology is itself a valuable contribution.

Chapter VIII presented an innovative efficient method for the fatigue assessment of railway bridges. This method was demonstrated thru an application to the new Álcacer do Sal railway bridge. The simulation of fatigue crack propagation in critical details can be achieved using minimal/optimized computational resources. Shell-to-solid submodelling proves to be an effective way to address multiple-scale structural

problems, such as localized fatigue crack propagation in large structures. Also, modal superposition of stress intensity factors confirms to be an adequate and efficient method when multiple and complex load histories are considered, such as multiple traffic events on bridges. For the current case study and selected detail, the assumption of mixed mode fatigue crack propagation impacted on fatigue crack propagation path. An important outcome of the proposed methodology is the quick response and assessment of different traffic scenarios, e.g. the consideration of an increase of annual traffic volume over time. Finally, it should be underlined that the simulation can be optimized, by the implementation of parallel computing, further increasing the computational efficiency.

9.2. FUTURE WORKS

Despite the extensive investigation performed in the last years, many aspects of the conducted research deserve to be continued and further developed in the future in order the progresses made in this work to understand and simulate the fatigue behaviour of bridge structural details could accomplish a matured plateau in order to gain the confidence of both bridge engineers and railway authorities.

One important aspect is related to the fatigue crack propagation under mixed-mode loading conditions. Due to the complex stress fields and loading histories, it is clear that cracks in bridge components will very likely propagate under mixed-mode conditions. Therefore the experimental work performed in this thesis covering mixed-mode fatigue crack propagation for one structural steel, needs to be extended to more representative structural steels and also to other mixicity ratios. To accomplish the last subject, distinct testing procedures needs to be pondered, such as the Arcan testing procedure. Also, further work will be necessary to develop the DIC technique that was used in this thesis in order to reduce the scatter found in the crack growth results.

Also, it is proposed in future fatigue tests of structural details to use systematically the DIC procedure. With this technique one may compute the stress intensity factors

directly from the displacement fields. The idea is to replicate the procedures used in Chapter III using simple specimen geometries, to more complex details.

Also the clarification that fatigue behaviour of bridge details is in general a multiaxial non-proportional problem, future experimental works should be focused on these aspects. Non-proportional multiaxial loading should be preferably used to test those details.

Since it was not possible to perform a multiaxial experimental fatigue characterization of the structural streels, it is proposed for future tasks specific tests covering multiaxial proportional and non-multiaxial loading conditions is order to understand what kind of models are more suitable for these materials. Also, random loading histories should be considered in order to derive significant data for validation/development of cycle counting techniques as well as damage models.

Concerning the numerical simulations, the XFEM approach needs to be further explored in order to make it possible for riveted joints, which involves the contact non-linearity. Concerning the modal superposition technique is could be extended to crack initiation simulation.

9.3. REFERENCES

[1] Kühn, B., Lukić, M., Nussbaumer, A., Günther, H.P., Helmerich, R., Herion, S., Kolstein, M.H., Walbridge, S., Androic, B., Dijkstra, O., Bucak, Ö., "Assessment of Existing Steel Structures: Recommendations for Estimation of Remaining Fatigue Life", in: G. Sedlacek, F. Bijlaard, M. Géradin, A. Pinto, S. Dimova (Eds.) JRC Scientific and Technical Reports, European Commission, Joint Research Centre, 2008.

[2] Haghani, R., Al-Emrani, M., Heshmati, M., "Fatigue-Prone Details in Steel Bridges", Buildings 2, pp.456-476, 2012.

[3] Miki, C., "Retrofitting Engineering for Fatigue Damaged Steel Structures", International Institute of Welding, pp. 70, 2010.

[4] J. Fisher, W., Roy, S., "Fatigue of steel bridge infrastructure", Structure and Infrastructure Engineering 7, pp.457-475, 2010.

[5] Zhou, H., Liu, K., Shi, G., Wang, Y.Q., Shi, Y.J., De Roeck, G., "Fatigue assessment of a composite railway bridge for high speed trains. Part I: Modeling and fatigue critical details", Journal of Constructional Steel Research 82, pp.234-245, 2013.

[6] Guo, T., Chen, Y.W., "Fatigue reliability analysis of steel bridge details based on field-monitored data and linear elastic fracture mechanics", Structure and Infrastructure Engineering 9, pp.496-505, 2013.

[7] Cremona, C., Eichler, B., Johansson, B., Larsson, T., "Improved Assessment Methods for Static and Fatigue Resistance of Old Metallic Railway Bridges", Journal of Bridge Engineering 18, pp.1164-1173, 2013.

[8] Vincenzi, L., Savoia, M., Salvatore, W., "Experimental modal analysis and fatigue assessment on the Lagoscuro viaduct", Crc Press-Taylor & Francis Group, Boca Raton, 2012.

[9] Lippi, F.V., Orlando, M., Salvatore, W., "Assessment of the dynamic and fatigue behaviour of the Panaro railway steel bridge", Structure and Infrastructure Engineering 9, pp.834-848, 2011.

[10] Caglayan, B.O., Ozakgul, K., Tezer, O., "Fatigue life evaluation of a through-girder steel railway bridge", Engineering Failure Analysis 16, pp. 765-774, 2009.

[11] Zhou, Y., "Assessment of Bridge Remaining Fatigue Life through Field Strain Measurement", Journal of Bridge Engineering 11, pp.737-744, 2006.

[12] Marques, F., Cunha, Á., Fernandes, A.A., Caetano, E., Magalhães, F., "Evaluation of dynamic effects and fatigue assessment of a metallic railway bridge", Structure and Infrastructure Engineering 6, pp.635-646, 2009.

[13] Lippi, F., Salvatore, W., Braconi, A., Finetto, M., Wenzel, H., De Roeck, G., Peeters, B., Könke C., Zabel, V., Cunha, A.,"Fatigue damage control and assessment for railway bridge", Research Fund for Coal and Steel, Directorate-General for Research and Innovation, 2009-2012

[14] Eurocode 3: Design of steel structures, Part 1-9: Fatigue, CEN: Brussels, Belgium,2004.

[15] Taras, A., Greiner, R., "Development and Application of a Fatigue Class Catalogue for Riveted Bridge Components", Institute for Steel Structure and Shell Structure, Graz, August 2009.

[16] Dong, P., "A Structural Stress Definition and Numerical Implementation for Fatigue Analysis of Welded Joints", International Journal of Fatigue,23, pp.865-876, 2001.